

THIS WEEK

EDITORIALS

EXOPLANETS The past, present and future of the hunt for extraterrestrials **p.272**

WORLD VIEW Global statistics need a new worldwide watchdog **p.273**



DEEP STORAGE Frozen turtles hibernate but stay sharp **p.274**

The maze of impact metrics

In deciding how to judge the impact of research, evaluators must take into account the effects of emphasizing particular measures — and be open about their methods.

So much science, so little time. Amid an ever-increasing mountain of research articles, data sets and other output, hard-pressed research funders and employers need shortcuts to identify and reward the work that matters. They have plenty of options: research impact is now recognized as a multidimensional affair.

The conventional measures of scholarly importance — citation metrics, publication in influential journals and the opinion of peers as expressed in letters and interviews — still loom large. But to those are now added metrics such as article downloads and views, and measures of importance beyond the academic realm, including influence on policy-makers or health and environment officials, effects on industry and the economy, and public outreach.

Researchers at the Center for the Study of Interdisciplinarity, part of the University of North Texas in Dalton, this year came up with 56 measures of impact (see *Nature* 497, 439; 2013), including influence on curriculum creation, authorship of textbooks and success in surveys of colleagues' esteem. Some of these measures are a little fanciful, but they demonstrate that it has never been easier for scientists to show off the various ways in which their work deserves attention — and funds.

That variety is worth celebrating, but it can lead to dizzying confusion. How are researchers and evaluators to choose between measures? In this issue, *Nature* looks at some traditional and emerging ways to track research quality (see page 287). Ultimately, it is for institutions and funders to choose their preferences, but in doing so they should take two important considerations into account.

First, it is important to be aware of the positive and negative effects of privileging certain measures.

For example, emphasizing that research is considered especially important if it is published in one of a few historically influential journals — *Cell*, *Nature*, *Science* — could be a laudable attempt to get scientists to think ambitiously about their research goals. But it can also result in excessive pressure to publish big claims, leading to problems of irreproducibility, for example. (*Nature's* position is that it has been publishing research using essentially the same criteria for decades; it is up to the scientific community and evaluators to decide how much importance they want to place on papers that appear in the journal).

It is a mistake to consider a research paper important because it is published in a journal with a good citation record, as measured by its impact factor. As this publication has highlighted many times (see in particular *Nature* 435, 1003–1004; 2005), two articles in the same journal may have very different citation records. It is much better to focus on the citations, views or downloads of an individual article — and to recognize that these metrics vary between research disciplines.

In another example, emphasizing the economic impacts of research may force scientists to think about justifying their taxpayer-funded work, but it also runs the risk of distracting them with the lure of meaningless patents and ill-considered spin-out companies.

The second important consideration is the need for research evaluators to be explicit about the methods they use to measure impact. Openness is an essential part of earning trust. Evaluators should publish worked examples showing how they score assessments, and the reasoning behind such scores; even better would be, where possible, to publish the full data. Otherwise, researchers might rightfully feel suspicious (see, for example, writer Colin Macilwain's scepticism towards performance metrics: *Nature* 500, 255; 2013).

"It has never been easier for scientists to show off the various ways in which their work deserves attention — and funds."

When scientists rail against the 'impact agenda', their arguments sometimes founder on irrelevant confusion between terms: too often, such discussion devolves into attacks on misuse of the impact factor, rather than looking at the range of possible metrics. The journal citation measure gains misleading prominence because its name happens to include the word impact — a semantic synergy that can cloud debate.

Arguments against impact metrics are strongest when they reference cases in which evaluators do not heed the considerations we mention above: in which evaluators choose metrics blindly, without sufficient thought for pernicious effects, or are secretive or inconsistent about their methodologies. If evaluators are to earn the acceptance — rather than the scorn — of the scientists whose work they want to fund, they had better pay attention to these concerns. ■

High hopes

Care must be taken not to raise unrealistic expectations for RTS,S malaria vaccine.

Vaccines have been an unparalleled public-health success: they have eradicated smallpox and driven polio to near extinction, and routine childhood immunization saves millions of children a year from death from diseases such as measles, diphtheria, tetanus and whooping cough. So it is not surprising that the public tend to view vaccines as synonymous with elimination, or near elimination, of our microbial foes.

This may help to explain last week's extensive and often upbeat media coverage of the 18-month results of a huge phase III trial of the malaria vaccine candidate RTS,S/AS01 in more than 15,000 children across 7 African countries. In the United Kingdom, for example, the front page of *The Guardian* stated that the vaccine "could save lives of millions of

children". Unfortunately, however, it won't. The 18-month results only confirm the disappointing results seen after 12 months.

The RTS,S vaccine is not what most people would think of as a vaccine. It provides only partial protection and most of those vaccinated, particularly those in areas with moderate to high malaria transmission rates, will eventually contract the disease. There is also confusion over its efficacy. Many media reports concluded that although the vaccine did not give the 90%-plus efficacy levels of most childhood vaccines, it might nonetheless be satisfactory, with a reported 46% reduction in cases in children vaccinated when they were aged 5 to 17 months, and 27% in 6–12-week-old babies.

Not so. The efficacy figures given for RTS,S are not directly comparable with those usually given for vaccines. The conventional measurement of a vaccine's success is how many people remain protected after a given period, such as 12 months. Because RTS,S is only partially protective, a different measurement of efficacy is used — a complex statistical model that computes hazard ratios on the basis of the first clinical episodes of malaria. As the designers of the method themselves concede, "a shortcoming of the vaccine efficacy calculated from hazard ratios could be that it is not intuitively understood". Too true. In the hands of experts, and regulatory agencies, this hazards-ratio model offers a valid measurement of the efficacy of a partially protective vaccine, but it can be easily misinterpreted by the media, politicians and policy-makers.

It is not possible for outside scientists to deduce a more conventional efficacy estimate from the 18-month data, as it was described only briefly in press releases from the vaccine's sponsors, the PATH Malaria Vaccine Initiative (MVI) based in Seattle, Washington, and GlaxoSmithKline (GSK), headquartered in Brentford, UK. (The paper and supporting data are under review at a journal.) But applying a conventional measurement of vaccine success to the published figures for 12-month estimates — for which detailed data are available — reduces the vaccine's efficacy by more than one-third (see *Nature* 478, 439–440; 2011). Its protective effect also seems to begin fading after about six months.

Perhaps more promising are the reductions seen in cases of severe malaria, which are reported in the conventional manner. However, although a 36% reduction was reported in children of 5–17 months, the 15% reduction seen in 6–12-week-old babies was not significant — and this age group was the main target of the trial because for logistical reasons it is likely that any malaria vaccine would need to be given alongside routine immunizations at this age.

"The vaccine falls short of the target set by the World Health Organization."

Many vaccine trial participants had access to other anti-malarial measures — including insecticide-treated bednets and effective drug treatment — so it is possible that the vaccine might offer greater benefit to people more exposed to malaria. Nonetheless, the vaccine falls short of the target for a partially protective malaria vaccine set in 2006 by the World Health Organization, which stated that it should have a "protective efficacy of more than 50% against severe disease and death" that "lasts longer than one year".

The work will continue. Data on the effects of a booster dose given after 18 months will not be available until next year, and RTS,S is also due to be tested in combination with a vaccine developed by researchers at the University of Oxford, UK, in an early-stage clinical trial. Meanwhile, the RTS,S trials are to be applauded for having left a lasting legacy in the unprecedented collaboration with African scientists who led the study, and a first-class clinical-trials infrastructure on the continent.

RTS,S has been in the works for almost 30 years. Since 2001, the MVI has put some US\$200 million into it, and GSK more than \$350 million, with a further \$260 million earmarked to complete its development. The huge past impact of vaccines risks fuelling illusions over the impact of having a malaria 'vaccine'. But the modest efficacy of RTS,S means that it falls squarely in competition with other malaria control measures, many of which might be more cost-effective. Care must be taken not to build excessive expectations that can only lead to disappointment over its potentially limited public-health impact. ■

Searching for life

A look into the past frames our attempts to find extraterrestrial intelligence.

Carl Sagan's 1993 *Nature* paper has, rather appropriately, a hint of science fiction about it. Twenty years ago this week, Sagan and a team of other astronomers announced that they had found life on a planet in the Galaxy. They used data from the Galileo space telescope to catch clear signatures of methane and carbon dioxide in the planet's atmosphere and abundant water in frozen and liquid states on its surface. They even confirmed the presence of radio emissions emanating from it — the canonical autograph of intelligence.

This month's *Nature* PastCast — one of a series of special audio treats available for free on the *Nature* website — recounts the tale. The twist, of course, was that this planet was Earth. Sagan and his team were trying out a method for finding life on other planets, using Earth as a calibration for future missions that might explore the depths of the Galaxy for signs of life.

Those were not friendly times for thinking about life elsewhere. At the time, the US Congress was debating whether to cut federal funding for NASA's SETI programme, the search for extraterrestrial intelligence. So Sagan and his team set about their task in as objective a way as they could, notwithstanding their foregone conclusion. They were careful to declare that "life is the hypothesis of last resort", and to show that this was a scientific question that needed an answer.

The bigger question, of course, goes unanswered, although not for want of trying. SETI was launched in the late 1950s, propelled

by the optimism of the space age. In 1959, a paper in *Nature* by Giuseppe Cocconi and Philip Morrison suggested that if civilizations elsewhere wanted to contact Earthlings, they would probably use electromagnetic signals. "We shall assume that long ago they established a channel of communication that would one day become known to us, and that they look forward patiently to the answering signals from the Sun which would make known to them that a new society has entered the community of intelligence," they wrote.

Soon after, astronomer Frank Drake was preparing for one of the first conferences to address the search for extraterrestrial life. As a loose agenda, he came up with a list of unknowns that would need to be resolved in order to predict whether intelligent life exists elsewhere in the Universe. For example, how many star systems exist that are suitable for the development of intelligent life? How many Earth-like planets are in orbit around them? What is the probability of life sparking into existence on any of them? Drake then formulated an equation that created a mathematical framework for such unknowns.

Research ongoing since Sagan's paper is making Drake's equation more solvable today than it has ever been. The control test was performed, so astronomers know that their tests for life would work. Meanwhile, the first exoplanet was found in 1992, and hundreds have been spotted since.

Scientists can use variants of Sagan's prescient control test to characterize the atmospheres and locations of exoplanets whizzing around their stars. Are we now in an era not of space-age optimism, but of realism? Life is still the hypothesis of last resort for astrobiologists. But if they find none, they will not be disillusioned. It would be just as interesting, they say, to find that habitable-looking environments do not all sprout life, and that Earth is unique in being so full of it. ■

➔ **NATURE.COM**
To comment online,
click on Editorials at:
go.nature.com/xhbnqy



Time for global statistics we can count on

Public policy is too often derailed by assessments based on faulty data, says Martin Rees, as he calls for the formation of an international data watchdog.

Science has become pervasive in public policy, and all of us who are active in this arena are aware of the intense scrutiny that scientific evidence rightly receives. Yet much of the data that shape and underpin crucial areas of public policy, such as improving health and reducing poverty, are substandard.

A report published this week makes a key recommendation to address this gap in data quality: the establishment of a new international agency, Worldstat. Worldstat would carry out quality control on global statistics. It would assess and improve data-collection practices and monitor for the misuse of statistics. Its role is crucial: unless all countries gather and publish reliable and comparable data on topics such as disease, income and employment, then international comparisons of economic growth, health, life expectancies and so forth cannot be relied on. Nor can such data form a firm basis for action by governments or international agencies.

This proposal is part of a wider set of recommendations that have emerged from a year-long process by the Oxford Martin Commission for Future Generations, in which I have participated as a member. It is chaired by Pascal Lamy, former director-general of the World Trade Organization. The commission's 19 members, who hail from many nations and have diverse political and professional backgrounds, collectively have broad experience and expertise. But what brought them all to the table was a shared concern that a prosperous, equitable and sustainable global future is in jeopardy because modern politics and businesses have become too preoccupied with short-term pressures at the expense of long-term needs.

The result of our work is the publication of 'Now for the Long Term', a report that proposes a set of principles aimed at overcoming deep political and cultural barriers that obstruct a longer-term vision (see www.oxfordmartin.ox.ac.uk/commission). It provides practical recommendations for action to deliver progress on climate change, reduce economic inequality, improve corporate practices and address the chronic burden of disease.

Data vary so much across the world that in many fields it is almost impossible to generate reliable comparisons. Often, the information is simply not there. The paucity of economic data on key indices — such as average income in poor countries, particularly in Africa — makes it difficult to assess the true level of inequality and its drivers. Even in the United Kingdom there is concern about proposals to scrap the decadal census in its conventional form; whatever changes are made after the current consultation period must not compromise the collection of key data or the ability to monitor long-term trends.

Unreliable or missing data block good governance. One cannot properly assess the effectiveness

of governments and international organizations unless there are reliable performance indicators. Such indicators help to reduce corruption and waste. There are currently serious weaknesses in data quality in areas as diverse as health spending, mortality rates, gender representation and biodiversity; assessments of success and failure in public policy are often based on distorted or subjective perceptions. As a result, indicators should come with a 'health warning' to emphasize their limitations.

Worldstat would not be a substitute for existing institutions such as the United Nations Statistical Commission or the UN Statistics Division (both within the UN Economic and Social Council). Instead, it would complement existing work by focusing on implementing agreed standards and improving the capabilities for archiving and interpreting data, particularly in the developing world. As a separate entity with a budget and resources on a scale comparable with Eurostat, World-

stat could also fast-track international efforts to adopt appropriate and robust indicators for sustainable development and direct attention to capacity building on this front. This week's report highlights, in particular, the need to devise a 'long-term impact index' that could comprehensively measure a country's long-term progress on a much broader range of indicators than the standard measure, gross domestic product.

The report also includes recommendations for corporate reform, such as a voluntary taxation and regulatory exchange, to address tax abuse and avoidance and to harmonize company taxation arrangements. It also offers specific proposals for dealing with youth unemployment and poverty

by removing price-distorting subsidies and investing in social protection measures, such as conditional cash-transfer programmes.

The commission's work allowed us to identify the need for Worldstat, and the next step is to work with existing organizations to decide how the agency could be funded and organized, and to which bodies it would be accountable. Yet we are mindful that it is all too easy to propose new international agencies, and that few twentieth-century agencies have closed down, even though some are now anachronistic. To counter such proliferation, we suggest the introduction of 'sunset clauses' that require regular reviews of accomplishments to ensure that publicly funded international institutions are fit for twenty-first-century purposes.

Science and engineering can enhance lives in the developing world and safeguard the welfare of future generations. But there is a dismaying gap between what should be done and what actually happens. 'Now for the Long Term' presents a practical agenda that is designed to help overcome the gap between knowledge and action. ■

*Martin Rees is a former president of the Royal Society and a fellow of Trinity College, University of Cambridge, UK.
e-mail: mjr36@cam.ac.uk*

THERE ARE
CURRENTLY
**SERIOUS
WEAKNESSES**
IN DATA
QUALITY.

➔ **NATURE.COM**
Discuss this article
online at:
go.nature.com/mreewb

RESEARCH HIGHLIGHTS

Selections from the
scientific literature

CANCER

Immune-cell block halts brain tumour

A drug that targets the white blood cells fostering brain tumours — rather than the cancer cells themselves — shrinks tumours in mice.

The aggressive brain cancer known as glioblastoma is notoriously difficult to treat. Johanna Joyce at the Memorial Sloan-Kettering Cancer Center in New York and her colleagues gave mice with glioblastomas a drug that inhibits a cell-surface protein called colony-stimulating factor-1 receptor. This protein is expressed mainly on the white blood cells, or macrophages, that surround the tumour.

The 22 mice that did not receive the drug all died within 8 weeks. By contrast, 64% of the mice given the drug were still alive after 26 weeks. Surprisingly, the drug did not kill the macrophages but instead altered their gene expression, presumably turning off tumour-promoting functions.

Nature Med. 19, 1264–1272 (2013)

ZOOLOGY

Shining light on cold turtles

Freshwater turtles can survive the winter at the bottom of frozen lakes despite a complete lack of oxygen. But they do not, as some have suggested, fall into a coma when hibernating, according to Jesper Madsen of Aarhus University in Denmark and his colleagues.

Madsen and his team submerged *Trachemys scripta* turtles (pictured) in cold, oxygen-depleted water to put them into false hibernation. The animals still responded

to light and increased temperatures, but not to vibrations or increased oxygen levels. The results suggest that hibernating turtles are in a low-energy but vigilant state.

The brains of chemically anaesthetized turtles also responded to light, indicating that these animals have adapted to remain responsive to this stimulus even when other body systems are shut down.

Biol. Lett. 9, 20130602 (2013)



ENVIRONMENTAL SCIENCE

Why bee colonies collapse

Environmental stresses can cause bee colonies to fail — even if the stress levels are not high enough to kill individual insects.

Habitat decline, parasites and insecticides have all been blamed for bee colony collapses, but finding the individual causes of collapse has been problematic.

John Bryden of Royal Holloway University of London and his colleagues modelled stresses on bees and found that colonies began to decline when the number of functionally impaired

bees reaches a critical threshold. The model accurately predicted the fate of 16 experimental colonies of bumblebees (*Bombus terrestris*), of which half were exposed to a neonicotinoid pesticide at levels that do not kill bees but do reduce their ability to learn and gather food.

Multiple stresses can put colonies on a knife edge between growth and failure, the authors say, which makes it hard to pin declines on one factor. *Ecol. Lett.* <http://dx.doi.org/10.1111/ele.12188> (2013)

DRUG MANUFACTURING

From synthesis to pill without pause

A factory that produces a continuous stream of drug tablets from the raw ingredients could save time and money over traditional stop-start methods, which spread manufacture over many locations. Bernhard Trout and

his colleagues at the Massachusetts Institute of Technology

in Cambridge report the first example of such a plant, an 18-square-metre factory that produces the hypertension drug aliskiren (developed by Novartis, which funded the project).

Chemical building blocks flow in at one end, followed by a series of reactions and separations in which the drug is synthesized, crystallized, dried and coated to produce tablets at the other.

Angew. Chem. Int. Edn <http://dx.doi.org/10.1002/anie.201305429> (2013)

NIGEL E. RAINE

C. STEIMER/ARCO IMAGES/ROBERT HARDING PICTURE LIBRARY



NASA/CXC/MIT/F. K. BAGANOFF ET AL

ASTRONOMY

Reflections from a black hole

Sagittarius A*, the unusually dim supermassive black hole at the heart of the Milky Way (pictured), may have flared up at times during the past few centuries.

Observations from NASA's Chandra X-ray Observatory between 1999 and 2011 reveal bright patches of X-rays in molecular clouds in the centre of the Galaxy. The glow, which has been rippling outwards, could be reflected radiation that was emitted from the black hole long ago, and then bounced off nearby clouds.

Maica Clavel of the Paris Diderot University and her colleagues calculate that two sudden surges in the black hole's activity — one lasting no more than two years, and the other about a decade — could produce the observed reflections. Charting them may help to reveal what the black hole has been consuming. *Astron. Astrophys.* 558, A32 (2013)

CANCER

Two-faced cancer gene

A genetic variant that greatly boosts the risk of testicular cancer may protect light-skinned individuals from skin cancer by helping them to tan.

A team led by Douglas Bell at the US National Institutes of Health in Bethesda, Maryland, and Gareth Bond at the University of Oxford, UK, surveyed data from

genome-wide association studies (GWAS). They focused on polymorphisms in DNA binding sites for the tumour-suppressor protein p53. One variant, in a gene called *KITLG*, has one of the strongest effects of any pro-cancer variant identified by GWAS and was vastly more common in caucasians. In mice, the p53–*KITLG* interaction boosted the growth of pigment-producing cells after exposure to ultraviolet radiation, and so might protect against excessive sun damage and cancer. *Cell* 155, 410–422 (2013)

CLIMATE SCIENCE

Ozone hole fans African heat

Much of the summer warming in southern Africa over recent decades seems to have been due to the ozone hole over Antarctica.

Desmond Manatsa, of Bindura University of Science in Zimbabwe, and colleagues compared regional climates before and after ozone depletion set in around 1993. Pronounced surface warming strongly correlated with shifts in the strength and position of pressure systems in the atmosphere that enhance the southward flow of warm tropical air. These shifts are often attributed to ozone depletion in the upper atmosphere.

The expected closure of the ozone hole by 2050 may help to mitigate climate warming in southern Africa, the authors conclude.

Nature Geosci. <http://doi.org/n8x> (2013)
For a longer story on this research, see go.nature.com/ph2nyo

NEUROSCIENCE

How exercise boosts the brain

A protein molecule secreted by muscles during exercise boosts the expression of factors that help to protect brain neurons.

Endurance exercise is known to induce production

COMMUNITY CHOICE

The most viewed papers in science

SUSTAINABILITY

Steel mesh sucks in fog

HIGHLY READ
on pubs.acs.org
in September

One square metre of high-tech mesh could capture 12 litres of potable water a day from morning fog.

Fog-harvesters are used in countries such as Chile to collect drinking water. Tiny fog droplets in humid air blow through mesh filaments, where they coalesce into larger drops that roll into a collecting trough.

To boost the amount of water captured, Robert Cohen and Gareth McKinley at the Massachusetts Institute of Technology in Cambridge and their colleagues systematically modelled and tested surface chemistries, fibre thicknesses and geometrical configurations of woven mesh. They produced a mesh of thin steel strands coated with a fluorinated polymer. In laboratory tests simulating Chilean mountain fog, the mesh collected water at rates fivefold higher than conventional fog-catching meshes and came close to the theoretical limit calculated by the researchers.

Langmuir <http://doi.org/n7n> (2013)

of a protein called irisin and to improve cognitive performance in patients with some neurological conditions, but the mechanism linking these observations has been unclear.

A team led by Michael Greenberg and Bruce Spiegelman at Harvard Medical School in Boston, Massachusetts, observed that irisin levels increased in a brain area associated with learning and memory after mice ran on exercise wheels. When levels of irisin or its progenitor were raised experimentally in the blood and in neurons, genes associated with learning and memory became active in the brain.

Cell Metab. <http://doi.org/n8z> (2013)

water flows around pulsing or paralysed moon jellyfish (*Aurelia aurita*). The animal's bell-shaped body produces vortex rings of water as it pulsates.

As the bell flattens and expands, one of the rings rolls inside the bell and sucks in more water. That pushes the jellyfish forward without any extra force from the creature's muscles. This makes the simple predator one of the most energy-efficient swimmers on the planet, the authors say.

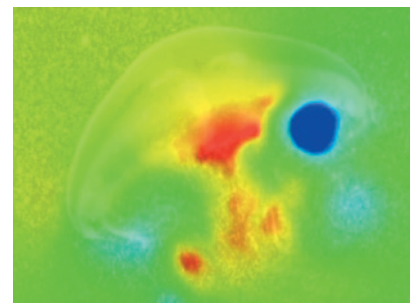
Proc. Natl Acad. Sci USA <http://doi.org/n7k> (2013)
For a longer story on this research, see go.nature.com/gbbmhv

BIOMECHANICS

Jellyfish wake makes power

When a jellyfish swims, its pulsing body gets an extra push from spinning water in its wake (pictured, red).

Brad Gemmell at the Marine Biological Laboratory in Woods Hole, Massachusetts, and his colleagues studied how



NATURE.COM

For the latest research published by Nature visit:
www.nature.com/latestresearch

BRAD GEMMELL

SEVEN DAYS

The news in brief

POLICY

US labs to close

The US Department of Energy is planning to temporarily close some of its national laboratories, as the ongoing US government shutdown prevents the agency from paying the contractors that run the labs. Los Alamos National Laboratory in New Mexico will close on 18 October, and the nearby Sandia National Laboratories in Albuquerque will close on 21 October. Other facilities, including Pacific Northwest National Laboratory in Richland, Washington, have funds to remain open until at least early November. See go.nature.com/eh1lbi for more.

Antarctic freeze

The US National Science Foundation is recalling staff and scientists from Antarctica as a result of the US government shutdown, it announced on 8 October. Almost all science at the three US bases will cease, and only a minimal crew will stay to maintain facilities. Depending on the length of the shutdown, which began on 1 October, the move could effectively end this year's fieldwork at McMurdo, Amundsen–Scott and Palmer stations. See go.nature.com/w48czc for more.

Mercury treaty

More than 90 countries signed a treaty to limit mercury use and pollution at a United Nations conference in Kumamoto, Japan, on 10 October. The Minamata Convention on Mercury seeks to curb emissions of the metal from power plants and other industrial facilities, and to limit its use in products from batteries and light bulbs to cosmetics and medical equipment (see go.nature.com/vqch6y). The treaty will enter into force once it has been

ratified by 50 countries, which is expected to take three to four years.

Stem-cell trial off

Italy's health minister put an end to a planned clinical trial of a controversial stem-cell therapy on 10 October, which the government had previously agreed to finance with €3 million (US\$4 million). In a stinging report, the scientific advisory committee appointed by the minister said that the clinical protocol proposed by the Brescia-based Stamina Foundation was inadequately described, lacked a scientific basis and was potentially dangerous. The therapy has divided Italian society for more than a year (see *Nature* 495, 418–419; 499, 125; 2013).

Fracking studies

The European Parliament proposed on 9 October to toughen regulations on the use of hydraulic fracturing for oil and gas exploration. The technique, also known as fracking, involves pumping a slurry of water, sand and chemicals underground to fracture shale formations and release hydrocarbons. Under the proposed rule, which was adopted by 332 votes to 311, companies seeking to exploit shale formations would first be required to conduct environmental-impact studies.

E-cigarette vote

On 8 October, the European Parliament voted to tighten regulations on tobacco products across the European Union (EU), but opted to

it made landfall, storm winds blew at up to 260 kilometres per hour: on a par with a 1999 cyclone that killed some 10,000 people in the region. Phailin weakened before it hit land; it caused hundreds of millions of dollars of damage, but, in contrast to the 1999 storm, only 27 deaths had been reported as *Nature* went to press.



BISSWARJAN ROUT/AP

Warnings save lives in Indian cyclone

India's strongest cyclone in 14 years tore up crops and blew away buildings, but caused fewer casualties than feared owing to advance evacuations of at least 1 million people. Cyclone Phailin hit northeastern India on 12 October, with satellite estimates from the US Joint Typhoon Warning Center suggesting that, before

scale back proposed rules for electronic cigarettes. The European Commission and the European Council, which represents the governments of the 28 EU member states, have pushed for regulation of e-cigarettes as medical devices. The parliament voted to treat them as tobacco products unless they are marketed with health claims. Europe's legislative bodies must now negotiate and agree on the final legislation. See go.nature.com/fpk7ra for more.

RESEARCH

Malaria trial

GlaxoSmithKline (GSK) will apply next year for European regulatory approval of the candidate malaria vaccine

SERGEY MAJONTOV/RIA NOVOSTI

RTS, S/AS01, the London-based pharmaceutical giant announced on 8 October. GSK and the PATH Malaria Vaccine Initiative, a global programme that is co-developing the treatment, released 18-month follow-up data from a phase III clinical trial of children in Africa, which largely reinforced results reported at 12 months (see go.nature.com/2bgpl8). The treatment offered only modest protection for most children. It showed especially weak results in babies treated at 6–12 weeks of age — the vaccine's target group (see go.nature.com/gmw9ib). See page 271 for more.

Badger beef

A UK experiment to control the spread of bovine tuberculosis by culling badgers (*Meles meles*) is causing political strife. After markedly fewer badgers were killed than originally mandated for the six-week pilot cull, the UK environment department said that it would extend the experiment. Environment minister Owen Patterson said that there were fewer badgers than thought in the pilot regions, so the cull had been successful. Asked last week if he was “moving the goalposts” to make this claim, he replied that “the badgers have moved the goalposts”.



PEOPLE

New space chief

Russian space agency chief Vladimir Popovkin was replaced on 10 October following a series of failed launches. In July, a Russian Proton-M rocket carrying navigation satellites crashed seconds after launching. Former deputy defence minister Oleg Ostapenko (pictured) was named to take over the federal space agency Roscosmos. See go.nature.com/vwuqun for more.

Chemistry Nobel

This year's Nobel Prize in Chemistry was won by computational biologist Michael Levitt at Stanford University School of Medicine, California, together with chemists

Martin Karplus at the University of Strasbourg in France and Harvard University in Cambridge, Massachusetts, and Arieh Warshel at the University of Southern California, Los Angeles, for their work on computer modelling of chemical interactions. See page 280 for more.

Nobel Peace Prize

The Organisation for the Prohibition of Chemical Weapons was awarded the 2013 Nobel Peace Prize on 11 October. The international body, which is based in The Hague, the Netherlands, was recognized for its extensive efforts to eliminate chemical weapons, which include overseeing the current process to destroy Syria's arsenal. See go.nature.com/3lf4kv for more.

BUSINESS

Carbon-capture fall

Plans for large-scale projects to capture and store carbon dioxide emissions are declining, according to the Global Carbon Capture and Storage (CCS) Institute, a non-profit CCS-supporting company based in Melbourne, Australia. In its annual report, published on 10 October, the institute counted 65 planned and ongoing projects, down from

COMING UP

21–27 OCTOBER
Improved assessment tools and science-based management of marine ecosystems are discussed at the 3rd International Marine Protected Areas Congress in Marseilles, France.

go.nature.com/hrtazt

22–25 OCTOBER
São Paulo, Brazil, hosts a conference celebrating 15 years of the SciELO Network, an open-access platform for scientific publishing. Topics include trends in open access, metrics for journal quality and research-communication policy.

go.nature.com/tw2tkd

75 in 2012 — a decrease it attributes in part to policy uncertainty. None of the 12 projects now in operation is at a power plant, but one large coal plant in Saskatchewan, Canada, is scheduled to start capturing carbon in April.

Lithium concerns

The US Government Accountability Office in Washington DC has warned of a looming shortage of lithium-7, a radioactive isotope used to maintain safe cooling at more than half of the 100 nuclear power plants in the United States. On 9 October, the agency said that previous government assessments underestimated the country's demand for the isotope and overlooked uncertainties about future supplies. The isotope has not been produced in the United States since 1963, and can be obtained only from Russia or China.

➔ NATURE.COM

For daily news updates see:
www.nature.com/news

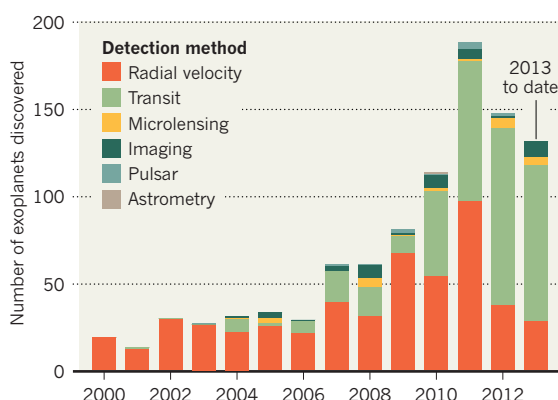
SOURCE: EXOPLANETEU

TREND WATCH

The number of planets detected outside the Solar System was expected to surpass 1,000 this week, according to the Extrasolar Planets Encyclopaedia, which is run by Jean Schneider of the Paris Observatory. But Schneider notes that the precise count is complicated by the lack of any consensus on what defines a planet, and uncertainty about some remote measurements. NASA's Kepler mission has identified thousands more candidate exoplanets that have yet to be confirmed.

EXOPLANET CATALOGUE NEARS 1,000

Most recent exoplanets were found by NASA's Kepler mission, which detected dips in starlight caused by a transiting planet.



NEWS IN FOCUS

CLIMATE CHANGE Social scientists apply to study the inner workings of the IPCC **p.281**

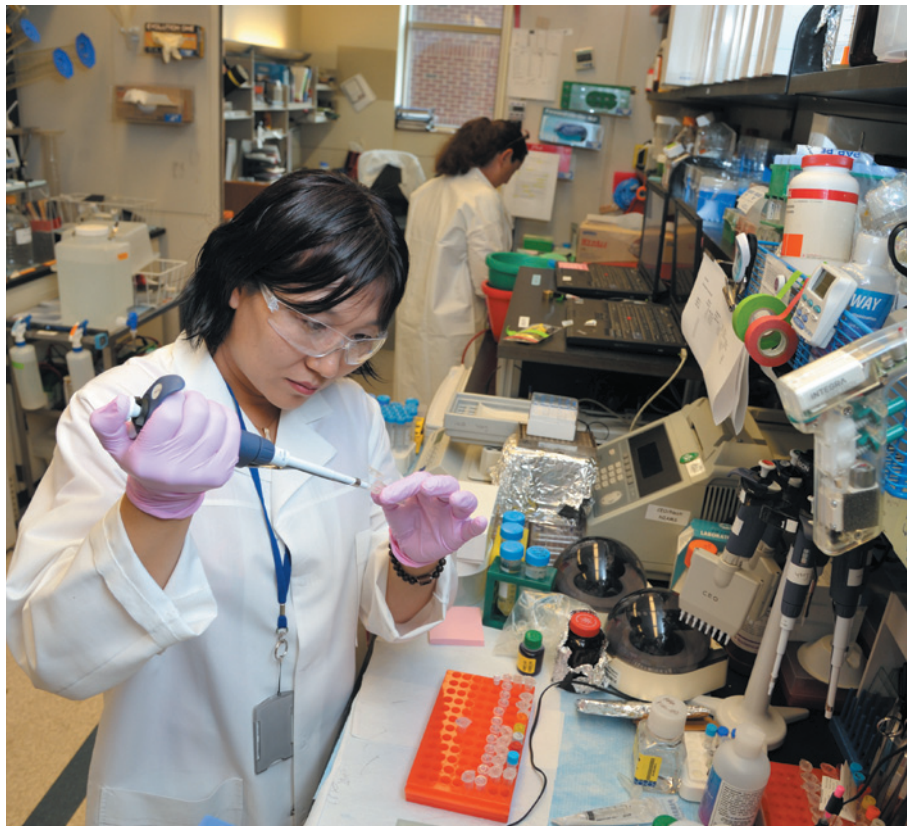
NUCLEAR FUSION Delays force ITER experiment to go all out for power **p.282**

MEDICAL DATA Researchers could soon get their hands on UK patient records **p.283**

IMPACT *Nature* looks at ways of tracking the influence of research **p.287**



BILL BRANSON/NIAMS/NIH



A skeleton staff at the US National Institutes of Health has struggled to keep experiments afloat.

GOVERNMENT

NIH campus endures slow decay

Experiments suffer from lack of lab materials and staff during US government shutdown.

BY SARA REARDON

Bleak grey skies mirror the mood of the skeleton staff trickling through the gates of the main US National Institutes of Health campus in Bethesda, Maryland. Most of the principal investigators are absent: without students to advise or meetings to attend, there is little point in being there. Perhaps one

out of every ten windows is lit up, revealing lonely postdocs working on what few experiments they are allowed to maintain as the US government shutdown drags on.

On 1 October, after federal budget negotiations reached an impasse and forced the shutdown, the NIH sent 73% of its 18,646 employees home. During the second week of the shutdown, the US Department

of Health and Human Services put nearly 1,000 more on unpaid furlough, or enforced leave. As *Nature* went to press, there were suggestions that the Republican-controlled US House of Representatives could come to a deal with the presidential administration and the Democratic-controlled Senate, which could reopen the government. But during a visit to the NIH on 9 October, *Nature* found remaining staff members grimly working to keep crucial research efforts afloat. Notably, 1,437 clinical studies are continuing and a few trials have been able to enrol a handful of desperately ill patients. Technicians at animal facilities have stayed on, ensuring that the NIH's 1.4 million rodents and 3,900 non-human primates receive care. And several hundred employees are allowed to maintain irreplaceable cell lines.

Yet researchers are still finding themselves severely hobbled. One of the worst problems, some say, is the ban on ordering necessary lab materials such as enzymes and chemicals for culturing cells. "We can hold out for maybe a couple weeks with what we have, then we're in real trouble," says one lab head from the National Institute of Allergy and Infectious Diseases (NIAID). Like all of the NIH employees who spoke to *Nature*, he asked to remain anonymous because he is not authorized to talk to the media. Many experiments are being frozen — in some cases literally — as labs decide which can continue, which must be put on hold and which have to be abandoned. "If this goes on, whole experiments will begin to crumble," says the NIAID researcher.

With confusion reigning, the shutdown is playing out in different ways across the NIH's 27 institutes and centres. At the NIAID, for instance, lab heads have been instructed that they cannot have more than two people in a lab at any given time. Some institutes are allowing lab heads to recall workers as needed, whereas others have issued no clear directives. A few postdocs are ignoring the furlough, saying that they have had no specific orders to leave campus. One says that he and his colleagues have not been bothered yet, but he worries about being revealed if an accident occurs in the lab.

Lab heads, some of whom are themselves barred from campus, say that they have been told to write out precisely what each employee should be doing each day, and to justify each project. Mike Askenase, a graduate student at the University of Pennsylvania in Philadelphia who does research at the NIAID, is allowed ▶

► to work for just eight hours a week and only on experiments “that would cost more to shut down than to continue”. He says his lab studies “mouse plague”: *Yersinia pseudotuberculosis*, which in mice causes cysts and gut problems over the course of two to three months. The disease progression cannot be rescheduled, he says, and most researchers did not count on a shutdown when they started their experiments months ago. With just two people at a time in the lab, some parts of the experiments may go unfinished.

Researchers working on animals are among the most worried. One postdoc from the National Cancer Institute says that her security access was revoked at first, but after her adviser pleaded her case, she was given permission to enter her building for one hour per day to advise the technicians who are caring for her mice. The rodents were injected with cancerous cells several months ago, she says, and some of their tumours have now grown so large that the animals need to be killed. She is grateful for that one hour, she says, because it allows her to direct the technicians to take tissue biopsies so that she will be able to pick her experiment back up once the shutdown ends.

Other animal researchers say that the shutdown is affecting their projects in more unpredictable ways. One NIH scientist who works with primates says that it is keeping him from retrieving samples from the primate facilities in Poolesville, Maryland, 40 kilometres from Bethesda. Regulations require that animal-tissue specimens be transported in a government car, but the shutdown has kept government vehicles out of use. And if he cannot do his work, which involves human therapeutics, the researcher questions the morality of keeping the primates. “I don’t think it’s ethical to have an animal in a cage if we’re not doing experiments on it,” he says.

There is one place on campus that still seems to be doing good business: the small cafeteria in the NIH’s Clinical Center. Normally used by patients, it is now the only place open to eat. The buzz of conversation there seems muffled. Discussions of science are overshadowed by doubt, worry and uncertainty. ■

NOBEL PRIZE

Modellers react to chemistry award

Prize proves that theorists can measure up to experimenters.

BY RICHARD VAN NOORDEN

Computer modelling is one of the many scientific fields that Alfred Nobel, understandably, failed to anticipate in his 1895 will. And so, as Michael Levitt points out, “there’s no Nobel prize for computer science”. But computation’s increasing importance in chemistry and biology was recognized last week, when Levitt, of Stanford University in California, was one of three scientists to receive the chemistry Nobel for their work on ways to simulate the activity of large molecules — from cellular enzymes to light-absorbing dyes.

“Computers in biology have not been sufficiently appreciated,” Levitt said at a press conference, joking that a fourth portion of the Nobel might have gone to the chip manufacturers, who have driven up computing power exponentially.

Together with Martin Karplus of the University of Strasbourg in France and Harvard University in Cambridge, Massachusetts, and Arieh Warshel of the University of Southern California in Los Angeles, Levitt was honoured for a specific modelling technique: working out how to stitch together descriptions of molecules at close-up and zoomed-out scales.

The three were trailblazers in the 1970s. At the time, finely detailed quantum-mechanical pictures of bond making and breaking could not be calculated for more than a cluster of atoms — even today they are too complex to be computable beyond a few hundred atoms, and cannot be used to model whole proteins. So Levitt, Warshel and Karplus worked out how to merge these models with simplified simulations that treat molecules as non-reacting, vibrating atomic balls

connected by springs. “The art is to find an approximation simple enough to be computable, but not so simple that you lose the useful detail,” Levitt says.

These multi-scale models have proved essential for studying the workings of enzyme reactions, and were pioneered in a 1976 paper in which Warshel and Levitt explained how lysozyme cleaves a glycosidic bond. Multi-scale techniques are not widely used in the drug industry, adds Kenneth Merz, who heads the Institute for Cyber-Enabled Research at Michigan State University in East Lansing. Instead, says theorist Christopher Cramer of the University of Minnesota in Minneapolis, they find uses in, for example, revealing how industrial catalysts work, or examining how light activates dyes on semiconducting nanoparticles.

The award is also being viewed as an acknowledgement of the three scientists’ lifetime work in molecular simulation, researchers told *Nature*. “They have made theory an equal partner to experiment,” said theoretical chemist Gunnar Karlström of Lund University in Sweden, a member of the Nobel committee.

Still, a question mark remains over whether theorists can make predictions that surprise experimenters. Computer modelling “is really good at helping people understand why things work the way they do, but not so good at predicting new things. We are good at guiding experimentalists,” says Ken Houk, who uses computer programs to design new enzymes at the University of California, Los Angeles.

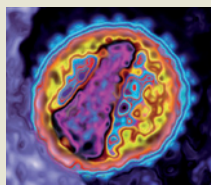
Experimenters should be cautious of simulation results, agrees Warshel. But “one day everything will be done by powerful computers”, he predicts.

Cramer adds: “Every year, hazardous-waste disposal gets more expensive, whereas computing power gets cheaper. So the progress curves favour the theoreticians.” ■

“We are good at guiding experimentalists.”


MORE ONLINE

VIDEO OF THE WEEK

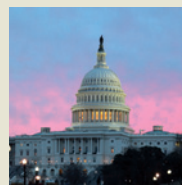


Mammals chop up viral RNA to attack infection
go.nature.com/sftmsh

MORE NEWS

- Quantum wavefunction collapse caught in slow motion go.nature.com/ryu8ny
- Diamond drizzle forecast for Saturn and Jupiter go.nature.com/r1pwmmt
- Ozone loss warmed southern Africa go.nature.com/ph2nyo

TOP STORY



Live updates on how science is being hit by the US government shutdown
go.nature.com/u5kntz



IPCC head Rajendra Pachauri (left) could be observed by sociologists studying meeting interactions.

CLIMATE POLICY

Study aims to put IPCC under a lens

Social scientists want to examine how climate panel's internal dynamics affect outcomes.

BY JEFF TOLLEFSON

Every six years or so, the Intergovernmental Panel on Climate Change (IPCC) reports on everything that is known about global warming. In between, at meetings behind closed doors, hundreds of scientists review studies, discuss the latest model results and assess humanity's options. The eventual result is a series of reports, such as the scientific analysis released last month — the first component in the fifth assessment on climate change, which will also cover adaptation and mitigation. But how, exactly, do these reports get written?

This week, at its latest plenary session in the Black Sea city of Batumi, Georgia, the IPCC will consider a request from social scientists who, armed with recorders, want to study the interactions that take place within the panel's many meetings. The proposal, part of a larger “assessment of assessments” funded by the US National Science Foundation, could offer insight into the ways that social dynamics, unconscious biases and seemingly mundane rules affect the final product — and what might be done to improve the process.

“Most previous studies have looked at how the IPCC interacts with the outside world, but we're interested in how it interacts with itself,” says Michael Oppenheimer, a climate scientist

at Princeton University in New Jersey, who recognizes his own biases as a participant in the past four climate assessments. “The truth is that very little is known about the actual process.”

Sociologists of science have long been interested in the way that social dynamics subtly tug at the scientific process, and the IPCC, a prominent target because of its international stature and political significance, has been studied before. In a pair of recent papers (K. Brysse *et al.* *Global Environ. Change* **23**, 327–337; 2013, and J. O'Reilly *et al.* *Soc. Stud. Sci.* **42**, 709–731; 2012), which centred on the treatment of rising sea levels in the 2007 assessment, Oppenheimer and his colleagues argued that the IPCC tends towards caution and errs “on the side of least drama”. Their results were based on IPCC documents and subsequent interviews, but the researchers did not have access to the meetings in which the issue was thrashed out.

In the studies, the researchers focused on the IPCC's decision to exclude melting of the West Antarctic Ice Sheet from its review, because of uncertainty in the models used to predict the ice sheet's behaviour. As a result, the final assessment projected a sea-level rise of up to 59 centimetres by 2100, even though new studies had suggested that an acceleration in ice-sheet melting could raise ocean levels

substantially higher. Oppenheimer and his colleagues found that the exclusion decision was driven by a few key scientists and a requirement for consensus, and also by an assessment structure that split the treatment of sea ice into three chapters covering the past, present and future. This complicated the assessment process by involving more scientists and overemphasized uncertainty, the researchers argued.

The social scientists now want to go deeper and get inside the IPCC meetings as they happen. That would allow the team to observe scientists' interactions and to interview pivotal actors on the spot, rather than trying to reconstruct events. Treating scientists as subjects, however, raises privacy issues, given that the deliberations are confidential, a policy that is intended to allow scientists to talk openly without fear of having off-the-cuff remarks broadcast to the world. The social scientists also recognize that the mere act of observation could affect the process, although they say that their protocols would be designed to minimize intrusion and maintain confidentiality.

Such fears led the IPCC to deny the team's first request for access in 2010. It came at a particularly sensitive time, when the panel was reviewing its procedures after an embarrassing mistake (regarding Himalayan glaciers) in the previous assessment, and following the ‘Climategate’ controversy, sparked by the leak of thousands of private e-mails from the University of East Anglia, UK, revealing private discussions between leading climate scientists.

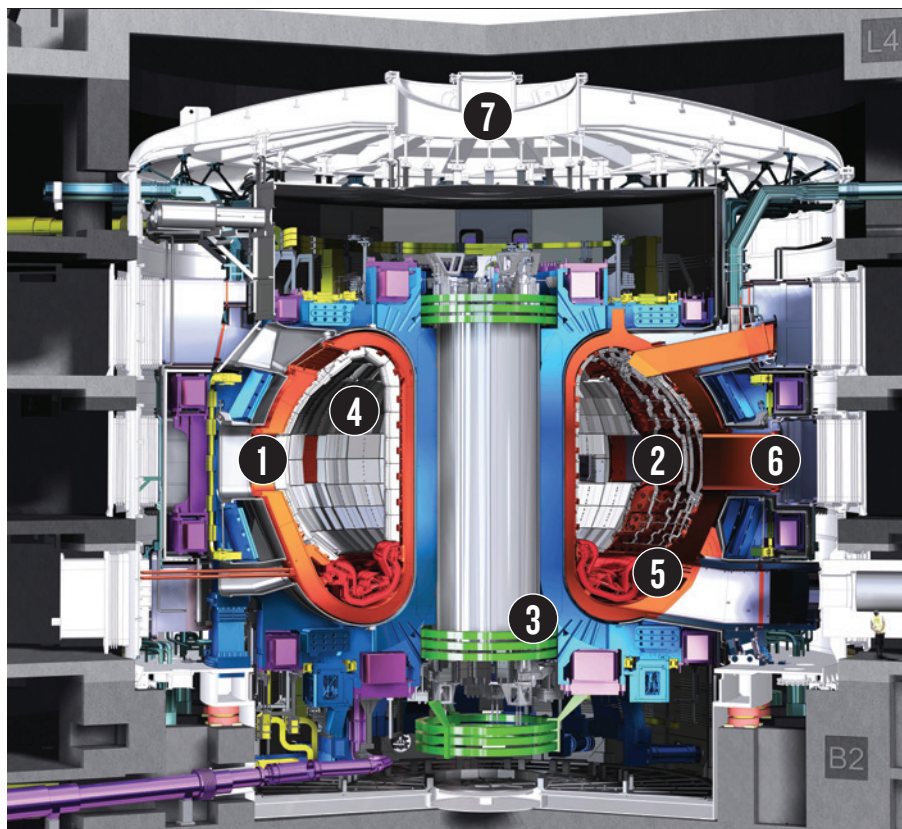
Procedure was also an issue: the request came after the IPCC had enlisted scientists and laid out the ground rules for the fifth assessment. “It was perceived by some as a change of the rules in the middle of the game,” says IPCC vice-chair Jean-Pascal van Ypersele, a climatologist at the Catholic University of Leuven in Belgium.

Ypersele suspects that the proposal will be received more warmly this time around by

“Most people on the outside have no idea what the IPCC does.”

member governments, because it could be folded into the IPCC assessment process from the outset. This week, the IPCC is likely to either approve the proposal, or delay action until after the fifth assessment is completed next year, he says.

Naomi Oreskes, a science historian at Harvard University in Cambridge, Massachusetts, and a member of the prospective study team, argues that allowing ethnographers inside the process will promote transparency and enhance the panel's credibility with the public and policy-makers. “Most people on the outside have no idea what the IPCC does,” she says, and the black box inevitably generates suspicion and fuels criticism among climate sceptics. Clarifying the process might make the IPCC's assessments seem a little less like magic — and a little more like sausage-making. ■



A FUSION OF IDEAS

ITER's reactor is a tokamak, in which the fuel is contained in a doughnut-shaped vessel and heated to ten times the temperature of the Sun's core, forming a plasma, a hot, electrically charged gas.

1. VACUUM VESSEL

A huge stainless steel container will hold the plasma and house the fusion reaction.

2. HEATING

Neutral beam injections and radio-frequency electromagnetic waves will heat the plasma to 150,000,000 °C.

3. MAGNETS

Ten thousand tonnes of superconducting magnets generating a field 200,000 times that of Earth's magnetic field will confine and shape the plasma.

4. BLANKET

Tiles weighing up to 4 tonnes will protect the vacuum vessel and magnets from heat and neutrons.

5. DIVERTOR

A series of tungsten tiles under the vacuum vessel take exhaust heat and gases away from the tokamak.

6. DIAGNOSTICS

Key experimental tools (including pressure gauges and neutron cameras) for measuring the physics of plasmas.

7. CRYOSTAT

A huge refrigerator surrounding the vacuum vessel, protecting the superconducting magnets and other equipment from heat.

NUCLEAR FUSION

ITER keeps eye on prize

Construction delays force rethink of research programme, but fusion target still on track.

BY DECLAN BUTLER

Delays in the installation of key parts of ITER, a multibillion-euro international nuclear-fusion experiment, are forcing scientists to change ITER's research programme to focus exclusively on the key goal of generating power by 2028. As a result, much research considered non-essential to the target, including some basic physics and studies of plasmas aimed at better understanding industrial-scale fusion, will be postponed.

Nature has learned that the plans form the main thrust of recommendations by a 21-strong expert panel of international plasma scientists and ITER staff, convened to reassess the project's research plan in the light of the construction delays. The plans were discussed this week at a meeting of ITER's Science and Technology Advisory Committee (STAC).

The meeting is the start of a year-long review by ITER to try to keep the experiment on track to generate 500 MW of power from an input of 50 MW by 2028, and so hit its target of attaining the so-called $Q \geq 10$, where power output is ten times input or more.

ITER, which will be the world's largest tokamak thermonuclear reactor (see 'A fusion of ideas'), is being built in St-Paul-lez-Durance in southern France by the European Union, China, India, Japan, South Korea, Russia and the United States at a cost of €15 billion (US\$20.3 billion). $Q \geq 10$ is seen as its *raison d'être*, and achieving it would be likely to revitalize public and political interest in fusion. Crucial to that is getting to the point, scheduled for 2027, when the first nuclear fuel would be injected into the reactor. The fuel will be a plasma of two heavy hydrogen isotopes, deuterium and tritium (DT).

The original 2010 research plan foresaw the entire reactor being built by 2020, when ITER was also scheduled to produce its first plasma, using hydrogen as a test fuel. But cost-cutting and cash-flow problems in member states mean that while the reactor is likely to be operating by then, the delivery of some parts is being deferred until several years later. These include some diagnostics devices for analysing the physics of plasmas at the very large scales of ITER, and elements of the heating system that will eventually take the plasmas to 150,000,000 °C.

"The plan was that everything would be procured and installed before first plasma, and then we would go straight into operation with a full set of systems," says David Campbell, head of ITER's plasma directorate. Instead, researchers will start with an initial set of instruments and systems, with others added later as upgrades. One of the main aims of the STAC meeting was for ITER to learn what elements of the research programme were essential to keeping it on track to reach DT phase and $Q \geq 10$ on schedule. A local plant that will produce tritium, for example, is one key element.

The outcome of the review is also expected to influence ITER member states' deferral plans, which will be modified to meet the key scientific priorities identified in the review. By fixing a timetable, Campbell says, STAC "will match up delivery schedules to the research plan, so that the research plan is not waiting for stuff to be delivered".

The likely consequence of capping costs is that some parts of the research plan will be postponed until after 2028. ITER initially aims to produce a $Q \geq 10$ for a few seconds, and then

for pulses of 300–500 seconds, and work up over the following decade to output ratios of 30 times more power out than in, with pulses lasting almost an hour. Eventually the aim is to develop steady-state plasmas, which will yield information relevant to industrial-scale fusion-power generation. It is experiments relating to the understanding of longer-pulse and steady-state ITER plasmas that are most likely to be delayed beyond 2028.

Research into better plasma performance, and with it greater energy output, may also be held back, along with experiments

investigating how to control turbulence, which can damage the reactor wall, and the stability and energy characteristics of plasmas.

Olivier Sauter at the Swiss Federal Institute of Technology in Lausanne, Switzerland, one of the reviewers of ITER's research plan, says that months or more might be cut from the time needed to reach DT. But ITER's decision to take shortcuts also carries risks, he adds. To help mitigate these, ITER is working closely with researchers at other tokamaks around the world, such as the Joint European Torus in Oxfordshire, UK, to address some of the

uncertainties likely to be encountered in plasma energies and stability.

"It is somewhat unfortunate that the compression of the ITER schedule will limit interesting research opportunities during the early stages of ITER operation, but the mission of ITER is clear," says Mickey Wade, director of the US national DIII-D fusion programme at General Atomics in San Diego, and a member of the review panel advising STAC. "The ITER physics team has done an admirable job of maintaining a single-minded focus on obtaining $Q \geq 10$ operation as early as possible." ■

HEALTH POLICY

UK push to open up patients' data

Government faces obstacles to mining medical records.

BY EWEN CALLAWAY

In August, posters began appearing in doctor's practices across England, urging patients to say yes to their medical records being used for scientific research — or, more precisely, not to say no.

The move, now gathering momentum, is part of a campaign by the UK government, alongside major research funders such as the Wellcome Trust in London, to convince a sceptical public to share their health details with researchers, through a system in which patients must expressly opt out. Privacy advocates are encouraging them to do just that.

The government's plans are part of a shake-up of health data in the National Health Service (NHS) in England, the world's largest public-health system, that cares for about 53 million people. Following reforms made in April, it will in the coming weeks begin radically changing the way it handles patients' records. This will involve establishing a central repository to connect hitherto disparate electronic data from general practitioners' (GP) practices, hospitals and disease registries.

Such linkage, already in place in Scotland and Wales, where the NHS is run separately, will deliver better health care, the government says, while establishing the world's most comprehensive patient database for research. It could be used to find new uses for existing drugs, and speed up the transfer of research to the clinic.

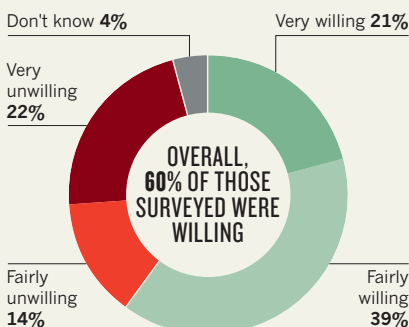
"The potential crown jewels in the UK are primary-care data that have been electronic for decades and have been coded for decades and have wide population coverage, nearly 100%," says Harry Hemingway, director of the Farr

Health Informatics Research Institute at University College London, which was established this year with funding from the UK Medical Research Council to mine such records. Such an archive would trump those in the United States, and even in Denmark and Sweden, which have had central health databases for years.

The immediate use of the linked data will be to help the NHS apportion resources, but the government is also keen to make patients' records more useful — and accessible — to researchers in academia and industry. Prime Minister David Cameron has said that every NHS patient should be a research participant. His administration is also hoping that access to patients' data will lure drug companies back to Britain, and catalyse a health-informatics industry potentially worth billions of pounds.

A QUESTION OF CONSENT

In a survey, 1,396 UK adults were asked: 'How willing or unwilling would you be to take part in a medical research project which involved allowing access to your personal health information (medical records), on an anonymous basis.'



This autumn, GPs' records will begin migration to a data centre, where they will be linked with other data, including already-centralized hospital records. Some of this information — stripped of identifying details or fully anonymized — will also be made available to approved researchers through a secure portal.

According to some proponents of the plan, patients have little reason to opt out. "People think their records are being shared much more than they already are," says Nicola Perin, head of policy at the Wellcome Trust, the UK's biggest funder of biomedical research. She worries that the public in England have not been adequately informed about the benefits of records sharing, such as improved health care, nor about measures intended to protect privacy. "I think there is underlying support for it, provided one can explain that there are safeguards, and that it isn't your most personal secrets that researchers want to get," she adds (see 'A question of consent').

Yet research funders worry that scaremongering in sections of the press could lead to large numbers of people opting out of the scheme, diluting its usefulness to researchers. In response, funders plan to become more vocal in touting the benefits of health-records research, such as very large epidemiological studies showing the effectiveness of smoking bans and the safety of vaccines. "When you explain that all of this research is only possible by using patient records, then people change their minds," says Janet Valentine, head of public health and ageing at the Medical Research Council, the UK's publicly funded agency for biomedical research, which spent £760 million (US\$1.2 billion) on research last year.

Phil Booth, head of a campaign called medConfidential that opposes the changes, worries that medical research is being used as a patient-friendly cover to collect data for other uses, such as the administration of social-security benefits. If privacy were compromised — an inevitability, Booth says — patients might lose faith in research and the NHS. His organization successfully fought for patients to be able to opt out. "I think research institutions are basically being rather short-sighted in aligning themselves with this initiative," he says. ■

Regulators weigh benefits of 'three-parent' fertilization

But critics say mitochondrial replacement carries safety and ethical concerns.

BY ERIKA CHECK HAYDEN

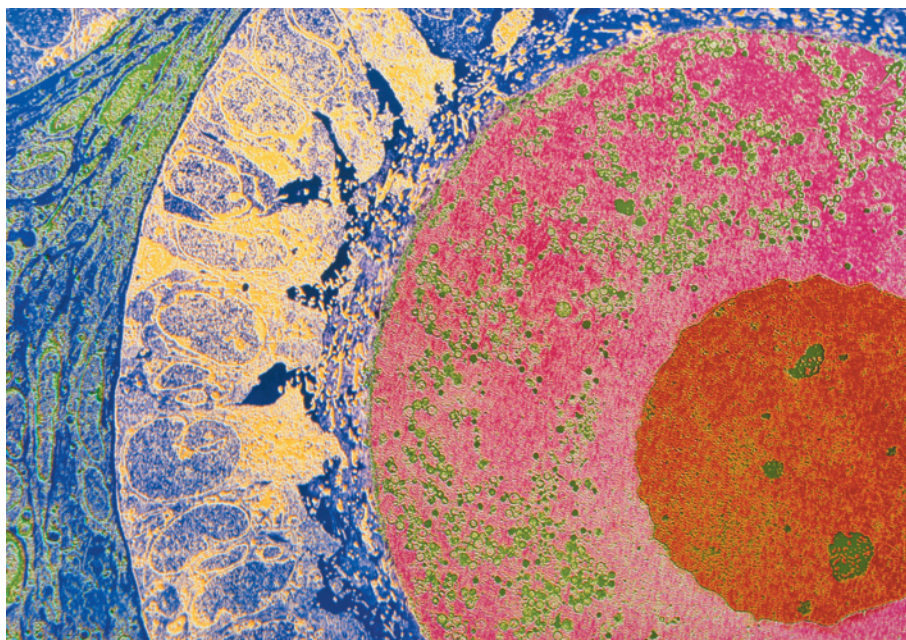
Regulators in the United States are considering whether to permit trials of a controversial assisted-reproduction technique intended to help women to avoid passing certain genetic defects on to their children.

On 22 October, the US Food and Drug Administration (FDA) is scheduled to meet in Silver Spring, Maryland, to discuss a method that could prevent transmission of defects in mitochondria — cellular components that contain a small amount of DNA — from mother to child. The defects, which can cause fatal developmental conditions, affect as many as 4,000 US births a year.

The technique places nuclear DNA from the egg of a woman with a mitochondrial defect into a donated egg that has had its nuclear DNA removed, but contains healthy mitochondrial DNA. Once the egg is fertilized, the resulting embryo would, in a sense, have three parents, because the donor mitochondrial DNA is passed down along with the mother and father's nuclear DNA.

The FDA was asked to look into the issue by developmental biologist Shoukhrat Mitalipov at Oregon Health and Science University in Beaverton, who last year created early human embryos with the technique (see *Nature* <http://doi.org/n76>; 2012). When the manipulated eggs were fertilized, genetic abnormalities were detected in half of them — but seemingly normal embryonic stem-cell lines could be extracted from 38% of the rest. Trying to obtain stem cells from unmanipulated eggs results in a similar success rate. Mitalipov had used the same technique in 2009 to create apparently healthy rhesus monkeys. Now he wants to begin a clinical trial in humans.

In 2001, the FDA began to regulate the technique as a form of gene therapy after researchers used fresh mitochondria in a handful of infertile women to help them to conceive (see 'Energizing eggs'). The regulation was widely, but incorrectly, reported as a ban. The FDA asked researchers to apply for permission to test the approach in clinical trials. But none did — until now. At the time, the agency said that the safety data "were not convincing", citing examples of genetic abnormalities such as a missing X chromosome



Mitochondria (green) in egg cells carry an independent lineage of DNA that can pass on genetic defects.

in a fetus created with the technique.

The anomalies seen in embryos created with mitochondrial transfer could have been due to the mothers' underlying fertility issues rather than to the technique itself, says embryologist Jacques Cohen, who was scientific director of assisted reproduction at Saint Barnabas Medical Center in Livingston, New Jersey, when such treatments were conducted there.

But other safety concerns have been raised since then. In September, a group of evolutionary biologists led by Klaus Reinhardt at the University of Tübingen in Germany, said that problems could arise if mitochondrial and nuclear DNA from different women proved to be incompatible. They pointed to dozens of experiments in mice, fruit flies and other animals in which mixing nuclear and mitochondrial DNA from individuals with different genetic backgrounds sometimes led to reduced growth, early death, fast ageing or reduced reproductive ability.

➔ NATURE.COM
For more on
mitochondrial
replacement, see:
go.nature.com/xhdcdw

Mitalipov and other scientists counter that those experiments were mostly done by mixing strains of inbred animals. In species such as

humans, individuals from different genetic backgrounds interbreed freely without ill effects. "If anything, children born from mixed-race couples, and [their] successive generations, are fitter than those from same-race couples," says developmental geneticist Robin Lovell-Badge of the Medical Research Council National Institute for Medical Research in London.

Paul Knoepfler, a stem-cell biologist at the University of California, Davis, has a different concern: epigenetics. He says that the donor egg's cytoplasm could reprogram chemical tags on the nuclear DNA which alter the expression of genes. But Mitalipov argues that reprogramming will not occur with his technique because he is transferring genetic material between cells that are in exactly the same developmental state. He points to the existence of the healthy monkeys that are now more than four years old — and are the product of mitochondrial transplants across different genetic backgrounds — as evidence that the technique is safe.

In March, the UK Human Fertilisation and Embryology Authority (HFEA) concluded that human trials could be done if, for instance, offspring were monitored long-term. The UK government is now drawing up regulations

P. MOTTA/DEPT. ANATOMY UNIV. ROMA LA SAPIENZA/SPL

ENERGIZING EGGS

Experimental fertility treatment faces scrutiny

As the US Food and Drug Administration (FDA) debates the merits of mitochondrial replacement in eggs, some observers will be looking for hints as to how the agency may regulate another mitochondrial manipulation — one with fewer ethical and safety concerns.

OvaScience, a biotechnology company in Cambridge, Massachusetts, wants to boost the success rate of *in vitro* fertilization (IVF) by infusing eggs with fresh mitochondria. The mitochondria are harvested from an IVF patient's own egg precursor cells, a cell type discovered by Jonathan Tilly, a reproductive biologist at Northeastern University in Boston, Massachusetts. Tilly says that these precursor cells can be coaxed to develop into mature eggs in adult women, challenging the dogma that women are born with all the eggs they will ever have. Tilly's results are disputed (see *Nature* **491**, 318–320; 2012), but OvaScience has long-term plans to harvest precursor cells and use them to create fresh eggs for women for whom conventional IVF has failed.

The company's first project, called AUGMENT, is to harvest precursor cells, isolate their mitochondria, and inject

them into mature eggs to see if they can revive eggs from infertile women, as work with mitochondria from donor eggs has suggested. Mitochondrial DNA from egg-precursor cells is thought to contain fewer mutations than mitochondrial DNA in the eggs themselves. Because OvaScience would be using mitochondria from a patient's own cells, the company hopes to sidestep ethical concerns raised by 'three-parent' embryos.

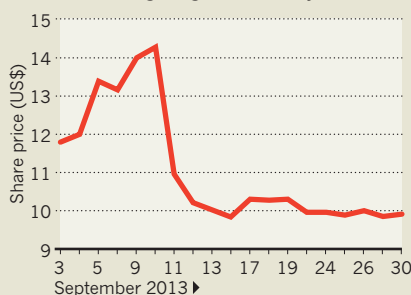
OvaScience has argued that AUGMENT involves 'minimal manipulation' — the same injection procedure, for example, is already used to put sperm into an egg — and therefore would not need FDA approval to be deployed in clinics. Regenerative Sciences in Broomfield, Colorado, has also argued that one of its stem-cell therapies involves 'minimal manipulation'. The FDA challenged that idea, and its injunction on the treatment was ultimately upheld in court (see *Nature* **488**, 14; 2012).

OvaScience investors clearly feared that AUGMENT would meet the same fate when, on 10 September, the company announced that the FDA had issued a letter questioning whether the project was exempt from agency review. OvaScience voluntarily suspended enrolment in the US arm of its AUGMENT clinical study, pending a meeting with regulators. The company's shares fell 23% that day, and have yet to recover (see 'Egg regs').

But analyst Jeffrey Cohen of Ladenburg Thalmann, a financial services company in Miami, Florida, says that the FDA letter has not changed his favourable assessment of OvaScience. The AUGMENT study is continuing in Europe, he notes, where the market for IVF is as much as three times larger than in the United States, and regulatory hurdles are not expected to be a barrier. **Heidi Ledford**

EGG REGS

OvaScience shares plummeted on 10 September, the day the company revealed that the US Food and Drug Administration might regulate its fertility treatment.



SOURCE: NASDAQ

on the technique, and Parliament, which had banned all germline modifications, will vote on whether to allow the procedure next year.

There are also ethical considerations. The HFEA said that the procedure should be considered in the same ways as a tissue donation, and that any resulting child should not have the right to know the identity of the donor of the healthy mitochondria. The FDA, unlike the HFEA, does not consider ethics, and that worries Marcy Darnovsky, executive director of the Center for Genetics and Society, an advocacy group in Berkeley, California. Her group has opposed such trials, in part because of concerns that acceptance of the technology might lead to the selection of embryos with

specific traits for non-medical reasons.

Mitalipov agrees that any trial would need to proceed with caution, but says that if he cannot perform the trials in the United States, he would consider going to the United Kingdom if it allows the procedure first. "Patients are suffering the same issues, no matter where they are." ■

CORRECTION

The print version of the World View by George Church (*Nature* **502**, 143; 2013) was published before the author had approved changes. The online version was amended to better reflect his views.

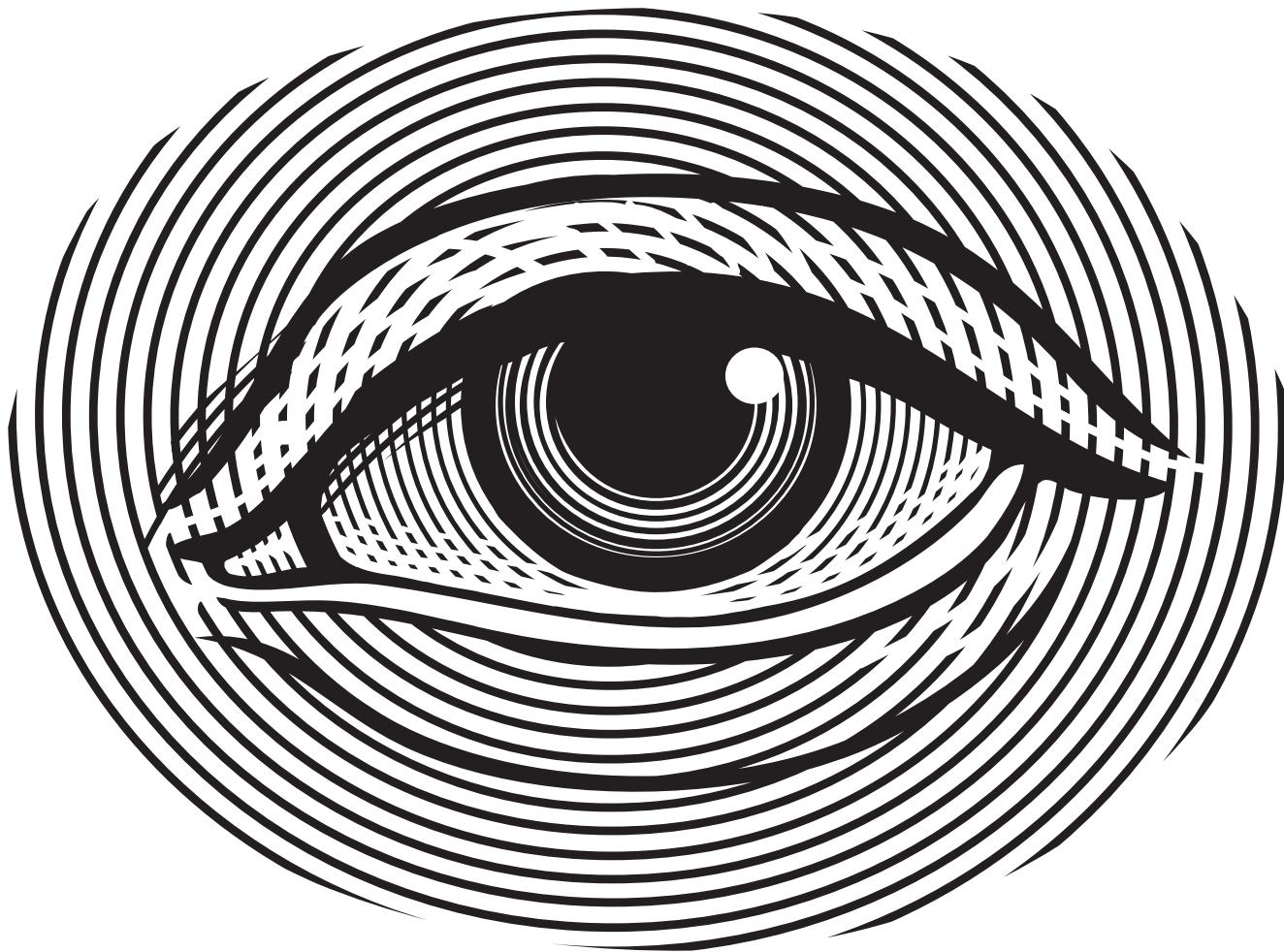
Every organization that funds research wants to support science that makes a difference. But there is no simple formula for identifying truly important research. And the job is becoming more difficult. As funding gets squeezed, scientists face stiffer competition for resources and jobs, and it becomes more crucial than ever to develop reliable ways of spotting and supporting the best work. This week, *Nature* examines how the impact of research is measured — and asks whether today's evaluation systems promote the most important science.

One way of assessing the influence of research is to track citations of papers, but there are concerns that such data are often proprietary and not easily evaluated, writes David Shotton on page 295. Shotton is the director of the Open Citations Corpus, a fledgling repository for open scholarly citation data. Researchers are increasingly producing output — data, videos and code, for example — that do not mesh well with older systems for evaluating scientific contributions. On page 298, Mark Hahnel, founder of figshare, an online tool that allows researchers to publish all their data in a citable, searchable and shareable manner, describes the complexities of tracking the impact of these diverse research products.

These stories and commentaries show how evaluation systems are having to evolve rapidly to keep up with changes in the way that science is practised and communicated (see Editorial, page 271). Separating the best from the rest has never been harder. ■



A *Nature* special issue
nature.com/impact



JUDGEMENT DAY

Many governments are assessing the quality of university research, much to the dismay of some researchers.

BY BRIAN OWENS

Two years ago, academics at Lancaster University, UK, found themselves in the uncomfortable position of being graded. They each had to submit the four best pieces of research that they had published in the previous few years, and then wait for months as small panels of colleagues — each containing at least one person from outside the university — judged the quality of the work. Those who failed their evaluations were offered various forms of help, including mentoring from a more experienced colleague, an early start on an upcoming sabbatical or a temporary break from teaching duties.

The university did not undertake this huge exercise just to make sure that the researchers

were pulling their weight. The assessment was a drill to prepare for the Research Excellence Framework (REF), a massive evaluation of the quality of research at every university and public research institute in the United Kingdom, which is set to take place in 2014.

The idea of the drill “was to identify areas where we could help people develop their profiles”, says Trevor McMillan, Lancaster University’s pro-vice-chancellor for research. Happily, he says, the results suggested that the university would score more highly than it did on the most recent national evaluation, in 2008.

But other mock evaluations have proceeded less smoothly. In a survey of more than 7,000 UK academics published on 3 October by the University and College Union (UCU) in

London, almost 12% reported having been told that failure to meet their university's REF benchmarks in a drill could lead them to be transferred to a teaching-only contract before the real REF (see go.nature.com/eqiirr). Almost 10% said that they faced denial of promotion. At Cardiff University, around ten academics were pressured to switch to teaching-focused contracts after they scored poorly on a practice exercise, so as not to drag down their department, says Peter Guest, an archaeologist at Cardiff and the university's UCU liaison on the REF. This form of game-playing is discouraged, but not expressly forbidden, by the REF — however, making career decisions solely on the basis of the evaluation is against the university's own policies, as well as those of many other institutions, says Guest.

All of the Cardiff cases were resolved in a day or two, with managers being “forcefully reminded” of the rules by the UCU, says Guest. But the experience shows how tempting it is for institutions to make career decisions on the basis of predicted REF scores, which are highly subjective. This is neither reliable nor fair, says Guest. (In response to questions about the incident, a spokesman for the university said in an e-mail: “We have been running a long-term programme for over four years to ensure our academic staff are on contracts that reflect what they actually do.”)

Even many academics who did score well in the mock evaluations resent them. Around the United Kingdom, researchers view these national assessments as a bureaucratic imposition that can stifle creativity.

UNDER PRESSURE

Most academics at Lancaster saw the mock REF as little more than a “mildly annoying” bit of bureaucracy, but the real thing is a different matter. “We have our department's top research professor working on preparing our REF submission, and it's taking up about a third of his time,” says one member of the mathematics and statistics department. “It seems like a waste of talent.” Too many researchers are focused on winning grants and trying to predict what kind of work will be rewarded in the next assessment, rather than doing the best science they can, says Dorothy Bishop, an experimental psychologist at the University of Oxford, UK. “I think a lot of science is just not very well done these days because people are trying to do too many things.”

But university administrators and the government have come to rely on these evaluations to help them decide how to disburse funding. And the idea has been so popular with educational leaders that other countries are following the United Kingdom's example, with similar exercises cropping up in Australia, Italy, Germany and elsewhere.

In the late 1980s, the United Kingdom became the first country to systematically evaluate the quality of its university research.

The REF is the latest incarnation of these check-ups. Previously known as the Research Assessment Exercise (RAE), the evaluations are widely credited with helping to improve the country's research system. Between 2006 and 2010, citations of UK articles grew by 7.2%, faster than the world average of 6.3%; and the country's share of citations grew by 0.9% per year, according to a 2011 analysis conducted by publishing company Elsevier for the government.

The assessment is used by the UK government to distribute more than £1.6 billion (US\$2.6 billion) a year in block grants to universities. More than 70% of the pot goes to the top-scoring 20 or so universities — last year, the University of Oxford got more than £130 million in quality-related funding — whereas the smallest, least research-intensive institutions make do with just a few tens of thousands of pounds. Assessment results are eagerly assembled into league tables, showing which universities are performing best in which subjects (see “Top 5”).

“The reputational aspects of it can be as important as the financial aspects,” says McMillan. Some smaller institutions that are strong in particular subjects — as Lancaster is in physics — have reported that they have an easier time attracting students in those areas as a result of the assessments. And it is not just students. “One of the consequences is that people really want to come to a department that did well in the RAE,” says McMillan. “We've found it easier to recruit high-quality staff in physics.”

For the REF, universities submit a selection of work from most of their active researchers to one of dozens of subject-specific panels known as Units of Assessment that correspond roughly, but not exactly, to university departments. The panels evaluate the quality of the research using peer review and metrics such as citation indexes. And they will also, for the first time, look at the economic and social impact of a university's research.

Even critics of the assessments agree that they have had some positive effects on the country's research system. Because the exercises judge academics on the quality of their

research, many departments have tried to cut back on other demands, such as administrative work, says Guest. Furthermore, the results make it clear which departments and academics are not pulling their weight, and allow universities to make strategic decisions about how to invest resources.

Royal Holloway, University of London, faced that very situation after the first research assessment in 1986, which ranked the university's psychology department in last place

nationwide, says Kathy Rastle, a cognitive psychologist and the department's director of research. Recognizing that it would not be able to boost its rating by hiring established stars, the department sought instead to attract and develop young talent. “We try to focus on people we feel have great potential,” says Rastle.

Early-career psychologists at Royal Holloway are now offered “substantial, but tailored” start-up packages, she says, with hardly any teaching commitments for the first two years. They also get help from more experienced colleagues in preparing funding proposals.

In the 2008 RAE, after two decades of nurturing junior staff, the department was ranked among the top ten in the country. It has ambitions to go even higher. “I look forward to the REF as an opportunity to show what we've done, and to move up the ranks,” says Rastle.

AN IDEA SPREADS

As other countries begin their own national research evaluations, they hope to achieve

the same kinds of benefits. This year, Italy published the results of an evaluation begun in 2011 (see *Nature* <http://doi.org/nrx>; 2013); its goal is to increase meritocracy in the country's universities, where academics of the same rank and seniority currently receive the same salary, regardless of output. “There are no incentives to improve your research performance,” says Giovanni Abramo, who studies bibliometrics and research evaluation at the National Research Council of Italy in Rome. “Now some of the money the government gives to universities will be based on this evaluation.”

The Italian effort evaluates only three journal articles from each researcher with teaching commitments, whereas Australia assesses all research output as part of its Excellence in Research for Australia (ERA) initiative, most recently in 2012. Only a relatively small pot of funding rides on the results: this year,

TOP 5

Analysts used information from the 2008 UK Research Assessment Exercise to rank academic departments by quality.

CHEMISTRY

1. University of Cambridge
2. University of Nottingham
3. University of Oxford
4. St Andrews/Edinburgh
5. University of Bristol

MATHEMATICS

1. Imperial College London
2. University of Warwick
3. University of Oxford
4. University of Cambridge
5. University of Bristol

PHYSICS

1. Lancaster University
2. University of Cambridge
3. University of Nottingham
4. University of St Andrews
5. University of Bath

PSYCHOLOGY

1. University of Cambridge
2. University of Oxford
3. University of Birmingham
4. University College London
5. Birkbeck

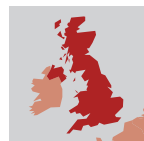


IMPACT

A *Nature* special issue
nature.com/impact

STAND AND BE COUNTED

Assessment of academics has spread throughout the world, but each country does it differently.



UNITED KINGDOM

Name: Research Excellence Framework

Next assessment: 2014

A sample of researchers submits four examples of work published since 2008;

department heads often decide who is included. Each department provides a description of the economic and social impact of its work.

Submissions are evaluated by expert panels that assign a quality profile to each university. Quality will account for 65% of the score, impact for 20% and research environment 15%.

Results are made public and used to distribute the government's 'quality-related' research funding, which in 2013 was worth more than £1.6 billion (US\$2.6 billion).



GERMANY

Name: Research Rating

Next assessment: Unknown

Four pilots of the Research Rating have been conducted so far, in chemistry, sociology, electrical engineering and

English and American studies.

Panels of 15–20 people evaluated the quality of a selection of publications from each research institute. Panels also sought to promote young researchers and technology transfer.

The government is considering a decision this month on whether to repeat the assessment and expand it to all disciplines.

The assessments are made public, but will not be used to distribute funding.



ITALY

Name: National Agency for the Evaluation of the University System and Research (ANVUR)

Next assessment: Unknown
Researchers submitted three selections of their work — six if

they had no teaching commitments — published between 2004 and 2010.

The research outputs were evaluated by 14 subject panels. Science panels made extensive use of bibliometrics. Large, medium and small universities were ranked separately, as were research agencies and inter-university consortia.

The results were made public and were used to distribute around €540 million (US\$729 million) as part of the 2013 university budget.



AUSTRALIA

Name: Excellence in Research for Australia

Next assessment: 2015

Universities track every piece of research output from their academics; more than 400,000

pieces were submitted in 2012.

Output is reviewed by expert panels, using metrics such as citation counts and patents filed, as well as research funding and signs of prestige including researchers' membership of learned academies.

The results are released publicly to allow comparisons between institutions, but just Aus\$68 million (US\$64 million) is distributed according to the outcome.

rankings determined the disbursement of just Aus\$68 million (US\$64 million). The outcome is mainly used to give institutions an idea of where they stand in terms of national and international quality, says Aidan Byrne, chief executive of the research council.

The exercise has added benefits, he says. For example, it helps to verify that the council is distributing its Aus\$800-million competitive-grants portfolio in a reasonable way. With a round of assessments costing Aus\$4 million,

the UCU's survey is the stipulation by many universities that researchers must have produced four high-quality publications between 2008 and 2013, says Stefano Fella, a national industrial-relations official at the union. Of the academics polled, 67% felt that they could not produce the required output without working excessive hours — and 34% said that the stress was affecting their health. Many have reported changing how they approach their work, says Fella — for

“You should do good science, and not think in this appallingly strategic way.”

says Byrne, “it’s a very efficient method of quality control”. Although there is no formal connection between the ERA and the grants process, the academics who peer-review grant applications are aware of ERA outcomes, and that feeds into their decisions, he says.

GROWING PAINS

It is too early to know how the newer assessment efforts in Italy, Australia and other countries will affect the research environment there (see ‘Stand and be counted’). But researchers say that they have seen enough of the long-lived UK programme to know some of the downsides.

One of the main worries that came up in

example, some might have rushed to get a publication in the assessment period, even if the work might have benefited from more time. “They don’t think about the best way to present the work,” says Fella, “but what would be best for the REF?”

Frederic Lee, an economist at the University of Missouri–Kansas City, has studied how the UK research-assessment system has affected his discipline. He experienced two rounds of assessments first-hand while working at De Montfort University in Leicester in the 1990s. He says that economists who study alternative theories such as Marxism have been squeezed out because the assessment has consistently favoured mainstream work at elite institutions,

published in a small subset of journals. “There has been a lemming effect that has led to a homogeneity of research topics,” he says.

Lee says that he was never pressured to abandon his research on the history of heterodox economic theories in the United Kingdom, but was encouraged to submit his work to particular mainstream journals, where it stood a slim chance of getting accepted. Other academics have told him that they have been pressured to switch to more conventional research topics, and some had been squeezed out of departments at major institutions. *Nature* spoke to one economist at the University of Manchester who studies alternative theories, and who left the department in part because the focus on RAE-friendly theories meant that prospects for advancement seemed essentially non-existent.

Academics are particularly worried about the move to assess the impact of research in the REF. They fear that this signals a preference for short-term, applied work over basic research that has no obvious, immediate public benefit. “As far as I’m concerned, you should do good science, and not think in this appallingly strategic way,” says Bishop. “Some good science takes a long time to do well.”

The time, effort and money being spent on submissions are also a major concern: preparations for the 2008 RAE cost universities £47 million, according to a 2009 review of the exercise. Even smaller universities such as Lancaster asked several academics to spend months reviewing applications for mock REFs. The time burden can be even worse for administrators, who might have to hire extra staff to work on the REF, says Bishop. University College London, for example, has recruited four editorial consultants to work on the impact portion of the assessment.

McMillan says that it is natural to spend a bit more time and money when preparing to tackle a new criterion. “It’s a dimension that we’re not used to.” He adds that administrators at Lancaster are hiring external professional editors to help with only the final part of the process: polishing the case studies and impact statements that are written by academics and the university’s research support office. Still, McMillan himself is currently spending two to three days a week tweaking Lancaster’s submissions. “I think the REF is probably taking up more time than previous exercises,” he says. “The shift to the impact agenda has seen a big increase in the workload.”

But some universities have seen the benefits of all that work. The vast improvements made by Royal Holloway’s psychology department demonstrate how much periodic evaluations can help, says Rastle. “Having the REF hanging over our heads makes sure we take all the steps we can to get the best out of our people.” ■

Brian Owens is a freelance writer based in New Brunswick, Canada.

THE GOLDEN CLUB

Publishing in the most prestigious journals can open doors, but their cachet is under attack.

BY EUGENIE SAMUEL REICH

Jeffrey Rimer has noticed a change in the way other scientists treat him since his paper on kidney-stone growth inhibitors appeared on the cover of *Science* three years ago. When his colleagues introduce him, they often mention his publications or the publicity he has garnered, which he interprets as a nod to his *Science* paper¹. “From the reaction of colleagues, it’s almost like you’ve joined a club,” says Rimer, a chemical engineer and assistant professor at the University of Houston in Texas. “Fair or unfair, it’s like you’ve proved you can do good science.”

Researchers often say that publishing in prestigious journals can make a career. And for decades, the most sought after of the bunch have been *Nature* and *Science* — broadly read journals that reject more than 90% of the manuscripts they receive. A paper in one of these journals, it is said, can bring job opportunities, invitations to speak, grants, promotions and even cash bonuses and prizes. Rimer believes that his *Science* paper contributed to his winning a grant from the Welch Foundation, a chemical-research funding organization based in Houston, in 2012, and he expects that it may help when he seeks tenure at his university.

His impressions echo what many other scientists say — often with gritted teeth — about premier journals. But the publishing world is rapidly changing, and the leading titles are facing increasing competition. The push for open-access publishing has gathered steady steam; more than 5,000 open-access journals have been launched since Rimer’s paper was published in October 2010. These journals, along with the more established open-access publications, are attracting a growing share of submissions, threatening the hold of the leading journals.

Beyond that trend, some advocates for the open-access movement have specifically attacked *Science* and *Nature*, which they label as ‘glamour journals’. They say that the journals’ prestige is part of a business model in which hot findings are flaunted as a way to justify their subscription rates. And many senior scientists worry that too much attention is paid to where people publish rather than to what they have done — that *Science*, *Nature* and similar publications hold too much sway over the careers of working scientists. “It’s like a kind of addiction,” says Stephen Curry, a structural biologist at Imperial College London who has been vocal about the issue on his blog, Reciprocal Space.

To get a sense of whether the changes in the publishing landscape have altered the allure and impact of top-tier journals, *Nature* interviewed Rimer and several



IMPACT

A *Nature* special issue
nature.com/impact

VIEWS FROM THE LAB BENCH

**ANKE BILL**

Says that her *Cell* paper helped her job search.

**YINGJIE PENG**

Says that astronomers do not generally care where papers appear.

**ANNELE VIRTANEN**

Says that her *Nature* paper opened doors outside her field.

**JEFFREY RIMER**

Says that his *Science* paper helped him to win a grant.

**PING CHI**

Says that her *Nature* paper helped to start a clinical trial.

other early-career researchers who published for the first time in *Nature*, *Science* or other journals in October 2010 (see 'Views from the lab bench').

Several of those researchers say that three years on, they feel that getting a paper in a premier journal helped their careers in concrete ways. Although they cannot know how their careers would have unfolded without these high-profile publications, what they believe is still telling. It is why some of them are reluctant to join established scientists who say that they will not submit to *Nature* and *Science* as a matter of principle, a step many younger researchers are unwilling to take.

Yet critics are working hard to change how researchers — and those who assess their work — judge the value of different publications. Sandra Schmid, head of the cell biology department at the University of Texas Southwestern Medical School in Dallas, is one of many academics advocating ways to identify promising candidates other than simply looking for leading journals on their CVs. "The drive to publish in these journals does more harm than good," she says.

PUBLICATION PUBLICITY

Ping Chi, a medical oncologist who landed a paper² in *Nature* three years ago, says that she got an important boost towards launching a clinical trial of new cancer drugs, which is now starting up. Her paper investigated how two proteins stabilize the survival of gastrointestinal tumours. Had it been published in a lesser-known journal, she says, she might still have been hired by Memorial Sloan-Kettering Cancer Center in New York, but she probably would not have received such a generous start-up package and would have spent some of the past two years raising funds. Instead, she put her energy into persuading her collaborators and pharmaceutical companies to support the clinical trial of a therapy that inhibits the proteins.

The *Nature* paper, Chi says, helped to establish her work as a significant advance, especially because it received media attention

(thanks in part to a press release issued by *Nature's* press office).

In some developing countries, publishing in top-tier journals has extra appeal; researchers in China and India sometimes receive bonuses or salary increases when they get papers into *Science* or *Nature*. Yingjie Peng, a Chinese-born astrophysicist and postdoctoral researcher at the Cavendish Laboratory of the University of Cambridge, UK, says that if he were to seek a faculty position in China, it would be invaluable to have a *Nature* or *Science* paper. "Government officials may not understand the work — the easy thing to do is compare journals," he says.

Peng argues that publishing in elite journals is less important in the United States and the United Kingdom. Most astronomers see papers as soon as they are posted to the arXiv.org preprint server. And where a paper is published is not as important as who did the work and how technically adept it is. Peng is doing well in terms of recognition; his paper³ on galaxy evolution, published in *The Astrophysical Journal* three years ago, has already received a substantial count of more than 150 citations.

The Astrophysical Journal allows longer papers than *Science* and *Nature* typically would, which gave Peng a chance to fully explain his method for extracting laws of galaxy evolution from data rather than deriving them entirely theoretically. He credits the paper with helping him to get his position at the Cavendish.

Anke Bill, a cell biologist at the Novartis Institutes for Biomedical Research in Cambridge, Massachusetts, had a similar experience with her 2010 paper⁴ in *Cell*, a specialized journal that is highly prestigious in the biological sciences. Her paper focused on cytohesins, proteins thought to be involved in human lung cancer. Bill says that she and her adviser had initially aimed for the wider exposure that would come from publishing in *Nature*. But they say that they received a tough set of reviews that required more experiments. When Bill resubmitted the paper with the extra data, *Nature's* editors decided that the paper was too long and technical, she says, but *Cell*

accepted the paper in its expanded form.

Bill says that beyond the world of biomedical science, a *Nature* or *Science* paper would have boosted her reputation more. But within her field, she says, the *Cell* paper had a big impact. It may have helped her to land her current position, especially because the laboratory at the German university where she did her PhD was not well known outside that country. The *Cell* paper showed that she could develop and test a promising novel hypothesis. "I got positive feedback everywhere I applied," she says.

Other researchers point to the advantages of less selective journals, such as *PLoS ONE*, which publishes a high volume of papers online. Nicholas Longrich, was a postdoc in palaeontology at Yale University in New Haven, Connecticut, when he published his 2010 paper⁵ in *PLoS ONE* showing evidence of cannibalism in *Tyrannosaurus rex*. "The fact that you probably won't get it rejected and have to submit elsewhere means you can get your work out quickly," he says.

Longrich also liked that *PLoS ONE* is open access, which made it easier for his *T. rex* work to be read by others. Still, he says that he did not land his current job as a lecturer at the University of Bath, UK, until he published three more papers, in subscription-based journals (*Nature*, *The Proceedings of the National Academy of Sciences* and *Current Biology*). "Did *Nature* help my career more than *PLoS*? I can't prove it, but I think so," he says.

MEASURING IMPACT

Critics of the status quo object to evaluating research on the basis of where it is published. The shorthand way to do this is by the journal impact factor — an index kept by Thomson Reuters, an information-services company based in New York. A journal's 2013 impact factor, for example, would be computed by summing the number of citations garnered this year to papers published in that journal in 2011–12 and then dividing that sum by the number of papers the journal published during that span.

Curry, who received hundreds of comments

ILLUSTRATIONS BY MARTIN HARGREAVES, BASED ON PHOTOGRAPHS BY PJ KASZAS/NOVARTIS (AB); KEVIN FAGAN/UNIV. CAMBRIDGE (TP); RAJJA TORRONEN (AV); MSHCC (PC)

SOURCES: NATURE, SCOPUS/ELSEVIER

on his blog when he criticized impact factors in 2012, says that *Nature* and *Science* may command high reputations in part because they have high impact factors (38.6 and 31, respectively, in 2012), but those figures are averages that are pulled upwards by a few very frequently cited papers. It is not rational, he says, for papers that are not cited as often to get a boost just because they come out in the same journal.

Some experts are taking active steps to challenge the sway of the leading journals. In December 2012, hundreds of scientific leaders, funding bodies, journals (including *Science*, but not *Nature*) and other organizations gathered in San Francisco, California, to sign the Declaration on Research Assessment (DORA), which criticizes reliance on the impact factor and commits signatories to evaluate research on the basis of its scientific merit. Schmid, the Texas cell-biology chair, signed DORA and published a commentary in *Science Careers*⁶ saying that her department will no longer filter applicants for faculty jobs on the basis of their publications.

Her department fills one or two faculty positions a year and receives as many as 300 applications for each one. In the past, the department weeded out candidates who had not published in top-tier journals, but Schmid dislikes that approach. "How many brilliant scientists are just outside the spotlight?" she says. She is now filtering candidates on the basis of a covering letter describing their past work and how they envision their future.

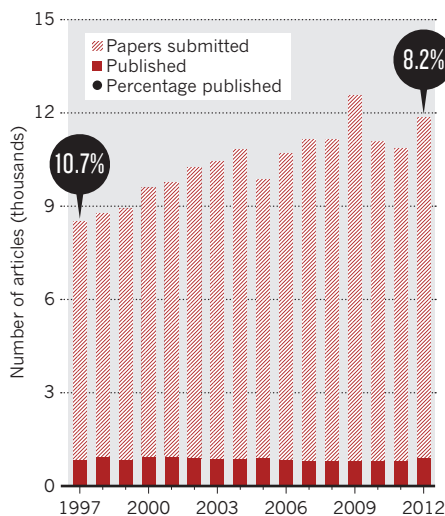
RANKINGS RACE

It is hard to assess how widespread such changes are, because research evaluations and hiring processes are often confidential. But Henk Moed, a bibliometrician and scientific adviser at Elsevier, a science publisher in Amsterdam, suspects that the journal impact factor still looms large in many hiring decisions. Evaluators may decide privately to average the impact factors of the journals listed on a CV as a way to rank candidates. He notes that some institutional rankings, such as the Academic Ranking of World Universities, compiled by Shanghai Jiao Tong University, give explicit weight to the number of *Nature* and *Science* papers an institution has produced — making it likely that some universities would then begin to rank prospective faculty by the same measure. "There is more and more evaluation, and a need for researchers to prove their quality," Moed says. "Journal reputations play a role, and that role has increased."

Others echo Moed's sense that *Nature* and *Science* papers are often relied upon implicitly. Amy Ruschak, a biochemist and assistant professor at Case Western Reserve University in Cleveland, Ohio, says that her 2010 *Nature* paper⁷ on a cellular apparatus that destroys toxic proteins was a highlight of her application for faculty positions and undoubtedly contributed to her success. "It's central, but no one will specifically say that," she says.

GROWING COMPETITION

Submissions to *Nature* have risen over the past 16 years, and the journal has become more selective. But the growth in submissions is slower than the worldwide increase in the number of published papers.



Moed notes that bibliometricians are trying to improve measures of journal quality while also educating researchers about the value and limitations of such metrics. And Stefano Bertuzzi, executive director of the American Society for Cell Biology in Bethesda, Maryland, which spearheaded DORA, says that although the current scientific culture unduly rewards *Nature* and *Science* publications, he thinks that the rapid growth of open access to articles online will change that. "Open-access articles get read a lot, so they should gain visibility," he says.

Visibility is what motivated Olga Momcilovic, a cell biology postdoc at the Buck Institute for Research on Aging in Novato, California, to send her paper⁸ on DNA damage in stem cells to *PLoS ONE* in 2010. "Social media and Google searches list papers by relevance, not by impact factor," she says.

There are some signs that the leading journals are not keeping pace with the overall growth in publishing. According to information made available by *Nature* and *Science*, submissions to both journals have climbed over the past ten years, reaching more than 10,000 per year for *Nature* and more than 12,000 for *Science*. However, the number of articles published worldwide in all journals has been rising much more rapidly, suggesting that many researchers are looking to publish elsewhere (see 'Growing competition').

A similar story emerges from data on the most highly cited papers. In 2012, Vincent Larivière, an information scientist at the University of Montreal in Canada, studied the clout of *Nature*, *Science* and other top journals by examining citation statistics⁹. He found that although these journals are publishing a growing number of highly cited papers each year, they are not keeping up with the industry as a whole; overall, their proportion of the total number of highly cited papers is declining.



Nature and *Science* have press offices that are more active than those of many other journals, however — making it more likely that papers published there will receive notice. And because electronic publishing has led to a flood of online information, journals that can claim to be highly selective fill a niche by elevating papers worthy of reading, says Larivière.

Annele Virtanen, an aerosol chemist who is now an assistant professor at the University of Eastern Finland in Kuopio, agrees. She was a postdoc in 2010, when she published a *Nature* paper¹⁰ showing that organic aerosol particles that most researchers had assumed were liquid were probably solid. The publication opened all kinds of doors for Virtanen. The journal's visibility meant that climate modellers and atmospheric chemists outside her original research field saw her paper, and many wrote to her, helping to drive her current research in a more generally relevant direction.

She now has more results and is thinking of submitting to *Nature* again — or to *Science*. Shooting for these publications, she believes, means reaching to do excellent research that will stand out. "It improves the level of science," she says. "I can't see so many bad sides." ■

Eugenie Samuel Reich reports for *Nature* from Boston.

1. Rimer, J. D. *et al.* *Science* **330**, 337–341 (2010).
2. Chi, P. *et al.* *Nature* **467**, 849–853 (2010).
3. Peng, Y. *et al.* *Astrophys. J.* **721**, 193–221 (2010).
4. Bill, A. *et al.* *Cell* **143**, 201–211 (2010).
5. Longrich, N. R., Horner, J. R., Erickson, G. M. & Currie, P. J. *PLoS ONE* **5**, e13419 (2010).
6. Schmid, S. L. *Science Careers* <http://dx.doi.org/10.1126/science.caredita.1300186> (2013).
7. Ruschak, A. M., Religa, T. L., Breuer, S., Witt, S. & Kay, L. E. *Nature* **467**, 868–871 (2010).
8. Momcilovic, O. *et al.* *PLoS ONE* **5**, e13410 (2010).
9. Lozano, G. A., Larivière, V. & Gingras Y. Preprint at <http://arxiv.org/abs/1304.6460> (2013).
10. Virtanen, A. *et al.* *Nature* **467**, 824–827 (2010).

COMMENT

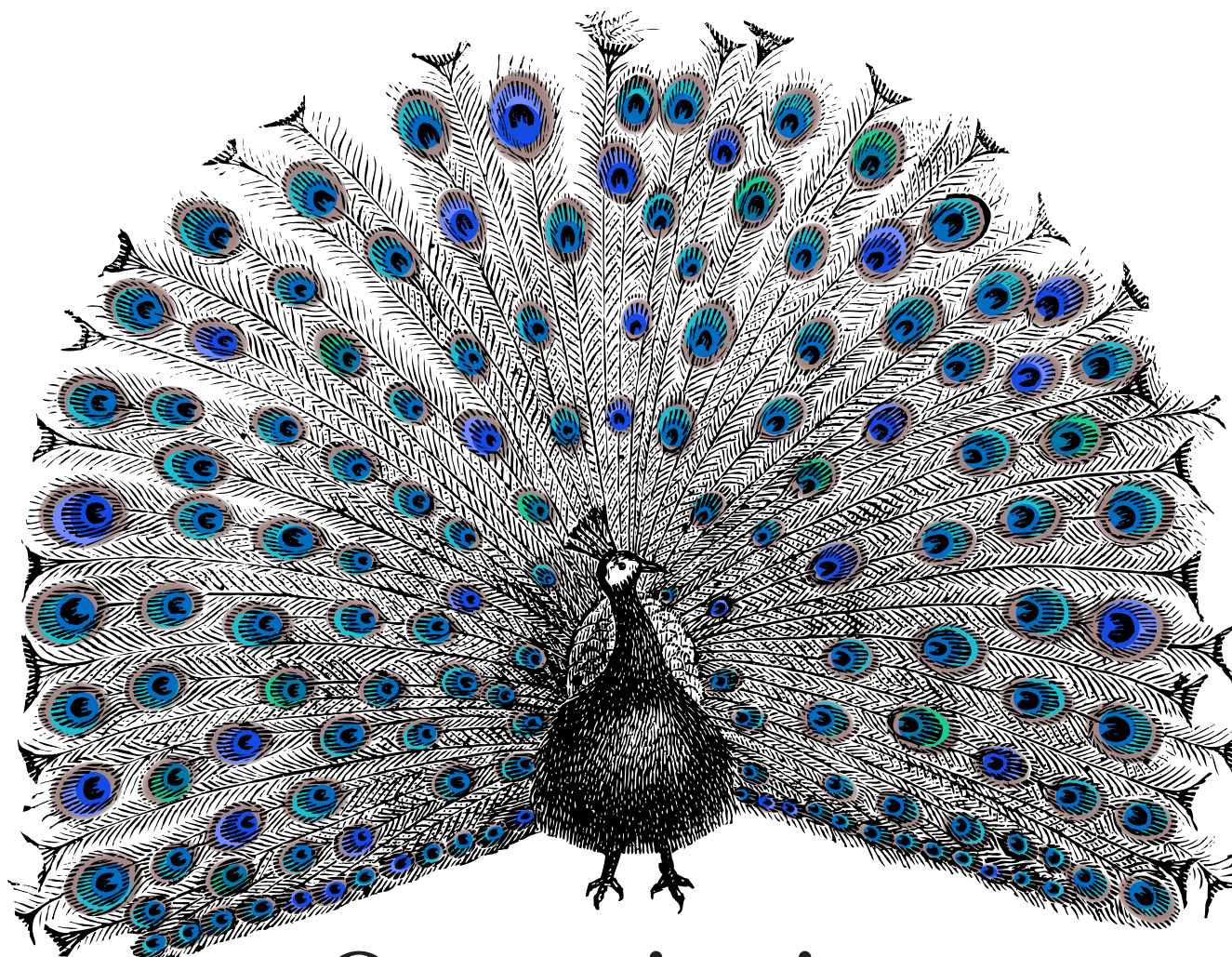
IMPACT Make data findable, shareable and citable urges Mark Hahnel **p.298**

TECHNOLOGY What could make our ever-expanding cities smarter? **p.299**

PHYSICS A celebration of Einstein's contributions to quantum theory **p.300**



OBITUARY David Barker, who linked early life with chronic disease, remembered **p.304**



Open citations

Make bibliographic citation data freely available and substantial benefits will flow, says **David Shotton**, director of the Open Citations Corpus.

When Heather Piwowar set out in May last year to investigate whether making research data publicly available increased the citation rates of articles¹, she never anticipated the difficulties. Piwowar, co-founder of ImpactStory², and who is based in Vancouver, Canada, was at the time a postdoc at Duke University in North Carolina. Lacking institutional access to Scopus, Elsevier's database of scholarly

citations, she eventually obtained access through a research-worker agreement with Canada's National Science Library. But this required her to be fingerprinted to obtain a police clearance certificate because she had



IMPACT
A Nature special issue
nature.com/impact

lived in the United States. "I wasted days trying to access the citation data required for my study," she told me. "It was just ridiculous." Piwowar needed to analyse citation counts for 10,000 articles, but the other major citation source, the Thomson Reuters Web of Science, did not at the time support queries using PubMed's unique identifier numbers. She explains: "Had there been open citation data, I could have written my own script!" ►

► Steven Greenberg, a neurologist at Harvard Medical School in Boston, Massachusetts, had a similar experience when he set about revealing how hypotheses can be converted into 'facts' simply by repeated citation³. Greenberg had manually to construct and analyse a citation network that contained 242 papers, 675 citations and 220,553 distinct citation paths that were relevant to a particular hypothesis. Had those citation data been readily accessible online, he would have been saved considerable effort. Research practice suffers because access to citation data is currently so difficult.

In this open-access age, it is a scandal that reference lists from journal articles — core elements of scholarly communication that permit the attribution of credit and integrate our independent research endeavours — are not readily and freely available for use by all scholars.

To rectify this, citation data now need to be recognized as a part of the commons — those works that are freely and legally available for sharing — and placed in an open repository. To that end, since 2010 I have led a project funded by two small grants totalling £132,000 (US\$212,000) from Jisc (www.jisc.ac.uk), a UK information technology research and development funding organization, to establish and develop the Open Citations Corpus (OCC). The OCC is a fledgling repository for open scholarly citation data that is now seeking sustainable funding to become a cornerstone of the digital research infrastructure that supports the academic enterprise.

CLOSED SHOP

Although alternative metrics for impact and esteem are being developed⁴, direct citation remains a keystone indicator of the significance of an output (see page 298). Scholarly communication involves the flow of information and ideas through the citation network, and analysis of changes in the network over time can reveal patterns of communication between scholars and the development and demise of academic disciplines. Such information is central to scholarly endeavour. It is also fundamental to good decision-making about research investment and strategy, to facilitate innovation, and to promote growth and prosperity, particularly in light of the increasingly international nature of research collaborations⁵.

The most authoritative sources of scholarly citation data are the Thomson Reuters Web of Science, which grew from the Science Citation Index created by US

FREEDOM OF INFORMATION

Bibliographic citation data are freely available from an estimated 4% of the world's scholarly literature.

204,637

Articles in the Open Access Subset of PubMed Central from which citation data are already available in the Open Citations Corpus (OCC)

468,805

New articles in the Open Access Subset of PubMed Central from which references are being added to the OCC

881,216

Preprints in arXiv from which references are being added to the OCC

Unquantified overlap

1,242,041

Articles in CiteSeerX from which citation information is available

545,641

Articles in CitEc from which citation information is available

~2,130,000

Articles in the rest of PubMed Central from which references are potentially available

~50,000,000

All scholarly journal articles and books from which bibliographic reference data could be extracted

scientist Eugene Garfield in 1964, and which was originally published by the Institute for Scientific Information (ISI); and its main commercial rival, Elsevier's Scopus, released in 2004. Both have wide coverage of the leading literature, but because neither is complete, they are widely regarded as complementary⁶.

For access to these two resources, UK research universities each pay tens of thousands of pounds a year⁶, with equivalent sums charged at institutions in other developed countries. The exact values of these subscriptions are closely guarded industrial secrets, and the university librarians who pay these fees are bound by confidentiality agreements from disclosing them. This high cost severely disadvantages all those who work outside such wealthy institutions, including most businesses and the general public. The other significant sources of citation information, also run by commercial companies but accessible without subscriptions, are Google Scholar and Microsoft Academic Search, released in 2004 and 2009, respectively. Google Scholar's coverage is wider than that of the others, because it includes books, theses, preprints, technical reports and other non-peer-reviewed 'grey' literature.

All these sources have licence restrictions that prevent the re-publication of their citation data. For this reason, bibliometrics papers are rarely permitted to publish the data on which their conclusions are based — hampering reuse, validation of findings and other advantages of open data.

Worse, the available citation data are not accurate. My own citation record differs considerably across the Web of Science, Scopus, Google Scholar and Microsoft Academic Search. For example, a 2009 paper⁷ on semantic publishing that I co-authored currently has citation counts of 22, 37, 88 and 16, respectively, in these four databases. Which to trust?

More worryingly, an earlier protein-crystallography paper⁸ has three separate entries in the Web of Science, with citation counts of 59, 19 and 0, respectively. In my view, this calls into question the reliability of the Thomson Reuters Impact Factor, which is based on such counts.

A SOLUTION

The OCC, as an open repository of scholarly citation data made available under a Creative Commons public domain dedication, is attempting to improve matters. It aims to provide accurate citation data that others may freely build upon, enhance and reuse for any purpose, without

restriction under copyright or database law.

We began building the OCC in mid-2010, and released the first version in mid-2011. This prototype provided open access to reference lists from the 204,637 articles that then comprised the Open Access Subset of PubMed Central (OA-PMC), containing 6,325,178 individual references to 3,373,961 unique papers. Despite its small size, this corpus contains references to about 20% of all the biomedical literature indexed in PubMed that had been published between 1950 and 2010, including all highly cited papers in every biomedical field. Available at <http://opencitations.net>, the OCC is structured to enable the information to be easily integrated with similar information from elsewhere — the data are encoded as Linked Open Data using the SPAR (Semantic Publishing and Referencing) Ontologies⁹ and the latest Semantic Web standards.

Other open citations resources exist. The two main ones are CiteSeerX (citeseerx.ist.psu.edu), which contains around 13,500,000 references from 1,242,041 articles, primarily in computer science; and CitEc (Citations in Economics; citec.repec.org), which contains 13,544,970 references from 545,641 documents. Together, these resources and the OCC have the references from some 1,980,000 articles — a mere 4% of the estimated 50 million articles that have been published (see 'Freedom of information').

We are currently revising the OCC data model, improving its hosting infrastructure and expanding its coverage, both by updating the OA-PMC holdings, which have more than doubled since the initial ingest to 672,442 articles, and by ingesting citation data from the 881,216 preprints in the arXiv server, thus adding citations in mathematics and the 'hard' sciences to augment the initial biomedical coverage. Future work will include integration with CiteSeerX, harvesting dataset-to-article references from the Dryad Digital Repository, and extracting references from the pre-digital 'legacy' literature that is poorly represented in other citation repositories. This applies particularly to fields in which such literature is both well organized and of enduring value — notably astronomy, and biodiversity and biological taxonomy.

Ideally, references will come directly from publishers at the time of article publication. Most publishers are sympathetic to the idea of putting article reference lists outside the journal-subscription payroll, as they do copyrighted abstracts. We already have agreements with several major journal publishers for the future routine harvesting of reference data. As well as the 'pure' open-access publishers, the references from which are open by definition, the publishers of subscription-access journals include Nature Publishing Group (NPG), Oxford University Press, the American Association for the

Advancement of Science (which publishes *Science*), Royal Society Publishing, Portland Press, MIT Press and Taylor & Francis, all of which will make references available either from some or from all of their journals. This represents a small but growing proportion of all the journal articles published in a year.

References will be harvested centrally from CrossRef, the organization that provides digital object identifiers (DOI) for

"Ideally, references will come directly from publishers at the time of article publication."

journal articles, to which these publishers already submit article reference lists as participants in its CitedBy Linking service. However, publishers need to indicate their consent in the article meta-data for the article's references to be made open (see go.nature.com/x4pzta), because by default references are kept private. No other action is required; it is straightforward and free.

The long-term aim of the OCC is to host citation information for most of the world's scholarly literature, in the arts and humanities as well as the sciences. This will require a major curatorial effort and underpinning technical innovation, on the scale of PubMed, which is run by the US National Library of Medicine.

OPEN SEASON

In an ideal world, publishers would host their own bibliographic and citation data, following the example of NPG (publishers of this journal) — the first and currently only company to make such information available as Linked Open Data, at data.nature.com.

But there are separate benefits to be gained from the aggregation of such data into a single corpus. The OCC will provide integrated access to citation data from a variety of sources, inside and outside traditional scholarly publishing, with clear provenance data. It will expose entity relationships, including article-to-article, article-to-database and database-to-article citations, and will reveal shared authorship and institutional membership, common funding, and semantic relationships between articles, where the data are available.

Once citation data are openly available, useful analytical services can be built, including faceted search-and-browse tools, recommendation and trend identification services, and timeline visualization. Some of these we have already developed in prototype. The OCC's usefulness for calculating citation metrics will, of course, increase in proportion to its expanding coverage.

There is one other service that we think could be of particular benefit to authors and editors — an erroneous reference

correction service. About 1% of references in published papers contain errors of varying severity, ranging from the trivial — for example, substitution of 'beta amylase' for 'β-amylase' in the reference title, or the omission of accents in author names — to the more serious, such as errors in the year, volume, page numbers or DOI. The OCC already uses citation-correction methods internally for reference targets that are multiply cited, or for which authoritative bibliographic records can be obtained externally. A similar Web service that could detect errors in uploaded reference lists might significantly reduce the number of mistakes in published papers.

HELP US

So what next? Just over a decade ago, a similar aim for open citation data was held by the Open Citation Project (opcit.eprints.org), a collaboration between Southampton University, UK; Cornell University in Ithaca, New York; and arXiv, that ran between 1999 and 2002. That project developed Citebase, a database of citation information, which its developers described as "the crown jewel of the Open Citation Project". Following the link to citebase.eprints.org today, one gets the message "No website currently exists at this URL."

Making the transition from a promising academic project to a robust sustainable global service is extremely difficult. For the OCC to avoid the fate of Citebase, and instead grow into a comprehensive and trustworthy source of well-curated open citation data serving the entire scholarly community across all disciplines, it requires champions, managers, developers and curators. It also needs genuine collaborations with similar endeavours, a sustained and sizeable income stream from funders, supporters and investors committed to achieving a social good rather than a financial return, direct support from the publishing community, and adoption by a major institution or international organization. Can you help? ■

David Shotton is director of the Open Citations Corpus and a senior research fellow in the Oxford e-Research Centre, University of Oxford, UK.
e-mail: david.shotton@oerc.ox.ac.uk

1. Piwowar, H. A. & Vision, T. J. *PeerJ* **1**, e175 (2013).
2. Piwowar, H. *Nature* **493**, 159 (2013).
3. Greenberg, S. A. *Br. Med. J.* **339**, b2680 (2009).
4. Priem, J. *Nature* **495**, 437–440 (2013).
5. Adams, J. *Nature* **490**, 335–336 (2012).
6. Chadevani, A. A. et al. *Asian Social Sci.* **9**, 18–26 (2013).
7. Shotton, D., Portwin, K., Klyne, G. & Miles, A. *PLoS Comput. Biol.* **5**, e1000361 (2009).
8. Shotton, D. M., White, N. J. & Watson, H. C. *Cold Spring Harb. Symp. Quant. Biol.* **36**, 91–105 (1972).
9. Peroni, S. & Shotton, D. *Web Semant.* **17**, 33–34 (2012).

The reuse factor

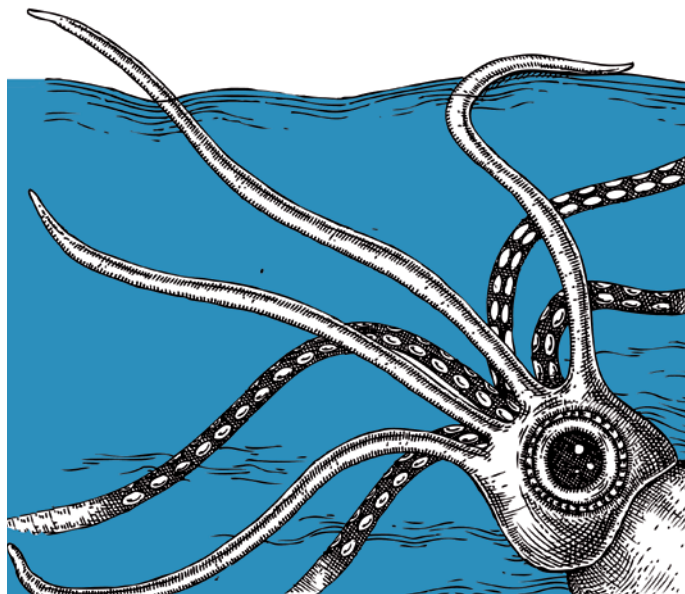
The reference is not dead — it is exploding to encompass the full spectrum of research outputs from lines of code to video frames, explains **Mark Hahnel**.

Researchers are still struggling to find, manipulate and cite research outputs other than published papers. Data-management plans for research — detailing what data will be created and how, and outlining plans for data sharing and preservation — are a core requisite of all grant applications for a long list of US and UK funding agencies. These include the US National Science Foundation, the US National Institutes of Health, NASA, the UK Biotechnology and Biological Sciences Research Council, the UK Medical Research Council and the Wellcome Trust. Funders require grantees to make all their products available in a citable, sharable and discoverable manner. As a result, tools such as the California Digital Library's Data Management Plan and the UK-based Digital Curation Centre's DMPonline have materialized to help optimistic grant applicants to fill in this section.

Even with the help of such tools, data-management plans are being rejected in some grant applications. This is a wake-up call. Researchers should be long past thinking that depositing their data in a file-hosting service such as Dropbox is sufficient. Yet the majority of academics still consider journal articles to be the only valid, formal record of their research — the main currency for credit.

In my view, the current model of grouping non-image files together in supplemental data appended to a paper is laughable. Data are the bedrock of a paper and come in myriad forms; for instance, videos for research on cell motility or biomechanics, or code for climate or epidemiology models. Scholars are increasingly sharing these sorts of raw data through repositories such as the Dryad Digital Repository and GenBank, which allow for the citation of data sets, videos, genetic sequences and other such files that publishers often struggle to accommodate.

In 2011, I set up another such company, figshare, to improve the way that the 'data behind the graph' is disseminated, exploiting visualization tools such as D3.js and Jmol¹. At figshare, we work with research groups and publishers to make data reusable, reproducible and interactive. (Macmillan Science and Education, the publisher of



PIKA/SHUTTERSTOCK

this journal, is an investor in figshare.)

But the generation of huge numbers of citable research outputs is confusing researchers who are accustomed to citing only papers. The FORCE11 Amsterdam manifesto on data-citation principles, drawn up in 2011 by a community of scholars, librarians, archivists, publishers and research funders, states: "A data citation in a publication should resemble a bibliographic citation and be located in the publication's reference list." A quick look at the most recent journal citations of data held in figshare shows that this recommendation is not enforced by publishers or authors: only one in five cited the data in the reference list; the rest mentioned it in methods or deposition sections.

There are standard protocols for citing static data such as genomes or clinical-trial results². But data is increasingly dynamic, coming from sensors that monitor, for example, geophysical and atmospheric changes in real time. Tracking these feeds in a way that is automated and machine-processable will lead to improved validation and verification, and help to prevent falsification of data that, in areas such as climate-change research, has led to much unnecessary wrangling³.

Scientists should appreciate that making their research outputs citable enables more of

their research to have quantifiable impact. To this end, the Research Data Alliance (RDA) was established in August 2012 by a steering group of funding agencies from the United States, Europe and Australia. The RDA aims to accelerate and facilitate research data sharing and exchange across multiple disciplines that have complicated funder mandates and a need to cite various unconventional research outputs. An RDA working group plans to provide prototypes and examples. For instance, individual cells of a spreadsheet or a few frames of a video can be cited in a way that does not dilute a paper's total number of citations.

Early adopters of open-data science are already seeing the benefits. Computer scientist

Titus Brown at Michigan State University in East Lansing, for example, blogged, "My career has already been immeasurably improved by my openness, including posting our software." And the efficiency gains are long overdue.

I believe that publishers should mandate that all the research that goes into forming the conclusions of a paper be made openly available, when ethically possible. Even better would be for raw data to be made available in the paper, as *F1000 Research*, an open-access journal, and PLoS journals already do for their articles. Publishers should also ensure that all citations — to products of all kinds — are included in reference lists, and should make this bibliometric data openly available in a searchable format (see page 295).

Are we witnessing the death of the reference? No, we are seeing the birth of an exponentially larger number of citations, crediting a much wider variety of outputs. The end is nigh for the measuring of impact using only citations to published papers: this is the age of the 'reuse factor'. ■

Mark Hahnel is founder of figshare.
e-mail: mark@figshare.com



IMPACT
A Nature special issue
nature.com/impact

1. Cowley, M. J., Huch, V., Rzepa, H. S. & Scheschke, D. *Nature Chem.* **5**, 876–879 (2013).
2. Altman, M. & King, G. 'A proposed standard for the scholarly citation of quantitative data' *D-Lib Magazine* (2007); available at <http://go.nature.com/sv314e>.
3. Heffernan, O. *Nature* **460**, 787 (2009).



The operations centre that IBM designed for Rio de Janeiro in Brazil helps to coordinate the city's activities.

INFORMATION TECHNOLOGY

Slouching towards utopia

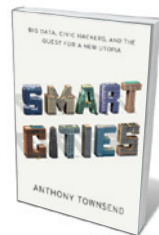
As interests vie for the soul of smart cities, **Melanie Moses** asks: “Smarter for whom?”

Some 3.5 billion people — half of humanity — now live in cities. Cities magnify human endeavours: they account for much more than half of humanity's pollution, energy consumption, crime and disease spread, while also incubating the lion's share of innovations, technology, art and entertainment. A sustainable, equitable future on our crowded planet will require fundamental changes in how cities operate. In *Smart Cities*, Anthony Townsend examines how information technology is shaping the development of 'smart' cities.

What makes them smart? Accessible and efficient services, transportation and infrastructure are essential to the mix. Bike-share programmes, for example, exemplify smart urban problem-solving by reducing traffic and pollution, encouraging exercise and providing cheap transport. Information technology makes it possible to adapt bike placement to the variable flow of riders, who use smart phones to find them. And smart cities need not reinvent the wheel: bike-share programmes have spread rapidly since the first large-scale launch in Paris in 2007, with now hundreds of thousands of bikes in cities from Beijing to Stockholm. Each scheme has evolved to meet local needs, leading to the emergence of solar-powered bike stations, stationless bike exchanges and new car-sharing

schemes. Pricing, funding and management also evolve in partnerships between non-profit organizations, governments and, increasingly, corporations. (It's no secret who funds New York's Citi Bike.)

But corporate involvement is a mixed blessing. Uproar greeted the recent revelation that the US National Security Agency has been monitoring communications across the globe, but Townsend cautions that city halls and their corporate partners may be intruding on your privacy at a more intimate scale. For example, in Rio de Janeiro, IBM's Intelligent Operations Center, which was originally designed for disaster management, has become a “mission control center for mayors” with “people looking into every corner of the city, 24 hours a day, 7 days a week” in order to reduce urban crime and ensure that buses run on time. South Korea has teamed up with Cisco Systems and invested US\$35 billion in Songdo, a model city for energy conservation through



Smart Cities: Big Data, Civic Hackers, and the Quest for a New Utopia
ANTHONY M. TOWNSEND
W. W. Norton: 2013.

ubiquitous computing. Millions of sensors are embedded in roads and power grids to track and predict people's movements. Townsend argues that a relentless focus on efficiency has been “engineering serendipity out of the urban equation”, damping the creative spark that makes cities dynamic and adaptable.

Townsend contrasts top-down, corporate urban management with bottom-up action by civic hackers and engaged citizens who provide creative, but not always scalable, technologies to empower people. Among his compelling examples is Access Together, a crowdsourced online mapping tool that provides information on accessibility for disabled New Yorkers. Another example is from Nairobi, where in 2009 activists literally put the Kibera slum on the map by walking the streets with Global Positioning System receivers. The lives of a quarter of a million people suddenly became visible; before Google Maps had shown just a forest. Such crowdsourced cartography is a first step in demanding water, sanitation and other government services. This is real inclusivity, Townsend notes, whereas many smart solutions deemed successes are developed by, and largely for, the privileged. Bike shares are great for young commuters, but they don't do much for the elderly, disabled or struggling families with young children. ▶

► With such caveats, Townsend conveys a cautious optimism that information technology might make cities smarter. But the book only nibbles at the edges of fundamental shifts in how data-driven cities might operate in future. Top-down versus bottom-up approaches to urban development are discussed anecdotally, neglecting a deeper analysis of cities that exemplify an organic “organized complexity”, as social critic Jane Jacobs described decades ago.

Perhaps the history of failed top-down urban planning models has left Townsend sceptical of systematic and quantitative scientific analyses of cities. However, we need a scientific understanding of what makes cities adaptive, resilient and prosperous, as we create ever more, and ever larger, urban environments.

In *The New Science of Cities* (MIT Press, 2013), urban planner Michael Batty proposes a new approach based on models grounded in volumes of data that reveal fine details of how individuals behave in urban environments. Equally important is a growing understanding of cities as dynamic systems driven by top-down and bottom-up processes. The macroscopic analysis of cities led by Luis Bettencourt and Geoffrey West at the Santa Fe Institute in New Mexico reveals regularities in how cities are distributed and grow, and common patterns in how transportation, the pace of innovation and economic activity vary across cities of different sizes.

“Cities will need to be smarter than the sum of their parts.”

This work, and my own, suggests that urban energy and information flow are governed by basic physical principles, even given cities’ different histories, politics and cultures. To understand cities, we need not just the abundant data that sensorised cities will produce, but also a new framework to understand how individual stories are woven into vibrant urban systems.

On a rapidly urbanizing planet, smart cities will dominate the human cultural landscape and affect how we live, consume resources and manage the environment. Cities will need to be smarter than the sum of their parts and founded on more than routers, protocols and social networking apps. Townsend begins a conversation, but we owe it to ourselves to develop a quantitative, integrated science of cities to guide our vision of how we will grow, govern, live and work in tomorrow’s smart cities.

Melanie E. Moses is an associate professor of computer science and biology at the University of New Mexico and external faculty of the Santa Fe Institute. e-mail: melaniem@cs.unm.edu

QUANTUM PHYSICS

Packet man

Graham Farmelo delights in a study of Albert Einstein’s under-appreciated contributions to quantum theory.

In 1941, US physicist John Wheeler visited Albert Einstein, the arch quantum sceptic, at his home in Princeton, New Jersey. Wheeler was hoping that the beauty of the new version of quantum theory developed by his brilliant student Richard Feynman would persuade Einstein to accept that the theory was simply a natural development of well-founded classical ideas. The sage of Princeton listened in silence as Wheeler set out his case, but afterwards was no more enthusiastic. “Of course, I may be wrong,” he said, “but perhaps I have earned the right to make my mistakes.”

Einstein was by that time a semi-detached member of the physics community, admired much less for his current work than for his achievements. Many of his colleagues thought his views on quantum theory cranky — Robert Oppenheimer dismissed them as “cuckoo”. That opinion is sometimes echoed today in popular books, many of which underestimate his contributions to the theory.

In *Einstein and the Quantum*, Douglas Stone attempts to put that right. He describes Einstein’s work on the theory using few equations, combining scientific and biographical accuracy with wide accessibility. Stone, a distinguished condensed-matter physicist at Yale University in New Haven, Connecticut, brings a wealth of physical insight and — less predictably — an impressive familiarity with the work of leading Einstein scholars.

In 1900, Max Planck introduced the revolutionary idea of energy quantization in the interaction between matter and radiation in black bodies. But, as Stone explains, it was Einstein who first understood the implications. In 1905, the 26-year-old physics wizard radically suggested that the energy of electromagnetic radiation is transferred in the discrete amounts that Planck called quanta. For physicists of the day, long familiar with James Clerk Maxwell’s wave description of light, Einstein’s notion was beyond heretical. Few leading theoreticians took it seriously, least of all Planck.

Even Einstein wavered. He strove for years to understand radiation quanta, for example by tinkering with Maxwell’s equations of electromagnetism. Eventually he abandoned this approach, having introduced the useful but murky concept of wave-particle duality.

Einstein and the Quantum: The Quest of the Valiant Swabian
A. DOUGLAS STONE
Princeton University Press: 2013.



Albert Einstein at his home in Berlin.

Yet, more than any other scientist, Einstein ran with the quantum idea. Applying it to the vibrational energies of atoms, he used it to predict that the specific heats of solids should vanish as the temperature is lowered towards absolute zero. Quoting an early statement of Einstein’s about atomic energy, Stone adds with characteristic pith that energy quantization “is not a mathematical trick; it is the way of the atomic world. Get used to it.”

Each of the 29 chapters in *Einstein and the*

UNDERWOOD & UNDERWOOD/CORBIS

Quantum is brief, pacy and lucid (although some titles are perhaps too clever: for example, 'Stalking the Planck'). The breadth and depth of Einstein's contribution in this area becomes overwhelmingly clear. Eleven years after his first great paper on the subject, he delivered a theory of transitions that introduced into quantum theory the idea of probabilities, which he came to despise. Finally, in 1924, he built on the thinking of Indian physicist Satyendra Bose about quantum gases and predicted that, under some conditions, a high proportion of particles could occupy the lowest quantum state, enabling quantum effects to appear in the everyday world. This was later called Bose–Einstein condensation and was first observed experimentally in 1995.

Stone covers all this with clarity and even tackles Einstein's little-known 1917 paper on the quantization of chaotic systems. This chapter will probably leave non-specialists scratching their heads, but it is worth a read because it demonstrates that there is more to Einstein's *oeuvre* than even most quantum physicists know. Stone concludes that Einstein's work was worthy of four Nobel prizes, and it is a measure of the book's achievement that his claim sounds quite reasonable.

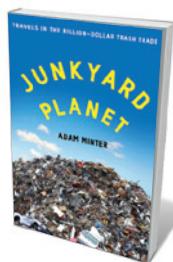
It was left to Werner Heisenberg, Erwin Schrödinger and Paul Dirac to set out the full-blown quantum theory of matter in the mid-1920s. Einstein was a formidable critic of the theory, although he was always outwitted in argument by his friend Niels Bohr — a topic treated only briefly in the book, probably because this ground is so well-trodden. Yet all the originators were indebted to Einstein's thinking. As Max Born later said, he was "clearly involved in the foundation of wave mechanics and no alibi can disprove it".

In old age, Einstein seemed indifferent to his reputation as a fuddy-duddy, but the criticisms may have hurt more than he let on. I have often wondered how he felt when he saw the Princeton University Players' production of William Shakespeare's *The Tempest* in July 1953, especially when Prospero contemplates the fleeting nature of existence that leaves "not a rack behind". Einstein died less than two years later. He was proud to have built the great edifice of relativity, but still profoundly dissatisfied with quantum theory, which he was confident would be superseded.

Was he wrong? Some theoretical physicists are now speculating that space and time might in some sense emerge from the more fundamental quantum, so it may be that scientists will one day regard Einstein's greatest achievement as pioneering a theory he believed was terribly flawed. In the meantime, Stone's rewarding book helps us to appreciate the remarkable extent of that feat. ■

Graham Farmelo is a By-Fellow at Churchill College, University of Cambridge, UK.
e-mail: graham@grahamfarmelo.com

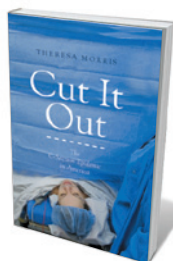
Books in brief



Junkyard Planet: Travels in the Billion-Dollar Trash Trade

Adam Minter BLOOMSBURY (2013)

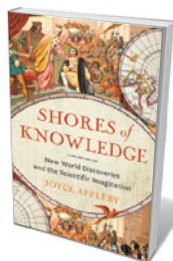
Junk really is filthy lucre — the basis of a global scrap trade worth up to US\$500 billion a year, writes Adam Minter. Scion of a professional recycling family, Minter anatomizes this complicated, half-hidden industry that he argues is, even at its dirtiest, greener than harvesting raw resources. He focuses on scrap metal, a prized commodity now recycled in innovative ways, and the kingpins of the trade. Leonard Fritz, for instance, rose from extreme poverty to run the Michigan-based Huron Valley Steel Corporation, which annually processes almost half a million tonnes of shredded automobile.



Cut It Out: The C-Section Epidemic in America

Theresa Morris NEW YORK UNIVERSITY PRESS (2013)

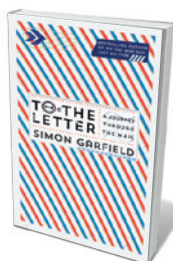
Birth by Caesarean section is expensive and carries a higher risk of medical complications than vaginal birth. Yet in 2011, 33% of US births were by Caesarean. To investigate why, sociologist Theresa Morris crunched the numbers and interviewed more than 100 medical staff and mothers. The culprit, she concludes in this excellent and detailed study, is a risk-averse US medical culture that favours heavily managed births — such as the overzealous use of fetal heart monitors, which restrict the mother's movement — and that frowns on women having vaginal births after Caesareans.



Shores of Knowledge: New World Discoveries and the Scientific Imagination

Joyce Appleby W. W. NORTON (2013)

A sea change gripped Europe from the late 1400s as word of the thrillingly strange New World spread. Maps were redrawn and the 'book of nature' swelled with new species, from penguins to chillies. In a history stretching from Christopher Columbus to Charles Darwin, Joyce Appleby reveals how a thirst for empiricism grew with the need to sift out tall tales from genuine reportage. She treads the trail of paper and specimens left by the likes of ethnographer Bernardino de Sahagún and "first ecologist" Alexander von Humboldt.



To the Letter: A Journey Through a Vanishing World

Simon Garfield CANONGATE (2013)

The letter — that pillar of the historical record — may itself soon be history. As Simon Garfield reminds us in this elegy to the post, letters uniquely revivify past eras and the psychological complexities of people living through them. The first stirrings and exponential rise of e-mail are touched on, but Garfield's focus is the physical missive and the depth of thought it allows. From wooden tablets dug up at the ancient Roman garrison Vindolanda, UK, to the epistolary gems of novelist Virginia Woolf, this is a billet-doux to two millennia of the impassioned, often life-changing power of private correspondence.



Survive! Inside the Human Body, Vol. 1: The Digestive System

Gomdori co., Suk-young Song and Hyun-dong Han NO STARCH PRESS (2013)

From volcanic burps to colonic bacteria, this comic-book ride through the human digestive system is a delirious joy for pretty much everyone aged eight and over. Hyun-dong Han's lurid images and zippy text by Suk-young Song deliver on facts even as they shamelessly milk the 'yuck' factor. Take the plunge with hero Geo and "self-proclaimed genius" Dr. Brain as they shrink and are sucked into the ever-hungry Phoebe: the ultimate inside story. [Barbara Kiser](#)



The eruption of Mount Pinatubo in the Philippines in June 1991 cooled the globe.

GEOENGINEERING

One cool solution

Nicola Jones finds a treatise on a proposed global-warming fix intriguing, but isn't converted to the cause.

It is 2030, and a fleet of ten Gulfstream business jets have been converted to a new purpose: dispensing 250,000 tonnes of sulphates a year into the lower stratosphere. Here the chemicals form sunlight-reflecting droplets that cool the planet below. This artificial volcanic haze, costing about US\$700 million a year, helps to mitigate the warming effect of greenhouse gases.

This is the vision of David Keith, a physicist and self-described “oddball environmentalist”. His company, Carbon Engineering, is currently pursuing a device that can suck carbon dioxide out of the air (see *Nature* **458**, 1094–1097; 2009). Now, in *A Case for Climate Engineering*, Keith considers the partner concept of cooling the world by deflecting sunlight. Unlike journalist Eli Kintisch's 2010 book *Hack the Planet*, this is not an exploration of all geoengineering schemes told through compelling stories and characters. Rather, it is a straightforward presentation of one controversial, planet-altering idea — along with an intriguing discussion of the philosophical roots of environmentalism.

Mopping up carbon dioxide, as Keith's company aims to do, is expensive but carries no global risk. Conversely, sulphate spraying

is very cheap: the cost of a decade's worth of Sun-blocking might be just a few billion dollars, compared to the \$300 billion being spent per year globally on clean-energy technologies, writes Keith. But the possible downsides range from disrupting rainfall and interfering with the ozone layer to creating acid rain and removing political incentives to reduce emissions.

Keith is a member of the ‘geo-clique’, a small group of researchers who have spent serious time considering such schemes. His work has earned him everything from being named a 2009 ‘Hero of the Environment’ by *Time* magazine to outrage from colleagues — and even death threats. Geoengineering has been labelled crazy: geophysicist Ray Pierrehumbert called it “barking mad”. And just last month, former Royal Society head Martin Rees dubbed it “an utter political nightmare”.

Sulphates are certainly effective coolants. Atmospheric sulphur dioxide from the 1991 eruption of Mount Pinatubo cooled the globe by 0.5 °C in less than a year. Since the 1970s, a few scientists have explored the logistics and risks of mimicking this process.

A Case for Climate Engineering

DAVID KEITH
MIT Press: 2013.

It has become apparent, for example, that counteracting all greenhouse-gas warming with sulphates would result in a world with less rainfall. Keith's group has found, however, that countering just a fraction of the world's warming with sulphates could mitigate the rainfall changes caused by our current emissions of greenhouse gases. For this reason, among others, Keith prefers to investigate a Sun-shading scheme that aims to counter just half of the world's temperature rise (for example, reducing a catastrophic rise of 4 °C to 2 °C, the “upper bound of acceptable warming”), and only for a limited time.

But there are problems. The cooling action of sulphates doesn't follow the same pattern as the warming action of carbon dioxide: sulphates are more effective during the day and in summer, for example, whereas carbon dioxide acts all year round. Nor can sulphates counteract ocean acidification. And the resulting air pollution would probably cause thousands of deaths each year from asthma, heart disease and lung cancer, writes Keith. There are few facts and figures in the book with which to weigh up these dangers: the risk of acid rain, for example, he simply dismisses as “relatively small” compared to the hazards of rapid climate change.

Strangely unmentioned in Keith's book is the United Nations ban against geoengineering. In 2008, the United Nations Convention on Biological Diversity enacted a moratorium against iron fertilization — the idea of sprinkling iron into the ocean to feed phytoplankton and thus soak up atmospheric carbon dioxide. This ban was extended in 2010 to all temperature-fiddling geoengineering projects, including Sun-blocking schemes.

The moratorium, which is intended to prevent commercial projects or large-scale efforts while allowing for small-scale experimentation, has been used by protestors to try to block all iron-fertilization experimentation. Keith's book might be a pre-emptive strike against things going the same way for solar geoengineering; he and his colleagues are contemplating small-scale experiments now.

Keith's goal with this book, he writes, is to convince us that deciding whether or not to pursue geoengineering is a “hard choice”, not an easy decision based on instinctive revulsion. He succeeds, but this is a low bar. Where he fails is in convincing us to agree with him that “deliberate haste” is called for.

General readers will probably find *A Case for Climate Engineering* a bit dry; academics might judge it too light. But it should stand as an enticing starter for the researchers who Keith hopes to rope into the field, thereby expanding the ‘geo-clique’ and helping to push the science into the mainstream. ■

Nicola Jones is a freelance science journalist based near Vancouver, Canada.
e-mail: nkjones@gmail.com

Correspondence

No bias behind pollinator research

We disagree with Ian Boyd's implication that bias may have influenced the commissioning and publication of research on pollinator declines (*Nature* **501**, 159–160; 2013).

Our paper on falls in European bee-species richness (J. C. Biesmeijer *et al.* *Science* **313**, 351–354; 2006), along with others on honeybee colony collapse and bumblebee declines, prompted widespread public concern. Subsequent decisions in continental Europe and the United Kingdom to commission further research in this area therefore seemed sensible and proportionate.

These calls for research used “pollinator declines” as a convenient shorthand, not to steer the work. This is borne out by results from the studies funded, including our own, indicating that past declines in some pollinator groups may have recently slowed or even partially reversed (L. G. Carvalheiro *et al.* *Ecol. Lett.* **16**, 870–878; 2013).

Publication bias undoubtedly occurs, but it can be identified only by reviewing whole fields, not individual papers. This should be addressed as part of a systematic review when policy issues arise, as carried out by the UK's Parliamentary Office of Science and Technology or by independent research teams.

We agree that there are uncertainties in our conclusions, as Boyd suggests; indeed, our papers list strong caveats pertaining to our data sets and methodology, which were largely ignored by the media.

A national pollinator-monitoring programme, recommended recently in a parliamentary report, would provide much more robust estimates of pollinator trends in future.

William E. Kunin* *University of Leeds, UK.*
w.e.kunin@leeds.ac.uk

**On behalf of 5 co-signatories (see go.nature.com/setpu6 for full list).*

Genetic engineering in conservation

Species bearing genetically engineered adaptive variants that are intended to save them from extinction might differ in important respects from the original species designated for protection — with unpredictable ecological consequences (see M. A. Thomas *et al.* *Nature* **501**, 485–486; 2013).

Introducing adaptive variants by genetic engineering might work for some long-lived plants in which disease resistance is primarily due to a single gene (J. M. Adams *et al.* *Conserv. Biol.* **16**, 874–879; 2002), and for economically important traits in agricultural crops grown in controlled environments. In wild endangered species, however, identifying ‘missing’ adaptive single-gene variants and increasing their frequency without causing negative side effects is almost certain to prove impossible.

Genetically based inferior fitness in endangered populations — including in the Florida panthers and Swedish vipers cited by Thomas and his colleagues — has been traced to an increased frequency of detrimental alleles from inbreeding or a loss of genetic variation, and not to a lack of adaptive variants.

Improving connectivity with outside populations would rescue the fitness of such endangered populations by introducing greater genetic variation, non-detrimental variants, and adaptive alleles that have already been well tested by evolution.

Philip W. Hedrick *Arizona State University, Tempe, USA.*
philip.hedrick@asu.edu

Fred W. Allendorf *University of Montana, Missoula, USA.*

Robin S. Waples *National Marine Fisheries Service, Seattle, Washington, USA.*

Safeguard species in warming flatlands

To protect the biodiversity of flatlands against the effects of climate change (M. Tingley *et al.* *Nature* **500**, 271–272; 2013), we need strategies to buy time for species to adapt to warmer environments or to move to cooler ones. This will mean adding more protected areas in cool regions and improving connectivity between protected sites.

One way to increase resilience among resident communities would be to reduce the intensity of summer grazing on flatlands. Shade from tall, dense swards helps to cool the soil by up to 5 °C (J. A. Thomas *et al.* *Science* **325**, 80–83; 2009), an effect that is enhanced as the land becomes more uneven (J. Settele and E. Kühn *Science* **325**, 41–42; 2009).

Conservation measures in existing protected sites, as in Europe's Natura 2000 programme (see go.nature.com/ykf7vt), remain important but may prove inadequate on their own and will need to be adapted and revived as the climate warms.

Josef Settele, Ingolf Kühn *Helmholtz Centre for Environmental Research, Halle, Germany.*

josef.settele@ufz.de

Jeremy A. Thomas *University of Oxford, UK.*

Metaphors advance scientific research

As a former collaborator in Eleonore Pauwels' research on the misuse of metaphors by synthetic biologists, I agree with many of her points but find her perspective too restrictive (*Nature* **500**, 523–524; 2013). In my view, the use of analogies, concepts and metaphors is crucial for advancing scientific research.

Pauwels tends to merge metaphors with analogies and theoretical concepts. Her

examples of oscillators, switches and logic gates, which have a precise meaning in engineering, are better viewed as the analogical transfer of a scientific concept (see also B. Calcott *Nature* **502**, 170; 2013). To treat them as though they were on a par with expressions such as ‘selfish gene’, ‘software of life’ or ‘household of nature’ does not capture the ways in which they are used in scientific practice.

Metaphors and analogies have long driven cross-disciplinary exchange. For example, the early mathematization of biology and economics in the nineteenth and twentieth centuries was largely built on analogies with physics. Analogies and metaphors have also contributed substantially to ideas developed in cognitive science and in the philosophy and history of science (reviewed in J. Maienschein *et al.* *Isis* **99**, 341–349; 2008).

Andrea Loettgers *University of Geneva, Switzerland.*

andrea.loettgers@unige.ch

Keep PubMed running at all costs

With more than 23 million citations to date from MEDLINE, life-science journals and online books, the giant National Institutes of Health database PubMed is arguably the most valuable tool available to biomedical scientists. Its vulnerability has been highlighted by this month's partial US government shutdown, with only minimal updates and maintenance to PubMed possible.

To avoid lapsing into another dark age of research, the ongoing maintenance of PubMed must be guaranteed. We urge the scientific community to push for PubMed to be entirely supported and commissioned by an international forum.

Alex W. Hewitt, David A. Mackey *Lions Eye Institute, Perth, Australia.*
hewitt.alex@gmail.com

David Barker

(1938–2013)

Epidemiologist who traced roots of chronic disease to early life.

David Barker was one of the most influential clinical epidemiologists of our time. He challenged the idea that chronic disorders such as diabetes and cardiovascular disease are explained only by bad genes and unhealthy adult lifestyles. His 'Barker hypothesis' proposed that the fetal environment and early infant health permanently programme the body's metabolism and growth, and thus determine the pathologies of old age. Initially controversial, his ideas triggered an explosion of research worldwide into the relationship between early development and adult disease.

Barker died suddenly from a cerebral haemorrhage on 27 August, aged 75. Born in 1938, he was educated at Oundle School, UK. His biology teacher encouraged him to roam the countryside hunting for beetles, and gave him access to the labs to classify his finds. When Barker left school, he led a project on the Icelandic island of Grimsey to collect plant specimens for the Natural History Museum in London.

During his medical training at Guy's Hospital in London, he took a year out to complete a bachelor's degree in physical anthropology, comparative anatomy, embryology and mammalian biology. He studied under the eminent zoologist J. Z. Young, and published his first paper, on the effects of testosterone on bone density, in *Nature* in 1962.

In 1966, Barker completed his PhD thesis on prenatal influences and subnormal intelligence, a forerunner to his later work on fetal programming. With a Medical Research Council (MRC) grant, he worked in Uganda on *Mycobacterium ulcerans* infection (Buruli ulcer). When the country descended into crisis in the 1970s under President Idi Amin, Barker, fearing for his family's safety, fled through the night with his wife and four young children into neighbouring Kenya. By then, he had done enough research to link the transmission of Buruli ulcer to wounds caused by the razor-sharp reeds growing near the river Nile, proving that it was not an insect-borne disease.

In 1972, Barker joined the University of Southampton, UK, where he remained for the rest of his career. An inspiring teacher,

he set up an annual course on epidemiology for clinicians, with fellow epidemiologist Geoffrey Rose. The course remains the definitive introduction to the field for researchers. In 1984, Barker became director of the MRC Environmental Epidemiology Unit in Southampton.



The unit's detailed mapping of mortality trends in England and Wales led to his observation that areas with the highest infant mortality in 1910 had the highest rate of cardiovascular deaths in the 1970s. With his lifelong research partner, Clive Osmond, Barker developed his hypothesis that an adverse environment in the womb, and during infancy, was causally linked to chronic-disease risk later in life.

He devoted the next three decades of his life to the pursuit of this idea. And through various and diverse collaborations, Barker made many significant advances. With colleagues at his MRC Unit and in Cambridge, he showed that people of lower weight at birth and in infancy were more prone to cardiovascular disease, hypertension and diabetes in middle

age. Collaborating with researchers from the Helsinki Birth Cohort study, which tracks the long-term health impacts of early growth, he linked patterns of childhood growth to these conditions. And with colleagues in India, he showed similar relationships in developing-world populations. His work also formed the basis for linking the until then separate worlds of fetal physiology and epidemiology, bringing together physiologists from Australia, New Zealand and Canada who were studying fetal development in animals. Ultimately, Barker published 500 research papers and 10 books, and had numerous honours to his name.

David never retired. After stepping down as director of the Southampton unit in 2003, he continued to work at what is now called the MRC Lifecourse Epidemiology Unit, and to contribute to the studies that he established — the Hertfordshire Cohort Study and the Southampton Women's Survey. He also helped to set up the Southampton Initiative for Health to find practical ways of improving the diets of low-income mothers in the United Kingdom. In his last few years, he turned his focus to the placenta as the channel of communication between mother and fetus, and spent several months a year working at the Oregon Health and Science University in Portland — a leading placental-research centre — and at Emory University in Atlanta, Georgia, working on the biology of human growth.

Of all his characteristics, I, like other colleagues, will most fondly remember David's humour; he was a brilliant raconteur and often sought as an after-dinner speaker. He was a private, thoughtful and caring man, for whom family life was central. After the death of his first wife, Angela, he married Jan in 1983. Their home housed four generations, and became a centre for scientific work, to which they welcomed visitors from around the world. ■

Cyrus Cooper is director of the Medical Research Council Lifecourse Epidemiology Unit, University of Southampton, UK. During the 1980s, he worked as a clinician for David Barker, who supervised his doctoral research at the MRC Unit. e-mail: cc@mrc.soton.ac.uk

BARKER FAMILY

FORUM Genomics

Comparisons across cancers

Analysis of cancer genomes is moving beyond the confines of a particular disease — researchers are now comparing the genetic and epigenetic characteristics of multiple tumour types. Two scientists comment on what such studies can teach us about cancer biology and how they may guide clinical practice. [SEE ARTICLE P.333](#)

THE PAPER IN BRIEF

- Research networks around the world are cataloguing DNA mutations, chemical changes to DNA-associated proteins, and expression of RNA transcripts and proteins in thousands of human tumours.
- In a series of 16 papers¹, one of which is published on page 333 of this issue (Kandoth *et al.*)², The Cancer Genome Atlas (TCGA) Research Network presents comparisons of such data across as many

as 12 tumour types (Fig. 1).

- The publications join other pan-cancer efforts in revealing commonalities between all cancer types, shared molecular abnormalities in tumours that superficially seem distinct, and mutations that are confined to specific tumours.

- The findings will guide the development of prognostic, diagnostic and therapeutic strategies.

Order from disorder sprung

ALAN ASHWORTH

During the past few years, the advent of hugely powerful DNA-sequencing technologies has delivered unprecedented insight into the nature of cancer genomes³. Hundreds of examples of genomes from several cancer types have already been produced, and this process will continue so that a definitive overview of cancer genomics can eventually be achieved. Nevertheless, it seems apposite to take stock of the themes that are emerging from comparisons of the genomes of different tumour types^{2,4} — studies that are giving us a fascinating first peek at the common mutational events and processes that shape cancer genomes.

The first impression that emerges from these comparisons is of the tremendous variation. Some types of cancer have, on average, relatively few genetic changes, whereas others show extraordinary mutational complexity. It is likely that most mutations in cancer genomes represent collateral damage that is unrelated to pathogenesis, but studies seeking candidates for driver mutations — those that contribute to the disease state⁵ — are revealing that both the number and nature of these candidates also differ considerably between cancers³. In some cases, we are seeing distinct cancer types with alterations in the same

cellular pathway brought about through driver mutations in different genes.

Mutual exclusivity of mutations in genes or pathways is also becoming apparent^{2,3}, providing clues as to which genes or pathways have non-redundant roles in oncogenesis. Using such data, we may eventually be able to understand the totality of biological perturbations that, acting together, result in the phenotypic diversity of human cancer. There is also the potential to deconvolve the order in which pathways are altered during disease progression, which is likely to be non-random owing to genetic interactions⁶. Gaining understanding of these two issues may be key to successful prevention and treatment strategies.

Comparing the type and frequency of genetic alterations, and the overall genomic structure, in different tumour classes also gives insight into the underlying mutational processes at play⁴. The accumulation of mutagenic cellular processes, endogenous and environmental exposures, and DNA-repair defects over many years or decades results in genomic 'scars'⁷ that can help us to understand the cause of the disease in an individual. The mutagenic fingerprints of tobacco smoking and sunlight exposure, for example, are obviously manifest in some cancers, but new phenomena are also being described and neologisms coined to describe them, such as chromothripsis for the shattering of individual chromosomes⁸ or kataegis for discrete genomic regions peppered with mutations⁹. Many other previously unknown mutational processes also seem to be involved in the development of

particular cancers. Studying these may reveal other influences on cancer development⁴.

An enormous amount has already been gleaned from these initial analyses, but much remains to be done. First, there is a strong case for completing a comprehensive and detailed survey of the entire panoply of human cancers. Paradoxically, rather than increasing complexity, this should allow further common themes to emerge from the noise. Second, most analyses of driver mutations have focused on protein-coding regions, which comprise only about 1% of the human genome. But it seems probable that studying non-coding regions will reveal a wealth of cancer-related mutations. Third, epigenetic alterations to the genome — which affect gene expression without changing the underlying DNA sequence — that cause or occur during cancer development need to be integrated into this landscape. Fourth, most of the tumours studied so far have been primary cancers before treatment; metastatic and treatment-resistant genomes also need to be studied in detail. Last, several studies have highlighted the genetic variation between individual cells within a tumour, and further analysis is needed to ascertain the prevalence of this phenomenon.

Alan Ashworth is at the Institute of Cancer Research, London SW7 3RP, UK.
e-mail: alan.ashworth@icr.ac.uk

A clinical perspective

THOMAS J. HUDSON

Classifying cancers using a broad, cross-tumour perspective provides not only biological insight, but also clinically relevant information. The value of the pan-cancer approach is demonstrated by Kandoth and colleagues' study² focusing on the simplest forms of mutation — single-nucleotide substitutions, or insertions or deletions of a few nucleotides, in the sequences of protein-coding genes. By

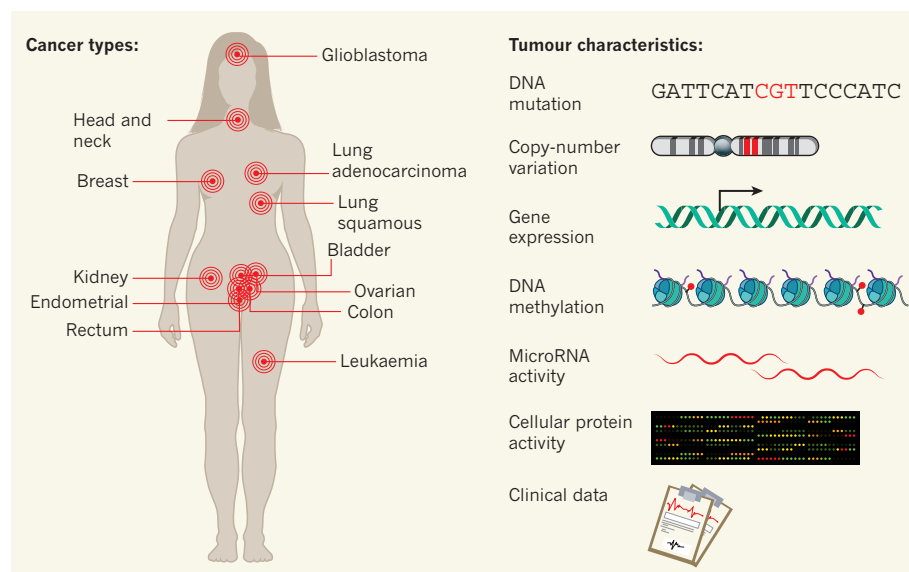


Figure 1 | Pan-cancer analysis. The Cancer Genome Atlas Research Network has presented a series¹ of initial findings from comparisons of the tumour characteristics and clinical data of thousands of patients, covering 12 major types of cancer.

applying stringent statistical tests based on the recurrence rates of such mutations, the authors identify 127 genes that are significantly mutated in a combined analysis of 3,281 tumours representing 12 tumour types. Although many genes in the list have previously been reported as mutated in cancer, the occurrence of these mutations across a wide range of cancers has not been appreciated until now.

Kandoth *et al.* also investigated these 127 genes as indicators of disease prognosis, using clinical data collected by the TCGA¹⁰, such as time to disease recurrence and time to death. Although survival analyses across cancer types are made difficult by the heterogeneity of clinical features related to different tumours, such as age of presentation, treatment modalities or metastatic potential, the large size of the study gave sufficient power to reveal several prognostic correlates. For example, mutations in several genes, including *BAP1*, *DNMT3A*, *KDM5C*, *FBXW7* and *TP53*, were found to correlate with poor prognosis, whereas mutations in two genes, *BRCA2* and *IDH1*, often correlated with improved prognosis.

It is worth noting that multi-tumour analyses can miss biomarkers that are prognostic indicators in single tumour types (such as *KDM6A* and *ARID1A* in bladder cancer), affirming the value of analysing data at both the individual tissue-type and pan-cancer levels. However, if the prognostic significance of pan-cancer genes is validated in large prospective studies of patients with cancer, clinical assessments of these genes may help to identify patients at higher risk of metastatic relapse, who could benefit from adjuvant therapies. This strategy has already been applied in patients with early-onset breast cancer through the use of multi-gene expression profiles^{11,12}.

In future, it will be useful to correlate genes identified as being relevant to multiple cancer types with drug responses, although this information will require greater integration of genomic profiles in clinical trials and cancer registries¹³, and new models of data sharing among research institutions¹⁴.

How can this pan-cancer project be exploited in drug development? One way is through the ranking of drug targets, which can be used to prioritize drug-development projects. More important, however, is the identification of functional relationships between groups of genes, or pathways. Pharmacological modulation of such pathways provides an alternative route for drug development when candidate genes encode proteins that are not deemed to be appropriate drug targets. Several

pathways implicated recently by other cancer-genome projects (such as pathways involved in RNA splicing, transcription regulation and metabolism) have been confirmed in the pan-cancer analysis, reinforcing the idea that these pathways should be considered as therapeutic targets.

We should anticipate many more surprises as additional tumour types¹⁵, mutation categories (including those in non-coding regions of the genome) and functional annotations of genomes¹⁶ are integrated in the next generation of pan-cancer studies. The determination of the common denominators — and the outliers — in cancer has the potential to benefit patients through improved laboratory tests, new drug-development opportunities and better-informed treatment decisions. ■

Thomas J. Hudson is at the Ontario Institute for Cancer Research, Toronto, Ontario M5G 0A3, Canada.

e-mail: tom.hudson@oicr.on.ca

1. www.nature.com/ng/focus/tcga/index.html
2. Kandoth, C. *et al.* *Nature* **502**, 333–339 (2013).
3. Garraway, L. A. & Lander, E. S. *Cell* **153**, 17–37 (2013).
4. Alexandrov, L. B. *et al.* *Nature* **500**, 415–421 (2013).
5. Lawrence, M. S. *et al.* *Nature* **499**, 214–218 (2013).
6. Ashworth, A., Lord, C. J. & Reis-Filho, J. S. *Cell* **145**, 30–38 (2011).
7. Lord, C. J. & Ashworth, A. *Nature* **481**, 287–294 (2012).
8. Stephens, P. J. *et al.* *Cell* **144**, 27–40 (2011).
9. Nik-Zainal, S. *et al.* *Cell* **149**, 979–993 (2012).
10. The Cancer Genome Atlas Research Network *Nature Genet.* **45**, 1113–1120 (2013).
11. Glas, A. M. *et al.* *BMC Genomics* **7**, 278 (2006).
12. Paik, S. *et al.* *N. Engl. J. Med.* **351**, 2817–2826 (2004).
13. Dancsey, J. E., Bedard, P. L., Onetto, N. & Hudson, T. J. *Cell* **148**, 409–420 (2012).
14. Check Hayden, E. *Nature* **498**, 16–17 (2013).
15. The International Cancer Genome Consortium *Nature* **464**, 993–998 (2010).
16. The ENCODE Project Consortium *Nature* **489**, 57–74 (2012).

PHYSICAL CHEMISTRY

Combs for molecules

Lasers known as frequency combs have been used to generate molecular spectra from samples within microseconds and with high spatial resolution. This offers fresh prospects for making microscopy observations in real time. SEE LETTER P.355

YARON SILBERBERG

Imagine a microscope that can be tuned to see specific molecules, or to analyse the molecular content of a sample. This dream has driven much of the work in advanced microscopy in recent years, particularly towards instruments that can be tuned to detect molecules through their specific vibration frequencies^{1–3}. In this issue, Ideguchi *et al.*⁴

report a crucial step in this direction: a microscopy method that uses light sources known as frequency combs. The work resolves a problem that has hindered the use of a technique called impulsive Raman spectroscopy in microscopy.

Molecules can be thought of as atoms connected by springs, and so their vibrations depend on their precise structure. This means that each molecule is characterized by a specific set of vibration frequencies, which

generate a 'fingerprint' that can be detected using Raman spectroscopy.

One simple way to induce vibrations in a molecule is to irradiate it with an intense pulse of light. Because molecular vibrations typically oscillate with periods of a few tens of femtoseconds (1 femtosecond is 10^{-15} seconds), the pulse should be no longer than this. To identify the molecule, a second pulse of light is then needed. This pulse may enhance or attenuate the vibration, depending on the delay between the two pulses — that is, depending on when the second pulse arrives relative to the molecular oscillation cycle. More importantly, the vibrating molecules slightly shift the frequency of the delayed light pulse up or down, depending on when exactly it arrives. This spectral shift is easy to detect.

To determine the molecule's vibration frequency, a series of pairs of pulses is used in which the delay between pulses is systematically varied. This causes a periodic change in the output spectrum, from which the molecular vibration frequency can be calculated. If the molecule vibrates at several frequencies, or if the sample contains a mixture of materials, the frequency-shift pattern is more complex, but a simple mathematical analysis can extract individual frequencies, thereby allowing molecules to be identified.

This spectroscopic method, known as impulsive Raman scattering, has been around for a few decades^{5,6}. It has even been adapted for microscopy⁷, but here it suffers from a major drawback: measurements must be performed repeatedly at every point in a sample, with each picture element being acquired quickly enough for a whole image to be obtained in a reasonable time frame. In all previously reported methods, the delay between pulses was varied by mechanically moving a mirror. Such back-and-forth mechanical motions of a mirror cannot be done faster than a few times per second, and therefore acquiring a complete image with a sufficient number of picture elements would take too long for most applications.

Enter the wizardry of frequency combs. These are lasers that produce a train of ultra-short pulses at a highly precise rate, typically around 100 million pulses per second. They generate a precise 'comb' of optical frequencies and so have revolutionized atomic spectroscopy, which requires exquisite frequency control⁸. Indeed, Theodor Hänsch, one of the co-authors of Ideguchi and colleagues' paper, was awarded the 2005 Nobel Prize in Physics for the development of these light sources.

Frequency combs are not obviously suited to molecular spectroscopy and microscopy, because these fields do not usually require the sensitive frequency control of atomic spectroscopy. But Ideguchi and co-workers show that frequency combs can be harnessed to speed up impulsive Raman scattering so that it can be

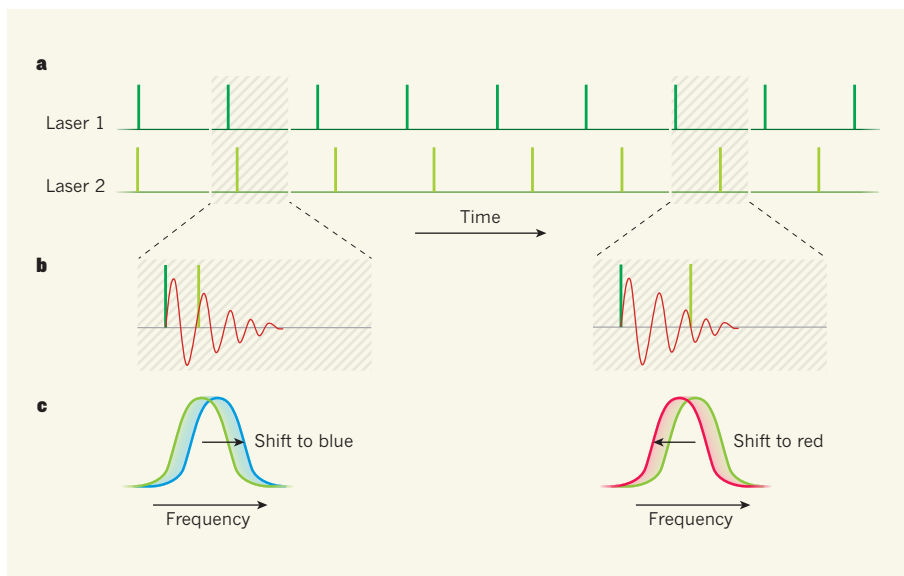


Figure 1 | Frequency combs for molecular spectroscopy. **a**, Ideguchi *et al.*⁴ have used two laser sources (known as frequency combs) that have different pulse-production rates to generate pairs of light pulses (vertical lines) so that the time between pulses varies. **b**, They used these sources to excite molecular vibrations in a sample (not shown). The red line indicates the amplitude of a molecular vibration stimulated by a pulse from laser 1 (dark-green line) over time; the light-green line indicates the arrival time of a pulse from laser 2. Vibration duration is not shown to scale; vibrations last for only a small fraction of the time between consecutive laser pulses. **c**, Vibrations excited by the first pulse shift the spectrum of the second pulse in different directions, depending on the point of the vibration cycle at which the second pulse arrived. The researchers analysed the spectral shifts to determine the frequency of the molecular vibrations.

used for microscopy. The authors combined light from two such lasers, which produce pulses at slightly different repetition rates; the delay between pulses from each laser therefore varies (Fig. 1). This approach to varying the delay requires no moving parts, and the rate of variation can be easily controlled by manipulating the lasers' pulse-production rates.

By using just such a combined laser source and monitoring the output, Ideguchi *et al.* were able to acquire the vibration Raman spectra of samples in just a few microseconds — thousands of times faster than is possible with a mechanically based system, and certainly fast enough to apply the technique to microscopy. They recorded these spectra with sufficient resolution and signal-to-noise ratios to identify the constituents of various mixtures of organic solvents, and to produce molecular images using a simple microscopy set-up.

The authors' system suffers from one major limitation: there is a long 'dead time' for each measurement. Molecular vibrations die out after a few picoseconds (1 picosecond is 10^{-12} seconds), but scanning continues for up to a few nanoseconds, as dictated by the repetition rates of the lasers. In other words, data are collected during only about one-thousandth of the whole measurement time. And not only is most of the measurement time wasted, but also the sample is irradiated with much more light than is necessary for obtaining information.

Ideguchi *et al.* are well aware of these problems, and argue that advances in frequency-comb technology will lead to sources that have

much higher pulse-production rates, which should reduce the amount of dead time considerably. Indeed, frequency-comb sources with a rate of 10^9 pulses per second, ten times higher than the one used by the authors, are already available, and more-exotic sources with even higher rates are being developed. As always, to be useful for microscopy, such sources will need to be engineered to a level that does not require a laser expert to run them, and to be accessibly priced. Such engineering has already brought ultrafast laser technology to a variety of surprising applications, and so the advent of practical, hands-off frequency-comb sources is probably just a matter of time. ■

Yaron Silberberg is in the Department of Physics of Complex Systems, Weizmann Institute of Science, Rehovot 76100, Israel. e-mail: yaron.silberberg@weizmann.ac.il

1. Zumbusch, A., Holtom, G. R. & Xie, X. S. *Phys. Rev. Lett.* **82**, 4142–4145 (1999).
2. Dudovich, N., Oron, D. & Silberberg, Y. *Nature* **418**, 512–514 (2002).
3. Freudiger, C. W. *et al. Science* **322**, 1857–1861 (2008).
4. Ideguchi, T. *et al. Nature* **502**, 355–358 (2013).
5. Yan, Y.-X., Gamble, E. B. & Nelson, K. A. *J. Chem. Phys.* **83**, 5391–5399 (1985).
6. Weiner, A. M., Leaird, D. E., Wiederrecht, G. P. & Nelson, K. A. *J. Opt. Soc. Am. B* **8**, 1264–1275 (1991).
7. Ogilvie, J. P., Beaurepaire, E., Alexandrou, A. & Joffe, M. *Opt. Lett.* **31**, 480–482 (2006).
8. Ye, J. & Cundiff, S. T. (eds) *Femtosecond Optical Frequency Comb: Principle, Operation, and Applications* (Springer, 2005).

STEM CELLS

Reprogramming *in situ*

Cellular reprogramming to a stem-cell state has now been achieved in tissues of genetically engineered mice. This work signals a future for regenerative medicine in which tissue fates might be manipulated in living organisms. [SEE ARTICLE P.340](#)

ALEJANDRO DE LOS ANGELES
& GEORGE Q. DALEY

Pluripotent stem cells sit atop the developmental hierarchy: they can self-renew indefinitely and form all tissues of the body. Embryonic stem (ES) cells, obtained from early mammalian embryos, are the quintessential pluripotent cell, but induced pluripotent stem (iPS) cells can be generated by simply introducing four specific transcription factors into cultured cells and allowing them to grow under the laboratory conditions used to maintain ES cells, a process termed direct reprogramming. Despite these remarkable *in vitro* manipulations, the capacity of the cellular milieu and tissue microenvironment to support reprogramming within living organisms has not been explored. On page 340 of this issue, Abad *et al.*¹ present the first report of such *in vivo* cellular reprogramming*.

A standard technique for assessing the pluripotency of human stem cells is to test their capacity to form teratomas when injected under the skin of immune-deficient mice. Teratomas consist of disorganized tissues of all three embryonic germ layers, and are believed to derive from abnormally growing germ cells or residual embryonic tissues. Occasionally, however, teratomas display a remarkable degree of organization, containing whole organs or limbs — a phenomenon termed *fetus in fetu*. This suggests that conditions supporting significant features of embryonic development do exist within our tissues, although the developmental origins of this event remain obscure.

Abad *et al.* generated mice carrying a drug-inducible 'gene cassette' of the four cell-reprogramming factors. To induce the expression of these transcription factors, the authors added the drug doxycycline to the animals' drinking water. Remarkably, after several weeks, teratomas appeared in various tissues, indicating that *in situ* reprogramming had occurred. This suggests that selective laboratory culture conditions are not essential for reprogramming to pluripotency, and that the *in vivo* environment can substitute for them.

During early mammalian development, the fertilized egg (zygote) and its immediate daughter cells are totipotent. Totipotency is defined as the potential to differentiate not

only into all cell types of the growing embryo (pluripotency), but also into extraembryonic cells of the placenta, such as trophoblasts, which sustain the growth and development of the entire organism.

Intriguingly, Abad *et al.* found that reprogrammed iPS cells isolated from the blood of the doxycycline-treated mice had totipotent-like features. In addition to generating cells from the three embryonic germ layers, the iPS cells could form trophoblast stem-like cells in the laboratory — evidence of these cells' expanded potential to generate derivatives of the trophoderm lineage. Moreover, the teratomas derived from the reprogrammed iPS cells from mice contained 'trophoblast giant cells.'

When the authors introduced the *in vivo*-derived iPS cells into preimplantation embryos, the cells efficiently contributed to the trophoderm lineage, including the

placenta. Strikingly, these iPS cells also generated embryo-like structures in the abdominal cavity of the reprogrammable mice (similar to *fetus in fetu*), suggesting that the iPS cells have the potential to self-organize into a complete organism. Such totipotent-like features are not seen in ES cells or in iPS cells that have been reprogrammed *in vitro*². The present landmark findings, therefore, have implications for our understanding of the relationship between pluripotency and totipotency, and for future attempts at mammalian regeneration *in situ* (Fig. 1).

It is well established that the cell-culture milieu profoundly influences the properties of pluripotent stem-cell lines, including their developmental potential and epigenetic features (chemical changes to genomic DNA and its associated histone proteins that influence cell identity and developmental potential)³. The growth conditions used for maintaining *in vivo*-derived iPS cells are similar to those for mouse ES cells and iPS cells derived *in vitro*. So one might assume that all three cell types would manifest similar developmental potential. However, it seems that *in vivo* reprogramming fixes iPS cells in a more pristine, totipotent-like state. Abad and co-workers' gene-expression profiling reveals that *in vivo*-derived iPS cells share transcriptional features with morulas (early-stage embryos), but more research is needed to dissect the functional

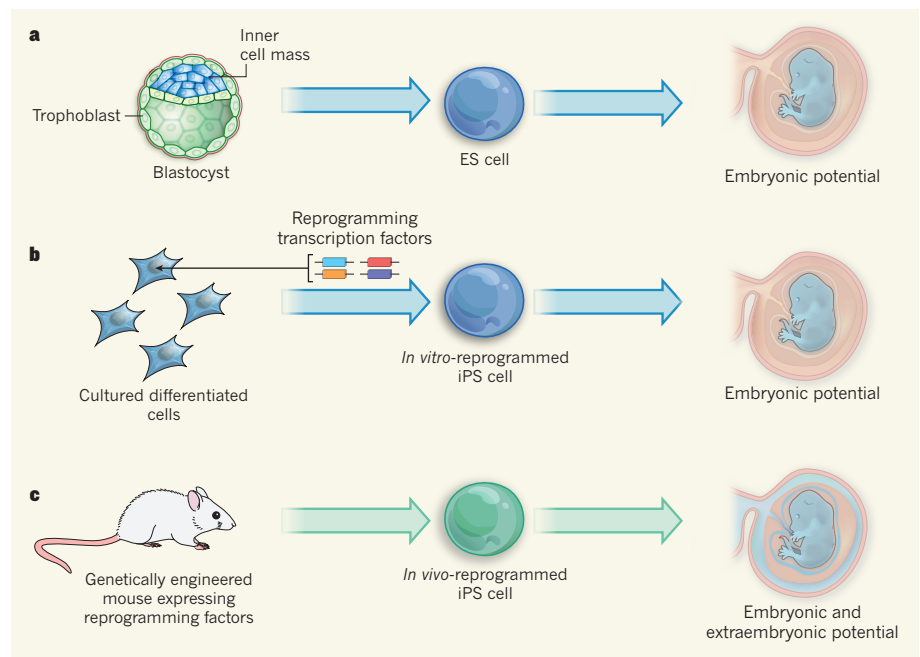


Figure 1 | Pluripotent stem cells and their potential. **a**, The preimplantation embryo, or blastocyst, consists of the inner cell mass that gives rise to the fetus. Its outer cells, the trophoblast, develop into the extraembryonic tissues of the placenta. Embryonic stem (ES) cells, derived from blastocysts, self-renew in culture and are pluripotent, giving rise to all cell types of the growing embryo. ES cells rarely exhibit totipotent-like features such as the potential to form extraembryonic tissues. **b**, Differentiated adult cells cultured in the laboratory can be reprogrammed by overexpression of reprogramming transcription factors. These *in vitro*-reprogrammed induced pluripotent stem (iPS) cells are also mainly pluripotent. **c**, Abad *et al.*¹ show that iPS cells generated by reprogramming of adult mouse cells *in vivo* maintain a totipotent-like developmental potential; the cells can contribute to extraembryonic tissues as well as embryonic tissues.

*This article and the paper under discussion¹ were published online on 11 September 2013.

relevance of the morula-enriched gene set.

Further investigation may also reveal the epigenetic mechanisms that underlie the expanded developmental potential of *in vivo*-derived iPS cells. Previous work^{4–6} has suggested that DNA methylation is crucial to safeguard pluripotency against commitment to extraembryonic lineages. Although the widely used mouse ES cells and *in vitro*-reprogrammed iPS cells are functionally pluripotent, the fact that they undergo an *in vitro*-programmed lineage restriction raises provocative questions regarding the fidelity of cell-state transitions induced in cell culture, and about the accuracy of cellular models generated by differentiation or manipulation in the laboratory.

Do human pluripotent stem cells have totipotent-like potential? Human ES cells were initially thought⁷ to generate trophectoderm on treatment with the protein BMP4. However, subsequent work showed that BMP4-treated human ES cells generate a subpopulation of cells that resemble extraembryonic mesoderm and do not correspond to genuine placental trophoblasts⁸. It is now thought that, rather than corresponding to an early totipotent-like state, human ES and iPS cells represent a distinct 'primed' state of pluripotency corresponding to a later stage of embryonic development than that of 'naïve' mouse pluripotent stem cells³. This fundamental distinction between mouse and human pluripotent stem cells may greatly influence the potential to produce extraembryonic lineages. We speculate that generation of human pluripotent stem cells with similar features to mouse ES cells may improve access to extraembryonic lineages *in vitro*. Generation of real placental derivatives from human pluripotent stem cells would enable modelling of placenta-associated disorders.

Abad and co-authors' work represents a landmark for what could become a powerful strategy in regenerative medicine — tissue reprogramming *in situ*. A hallmark of limb regeneration in amphibians is the formation of a blastema, a mass of dedifferentiated proliferating cells that undergoes morphogenesis and redifferentiates to replace structures that have been lost by amputation. However, there is currently no mammalian counterpart to the amphibian blastema, although there is a growing interest in strategies to induce regenerative responses in mammals, especially humans. In this regard, *in vivo* application of the latest transgene-free reprogramming technologies, such as those using modified messenger RNA sequences⁹ or a recently reported reprogramming cocktail of small molecules¹⁰, may allow reprogramming *in situ* to proceed in a controlled manner. The growing parallels between reprogramming and regeneration should inspire the application of reprogramming technologies in living organisms for regenerative ends. ■

Alejandro De Los Angeles and George Q. Daley are in the Stem Cell Transplantation Program, Division of Pediatric Hematology and Oncology, Children's Hospital Boston and Dana Farber Cancer Institute, Boston, Massachusetts 02115, USA. They are also at the Howard Hughes Medical Institute, at the Harvard Stem Cell Institute and in the Department of Biological Chemistry and Molecular Pharmacology, Harvard Medical School, Boston.
e-mail: george.daley@childrens.harvard.edu

ASTROPHYSICS

Super-luminous supernovae on the rise

New observations suggest that certain extremely bright supernovae are not the nuclear explosions of very massive stars. Instead, they may be ordinary-mass events lit up by a potent central fountain of magnetic energy. [SEE LETTER P.346](#)

DANIEL KASEN

Although every supernova is remarkably brilliant — at its peak, the average stellar explosion shines about a billion times brighter than the Sun — astronomers have recently discovered an astonishing class of super-luminous supernovae that outshine the ordinary ones by almost a hundredfold^{1,2}. These are very rare examples of extreme stellar death, and their progenitors are unclear, although it has been tempting to associate them with the most massive stars in the Universe. On page 346 of this issue, Nicholl *et al.*³ present data that, for certain events, point to a different origin.

The origin of ordinary supernovae has been agreed on for decades; the most common events occur when a moderately massive star (one of around 10–20 solar masses) has nearly exhausted its nuclear fuel. The stellar core, now filled with ash, cannot maintain the pressure to withstand its own gravity, and collapses to a dense, compact nugget — a neutron star — releasing enough energy in the process to blow away the outer layers in a supernova explosion.

For extremely massive stars, however, a different, and much more energetic, outcome may be possible. A star initially larger than about 140 solar masses becomes so hot in its interior that pairs of electrons and anti-electrons are spontaneously produced from the thermal bath. The energy expended in making these particles depletes the pressure support, and the star becomes 'pair unstable'. The core begins to fall inwards, but this time with its fuel tank still completely full.

The outcome is, predictably, catastrophic.

1. Abad, M. *et al.* *Nature* **502**, 340–345 (2013).
2. Macfarlan, T. S. *et al.* *Nature* **487**, 57–63 (2012).
3. Tesar, P. J. *et al.* *Nature* **448**, 196–199 (2007).
4. Ng, R. K. *et al.* *Nature Cell Biol.* **10**, 1280–1290 (2008).
5. Leitch, H. G. *et al.* *Nature Struct. Mol. Biol.* **20**, 311–316 (2013).
6. Fic, G. *et al.* *Cell Stem Cell* **13**, 351–359 (2013).
7. Xu, R. H. *et al.* *Nature Biotechnol.* **20**, 1261–1264 (2002).
8. Bernardo, A. S. *et al.* *Cell Stem Cell* **9**, 144–155 (2011).
9. Warren, L. *et al.* *Cell Stem Cell* **7**, 618–630 (2010).
10. Hou, P. *et al.* *Science* **341**, 651–654 (2013).

As the core contracts and becomes compressed, burning accelerates exponentially, and nearly all the remaining fuel is consumed within seconds. That extreme energy release completely blows the star apart, expelling a massive cloud of highly radioactive debris. The radioactive glow of the expanding cloud can be visible from more than a billion light years away.

The theory of these hyper-energetic nuclear explosions, called pair-instability supernovae (pair-SNe), was proposed⁴ in the 1960s, but it was only a few years ago that astronomers found evidence of an actual event⁵. A remarkably luminous supernova, named SN 2007bi, resembled the theoretical predictions; in particular, its brightness gradually faded at a rate consistent with the half-life of cobalt-56, a radioisotope produced abundantly in pair-SNe.

The discovery excited but confused theorists. Pair-SNe are expected to occur in pristine regions of pure hydrogen and helium gas. SN 2007bi was found in a galaxy mildly polluted by chemical elements heavier than hydrogen and helium — what astronomers call metals. Theory suggests that stars containing even small traces of metals will continuously shed material in winds, losing so much mass early in their lives that they avoid the pair instability. If SN 2007bi was indeed a pair-SN, our understanding of the formation and evolution of very massive stars needed to be reconsidered.

As it turns out, there is a relatively simple test of whether a supernova is big enough to be a pair-SN. The more massive and opaque a debris cloud, the longer it takes light to diffuse

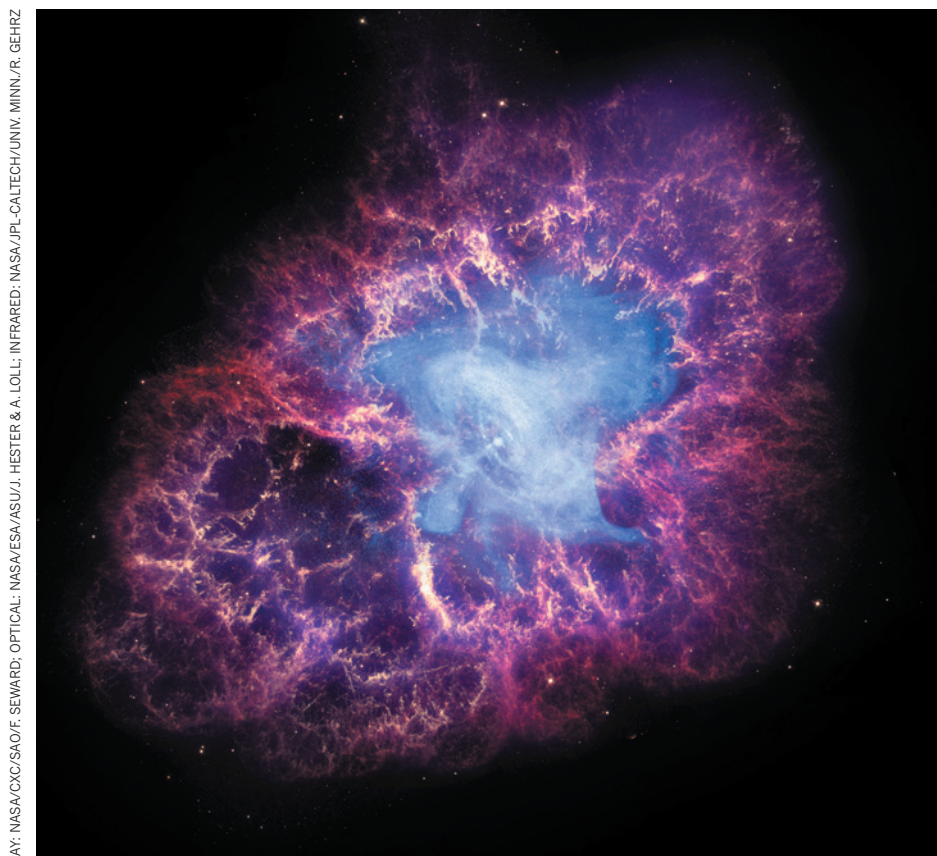


Figure 1 | The Crab nebula. At the centre of the Crab nebula — the remnant of a supernova that exploded nearly 1,000 years ago — a spinning, magnetized neutron star is slowly injecting energy into the surrounding gas cloud, lighting it up. A similar, but more extreme, physical process may explain the super-luminous supernovae observed by Nicholl and colleagues³. A neutron star spinning ten times faster than the one in the Crab nebula, and with magnetic fields 100 times stronger, would inject its spin energy much more rapidly, within a few months, and shine more than a million times more brightly.

out of it. The radioactive glow of a giant pair-SN should therefore rise to its peak brightness unusually slowly, over a period of about a year^{6,7}. That is several times longer than the rise of an ordinary-mass supernova. Unfortunately, astronomers did not catch the rise of SN 2007bi; they discovered it just as it was peaking.

But now Nicholl *et al.* have discovered two super-luminous supernovae that are dead ringers for SN 2007bi. This time the events were caught early, and the rise time to peak could be measured. The rise was relatively rapid, about two months, implying a moderate debris mass of only 10–20 solar masses. Their conclusion: these two new supernovae — and presumably SN 2007bi, by association — are not pair-SNe.

What could they be? One existing idea^{8,9}, favoured by Nicholl and colleagues, is that the emission is powered not by radioactivity, but by the activity of a spinning, highly magnetized neutron star (a ‘magnetar’). In this picture, the progenitor star was not extraordinarily massive, but it was rotating rapidly, and on collapse formed a magnetar spinning nearly 1,000 times per second. The kinetic energy stored in that dense, whirling flywheel would be enormous, with the strong magnetic fields

providing a mechanism to steadily transport the spin energy to the surrounding debris cloud, lighting it up¹⁰. This would be an extreme version of the emission seen from the remnants of some ancient supernovae (Fig. 1). Simplistic models of this process nicely explain the rise and fall of SN 2007bi and its doppelgängers^{3,4}.

Hints of magnetar activity have been noted¹¹ in a few other supernovae that reach similar peak brightnesses to SN 2007bi, but fade more rapidly after peak, perhaps pointing to a unifying mechanism for a range of super-luminous events. But other mechanisms for producing very bright supernovae are possible; for example, expanding supernova debris may encounter a dense shell of gas, and light up in a violent collision¹². Nicholl and colleagues’ data should be valuable in discriminating between different models.

Meanwhile, the pair-SNe, after a brief fling with reality, seem to have crept back into the realm of theoretical conjecture. Having failed to find a convincing candidate in their survey, Nicholl *et al.* argue that these events must be rare in the nearby Universe, less than 1 for every 100,000 ordinary supernovae. But our best chance of finding one may be to look into the very distant, very early Universe. Back

then, stars were probably bigger, and mostly free of metals. Future telescopes should be able to see a long way there; maybe they will catch a glimpse of these largest of nuclear explosions. ■

Daniel Kasen is in the Departments of Physics and Astronomy, University of California, Berkeley, and in the Nuclear Science Division, Lawrence Berkeley National Laboratory, Berkeley, California 94720, USA.
e-mail: kasen@berkeley.edu

1. Quimby, R. M. *et al. Nature* **474**, 487–489 (2011).

2. Cooke, J. *et al. Nature* **491**, 228–231 (2012).
3. Nicholl, M. *et al. Nature* **502**, 346–349 (2013).
4. Barkat, Z., Rakavy, G. & Sack, N. *Phys. Rev. Lett.* **18**, 379–381 (1967).
5. Gal-Yam, A. *et al. Nature* **462**, 624–627 (2009).
6. Kasen, D., Woosley, S. E. & Heger, A. *Astrophys. J.* **734**, 102 (2011).
7. Dessart, L., Waldman, R., Livne, E., Hillier, D. J. & Blondin, S. *Mon. Not. R. Astron. Soc.* **428**, 3227–3251 (2013).
8. Kasen, D. & Bildsten, L. *Astrophys. J.* **717**, 245–249 (2010).
9. Woosley, S. E. *Astrophys. J.* **719**, L204–L207 (2010).
10. Maeda, K. *et al. Astrophys. J.* **666**, 1069–1082 (2007).
11. Inserra, C. *et al. Astrophys. J.* **770**, 128 (2013).
12. Woosley, S. E., Blinnikov, S. & Heger, A. *Nature* **450**, 390–392 (2007).

specifically binds to a negatively charged lipid called bis(monoacylglycero)phosphate (BMP), which is found in the membrane of vesicles in the lysosome lumen⁶. This binding activates acid sphingomyelinase (ASM), an enzyme that breaks down the lipid sphingomyelin⁷, which is a typical and important component of cell membranes. Interestingly, increased ASM activity seems to support lysosomal integrity. Prompted by this observation, Petersen *et al.* hypothesized that inhibiting ASM in cancer cells would increase lysosomal fragility, LMP and cell death (Fig. 1).

It was already known that cationic amphiphilic drugs (CADs) — substances that are well established for the treatment of depression, allergies and hypertension — act as ASM modulators. At the low pH of the lysosome, the drugs interfere with the electrostatic interaction between ASM, which is cationic, and the anionic surface of BMP-rich intralysosomal membranes^{8,9}. The displaced ASM is then rapidly degraded by cathepsins. Petersen and colleagues tested the effects of CAD treatment on several types of cancer cell, and found that the drugs killed the cells at much lower concentrations and shorter exposure times than was required for them to affect the viability of non-transformed cells. CAD treatment also led to reduced tumour growth in animal models. Furthermore, the authors found that cancer cells that were resistant to many other anticancer drugs were susceptible to CADs. Fascinatingly, this treatment restored the cells' susceptibility to the other drugs.

CANCER

Killing from the inside

Lysosomes are the main degradative compartment in cells, but they are also involved in cell-death pathways. Studies using existing drugs show that lysosomes are excellent pharmacological targets for selectively destroying cancer cells.

PAUL SAFTIG & KONRAD SANDHOFF

There have been numerous efforts to identify the Achilles heel of cancer and to find ways of killing tumour cells while leaving normal cells unaffected. The development of cancer chemotherapy started in the 1940s, and our increasing understanding of cancer biology has led to ever more precisely targeted therapies. Most of these strategies target the abnormal proliferative behaviour of cancer cells. Now, writing in *Cancer Cell*, Petersen *et al.*¹ propose an alternative intracellular anticancer target — the lysosome*.

For a long time, lysosomes were misleadingly regarded as the cell's waste bin, but we now know that they are more akin to cellular stomachs. In the lysosome, macromolecules are degraded by hydrolase enzymes, including protein-degrading cathepsin enzymes, and the resulting components are released as nutrients into the cytoplasm. Importantly, lysosomes are involved in several cellular processes, such as membrane repair, pathogen defence, autophagy and signalling². The lysosomes in cancer cells are more numerous, larger and have greater cathepsin activity than those in normal cells, and the release of cathepsins from cancer-cell lysosomes into the extracellular space can promote tumour progression³.

Lysosomes are also involved in cell death — the release of certain cathepsins from the lysosome into the cytoplasm is thought to trigger death by apoptosis and apoptosis-like pathways⁴. This release occurs by a process known as lysosome membrane permeabilization (LMP), which possibly occurs following

certain changes to the composition of membrane lipids and major lysosomal membrane proteins⁵. LMP can be induced by various stimuli, including reactive oxygen species and endogenous apoptotic stimuli. However, cancer cells seem to overcome this threat of death by invoking the action of the protein Hsp70, which is expressed in many tumour types. Hsp70

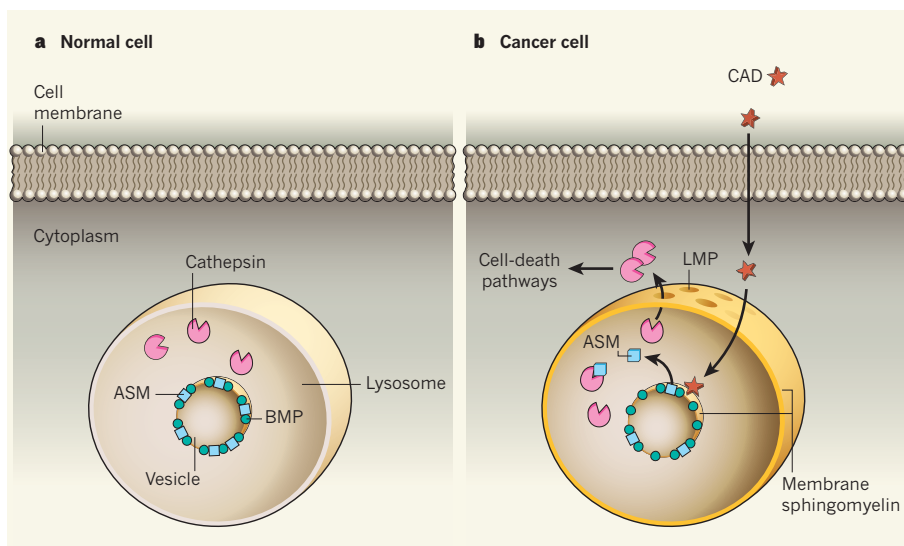


Figure 1 | Lysosomes as a therapeutic cancer target. **a**, The degradation of macromolecules in lysosomes is achieved by hydrolase enzymes, including cathepsins. Another lysosomal enzyme is acid sphingomyelinase (ASM), which breaks down the membrane lipid sphingomyelin. ASM is positively charged and associates with another, negatively charged, lipid called BMP, which is found in the membranes of vesicles in the lysosome lumen. **b**, ASM activity is lower in cancer cells than in normal cells, and thus sphingomyelin levels are higher. Petersen and colleagues¹ show that cationic amphiphilic drugs (CADs) selectively kill cancer cells. CADs are positively charged, so they can displace ASM from vesicular membranes such that it is degraded by cathepsins. It is possible that this blocks the residual ASM activity in cancer cells, leading to even higher levels of sphingomyelin, which may disturb membrane homeostasis and cause lysosome membrane permeabilization (LMP). This allows cathepsins to be released into the cytoplasm, triggering cell-death pathways.

*This News & Views article was published online on 2 October 2013.

The reason for the high susceptibility of cancer cells to ASM targeting is not completely understood. However, it might be explained by the fact that ASM activity is already low in cancer cells, and a further decrease could lead to a membrane-destabilizing level of sphingomyelin in the lysosomes of these cells. Cancer cells have higher levels of membrane dynamics and cellular signalling than normal cells, and high concentrations of sphingomyelin might inhibit these processes. It is likely that other lipids that are ASM substrates also contribute to the fragility of lysosomal membranes in tumour cells. An additional aspect of the high sphingomyelin levels in cancer cells is that the export of cholesterol from lysosomes is inhibited¹⁰; this leads to the inactivation of saposins (essential cofactors for sphingolipid-degrading enzymes), and thereby a further reduction in sphingolipid degradation.

Thus, it seems that CAD treatment may lead to a generally dysfunctional lysosomal-lipid homeostasis that severely affects the physiology of this cellular compartment and favours lysosome-related cell-death pathways. It would

be useful to analyse the specificity of CADs for tumour-cell targeting in genetically defined animal models, such as mice lacking or over-expressing ASM. Another aspect yet to be investigated is the rate of uptake of CADs in tumour cells compared with healthy cells. Surprisingly, although the events following LMP are well understood, a long-standing question is how LMP is mediated at a molecular level. Further studies of the role of CADs may help to explain how alterations in the lipid or protein composition of lysosomal membranes lead to transient and enzyme-specific lysosomal leakage.

Despite these remaining questions, Petersen and colleagues' findings argue for an in-depth pharmacological and epidemiological study of the effect of CAD treatment on cancer outcomes. CADs are relatively cheap drugs that have limited side effects, but their activity in lysosomal killing pathways is probably not sufficient for effective cancer therapy when used alone, so combination treatments with other chemotherapeutic compounds might be advisable. Future research might also reveal specific and potent modulators of

lysosomal-sphingolipid metabolism that are even more effective than CADs at inducing the death of cancer cells through this pathway. ■

Paul Saftig is at the *Biochemisches Institut, Christian Albrechts-Universität Kiel, 24118 Kiel, Germany*. **Konrad Sandhoff** is at the *Life and Medical Sciences Institute, Universität Bonn, 53121 Bonn, Germany*.
e-mail: psaftig@biochem.uni-kiel.de

1. Petersen, N. H. T. *et al. Cancer Cell* **24**, 379–393 (2013).
2. Saftig, P. & Klumperman, J. *Nature Rev. Mol. Cell Biol.* **10**, 623–635 (2009).
3. Mohamed, M. M. & Sloane, B. F. *Nature Rev. Cancer* **6**, 764–775 (2006).
4. Boya, P. & Kroemer, G. *Oncogene* **27**, 6434–6451 (2008).
5. Fehrenbacher, N. *et al. Cancer Res.* **68**, 6623–6633 (2008).
6. Kirkegaard, T. *et al. Nature* **463**, 549–553 (2010).
7. Linke, T. *et al. Biol. Chem.* **382**, 283–290 (2001).
8. Hurwitz, R., Ferlinz, K. & Sandhoff, K. *Biol. Chem.* **375**, 447–450 (1994).
9. Kornhuber, J. *et al. Cell Physiol. Biochem.* **26**, 9–20 (2010).
10. Abdul-Hammed, M. *et al. J. Lipid Res.* **51**, 1747–1760 (2010).

MATERIALS SCIENCE

To bind or not to bind

Finding a way to control how particles bind to cells could open up opportunities for biomedical research. The discovery of a method for directing the orientation of particle–cell interactions is therefore a cause for excitement.

ANDREA J. O'CONNOR & FRANK CARUSO

The interactions of small particles with cells are crucial in biology, such as when immune-system cells remove dirt and bacteria to stop an infection. Such interactions have many potential applications in promising medical therapies, and have fuelled the growing field of nanomedicine. Writing in *Advanced Materials*, Gilbert *et al.*¹ report a significant contribution to this field: the preparation of tube-shaped particles that attach to cells in different ways depending on the tubes' surface properties. This could lead to new ways to deliver drugs into target cells and to create constructs from cells.

Small particles (nanometres to micrometres in size) can interact with cells in many different ways, depending on the type of cell, the local environment and, notably, the physico-chemical properties of the particles. Scientists and engineers are therefore working on approaches to tailor both the physical and the chemical properties of particles in order to develop control over their interactions with cells and tissues.

The size, stiffness, shape and chemical make-up of small particles all strongly

influence how such particles interact with cells — they may bind to the outside of a cell, be taken up by the cell and trafficked through different pathways within it, and ultimately even change aspects of the cell's functions. Gilbert *et al.* have designed and made hollow, tubular, polymeric particles that can have non-uniform chemical properties, to see how this affected the particles' interactions with cells.

Gilbert *et al.* made the microtubes by assembling layers of oppositely charged polymers

— polyelectrolytes — in the pores of a special type of filtration membrane that has straight pores. They then chemically cross-linked the polyelectrolytes to stabilize them, and dissolved away the membrane. Benefits of this method are that it can be used to make millions of microtubes at a time, and that it could be scaled up using multiple membranes. The dimensions of the microtubes could also be easily changed by altering the pore size or the thickness of the templating membrane.

The authors prepared microtubes that were either cell-resistant or cell-adhesive by changing the polymers used to make them. In a smart variation, they also made microtubes that were cell-resistant along their length on the outside but cell-adhesive inside. Because cells cannot fit inside the tubes, they can bind only to the ends of the microtubes where the adhesive molecules are exposed. The researchers therefore observed that these particles tend

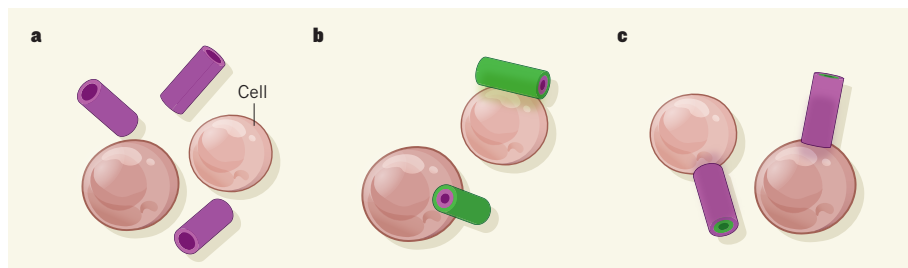


Figure 1 | Surface properties control interactions of polymer tubes with cells. Gilbert *et al.*¹ have prepared polymeric, micrometre-scale tubes from cell-resistant (pink) and cell-adhesive (green) polymers. **a**, When incubated with mouse cells, the microtubes made from only the cell-resistant polymer did not bind to the cells. **b**, Microtubes that were cell-adhesive along the sides but cell-resistant on the ends bound to cells side-on. **c**, Microtubes that were cell-resistant along the sides, but cell-adhesive at the ends, bound to the cells end-on.

to bind to cells end-on — that is, the particles' chemical properties control their orientation upon interaction with the cells. Conversely, the authors also made microtubes that have adhesive molecules along their outer length but not on the ends; these tend to bind to cells side-on.

Much of our knowledge about particle interactions with cells originates from studies of spherical particles that have uniform surface chemistry. However, it has become clear that particle shape has a major role in these interactions. For example, two particles made of the same polymer may have different rates of uptake by cells, solely because of differences in their shape and in their orientation relative to the cells². Furthermore, different surface patterns on particles can have distinctively different effects on the particles' interactions with cells³. These effects are important for many potential medical applications of nano- and microparticles, particularly drug delivery.

Particles that have tunable orientations for cell attachment, like those developed by Gilbert *et al.*, might provide another level of control over drug delivery into targeted cells. Cell-binding 'patches' on particles could regulate how those particles bind to cells, and even which cells they bind to, if biochemical molecules that target particular proteins or receptors are added to the patches. Furthermore, the other key properties of such particles, including their size, aspect ratio (the ratio of width to length) and stiffness, could be used to influence rates of particle binding and uptake into the cells.

It can also be envisaged that new biomaterial-cell constructs could be created by using such particles to connect cells into a network whose properties are highly tunable, for example by changing the numbers, dimensions and cell-binding tendencies of the particles. This could facilitate the formation of biomimetic or tissue-like hybrid materials that contain living cells in an environment more like their native milieu than the current commonly used *in vitro* supports.

Furthermore, regulation of the cellular microenvironment can alter cell functions such as differentiation of stem cells, cell-growth rates and gene expression⁴. So, if cells bind particles in a selective orientation, the particles could potentially also shape how these functions are organized in three dimensions within a tissue construct. Such orientation-specific interactions could be valuable for generating scaffold-free constructs for tissue engineering. In the future, it might also be possible to form cell-based 'polymers', using microtubes with engineered regions to link cells to form different architectures, including linear and branched systems.

Several obstacles need to be overcome to apply the microtubes therapeutically. These include the formation of microtubes that are

biocompatible and which can respond to, and degrade in, cellular or physiological conditions. It is likely that Gilbert and colleagues' work will trigger research into optimizing the efficiency with which such particles can be produced and attached to cells, and also into what happens to the particles and cells when they interact over extended times *in vitro* and *in vivo*. This will be well worth it, because the prospect of being able to design particles to deliver payloads of drugs and organize cells in new ways is exciting. ■

MULTIPLE SCLEROSIS

An old drug plays a new trick

A drug already used to treat Parkinson's disease induces repair of the damage that occurs to the myelin sheath around nerve fibres during multiple sclerosis. The finding offers new therapeutic avenues for this disease. [SEE ARTICLE P.327](#)

HARTMUT WEKERLE & EDGAR MEINL

What a change: just 20 years ago, multiple sclerosis was a disease without any promising treatment. Today, it has become treatable. Indeed, the number of drugs that effectively mitigate, although unfortunately do not cure, the disease is impressive, and is growing. But these drugs work well only in blunting the early inflammatory phase of multiple sclerosis, they do not help to restore myelin¹ — the protective sheath surrounding the axons of neurons in the brain and spinal cord that is damaged in the disease. In this issue, Deshmukh *et al.*² (page 327) identify a drug, benztropine, that may finally raise the hope of myelin repair*.

The authors show that benztropine promotes the differentiation of oligodendrocytes (the myelin-forming cells in the brain) *in vitro* and supports remyelination in animal models of multiple sclerosis (MS). What's more, the drug is an old acquaintance: benztropine is well established as an approved treatment for Parkinson's disease³.

The finding came from a monumental experimental effort that was organized in three stages. First, in a high-throughput set-up, the researchers exposed immature oligodendrocyte progenitor cells to 100,000 different small molecules in individual culture wells (Fig 1a). The progenitors came from the optic nerves of newborn rats, in which myelin formation was just about to start. After 6 days of exposure, the cultures were screened for production of intracellular myelin basic protein (MBP), a key

*This article and the paper under discussion² were published online on 9 October 2013.

Andrea J. O'Connor and Frank Caruso are in the Department of Chemical and Biomolecular Engineering, University of Melbourne, Victoria 3010, Australia. e-mail: fcaruso@unimelb.edu.au

1. Gilbert, J. B., O'Brien, J. S., Suresh, H. S., Cohen, R. E. & Rubner, M. F. *Adv. Mater.* <http://dx.doi.org/10.1002/adma.201302673> (2013).
2. Mitragotri, S. & Lahann, J. *Nature Mater.* **8**, 15–23 (2009).
3. Verma, A. *et al. Nature Mater.* **7**, 588–595 (2008).
4. Discher, D. E., Janmey, P. & Wang, Y. L. *Science* **310**, 1139–1143 (2005).

product of myelin-forming cells. This process identified compounds in more than a dozen functional classes that drove MBP formation; these molecules were then considered further.

MBP production is necessary but not sufficient for the formation of intact, compacted, myelin sheaths. To test the effects of their compounds on this latter process, the authors used a second, medium-throughput step to examine effects on the myelination of axons of neurons co-cultured with oligodendrocyte precursors (Fig. 1b). In the presence of one of the compounds, benztropine, more myelin wraps appeared around the axons than in untreated cultures. Additional pharmacological experiments revealed that the benztropine-driven myelination involved blocking the activity of muscarinic cholinergic receptors, extending a previous observation about the function of these receptors on oligodendrocytes⁴.

These findings were made using cultures of rodent cells, but, as readers (and drug-regulatory agencies) would ask, could the drug promote myelin repair in live animals with an MS-like disease? In the third, low-throughput, stage (Fig. 1c), the investigators tested benztropine in two mouse models of demyelinating disease. The first, called experimental autoimmune encephalomyelitis, involves inducing an autoimmune response against myelin by immunizing the animals with a myelin auto-antigen. This condition recapitulates *in vivo* some essential features of human MS, such as large-scale demyelinated lesions accompanied by axonal damage⁵. Benztropine substantially mitigated ongoing disease and promoted remyelination in these mice. But these findings

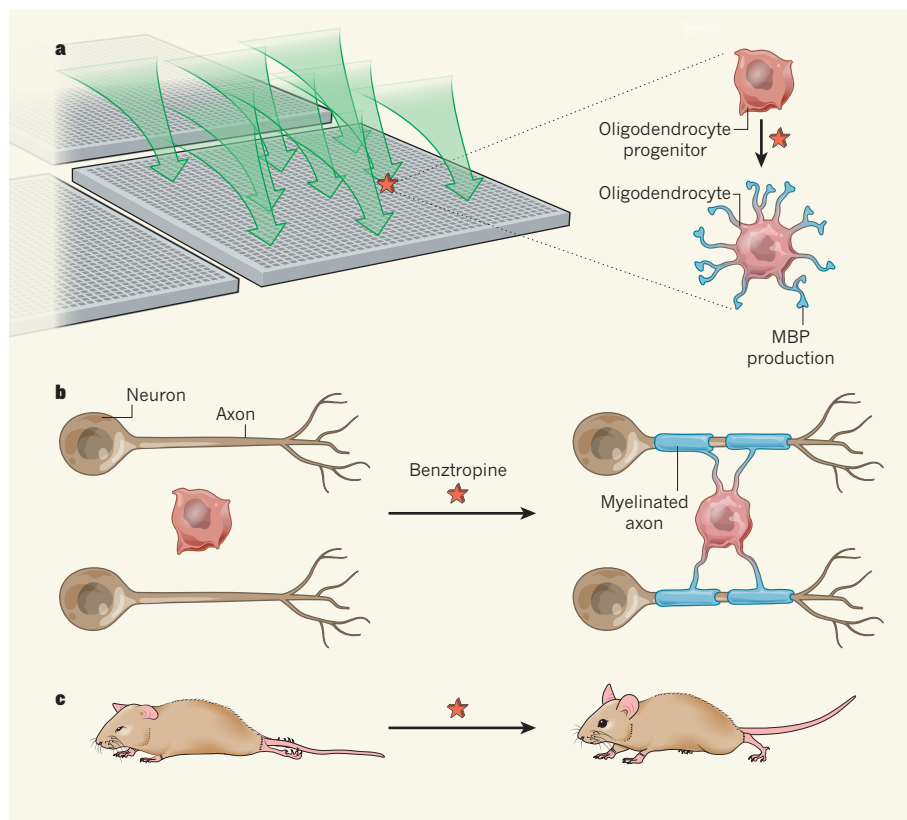


Figure 1 | Identification of a myelin-promoting drug. Deshmukh *et al.*² used a three-stage screening and validation protocol to search for drugs that might restore the damage to myelin that occurs during multiple sclerosis. **a**, In the high-throughput stage, the authors tested the effects of 100,000 compounds on cultured rat oligodendrocyte progenitor cells, searching for agents that would induce differentiation of oligodendrocytes, which produce myelin basic protein (MBP). One compound, benzotropine, particularly enhanced MBP production. **b**, In the medium-throughput stage, the authors show that benzotropine enhanced axon myelination when added to a co-culture of oligodendrocyte progenitors and neurons. **c**, The authors then tested the effect of benzotropine in two animal models of demyelination — one immune-mediated and the other chemically induced. In both models, the drug promoted remyelination, and in the immune-mediated model, it alleviated disease symptoms such as hind-leg and tail paralysis.

do not unequivocally prove remyelination to be the sole therapeutic mechanism. Although the drug did not grossly alter the function of the immune cells involved in MS (which include peripheral T lymphocytes and macrophages), an action on immune-effector mechanisms within the central nervous system cannot be excluded.

In another remarkable result, the authors report that, when given prophylactically, benzotropine enhanced the density of mature oligodendrocytes in the animals' central nervous systems even before disease onset. Is this effect welcome, or could an excess of oligodendrocytes be detrimental? That is not yet clear, but proof of benzotropine's myelin-promoting potential came from a second animal model, in which myelin is destroyed not through an inflammatory process, but by an orally administered toxin called cuprizone⁶. In these mice, spontaneous myelin repair following discontinuation of cuprizone treatment was clearly accelerated by benzotropine therapy.

In MS, although most lesions remain permanently demyelinated, certain lesions called shadow plaques show evidence of spontaneous

remyelination. But, as a rule, the renewed myelin formation remains incomplete, with axons wrapped only by solitary myelin segments, or internodes, that are abnormally thin⁷. Furthermore, the degree of remyelination does not directly correlate with disease severity⁸. This failed repair effort mostly seems to reflect a failure of oligodendrocyte progenitors to myelinate, rather than a lack of locally available progenitors⁹. Thus, one would conclude that drugs that support myelin reformation are a more promising treatment for repair than the supply of additional progenitors, for example by cell transplants. The investigators conclude that benzotropine acts mainly by promoting the differentiation of oligodendrocyte precursors to mature myelin-producing cells, although their results do not rule out local progenitor proliferation as an alternative or additional mechanism.

There have been many different approaches to seeking drugs for MS. Some successful drugs were discovered by serendipity. Interferon- β , for example, was initially applied with the intention to clear affected brains of what were assumed to be pathogenic viruses¹⁰.

Other drugs were found by directed screening or design: natalizumab, for example, is an antibody designed to block the entry of inflammatory cells to the brain. It was identified as effective in animal studies and from there moved directly into the clinic¹¹.

Deshmukh and colleagues opted for the latter approach, and their platform has been remarkably successful. But a few caveats remain. Benzotropine was identified using rodent cells and models only, without a test stage using human cells. Will the drug's anticholinergic activity induce the differentiation of human progenitor cells in the same way? In this context it is worth noting that not all anticholinergic agents tested by the authors were as effective at inducing MBP as benzotropine. Furthermore, anti-cholinergic drugs are routinely used to treat urinary complications in people with MS¹², but changes in the general disease course of these patients have not been reported, to our knowledge. Finally, it remains to be seen how benzotropine will affect remyelination in people with MS, both at sites of active demyelination and in chronic, 'burnt out' lesions.

Numerous therapeutic trials have tested a diversity of potential myelin-protective drugs, but so far with disappointing outcomes¹³. Will Deshmukh and colleagues' study change this dire situation? Here, the authors keep a low profile. They cite the nature and severity of the side effects of benzotropine that have been observed following its use in Parkinson's disease. But the present results will motivate the group to search for drug variants that maintain benzotropine's virtues — its myelin-repairing activity and its ability to cross the blood-brain barrier — but lack its dark side. ■

Hartmut Wekerle is in the Hertie Senior Professor Group, Max Planck Institute of Neurobiology, 82152 Martinsried, Germany.

Edgar Mehl is at the Institute of Clinical Neuroimmunology, LMU Munich, 81377 Munich, Germany.

e-mail: hwekerle@neuro.mpg.de

1. Hauser, S. L., Chan, J. R. & Oksenberg, J. R. *Ann. Neurol.* **74**, 317–327 (2013).
2. Deshmukh, V. A. *et al. Nature* **502**, 327–332 (2013).
3. Burgoyne, K., Aduri, K., Ananth, J. & Parameswaran, S. *Curr. Pharm. Des.* **10**, 2239–2248 (2004).
4. De Angelis, F., Bernardo, A., Magnaghi, V., Minghetti, L. & Tata, A. M. *Dev. Neurobiol.* **72**, 713–728 (2012).
5. Gold, R., Linington, C. & Lassmann, H. *Brain* **129**, 1953–1971 (2006).
6. Ludwin, S. K. *Lab. Invest.* **43**, 382–387 (1980).
7. Franklin, R. J. M. & Ffrench-Constant, C. *Nature Rev. Neurosci.* **9**, 839–855 (2008).
8. Patrikios, P. *et al. Brain* **129**, 3165–3172 (2006).
9. Chang, A., Tourtellotte, W. W., Rudick, R. & Trapp, B. D. *N. Engl. J. Med.* **346**, 165–173 (2002).
10. Jacobs, L. & Johnson, K. P. *Arch. Neurol.* **51**, 1245–1252 (1994).
11. Steinman, L. *Science* **305**, 212–216 (2004).
12. Nicholas, R., Young, C. & Friede, T. *Expert Opin. Drug Safety* **9**, 905–915 (2010).
13. van der Walt, A. *et al. Pharmacol. Ther.* **126**, 82–93 (2010).

Criteria for the use of omics-based predictors in clinical trials

Lisa M. McShane¹, Margaret M. Cavenagh¹, Tracy G. Lively¹, David A. Eberhard², William L. Bigbee³, P. Mickey Williams⁴, Jill P. Mesirov⁵, Mei-Yin C. Polley¹, Kelly Y. Kim¹, James V. Tricoli¹, Jeremy M. G. Taylor⁶, Deborah J. Shuman¹, Richard M. Simon¹, James H. Doroshow¹ & Barbara A. Conley¹

The US National Cancer Institute (NCI), in collaboration with scientists representing multiple areas of expertise relevant to ‘omics’-based test development, has developed a checklist of criteria that can be used to determine the readiness of omics-based tests for guiding patient care in clinical trials. The checklist criteria cover issues relating to specimens, assays, mathematical modelling, clinical trial design, and ethical, legal and regulatory aspects. Funding bodies and journals are encouraged to consider the checklist, which they may find useful for assessing study quality and evidence strength. The checklist will be used to evaluate proposals for NCI-sponsored clinical trials in which omics tests will be used to guide therapy.

High-throughput ‘omics’ technologies hold great promise to provide detailed characterization of diseases to more effectively predict a patient’s clinical course or to select the most beneficial therapies (see Box 1). These technologies have been embraced enthusiastically in oncology, as the heterogeneous character of malignant diseases presents substantial challenges for cancer detection, prognosis and optimal selection of therapy. Many preclinical studies using these technologies to elucidate biological features and mechanisms have been published, and retrospective studies applying omics assays to stored human biospecimens have been conducted to develop mathematical models to predict clinical endpoints such as survival or response to therapy.

Despite numerous publications, however, few omics-based predictors have been translated successfully into clinically useful tests. A factor that contributes to the slow pace of clinical translation is the challenge of assessing whether the body of evidence for an omics-based test is sufficiently comprehensive and reliable that the test is ready for definitive evaluation in a clinical trial in which it could be used to direct patient care. Translation from research-grade omics assays to clinical-grade omics-based tests¹ requires a rigorous development and validation process with attention to the complexities of omics assays and their application to clinical specimens, specialized expertise required to appropriately develop and evaluate mathematical predictor models built from high-dimensional data, and multiple ethical, legal and regulatory issues.

Recently there have been some widely publicized cases of premature advancement of omics-based tests to use in trials in which they were used to guide patient treatment decisions. These cases led to calls for examination of the field of translational omics. The Institute of Medicine (IOM) conducted a study¹ to review the field and formed the Committee on the Review of Omics-Based Tests for Predicting Patient Outcomes in Clinical Trials. The group’s task statement included recommending an evaluation process for determining when omics tests are fit for use in clinical trials and applying it to several specific cases of premature use of omics-based tests¹. The resulting report laid out a three-phase process for the development and evaluation of omics-based tests for use in clinical trials: the discovery phase, the test validation phase, and the evaluation for clinical utility and use stage.

During the IOM committee deliberations, the NCI convened a workshop to bring together scientists and stakeholders who had an interest in this area of research to stimulate community dialogue. Subsequently, a working group was formed to develop a checklist that would operationalize the principles set forth in the IOM report and the NCI workshop discussions.

The results of those efforts are presented in Table 1, which lists 30 criteria that should be addressed to determine the readiness of an omics test for use in a prospective clinical trial. These criteria apply to any clinical trial involving the investigational use of an omics test that will influence the clinical management of patients in the trial; for example, the selection of therapy. These criteria cover not only the strength of evidence in support of an omics test but also the practical issues that must be considered before the test is used in a clinical setting. The criteria can also be helpful in assessing the reliability and credibility of an omics predictor to justify its use on valuable non-renewable archived specimens collected from patients who were prospectively enrolled in previous clinical studies. This paper presents the criteria in checklist form with brief background. Readers are referred to a recently published companion paper² for a more complete explanation and elaboration of the rationale for each criterion.

BOX 1

Definition of ‘omics’

In its report, *Evolution of Translational Omics: Lessons Learned and the Path Forward*, the Institute of Medicine Committee on the Review of Omics-Based Tests for Predicting Patient Outcomes in Clinical Trials defines ‘omics’ as the study of related sets of biological molecules in a comprehensive fashion. Examples of omics disciplines include genomics, transcriptomics, proteomics, metabolomics and epigenomics. An omics-based test is defined as “an assay composed of or derived from multiple molecular measurements and interpreted by a fully specified computational model to produce a clinically actionable result”¹.

¹Division of Cancer Treatment and Diagnosis, National Cancer Institute, National Institutes of Health, Bethesda, Maryland 20892, USA. ²Department of Pathology and Lineberger Comprehensive Cancer Center, University of North Carolina, Chapel Hill, North Carolina 27599, USA. ³Department of Pathology and University of Pittsburgh Cancer Institute, Hillman Cancer Center, University of Pittsburgh School of Medicine, Pittsburgh, Pennsylvania 15213, USA. ⁴Frederick National Laboratory for Cancer Research, National Cancer Institute, National Institutes of Health, Frederick, Maryland 21702, USA. ⁵Broad Institute of Massachusetts Institute of Technology and Harvard University, Cambridge, Massachusetts 02142, USA. ⁶Department of Biostatistics, University of Michigan, Ann Arbor, Michigan 48109, USA.

Table 1 | Criteria for the use of omics-based predictors in NCI-supported clinical trials

Domain	Criteria
Specimen issues	<ol style="list-style-type: none"> 1. Establish methods for specimen collection and processing and appropriate storage conditions to ensure the suitability of specimens for use with the omics test. 2. Establish criteria for screening out inadequate or poor-quality specimens or analytes isolated from those specimens before performing assays. 3. Specify the minimum amount of specimen required. 4. Determine the feasibility of obtaining specimens that will yield the quantity and quality of isolated cells or analytes needed for successful assay performance in clinical settings.
Assay issues	<ol style="list-style-type: none"> 5. Review all available information about the standard operating procedures (SOPs) used by the laboratories that performed the omics assays in the developmental studies, including information on technical protocol, reagents, analytical platform, assay scoring, and reporting method, to evaluate the comparability of the current assay to earlier versions and to establish the point at which all aspects of the omics test were definitively locked down for final validation. 6. Establish a detailed SOP to conduct the assay, including technical protocol, instrumentation, reagents, scoring and reporting methods, calibrators and analytical standards, and controls. 7. Establish acceptability criteria for the quality of assay batches and for results from individual specimens. 8. Validate assay performance by using established analytical metrics such as accuracy, precision, coefficient of variation, sensitivity, specificity, linear range, limit of detection, and limit of quantification, as applicable. 9. Establish acceptable reproducibility among technicians and participating laboratories and develop a quality assurance plan to ensure adherence to a detailed SOP and maintain reproducibility of test results during the clinical trial. 10. Establish a turnaround time for test results that is within acceptable limits for use in real-time clinical settings.
Model development, specification, and preliminary performance evaluation	<ol style="list-style-type: none"> 11. Evaluate data used in developing and validating the predictor model to check for accuracy, completeness, and outliers. Perform retrospective verification of the data quality if necessary. 12. Assess the developmental data sets for technical artefacts (for example, effects of assay batch, specimen handling, assay instrument or platform, reagent, or operator), focusing particular attention on whether any artefacts could potentially influence the observed association between the omics profiles and clinical outcomes. 13. Evaluate the appropriateness of the statistical methods used to build the predictor model and to assess its performance. 14. Establish that the predictor algorithm, including all data pre-processing steps, cutpoints applied to continuous variables (if any), and methods for assigning confidence measures for predictions, are completely locked down (that is, fully specified) and identical to prior versions for which performance claims were made. 15. Document sources of variation that affect the reproducibility of the final predictions, and provide an estimate of the overall variability along with verification that the prediction algorithm can be applied to one case at a time. 16. Summarize the expected distribution of predictions in the patient population to which the predictor will be applied, including the distribution of any confidence metrics associated with the predictions. 17. Review any studies reporting evaluations of the predictor's performance to determine their relevance for the setting in which the predictor is being proposed for clinical use. 18. Evaluate whether clinical validations of the predictor were analytically and statistically rigorous and unequivocally blinded. 19. Search public sources, including literature and citation databases, journal correspondence, and retraction notices, to determine whether any questions have been raised about the data or methods used to develop the predictor or assess its performance, and ensure that all questions have been adequately addressed.
Clinical trial design	<ol style="list-style-type: none"> 20. Provide a clear statement of the target patient population and intended clinical use of the predictor and ensure that the expected clinical benefit is sufficiently large to support its clinical utility. 21. Determine whether the clinical utility of the omics test can be evaluated by using stored specimens from a completed clinical trial (that is, a prospective-retrospective study). 22. If a new prospective clinical trial will be required, evaluate which aspects of the proposed predictor have undergone sufficiently rigorous validation to allow treatment decisions to be influenced by predictor results; where treatment assignments are randomized, provide justification for equipoise. 23. Develop a clinical trial protocol that contains clearly stated objectives and methods and an analysis plan that includes justification of sample size; lock down and fully document all aspects of the omics test and establish analytical validation of the predictor. 24. Establish a secure clinical database so that links among clinical data, omics data, and predictor results remain appropriately blinded, under the control of the study statistician.
Ethical, legal and regulatory issues	<ol style="list-style-type: none"> 25. Include in the protocol the names of the primary individuals who are responsible for each aspect of the study. 26. Establish communication with the individuals, offices, and agencies that will oversee the ethical, legal, and regulatory issues that are relevant to the conduct of the trial. 27. Ensure that the informed consent documents to be signed by study participants accurately describe the risks and potential benefits associated with use of the omics test and include provisions for banking of specimens, particularly to allow for 'bridging studies' to validate new or improved assays. 28. Address any intellectual property issues regarding the use of the specimens, biomarkers, assays, and computer software used for calculation of the predictor. 29. Ensure that the omics test is performed in a Clinical Laboratory Improvement Amendments-certified laboratory if the results will be used to determine treatment or will be reported to the patient or the patient's physician at any time, even after the trial has ended or the patient is no longer participating in the study. 30. Ensure that appropriate regulatory approvals have been obtained for investigational use of the omics test. If a prospective trial is planned in which the test will guide treatment, consider a pre-submission consultation with the US Food and Drug Administration.

Specimen issues

Molecular profiles generated by the use of omics technologies can be sensitive to specimen collection, processing and storage conditions³. Investigators should consider the conditions under which specimens

used in developmental studies were collected and handled to assess the robustness of an omics test to various specimen conditions. It may be necessary to conduct additional feasibility studies to document that the omics test will perform satisfactorily under the range of conditions in

which the specimens will be obtained and stored in typical clinical settings; alternatively, more restrictive requirements for specimen collection, processing and storage should be clearly specified before the test is used in a clinical trial or other clinical validation study.

Criteria for specimen quality, amount (mass or volume), and composition should be clearly specified in order to qualify a specimen or its isolated analytes as suitable for assay by the omics test. Appropriate criteria will depend on the specimen type and the particular omics assay platform to be used. Details of the specification might include per cent purity of the target cells or intact analyte of interest and specific mass or volume of the specimen or analytes isolated from the specimen. It should be established that it is feasible to achieve these criteria in clinical settings.

Assay issues

Variations in assay procedures due to differences in technical protocols, reagents, and scoring and reporting methods can have a substantial impact on the analytical performance of an omics assay and its comparability among laboratories^{4,5}. Many omics tests are developed using data from retrospective studies in which these aspects of the assay were not standardized. This can lead to uncertainties in how the test will perform when based on assay data from a new laboratory, including the laboratory or laboratories that will generate the assay data for a prospective trial. It is important to develop detailed standard operating procedures (SOPs) for the assay underlying the omics test and to establish that studies conducted previously to clinically validate the omics test were based on data expected to be comparable to new data generated under the specified SOPs.

Analytical performance of the omics assay under the proposed SOPs must be documented and found to be acceptable in terms of metrics such as accuracy, precision, coefficient of variation, sensitivity, specificity, linear range, limit of detection, and limit of quantification, as applicable. Calibrators, analytical standards, and controls are essential components of the SOPs and should be described clearly. Quality assurance procedures should include criteria for acceptance or rejection of assay batches and results from individual specimens. When multiple technicians or laboratories will conduct the assays, monitoring procedures should be in place to ensure comparability across technicians and laboratories. Methods for assay scoring and reporting should be clearly specified. Turnaround times for return of test results should be within acceptable limits that will be dependent on the particular clinical situation and should be sufficiently rapid to not impede clinical management timelines. Feasibility studies to assess assay analytical performance, reproducibility and turnaround times may be required in advance of initiating a clinical trial to firmly establish the suitability of the omics test for use in a real-time clinical setting.

Model development and evaluation

Many omics tests are developed using existing omics, clinical and pathology data or using data generated from retrospective specimen collections. These data may be incomplete or unreliable and should be examined for errors, inconsistencies or bias. Omics assays can be sensitive to a variety of ancillary technical influences that result in artefacts in the generated data. Of particular concern is the potential for such artefacts to be confounded with clinical variables or endpoints. Efforts should be made to identify potential confounders, including source of specimens (for example, clinical sites processing specimens differently), laboratory performing the omics assay, and assay batches⁶.

Examples of flawed applications of statistical approaches for development of omics predictors and for evaluation of their performance are abundant in the literature^{7–9}. Model overfitting, which occurs when a statistical model describes random noise instead of capturing the true association between predictor variables and a clinical endpoint, is a common problem in omics research projects, in which the number of analytes measured per specimen exceeds the number of specimens studied. Overfitting can be reduced by the use of model ‘regularization’ approaches that constrain the complexity of the model, but these approaches do not completely eliminate overfitting risk. It is common for researchers without

the appropriate expertise to misunderstand and misapply modelling techniques. In addition, if flawed methods for model performance assessment are used, then overfitting may escape detection. A common mistake is failure to maintain strict separation between data used to build a model (‘training set’) and data used to assess model performance (‘testing set’). Numerous published papers have inappropriately reported model performance estimates based on resubstitution of data used to build a model back into that same model. These so-called ‘resubstitution estimates’ are severely (optimistically) biased. Assessment of model performance on the combined training and testing data sets is similarly problematic. Re-use of training data is acceptable only if performed properly using data resampling methods¹⁰ that iteratively split the training data to hold out subsets of the data that are not used for model building and can therefore be used to check model performance.

Development of an omics predictor can be an iterative process involving several adjustments to improve performance. With regard to the three phases of the development and evaluation process in the IOM report¹ on omics tests, it is noted in the report that preliminary validations may occur in the test validation phase, and the definitive evaluation of clinical utility takes place in the final phase. It is important to be able to discern the point at which the omics test is ‘locked down’, or finalized, in all aspects, including specimen requirements, technical protocol for assay, data preprocessing, the form of mathematical predictor model, and interpretation of the test result. The test is then ready to enter the final evaluation for clinical utility and use stage, at which there are three basic options for clinical utility evaluation: first, a prospective evaluation of the omics test on a retrospective specimen collection from a clinical trial or prospective cohort study; second, a prospective clinical trial in which the test does not direct patient management; and third, a prospective clinical trial in which the omics test is used to direct patient management. Ideally, there should have been a blinded and rigorous preliminary validation of performance of the locked-down model on an external independent specimen set during the test validation phase. If an independent external validation set is not possible because adequate specimen collections do not exist, then existing performance evaluations based on internal validations should be carefully reviewed to ensure that they were rigorous and used appropriate methods. In this situation, it may be necessary to use a clinical trial design that does not allow the test to influence patient care.

When further adjustments are made to the omics test or data after the final validation data have been unblinded, there is a risk of compromising the validation. If the omics test is adjusted, either a new validation must be performed or additional evidence must be obtained; for example, by conducting an assay-bridging study to ensure that the adjustments to the test have not adversely affected its performance.

Investigators should be prepared to supply data and computer code as part of the review process for proposals to use omics tests in clinical trials. It is highly recommended that investigators follow reproducible research practices so that they will be able to supply the needed information quickly and easily for verification of the validation of the test and its locked-down form. Readers are referred to the companion publication² for further discussion of recommended reproducible research practices.

Clinical trial design

A clinical trial for definitive evaluation of an omics test should be conducted using the same rigorous standards expected for clinical trials evaluating experimental therapies. In some circumstances, high-level evidence can be obtained by use of specimens from an already-completed clinical trial¹¹. Accepted standards for good clinical practice must be followed^{12,13}, including development of a formal protocol with clearly stated objectives and eligibility criteria, an informatics plan for management of clinical and omics data, a pre-specified study design¹⁴ and statistical analysis plan, complete specification of the omics test, and justification for equipoise for any treatment randomizations (if the trial is conducted prospectively). The study team must include individuals with appropriate expertise to assume responsibility for the clinical, laboratory, pathology, bioinformatics, data management and statistical aspects of the study.

Ethical, legal and regulatory issues

Numerous ethical, legal and regulatory issues must be addressed in the course of developing an omics test for clinical use. Research involving human subjects, which includes retrospective use of specimens from living subjects, requires that adequate protection is in place to ensure the safety of patients and the privacy and confidentiality of patient information¹⁵. Ensuring appropriate protections has become more challenging as omics technologies make it possible to provide detailed genetic characterizations of individuals and much research data are made publicly available. Informed consent documents for a clinical trial using an omics test to guide patient management must accurately describe any potential risks from participation in a study and all potential conflicts of interest on the part of study investigators or sponsoring institutions. Laboratory tests must be conducted in environments that meet Clinical Laboratory Improvement Amendments certification requirements if the results will be reported to the patient or the patient's physician¹⁶. Responsible parties at participating institutions (for example, institutional review boards, protocol review committees), trial sponsors (for example, the NCI, universities, companies), and the US Food and Drug Administration (FDA) (for example, for Investigational Device Exemption (IDE)¹⁷ or Investigational New Drug¹⁸ applications) must be fully informed of study details and approve the study before it proceeds.

If the omics assay to be used in a clinical trial could be considered a significant-risk assay, including—but not limited to—one used to choose among treatments, investigators must consult with the FDA to determine whether an IDE from the Center for Devices and Radiologic Health, or a similar evaluation carried out through the Investigational New Drug process, is required. The complexities of omics-based tests, together with the FDA's evolving view of regulatory enforcement discretion for these tests, make it important to have early communications with the FDA. Investigators may find it helpful to discuss the trial formally with the FDA in a pre-submission process if they are not familiar with IDE requirements¹⁹.

Intellectual property issues may apply to the use of the specimens, biomarkers, assays, and computer software used for calculation of the predictor. Intellectual property rights should be documented and respected by all parties involved. Potential conflicts of interest of study investigators must be disclosed and managed.

Summary

Evaluation of the readiness of an omics test to be used for clinical care requires careful consideration of the body of evidence supporting the test's analytical and clinical validity and potential clinical utility, as well as an understanding of ethical, legal and regulatory issues. Funding bodies and journals are encouraged to consider using the checklist as an evaluation guide in their review processes. The NCI plans to use the checklist presented here to evaluate proposals for the use of omics tests in clinical trials where the test will be used to guide patient care. Although it is not expected that exploratory studies using omics assays or studies aiming to develop omics tests will meet all of the checklist criteria, the checklist does provide a convenient framework by which to assess the stage of development of an omics test and the strength and quality of the accumulated evidence. Several of the checklist criteria (those that are not specific to the development of models from high-dimensional data) also apply to studies of single biomarkers, or limited panels of biomarkers, measured by a variety of conventional assay methods. The checklist may, therefore, serve as a useful reference in a variety of review settings.

It is hoped that this 30-point checklist will guide investigators towards the use of best practices in omics test development, help them to more reliably evaluate the quality of evidence in support of omics tests, and assist them in planning appropriately for the clinical use of omics predictors. The ultimate goal is to develop a more efficient, reliable and transparent process to move omics assays from promising research results to clinically useful tests that improve patient care and outcome.

Received 23 April; accepted 15 August 2013.

1. Institute of Medicine. *Evolution of Translational Omics: Lessons Learned and the Path Forward* (eds Miceel, C. M., Nass, S. & Omenn, G. S.) (The National Academies Press, 2012).
A report produced by a committee formed in response to an NCI request for recommendations to strengthen omics-based test development and evaluation; this identifies best practices to enhance the development, evaluation and translation of omics-based tests while reinforcing steps to ensure that these tests are appropriately assessed for scientific validity before they are used to guide patient treatment in clinical trials.
2. McShane, L. M. *et al.* Criteria for the use of omics-based predictors in clinical trials: explanation & elaboration. *BMC Med.* **11**, 220 (2013).
This paper is an annotated companion to the short version of the guidelines presented here, elucidating the rationale underlying the development of the criteria in greater detail.
3. Moore, H. M. *et al.* Biospecimen Reporting for Improved Study Quality (BRISQ). *Cancer Cytopath.* **119**, 92–101 (2011).
4. Dobbin, K. K. *et al.* Interlaboratory comparability study of cancer gene expression analysis using oligonucleotide microarrays. *Clin. Cancer Res.* **11**, 565–572 (2005).
5. Shi, L. *et al.* The MicroArray Quality Control (MAQC) project shows inter- and intraplatform reproducibility of gene expression measurements. *Nature Biotechnol.* **24**, 1151–1161 (2006).
6. Leek, J. T. *et al.* Tackling the widespread and critical impact of batch effects in high-throughput data. *Nature Rev. Genet.* **11**, 733–739 (2010).
7. Dupuy, A. & Simon, R. M. Critical review of published microarray studies for cancer outcome and guidelines on statistical analysis and reporting. *J. Natl. Cancer Inst.* **99**, 147–157 (2007).
8. Simon, R., Radmacher, M. D., Dobbin, K. & McShane, L. M. Pitfalls in the use of DNA microarray data for diagnostic and prognostic classification. *J. Natl. Cancer Inst.* **95**, 14–18 (2003).
9. Subramanian, J. & Simon, R. Gene expression-based prognostic signatures in lung cancer: ready for clinical use? *J. Natl. Cancer Inst.* **102**, 464–474 (2010).
10. Molinaro, A. M., Simon, R. & Pfeiffer, R. M. Prediction error estimation: a comparison of resampling methods. *Bioinformatics* **21**, 3301–3307 (2005).
11. Simon, R. M., Paik, S. & Hayes, D. F. Use of archived specimens in evaluation of prognostic and predictive biomarkers. *J. Natl. Cancer Inst.* **101**, 1446–1452 (2009).
12. ICH Expert Working Group International Conference on Harmonisation of Technical Requirements for Registration of Pharmaceuticals for Human Use; http://www.ich.org/fileadmin/Public_Web_Site/ICH_Products/Guidelines/Quality/Q2_R1/Step4/Q2_R1_Guideline.pdf (accessed 19 February 2013).
13. US Food and Drug Administration. *Guidance for Industry: Computerized Systems Used in Clinical Investigations* (US Department of Health and Human Services, 2007).
14. Freidlin, B., McShane, L. M. & Korn, E. L. Randomized clinical trials with biomarkers: design issues. *J. Natl. Cancer Inst.* **102**, 152–160 (2010).
15. US Department of Health & Human Services. SACHRP Letter to the Secretary: FAQs, Terms and Recommendations on Informed Consent and Research Use of Biospecimens; http://www.hhs.gov/ohrp/sachrp/20110124_attachmenttosecretletter.html (accessed 19 February 2013).
16. Center for Medicare and Medicaid Services. Clinical Laboratory Improvement Amendments (CLIA); <http://www.cms.gov/Regulations-and-Guidance/Legislation/CLIA/index.html?redirect=/CLIA> (accessed 19 February 2013).
17. US Food and Drug Administration. Device Advice: Comprehensive Regulatory Assistance; <http://www.fda.gov/MedicalDevices/DeviceRegulationandGuidance/default.htm> (accessed 19 February 2013).
18. US Food and Drug Administration. Investigational New Drug (IND) Application; <http://www.fda.gov/Drugs/DevelopmentApprovalProcess/HowDrugsareDevelopedandApproved/ApprovalApplications/InvestigationalNewDrugINDApplication/default.htm> (accessed 19 February 2013).
19. US Food and Drug Administration. Draft Guidance for Industry and FDA Staff: Medical Devices: the Pre-submission Program and Meetings with FDA Staff (US Department of Health & Human Services); <http://www.fda.gov/MedicalDevices/DeviceRegulationandGuidance/GuidanceDocuments/ucm310375.htm> (accessed 19 February 2013).

Author Contributions B.A.C. and L.M.M. conceived the idea for this paper and the checklist. The initial draft of the manuscript was the joint effort of several authors contributing according to their particular areas of expertise (W.L.B., M.M.C., B.A.C., D.A.E., T.G.L. and L.M.M.). All authors provided comments, suggested edits, and contributed additional expertise to enhance the initial draft and produce the final version of the manuscript.

Author Information Reprints and permissions information is available at www.nature.com/reprints. The authors declare no competing financial interests. Readers are welcome to comment on the online version of the paper. Correspondence and requests for materials should be addressed to L.M.M. (mcsanel@ctep.nci.nih.gov).



This work is licensed under a Creative Commons Attribution-NonCommercial-Share Alike 3.0 Unported licence. To view a copy of this licence, visit <http://creativecommons.org/licenses/by-nc-sa/3.0>

Olivine crystals align during diffusion creep of Earth's upper mantle

Tomonori Miyazaki¹, Kenta Sueyoshi¹ & Takehiko Hiraga¹

The crystallographic preferred orientation (CPO) of olivine produced during dislocation creep is considered to be the primary cause of elastic anisotropy in Earth's upper mantle and is often used to determine the direction of mantle flow. A fundamental question remains, however, as to whether the alignment of olivine crystals is uniquely produced by dislocation creep. Here we report the development of CPO in iron-free olivine (that is, forsterite) during diffusion creep; the intensity and pattern of CPO depend on temperature and the presence of melt, which control the appearance of crystallographic planes on grain boundaries. Grain boundary sliding on these crystallography-controlled boundaries accommodated by diffusion contributes to grain rotation, resulting in a CPO. We show that strong radial anisotropy is anticipated at temperatures corresponding to depths where melting initiates to depths where strongly anisotropic and low seismic velocities are detected. Conversely, weak anisotropy is anticipated at temperatures corresponding to depths where almost isotropic mantle is found. We propose diffusion creep to be the primary means of mantle flow.

Observations of anisotropy in the velocity of seismic waves have given us a dynamic view of Earth's interior¹. Interpretation of seismic anisotropy in the mantle is based on our understanding of mineral physics and the anisotropic deformation characteristics of the olivine lattice². Dislocation creep, which is considered to be one of the main deformation mechanism in Earth's interior, involves not only slip on specific crystallographic planes, but also grain rotation. As a consequence, the primary crystal slip plane and axis align with the direction of mantle flow³. All minerals are elastically anisotropic to some extent, such that crystallographic alignment of minerals with a specific direction results in anisotropy in elastic-wave velocity. Consequently, observed seismic anisotropy is often interpreted as the result of slip on a particular slip system. The recent discovery of the various patterns of CPO of olivine formed under various experimental conditions such as different stresses, pressures and water concentrations has resulted in new interpretations of seismic anisotropy and CPO observed in nature^{4–6}. The common principle underlying these interpretations is that the anisotropy is a consequence of dislocation creep. Here we describe experimental evidence showing that significant olivine crystallographic alignment occurs during diffusion creep, which may alter the simple, long-held view of CPO development in Earth's interior.

Creep tests and microstructural analyses

We conducted uniaxial tensile and compression creep experiments on fine-grained iron-free olivine (that is, forsterite) plus 20 vol.% diopside (a combination that we denote Fo + Di) and the same compression tests on forsterite plus 20 vol.% anorthitic melt (An) at atmospheric pressure, temperatures of 1,150–1,385 °C (the solidus temperature, T_s , for Fo + Di is 1,382 °C) and strain rates of $\dot{\epsilon} = 10^{-6}$ – 10^{-4} s⁻¹. We anticipated that tension experiments would give us an indication of the easy slip direction and that compression experiments would indicate the easy slip plane for forsterite if we detected a CPO in our samples.

In all the tests, a piece of the same starting material was placed next to the creep sample but not under load, to observe changes in the microstructure due to static annealing (we refer to this sample as a reference sample). We rapidly changed displacement rates (\dot{v}) during the compression experiments, to obtain the stress dependence of the strain rate.

Unless melt was involved, we also conducted independent compression experiments at lower but constant values of \dot{v} and to a constant final strain ($\epsilon = 0.6$). These constant- \dot{v} experiments were conducted to eliminate any effect of changing strain rate and strain on the sample microstructure, especially CPO. Typical stress (σ)– ϵ curves showed strain hardening, which is attributed to grain growth (Extended Data Fig. 1). Such growth is identified in the change in grain size (d) measured before and after the creep experiments. Grain growth during the experiments was estimated using static and dynamic grain growth laws^{7,8} (Methods). Rheological data were analysed on the basis of the power-law relationship $\dot{\epsilon} = A(\sigma^n/d^p)$, where A is a constant and n and p are respectively the stress and grain size exponents. We estimate that $p = 1$ – 2 from the relationship between sample hardening and the estimated grain growth during the deformation. By using $p = 2$ to normalize the grain size to 1 μm in all samples⁹, including those from individual experiments conducted for CPO analyses, we find a linear dependence between strain rate and stress with $n = 1.1 \pm 0.2$ for temperatures from 1,200 to 1,350 °C (Fig. 1).

In Fig. 2, the crystallographic orientations of more than 300 forsterite grains, taken from the centre part of each sample, are plotted on lower-hemispheric projections, where the x (or y) and z axes respectively correspond to directions perpendicular and parallel to the direction of applied force. Because we conducted uniaxial tests, the x and y axes are equivalent. We found a systematic change in CPO patterns with temperature. At $T \leq 1,250$ °C in Fo + Di samples deformed in compression, the forsterite c axes ([001]) are weakly oriented in the z direction and the a axes ([100]) are weakly but homogeneously oriented in the x – y plane (we denote this as an a girdle), whereas in samples deformed in tension, the a axes are weakly oriented in the z direction. CPOs developed in this temperature range are very weak (J index < 3 ; see Extended Data Table 1, where the J index is a measure of the density distribution of the crystallographic orientations, that is, J is respectively unity and infinity for a random distribution and for a single crystal (perfect CPO)¹⁰); nevertheless, the observed CPO patterns are characteristic of all the samples deformed under these conditions. At 1,300–1,350 °C, the b axes ([010]) are strongly oriented in the z direction and a and c girdles form in the x – y plane in samples deformed in compression,

¹Earthquake Research Institute, University of Tokyo, 1-1-1 Yayoi, Bunkyo-ku, Tokyo 113-0032, Japan.

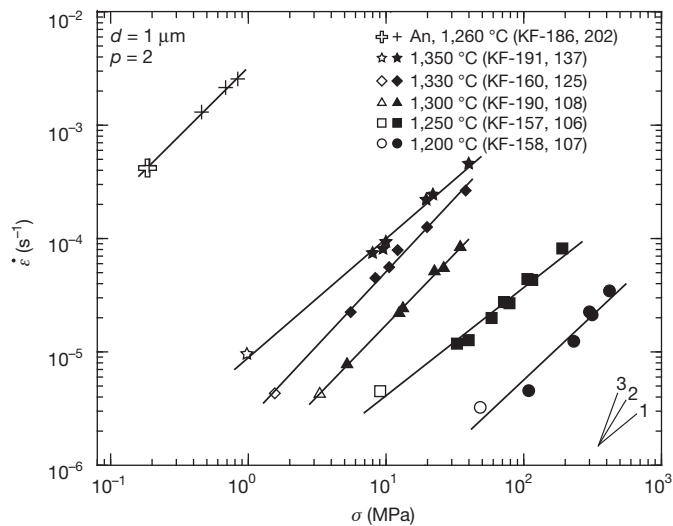


Figure 1 | Strain rate as a function of stress. Data from Fo+Di samples at five different temperatures and from the Fo+An sample at 1,260 °C are presented. Open symbols represent the data from samples that were used to determine the crystallographic orientation of forsterite grains shown in Fig. 2. Three different slopes corresponding to three different stress exponents ($n = 1-3$) are shown at lower right.

whereas in samples deformed in tension, the a axes are oriented towards the z direction and b girdles form in the $x-y$ plane. The CPO formed in samples deformed at 1,250 °C has characteristics of the patterns observed for samples deformed at $T < 1,250$ °C and $T \geq 1,300$ °C. At 1,385 °C, where melting of all diopside grains and some of the forsterite produces samples of Fo plus 30 vol.% melt, we observe very weak orientation of b axes in the z direction, which was also identified in Fo+An samples. Most of the CPOs are weak, but their intensity increases with strain, as confirmed in a sample deformed at 1,330 °C (Extended Data Fig. 2). CPO patterns change systematically with temperature and the presence of melt. To reflect this, in what follows we refer to subsolidus temperatures of $T \leq 1,250$ °C as 'low T ', subsolidus temperatures between 1,250 °C and T_s as 'high T ', and temperatures at which the samples are melt bearing as ' $>T_s$ '.

The CPO patterns were identified from samples deformed at the lowest stresses for each temperature where linear σ - $\dot{\epsilon}$ relationships were observed under all experimental conditions (Fig. 1). Thus, these samples were necessarily deformed by a diffusional creep mechanism, and it is difficult to explain the CPO patterns as a result of dislocation creep on specific slip systems in forsterite. In the reference samples, forsterite grains at low T have an equigranular (that is, isotropic) shape, whereas grains at high T develop a weakly to strongly elongated (tabular) shape (Fig. 3). Grains in $>T_s$ samples have a polygonal-equigranular shape. These characteristic shapes align towards the direction of maximum strain in the deformed samples. In Fig. 4, we plot the J index as a function of aspect ratio for the reference samples determined from the

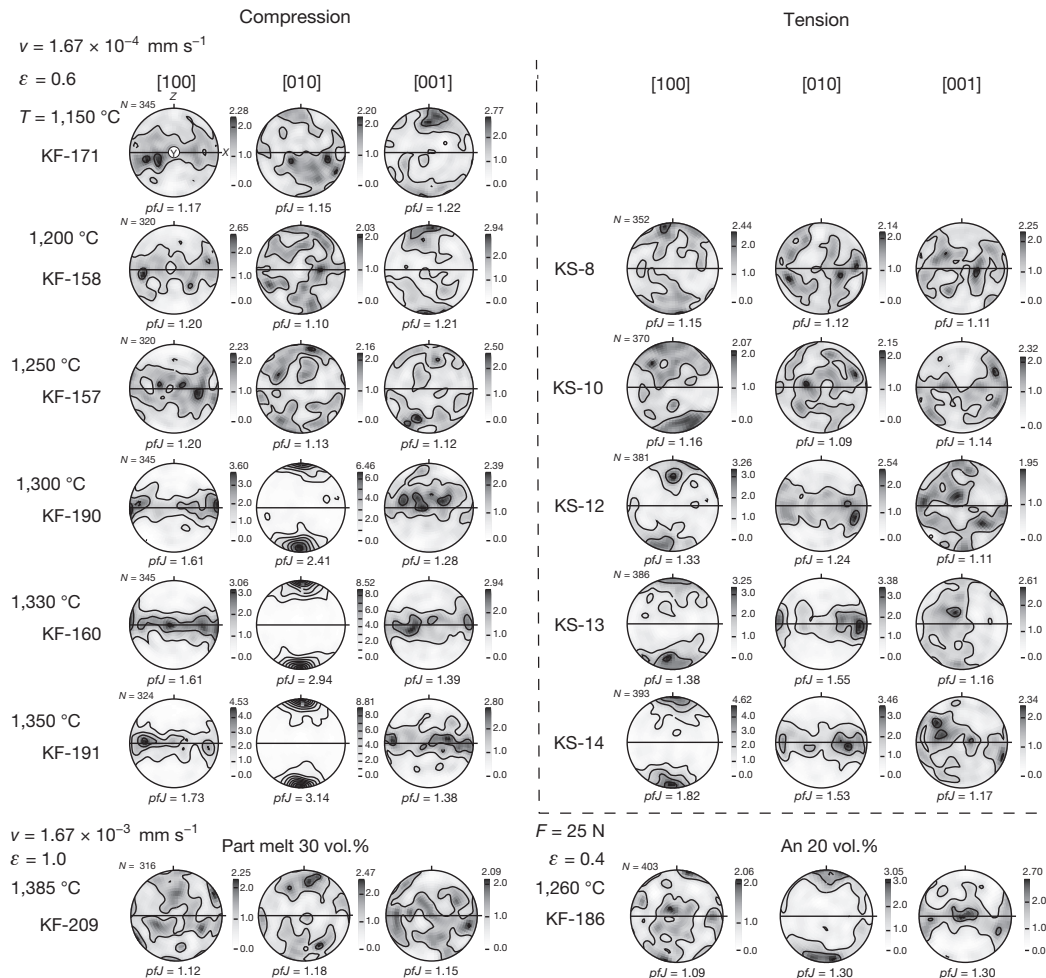


Figure 2 | Lower-hemispheric projections of the crystallographic orientations of forsterite grains. The Fo+Di orientations are at a strain of $\epsilon = 0.6$ ($\epsilon = 1.0$ for the partly molten Fo+Di) and are deformed at constant displacement rate (ν). The Fo+An orientations are at $\epsilon = 0.4$ and are deformed

at constant force (F). N , number of measured grains. Measurements were made by scanning electron microscopy (SEM) and SEM electron backscatter diffraction (EBSD). p/J , sharpness of a pole figure¹⁰.

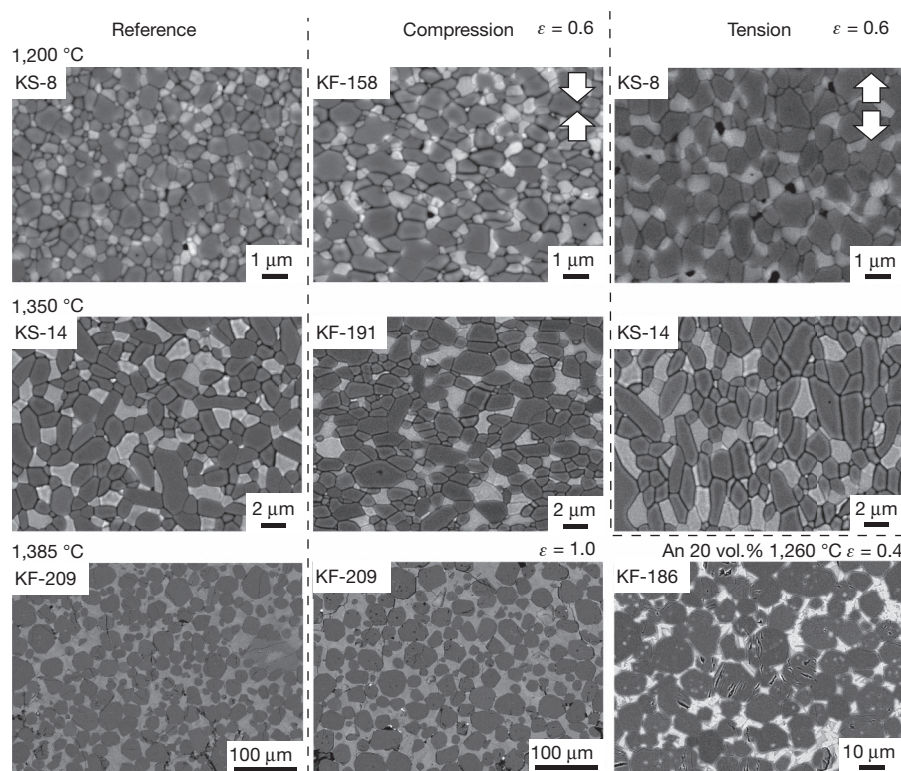


Figure 3 | SEM backscatter images of reference and deformed samples of Fo+Di, partly molten Fo+Di and Fo+An. Dark-grey grains are forsterite and light-grey grains are diopside. Diopside grains are weakly aggregated and aligned in the direction of compression, whereas grains of forsterite and

diopside phases are weakly to strongly elongated and aligned in the tensile direction. All the reference samples were annealed during the tensile experiments. In the melt-bearing samples (KF-209 and KF-186), the melt phase is light grey or dark grey and the forsterite grains are darker still.

CPOs shown in Fig. 2. At low T , the grains have a constant aspect ratio of 1.3–1.4, whereas at high T the aspect ratio increases with temperature. The aspect ratio is smaller in melt-bearing samples. The aspect ratios in reference samples and J index values from high- T deformation experiments correlate positively, indicating that anisotropic grain growth with temperature controls the CPO.

In addition to grains with highly anisotropic shape appearing even in the reference samples, grain boundaries are frequently straight and parallel on opposite sides of the grains. We found that the long axes of forsterite grains in the high- T reference and deformed samples are frequently perpendicular to [010] and occasionally to [001], and that

they are parallel to [100] (Extended Data Fig. 3). Consequently, the longest straight grain boundaries parallel to the long axes of forsterite grains in the high- T samples also lie in the (010) plane (the plane perpendicular to the b axis) (Fig. 3), a conclusion that is supported by our transmission electron microscopy study (Extended Data Fig. 4). This type of the boundary is referred to as a low-index plane boundary¹¹ and has been previously identified in iron-bearing olivine aggregates^{12,13}. Forsterite grains at low T and $>T_s$ have aspect ratios low enough that it was difficult to analyse their shape with respect to their crystallographic axes. However, especially in $>T_s$ samples, forsterite has straight interfaces indicative of the crystal habit. Thus, we conclude that the development of low-index plane boundaries controls the grain shape and, furthermore, the development of CPO during deformation at all temperature conditions.

Condition for CPO formation

We observe aggregation of like phases in the direction of compression in melt-free samples (Fig. 3). This aggregation is due to significant grain boundary sliding (GBS), which allows isolated grains of the secondary phase to contact each other through grain switching events^{7,14}. In addition, Fo+Di samples at high T exhibited superplasticity (that is, a tensile strain of $\gg 100\%$; Extended Data Fig. 5), which also requires a significant contribution from GBS¹⁵. Thus, it is reasonable to consider CPO development in a regime where GBS is accommodated by diffusion. Because the orientation of many grain boundaries is crystallography controlled, GBS should frequently occur on specific crystallographic planes and even in specific directions. Preferential GBS on specific boundaries contributes to grain rotation followed by an alignment of easy slip grain boundaries in the direction of flow¹⁶ (Extended Data Fig. 6). As a result, we can identify an apparent easy slip plane and direction for GBS from the CPO patterns, which can be compared with results on dislocation creep showing that slip occurs along preferential intergranular crystallographic planes.

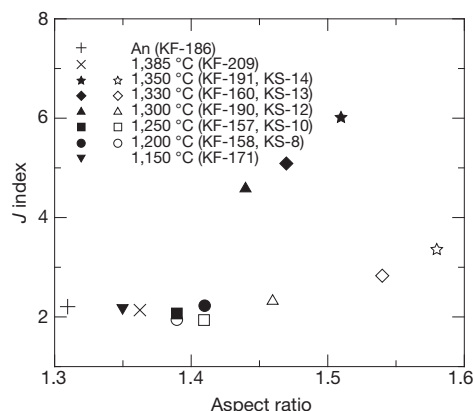


Figure 4 | J index determined from EBSD analyses of the deformed samples as a function of aspect ratio of forsterite grains in the reference sample. Data come from both tension experiments (open symbols) and compression experiments (filled symbols). A different effect of the aspect ratio on J index is observed in compression and tension samples owing to the strong alignment of b axes in the z direction in high- T compression samples (Fig. 2).

Our proposal that CPO is controlled by grain shape is strongly supported by the characteristic high- T CPO pattern formed during low- T compression experiments, where the starting material was prepared at high T (Extended Data Fig. 7). Little grain shape modification is expected after the saturation of grain size at high T (Extended Data Table 1), and, consequently, the CPO pattern must have developed as a result of the inherited high- T grain shape. Essentially the same observations and conclusions have been made for CPO formation in deformed alumina aggregates, which yielded crystallographically controlled anisotropic alumina grains in a certain sintering temperature range and deformed by means of GBS plus grain rotation without the help of dislocation glide¹⁷. In silicates, the development of CPO during deformation with a stress exponent of ~ 1 has been identified previously^{18,19} and was thought to be due to a contribution from dislocation glide or chemical reaction, neither of which is required to explain CPO development in our experiments.

Assuming that the observed CPO patterns reflect the elongated forsterite shape, we estimate the relative axial dimensions of forsterite as $a > b > c$ at low T , indicating that the plane perpendicular to the c axis (the ' c plane') defines the most developed grain boundary elongated in the a direction, and as $a > c > b$ at high T , where the b plane is the most developed grain boundary elongated in the a direction. For samples deformed in compression at $T > T_s$, it is difficult to estimate the forsterite dimensions from CPO patterns alone. However, if we use the previously known euhedral shape of forsterite with its free surfaces (that is, the crystal–fluid or crystal–melt interfaces)²⁰, then we predict that $c > a > b$ at $T > T_s$, where the b plane is the most developed grain boundary elongated in the c direction, which is consistent with the observed CPO patterns and grain shape.

We have identified anisotropic forsterite grains similar to those observed in high- T samples in the forsterite system with different chemical environments. In calcium-free samples of forsterite plus enstatite (MgSiO_3) at $T \leq 1,360^\circ\text{C}$, we observed equigranular grains similar to those present at low T (see figure 1 in refs 8, 21), whereas in annealed samples at $1,400^\circ\text{C}$ we identified elongated grains (data not shown). In a system of forsterite plus MgO , we observed equigranular grains with almost random to weak CPO even at $1,450^\circ\text{C}$, which respectively resemble the grain shape and CPO pattern seen at low T in this study⁷. In aggregates of forsterite plus diopside (plus water) at $1,200^\circ\text{C}$ and 1.2 GPa, very anisotropic (tabular) forsterite grains were formed²². All these results demonstrate that the equigranular or anisotropic forsterite grains form under different conditions in different forsterite-bearing systems. However, if we consider the experimental temperatures relative to T_s for each system (Supplementary Information), all the observed grain shapes are well explained by a transition temperature of $\sim 0.92T_s$ (in K), with equigranular and anisotropic grains appearing below and above $0.92T_s$, respectively. As a consequence, we can simply think of low T and high T as $T < 0.92T_s$ and $0.92T_s < T < T_s$, respectively, where T_s changes with different geological conditions including different chemical environments. At present, we have not determined a physical explanation for this transition temperature. However, it is reasonable that the shape transition is related to T_s , because elements that can reduce T_s are predicted to segregate to olivine grain boundaries²³. Some elements, for example calcium in this study, are confirmed to partition into olivine boundaries in a chemically equilibrated state¹³. Structural transitions of the grain boundary including pre-melting at the boundary below T_s have also been identified in some materials²⁴ where such transition should occur within a scale of 1 nm width (Extended Data Fig. 4).

Although our CPO results come from uniaxial deformation tests, we can estimate what type of CPO patterns will be formed during simple shear, which is more relevant to the deformation geometry in Earth's interior. The type of fabric was previously classified for olivine depending on flow and crystallographic geometry⁵. At high T , A-type fabric (that is, (010)[100], in which the olivine b plane is almost parallel to the shear plane and the a axis is almost parallel to the shear direction), which is the most common fabric found in nature, will be formed. At low T , despite its weak development, E-type fabric (that is, (001)[100]), which

has also been identified in nature^{25,26}, will be formed. At $T > T_s$, we predict B-type fabric (that is, (010)[001]) on the basis of the grain shape observed at this condition.

Discussion

In Earth's interior, changes in temperature from $T < 0.92T_s$ to $T > T_s$ occur mainly along adiabatic gradients during upwelling (that is, as pressure decreases) and as a result of changing chemical environments (for example, an increase in water content). Assuming (1) an adiabatic temperature gradient in the uppermost mantle of 0.5 K km^{-1} , (2) a melting point, $T_s = 1,650\text{--}1,900\text{ K}$, depending on the water concentration, and (3) geologic settings where upwelling is occurring, such as beneath a ridge or a plume, we estimate that the region in which $T = 0.92T_s$ will vary in depth from the point of initial melting to 50–100 km deeper.

We apply our prediction to the asthenosphere beneath the Pacific basin, where the horizontal flow of the mantle starting from beneath the East Pacific Rise is well resolved by seismic tomography²⁷ (Fig. 5). Electrical conductivity measurements across the East Pacific Rise showed the bottom of the conductive region to have a depth of $\sim 130\text{ km}$ (ref. 28). This depth is geochemically consistent with the initiation of silicate melting²⁹. With the same assumptions as above, if $T = T_s$ at this depth then $T = 0.92T_s$ at $\sim 210\text{ km}$. We thus predict, first, that the region at 130–210-km depth exhibits strong anisotropy with A-type fabric, which can produce radial and azimuthal seismic anisotropy with the fast axis almost parallel to the direction of mantle flow³ (that is, with the velocity of horizontally polarized shear waves greater than that of vertically polarized shear waves), and, second, that the intensity of the anisotropy increases with decreasing depth. Generally, a depth range of 130–210 km corresponds to the low-seismic-velocity zone, whose existence has been explained by thermal and grain size effects on seismic attenuation by extrapolating experimental results to mantle conditions³⁰; however, it has been questioned whether peridotite with the assumed grain size (that is, $\sim 1\text{ mm}$) could deform by dislocation creep at the conditions of the low-seismic-velocity zone, and it is claimed that a grain size $> 15\text{ mm}$ is necessary³¹.

Our results showing the presence of a strong A-type fabric during diffusion creep may explain not only the observed seismic anisotropy but also the apparent contradiction between the presence of larger seismic attenuation and strong radial anisotropy at grain sizes commonly observed in nature³². At depths $> 210\text{ km}$, the anisotropy becomes undetectable or very weak²⁷, which has been explained to result from a switch from dislocation creep to diffusion creep³³ or from a pressure-induced transition of an easy slip system of olivine crystal^{34–36}. Our results showing a very weak E-type fabric at $T < 0.92T_s$ may account for the seismic characteristics of this deeper region. In the shallow portion of the upper mantle with $T > T_s$, we predict the presence of A- and B-type fabrics in melt-poor and melt-rich regions, respectively, because such a fabric transition requires a change in the ratio of crystal–crystal interfaces to crystal–melt interfaces in the rock. Our prediction is supported by preliminary deformation experiments in the presence of $< 1\text{ vol.}\%$ melt (Extended Data Fig. 8).

Recent seismological studies indicate the presence of melt layers at the lithosphere–asthenosphere boundary, where the rock is considered to lose grain-to-grain contact within the layers and to be essentially free of melt outside the layers³⁷. The presence of such layers was experimentally reproduced in sheared olivine-plus-basalt aggregates with development of olivine CPO in B- or AG-type fabric³⁸ (AG-type is a mixture of A and B types). Grain growth is a thermally activated process, and so grain size will be almost maximized beneath the ridge and will remain constant during horizontal flow of the mantle, which will cool with distance from the ridge. Because grain growth is saturated, the grain shape will remain the same, and subsequent deformation will consequently produce a CPO determined by grain shape rather than by the deformation conditions, as in the experimental result of Extended Data Fig. 7. This prediction explains the $\sim 210\text{-km}$ depth of the bottom of the anisotropic mantle beneath the Pacific very far from the East Pacific Rise (Fig. 5).

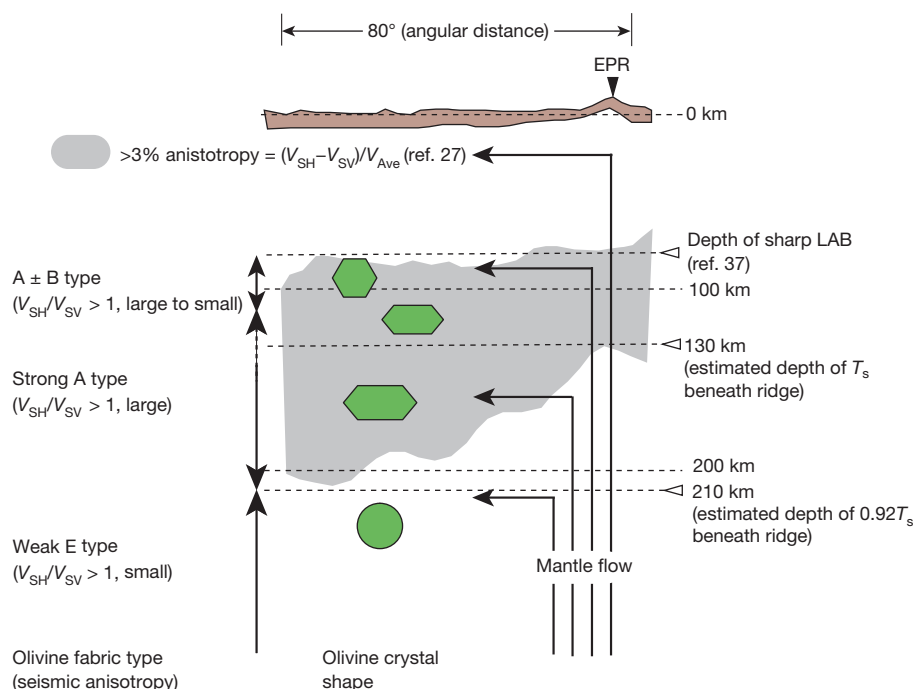


Figure 5 | Proposed depth distributions of olivine crystal shape and fabrics during diffusion-accommodated GBS creep of peridotite in the asthenosphere. Estimated depths corresponding to T_s and $0.92T_s$ for the East Pacific Rise (EPR) are added for comparison with the seismic anisotropy profile beneath the Pacific basin²⁷. Circular, tabular and hexagonal grains represent

olivine appearing at low T , high T and $>T_s$, respectively. Characteristics of seismic anisotropy are estimated from the olivine fabric types and intensity. LAB, lithosphere–asthenosphere boundary; V_{Ave} , average shear-wave velocity; V_{SH} , velocity of horizontally polarized shear wave; V_{SV} , velocity of vertically polarized shear wave; A ± B, A type with or without B type.

Because diffusion creep operates at finer grain size for a given stress and temperature, we may ask whether our observations are limited to very fine-grained aggregates such as those used in our study. Taking into account plausible stress and grain sizes in Earth's mantle, olivine aggregates are predicted to deform either by diffusion or dislocation creep³⁹. Furthermore, a significant contribution of GBS to sample strain, sometimes referred as GBS creep irrespective of its rate-controlling process, often appears near the transition between diffusion and dislocation creep⁴⁰. The effects of dynamic recrystallization during dislocation creep are easily identified in rocks; however, dislocation creep may be limited to very shallow portions of Earth's interior, such as within the lithosphere, where stresses of >10 MPa may drive deformation. Historically, diffusion creep was believed to dominate in Earth's interior owing to its occurrence at high temperature and low stress^{41,42}. Soon after the discovery of the anisotropic nature of Earth's interior, especially in the upper portion of the mantle, the importance accorded to diffusion creep decreased. We have reported experimental evidence showing that the mantle anisotropy can be formed during diffusion creep and that the predicted anisotropy based on our observed CPO does not contradict seismic observations. Diffusion creep is thus once again the favoured mechanism of mantle flow.

METHODS SUMMARY

Experimental samples were prepared through vacuum sintering of mineral powders with nanometre-sized grains. A uniaxial mechanical testing machine was used for creep tests. We used SEM and SEM EBSD to analyse sample microstructures and the crystallographic orientation of forsterite grains.

Online Content Any additional Methods, Extended Data display items and Source Data are available in the online version of the paper; references unique to these sections appear only in the online paper.

Received 29 April; accepted 9 August 2013.

1. Tanimoto, T. & Anderson, D. L. Mapping mantle convection. *Geophys. Res. Lett.* **11**, 287–290 (1984).
2. Carter, N. L. & Avé Lallemant, H. G. High temperature flow of dunite and peridotite. *Geol. Soc. Am. Bull.* **81**, 2181–2202 (1970).

3. Nicolas, A. & Christensen, N. I. in *The Composition, Structure and Dynamics of the Lithosphere-Asthenosphere System* (eds Froidevaux, C. & Fuchs, K.) 111–123 (American Geophysical Union, 1987).
4. Couvy, H. *et al.* Shear deformation experiments of forsterite at 11 GPa–1400 °C in the multianvil apparatus. *Eur. J. Mineral.* **16**, 877–889 (2004).
5. Jung, H. & Karato, S.-I. Water-induced fabric transitions in olivine. *Science* **293**, 1460–1463 (2001).
6. Karato, S. in *Inside the Subduction Factory* (ed. Eiler, J.) 135–152 (American Geophysical Union, 2003).
7. Hiraga, T., Miyazaki, T., Tasaka, M. & Yoshida, H. Mantle superplasticity and its self-made demise. *Nature* **468**, 1091–1094 (2010).
8. Tasaka, M. & Hiraga, T. Influence of mineral fraction on the rheological properties of forsterite + enstatite during grain size sensitive creep: 1. Grain size and grain growth laws. *J. Geophys. Res.* **118**, <http://dx.doi.org/10.1002/jgrb.50285> (2013).
9. Tasaka, M., Hiraga, T. & Zimmerman, M. E. Influence of mineral fraction on the rheological properties of forsterite + enstatite during grain size sensitive creep: 2. Deformation experiments. *J. Geophys. Res.* **118**, <http://dx.doi.org/10.1002/jgrb.50284> (2013).
10. Mainprice, D., Barruol, G. & Ismail, W. in *Earth's Deep Interior: Mineral Physics and Seismic Tomography from the Atomic to the Global Scale* (eds Karato, S., Forte, A. M., Liebermann, R. C., Masters, G. & Stixrude, L.) 237–264 (Geophys. Monogr. Ser. 117, American Geophysical Union, 2000).
11. Hiraga, T., Nagase, T. & Akizuki, M. The structure of grain boundaries in granite-origin ultramylonite studied by high-resolution electron microscopy. *Phys. Chem. Miner.* **26**, 617–623 (1999).
12. Hiraga, T., Anderson, I. M., Zimmerman, M. E., Mei, S. & Kohlstedt, D. L. Structure and chemistry of grain boundaries in deformed, olivine + basalt and partially molten lherzolite aggregates: evidence of melt-free grain boundaries. *Contrib. Mineral. Petrol.* **144**, 163–175 (2002).
13. Hiraga, T., Anderson, I. M. & Kohlstedt, D. L. Grain boundaries as reservoirs of incompatible elements in the Earth's mantle. *Nature* **427**, 699–703 (2004).
14. Hiraga, T., Miyazaki, T., Yoshida, H. & Zimmerman, M. E. Comparison of microstructures in superplastically deformed synthetic materials and natural mylonites: mineral aggregation via grain boundary sliding. *Geology* **41**, 959–962 (2013).
15. Ashby, M. F. & Verrall, R. A. Diffusion-accommodated flow and superplasticity. *Acta Metall.* **21**, 149–163 (1973).
16. Beere, W. Stresses and deformation at grain boundaries. *Phil. Trans. R. Soc. Lond. A* **288**, 177–196 (1978).
17. Yoshizawa, Y., Toriyama, M. & Kanzaki, S. Fabrication of textured alumina by high-temperature deformation. *J. Am. Ceram. Soc.* **84**, 1392–1394 (2001).
18. Barreiro, G. *et al.* Preferred orientation of anorthite deformed experimentally in Newtonian creep. *Earth Planet. Sci. Lett.* **264**, 188–207 (2007).
19. Sundberg, M. & Cooper, R. F. Crystallographic preferred orientation produced by diffusional creep of harzburgite: effects of chemical interactions among phases during plastic flow. *J. Geophys. Res.* **113**, B12208 (2008).

20. Deer, W. A. Howie, R. A. & Zussman, J. *Rock-Forming Minerals: Volume 1A: Orthosilicates* 194–200 (Longman, 1982).
21. Hiraga, T., Tachibana, C., Ohashi, N. & Sano, S. Grain growth systematics for forsterite \pm enstatite aggregates: effect of lithology on grain size in the upper mantle. *Earth Planet. Sci. Lett.* **291**, 10–20 (2010).
22. Ohuchi, T. & Nakamura, M. Grain growth in the system forsterite–diopside–water. *Phys. Earth Planet. Inter.* **161**, 281–304 (2007).
23. Hiraga, T., Hirschmann, M. M. & Kohlstedt, D. L. Equilibrium interface segregation in the diopside–forsterite system II: applications of interface enrichment to mantle geochemistry. *Geochim. Cosmochim. Acta* **71**, 1281–1289 (2007).
24. Straumal, B. & Baretzky, B. Grain boundary phase transitions and their influence on properties of polycrystals. *Interface Sci.* **12**, 147–155 (2004).
25. Mehl, L., Hacker, B. R., Hirth, G. & Kelemen, P. B. Arc-parallel flow within the mantle wedge: evidence from the accreted Talkeetna arc, south central Alaska. *J. Geophys. Res.* **108**, 2375 (2003).
26. Fernando, L., Morales, G. & Tommasi, A. Composition, textures, seismic and thermal anisotropies of xenoliths from a thin and hot lithospheric mantle (Summit Lake, southern Canadian Cordillera). *Tectonophysics* **507**, 1–15 (2011).
27. Nettles, M. & Dziewonski, A. M. Radially anisotropic shear-velocity structure of the upper mantle beneath North America. *J. Geophys. Res.* **113**, B02303 (2008).
28. Evans, R. L. *et al.* Geophysical evidence from the MELT area for compositional controls on oceanic plates. *Nature* **437**, 249–252 (2005).
29. Hirschmann, M. M. Water melting and the deep Earth H₂O cycle. *Annu. Rev. Earth Planet. Sci.* **34**, 629–653 (2006).
30. Faul, U. H. & Jackson, I. The seismological signature of temperature and grain size variations in the upper mantle. *Earth Planet. Sci. Lett.* **234**, 119–134 (2005).
31. Behn, M. D., Hirth, G. & Elsenbeck, J. R. Implications of grain-size evolution on the seismic structure of the oceanic upper mantle. *Earth Planet. Sci. Lett.* **282**, 178–189 (2009).
32. Mercier, J.-C. C. Magnitude of the continental lithospheric stresses inferred from rheomorphic petrology. *J. Geophys. Res.* **85**, 6293–6303 (1980).
33. Karato, S. On the Lehmann discontinuity. *Geophys. Res. Lett.* **19**, 2255–2258 (1992).
34. Mainprice, D., Tommasi, A., Couvy, H., Cordier, P. & Frost, D. J. Pressure sensitivity of olivine slip systems: implications for the interpretation of seismic anisotropy of the Earth's upper mantle. *Nature* **433**, 731–733 (2005).
35. Raterron, P., Chen, J., Li, L., Weidner, D. J. & Cordier, P. Pressure-induced slip system transition in forsterite: single-crystal rheological properties at mantle pressure and temperature. *Am. Mineral.* **92**, 1436–1445 (2007).
36. Ohuchi, T., Kawazoe, T., Nishihara, Y., Nishiyama, N. & Irifune, T. High pressure and temperature fabric transitions in olivine and variations in upper mantle seismic anisotropy. *Earth Planet. Sci. Lett.* **304**, 55–63 (2011).
37. Kawakatsu, H. *et al.* Seismic evidence for sharp lithosphere–asthenosphere boundaries of oceanic plates. *Science* **324**, 499–502 (2009).
38. Holtzman, B. K. *et al.* Melt segregation and strain partitioning: implications for seismic anisotropy and mantle flow. *Science* **301**, 1227–1230 (2003).
39. Karato, S.-I. Rheology of the deep upper mantle and its implications for the preservation of the continental roots: a review. *Tectonophysics* **481**, 82–98 (2010).
40. Nieh, T. G., Wadsworth, J. & Sherby, O. D. *Superplasticity in Metals and Ceramics* 32–57 (Cambridge Univ. Press, 1997).
41. Nabarro, F. R. N. in *Strength of Solids* (ed. Mott, N. F.) 75–90 (Physical Society, 1948).
42. Gordon, R. B. Diffusion creep in the Earth's mantle. *J. Geophys. Res.* **70**, 2413–2418 (1965).

Supplementary Information is available in the online version of the paper.

Acknowledgements Discussions with H. Yoshida, K. Morita, M. E. Zimmerman, Y. Takei, S. Michibayashi, B. K. Holtzman, K. Baba, T. Isse and H. Kawakatsu were very helpful. We thank Ube Material Industries, S. Ohtsuka, K. Ibe, M. Uchida and A. Yasuda for technical assistance. A portion of this work was conducted at the Center for Nano Lithography and Analysis of the University of Tokyo, supported by the Ministry of Education, Culture, Sports, Science and Technology (MEXT), Japan. This study was supported by the JSPS through Grants-in-Aid for Scientific Research 23684043, 22000003 and 21109005, and through the Earthquake Research Institute's cooperative research programme (T.H.).

Author Contributions T.M., K.S. and T.H. organized the project, and T.H. and T.M. completed the manuscript.

Author Information Reprints and permissions information is available at www.nature.com/reprints. The authors declare no competing financial interests. Readers are welcome to comment on the online version of the paper. Correspondence and requests for materials should be addressed to T.H. (hiraga@eri.u-tokyo.ac.jp).

METHODS

Mineral powders for sintering Fo+Di were prepared through solid-state reactions of nano-sized powders of $\text{Mg}(\text{OH})_2$, colloidal SiO_2 and CaCO_3 at 1,000 °C, and those for Fo+An were prepared using $\text{Mg}(\text{OH})_2$, colloidal SiO_2 , CaCO_3 and Al_2O_3 at 800–1,000 °C (see details in refs. 21, 43). We applied a vacuum sintering technique at 1,150–1,280 °C to obtain aggregates with >99.9% density and a homogeneous phase distribution. We changed time durations for the sintering to minimize grain size differences among the creep experiments, resulting in an almost constant grain size of $\sim 0.4 \mu\text{m}$ for melt-free samples and, owing to faster grain growth, 10–20 μm for melt-bearing samples (Extended Data Table 1). Introduction of diopside as a secondary phase helps to stabilize the microstructure through grain boundary pinning in melt-free samples⁴³.

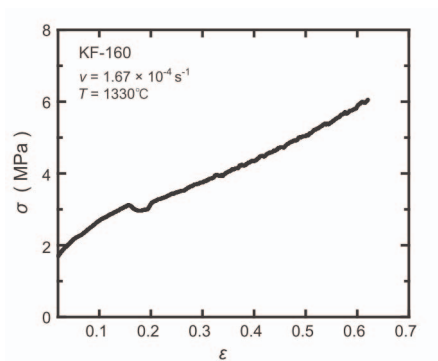
The resultant calcined powders were cold-pressed at an isostatic pressure of 200 MPa into 5 mm \times 10 mm \times 30 mm bars and cylinders 8 mm in diameter and 15 mm long. Subsequently, they were vacuum-sintered at 1,150, 1,200 or 1,280 °C depending on the temperature conditions for subsequent creep experiments. In general, the sintering temperatures and time duration were lower than those for subsequent creep experiments, to achieve equilibrium grain shape at each deformation temperature via grain growth. However, Fo+Di samples deformed in tension were all sintered at 1,280 °C. The effect of the higher sintering temperature on CPO development in the tension experiments at 1,200 and 1,250 °C is limited, because grain growth that could help to change grain shape was detected in these experiments and the grains were, as a result, expected to acquire equilibrium grain shape at the experimental temperatures (Extended Data Table 1). The bar-shaped sintered aggregates for tension experiments were machined to a gauge length of 12 mm, a width of 2 mm and a thickness of 2 mm (Extended Data Fig. 5a). Samples were deformed in a uniaxial mechanical testing machine with a furnace attached. Silicon carbide rods consisting of two to three parts with flexible joints were used to align samples to the tensile geometry after a small amount of displacement. The samples for the compression experiments were pressed using SiC rods with Al_2O_3 and SiC spacers. Testing temperatures were established by increasing the temperature at 650 °C h^{-1} . Tension experiments on melt-bearing samples and Fo+Di at 1,150 °C were limited owing to sample failure at the beginning of the experiments. Strain was determined from the crosshead displacement by considering the compliance of the apparatus and by assuming uniform elongation in the gauge portion. Thus, we use true strain (ϵ) instead of nominal strain when discussing the strain effect on creep characteristics. The force was determined using a load cell attached to the crosshead of the testing machine. Data were collected every 1–2 s. All samples were quenched at a rate of 20 °C min^{-1} to preserve deformation microstructure.

After the tests, all the samples were polished in the plane parallel to the tension or compression direction. Mechanochemical polishing with colloidal silica was used to prepare samples for EBSD analyses. A thermal grooving technique at

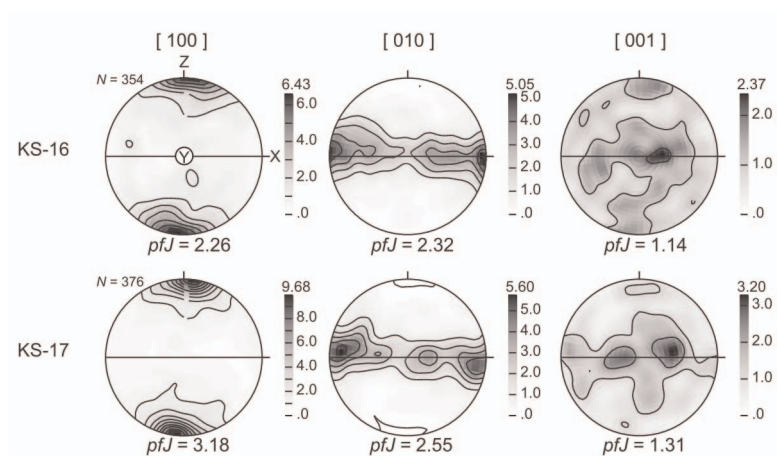
temperatures >100 °C lower than those used for the experiments was applied for 0.5 h in air to expose grain and interphase boundaries to analyse grain size, shapes and phase distributions (Fig. 3). Microstructural changes during the thermal etching were negligible. We did not apply any etching techniques to the specimens for transmission electron microscopy (TEM) observations. An ion slicer was used to obtain a thin section for TEM. We measured the diameter of each grain before and after deformation by approximating the grain shape to an ellipse using imaging software. The mean diameter of the ellipse was assumed to represent the grain size of the sample. Aspect ratios were determined from the long and short axes of the ellipse. The ratios were used in the analyses of the effect of grain shape on CPO intensity (Fig. 4). More than 170 grains were measured in each sample.

We estimate grain size at any point of the deformation using a dynamic grain growth law, $d_e = d_{\text{ref}} \exp(\alpha \epsilon)$, where d_e is grain size after a strain of ϵ , d_{ref} is grain size in the reference sample and α is a coefficient of ~ 0.2 for melt-free samples^{7,8} in which the applicability of the law to forsterite system was confirmed. Here we use d as an average grain size without distinguishing between phases. We estimated d_{ref} from a static grain growth law, $d_{\text{ref}}^m - d_0^m = kt$, where k is a growth coefficient estimated from a fit of the observed grain sizes as a function of time (t) and m is a growth exponent characteristic of the growth process. We use $m = 5$ for melt-free samples, which best explains the observed grain growth under static conditions. This value was also obtained in our grain growth experiments of forsterite plus enstatite²¹. The procedures used here to determine grain size during the deformation experiments are well described in ref. 8. We estimated grain growth in melt-bearing samples by using a static grain growth law, because we did not observe deformation-induced grain growth in these samples (Extended Data Table 1). This result is predicted from the dynamic grain growth model, in which the growth is controlled by a reduction of the number of the boundary-pinning grains (that is, the secondary crystalline phase) such that dynamic growth is not expected in the forsterite-plus-melt system. We use $m = 4$ for melt-bearing samples, which best explains our observed grain growth. This value is consistent with previous results from a grain growth experiment on partly molten olivine⁴⁴. All the estimated grain sizes (d_e in Extended Data Table 1) were used to correct the flow stress to a grain size of 1 μm by imposing $p = 2$ (Fig. 1). This value is consistent with previously obtained values in the forsterite system at low stress^{7,9}. Based on sample hardening and predicted grain size, our value of p contains a large uncertainty; however, n is still constrained to lie between 0.9 and 1.3 even with values of p ranging from 1 to 3.

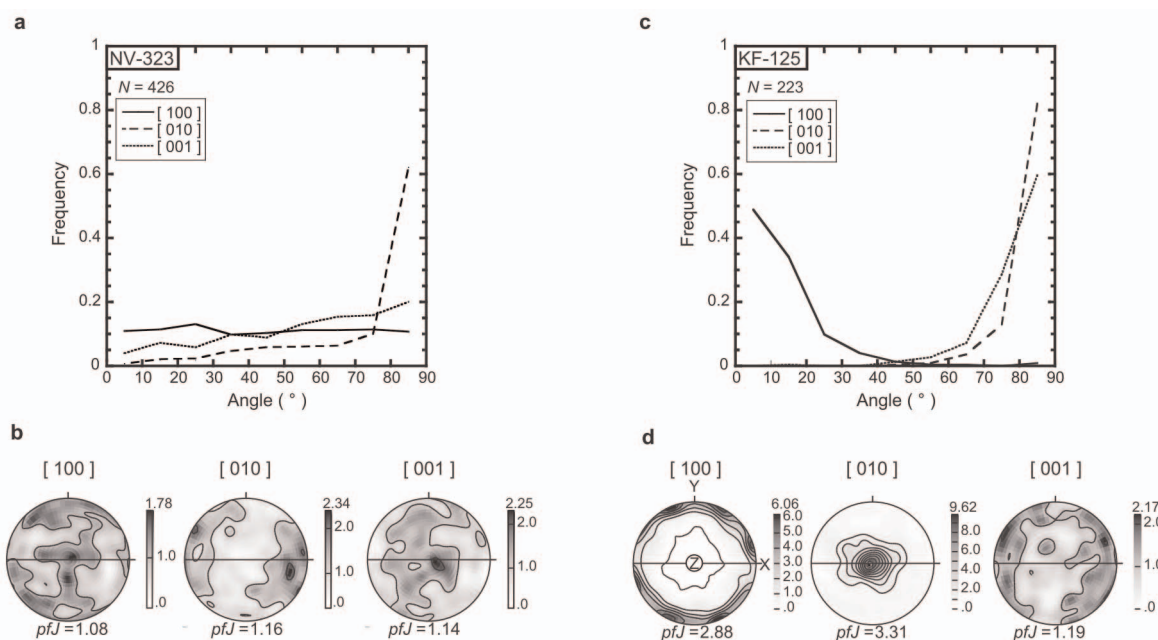
43. Koizumi, S. *et al.* Synthesis of highly dense and fine-grained aggregates of mantle composites by vacuum sintering of mineral nano-powders. *Phys. Chem. Miner.* **37**, 505–518 (2010).
44. Faul, U. H. & Scott, D. Grain growth in partially molten olivine aggregates. *Contrib. Mineral. Petrol.* **151**, 101–111 (2006).

**Extended Data Figure 1 | Typical stress–strain curve for a Fo+Di sample.**

The result was obtained from the compression experiment on the sample KF-160 at a constant displacement rate (ν). The CPO of forsterite for this sample is shown in Fig. 2.



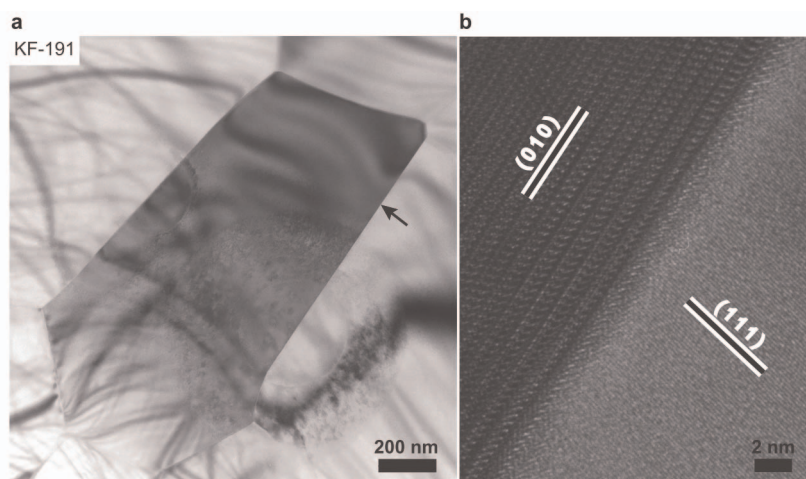
Extended Data Figure 2 | The CPO of forsterite grains from tension experiments on Fo+Di samples at 1,330 °C with different amounts of strain (KS-16, $\varepsilon = 1.1$; KS-17, $\varepsilon = 1.5$). The CPO of the sample with the smallest strain (KS-13, $\varepsilon = 0.6$) is shown in Fig. 2.



Extended Data Figure 3 | Angles between crystallographic axes of forsterite and apparent long axes of forsterite grains in the Fo+Di samples.

Crystallographic a , b and c axes were measured by SEM/EBSD, whereas the long axes were determined from the grain shapes. Highly anisotropic grains were selectively measured. N , number of measured grains. **a**, Angle frequency in the sample statically annealed at 1,330 °C for 20 h (NV-323). **b**, CPO of the grains analysed in **a**. **c**, Angle frequency in the sample compressed at 1,330 °C (KF-125). The angles were measured in sections cut perpendicularly to the compression axis in the deformed sample. **d**, CPO of the grains analysed in **c**. Note that b and c axes are perpendicular to the long axes in the deformed

samples, whereas only b axes are clearly perpendicular to the long axes in the non-deformed samples. The CPO in **b** indicates that the highly anisotropic grains were well identified when the b axes of forsterite grains were parallel to the sample section when the grains were randomly oriented, whereas the CPO in **d** indicates that the highly anisotropic grains were well identified when the b axes of the grains were perpendicular when the grains were preferentially oriented in the sample. Thus, we can conclude that the longest axis of each grain was parallel to the a axis and that the second longest axis was parallel to the c axis. The shortest grain axis should be parallel to the b axis.

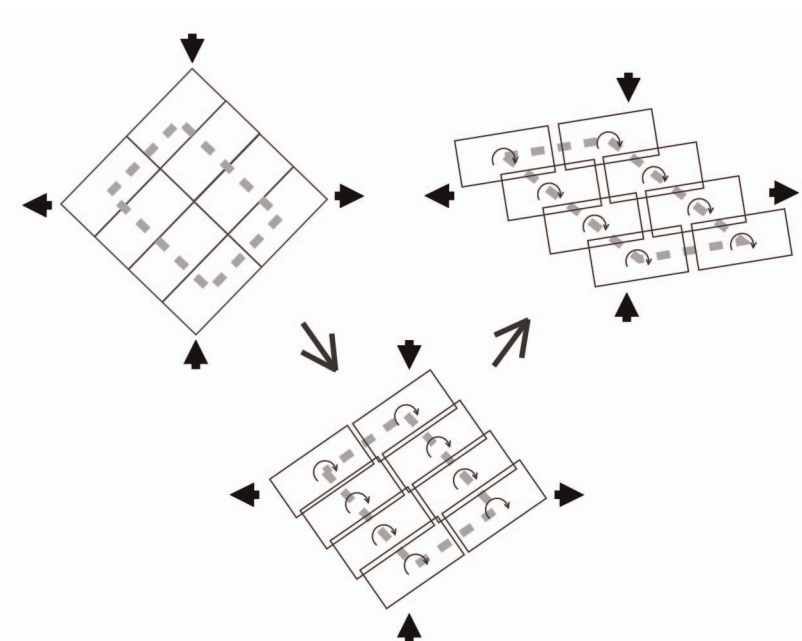


Extended Data Figure 4 | TEM and high-resolution TEM images of a Fo+Di sample after the compression experiment at 1,350 °C (KF-191). **a**, TEM image of multiple grains showing the large-scale structure of grain boundaries. **b**, High-resolution TEM image of the forsterite grain boundary

indicated by the arrow in **a**, showing that the boundary is parallel to the (010) plane of the central forsterite grain. Bending contrasts and a circular contrast from beam damage are observed. No dislocations are identified.

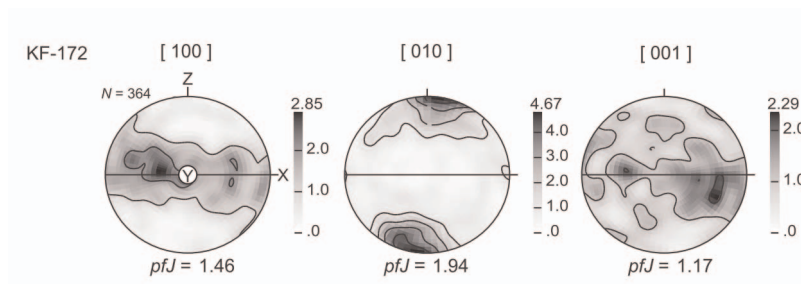


Extended Data Figure 5 | Specimens of Fo+Di. **a**, Before the tension deformation experiment. **b**, After the deformation experiment at 1,330 °C (KS-17) achieving $\varepsilon = 1.5$. The CPO of this sample is shown in Extended Data Fig. 2.

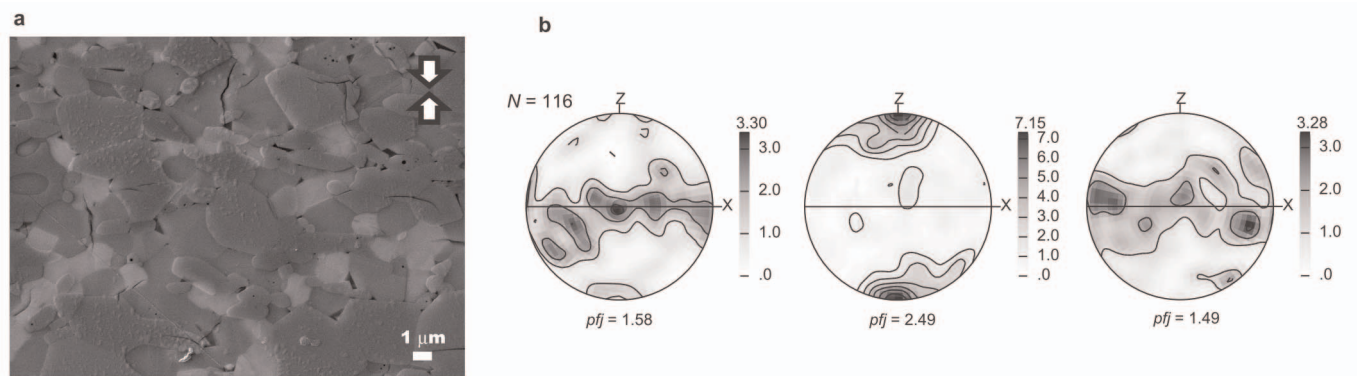


Extended Data Figure 6 | Schematic illustration of CPO formation during GBS. Anisotropic grains rotate under the operation of GBS, where GBS is easy on the long straight grain boundaries relative to the short grain boundaries (modified after ref. 16). Overlap and cavities formed at intergranular regions

during GBS are removed and compensated, respectively, by atomic diffusion. Easy GBS planes align in the flow direction followed by the grain rotation, resulting in the formation of CPO in our samples.



Extended Data Figure 7 | The CPO of forsterite grains in a Fo+Di sample (KF-172). The sample was statically annealed at 1,330 °C for 10 h and then deformed under compression ($\varepsilon = 0.6$) at 1,200 °C. The initial grain size of this sample before the creep test was already large (Extended Data Table 1).



Extended Data Figure 8 | Sample of spinel (0.5 vol.%) -doped forsterite (50 vol.%) plus Ca-bearing pyroxene deformed at $\sim 1,320^\circ\text{C}$ with $\varepsilon = 1.0$.
a, Secondary electron image of the sample. A very small amount of melt (~ 1 vol.%; black) is present, mostly at triple-grain junctions. Dark grey,

forsterite; light grey, pyroxene. **b**, Lower-hemispheric projections of the crystallographic orientations of forsterite grains measured by SEM/EBSD. N , number of measured grains. Both grain shape and CPO resemble that observed at high T .

Extended Data Table 1 | Experimental data

Composition	Experiments KF: compression KS: tension	T (K)	v (mm/s)	t (sec)	$\varepsilon(t)$	$\dot{\varepsilon}(t)$ (/sec)	d_0 (μm)	d_{fin} (μm)	$d_{ref}(t)$ (μm)	$d_e(t)$ (μm)	$\sigma(t)$ (MPa)	$\dot{\varepsilon}(t, d=1\ \mu\text{m})$ (/sec)	LPO J-index	Fo aspect ratio
Fo+Di	KF-171	1423	1.7E-04	779	0.02	1.9E-05	0.25	0.31	0.28	0.28	18.6	1.5E-06	2.16	1.35
	KF-158	1473	1.7E-04	3720	0.06	1.9E-05	0.39	0.46	0.40	0.41	48.0	3.1E-06	2.21	1.41
	KF-107	1473	1.2E-03	960	0.09	1.3E-04	0.41	0.44	0.41	0.41	300.0	2.2E-05	2.03	1.39
		1473	1.7E-03	1200	0.13	1.9E-04	0.41	-	0.41	0.42	418.0	3.4E-05	-	-
		1473	1.0E-03	1530	0.18	1.2E-04	0.41	-	0.41	0.42	313.0	2.1E-05	-	-
		1473	5.0E-04	2570	0.28	6.7E-05	0.41	-	0.41	0.42	230.0	1.2E-05	-	-
		1473	1.7E-04	3870	0.37	2.4E-05	0.41	-	0.41	0.43	108.0	4.5E-06	-	-
	KF-157	1523	1.7E-04	1674	0.10	1.9E-05	0.39	0.54	0.40	0.48	9.0	4.5E-06	2.04	1.39
	KF-106	1523	6.7E-04	671	0.04	6.6E-05	0.41	0.57	0.42	0.42	32.5	1.2E-05	2.02	1.37
		1523	1.3E-03	1431	0.10	1.4E-04	0.41	-	0.42	0.44	71.7	2.7E-05	-	-
		1523	2.0E-03	1639	0.14	2.2E-04	0.41	-	0.43	0.44	106.0	4.3E-05	-	-
		1523	3.3E-03	1836	0.21	3.9E-04	0.41	-	0.43	0.45	192.0	8.0E-05	-	-
		1523	1.0E-03	2137	0.27	1.2E-04	0.41	-	0.43	0.46	77.3	2.7E-05	-	-
		1523	6.7E-04	2639	0.33	8.8E-05	0.41	-	0.44	0.47	58.0	2.0E-05	-	-
		1523	3.3E-04	5339	0.42	4.8E-05	0.41	-	0.46	0.51	39.7	1.2E-05	-	-
		1523	1.0E-03	5930	0.49	1.6E-04	0.41	-	0.46	0.52	114.0	4.2E-05	-	-
	KF-190	1573	1.7E-04	1625	0.03	1.8E-05	0.39	0.75	0.47	0.48	3.2	4.2E-06	4.56	1.44
	KF-108	1573	3.3E-04	1550	0.03	3.3E-05	0.41	0.79	0.47	0.48	5.1	7.5E-06	3.37	1.40
		1573	6.7E-04	4457	0.15	7.4E-05	0.41	-	0.54	0.56	13.1	2.3E-05	-	-
		1573	1.3E-03	4777	0.18	1.5E-04	0.41	-	0.55	0.57	22.3	5.0E-05	-	-
		1573	2.0E-03	5054	0.23	2.4E-04	0.41	-	0.55	0.58	34.0	8.2E-05	-	-
		1573	1.2E-03	5354	0.29	1.5E-04	0.41	-	0.56	0.60	25.7	5.3E-05	-	-
		1573	1.7E-04	9090	0.88	3.8E-05	0.41	-	0.61	0.75	12.4	2.2E-05	-	-
	KF-160	1603	1.7E-04	555	0.01	1.8E-05	0.39	0.99	0.46	0.48	1.5	4.2E-06	5.09	1.47
	KF-125*	1603	1.3E-03	2326	0.07	1.4E-04	0.41	0.84	0.56	0.57	8.3	4.3E-05	6.55	1.45
		1603	6.7E-03	2643	0.16	7.4E-04	0.41	-	0.57	0.59	37.0	2.6E-04	-	-
		1603	1.7E-03	2938	0.26	2.0E-04	0.41	-	0.58	0.62	11.8	7.8E-05	-	-
		1603	3.3E-04	4505	0.40	4.7E-05	0.41	-	0.62	0.69	5.4	2.2E-05	-	-
		1603	6.7E-04	6225	0.46	1.0E-04	0.41	-	0.66	0.74	10.3	5.4E-05	-	-
		1603	1.3E-03	6760	0.52	2.1E-04	0.41	-	0.67	0.76	19.5	1.2E-04	-	-
	KF-191	1623	1.7E-04	3525	0.07	2.0E-05	0.39	1.05	0.66	0.69	1.0	9.3E-06	6.00	1.51
	KF-137	1623	3.3E-03	500	0.07	3.6E-04	0.41	0.94	0.49	0.50	9.8	8.9E-05	11.79	1.49
		1623	6.7E-03	830	0.20	8.1E-04	0.41	-	0.52	0.54	21.6	2.4E-04	-	-
		1623	1.0E-02	920	0.33	1.4E-03	0.41	-	0.53	0.56	39.2	4.4E-04	-	-
		1623	1.7E-03	1015	0.39	2.5E-04	0.41	-	0.54	0.58	9.4	8.2E-05	-	-
		1623	3.3E-03	1400	0.51	5.6E-04	0.41	-	0.57	0.62	19.2	2.1E-04	-	-
		1623	1.0E-03	1600	0.58	1.8E-04	0.41	-	0.58	0.64	8.0	7.3E-05	-	-
	KF-172	1473	1.7E-04	26685	0.62	3.2E-05	0.86	0.88	1.01**	0.88	181.6	2.5E-05	3.41	1.59***
Fo+Di (molten)	KF-209	1658	1.7E-03	2580	0.11	1.7E-04	-	21.80	18.30**	-	0.3	-	2.09	1.36
Fo+Di	KS-8	1473	1.7E-04	61835	0.62	7.5E-06	0.41	0.54	0.51**	-	48.9	-	1.96	1.39
	KS-10	1523	1.7E-04	61845	0.62	7.5E-06	0.41	0.76	0.73**	-	29.2	-	1.91	1.41
	KS-12	1573	2.2E-04	48000	0.62	9.7E-06	0.41	1.02	0.96**	-	26.2	-	2.31	1.46
	KS-13*	1603	2.2E-04	48000	0.62	9.7E-06	0.41	1.22	1.20**	-	17.7	-	2.81	1.54
	KS-14	1623	2.2E-04	48020	0.62	9.7E-06	0.41	1.24	1.15**	-	9.81	-	3.36	1.58
	KS-16	1603	7.5E-04	34080	1.14	2.0E-05	0.41	1.33	0.94**	-	26.0	-	5.12	1.56
	KS-17*	1603	8.3E-04	48060	1.47	1.4E-05	0.41	1.40	-	-	37.4	-	6.88	1.54
Fo+An-melt	NV-323	1603	-	72000	0.00	-	0.41	-	1.06**	-	-	-	-	-
	KF-186	1533	-	76563	0.37	4.8E-06	-	9.26	10.33**	9.26**	0.2	4.1E-04	2.19	1.31
	KF-202	1533	5.0E-04	650	0.03	5.0E-05	7.07	7.23	7.07	7.07	0.8	2.5E-03	-	1.32
		1533	4.2E-04	900	0.04	4.2E-05	7.07	-	7.07	7.07	0.7	2.1E-03	-	-
		1533	2.5E-04	1300	0.05	2.5E-05	7.07	-	7.07	7.07	0.5	1.3E-03	-	-
		1533	8.3E-05	2000	0.06	8.5E-06	7.07	-	7.08	7.08	0.2	4.3E-04	-	-

* Data were partially reported in ref. 14

** Observed grain size

*** Initial aspect ratio

KF, compression experiments; KS, tension experiments; NV, statically annealed experiments; v , displacement rate; t , experimental time; $\epsilon(t)$, strain at t ; $\dot{\epsilon}(t)$, strain rate at t ; d_0 , initial grain size ($t = 0$); $d_{ref}(t)$, estimated grain size in reference (and/or statically annealed) samples at t ; $\sigma(t)$, stress at t ; d_{fin} , final grain size observed in deformed samples; d_{es} , estimated grain size in deformed samples; $\dot{\epsilon}(t, d = 1 \mu\text{m})$, corrected strain rate at t and grain size of $1 \mu\text{m}$.

A regenerative approach to the treatment of multiple sclerosis

Vishal A. Deshmukh¹, Virginie Tardif², Costas A. Lyssiotis^{1†}, Chelsea C. Green¹, Bilal Kerman³, Hyung Joon Kim³, Krishnan Padmanabhan³, Jonathan G. Swoboda¹, Insha Ahmad¹, Toru Kondo⁴, Fred H. Gage³, Argyrios N. Theofilopoulos², Brian R. Lawson^{2*}, Peter G. Schultz^{1,5*} & Luke L. Lairson^{1,5*}

Progressive phases of multiple sclerosis are associated with inhibited differentiation of the progenitor cell population that generates the mature oligodendrocytes required for remyelination and disease remission. To identify selective inducers of oligodendrocyte differentiation, we performed an image-based screen for myelin basic protein (MBP) expression using primary rat optic-nerve-derived progenitor cells. Here we show that among the most effective compounds identified was benztropine, which significantly decreases clinical severity in the experimental autoimmune encephalomyelitis (EAE) model of relapsing-remitting multiple sclerosis when administered alone or in combination with approved immunosuppressive treatments for multiple sclerosis. Evidence from a cuprizone-induced model of demyelination, *in vitro* and *in vivo* T-cell assays and EAE adoptive transfer experiments indicated that the observed efficacy of this drug results directly from an enhancement of remyelination rather than immune suppression. Pharmacological studies indicate that benztropine functions by a mechanism that involves direct antagonism of M1 and/or M3 muscarinic receptors. These studies should facilitate the development of effective new therapies for the treatment of multiple sclerosis that complement established immunosuppressive approaches.

Remyelination persists throughout adulthood in the central nervous system and involves the generation of new myelinating oligodendrocytes¹. Despite some controversy regarding their intrinsic *in vitro* and *in vivo* lineage potential^{2–4}, compelling evidence indicates that a widespread proliferating population of nerve and glial antigen-2 (NG2), platelet-derived growth factor receptor alpha (PDGFR- α) positive cells, termed NG2-glia or oligodendrocyte precursor cells (OPCs), are the major source of newly formed mature oligodendrocytes required for remyelination^{5–7}. Remyelination in multiple sclerosis is largely dependent on migration of OPCs to sites of injury and subsequent differentiation to mature cells capable of repair^{1,2,8}. Studies evaluating the presence and relative densities of OPCs at sites of chronically demyelinated multiple sclerosis lesions indicate that it is not a failure of repopulation or migration of OPCs, but rather inhibition of OPC differentiation at sites of injury that contributes to disease progression^{9–12}. As such, the identification of small molecules that selectively induce differentiation of OPCs at sites of demyelinated lesions and thereby enhance remyelination would have a considerable impact on the development of new effective treatments for multiple sclerosis¹³.

High-throughput OPC differentiation screen

To identify drug-like small molecules that selectively induce OPC differentiation, we developed a high content imaging assay based on the induction of MBP expression in primary rat optic nerve-derived OPCs cultured for 6 days under basal differentiation conditions. Primary rodent OPCs proliferate *in vitro* when cultured in serum-free media containing PDGF-AA¹⁴. Upon withdrawal of PDGF-AA, immature A2B5⁺ OPCs cease to proliferate, but also fail to efficiently differentiate into MBP producing mature oligodendrocytes. Addition of thyroid hormone (triiodothyronine; T3), a known inducer of OPC differentiation^{15–19},

at the time of mitogen withdrawal results in the differentiation of OPCs to MBP-positive oligodendrocytes after 6 days of culture (Extended Data Fig. 1a). However, T3 has several physiological effects that make it unattractive as a therapeutic agent for multiple sclerosis. This assay was adapted to a high-throughput format and used to screen a collection of ~100,000 structurally diverse molecules (Extended Data Fig. 1b). This led to the identification of several previously identified inducers of OPC differentiation^{19–23} (Extended Data Fig. 1c, summarized in Supplementary Table 1). Unfortunately, these molecules have limited therapeutic potential due to off-target activities, toxicity, poor brain exposure and/or demonstrated lack of *in vivo* efficacy. Among the most effective inducers of OPC differentiation was benztropine (half-maximum effective concentration (EC₅₀) ~500 nM) (Fig. 1a and Extended Data Fig. 2a, b), which we chose to investigate further because it is an orally available approved drug that readily crosses the blood–brain barrier.

Benzotropine-induced *in vitro* differentiation of rodent OPCs was confirmed by evaluating the transcription and translation levels of the oligodendrocyte-specific markers MBP and myelin oligodendroglial glycoprotein (MOG) by western blot and quantitative polymerase chain reaction with reverse transcription (qRT-PCR) analysis (Extended Data Fig. 2c, d). Additionally, *in vitro* OPC differentiation activity was confirmed by immunofluorescence analysis using multiple markers specifically expressed in mature oligodendrocytes following 6 days of compound treatment (Extended Data Fig. 2e). Furthermore, transcript levels of cyclin D1, cyclin D2, *c-Fos* and *c-Jun* were significantly decreased in benztropine-treated OPCs, consistent with general inhibition of cell cycle progression (Extended Data Fig. 2f). To determine the stage of OPC differentiation at which benztropine is active^{24,25}, we treated OPCs for differing durations starting at several time points (Extended Data Fig. 2g, h). Maximal induction of MBP expression

¹Department of Chemistry, The Scripps Research Institute, 10550, North Torrey Pines Road, La Jolla, California 92037, USA. ²Department of Immunology and Microbial Science, The Scripps Research Institute, 10550 North Torrey Pines Road, La Jolla, California 92037, USA. ³Laboratory of Genetics, The Salk Institute for Biological Sciences, 10010 North Torrey Pines Road, La Jolla, California 92037, USA. ⁴Division of Stem Cell Biology, Institute for Genetic Medicine, Hokkaido University, Kita-15, Nishi-7, Kita-ku, Sapporo 060-0815, Japan. ⁵The California Institute for Biomedical Research, 11119 North Torrey Pines Road, La Jolla, California 92037, USA. [†]Present Address: Weill Cornell Medical College, 1300 York Avenue, New York, New York 10065, USA.

*These authors contributed equally to this work.

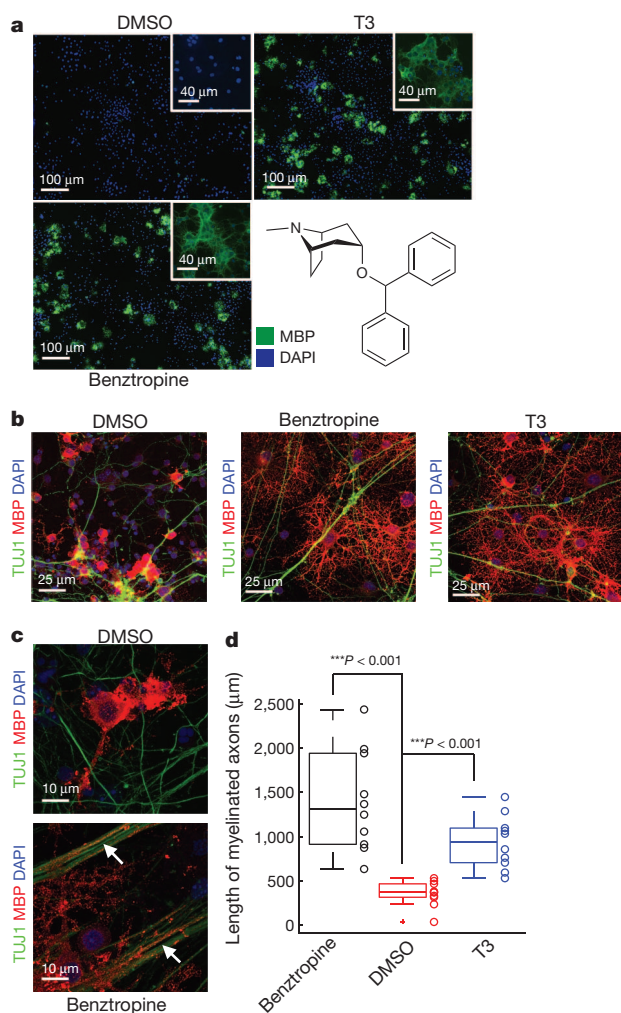


Figure 1 | Benztropine induces oligodendrocyte precursor cell differentiation and *in vitro* myelination of co-cultured axons. **a**, Benztropine (1.5 μM)- and T3 (1.0 μM)-treated rat OPCs immunostained for MBP (green) and 4',6-diamidino-2-phenylindole (DAPI, blue). Structure of benztropine. **b**, Benztropine (1.0 μM)- and T3 (1.0 μM)-treated co-culture of mouse embryonic-stem-derived neurons with rat OPCs immunostained for TUJ1 (tubulin marker, axons), MBP (oligodendrocytes) and DAPI (nuclei). **c**, Effect of benztropine (1.0 μM) treatment on the myelination of axons. Arrows denote myelinated axons. **d**, Quantification of total axonal myelination in OPC with neuron co-cultures ($n = 10$, mean and s.e.m., *** $P < 0.001$, ANOVA with Bonferroni correction).

was observed when the compound was added within 48 h of PDGF-AA withdrawal and cells were further cultured for at least 5 days, indicating that this drug probably acts on immature A2B5⁺ OPCs and not the intermediate 'pre-oligodendrocyte' stage of differentiation.

Benzotropine was also found to induce robust differentiation of rat and mouse OPCs when co-cultured with mouse embryonic-stem-cell-derived neurons²⁶ or mouse cortex-derived cells²⁷ (Fig. 1b and Extended Data Fig. 3a, b, respectively). We also quantified the effect of benztropine on the *in vitro* myelination of axons by quantifying the co-localization of MBP positive oligodendrocyte processes and axons (Extended Data Fig. 3c). The results showed a significant increase in the absolute amount of myelination in benztropine-treated co-cultures (Fig. 1c, d). This increase could result from enhanced maturation of oligodendrocytes and/or may reflect elevated myelination capacity of mature oligodendrocytes. To evaluate these two possibilities, we normalized the absolute amount of myelin to the total number of oligodendrocytes. Benzotropine treated cultures had a significantly higher percentage of myelinating

oligodendrocytes (Extended Data Fig. 3d), which indicates that benztropine not only enhances maturation of oligodendrocytes, but also promotes myelination.

M1/M3 muscarinic receptor antagonism

Benzotropine is used clinically for the management of Parkinson's disease and its pharmacological effects are thought to result from its anticholinergic activity²⁸. However, benztropine is also a centrally acting anti-histamine²⁹ and dopamine re-uptake inhibitor³⁰. To determine which, if any, of these activities play a role in OPC differentiation, we evaluated the ability of selective agonists of muscarinic acetylcholine receptors (mAChRs) or nicotinic acetylcholine receptors (the agonists carbachol or nicotine, respectively) to block benztropine activity. Inhibition of benztropine-induced OPC differentiation was observed in the presence of carbachol (Extended Data Fig. 3e, f), whereas nicotine had no effect on OPC differentiation (Extended Data Fig. 3g). The dopamine receptor antagonist haloperidol, the dopamine receptor agonist quinpirole and the histaminergic receptor agonists histamine and histamine trifluoromethyl-toluidine (HTMT) had no effect on benztropine-induced OPC differentiation (Extended Data Fig. 3h–k). Moreover, neither quinpirole nor nicotinic receptor antagonists (for example, tubocurarine, mivacurium, mecamlamine, pancuronium, atracurium or trimethopran) induced significant OPC differentiation (Extended Data Fig. 3l). We then evaluated a panel of mAChR antagonists (atropine, oxybutynin, scopolamine, ipratropium and propiverine) and found that all induced OPC differentiation in a dose-dependent manner with differing potencies (Supplementary Table 2), consistent with a mechanism of action that is dependent on muscarinic receptor antagonism.

To examine further the role of muscarinic receptor antagonism in benztropine-induced OPC differentiation and determine if a more potent and/or clinically useful drug could be identified, we evaluated a broader panel of structurally diverse muscarinic receptor antagonists. Of the 42 compounds tested, 20, which cluster amongst 4 related structural classes, were found to be active (Supplementary Tables 2 and 3). However, none were found to be more potent than benztropine. The ability of muscarinic receptor agonists to inhibit benztropine-induced OPC differentiation provides strong evidence that muscarinic receptor antagonism is an essential component of the mechanism of action. The inactivity of several of the muscarinic antagonists we evaluated could be the result of off-target inhibitory activities or toxicity-related effects. We cannot rule out the possibility that an additional biological activity, common among the active muscarinic receptor antagonists identified, is required for OPC differentiation. However, consistent with the proposed mechanism, it has recently been demonstrated that muscarinic activation causes decreased expression of myelin proteins in mature oligodendrocytes and modulates the expression of known regulators of differentiation (for example, PDGFRα) in immature OPCs³¹. Furthermore, Notch1 is a known negative regulator of OPC differentiation^{32,33} and, consistent with the observation that muscarinic receptor activation causes increased expression of Notch1 (ref. 31), we found that treatment of OPCs with benztropine results in a significant decrease in Notch1 expression in immature OPCs (Extended Data Fig. 3m).

OPCs are known to express mAChRs, predominantly subtypes M1, M3 and M5 (ref. 34). We confirmed expression of these receptors, as well as that of the acetylcholine-synthesizing enzyme choline acetyltransferase (ChAT), by qRT-PCR (Extended Data Fig. 3n, o). Activation of mAChRs triggers protein-kinase-C-dependent activation of the MAPK/ERK pathway leading to modulation of c-Fos expression³⁵. Western blot analysis of benztropine-treated OPCs is consistent with general inhibition of this pathway (decreased phospho-Akt and stimulated phosphorylation of p38 MAPK and CREB) (Extended Data Fig. 3p). Activation of M1 and M3 mAChRs is coupled to downstream signalling events through phospholipase C, which results in increased intracellular calcium concentrations³⁵, whereas M2 and M4 mAChR

activation inhibits adenylate cyclase, leading to decreased intracellular cAMP levels³¹. In OPCs, benztropine and the muscarinic antagonist atropine both inhibited carbachol-induced calcium influx (Extended Data Fig. 3q), but had no effect on cAMP levels (Extended Data Fig. 3r). Together, these results suggest that benztropine induces OPC differentiation by a mechanism involving direct antagonism of M1/M3 muscarinic receptors. Acetylcholine is a known regulator of OPC proliferation and, as such, muscarinic receptor subtypes represent a promising class of therapeutic targets for the modulation of OPC proliferation and differentiation^{31–35}.

Efficacy in the PLP-induced EAE model

We next examined the activity of benztropine in the proteolipid protein (PLP)-induced EAE rodent model of relapsing-remitting multiple sclerosis^{36,37}. Despite some inherent limitations of this model, all therapies approved for the treatment of MS decrease the clinical severity of EAE^{38,39}. This model is most commonly used to evaluate the potential efficacy of immunosuppressive agents, but can also be used to determine the effectiveness of promyelinating agents that function by enhancing OPC differentiation^{40,41}. Benztropine (10 mg per kg) was administered prophylactically by a daily intraperitoneal (i.p.) injection regimen initiated at the onset of PLP immunization. Benztropine dramatically decreased the severity of the acute phase of disease and virtually eliminated the relapse phase compared to vehicle-treated controls (Fig. 2a and Extended Data Fig. 4a). We next evaluated efficacy

when the drug was administered therapeutically, by starting daily injections at the first sign of disease. Treatment with benztropine in this mode again led to functional recovery; significant decreases in clinical severity during remission phases were observed and the occurrence of relapse was again virtually eliminated (Fig. 2a). In fact, treatment with benztropine in this mode resulted in decreased clinical severity comparable to, or better than, that observed for the immunosuppressive multiple sclerosis drugs FTY720 or interferon- β (administered at reported therapeutic doses in mice) (Fig. 2a).

In parallel experiments, when benztropine was dosed in a prophylactic mode, we isolated spinal cords from drug- or vehicle-treated mice at various time points before the onset of symptoms and during the acute and relapse phases of disease. Sections from many regions were stained with Luxol fast blue to visualize myelin or Luxol fast blue and hematoxylin and eosin (H&E) to visualize both myelin and infiltrating immune cells. Immunohistochemical analysis was also performed using antibodies that recognize markers of mature oligodendrocytes (MBP and glutathione *S*-transferase; GST- π), immature OPCs (NG2) or infiltrating immune cells (CD45). During acute and relapse phases of disease, sections from both vehicle- and benztropine-treated mice showed significant infiltration by H&E- and CD45-positive immune cells (Extended Data Fig. 4b–d). In vehicle-treated mice, infiltration corresponded to areas of significant demyelination (Extended Data Fig. 4b, e). In contrast, in benztropine-treated mice, a large number of immune-cell-infiltrated areas stained positive for Luxol fast blue or MBP, a finding consistent with a regenerative versus immunosuppressive mechanism (Extended Data Fig. 4b, e). We further evaluated drug-enhanced remyelination using confocal microscopy (Fig. 2b). Quantitative image analysis of many random fields per group indicated that benztropine treatment caused a significant increase in the number of GST- π^+ mature oligodendrocytes from ~ 500 to $\sim 1,100$ per field compared to vehicle (Fig. 2c and Extended Data Fig. 4d). The observed increase in mature oligodendrocyte numbers is consistent with a mechanism of benztropine-induced clinical recovery that involves the stimulation of OPC differentiation, leading to enhanced remyelination, in the context of an inflammatory environment. Notably, at time points before any observable immune cell infiltration or disease onset (day 8), a similar (\sim twofold) increase in the number of mature oligodendrocyte was observed in the spinal cords of benztropine-treated mice (Extended Data Fig. 4c, d). This observation is consistent with the time frame of *in vitro* activity. Furthermore, it is consistent with the occurrence of benztropine-induced OPC differentiation *in vivo* in the absence of inflammatory insult and provides an explanation for the substantial decrease in clinical severity observed during the acute phase of disease when the drug is dosed in a prophylactic mode. Mature oligodendrocytes capable of remyelination are poised for repair (or possibly protection) before immunological attack. Importantly, general toxicity was not observed either microscopically or macroscopically in drug-treated mice following 4 weeks of daily injections at 10 mg per kg.

Electron microscopy was used to observe myelin surrounding spinal cord axons in benztropine- and vehicle-treated mice during the peak of the acute phase of disease. Immune-cell-infiltrated areas of spinal cords from vehicle-treated mice exhibited characteristic oligodendroglial pathology along with damaged axons with loose and separated layers of myelin sheaths⁴² (Fig. 3a, b and Extended Data Fig. 4f). Benztropine treatment did not influence the infiltration or relative abundance of encephalogenic T cells and other inflammatory immune effector cells, nor did it affect the ability of these cells to cause demyelination during the acute phase of disease. Evidence for demyelination at this time point is provided by the significant ($P < 0.01$) increases in observed g-ratios (ratio of axon diameter to myelinated axon diameter) for both drug- and vehicle-treated mice compared to non-diseased controls (Fig. 3c and Extended Data Fig. 4g–i). Drug treatment resulted in extensive remyelination, as evidenced by the presence of abundant newly formed and notably thinner (compared to those of non-diseased mice) myelin sheaths (a characteristic associated with remyelination⁵) (Fig. 3a, b and

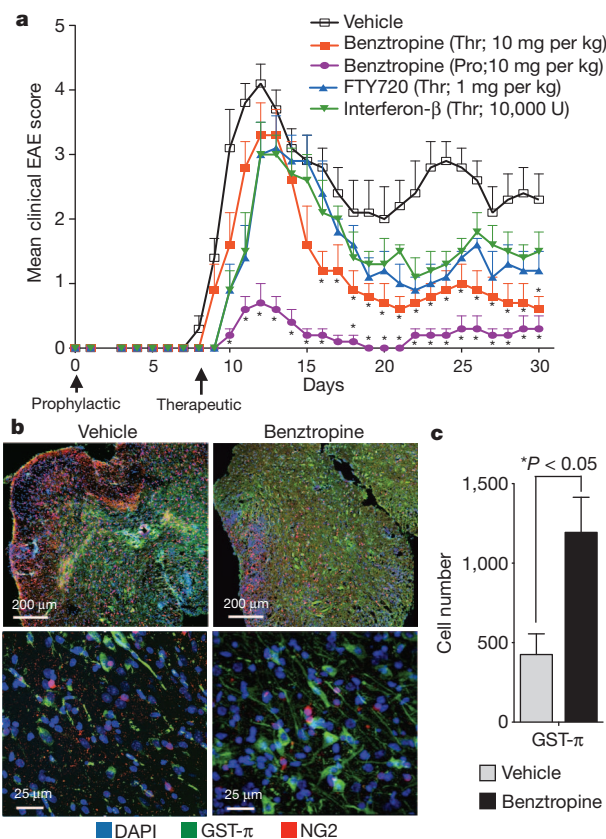


Figure 2 | Benztropine decreases disease severity in the PLP-induced EAE model. **a**, EAE severity scores (ranging from no observable disease to moribund/dead) following prophylactic (Pro, day 0) or therapeutic (Thr, time of initial symptoms) treatment with benztropine compared to therapeutically administered FTY720 or interferon- β ($n = 8$, mean and s.e.m., $*P < 0.05$; *t*-test). **b**, Confocal images of spinal cord sections isolated at day 14 from EAE mice treated prophylactically with benztropine (10 mg per kg) or vehicle and immunostained for GST- π (mature oligodendrocytes) and NG2. **c**, Quantification of GST- π^+ cells ($n = 30$, mean and s.e.m., $*P < 0.05$, *t*-test).

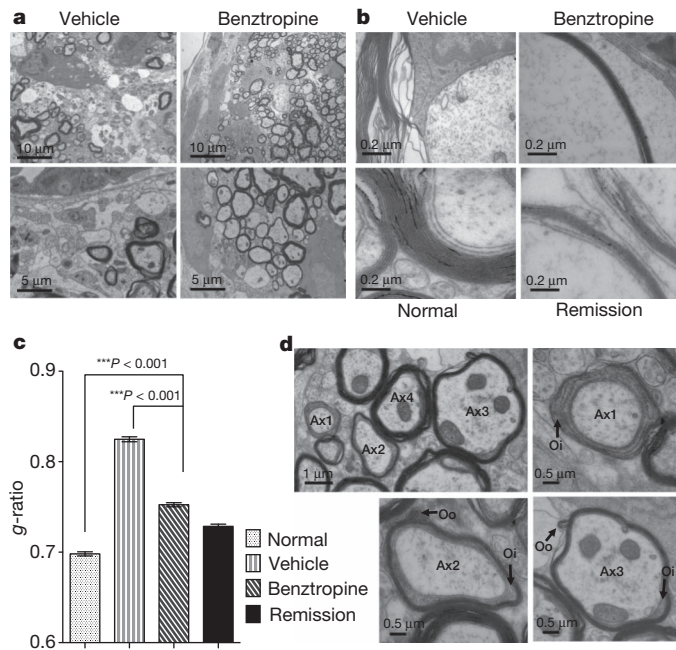


Figure 3 | Benztropine-induced remyelination in the PLP-induced EAE model. **a, b,** Electron microscopy images of spinal cords isolated from benztropine (Pro, 10 mg per kg) and vehicle-treated EAE mice. **c,** g-ratios of spinal cord axons in normal and EAE mice ($n = 1,000$, mean and s.e.m., $***P < 0.001$, two-way ANOVA). **d,** Electron microscopy images of spinal cords isolated from benztropine-treated EAE mice highlighting different phases of remyelination (initial wrapping (Ax1), partial remyelination (Ax2), almost remyelinated (Ax3) and normal axon (Ax4)) and associated morphological features (outer (Oo) and inner (Oi) ends of cytoplasmic processes of oligodendrocytes wrapped around axons (Ax)).

Extended Data Fig. 4f). Specifically, the g-ratios in benztropine-treated mice were significantly lower ($P < 0.01$) than in vehicle-treated mice, yet still significantly higher ($P < 0.01$) than in non-diseased mice (Fig. 3c and Extended Data Fig. 4g–i). Moreover, in these areas, myelin sheaths were observed in different phases of remyelination (axons undergoing initial wrapping, partial remyelination and almost complete remyelination⁴²) (Fig. 3d and Extended Data Fig. 4j), strongly supporting a benztropine-induced remyelination effect.

Effect on the immune system of EAE mice

The primary immunological processes involved in multiple sclerosis and EAE are thought to be T-cell mediated. To determine the extent to which the efficacy of benztropine in the EAE model results from T cell inhibitory activity, we evaluated the effects of benztropine and other muscarinic antagonists (atropine, oxybutynin, scopolamine, ipratropium and propiverine) on T-cell activation and proliferation. Notably, it has been reported that muscarinic receptors are expressed on T cells⁴³. However, neither benztropine nor the other muscarinic antagonists had an effect on T-cell proliferation *in vitro*, as measured using a carboxyfluorescein succinimidyl ester (CFSE) labelling assay (Extended Data Fig. 5a), nor did they affect T-cell activation as determined by assessing CD4⁺CD69⁺ and CD4⁺CD25⁺ populations (Extended Data Fig. 5b, c). We also evaluated the effect of benztropine on the immune system *in vivo* in SJL/J mice in which EAE had or had not been induced with PLP. In both diseased and healthy animals, benztropine had no effect on the number of splenic naive (CD44^{lo}) or activated (CD44^{hi}) CD4⁺ and CD8⁺ T cells (Extended Data Fig. 5d–f). A minor, but significant, decrease in B cell numbers was observed following treatment with benztropine (Extended Data Fig. 5e, f), and benztropine had no effect on cytokine (IL-2, IL-10, IFN- γ , TNF- α) producing T-cell populations isolated from drug- or vehicle-treated normal or diseased mice (Extended Data Fig. 5e, f). We also found that benztropine had no

effect on antigen-induced IgG production (Extended Data Fig. 5g). Next, we analysed the effect of benztropine on *in vitro* macrophage development and M1/M2 polarization and observed no significant differences between benztropine-treated cultures and controls (Extended Data Fig. 6). Additionally, the expression of M1 or M2 polarization markers in spleens, spinal cords, as well as spinal-infiltrating leukocytes isolated from EAE mice treated with benztropine for 14 days, were equivalent to those of controls (Extended Data Fig. 7).

We next performed the adoptive transfer model of EAE⁴⁴ to further demonstrate that benztropine does not affect T-cell development or function. Splenocytes were isolated from SJL/J donor mice, following immunization with PLP and immediate daily injection with benztropine (10 mg per kg) or saline for 10 days, and then cultured *in vitro* in the presence of benztropine (5 μ M) or vehicle, respectively (Extended Data Fig. 8). Injection of splenocytes from either donor group resulted in equally severe transfer of EAE disease to recipient mice (Extended Data Fig. 8: groups 1 and 3), providing evidence that benztropine had no effect on the development and function of PLP-specific T cells *in vivo* or *in vitro*. Benztropine (10 mg per kg) treatment of recipient mice, injected with splenocytes from vehicle- or benztropine-treated donor mice, resulted in significant reductions in clinical severity scores (Extended Data Fig. 8: groups 2 and 4) compared to controls (Extended Data Fig. 8: groups 1 and 3). Taken together, these results strongly suggest that the observed efficacy of benztropine in the EAE model results from remyelination arising from enhanced oligodendrogenesis rather than immune suppression.

Efficacy of benztropine in the cuprizone model

We further evaluated the ability of benztropine to induce OPC differentiation and enhance remyelination *in vivo* using the T-cell-independent cuprizone-induced model of demyelination. Inclusion of 0.2% (w/w) cuprizone in the diet of C57BL/6 mice induces a demyelination program that proceeds with a defined series of events over a characteristic time course in which the corpus callosum shows peak demyelination following 6–7 weeks⁴⁵. Spontaneous remyelination is observed 2–4 weeks following cuprizone withdrawal⁴⁶. By administering drugs when a cuprizone-free diet is reintroduced, the efficacy of promyelinating agents can be examined by evaluating the relative kinetics of OPC-dependent remyelination^{45,46}. Upon withdrawal of cuprizone, we administered vehicle or benztropine (10 mg per kg) by daily i.p. injections for 5 weeks. During this time, mice were euthanized weekly and the degree of remyelination was quantitatively established by staining the corpus callosum regions of harvested brains with Luxol fast blue and anti-GST- π ⁺ antibody. Significant demyelination was clearly observed after seven weeks of cuprizone treatment compared to naive animals (Fig. 4a, top left and bottom left panels). Consistent with enhanced OPC differentiation and accelerated remyelination, overall myelin staining (Fig. 4a, middle and right panels; 4b; Extended Data Fig. 9) and the number of GST- π ⁺ mature oligodendrocytes (Fig. 4c, d) increased significantly in the corpus callosum at week 2 following benztropine treatment compared to the spontaneous remyelination observed in vehicle controls. As expected, at later time points, spontaneous remyelination was relatively complete and no significant differences between drug- and vehicle-treated animals were observed. A lack of difference at these later time points indicates that, even after five weeks of treatment, benztropine is not toxic to mature oligodendrocytes. These data again indicate that benztropine enhances the process of *in vivo* remyelination by directly inducing OPC differentiation.

Benztropine is dose-sparing with FTY720

For the treatment of multiple sclerosis, an OPC differentiation-inducing drug would most probably be introduced clinically as part of a combination therapy with an immunosuppressive drug. Using the PLP-induced EAE model, we therefore evaluated the clinical efficacy of benztropine when combined with either of two immunosuppressive drugs approved for the treatment of multiple sclerosis, interferon- β

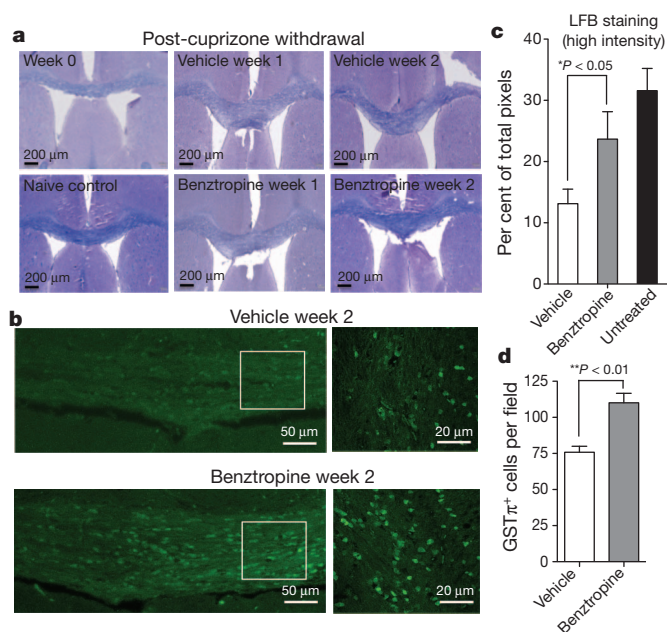


Figure 4 | Benztropine treatment enhances remyelination in the cuprizone model. **a**, Sections from the corpus callosum region of brains isolated from either benzotropine- or vehicle-treated mice stained with Luxol fast blue. **b**, Quantification of Luxol fast blue (LFB) staining ($n = 6$ images each from 4 mice per group, mean and s.d., $*P < 0.05$, t -test). **c**, Confocal microscopy images of sections from the corpus callosum region of brains isolated from either benzotropine- or vehicle-treated mice immunostained for GST- π . **d**, Quantification of GST- π^+ mature oligodendrocytes. ($n = 20$ images each from 4 mice per group, mean and standard deviation, $**P < 0.01$, t -test).

and FTY720 (refs 47, 48). The former reduces T-cell proliferation and alters cytokine expression⁴⁹, whereas the latter is an S1P agonist that blocks T-cell trafficking⁵⁰. Initially, all three drugs were dosed individually over a range of concentrations to determine suboptimal and maximal effective/tolerated doses in the EAE model (Extended Data Figs 4a and 10a, b). Addition of 2.5 mg per kg of benzotropine (suboptimal dose) to reported therapeutic doses of FTY720 (1 mg per kg) (Extended Data Fig. 10c) or interferon- β (10,000 U per mouse) (Extended Data Fig. 10d) resulted in decreased clinical severity comparable to, or greater than, either FTY720 or interferon- β alone. Furthermore, the combination of a suboptimal dose of benzotropine (2.5 mg per kg) with a suboptimal dose of FTY720 (0.1 mg per kg) resulted in a significant decrease in clinical severity (Extended Data Fig. 10e) comparable to the clinical efficacy observed when FTY720 was given alone at the reported therapeutically effective dose of 1 mg per kg (Extended Data Fig. 10f). Addition of benzotropine to FTY720 does not result in a decrease in immune cell infiltration compared to FTY720 treatment alone (Extended Data Fig. 10g, h), and addition of FTY720 to benzotropine does not result in an increase in the number of oligodendrocytes compared to benzotropine treatment alone (Extended Data Fig. 10i, j). This finding indicates that the observed benefit (Extended Data Fig. 10k) that results from this drug combination is derived from an additive effect that occurs when both immunological and remyelination mechanisms are targeted simultaneously. This observation may prove clinically relevant, because FTY720 treatment is associated with a dose-dependent bradycardia, which might be reduced by combination therapy with benzotropine, and benzotropine is associated with dose-dependent adverse neurological side effects.

Discussion

We have identified a centrally acting drug that, when administered in a clinically relevant model of multiple sclerosis, significantly decreases disease severity by directly stimulating the differentiation of a progenitor

cell population leading to enhanced remyelination and functional recovery. Pharmacological data clearly indicates that the mechanism of action of benzotropine is dependent on muscarinic receptor antagonism, but not any of its other known biological activities. However, based on the lack of activity of some of the anti-muscarinics tested, we cannot rule out the possibility that an additional unidentified target may exist that is common to all of the active anti-muscarinics identified. Further, although experimental evidence clearly indicates that benzotropine induces OPC differentiation and remyelination *in vitro* and *in vivo*, it is possible that the therapeutic effect observed in the EAE model could also result in part from a protective effect derived from increased glial cell density. Inclusion of benzotropine in EAE treatment regimens involving existing approved immunosuppressive drugs results in enhanced functional recovery and, in the case of FTY720, significantly decreases the dosages of both drugs that are required to achieve equivalent efficacy. Successful translation of these findings to multiple sclerosis patient populations will require further preclinical and clinical evaluation, as benzotropine and other anti-muscarinics have significant dose-dependent neurological and psychiatric side effects. To our knowledge, these results provide the first *in vivo* evidence supporting the notion that benefit can be achieved by treating multiple-sclerosis-like symptoms using the combination of an immunosuppressive drug with a remyelination enhancer and may have a significant effect on the development of new and more effective therapies for the treatment of multiple sclerosis. Finally, we are evaluating other hits from our screen to identify compounds that induce remyelination by mechanisms distinct from that of benzotropine.

METHODS SUMMARY

Cell culture and high-throughput screening. Primary rat optic nerve-derived OPCs were screened in 384-well format (1.5 μ M compound) using basal differentiation conditions. Following immunostaining using an MBP-specific antibody, plates were imaged and analysed using Opera (Perkin Elmer) or Cell Insight (Thermo) high content imaging systems.

***In vivo* animal models.** The PLP-induced EAE model was performed and scored using 8-week-old female SJL/J mice as described³⁷. Mice received daily i.p. injections with vehicle or drug using either prophylactic or therapeutic regimens. For the cuprizone model, C57BL/6 mice were fed 0.2% w/w cuprizone with chow for 7 weeks and thereafter with normal chow, at which point benzotropine (10 mg per kg) or saline was injected daily (i.p.) starting for 5 weeks. Spinal cords were isolated and histological analysis was performed at weeks 0–5 following cuprizone withdrawal.

Online Content Any additional Methods, Extended Data display items and Source Data are available in the online version of the paper; references unique to these sections appear only in the online paper.

Received 4 January; accepted 10 September 2013.

Published online 9 October 2013.

- Franklin, R. J. & Ffrench-Constant, C. Remyelination in the CNS: from biology to therapy. *Nature Rev. Neurosci.* **9**, 839–855 (2008).
- Franklin, R. J. Why does remyelination fail in multiple sclerosis? *Nature Rev. Neurosci.* **3**, 705–714 (2002).
- Nunes, M. C. *et al.* Identification and isolation of multipotential neural progenitor cells from the subcortical white matter of the adult human brain. *Nature Med.* **9**, 439–447 (2003).
- Nunes, M. C. *et al.* Postnatal NG2 proteoglycan-expressing progenitor cells are intrinsically multipotent and generate functional neurons. *J. Cell Biol.* **161**, 169–186 (2003).
- Huang, J. K. *et al.* Retinoid X receptor gamma signaling accelerates CNS remyelination. *Nature Neurosci.* **14**, 45–53 (2011).
- Gensert, J. M. & Goldman, J. E. Endogenous progenitors remyelinate demyelinated axons in the adult CNS. *Neuron* **19**, 197–203 (1997).
- Horner, P. J. *et al.* Proliferation and differentiation of progenitor cells throughout the intact adult rat spinal cord. *J. Neurosci.* **20**, 2218–2228 (2000).
- Kremer, D., Aktas, O., Hartung, H. P. & Kury, P. The complex world of oligodendroglial differentiation inhibitors. *Ann. Neurol.* **69**, 602–618 (2011).
- Patel, J. R. & Klein, R. S. Mediators of oligodendrocyte differentiation during remyelination. *FEBS Lett.* **585**, 3730–3737 (2011).
- Chang, A., Tourtellotte, W. W., Rudick, R. & Trapp, B. D. Premyelinating oligodendrocytes in chronic lesions of multiple sclerosis. *N. Engl. J. Med.* **346**, 165–173 (2002).
- Chari, D. M., Huang, W. L. & Blakemore, W. F. Dysfunctional oligodendrocyte progenitor cell (OPC) populations may inhibit repopulation of OPC depleted tissue. *J. Neurosci. Res.* **73**, 787–793 (2003).

12. Wolszijk, G. Chronic stage multiple sclerosis lesions contain a relatively quiescent population of oligodendrocyte precursor cells. *J. Neurosci.* **18**, 601–609 (1998).
13. Kuhlmann, T. *et al.* Differentiation block of oligodendroglial progenitor cells as a cause for remyelination failure in chronic multiple sclerosis. *Brain* **131**, 1749–1758 (2008).
14. Hart, I. K., Richardson, W. D., Bolsover, S. R. & Raff, M. C. PDGF and intracellular signaling in the timing of oligodendrocyte differentiation. *J. Cell Biol.* **109**, 3411–3417 (1989).
15. Billon, N., Tokumoto, Y., Forrest, D. & Raff, M. Role of thyroid hormone receptors in timing oligodendrocyte differentiation. *Dev. Biol.* **235**, 110–120 (2001).
16. Tokumoto, Y. M., Tang, D. G. & Raff, M. C. Two molecularly distinct intracellular pathways to oligodendrocyte differentiation: role of a p53 family protein. *EMBO J.* **20**, 5261–5268 (2001).
17. Fernandez, M. *et al.* Thyroid hormone administration enhances remyelination in chronic demyelinating inflammatory disease. *Proc. Natl Acad. Sci. USA* **101**, 16363–16368 (2004).
18. Calzà, L., Fernandez, M. & Giardino, L. Cellular approaches to central nervous system remyelination stimulation: thyroid hormone to promote myelin repair via endogenous stem and precursor cells. *J. Mol. Endocrinol.* **44**, 13–23 (2010).
19. Barres, B. A., Lazar, M. A. & Raff, M. C. A novel role for thyroid hormone, glucocorticoids and retinoic acid in timing oligodendrocyte development. *Development* **120**, 1097–1108 (1994).
20. Buckley, C. E. *et al.* Drug reprofiling using zebrafish identifies novel compounds with potential pro-myelination effects. *Neuropharmacology* **59**, 149–159 (2010).
21. Ibanez, C. *et al.* Steroids and the reversal of age-associated changes in myelination and remyelination. *Prog. Neurobiol.* **71**, 49–56 (2003).
22. Baer, A. S. *et al.* Myelin-mediated inhibition of oligodendrocyte precursor differentiation can be overcome by pharmacological modulation of Fyn-RhoA and protein kinase C signalling. *Brain* **132**, 465–481 (2009).
23. Joubert, L. *et al.* Chemical inducers and transcriptional markers of oligodendrocyte differentiation. *J. Neurosci. Res.* **88**, 2546–2557 (2010).
24. Gard, A. L. & Pfeiffer, S. E. Two proliferative stages of the oligodendrocyte lineage (A2B5⁺O4[−] and O4⁺GalC[−]) under different mitogenic control. *Neuron* **5**, 615–625 (1990).
25. Pfeiffer, S. E., Warrington, A. E. & Bansal, R. The oligodendrocyte and its many cellular processes. *Trends Cell Biol.* **3**, 191–197 (1993).
26. Gaspard, N. *et al.* Generation of cortical neurons from mouse embryonic stem cells. *Neural Protocols* **4**, 1454–1463 (2009).
27. Barres, B. A. *et al.* Cell death and control of cell survival in the oligodendrocyte lineage. *Cell* **70**, 31–46 (1992).
28. Eshleman, A. J., Henningsen, R. A., Neve, K. A. & Janowsky, A. Release of dopamine via the human transporter. *Mol. Pharmacol.* **45**, 312–316 (1994).
29. McKearney, J. W. Stimulant actions of histamine H1 antagonists on operant behavior in the squirrel monkey. *Psychopharmacol.* **77**, 156–158 (1982).
30. Agoston, G. E. *et al.* Novel N-substituted 3α-[bis(4'-fluorophenyl)methoxy]tropane analogues: selective ligands for the dopamine transporter. *J. Med. Chem.* **40**, 4329–4339 (1997).
31. De Angelis, F., Bernardo, A., Magnaghi, V., Minghetti, L. & Tata, A. M. Muscarinic receptor subtypes as potential targets to modulate oligodendrocyte progenitor survival, proliferation and differentiation. *Dev. Neurobiol.* **72**, 713–728 (2012).
32. Stidworthy, M. F. *et al.* Notch1 and Jagged1 are expressed after CNS demyelination, but are not a major rate-determining factor during remyelination. *Brain* **127**, 1928–1941 (2004).
33. Taveggia, C., Feltri, M. L. & Wrabetz, L. Signals to promote myelin formation and repair. *Nature Rev. Neurol.* **6**, 276–287 (2010).
34. Ragheb, F. *et al.* Pharmacological and functional characterization of muscarinic receptor subtypes in developing oligodendrocytes. *J. Neurochem.* **77**, 1396–1406 (2001).
35. Felder, C. C. Muscarinic acetylcholine receptors: signal transduction through multiple effectors. *FASEB J.* **9**, 619–625 (1995).
36. Owens, T. & Sriram, S. The immunology of multiple sclerosis and its animal model, experimental allergic encephalomyelitis. *Neurol. Clin.* **13**, 51–73 (1995).
37. Lawson, B. R. *et al.* Inhibition of transmethylation down-regulates CD4 T cell activation and curtails development of autoimmunity in a model system. *J. Immunol.* **178**, 5366–5374 (2007).
38. Mix, E., Meyer-Rienecker, H. & Zettl, U. K. Animal models of multiple sclerosis for the development and validation of novel therapies—potential and limitations. *J. Neurol.* **255** (Suppl 6), 7–14 (2008).
39. Steinman, L. & Zamvil, S. S. Virtues and pitfalls of EAE for the development of therapies for multiple sclerosis. *Trends Immunol.* **26**, 565–571 (2005).
40. Aharoni, R. *et al.* Distinct pathological patterns in relapsing-remitting and chronic models of experimental autoimmune encephalomyelitis and the neuroprotective effect of glatiramer acetate. *J. Autoimmun.* **37**, 228–241 (2011).
41. Liu, L. *et al.* Myelin repair is accelerated by inactivating CXCR2 on nonhematopoietic cells. *J. Neurosci.* **30**, 9074–9083 (2010).
42. Mi, S. *et al.* LINGO-1 antagonist promotes spinal cord remyelination and axonal integrity in MOG-induced experimental autoimmune encephalomyelitis. *Nature Med.* **13**, 1228–1233 (2007).
43. Kawashima, K. & Fujii, T. Basic and clinical aspects of non-neuronal acetylcholine: overview of non-neuronal cholinergic systems and their biological significance. *J. Pharmacol. Sci.* **106**, 167–173 (2008).
44. Stern, J. N. *et al.* Promoting tolerance to proteolipid protein-induced experimental autoimmune encephalomyelitis through targeting dendritic cells. *Proc. Natl Acad. Sci. USA* **107**, 17280–17285 (2010).
45. Steelman, A. J., Thompson, J. P. & Li, J. Demyelination and remyelination in anatomically distinct regions of the corpus callosum following cuprizone intoxication. *Neurosci. Res.* **72**, 32–42 (2012).
46. Matsushima, G. K. & Morell, P. The neurotoxicant, cuprizone, as a model to study demyelination and remyelination in the central nervous system. *Brain Pathol.* **11**, 107–116 (2001).
47. Kappos, L. *et al.* Oral fingolimod (FTY720) for relapsing multiple sclerosis. *N. Engl. J. Med.* **355**, 1124–1140 (2006).
48. Durelli, L. *et al.* Every-other-day interferon beta-1b versus once-weekly interferon beta-1a for multiple sclerosis: results of a 2-year prospective randomised multicentre study (INCOMIN). *Lancet* **359**, 1453–1460 (2002).
49. Noronha, A., Toscas, A. & Jensen, M. A. Interferon β decreases T cell activation and interferon γ production in multiple sclerosis. *J. Neuroimmunol.* **46**, 145–153 (1993).
50. Brinkmann, V. *et al.* The immune modulator FTY720 targets sphingosine 1-phosphate receptors. *J. Biol. Chem.* **277**, 21453–21457 (2002).

Supplementary Information is available in the online version of the paper.

Acknowledgements This work was supported by the Skaggs Institute for Chemical Biology and the California Institute for Regenerative Medicine grant TR3-05617 (to P.G.S.), the California Institute for Regenerative Medicine (TG2-01165) and National Science Foundation pre-doctoral fellowships (to V.A.D. and C.A.L. respectively). We are grateful to T. Hasnat, M. Chadwell, W. Kiosses and M. Wood for technical support. This is manuscript number 21786 of The Scripps Research Institute.

Author Contributions L.L.L., P.G.S., C.A.L. and V.A.D. initiated the project and developed strategy. V.A.D., V.T., C.C.G., B.K., H.J.K., K.P., J.G.S. and I.A. performed the experiments. L.L.L., P.G.S. and V.A.D. wrote the manuscript. B.R.L., C.A.L., A.N.T., F.H.G. and T.K. contributed essential ideas and comments.

Author Information Reprints and permissions information is available at www.nature.com/reprints. The authors declare no competing financial interests. Readers are welcome to comment on the online version of the paper. Correspondence and requests for materials should be addressed to B.L. (blawson@scripps.edu), P.G.S. (schultz@scripps.edu) or L.L.L. (llairson@scripps.edu).

METHODS

Statistical methods and experimental design. High-throughput screening was performed at a single concentration (1.5 μM) and primary hits were reconfirmed in triplicate. In all *in vivo* animal studies, we calculated that we required 8–12 mice per group in order to have 80% power of detecting approximately a 30% change, assuming a standard deviation of 30% at a significance level of $\alpha = 0.05$. It has been our experience that this is sufficient to detect clinically and statistically significant differences with repetitive studies. As per standard scoring methods for EAE, mice found moribund or dead were scored as 5 for the remainder of the study. For therapeutic dosing, just before drug treatment, mice were randomized, based on clinical severity such that each treatment group had equivalent mean clinical EAE scores. Mice were scored non-blinded. For all experiments, assuming normal distribution, two-sided *t*-tests were used to evaluate comparisons between 2 groups and ANOVA was used when >2 groups were compared. For the quantitative analysis of *in vitro* myelination, ANOVA with Bonferroni correction was used. Where possible, data are represented as mean \pm s.e.m., otherwise data are represented as mean \pm s.d., as indicated in the figure legends.

Cell culture. Rat primary optic nerve OPCs were isolated by panning^{27,51} ($>99\%$ A2B5⁺) and cultured in poly-D-lysine (10 $\mu\text{g ml}^{-1}$)-coated flasks in OPC proliferation media (Neurobasal Media, Invitrogen) supplemented with B27-without vitamin A (Invitrogen), non-essential amino acids, L-glutamine and PDGF-AA (30 ng ml^{-1} ; Peprotech) at 37 °C with 5% CO₂. OPCs were used between passage 10 and 15 and were never allowed to reach confluence to maintain a naive state. For differentiation, OPCs were plated in differentiation media (Neurobasal Media (Invitrogen) supplemented with B27-without vitamin A (Invitrogen), non-essential amino acids, L-glutamine and PDGF-AA (2 ng ml^{-1} ; Peprotech)).

Mouse cortical neural cell mixture was prepared from E18.5 brain using the Papain dissociation system, according to the supplier's instructions kit (Worthington Biochemical). Then, both oligodendrocytes and OPCs were depleted from the mixture by sequential immunopanning as described previously^{27,52}. The cells were then cultured on poly-D-lysine-coated 8-well chamber slide (Nunc) as described previously⁵³. Mouse neural stem cells (Invitrogen) were cultured in OPC medium as described previously⁵⁴. Induced mouse OPCs (5,000 cells per well) were cultured with benzotropine on the cortex-derived culture for 7 days. Cells were immunolabelled as described previously⁵¹.

High-throughput screening and imaging. OPCs were plated at a density of 1,000 cells per well on poly-D-lysine (10 $\mu\text{g ml}^{-1}$) coated 384-well plates (Greiner) in differentiation media. Compounds were added at a final concentration of 1.5 μM within 12 h after plating the cells and incubated at 37 °C with 5% CO₂ for 6 days. Cells were then fixed for 20 min with 4% formaldehyde solution and stained with mouse anti-rat MBP antibody (Millipore) in 3% BSA, 0.3% Triton X-100 with overnight incubation at 4 °C. The cells were washed and incubated with secondary antibody (goat anti-mouse Alexa Fluor488) and DAPI (Invitrogen) for 1 h at room temperature. The cells were washed and plates were sealed and imaged using an Opera confocal imaging reader (Perkin Elmer) or a Cellomics Cell Insight imaging reader (Thermo). An air $\times 10$ lens was used to capture 9 images per well at both wavelengths (488 and 365 nm), representing different locations in a single well. For image analysis, DAPI-stained nuclei and MBP-positive cell bodies were detected using an algorithm that selects for positive cell bodies and nuclei within a range of fluorescent emission values and sizes as determined by fitting parameters to positive (thyroid hormone (T3), 1 μM) and negative controls (DMSO, 0.1%). Numerical results from the analysed images were later exported for analysis in Excel (Microsoft) and Spotfire (Tibco).

Data analysis. EC₅₀ values were obtained by fitting the data using the sigmoidal dose–response curve-fitting function (Prism; GraphPad Software). Eight or twelve different concentrations and three data points per concentration were usually used for curve fitting. Experiments were repeated 2 or more times.

Compounds. Hit compounds were purchased as powders and dissolved in DMSO for *in vitro* studies or saline for *in vivo* studies. Benzotropine mesylate (MP Biochemicals), mycophenolate mofetil (Selleck Chemicals), FTY720 (Cayman Chemical), carbachol (EMD Chemicals), haloperidol (Sigma), quinpirole (Sigma), interferon- β , ipratropium (Sigma), oxybutynin (Sigma), histamine (Acros Organics), scopolamine (Sigma), atropine (Sigma), histamine trifluoromethyl toluidide (HTMT; Tocris Bioscience).

In vitro myelination. Mouse embryonic stem cells (ES cells) were differentiated into neurons using a previously published protocol²⁶. Neurons were allowed to mature and extend axons for about one week before plating rat primary OPCs. Cells were treated with either DMSO or 1 μM T3 or 1 μM benzotropine for two weeks and myelination under different conditions was quantified. For quantification, co-cultures were fixed for 15 min in 4% PFA and stained with TUJ1 (rabbit; Covance) and MBP (mouse; Millipore) antibodies. A total of 10 randomly selected regions on 2 plates per experiment were imaged. Images were imported to Imapis (Bitplane), and axon, oligodendrocyte processes were identified. Rendered channels

of the processes were exported as TIFF files to be analysed further using a custom script in MATLAB (Mathworks). Myelination was identified as regions of co-localization between MBP positive oligodendrocyte processes and TUJ1 positive neurites. Cell bodies were eliminated from the analysis to reduce the error due to non-specific overlap of MBP and TUJ1 staining.

Immunocytochemistry and antibodies. Immunostaining of cells was performed using standard protocols. Primary antibodies and dilutions are provided in Supplementary Table 4. Secondary antibodies were Alexa Fluor488 or Alexa Fluor647 conjugated anti-rabbit or anti-mouse (1:500; Invitrogen). Nuclei were counterstained with DAPI. Cells were imaged using a Nikon confocal microscope with a $\times 10$ air lens.

Western blot analysis. OPCs were plated in basal differentiation medium and treated for 6 days with benzotropine (1.5 μM), T3 (1 μM) or DMSO. Cells were collected by scraping, pelleted and washed with ice-cold phosphate buffered saline (PBS) before lysis with PBS containing protease inhibitors (Roche), phosphatase inhibitors (Sigma), Triton X-100 and EDTA. Following incubation on ice for 20 min, lysed cells were centrifuged (16,000g, 15 min at 4 °C). Total protein was quantified using a NanoDrop and equal amounts of protein from each sample was denatured by boiling with 4 \times SDS sample buffer (Invitrogen) containing β -mercaptoethanol (5%). Proteins were electrophoresed using 4–20% SDS-PAGE gels (BioRad) and transferred on to a nitrocellulose membrane (BioRad). The membrane was blocked with 5% non-fat dry milk in TRIS buffered saline with Tween-20 (0.2%) and reacted with appropriate antibodies. Blots were incubated with HRP-conjugated secondary antibodies and visualized using film and Super Signal West peroxide solution (Pierce).

Semi-quantitative RT-PCR analysis. Total RNA from different samples was isolated and purified using the RNeasy mini kit (Qiagen) with on-column DNase digestion according to the manufacturer's protocol. Single-stranded cDNA was synthesized from 3 μg of total RNA with the SuperScript III First-Strand Synthesis System for RT-PCR using oligo(dT)₂₀ primers (Invitrogen). PCRs were performed using the Phusion High Fidelity polymerase and gene-specific primers (Supplementary Table 5). Cycle parameters for all genes were 30 s at 94 °C, 60 s at 57 °C and 60 s at 72 °C for 25 cycles.

Quantitative RT-PCR. For expression analysis of MBP, MOG, cyclin D1, cyclin D2, *c-Fos* and *c-Jun*, RNA was isolated and reverse-transcribed to complementary DNA (cDNA) as previously described. cDNA was used for qRT-PCR with gene-specific Taqman probes labelled with FAM (Applied Biosystems). qRT-PCR was performed using the ABI 7900HT instrument (Applied Biosystems) with standard parameters. The amount of cDNA was optimized so that amplification of both control genes and the cDNAs of interest were in the exponential phase. Transcripts were quantitated by comparative C_t method and normalized to endogenous controls, β -actin and GAPDH.

For expression analysis of other genes, RNA was isolated and reverse-transcribed to cDNA as previously described. cDNA was used for SBYR-green based qRT-PCR using gene-specific primers (Supplementary Table 5). Transcripts were quantitated by comparative C_t method and normalized to endogenous controls, 18S, β -actin and GAPDH.

Cyclic AMP HTRF assay. OPCs were plated at a density of 8,000 cells per well onto a 384-well plate and incubated at 37 °C overnight. The assay was performed using the HTRF cAMP dynamic 2 kit (CisBio Bioassays) per the manufacturer's protocol. IBMX (1 μM final concentration) was added as a cAMP stabilizer. Data acquisition was performed in the time-resolved fluorescence resonance energy transfer (FRET) mode on Envision (PerkinElmer). The ratio between the acceptor fluorescence signal ($A_{665\text{ nm}}$) and donor fluorescence signal ($A_{620\text{ nm}}$) $\times 10^4$, representing the FRET between the conjugated cAMP and the anti-cAMP antibody, was calculated and plotted on the y axis. The ratio is inversely proportional to the endogenous cAMP levels in the sample.

Calcium influx assay. Effect of compound treatment on the release of Ca²⁺ ions from the ER was measured using the FLIPR Tetra system (Molecular Devices). Briefly, cells were treated with carbachol as an M1/M3 agonist and the compounds were assayed for M1/M3 receptor antagonism using a Ca²⁺ sensitive Fluo-3AM dye.

EAE model. SJL/J (8-week-old female) mice were purchased from The Jackson Laboratory. Mice were immunized subcutaneously with murine proteolipid peptide (PLP_{139–151}; Peptides International) mixed 1:1 with supplemented complete Freund's adjuvant (CFA, Fisher) followed by *Bordetella pertussis* toxin (200 μg per mouse, Sigma) on day 0 and day 2 as described³⁷. Clinical EAE was graded on a scale of 1–5 by established standard criteria as follows: score 0, no observable disease; score 1, limp tail; score 2, limp tail and partial limb weakness; score 3, one hind limb paralyzed; score 4, both hind limbs paralyzed; score 5, moribund/dead. Mice received daily i.p. injections with compounds dissolved in saline. Dosing was commenced either on the day of PLP injections defined as prophylactic regimen or at the first appearance of EAE symptoms defined as therapeutic regimen and continued until day 30.

Immunohistochemistry and antibodies. Spinal cords were isolated from mice using standard protocols, fixed in Formalin-Zinc overnight followed by incubation in 30% sucrose at 4 °C overnight. Spinal cords were cross-sectioned into 8 pieces and embedded in Tissue-Tek OCT (Electron Microscopy Sciences). Thin sections were cut using a Leica cryostat and stained for myelin and infiltrating cells using Luxol fast blue, PAS, haematoxylin and eosin using standard protocols. For OPC and oligodendrocyte staining, sections were treated with Cirtisolve (Fisher) antigen retrieval solution, followed by incubation with primary antibodies (Supplementary Table 3). Secondary antibodies were Alexa Fluor488 or Alexa Fluor647-conjugated anti-rabbit or anti-mouse (1:500; Invitrogen). Nuclei were counterstained with DAPI. Cells were imaged using a Zeiss confocal microscope. Quantitative image analysis was performed using ImageJ (NIH) and ImagePro (Media Cybernetics). Numerical results from the analysed images were exported for analysis in Excel (Microsoft).

Brains from cuprizone-treated mice were isolated using standard protocols, fixed in formalin-zinc overnight, and embedded in paraffin. Sections were deparaffinized using a standard protocol and stained with Luxol fast blue (LFB) and haematoxylin and eosin as previously described. Slides were scanned using a Leica scanner. Images from at least 6 sections were collected and quantitative image analysis was performed using ImageJ (National Institutes of Health) and ImagePro (Media Cybernetics). Numerical results from the analysed images were exported for analysis in Excel (Microsoft).

Electron microscopy. Mice were exsanguinated with 0.9% saline followed by perfusion fixation with 4% paraformaldehyde, 1.5% glutaraldehyde and 1 mM CaCl_2 in 0.1 M cacodylate buffer and the spinal cords were exposed and fixed *in situ* overnight. Following complete removal, immersion fixation continued overnight at 4 °C in cacodylate buffered 2.5% glutaraldehyde with 1 mM CaCl_2 and then sliced into individual blocks. The tissues were then buffer washed, fixed in 1% osmium tetroxide and subsequently dehydrated in graded ethanol series, transitioned in propylene oxide and embedded in EMbed 812 / Araldite (Electron Microscopy Sciences). Thick sections (1.5 μm) were cut, mounted on glass slides and stained in toluidine blue for general assessment in the light microscope. Subsequently, 70-nm thin sections were cut with a diamond knife (Diatome), mounted on copper slot grids coated with parlodion and stained with uranyl acetate and lead citrate for examination on a Philips CM100 electron microscope (FEI) at 80 kV. Images were documented using a Megaview III CCD camera (Olympus Soft Imaging Solutions). Images were analysed in Image-Pro for g-ratio measurements by manually drawing lines across 2 perpendicular diameters each for axons and axons plus myelin. Lengths of the lines (in pixels) as generated by Image-Pro were averaged across the 2 perpendicular measurements and converted to micrometres (μm) using the image scale bars. g-ratio is defined as the ratio of the diameter of a given axon and the diameter of the axon plus myelin unit. Approximately 1,000 axons and axon plus myelin units were measured for each treatment group.

In vitro T-cell assay. Spleens were isolated from SJL/J, teased apart to single cell suspensions, red blood cells were lysed and remaining cells were isolated by centrifugation, resuspended in complete media and counted. The cells were then plated with soluble anti-CD28 ($5 \mu\text{g ml}^{-1}$) at 2×10^5 cells per well on plates pre-coated with anti-CD3 ($10 \mu\text{g ml}^{-1}$). Compounds dissolved in dimethylsulphoxide (DMSO) ($<0.1\%$) were added at 4 different dilutions (5 mM, 500 μM , 50 μM , 5 μM) and incubated at 37 °C, 5% CO_2 for 24, 48, 72 and 96 h. Cells were analysed by flow cytometry for CFSE dilution and CD25 and CD69 expression. Cells were labelled with CFSE (3 μM) in PBS supplemented with bovine serum albumin (BSA, 0.1%). Labelling was performed in the dark at 37 °C for 10 min with occasional mixing. Labelling was stopped by addition of 5 volumes of ice-cold PBS (0.1% BSA). Labelled cells were cultured for two days and analysed on a LSR II flow cytometer (Becton Dickinson). The data was analysed using the FloJo software (Tree Star).

In vivo T-cell assay. SJL/J (8-week-old female) mice were injected with PLP and Pertussis toxin to induce EAE as described in the previous section. On the same day, a prophylactic dosing regimen of compounds dissolved in saline was commenced by i.p. injections. The mice were scored and dosed daily. Mice usually developed symptoms of EAE by day 9, with the peak of symptoms appearing around day 14. Mice were sacrificed on day 14 and spleens were removed. Blood was collected for sera. Spleens were teased apart to single cell suspensions, red blood cells were lysed and splenocytes were isolated by centrifugation. Cells were resuspended in complete medium defined as Dulbecco's modified eagle medium (Gibco) supplemented with 10% fetal bovine serum (Gibco) and counted. Cells were then plated at 2×10^5 cells per well on a 96-well plate and treated with either $20 \mu\text{g ml}^{-1}$ PLP peptide or 10 ng ml^{-1} phorbol myristate acetate (PMA) and 300 ng ml^{-1} ionomycin for 48 h to stimulate cytokine production. Cytokine secretion was blocked during the last 5 h by treatment with monensin. Supernatants were collected for ELISAs of IL-2, IFN- γ , IL-10 and TNF- α . Cells were stained for flow cytometry using antibodies against CD4,

CD8, B220 and CD44. Cells were also stained for intracellular cytokines such as IL-2, IFN- γ , IL-10 and TNF- α along with anti-CD4. Flow cytometry analysis was performed on a LSR II flow cytometer (Becton Dickinson) and the data was analysed using the FloJo software (Tree Star).

In vivo assays for T-cell-dependent B-cell responses. SJL/J mice were injected i.p. with TNP-KLH (Biosearch Technology; $25 \mu\text{g}$ per mouse in complete Freund's adjuvant). Benztropine (10 mg per kg) or vehicle was injected i.p. daily for 21 days. Sera were collected on day 0, 7, 14 and 21. The collected sera was analysed by ELISA for anti-TNP IgG levels.

Bone marrow-derived macrophages and M1/M2 polarization. Bone marrow-derived macrophage (BMM) cultures were generated from adult SJL/J mice. Briefly, femurs and tibias were collected bilaterally and marrow cores were flushed using syringes filled with DMEM medium supplemented with 1% penicillin/streptomycin, 1% HEPES, 1% sodium pyruvate, 0.1% β -mercaptoethanol and 10% FBS (complete DMEM) (Gibco). Cells suspension were filtered through a $0.2 \mu\text{m}$ cell strainer, counted, plated in complete DMEM supplemented with 5% of horse serum and 20% supernatant from macrophage colony stimulating factor secreting L929 (sL929) cells. The sL929 drives bone marrow cells towards a macrophage phenotype (10 days). Non-adherent cells were removed at day 4. At collection (day 10), $90 \pm 0.7\%$ of cells were macrophages (assessed by F4/80 immunostaining). To promote differentiation into M1 or M2 macrophages, cells were treated with LPS (100 ng ml^{-1} ; Sigma-Aldrich) plus IFN γ (20 ng ml^{-1} ; Peprotech) or IL-4 plus IL-13 (20 ng ml^{-1} ; Peprotech), respectively, for 16 h, in the presence or absence of benztropine (5 μM). After M1 or M2 polarization, some cells (cultured without benztropine) were saved and treated once again, as described above. The viability of M1/M2 macrophages was analysed in every experiment by flow cytometry of DAPI-stained cells (Invitrogen). Supernatants and cells were subsequently collected for cytokine (TNF- α) and phenotypic analysis, respectively. M1 and M2 polarization was assessed using the following fluorochrome-labelled antibodies: anti-F4/80, rat anti-mouse mannose receptor (CD206), rat anti-mouse CD86, rat anti-mouse CD80 and anti-mouse I-A/I-E antibodies (BioLegend).

Isolation of spleen and leukocyte isolation from spinal cords. EAE mice were euthanized, spleens were isolated from the mice as per standard protocols and crushed by mechanical disruption using a tissue homogenizer. Spinal cords were isolated from the mice, treated with collagenase and ground to a single cell suspension. Suspensions from 2 spinal cords from mice with similar clinical severity scores were combined and centrifuged through gradients of 30% and 70% Percoll to isolate infiltrating leukocytes. Total RNA was isolated and used for gene expression analysis as previously described.

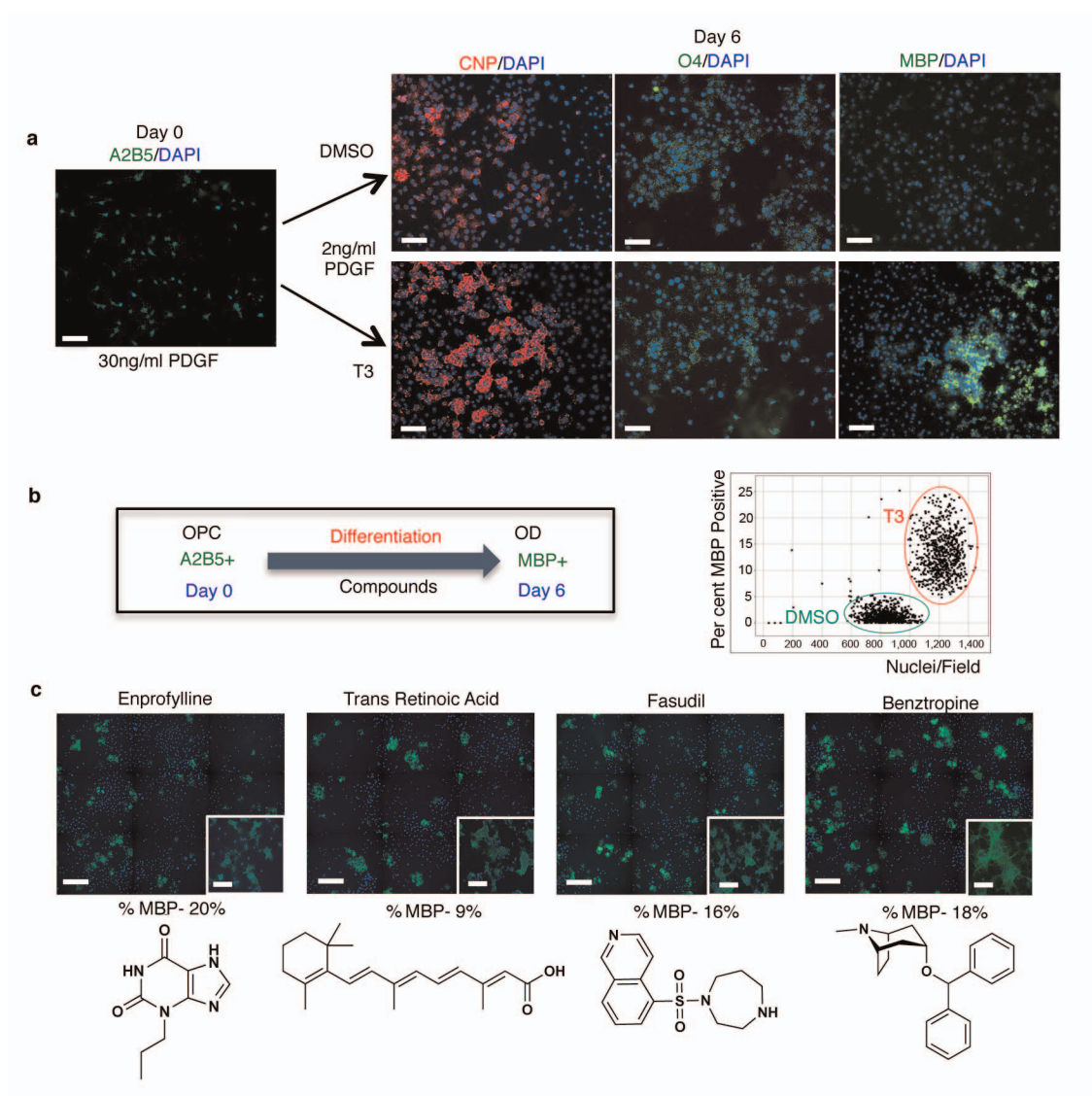
Adoptive transfer EAE. SJL/J donor mice were purchased from The Jackson Laboratories. Mice were immunized subcutaneously with murine proteolipid peptide (PLP₁₃₉₋₁₅₁; Peptides International) mixed 1:1 with supplemented complete Freund's adjuvant (CFA, Fisher). Mice were then either injected with saline or benztropine (10 mg per kg, daily, i.p.) for 7 days, and re-immunized with murine PLP emulsified 1:1 with incomplete Freund's adjuvant. Daily benztropine or vehicle injections were continued until day 10, when spleens were isolated, teased apart to single cell suspensions, red blood cells lysed and splenocytes isolated by centrifugation. Cells were resuspended in complete media (RPMI 1640 supplemented with 10% fetal bovine serum (FBS), 1.25% HEPES buffer, 1% sodium pyruvate, 1% penicillin-streptomycin, 1% glutamine, 1% non-essential amino acids, 0.01% 2-mercaptoethanol (2-ME)) (Sigma-Aldrich) and counted. Splenocytes were analysed by flow cytometry to determine cell viability and percentage of CD4^+ T cells as described earlier. Splenocytes from vehicle-treated mice were further cultured *in vitro* in the presence of PLP₁₃₉₋₁₅₁ ($30 \mu\text{g ml}^{-1}$), interleukin 12 (IL-12) (10 ng ml^{-1}) and DMSO ($<0.1\%$), whereas splenocytes from benztropine-treated donor mice were further cultured *in vitro* in the presence of PLP₁₃₉₋₁₅₁, interleukin 12 (IL-12) (10 ng ml^{-1}) and benztropine (5 μM) for 72 h at 37 °C. At the end of 72 h, cells were analysed by flow cytometry to determine cell viability and percentage of CD4^+ T cells as described earlier ($\sim 80\%$ activated T cells after *in vitro* culture). Cells were then washed and resuspended in PBS (50 million cells ml^{-1}) and $200 \mu\text{l}$ of cell suspension was injected into 4 groups (according to the following table) of naive recipient SJL/J mice by intravenous injection followed by *Bordetella pertussis* toxin (i.p., $200 \mu\text{g}$ per mouse, Sigma) on day 0 and day 2. Clinical EAE was graded on a scale of 1–5 by established standard criteria as follows: score 0, no observable disease; score 1, limp tail; score 2, limp tail and partial limb weakness; score 3, one hind limb paralyzed; score 4, both hind limbs paralyzed; score 5, moribund/dead. Mice received daily i.p. injections of either saline or benztropine (10 mg per kg) according to Extended Data Fig. 8c, d. **Cuprizone model.** C57BL/6 mice (8-week-old females) were purchased from the breeding colony at The Scripps Research Institute. Mice were fed 0.2% w/w cuprizone (bis-cyclohexanone oxaldihydrazone, Sigma-Aldrich) mixed into a ground standard rodent chow (Harlan). Cuprizone diet was maintained for 7 weeks; thereafter mice were put on a normal chow for another 5 weeks. Compounds were

dissolved in saline and daily i.p. injections were initiated at the withdrawal of the cuprizone diet. At different time points (0, 1, 2, 3, 4 and 5 weeks after cuprizone withdrawal), animals were euthanized. Brains were extracted, fixed in formalin-zinc, paraffin-embedded, sectioned and stained as described in the immunohistochemistry section.

Image analysis of brain sections. Using ImageJ (NIH), images were converted to a 256-shade grey scale. The 256 shades of grey were then divided into 5 bins of 50 shades each: 0–50, 50–100, 100–150, 150–200 and 200–256, with 0 being the pixel with darkest shade of grey and 256 being the pixel with the lightest shade of grey. Each bin was assigned an arbitrary colour: 0–50 (red), 50–100 (yellow), 100–150 (green), 150–200 (light blue) and 200–256 (dark blue). Based on the intensity of staining, each pixel was classified into one of the 5 bins using Image-Pro plus software. The number of objects in the corpus callosum region classified into each bin was counted. Data was exported to Excel (Microsoft) for analysis.

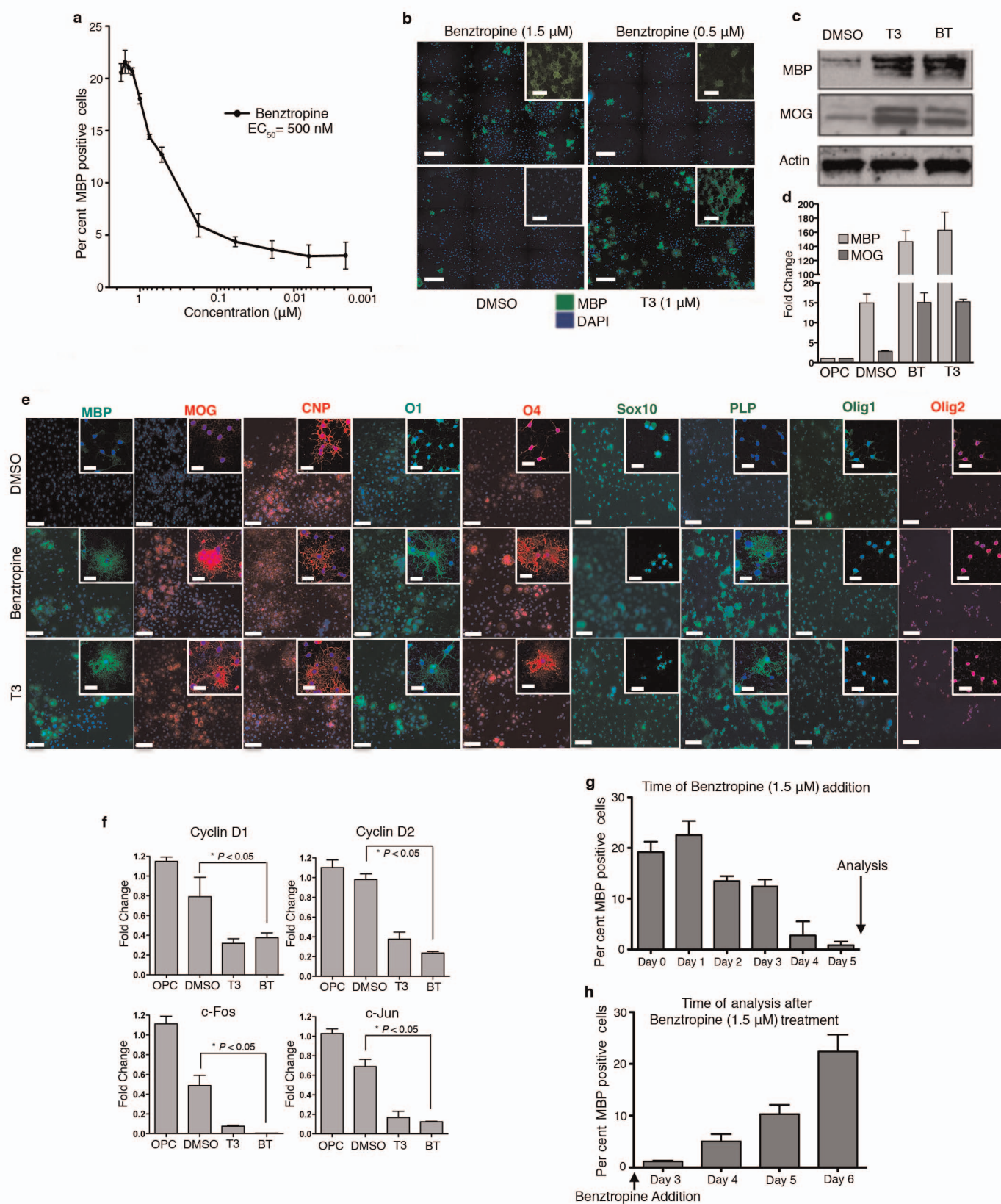
Animal use statement: All experiments were performed in accordance with approved Institutional Animal Care and Use Committee (IACUC) protocols of The Scripps Research Institute or Hokkaido University Institute for Genetic Medicine.

51. Kondo, T. & Raff, M. The Id4 HLH protein and the timing of oligodendrocyte differentiation. *EMBO J.* **19**, 1998–2007 (2000).
52. Wang, S., Sdrulla, A., Johnson, J. E., Yokota, Y. & Barres, B. A. A role for the helix-loop-helix protein Id2 in the control of oligodendrocyte development. *Neuron* **29**, 603–614 (2001).
53. Pang, Y. *et al.* Neuron-oligodendrocyte myelination co-culture derived from embryonic rat spinal cord and cerebral cortex. *Brain Behav.* **2**, 53–67 (2012).
54. Izrael, M. *et al.* Human oligodendrocytes derived from embryonic stem cells: Effect of noggin on phenotypic differentiation *in vitro* and on myelination *in vivo*. *Mol. Cell. Neurosci.* **34**, 310–323 (2007).



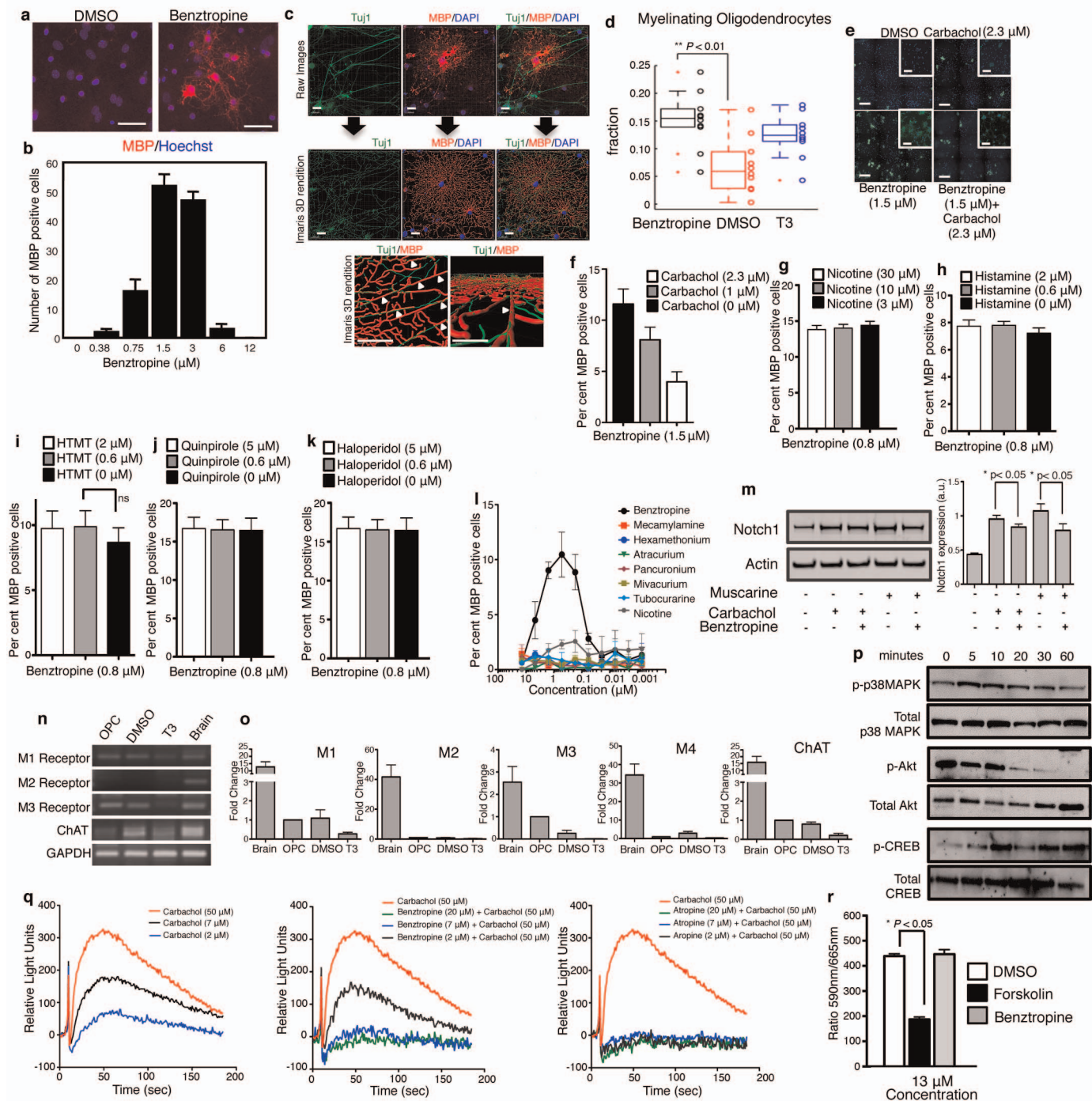
Extended Data Figure 1 | High-throughput screen to identify inducers of OPC differentiation. **a**, Rat primary OPCs in basal differentiation media treated with DMSO (<0.1%) or thyroid hormone (T3; 1 μ M) for 6 days in culture, fixed and stained using antibodies for myelin basic protein (MBP), 2',3'-cyclic-nucleotide 3'-phosphodiesterase (CNP) and oligodendrocyte marker O4. A2B5⁺ OPCs differentiated into immature oligodendrocytes that

express CNP and O4, but not MBP, upon reduction of PDGF-AA. T3 added as a positive control induced differentiation to mature cells that express MBP. Scale bars, 100 μ m. **b**, Schematic representation of the high-throughput screening platform used to identify inducers of OPC differentiation. **c**, Inducers of OPC differentiation identified as hits from a screen of known biologically active compounds. Scale bars, 100 μ m; inset, 40 μ m.



Extended Data Figure 2 | Benztropine induces dose-dependent OPC differentiation *in vitro* to mature oligodendrocytes. **a**, Dose response assay used to confirm primary screening activity of benztropine and determine potency (EC_{50}). OPCs were treated with benztropine and immunostained using antibodies for MBP ($n = 3$, mean and s.d.). **b**, Images showing dose-dependent induction of OPC differentiation after treatment with benztropine. (Scale bars, 100 μ m; inset, 40 μ m). OPCs in basal differentiation media treated with DMSO ($<0.1\%$), T3 (1 μ M) or benztropine (1.5 μ M) for 6 days and analysed for MBP and MOG expression by western blot (**c**) and by qRT-PCR (**d**) ($n = 3$, mean and s.d.). **e**, OPCs were plated in differentiation medium and treated with DMSO ($<0.1\%$), benztropine (1.5 μ M) or T3 (1 μ M) for 6 days. Cells were fixed and immunostained for myelin basic protein (MBP), myelin oligodendroglial

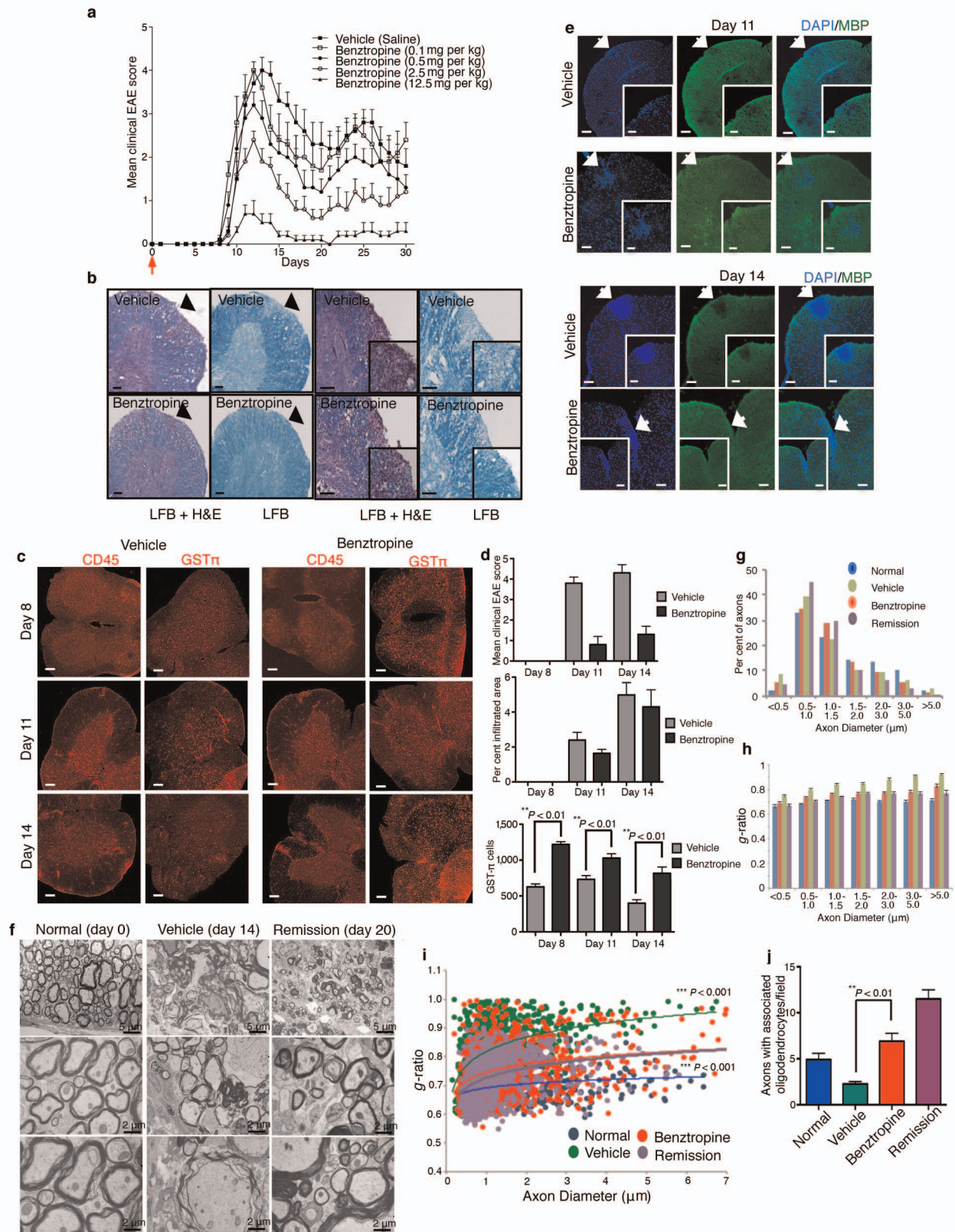
glycoprotein (MOG), CNP, oligodendrocyte marker O1, oligodendrocyte marker O4, glial marker SOX10, proteolipid peptide (PLP), OLIG1 and OLIG2. Representative images showing expression of mature oligodendrocyte markers in benztropine- and T3-treated cells, but not DMSO-treated cells. Scale bars, 100 μ m; inset, 40 μ m. **f**, Expression of cell cycle genes by qRT-PCR. ($n = 3$, mean and s.d., $*P < 0.05$, *t*-test). **g**, OPCs plated in basal differentiation medium and treated with benztropine (1.5 μ M) on various days (0, 1, 2, 3, 4 and 5), fixed on day 6 and immunostained for MBP ($n = 3$, mean and s.d.). **h**, OPCs plated in basal differentiation medium, treated with benztropine (1.5 μ M) on the same day, fixed on various days (3, 4, 5 and 6) following compound treatment and immunostained for MBP ($n = 3$, mean and s.d.).



Extended Data Figure 3 | Benztropine induces OPC differentiation and *in vitro* myelination through M1/M3 muscarinic receptor antagonism and has no effect on histamine or nicotinic signalling.

a, Mouse OPCs co-cultured with mouse cortex-derived cells in the presence of DMSO or benztropine and immunostained for MBP (red) and nuclei with Hoechst 33342 (blue). Scale bars, 100 μ m. **b**, Quantification of MBP staining of mouse OPCs treated with DMSO or benztropine. **c**, Analysis of myelination in OPCs with neurons co-culture. Arrowheads point to regions of myelination. Scale bars, 20 μ m. **d**, Quantification of fraction of myelinating oligodendrocytes in OPCs with neurons co-cultures ($n = 10$, mean and s.e.m., $**P < 0.01$, ANOVA with Bonferroni correction). OPCs co-treated with benztropine (1.5 μ M) and carbachol (2.3 μ M) for 6 days and stained for MBP (green) (Scale bars, 100 μ m; inset, 40 μ m). **e**, Antagonism of benztropine-induced OPC differentiation by muscarinic agonist carbachol. **f**, Quantification of MBP staining of OPCs co-treated with benztropine (1.5 μ M) and muscarinic receptor agonist carbachol for 6 days under basal differentiation conditions ($n = 3$, mean and s.d.). **g–k**, OPCs plated co-treated with benztropine (0.8 μ M) and either nicotine (**g**), histamine (**h**), histamine receptor agonist histamine trifluoromethyl

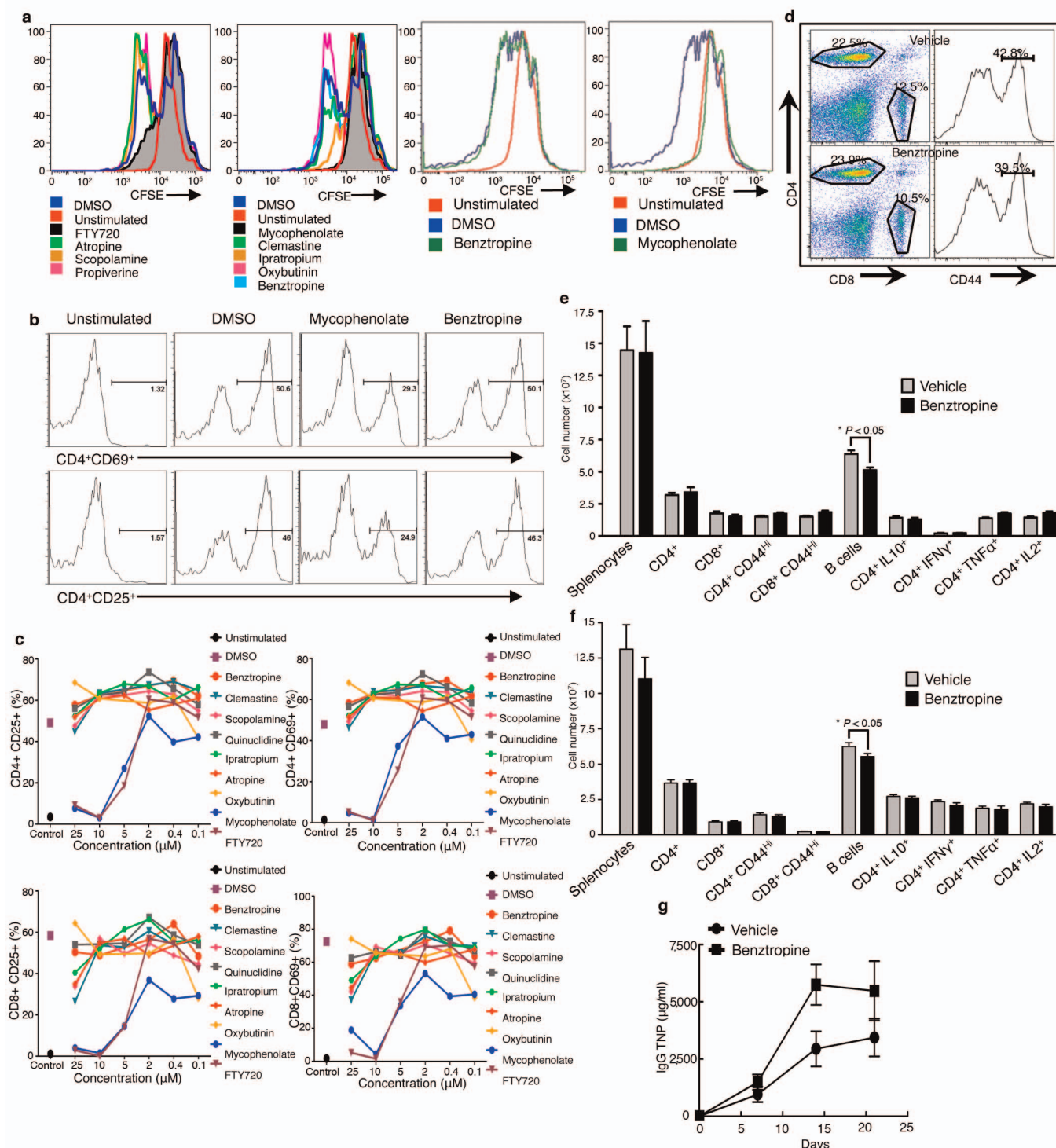
toluidide (HTMT) (**i**), dopamine receptor agonist quinpirole (**j**) or dopamine receptor antagonist haloperidol (**k**) ($n = 3$, mean and s.d., ns = not significant). **l**, Various nicotinic receptor antagonists have no effect on OPC differentiation. **m**, Benztropine blocks carbachol- and muscarine-induced activation of Notch signalling measured by western blot for intracellular domain of Notch1. (a.u., arbitrary unit, $n = 3$, mean and s.d., $*P < 0.05$, t -test). **n**, Naive whole rat brain and rat primary OPCs treated with DMSO (<0.1%) or T3 (1 μ M) for 6 days tested for expression of muscarinic receptors and choline acetyl transferase (ChAT) by PCR using gene-specific primers. **o**, Quantification of M1, M2, M3, M4 and ChAT expression by qRT-PCR. ($n = 3$, mean and s.d., expression fold change normalized to OPCs). **p**, OPCs treated with benztropine (25 μ M) and pelleted for western blot analysis of total protein. **q**, Carbachol induced a dose-dependent increase in intracellular Ca^{2+} levels, whereas benztropine and atropine (a muscarinic antagonist) dose-dependently blocked carbachol (50 μ M) induced calcium influx through antagonism of M1/M3 muscarinic receptors. **r**, Benztropine (13 μ M) had no effect on the levels of cAMP. Forskolin is a positive control for increasing intracellular cAMP ($n = 3$, mean and s.d., $*P < 0.05$, t -test).



Extended Data Figure 4 | Benztropine dose-dependently reduces clinical severity and induces remyelination in the PLP-induced EAE model.

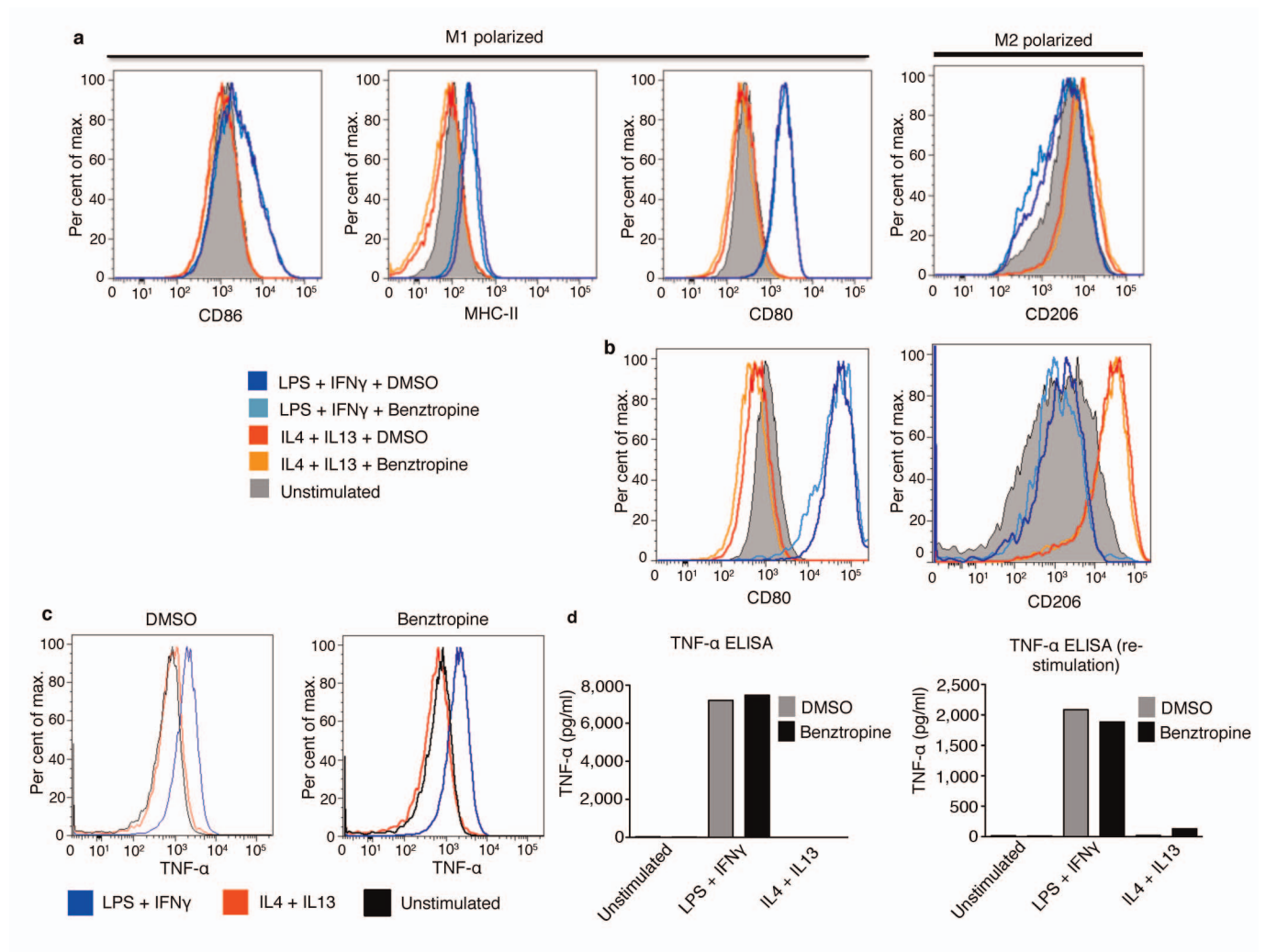
a, Clinical severity scores of EAE mice treated with various doses of benztropine in the prophylactic mode ($n = 8$, mean and s.e.m.). **b**, EAE mice treated with benztropine (10 mg per kg) or vehicle in the therapeutic mode and spinal cord sections from mice representative of the average group scores during the relapse phase of EAE stained with Luxol fast blue and H&E, or Luxol fast blue only. Arrows point to regions of lymphocyte infiltration (LFB + H&E) or demyelination (LFB). Scale bars represent 100 μm . EAE mice treated with benztropine (10 mg per kg) or vehicle in prophylactic mode. **c**, Spinal cord sections from mice representative of the average group scores on day 8, 11 and 14 immunostained with antibodies specific to CD45 and GST π . **d**, Mean clinical scores of mice at the time of spinal cord isolation and quantification of the infiltrated areas (CD45 $^{+}$) and number of GST π^{+} cells ($n = 8$, mean and

s.e.m., $**P < 0.01$, t -test). Scale bars, 100 μm . **e**, EAE mice treated with benztropine (10 mg per kg) or vehicle in prophylactic mode and spinal cord sections from mice representative of the average group scores on day 11 and 14, immunostained with antibody specific to MBP. Arrows point to regions of lymphocyte infiltration. Scale bars, 100 μm . **f**, Electron microscopy images showing myelin around axons in normal mice, vehicle-treated mice and mice in remission. Scale bars as indicated. **g**, Analysis of electron microscopy images indicating distribution of axonal diameters measured for 4 groups. **h**, Analysis of electron microscopy images indicating distribution of g -ratios of axons for 4 groups. **i**, Scatterplot of g -ratios in relation to spinal cord axonal diameters ($n = 1,000$, $***P < 0.001$, one-way ANOVA, exponential trend line). **j**, Quantification of the number of axons associated with oligodendrocytes ($n = 25$, mean and s.e.m., $**P < 0.01$, t -test). Oligodendrocytes were identified visually by their cytoplasmic processes wrapping around axons.



Extended Data Figure 5 | Benztropine has no effect on *in vitro* and *in vivo* immunological responses in EAE mice. **a**, Benztropine and various muscarinic antagonists have no effect on *in vitro* T-cell proliferation measured using carboxyfluorescein succinimidyl ester (CFSE) labelling, whereas mycophenolate and FTY720 suppress T-cell proliferation as determined by the percentage of CD4⁺ T-cell-gated populations positive for the given marker. **b**, **c**, Various muscarinic antagonists have no effect on T-cell activation as measured by CD4⁺CD25⁺, CD4⁺CD69⁺, CD8⁺CD25⁺ and CD8⁺CD69⁺ cell populations. FTY720 and mycophenolate serve as positive controls for suppression of T-cell activation. **d**, Representative flow cytometry scatter plots show similar numbers of CD4⁺, CD8⁺, and CD44⁺ cells in spleens isolated from vehicle- and benztropine-treated mice. **e**, **f**, Total splenocytes isolated from benztropine (10 mg per kg) or vehicle treated (14 days in the prophylactic

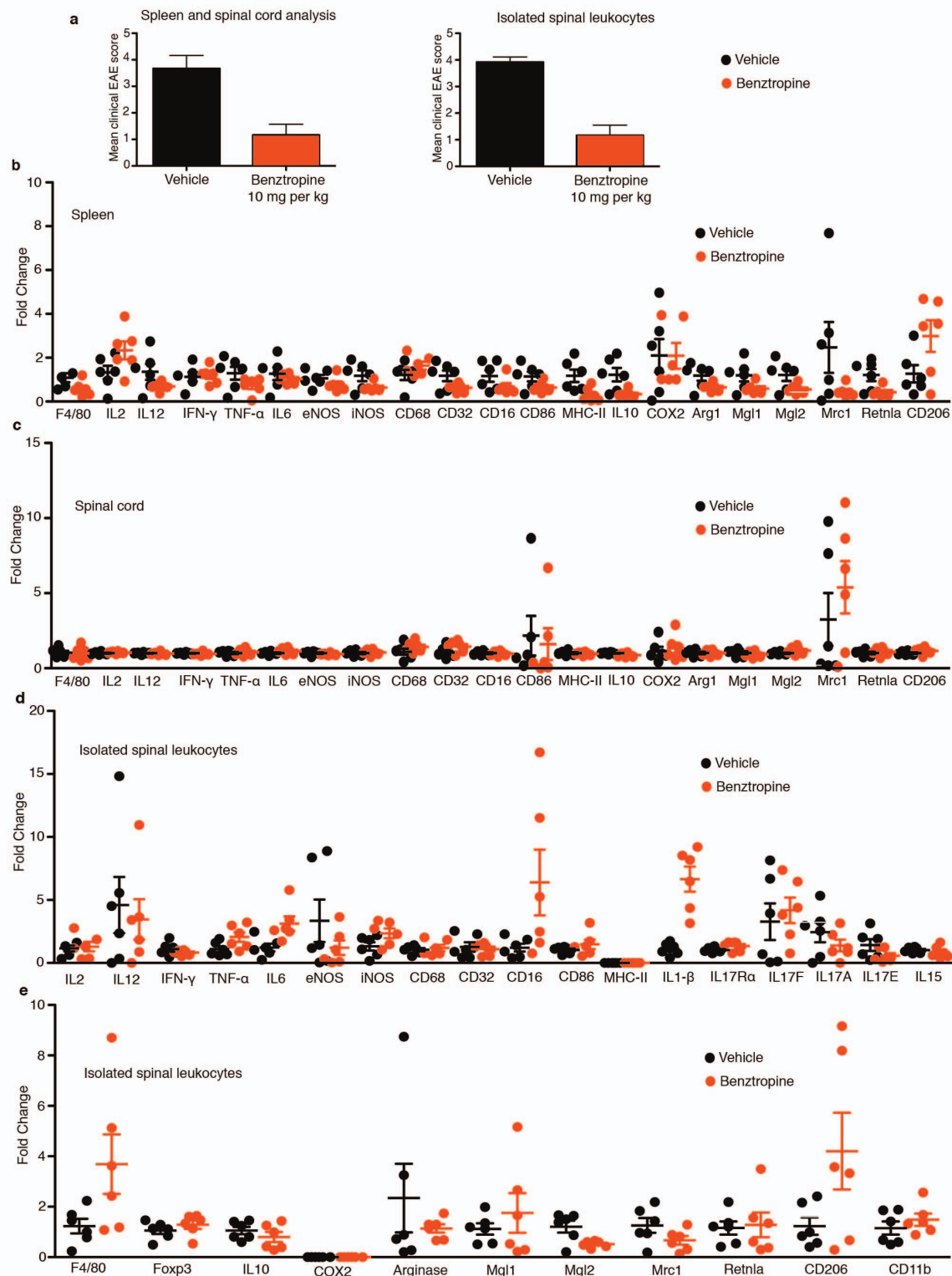
mode) naive SJL/J (**e**) or EAE (**f**) mice analysed for various populations of immune cells and cytokine secretion. Benztropine treatment had no effect on the numbers of total splenocytes, CD4⁺ T cells, CD8⁺ T cells, CD4⁺CD44⁺ T cells and CD8⁺CD44⁺ T cells. Benztropine treatment showed a minor, but significant decrease in the number of B cells ($n = 5$, mean and s.e.m., * $P < 0.05$, t -test). Benztropine had no effect on cytokine production from CD4⁺ T cells expressing IL-2, IL-10, TNF- α or IFN- γ . ($n = 5$, mean and s.e.m.). **g**, Benztropine showed no effect on keyhole limpet hemocyanin protein conjugated to 2,4,6-trinitrophenyl hapten (TNP-KLH)-induced T-cell-dependent B-cell response. Mice were injected with TNP-KLH in adjuvant and treated with vehicle or benztropine (10 mg per kg) daily. Serum was isolated at various time points and anti-TNP-IgG levels were measured by ELISA. (3 replicate ELISAs, $n = 5$ mice per group, mean and s.e.m.).



Extended Data Figure 6 | Benztropine does not affect derivation and *in vitro* polarization of macrophages from bone marrow derived monocytes.

a, Flow cytometry analysis of bone marrow derived monocytes treated *in vitro* with either DMSO (<0.1% v/v) or benztropine (5 μ M) for 24 h followed by 24 h treatment with LPS (100 ng ml⁻¹) plus IFN γ (20 ng ml⁻¹) for the expression of M1 markers: CD86, MHC-II and CD80, or 24 h treatment with IL-4 plus IL-13 (20 ng ml⁻¹ each) for the expression of M2 marker CD206. **b**, M1/M2 polarized macrophages re-stimulated using either LPS (100 ng ml⁻¹)

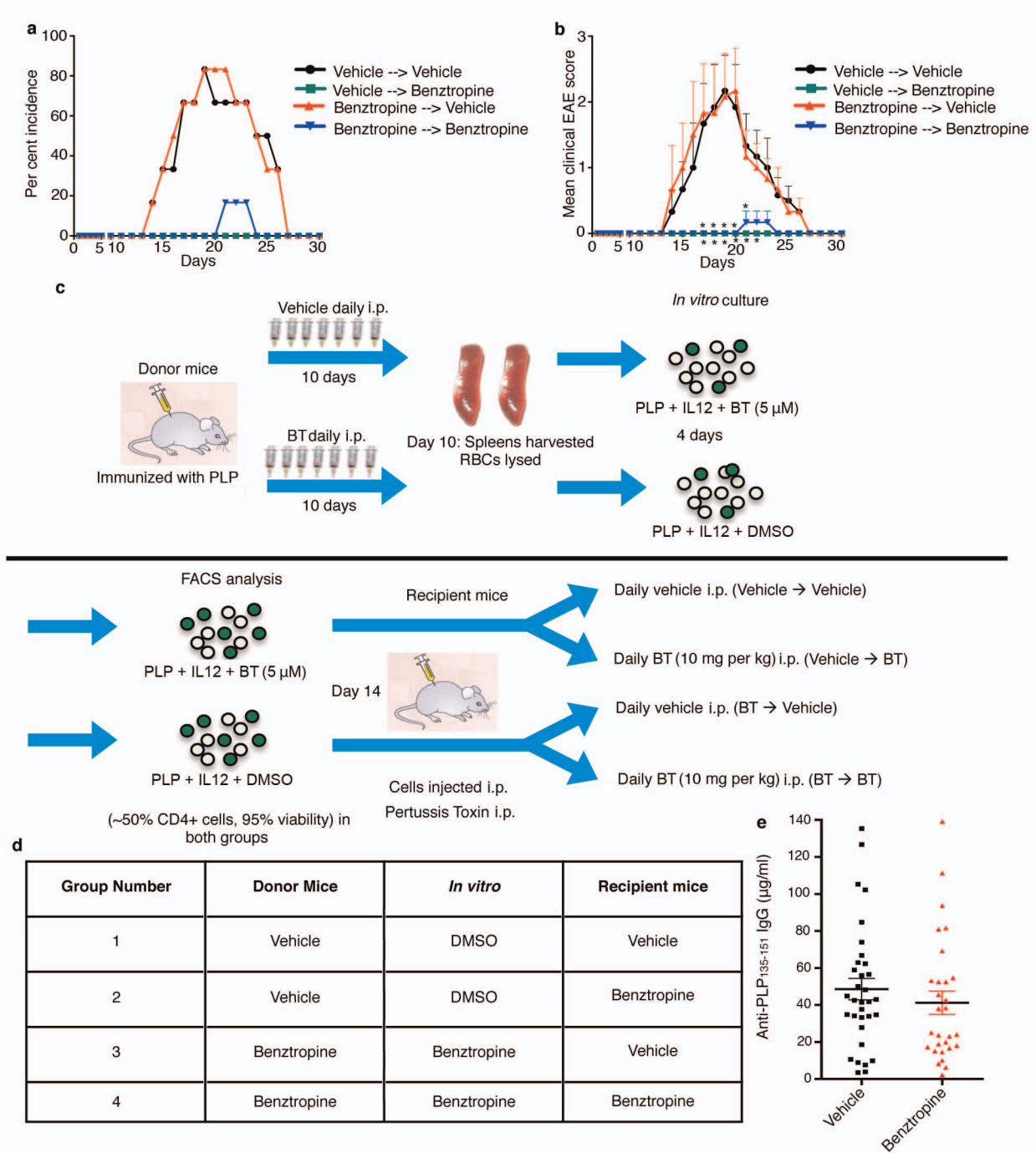
plus IFN γ (20 ng ml⁻¹) (M1) or IL-4 plus IL-13 (20 ng ml⁻¹ each) (M2) for 16 h in the presence of either benztropine (5 μ M) or DMSO and analysed for the expression of M1 (CD80) or M2 (CD206) markers by flow cytometry. **c**, **d**, Treatment with LPS (100 ng ml⁻¹) plus IFN γ (20 ng ml⁻¹) induced the expression of the prototypical M1 cytokine TNF- α as detected by intracellular flow cytometry (**c**) and ELISA (**d**) with no significant differences between DMSO or benztropine (5 μ M) treated cells (data representative of 2 replicate experiments).



Extended Data Figure 7 | Benzotropine does not affect *in vivo* polarization of macrophages in the spleen or spinal cord. EAE mice were treated with benzotropine (10 mg per kg) or vehicle for 14 days in the prophylactic mode.

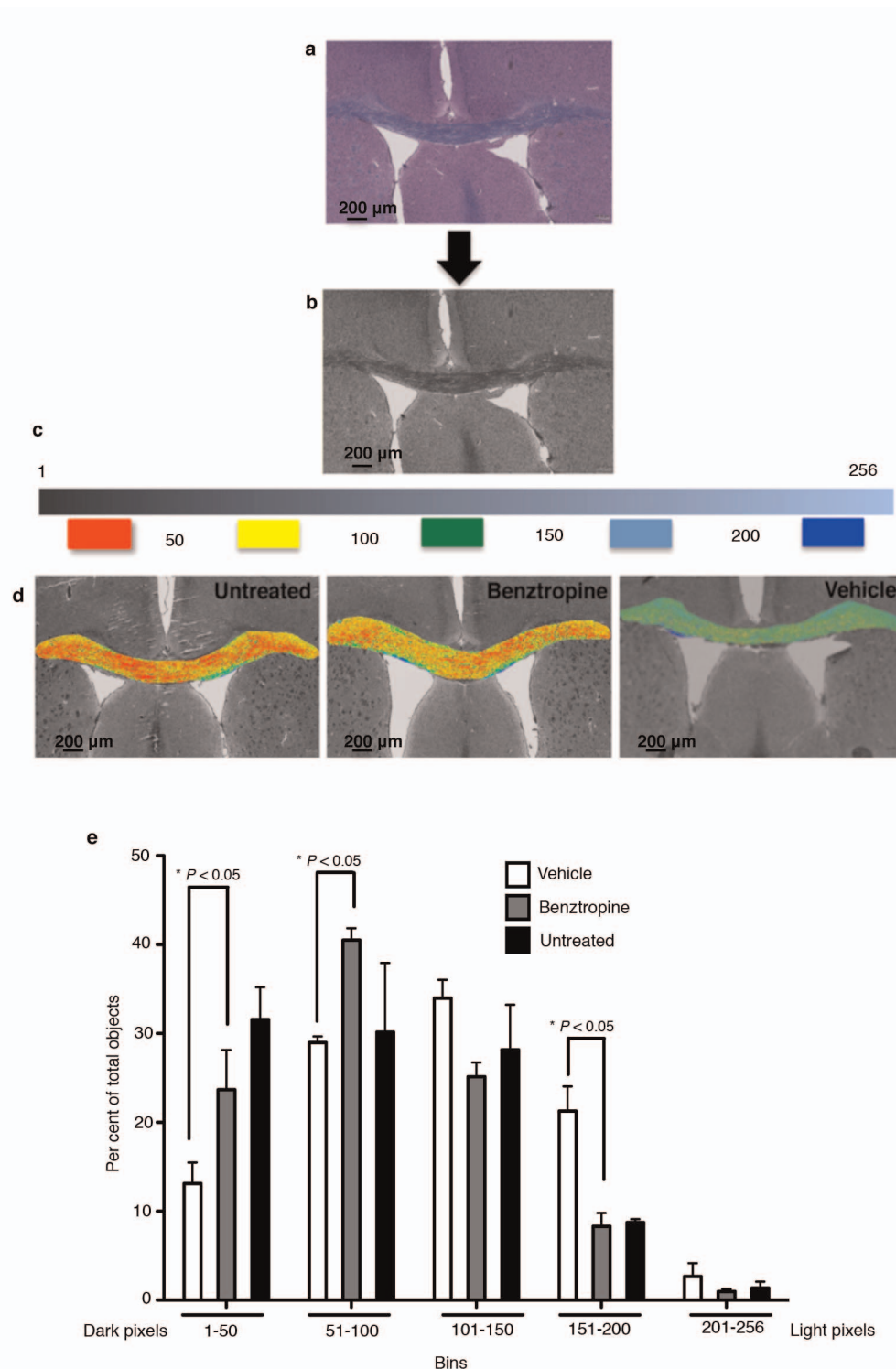
a, Mean clinical EAE scores for mice treated with vehicle or benzotropine ($n = 6$, mean and s.e.m. for spleens and spinal cords, $n = 12$ for isolated spinal leukocytes analysis). **b–e**, Spleens and spinal leukocytes were isolated from the mice as described in Methods. Total RNA was isolated, reverse transcribed and

gene expression was measured by qRT-PCR. Expression for each marker was normalized to the average gene expression of the vehicle group. No significant differences were observed in the expression of markers of macrophage polarization in the spleen (**b**), whole spinal cords (**c**) and leukocytes (**d, e**) isolated from spinal cords ($n = 6$ mice per group for spleens and spinal cords, $n = 12$ mice per group ($n = 6$ for qRT-PCR) for spinal leukocytes analysis. Error bars represent s.e.m.).



Extended Data Figure 8 | Benztropine does not affect clinical severity in an adoptive transfer model of EAE. **a, b**, Incidence of adoptive transfer of EAE (**a**) and mean clinical EAE scores (**b**) in mice injected with splenocytes isolated from benztropine- or vehicle-treated donor groups. T cells obtained from either benztropine- (BT, 10 mg per kg) or vehicle-treated donor EAE mice and further expanded in the presence or absence of benztropine (5 μ M) were able to adoptively transfer EAE to naive recipient mice. Benztropine-treated recipient

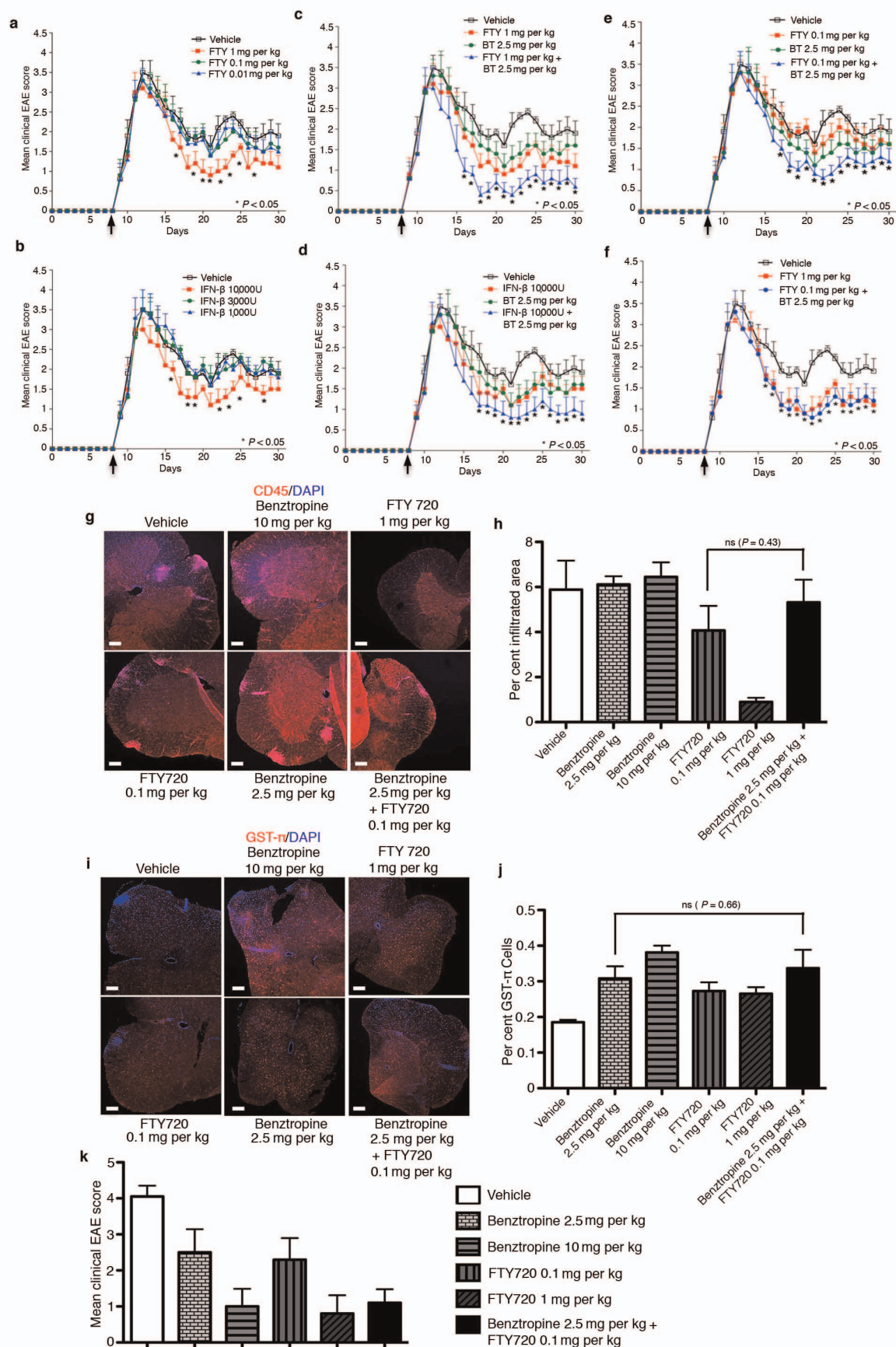
mice showed little to no clinical symptoms of EAE compared to vehicle-treated recipient mice, whether injected with benztropine- or vehicle-treated donor splenocytes ($n = 6$ mice, mean and s.e.m., $*P < 0.05$, t -test). **c**, Schematic for the adoptive transfer EAE model. **d**, Table showing various groups and treatments. **e**, ELISA for anti-PLP IgG shows equivalent PLP response in donor mice treated with either vehicle or benztropine ($n = 30$, mean and s.e.m).



Extended Data Figure 9 | Quantification of myelin staining in the cuprizone model. **a**, Luxol fast blue (LFB) and H&E staining was performed on sections from the corpus callosum region of brains isolated from mice treated either with benztropine (10 mg per kg) or vehicle after 7 weeks of exposure to cuprizone. **b**, Images were converted to a 256 shade grey scale. **c**, The 256 shades of grey were divided into 5 bins of 50 shades each (1–50, 51–100, 105–150, 151–200 and 201–256). Number of objects in the corpus

callosum region in each bin were counted using Image-Pro plus.

d, Representative images of Image-Pro rendering of the quantification of objects in each bin. **e**, Quantification of Luxol fast blue staining on week 2 shows an increase in the darker pixels (1–50 and 51–100) with benztropine treatment along with corresponding reduction in the number of lighter pixels (151–200). Six images per mouse were analysed and four mice per group were used at each time point (mean and s.d., * $P < 0.05$, t -test). Scale bars, 200 μ m.



Extended Data Figure 10 | Effect of the addition of benztropine to

interferon- β and FTY720 treatments. **a, b**, EAE severity scores for mice treated with various doses of FTY720 (**a**) or interferon- β (**b**). **c**, Mice treated therapeutically with FTY720 (1 mg per kg) in combination with a sub-optimal dose of benztropine (BT, 2.5 mg per kg) show significantly decreased clinical severity compared to FTY720 (1 mg per kg) or benztropine (2.5 mg per kg) alone. **d**, EAE mice treated with interferon- β (IFN; 10,000 U per mouse) in combination with benztropine (2.5 mg per kg) show significantly decreased clinical severity compared to interferon- β (IFN; 10,000 U per mouse) or benztropine (2.5 mg per kg) alone. **e**, EAE mice treated with a tenfold lower dose of FTY720 (0.1 mg per kg) in combination with benztropine (2.5 mg per kg). **f**, EAE mice treated with a tenfold lower dose of FTY720 (0.1 mg per kg) in

combination with benztropine (2.5 mg per kg) show clinical severity comparable to optimal dose of FTY720 (1 mg per kg) ($n = 8$ mice per group, mean and s.e.m., $*P < 0.05$; t -test). **g, i**, Spinal cord sections from EAE mice treated with the indicated drug(s) for 14 days in the prophylactic mode and immunostained for CD45 (immune cells) and GST π (oligodendrocytes) showing infiltration (**g**) and oligodendrocytes (**i**). **h, j**, Quantification of the number of CD45 $^{+}$ (**h**) and GST π $^{+}$ (**j**) cells showing a decrease in infiltrating cells with FTY720 treatment and an increase in oligodendrocytes numbers with benztropine treatment and synergy between benztropine (2.5 mg per kg) and FTY720 (0.1 mg per kg) ($n = 5$, mean and s.e.m., ns, not significant). Scale bars, 100 μ m. **k**, Mean clinical EAE scores for mice at the time of spinal cord isolation ($n = 8$, mean and s.e.m.).

Mutational landscape and significance across 12 major cancer types

Cyriac Kandoth^{1*}, Michael D. McLellan^{1*}, Fabio Vandin², Kai Ye^{1,3}, Beifang Niu¹, Charles Lu¹, Mingchao Xie¹, Qunyan Zhang^{1,3}, Joshua F. McMichael¹, Matthew A. Wyczalkowski¹, Mark D. M. Leiserson², Christopher A. Miller¹, John S. Welch^{4,5}, Matthew J. Walter^{4,5}, Michael C. Wendl^{1,3,6}, Timothy J. Ley^{1,3,4,5}, Richard K. Wilson^{1,3,5}, Benjamin J. Raphael² & Li Ding^{1,3,4,5}

The Cancer Genome Atlas (TCGA) has used the latest sequencing and analysis methods to identify somatic variants across thousands of tumours. Here we present data and analytical results for point mutations and small insertions/deletions from 3,281 tumours across 12 tumour types as part of the TCGA Pan-Cancer effort. We illustrate the distributions of mutation frequencies, types and contexts across tumour types, and establish their links to tissues of origin, environmental/carcinogen influences, and DNA repair defects. Using the integrated data sets, we identified 127 significantly mutated genes from well-known (for example, mitogen-activated protein kinase, phosphatidylinositol-3-OH kinase, Wnt/ β -catenin and receptor tyrosine kinase signalling pathways, and cell cycle control) and emerging (for example, histone, histone modification, splicing, metabolism and proteolysis) cellular processes in cancer. The average number of mutations in these significantly mutated genes varies across tumour types; most tumours have two to six, indicating that the number of driver mutations required during oncogenesis is relatively small. Mutations in transcriptional factors/regulators show tissue specificity, whereas histone modifiers are often mutated across several cancer types. Clinical association analysis identifies genes having a significant effect on survival, and investigations of mutations with respect to clonal/subclonal architecture delineate their temporal orders during tumorigenesis. Taken together, these results lay the groundwork for developing new diagnostics and individualizing cancer treatment.

The advancement of DNA sequencing technologies now enables the processing of thousands of tumours of many types for systematic mutation discovery. This expansion of scope, coupled with appreciable progress in algorithms^{1–5}, has led directly to characterization of significant functional mutations, genes and pathways^{6–18}. Cancer encompasses more than 100 related diseases¹⁹, making it crucial to understand the commonalities and differences among various types and subtypes. TCGA was founded to address these needs, and its large data sets are providing unprecedented opportunities for systematic, integrated analysis.

We performed a systematic analysis of 3,281 tumours from 12 cancer types to investigate underlying mechanisms of cancer initiation and progression. We describe variable mutation frequencies and contexts and their associations with environmental factors and defects in DNA repair. We identify 127 significantly mutated genes (SMGs) from diverse signalling and enzymatic processes. The finding of a *TP53*-driven breast, head and neck, and ovarian cancer cluster with a dearth of other mutations in SMGs suggests common therapeutic strategies might be applied for these tumours. We determined interactions among mutations and correlated mutations in *BAP1*, *FBXW7* and *TP53* with detrimental phenotypes across several cancer types. The subclonal structure and transcription status of underlying somatic mutations reveal the trajectory of tumour progression in patients with cancer.

Standardization of mutation data

Stringent filters (Methods) were applied to ensure high quality mutation calls for 12 cancer types: breast adenocarcinoma (BRCA), lung adenocarcinoma (LUAD), lung squamous cell carcinoma (LUSC), uterine corpus endometrial carcinoma (UCEC), glioblastoma multiforme

(GBM), head and neck squamous cell carcinoma (HNSC), colon and rectal carcinoma (COAD, READ), bladder urothelial carcinoma (BLCA), kidney renal clear cell carcinoma (KIRC), ovarian serous carcinoma (OV) and acute myeloid leukaemia (LAML; conventionally called AML) (Supplementary Table 1). A total of 617,354 somatic mutations, consisting of 398,750 missense, 145,488 silent, 36,443 nonsense, 9,778 splice site, 7,693 non-coding RNA, 523 non-stop/readthrough, 15,141 frameshift insertions/deletions (indels) and 3,538 inframe indels, were included for downstream analyses (Supplementary Table 2).

Distinct mutation frequencies and sequence context

Figure 1a shows that AML has the lowest median mutation frequency and LUSC the highest (0.28 and 8.15 mutations per megabase (Mb), respectively). Besides AML, all types average over 1 mutation per Mb, substantially higher than in paediatric tumours²⁰. Clustering²¹ illustrates that mutation frequencies for KIRC, BRCA, OV and AML are normally distributed within a single cluster, whereas other types have several clusters (for example, 5 and 6 clusters in UCEC and COAD/READ, respectively) (Fig. 1a and Supplementary Table 3a, b). In UCEC, the largest patient cluster has a frequency of approximately 1.5 mutations per Mb, and the cluster with the highest frequency is more than 150 times greater. Multiple clusters suggest that factors other than age contribute to development in these tumours^{14,16}. Indeed, there is a significant correlation between high mutation frequency and DNA repair pathway genes (for example, *PRKDC*, *TP53* and *MSH6*) (Supplementary Table 3c). Notably, *PRKDC* mutations are associated with high frequency in BLCA, COAD/READ, LUAD and UCEC, whereas *TP53* mutations are related with higher frequencies in AML, BLCA, BRCA, HNSC, LUAD, LUSC and UCEC (all $P < 0.05$). Mutations in

¹The Genome Institute, Washington University in St Louis, Missouri 63108, USA. ²Department of Computer Science, Brown University, Providence, Rhode Island 02912, USA. ³Department of Genetics, Washington University in St Louis, Missouri 63108, USA. ⁴Department of Medicine, Washington University in St Louis, Missouri 63108, USA. ⁵Siteman Cancer Center, Washington University in St Louis, Missouri 63108, USA. ⁶Department of Mathematics, Washington University in St Louis, Missouri 63108, USA.

*These authors contributed equally to this work.

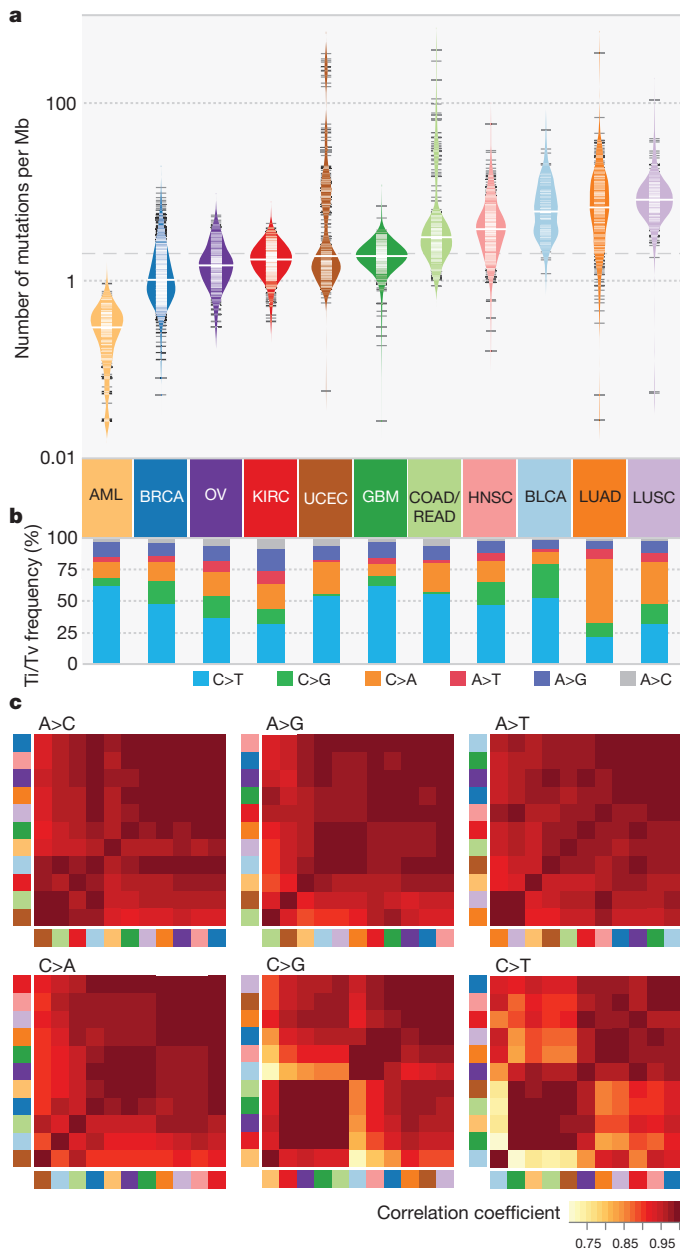


Figure 1 | Mutation frequencies, spectra and contexts across 12 cancer types. **a**, Distribution of mutation frequencies across 12 cancer types. Dashed grey and solid white lines denote average across cancer types and median for each type, respectively. **b**, Mutation spectrum of six transition (Ti) and transversion (Tv) categories for each cancer type. **c**, Hierarchically clustered mutation context (defined by the proportion of A, T, C and G nucleotides within ± 2 bp of variant site) for six mutation categories. Cancer types correspond to colours in **a**. Colour denotes degree of correlation: yellow ($r = 0.75$) and red ($r = 1$).

POLQ and *POLE* associate with high frequencies in multiple cancer types; *POLE* association in UCEC is consistent with previous observations¹⁴.

Comparison of spectra across the 12 types (Fig. 1b and Supplementary Table 3d) reveals that LUSC and LUAD contain increased C>A transversions, a signature of cigarette smoke exposure¹⁰. Sequence context analysis across 12 types revealed the largest difference being in C>T transitions and C>G transversions (Fig. 1c). The frequency of thymine 1-bp (base pair) upstream of C>G transversions is markedly higher in BLCA, BRCA and HNSC than in other cancer types (Extended Data Fig. 1). GBM, AML, COAD/READ and UCEC have similar contexts in that the proportions of guanine 1 base downstream

of C>T transitions are between 59% and 67%, substantially higher than the approximately 40% in other cancer types. Higher frequencies of transition mutations at CpG in gastrointestinal tumours, including colorectal, were previously reported²². We found three additional cancer types (GBM, AML and UCEC) clustered in the C>T mutation at CpG, consistent with previous findings of aberrant DNA methylation in endometrial cancer²³ and glioblastoma²⁴. BLCA has a unique signature for C>T transitions compared to the other types (enriched for TC) (Extended Data Fig. 1).

Significantly mutated genes

Genes under positive selection, either in individual or multiple tumour types, tend to display higher mutation frequencies above background. Our statistical analysis³, guided by expression data and curation (Methods), identified 127 such genes (SMGs; Supplementary Table 4). These SMGs are involved in a wide range of cellular processes, broadly classified into 20 categories (Fig. 2), including transcription factors/regulators, histone modifiers, genome integrity, receptor tyrosine kinase signalling, cell cycle, mitogen-activated protein kinases (MAPK) signalling, phosphatidylinositol-3-OH kinase (PI(3)K) signalling, Wnt/ β -catenin signalling, histones, ubiquitin-mediated proteolysis, and splicing (Fig. 2). The identification of MAPK, PI(3)K and Wnt/ β -catenin signalling pathways is consistent with classical cancer studies. Notably, newer categories (for example, splicing, transcription regulators, metabolism, proteolysis and histones) emerge as exciting guides for the development of new therapeutic targets. Genes categorized as histone modifiers ($Z = 0.57$), PI(3)K signalling ($Z = 1.03$), and genome integrity ($Z = 0.66$) all relate to more than one cancer type, whereas transcription factor/regulator ($Z = 0.40$), TGF- β signalling ($Z = 0.66$), and Wnt/ β -catenin signalling ($Z = 0.55$) genes tend to associate with single types (Methods).

Notably, 3,053 out of 3,281 total samples (93%) across the Pan-Cancer collection had at least one non-synonymous mutation in at least one SMG. The average number of point mutations and small indels in these genes varies across tumour types, with the highest (~ 6 mutations per tumour) in UCEC, LUAD and LUSC, and the lowest (~ 2 mutations per tumour) in AML, BRCA, KIRC and OV. This suggests that the numbers of both cancer-related genes (only 127 identified in this study) and cooperating driver mutations required during oncogenesis are small (most cases only had 2–6) (Fig. 3), although large-scale structural rearrangements were not included in this analysis.

Common mutations

The most frequently mutated gene in the Pan-Cancer cohort is *TP53* (42% of samples). Its mutations predominate in serous ovarian (95%) and serous endometrial carcinomas (89%) (Fig. 2). *TP53* mutations are also associated with basal subtype breast tumours. *PIK3CA* is the second most commonly mutated gene, occurring frequently ($> 10\%$) in most cancer types except OV, KIRC, LUAD and AML. *PIK3CA* mutations frequented UCEC (52%) and BRCA (33.6%), being specifically enriched in luminal subtype tumours. Tumours lacking *PIK3CA* mutations often had mutations in *PIK3R1*, with the highest occurrences in UCEC (31%) and GBM (11%) (Fig. 2).

Many cancer types carried mutations in chromatin re-modelling genes. In particular, histone-lysine *N*-methyltransferase genes (*MLL2* (also known as *KMT2D*), *MLL3* (*KMT2C*) and *MLL4* (*KMT2B*)) cluster in bladder, lung and endometrial cancers, whereas the lysine (K)-specific demethylase *KDM5C* is prevalently mutated in KIRC (7%). Mutations in *ARID1A* are frequent in BLCA, UCEC, LUAD and LUSC, whereas mutations in *ARID5B* predominate in UCEC (10%) (Fig. 2).

KRAS and *NRAS* mutations are typically mutually exclusive, with recurrent activating mutations (*KRAS* (Gly 12), *KRAS* (Gly 13) and *NRAS* (Gln 61)) common in COAD/READ (30%, 5% and 5%, respectively), UCEC (15%, 4% and 2%) and LUAD (24%, 1% and 2%). *EGFR* mutations are frequent in GBM (27%) and LUAD (11%). Recurrent,

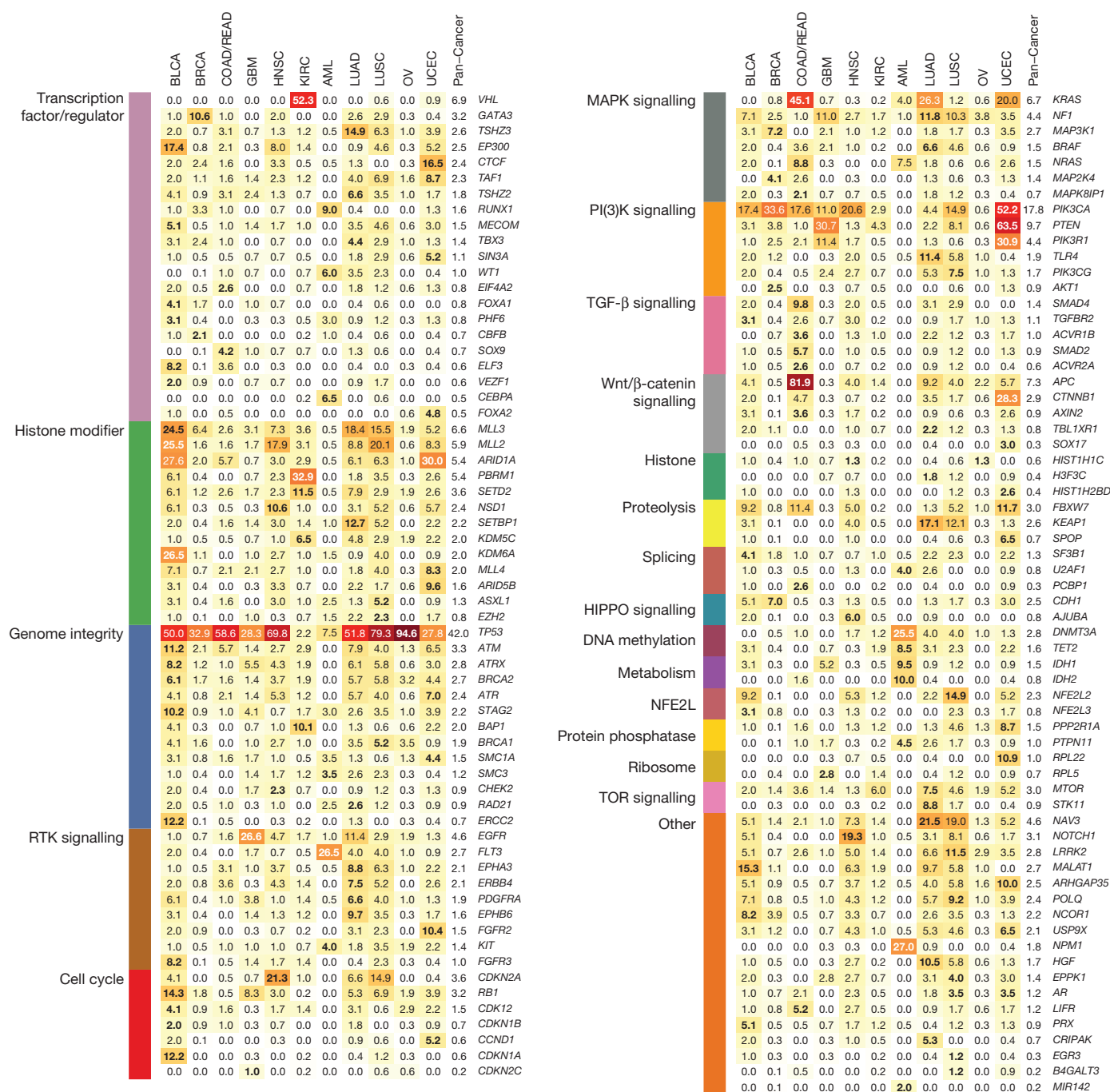


Figure 2 | The 127 SMGs from 20 cellular processes in cancer identified in 12 cancer types. Percentages of samples mutated in individual tumour types

gain-of-function mutations in *IDH1* (Arg 132) and/or *IDH2* (Arg 172) typify GBM and AML (Supplementary Table 2 and Fig. 2). Although KRAS residues Gly 12 and Gly 13 are commonly mutated in LUAD, COAD/READ and UCEC, the proportion of Gly12Cys changes is significantly higher in lung cancer ($P < 3.2 \times 10^{-10}$), resulting from the high C>A transversion rate (Extended Data Fig. 2).

Tumour-type-specific mutations

Signature mutations exclusive to KIRC include those affecting *VHL* (52%) and *PBRM1* (33%) (Fig. 2). Mutations to *BAP1* (10%) and *SETD2* (12%) are also most common in KIRC. Transcription factor *CTCF*, ribosome component *RPL22*, and histone modifiers *ARID1A* and *ARID5B* have the highest frequencies in UCEC. Predominant COAD/READ-specific mutations are those affecting *APC* (82%) and

and Pan-Cancer are shown, with the highest percentage in each gene among 12 cancer types in bold.

Wnt/β-catenin signalling (93% of samples). Several mutations occur exclusively in AML, including recurrent mutations in *NPM1* (27%) and *FLT3* (27%), and rare mutations affecting *MIR142* (Fig. 2). Mutations of methylation and chromatin modifiers are also typical in AML, mostly affecting *DNMT3A* and *TET2*. BRCA-specific mutations include *GATA3* and *MAP3K1*, whereas *KEAP1* mutations predominate in lung cancer (LUAD 17%, LUSC 12%). *EPHA3* (9%), *SETBP1* (13%) and *STK11* (9%) are characteristic in LUAD.

Shared and cancer type-specific mutation signatures

Cluster analysis on mutations in SMGs (Fig. 4 and Extended Data Fig. 3) showed 72% (1,881 of 2,611) of tumours are adjacent to those from the same tissue type. Notably, clustering identified several dominant groups in UCEC, COAD, GBM, AML, KIRC, OV and BRCA. Two major

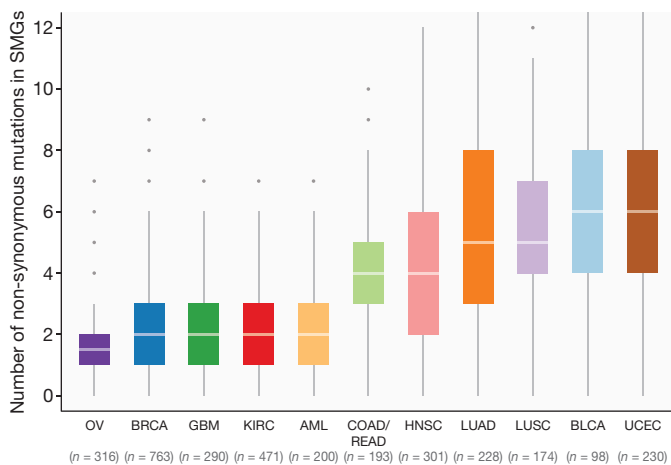


Figure 3 | Distribution of mutations in 127 SMGs across Pan-Cancer cohort. Box plot displays median numbers of non-synonymous mutations, with outliers shown as dots. In total, 3,210 tumours were used for this analysis (hypermutators excluded).

endometrial endometrioid clusters were found, one having mutations in *PIK3CA*, *PTEN* and *ARID1A*, and the other containing mutations in two additional genes (*PIK3R1* and *CTNNB1*). Five major breast cancer clusters were observed, with mutations in *CDH1*, *GATA3*, *MAP3K1*, *PIK3CA* and *TP53* as drivers for respective clusters. The *TP53*-driven cluster is adjacent to an HNSC cluster and an ovarian cancer cluster, all having a dearth of other SMG mutations (Fig. 4). The glioblastoma cluster is characterized by mutations in *EGFR*. Two kidney clear cell cancer clusters were detected; both have *VHL* as the common driver and one has additional mutations in *PBRM1* and/or *BAP1* (refs 25–27). *PBRM1* and *BAP1* mutations are mutually exclusive in KIRC ($P = 0.006$), consistent with previous reports^{26,28}. AML has three major clusters represented by various combinations of *DNMT3A*, *NPM1* and *FLT3* mutations, and one cluster dominated by *RUNX1* mutations. One cluster having *APC* and *KRAS* mutations was almost exclusively detected in COAD/READ. Tumours from BLCA, HNSC, LUAD and LUSC are largely scattered over the Pan-Cancer cohort, indicating extensive heterogeneity in these diseases.

Mutual exclusivity and co-occurrence among SMGs

Pairwise exclusivity and co-occurrence analysis for the 127 SMGs found 14 mutually exclusive (false discovery rate (FDR) < 0.05) and 148 co-occurring (FDR < 0.05) pairs (Supplementary Table 6). *TP53* and *CDH1* are exclusive in BRCA, with mutations enriched in different subtypes¹³, as are *TP53* and *CTNNB1* in UCEC. Cohort analysis identified pairs where at least one gene has mutations strongly associated (corrected $P < 0.05$) to one cancer type, and also identifies *TP53* and *PIK3CA* with significant exclusivity (Extended Data Fig. 4). Pairs with significant co-occurrence include *IDH1* and *ATRX* in GBM²⁹, *TP53* and *CDKN2A* in HNSC, and *TBX3* and *MLL4* in LUAD.

Dendrix³⁰ identified a set of five genes (*TP53*, *PTEN*, *VHL*, *NPM1* and *GATA3*) having strong mutual exclusivity ($P < 0.01$) (Extended Data Fig. 5a and Supplementary Table 7). Not surprisingly, many are associated ($P < 0.05$) with one cancer type (for example, *VHL* mutations in KIRC), demonstrating a strong relationship between exclusivity and tissue of origin. When 600 non-cancer-type-specific genes were added to the analysis (Methods), we identified another set consisting of *TP53*, *PIK3CA*, *PIK3R1*, *SETD2* and *WT1* ($P < 0.01$; Extended Data Fig. 5b and Supplementary Table 7). Dendrix also finds genes with strong mutual exclusivity from each cancer type separately (Extended Data Fig. 5c), allowing calculation of ‘cancer exclusivity’. KIRC has the strongest exclusivity from the other 11 cancer types, followed by AML with clear exclusivity from BRCA and UCEC. Conversely, COAD/READ displayed the greatest co-occurrence with other cancer types (Extended Data Fig. 5d).

Clinical correlation across tumour types

We examined how clinical features (Supplementary Table 8) correlate with somatic events in 127 SMGs within tumour types. Some findings are unsurprising, such as the correlation of *TP53* mutations with generally unfavourable indicators, for example in tumour stage ($P = 0.01$, Fisher’s exact test) and elapsed time to death ($P = 0.006$, Wilcoxon) in HNSC, age ($P = 0.002$, Wilcoxon rank test) and time to death ($P = 0.09$, Wilcoxon) in AML, and vital status in OV ($P = 0.04$, Fisher). In UCEC, mutations in several genes are correlated with the endometrioid rather than serous subtype: *PTEN*, *CTNNB1*, *PIK3R1*, *KRAS*, *ARID1A*, *CTCF*, *RPL22* and *ARID5B* (all $P < 0.03$) (Supplementary Table 9).

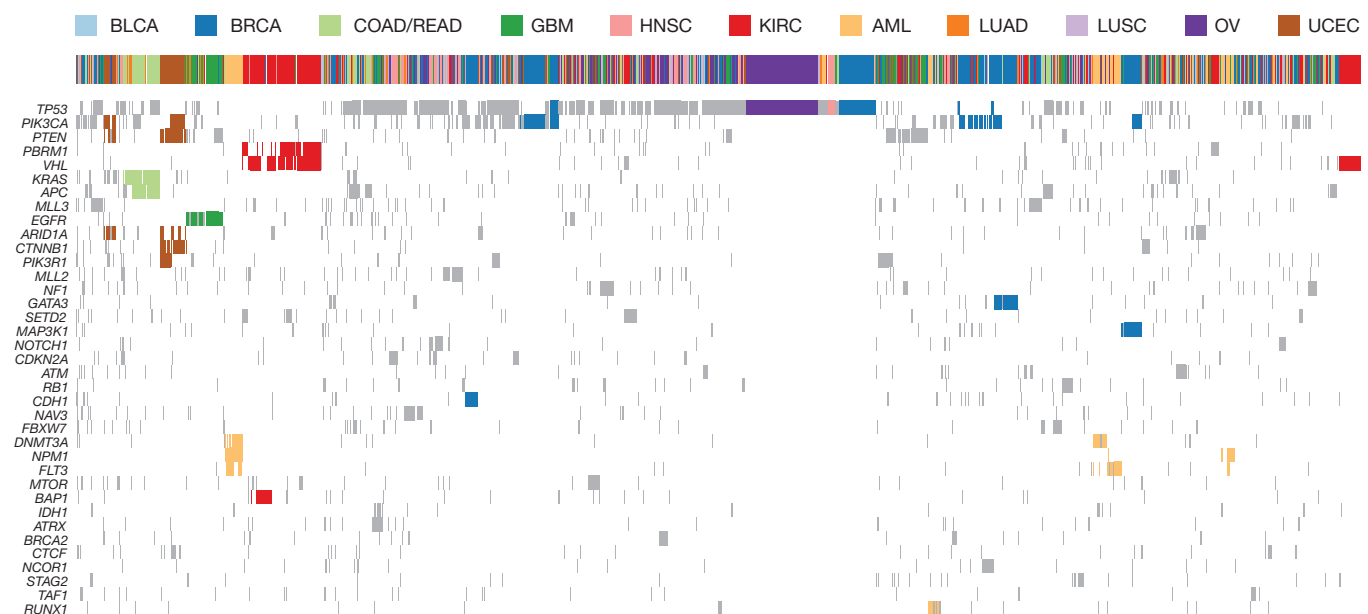


Figure 4 | Unsupervised clustering based on mutation status of SMGs. Tumours having no mutation or more than 500 mutations were excluded. A mutation status matrix was constructed for 2,611 tumours. Major clusters of

mutations detected in UCEC, COAD, GBM, AML, KIRC, OV and BRCA were highlighted. Complete gene list shown in Extended Data Fig. 3.

We examined which genes correlate with survival using the Cox proportional hazards model, first analysing individual cancer types using age and gender as covariates; an average of 2 genes (range: 0–4) with mutation frequency $\geq 2\%$ were significant ($P \leq 0.05$) in each type (Supplementary Table 10a and Extended Data Fig. 6). *KDM6A* and *ARID1A* mutations correlate with better survival in BLCA ($P = 0.03$, hazard ratio (HR) = 0.36, 95% confidence interval (CI): 0.14–0.92) and UCEC ($P = 0.03$, HR = 0.11, 95% CI: 0.01–0.84), respectively, but mutations in *SETBP1*, recently identified with worse prognosis in atypical chronic myeloid leukaemia (aCML)³¹, have a significant detrimental effect in HNSC ($P = 0.006$, HR = 3.21, 95% CI: 1.39–7.44). *BAP1* strongly correlates with poor survival ($P = 0.00079$, HR = 2.17, 95% CI: 1.38–3.41) in KIRC. Conversely, *BRCA2* mutations ($P = 0.02$, HR = 0.31, 95% CI: 0.12–0.85) associate with better survival in ovarian cancer, consistent with previous reports^{32,33}; *BRCA1* mutations showed positive correlation with better survival, but did not reach significance here.

We extended our survival analysis across cancer types, restricting our attention to the subset of 97 SMGs whose mutations appeared in $\geq 2\%$ of patients having survival data in ≥ 2 tumour types. Taking type, age and gender as covariates, we found 7 significant genes: *BAP1*, *DNMT3A*, *HGF*, *KDM5C*, *FBXW7*, *BRCA2* and *TP53* (Extended Data Table 1). In particular, *BAP1* was highly significant ($P = 0.00013$,

HR = 2.20, 95% CI: 1.47–3.29, more than 53 mutated tumours out of 888 total), with mutations associating with detrimental outcome in four tumour types and notable associations in KIRC ($P = 0.00079$), consistent with a recent report²⁸, and in UCEC ($P = 0.066$). Mutations in several other genes are detrimental, including *DNMT3A* (HR = 1.59), previously identified with poor prognosis in AML³⁴, and *KDM5C* (HR = 1.63), *FBXW7* (HR = 1.57) and *TP53* (HR = 1.19). *TP53* has significant associations with poor outcome in KIRC ($P = 0.012$), AML ($P = 0.0007$) and HNSC ($P = 0.00007$). Conversely, *BRCA2* ($P = 0.05$, HR = 0.62, 95% CI: 0.38 to 0.99) correlates with survival benefit in six types, including OV and UCEC (Supplementary Table 10a, b). *IDH1* mutations are associated with improved prognosis across the Pan-Cancer set (HR = 0.67, $P = 0.16$) and also in GBM (HR = 0.42, $P = 0.09$) (Supplementary Table 10a, b), consistent with previous work³⁵.

Driver mutations and tumour clonal architecture

To understand the temporal order of somatic events, we analysed the variant allele fraction (VAF) distribution of mutations in SMGs across AML, BRCA and UCEC (Fig. 5a and Supplementary Table 11a) and other tumour types (Extended Data Fig. 7). To minimize the effect of copy number alterations, we focused on mutations in copy neutral segments. Mutations in *TP53* have higher VAFs on average in all three cancer types, suggesting early appearance during tumorigenesis, although

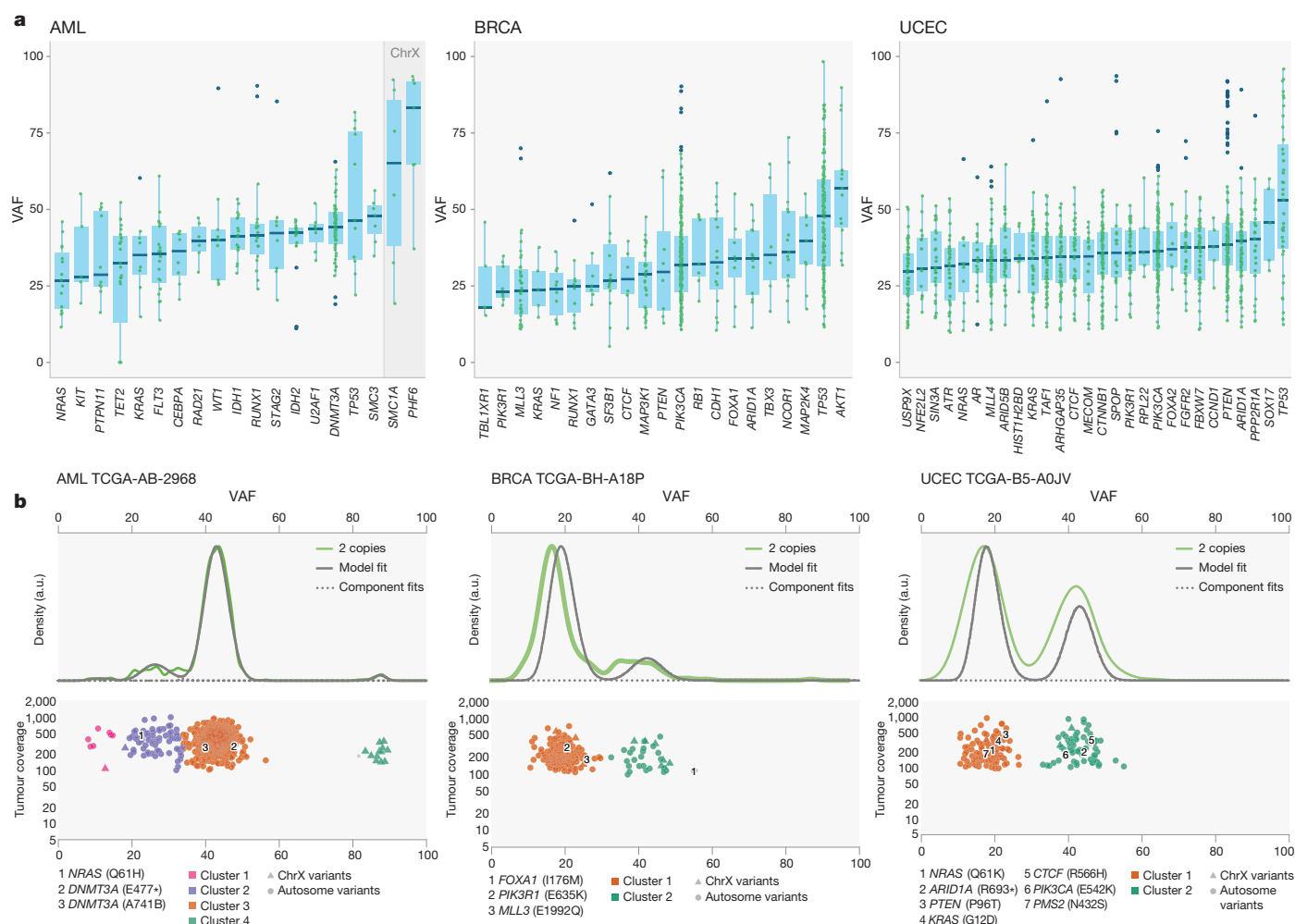


Figure 5 | Driver initiation and progression mutations and tumour clonal architecture. **a**, Variant allele fraction (VAF) distribution of mutations in SMGs across tumours from AML, BRCA and UCEC for mutations ($\geq 20\times$ coverage) in copy neutral segments. SMGs having ≥ 5 mutation data points were included. ChrX, chromosome X. **b**, In AML sample TCGA-AB-2968 (WGS), two *DNMT3A* mutations are in the founding clone, and one *NRAS*

mutation is in the subclone. In BRCA tumour TCGA-BH-A18P (exome), one *FOXA1* mutation is in the founding clone, and *PIK3R1* and *MLL3* mutations are in the subclone. In UCEC tumour TCGA-B5-A0JV (exome), *PIK3CA*, *ARID1A* and *CTCF* mutations are in the founding clone, and *NRAS*, *PTEN* and *KRAS* mutations are in the secondary clone. Asterisk denotes stop codon.

it is possible that a later mutation contributing to tumour cell expansion might have a high VAF. It is worth noting that copy neutral loss of heterozygosity is commonly found in classical tumour suppressors such as *TP53*, *BRCA1*, *BRCA2* and *PTEN*, leading to increased VAFs in these genes. In AML, *DNMT3A* (permutation test $P = 0$), *RUNX1* ($P = 0.0003$) and *SMC3* ($P = 0.05$) have significantly higher VAFs than average among SMGs (Fig. 5a and Supplementary Table 11b). In breast cancer, *AKT1*, *CBFB*, *MAP2K4*, *ARID1A*, *FOXA1* and *PIK3CA* have relatively high average VAFs. For endometrial cancer, multiple SMGs (for example, *PIK3CA*, *PIK3R1*, *PTEN*, *FOXA2* and *ARID1A*) have similar median VAFs. Conversely, *KRAS* and/or *NRAS* mutations tend to have lower VAFs in all three tumour types (Fig. 5a), suggesting *NRAS* (for example, $P = 0$ in AML) and *KRAS* (for example, $P = 0.02$ in BRCA) have a progression role in a subset of AML, BRCA and UCEC tumours. For all three cancer types, we clearly observed a shift towards higher expression VAFs in SMGs versus non-SMGs, most apparent in BRCA and UCEC (Extended Data Fig. 8a and Methods).

Previous analysis using whole-genome sequencing (WGS) detected subclones in approximately 50% of AML cases^{15,36,37}; however, analysis is difficult using AML exome owing to its relatively few coding mutations. Using 50 AML WGS cases, sciClone (<http://github.com/genome/sciclone>) detected *DNMT3A* mutations in the founding clone for 100% (8 out of 8) of cases and *NRAS* mutations in the subclone for 75% (3 out of 4) of cases (Extended Data Fig. 8b). Among 304 and 160 of BRCA and UCEC tumours, respectively, with enough coding mutations for clustering, 35% BRCA and 44% UCEC tumours contained subclones. Our analysis provides the lower bound for tumour heterogeneity, because only coding mutations were used for clustering. In BRCA, 95% (62 out of 65) of cases contained *PIK3CA* mutations in the founding clone, whereas 33% (3 out of 9) of cases had *MLL3* mutations in the subclone. Similar patterns were found in UCEC tumours, with 96% (65 out of 68) and 95% (62 out of 65) of tumours containing *PIK3CA* and *PTEN* mutations, respectively, in the founding clone, and 9% (2 out of 22) of *KRAS* and 14% (1 out of 7) of *NRAS* mutations in the subclone (Extended Data Fig. 8b and Supplementary Table 12).

Discussion

We have performed systematic analysis of the TCGA Pan-Cancer mutation data set, finding key insights for cancer genomes, as summarized in Extended Data Fig. 9. The data set contains 127 diverse SMGs, demonstrating that many cellular and enzymatic processes are involved in tumorigenesis. Notably, 66 of them are also on the 'mut-driver genes' list generated by a ratiometric method using COSMIC mutations³⁸. Although a common set of driver mutations exists in each cancer type, the combination of drivers within a cancer type and their distribution within the founding clone and subclones varies for individual patients. This suggests that knowing the clonal architecture of each patient's tumour will be crucial for optimizing their treatment.

Given the rate at which TCGA and International Cancer Genome Consortium projects are generating genomic data, there are reasonable chances of identifying the 'core' cancer genes and pathways and tumour-type-specific genes and pathways in the near term. These results will be immediately circulated within the research community to assess their potential for candidate targets for diverse tumour types or for specific tumour type. Ultimately, these data and their associations with different clinical features and subtypes should contribute to the formulation of a reference candidate gene panel for all tumour types that could be helpful for prognosis at various clinical time points.

METHODS SUMMARY

Mutation data were standardized for 12 cancer types and tracked on Synapse with documentation (<http://dx.doi.org/10.7303/syn1729383.2>). All mutation annotation format files were downloaded from the TCGA data coordinating centre, each being reprocessed to eliminate known, recurrent false positives and germline single nucleotide polymorphisms (SNP) present in the dbSNP database. All variant coordinates were converted to GRCh37 and re-annotated using the Gencode

human transcript annotation imported from Ensembl release 69. Mutation context (−2 to +2 bp) was calculated for each somatic variant in each mutation category, and hierarchical clustering was then performed using the pairwise mutation context correlation across all cancer types. The mutational significance in cancer (MuSiC)³ package was used to identify significant genes for both individual tumour types and the Pan-Cancer collective. An R function 'hclust' was used for complete-linkage hierarchical clustering across mutations and samples, and Dendrix³⁰ was used to identify sets of approximately mutual exclusive mutations. Cross-cancer survival analysis was based on the Cox proportional hazards model, as implemented in the R package 'survival' (<http://cran.r-project.org/web/packages/survival/>), and the sciClone algorithm (<http://github.com/genome/sciclone>) generated mutation clusters using point mutations from copy number neutral segments. A complete description of the materials and methods used to generate this data set and its results is provided in the Methods.

Online Content Any additional Methods, Extended Data display items and Source Data are available in the online version of the paper; references unique to these sections appear only in the online paper.

Received 21 June; accepted 13 September 2013.

- Larson, D. E. *et al.* SomaticSniper: identification of somatic point mutations in whole genome sequencing data. *Bioinformatics* **28**, 311–317 (2012).
- Koboldt, D. C. *et al.* VarScan 2: somatic mutation and copy number alteration discovery in cancer by exome sequencing. *Genome Res.* **22**, 568–576 (2012).
- Dees, N. D. *et al.* MuSiC: Identifying mutational significance in cancer genomes. *Genome Res.* **22**, 1589–1598 (2012).
- Roth, A. *et al.* JointSNVMix: a probabilistic model for accurate detection of somatic mutations in normal/tumour paired next-generation sequencing data. *Bioinformatics* **28**, 907–913 (2012).
- Cibulskis, K. *et al.* Sensitive detection of somatic point mutations in impure and heterogeneous cancer samples. *Nature Biotechnol.* **31**, 213–219 (2013).
- Jones, S. *et al.* Core signaling pathways in human pancreatic cancers revealed by global genomic analyses. *Science* **321**, 1801–1806 (2008).
- Parsons, D. W. *et al.* An integrated genomic analysis of human glioblastoma multiforme. *Science* **321**, 1807–1812 (2008).
- Sjöblom, T. *et al.* The consensus coding sequences of human breast and colorectal cancers. *Science* **314**, 268–274 (2006).
- The Cancer Genome Atlas Research Network. Comprehensive genomic characterization defines human glioblastoma genes and core pathways. *Nature* **455**, 1061–1068 (2008).
- Ding, L. *et al.* Somatic mutations affect key pathways in lung adenocarcinoma. *Nature* **455**, 1069–1075 (2008).
- Wood, L. D. *et al.* The genomic landscapes of human breast and colorectal cancers. *Science* **318**, 1108–1113 (2007).
- The Cancer Genome Atlas Research Network. Integrated genomic analyses of ovarian carcinoma. *Nature* **474**, 609–615 (2011).
- The Cancer Genome Atlas Network. Comprehensive molecular portraits of human breast tumours. *Nature* **490**, 61–70 (2012).
- Cancer Genome Atlas Research Network. Integrated genomic characterization of endometrial carcinoma. *Nature* **497**, 67–73 (2013).
- The Cancer Genome Atlas Research Network. Genomic and epigenomic landscapes of adult *de novo* acute myeloid leukemia. *N. Engl. J. Med.* **368**, 2059–2074 (2013).
- The Cancer Genome Atlas Network. Comprehensive molecular characterization of human colon and rectal cancer. *Nature* **487**, 330–337 (2012).
- Ellis, M. J. *et al.* Whole-genome analysis informs breast cancer response to aromatase inhibition. *Nature* **486**, 353–360 (2012).
- The Cancer Genome Atlas Research Network. Comprehensive molecular characterization of clear cell renal cell carcinoma. *Nature* **499**, 43–49 (2013).
- Hanahan, D. & Weinberg, R. A. The hallmarks of cancer. *Cell* **100**, 57–70 (2000).
- Downing, J. R. *et al.* The Pediatric Cancer Genome Project. *Nature Genet.* **44**, 619–622 (2012).
- Ma, Z. & Leijon, A. Bayesian estimation of beta mixture models with variational inference. *IEEE Trans. Pattern Anal. Mach. Intell.* **33**, 2160–2173 (2011).
- Lawrence, M. S. *et al.* Mutational heterogeneity in cancer and the search for new cancer-associated genes. *Nature* **499**, 214–218 (2013).
- Tao, M. H. & Freudenheim, J. L. DNA methylation in endometrial cancer. *Epigenetics* **5**, 491–498 (2010).
- Etcheberry, A. *et al.* DNA methylation in glioblastoma: impact on gene expression and clinical outcome. *BMC Genomics* **11**, 701 (2010).
- Varela, I. *et al.* Exome sequencing identifies frequent mutation of the SWI/SNF complex gene *PBRM1* in renal carcinoma. *Nature* **469**, 539–542 (2011).
- Peña-Llopis, S. *et al.* BAP1 loss defines a new class of renal cell carcinoma. *Nature Genet.* **44**, 751–759 (2012).
- Clapier, C. R. & Cairns, B. R. The biology of chromatin remodeling complexes. *Annu. Rev. Biochem.* **78**, 273–304 (2009).
- Kapur, P. *et al.* Effects on survival of *BAP1* and *PBRM1* mutations in sporadic clear-cell renal-cell carcinoma: a retrospective analysis with independent validation. *Lancet Oncol.* **14**, 159–167 (2013).
- Jiao, Y. *et al.* Frequent ATRX, CIC, FUBP1 and IDH1 mutations refine the classification of malignant gliomas. *Oncotarget* **3**, 709–722 (2012).
- Vandin, F., Upfal, E. & Raphael, B. J. *De novo* discovery of mutated driver pathways in cancer. *Genome Res.* **22**, 375–385 (2012).

31. Piazza, R. *et al.* Recurrent *SETBP1* mutations in atypical chronic myeloid leukemia. *Nature Genet.* **45**, 18–24 (2013).
32. Yang, D. *et al.* Association of *BRCA1* and *BRCA2* mutations with survival, chemotherapy sensitivity, and gene mutator phenotype in patients with ovarian cancer. *J. Am. Med. Assoc.* **306**, 1557–1565 (2011).
33. Bolton, K. L. *et al.* Association between *BRCA1* and *BRCA2* mutations and survival in women with invasive epithelial ovarian cancer. *J. Am. Med. Assoc.* **307**, 382–390 (2012).
34. Ley, T. J. *et al.* *DNMT3A* mutations in acute myeloid leukemia. *N. Engl. J. Med.* **363**, 2424–2433 (2010).
35. Myung, J. K. *et al.* IDH1 mutation of gliomas with long-term survival analysis. *Oncol. Rep.* **28**, 1639–1644 (2012).
36. Ding, L. *et al.* Clonal evolution in relapsed acute myeloid leukaemia revealed by whole-genome sequencing. *Nature* **481**, 506–510 (2012).
37. Welch, J. S. *et al.* The origin and evolution of mutations in acute myeloid leukemia. *Cell* **150**, 264–278 (2012).
38. Vogelstein, B. *et al.* Cancer genome landscapes. *Science* **339**, 1546–1558 (2013).

Supplementary Information is available in the online version of the paper.

Acknowledgements This work was supported by the National Cancer Institute grants R01CA180006 to L.D. and P01CA101937 to T.J.L., and National Human Genome

Research Institute grants R01HG005690 to B.J.R., U54HG003079 to R.K.W., and U01HG006517 to L.D., and National Science Foundation grant IIS-1016648 to B.J.R. We gratefully acknowledge the contributions from TCGA Research Network and its TCGA Pan-Cancer Analysis Working Group. We also thank M. Bharadwaj for technical assistance.

Author Contributions L.D. and R.K.W. supervised the research. L.D., C.K., M.D.M., F.V., K.Y., B.N., C.L., M.X., M.D.M.L., M.A.W., J.F.M., M.J.W., C.A.M., J.S.W. and B.J.R. analysed the data. M.C.W. and Q.Z. performed statistical analysis. M.D.M., C.K., F.V., C.L., M.X., K.Y., B.N., Q.Z., M.C.W., J.F.M., M.D.M., M.A.W. and L.D. prepared the figures and tables. L.D., T.J.L., C.K. and B.J.R. conceived and designed the experiments. L.D., M.D.M., C.K., F.V., C.L., B.J.R., K.Y. and M.C.W. wrote the manuscript.

Author Information Reprints and permissions information is available at www.nature.com/reprints. The authors declare no competing financial interests. Readers are welcome to comment on the online version of the paper. Correspondence and requests for materials should be addressed to L.D. (lding@genome.wustl.edu).



This work is licensed under a Creative Commons Attribution-NonCommercial-Share Alike 3.0 Unported licence. To view a copy of this licence, visit <http://creativecommons.org/licenses/by-nc-sa/3.0>

METHODS

Standardization and tracking of mutation data from 12 cancer types. The three TCGA genome sequencing centres (GSCs; Baylor Human Genome Center, Broad Institute, and The Genome Institute at Washington University) collectively performed exome sequencing on thousands of tumour samples and matched normal tissues, the latter being used as controls to distinguish somatic mutations from inherited variants. These controls were most often peripheral blood, but skin tissue was used in 199 AML samples as well as 1 buccal source, and adjacent tumour-free tissue was used for 927 cases, with 120 cases having normal DNA from blood and adjacent solid normal tissue.

Exome capture targets may differ among GSCs, as well as across cohorts at the same GSC because the capture technologies and sequencing platforms continue to evolve over time. Therefore, collecting sequencing coverage data for each sample is crucial for most variant significance analyses. Somatic variant calling methods also differ among GSCs for similar reasons, in addition to the fact that filtering strategies may be tuned to emphasize either sensitivity or specificity of calls. Finally, the TCGA disease analysis working groups (AWGs) may optionally perform manual curation of the variant calls, in which false positives are removed and true negatives are recovered. AWGs and GSCs also collaboratively select putative variants for validation or for recovering variants from regions that reported low coverage in the first pass of exome sequencing. These steps mean that somatic variant sensitivity and specificity are mostly comparable across samples of a given TCGA tumour type, but that they differ considerably among tumour types, creating significant challenges for Pan-Cancer analyses.

Complete standardization of sensitivity could not be attained, as it would have required a uniform variant calling and filtering workflow across all tumour-normal pairs. Instead, publicly available somatic variant calls in mutation annotation format (MAF) files from the TCGA were used to both ensure reproducibility and take advantage of extensive manual curation performed over the years by experts in the disease or in genomic sequence analysis and annotation. Specifically, all MAF files were downloaded from the TCGA data coordinating centre, each being reprocessed to eliminate known, recurrent false positives and germline single nucleotide polymorphisms (SNP) present in the dbSNP database. All variant coordinates were transferred to GRCh37 and re-annotated using the Gencode human transcript annotation imported from Ensembl release 69. Per sample, per gene coverage values were obtained using WIG-formatted reference coverage files associated with the BAMs or by processing the original BAM files directly. Details were tracked on Synapse with provenance and documentation (<https://www.synapse.org/#!Synapse:syn1729383>).

Mutation frequency and spectrum analysis. We calculate mutation frequency by dividing the number of validated somatic variants by the number of base pairs that have sufficient coverage. Minimum coverage is six and eight reads for normal and tumour BAMs, respectively. For mutation spectrum we classify the mutation by six types (transitions/transversions). Mutation context is generated by counting the frequency of A, T, C and G nucleotides that are 2 bp 5' and 3' to each variant within the six mutation categories. For the clustering, we pooled all samples (excluding hypermutators having >500 mutations) for each cancer type. We calculated the mutation context (−2 to +2 bp) for each somatic variant in each mutation category. A hierarchical clustering was then done using the pairwise correlation of the mutation context across all cancer types. We used correlation modules in the mutational significance in cancer (MuSiC) package to identify genes with mutations that are positively correlated with the number of mutations in the tumour sample. This analysis was performed for all 12 cancer types. Only genes mutated in at least 5% of tumours were included in the analysis. A list of genes known to be involved in DNA mismatch repair is included Supplementary Table 13.

SMG analysis. We used the SMG test in the MuSiC suite³ to identify significant genes for each tumour type and also for Pan-Cancer tumours. This test assigns mutations to seven categories: AT transition, AT transversion, CG transition, CG transversion, CpG transition, CpG transversion and indel, and then uses statistical methods based on convolution, the hypergeometric distribution (Fisher's test), and likelihood to combine the category-specific binomials to obtain overall *P* values. All *P* values were combined using the methods described previously³. SMGs are listed in Fig. 2. Finally, for the analysis of SMGs, genes not typically expressed in individual tumour type or/and Pan-Cancer tumour samples were filtered if they had an average read per kilobase per million (RPKM) ≤ 0.5. For the RNA sequencing (RNA-seq)-based gene expression analysis, we used the 'Pancan12 per-sample log₂-RSEM' matrix from Synapse (<https://www.synapse.org/#!Synapse:syn1734155>). A gene qualified as 'expressed' if it had at least three reads in at least 70% of samples. Annotation based curation was also performed.

Tumour specificity analysis. To make quantitative inferences as to the number of cancer types with which an individual gene associates, we calculated the empirical distributions of frequency for each cancer (tissue) type and declared

an association (setting indicator variable to 1) if a given gene frequency within a type exceeded a threshold. Otherwise we set the indicator to 0, indicating no association. We took the threshold as a standardized Z-score of 0.2 above the mean based on the estimated level of noise in the 127 significant genes as quantified by the coefficient of variation for each cancer type. We then computed an overall distribution on the indicator variable. The mean for each functional category having at least five genes was then converted to a Z-score based on the descriptive statistics (mean and standard deviation) of the indicator distribution.

Unsupervised clustering. Somatic point mutations and small indels of 127 SMGs across the 3,281 tumours were collected. To reduce noise from passenger mutations, tumours having more than 500 somatic mutations (considered hypermutators) were excluded from this analysis. Tumours with zero detected somatic mutations were also excluded, resulting in mutations from 2,611 tumours for downstream clustering analysis. A mutation status matrix (sample × gene) was constructed and passed to the R function 'hclust' for complete-linkage hierarchical clustering and a respective heatmap with a dendrogram was plotted. Tumours from BLCA, HNSC, LUAD and LUSC are largely scattered over the Pan-Cancer cohort, indicating extensive heterogeneity in these diseases. For instance, eight LUAD and two LUSC tumours are in the solid colorectal cluster, largely owing to their *KRAS* mutations (Fig. 4). Three UCEC, two GBM, one OV and one HNSC samples are in the *BRCA* cluster courtesy of *TP53* and *PIK3CA* mutations. The resolution of this analysis could be improved by incorporating copy number data, structural variants, gene expression, proteomics and methylation.

Dendrix analysis of mutation relationships. We used Fisher's exact test to identify pairs of SMGs with significant (FDR = 0.05 by Benjamini–Hochberg) exclusivity and co-occurrence. We identified significant pairs by analysing all samples together and by analysing samples in each cancer type separately. A large number of pairs (142) with significant co-occurring mutations is identified only considering the Pan-Cancer data set (Extended Data Fig. 4); these pairs include several candidate genes (for example, *NAV3*, *RPL22* and *TSHZ3*) whose function in carcinogenesis is not well characterized.

We applied our *de novo* driver exclusivity (Dendrix) algorithm to identify sets of approximately mutually exclusive mutations on all samples together. Dendrix finds a set *M* of genes of maximum weight *W*(*M*), in which *W*(*M*) is the difference between the number of samples with a mutation in *M* and the number of samples with more than one mutation in *M*. The maximum scoring set of genes of a given size is identified using a Markov chain Monte Carlo approach. We first applied Dendrix considering only the 127 SMGs, and then extended our analysis to consider the 1,000 genes of smallest median *q* value among the three *q* values (convolution, Fisher's combined test, and likelihood ratio) reported by MuSiC. From these 1,000 genes, we discarded the ones with mutations strongly associated (Bonferroni corrected *P* ≤ 0.05 by Fisher's exact test) with a cancer type, and this resulted in 600 genes for Dendrix analysis.

We also applied Dendrix to identify sets of exclusive mutations among the SMGs in each cancer type separately. The exclusivity and co-occurrence between different sets of mutations was assessed using Fisher's exact test, and the mutation status ('mutated' if at least one gene in the set is mutated, 'not mutated' otherwise) of the two sets as categories for the 2 × 2 contingency table.

Cross-cancer-type survival analysis using Cox proportional hazards model.

We used the clinical correlation module of MuSiC to examine how clinical features correlate with somatic events within individual tumour types. Fisher's exact test was used for analysing categorical features, and the Wilcoxon rank sum test was used for quantitative variables. We used the standard Cox proportional hazards model for individual cancer types as well as cross-cancer survival analysis, as implemented in the R package 'survival' (<http://cran.r-project.org/web/packages/survival/>). Here, the effects of all mutations are taken to be constant over time, that is, they are 'stationary coefficients'. Hazard ratios exceeding 1 indicate an overall detrimental effect across cancers, whereas those below 1 associate with better outcome. Calculations included only those genes having mutation frequencies of at least 2% (for both individual cancer types and Pan-Cancer) in at least two cancer types (for Pan-Cancer). In practice, this means that although some genes encompass many types, for example, *TP53* is calculated over 12 types, most are based on only a few (Extended Data Table 1 and Supplementary Table 10a, b). There is no basis for calculation of genes having 2% mutation in only a single type, although single-type analysis was computed similarly for all genes having at least 2% in all cancer types. Analyses were performed using age and gender as covariates.

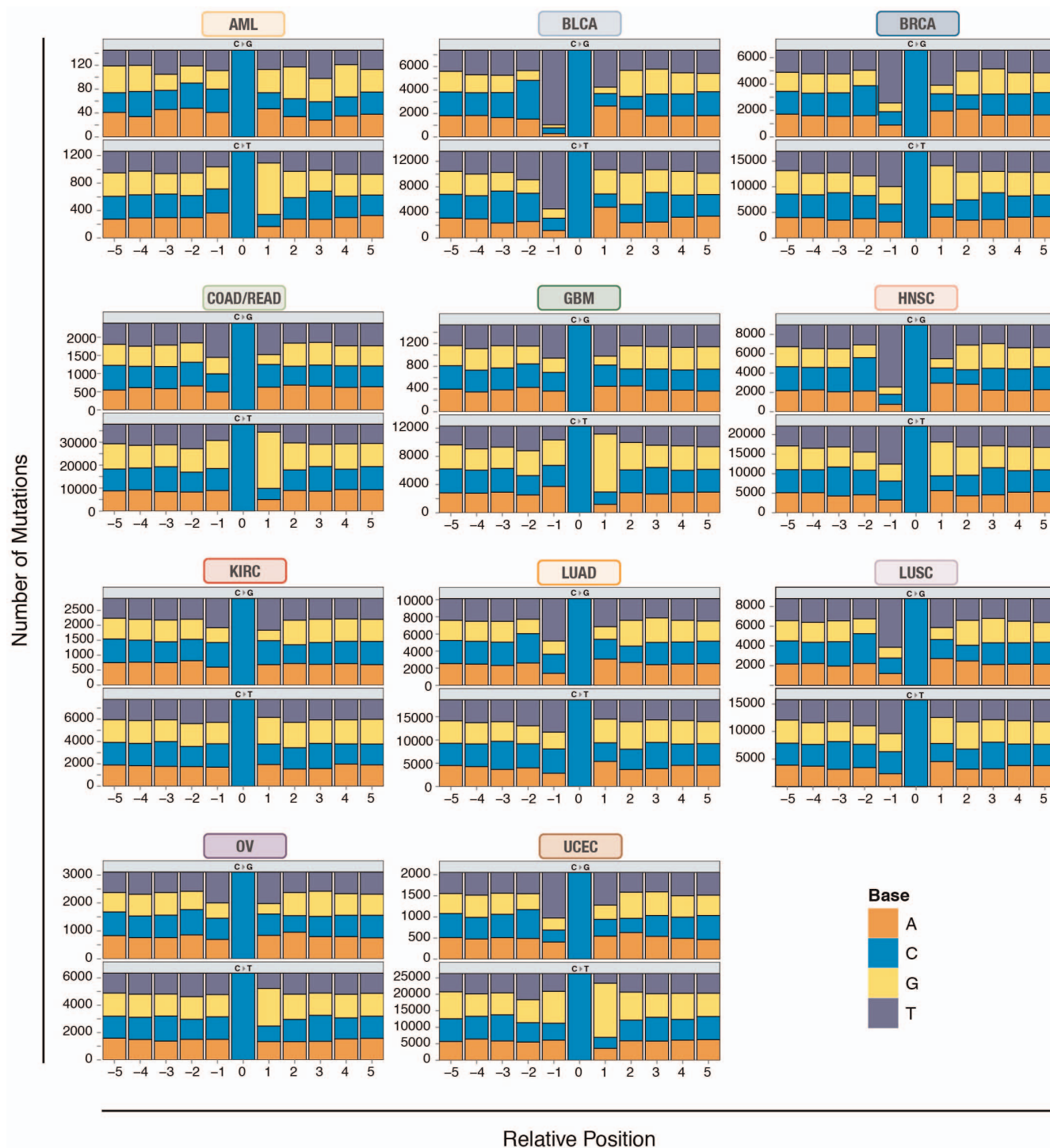
We also performed Pan-Cancer survival analysis by stratifying on cancer type in the Cox regression model and found the results are largely consistent with taking cancer type as a covariate (14 out of top 15 significant genes are overlapping from these two analyses) (Supplementary Table 10b). Furthermore, stage was used as a covariate for individual cancer type survival analysis (AML and COAD/READ not included). Again, the results are fairly consistent with taking

only age and gender as covariates (for example, 12 out of top 15 significant genes are overlapping from these two analyses for UCEC) (Supplementary Table 14).

Clonality and mutation VAF analysis. We computed the VAFs of somatic mutations in SMGs using TCGA targeted validation data or/and exome and RNA sequencing data for AML, BRCA and UCEC. An internally developed tool called Bam2ReadCount (unpublished), which counts the number of reads supporting the reference and variant alleles, was used for computing VAFs for point mutations and short indels in copy number neutral segments. Only mutation sites having $\geq 20\times$ coverage and SMGs having at least five data points were included in downstream analyses. Permutation and *t*-tests were used to identify genes with significantly higher or lower VAFs than the average (Supplementary Table 11a, b). These indicate chronological order-of-appearance of somatic events during tumorigenesis. VAFs for mutations from genes that are not identified as significantly mutated were similarly computed for generating control VAF density distribution. We also computed VAF distribution for the other nine cancer types, and plots are included in Extended Data Fig. 7. In total, 91 BLCA, 772 BRCA, 144 COAD/READ, 62 GBM, 144 HNSC, 195 KIRC, 197 LAML, 216 LUAD, 146 LUSC, 278 OV and 248 UCEC tumours were used for SMG VAF distribution analysis.

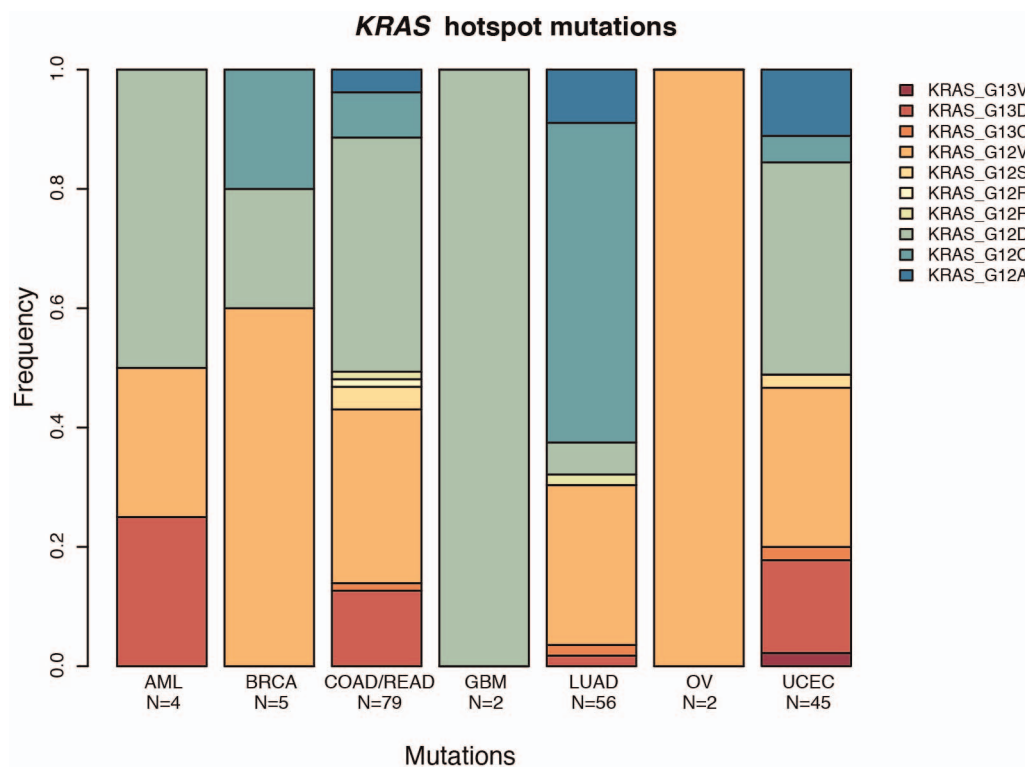
We further investigated the expression level of somatic mutations using available RNA sequencing data for AML, BRCA and UCEC, and then compared observed mutant allele expressions with expected levels based on DNA VAFs (assuming no allelic expression bias). A total of 671 BRCA, 170 AML and 190 UCEC tumours with RNA-seq BAMs were used for this analysis. Notably, we observed at least a twofold increase of variant allele expressions in 3.9%, 12.9% and 5.9% of mutations from SMGs in AML (for example, *TP53*, *STAG2* and *SMC3*), BRCA (for example, *CDH1*, *TP53*, *GATA3* and *MLL3*), and UCEC (for example, *ARID1A* and *FGFR2*), respectively (Supplementary Table 11a). We further compared expression level distributions across mutations from SMGs and non-SMGs. For all three cancer types, we clearly observed a shift towards higher expression VAFs in SMGs versus non-SMGs, which was most apparent in BRCA and UCEC (Extended Data Fig. 8a). This result suggests potential selection of these mutations during tumorigenesis.

SciClone (<http://github.com/genome/sciclon>) was used for generating mutation clusters using point mutations from copy number neutral segments. Only variants with greater than or equal to $100\times$ coverage were used for clustering and plotting. Validation data were used for AML, and exome sequencing data were used for BRCA and UCEC. SMGs were highlighted automatically by sciClone to show their clonal association (Extended Data Fig. 8b).



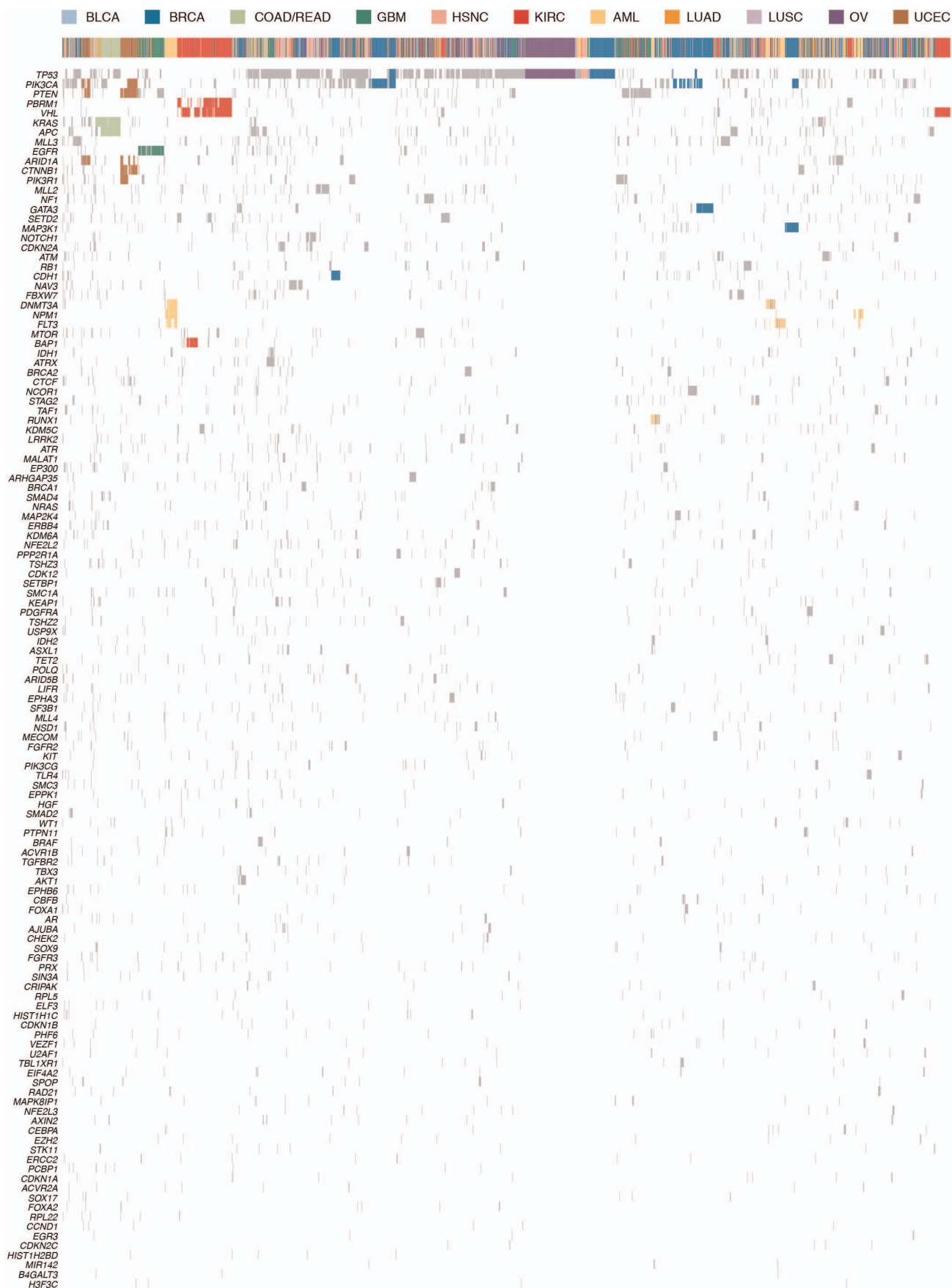
Extended Data Figure 1 | Mutation context across 12 cancer types. Mutation context showing proportions of A, T, C and G nucleotides within ± 5 bp for all validated mutations of type C>G/G>C and C>T/G>A

across all 12 cancer types. The y axis denotes the total number of mutations in each category.



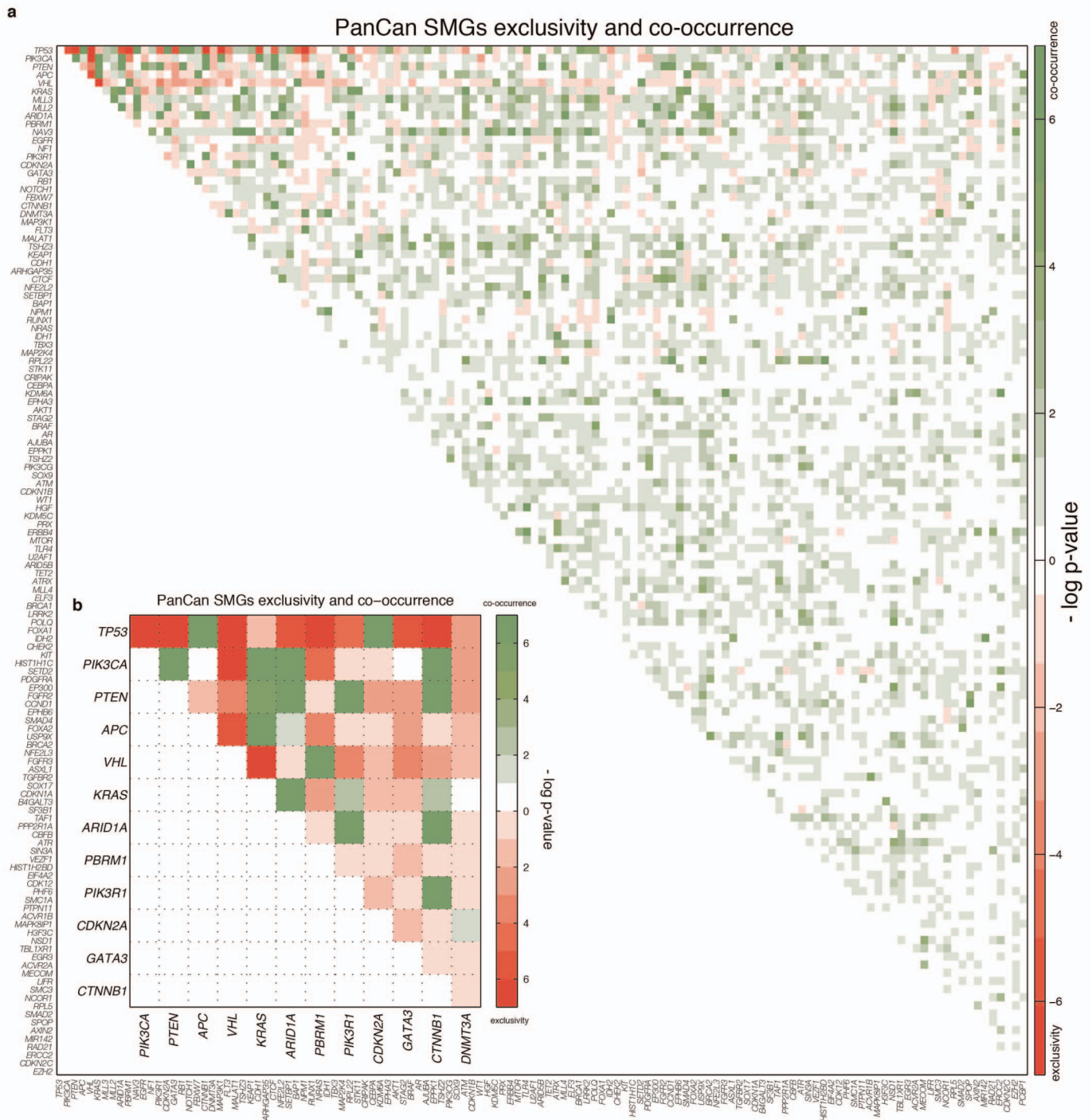
Extended Data Figure 2 | The distribution of *KRAS* hotspot mutations across tumour types. Distribution of changes caused by mutations of the *KRAS* hotspot at amino acids 12 and 13. Lung adenocarcinoma has a

significantly higher proportion of Gly12Cys mutations than other cancers ($P < 3.2 \times 10^{-10}$), caused by the increase in C>A transversions in the genomic DNA at that location.



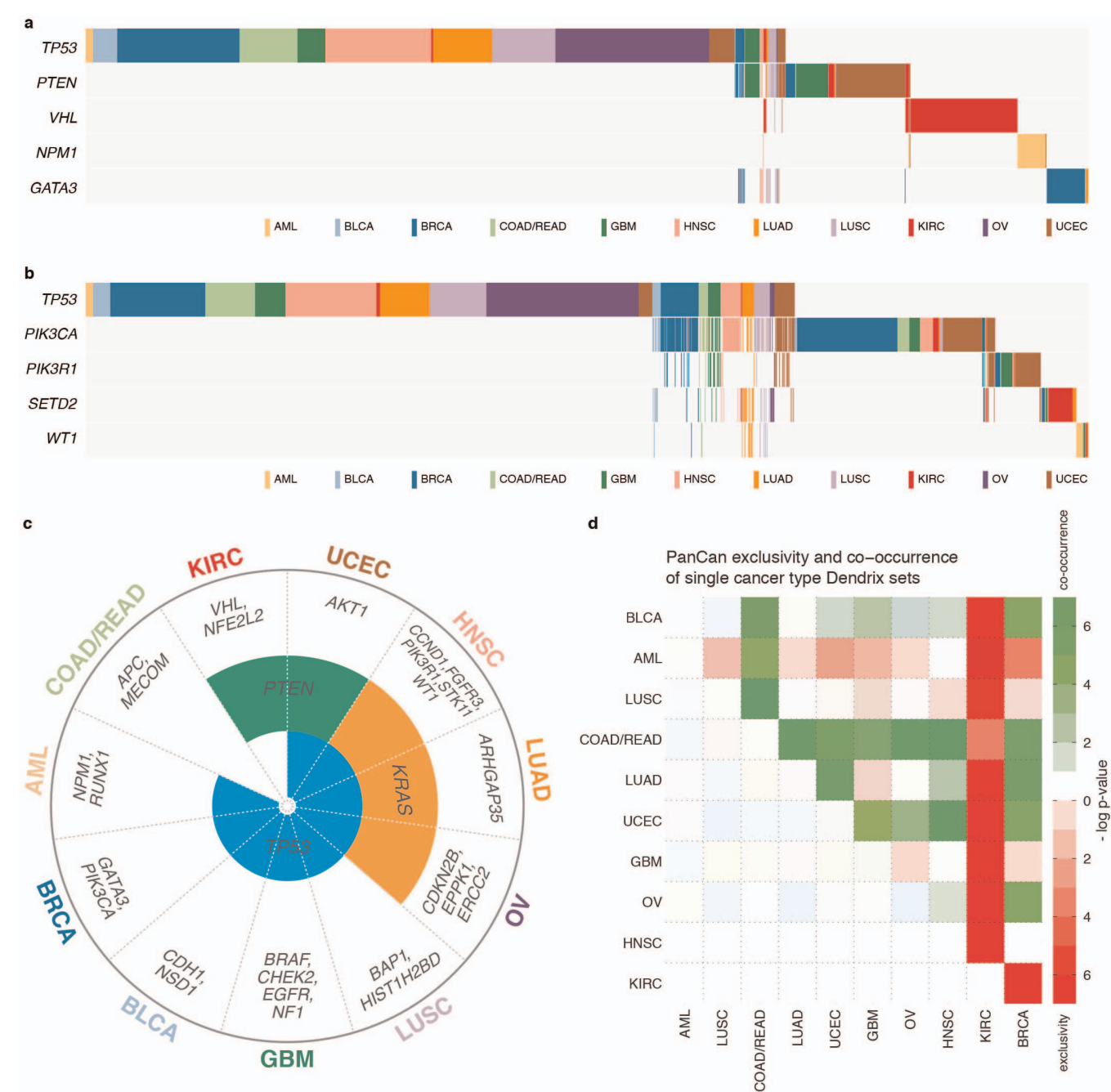
Extended Data Figure 3 | Unsupervised clustering based on mutation status of SMGs. Tumours having no mutation or more than 500 mutations were excluded to reduce noise. A mutation status matrix was constructed for 2,611

tumours. Major clusters of mutations detected in UCEC, COAD, GBM, AML, KIRC, OV and BRCA were highlighted. The shorter version is shown in Fig. 4.



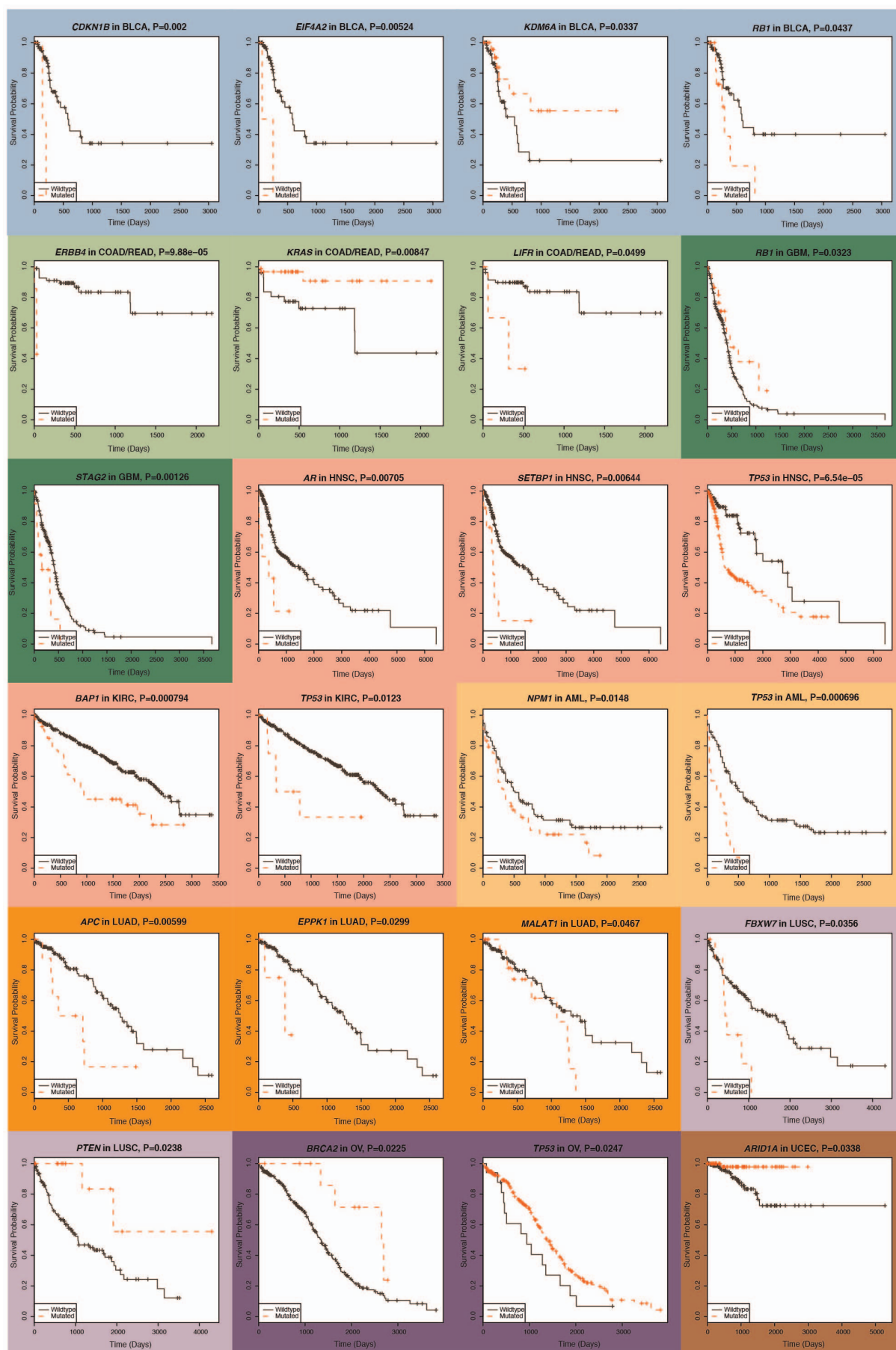
Extended Data Figure 4 | Mutation relation analysis in individual tumour types and the Pan-Cancer set. a, Exclusivity and co-occurrence between SMGs in each tumour type. The $-\log_{10} P$ value appears in either red or green if

the pair shows exclusivity or co-occurrence, respectively. **b,** Exclusivity and co-occurrence between genes in the most significant ($q < 0.05$) pairs in Pan-Cancer set. Colour scheme is as in **a**.



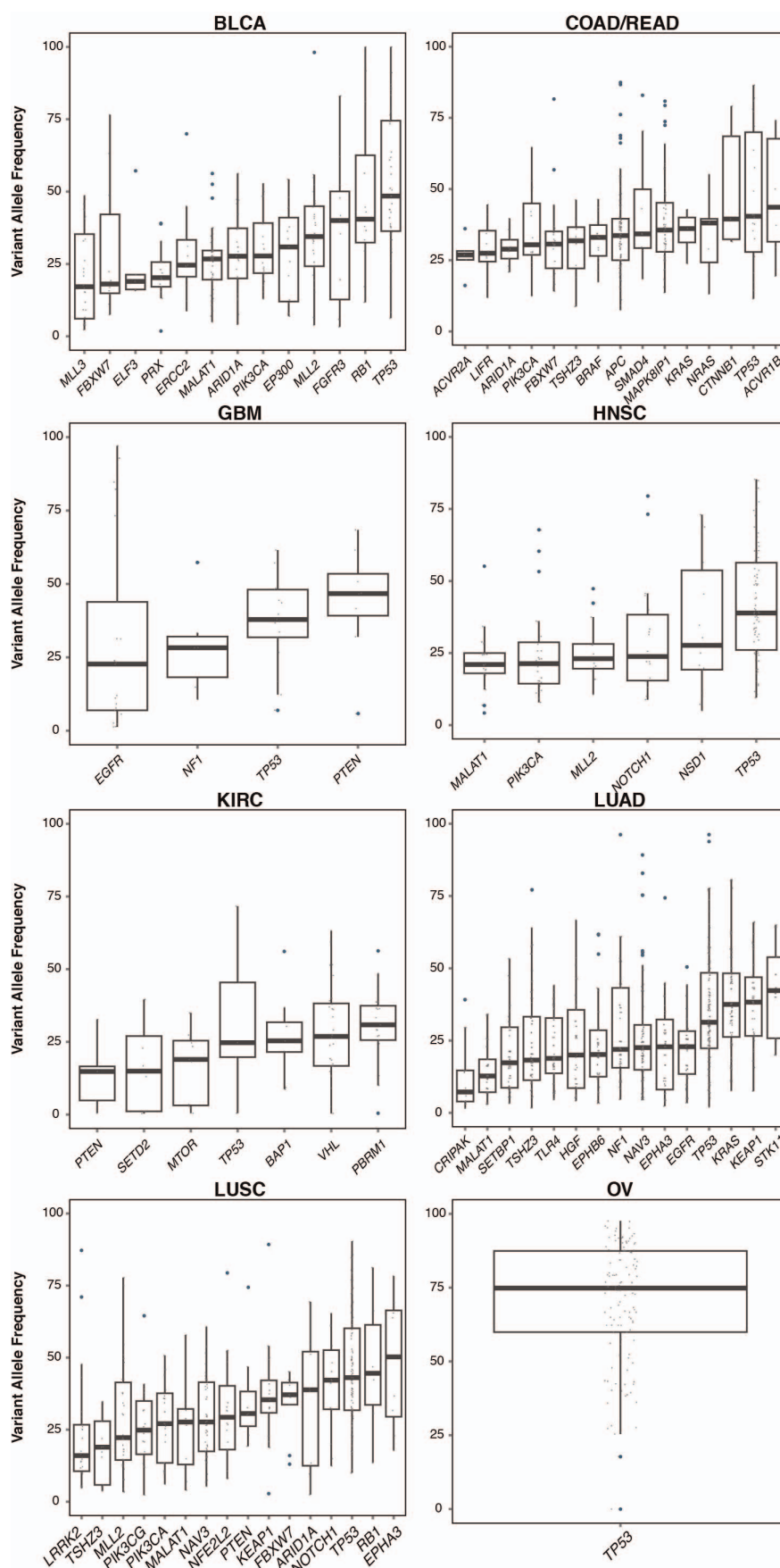
Extended Data Figure 5 | Mutually exclusive mutations identified by Dendrix in the Pan-Cancer and individual cancer type data sets. **a**, The highest scoring exclusive set of mutated genes in 127 SMGs contains several genes that are strongly associated with one cancer type. **b**, The highest scoring exclusive set of mutations in the top 600 genes (not enriched for mutations in one cancer type) reported by MuSiC. **c**, Relationships between exclusive gene sets identified by Dendrix in individual cancer types. Eight types include *TP53*

in the most exclusive set, three include *KRAS*, and two include *PTEN*, with the remaining genes appearing in only a single type. **d**, Exclusivity and co-occurrence assessed at the Pan-Cancer level. The $-\log_{10} P$ value appears in red or green if the pair shows exclusivity or co-occurrence, respectively. KIRC is most exclusive to other tumour types, whereas COAD/READ presented strong co-occurrence with other types.



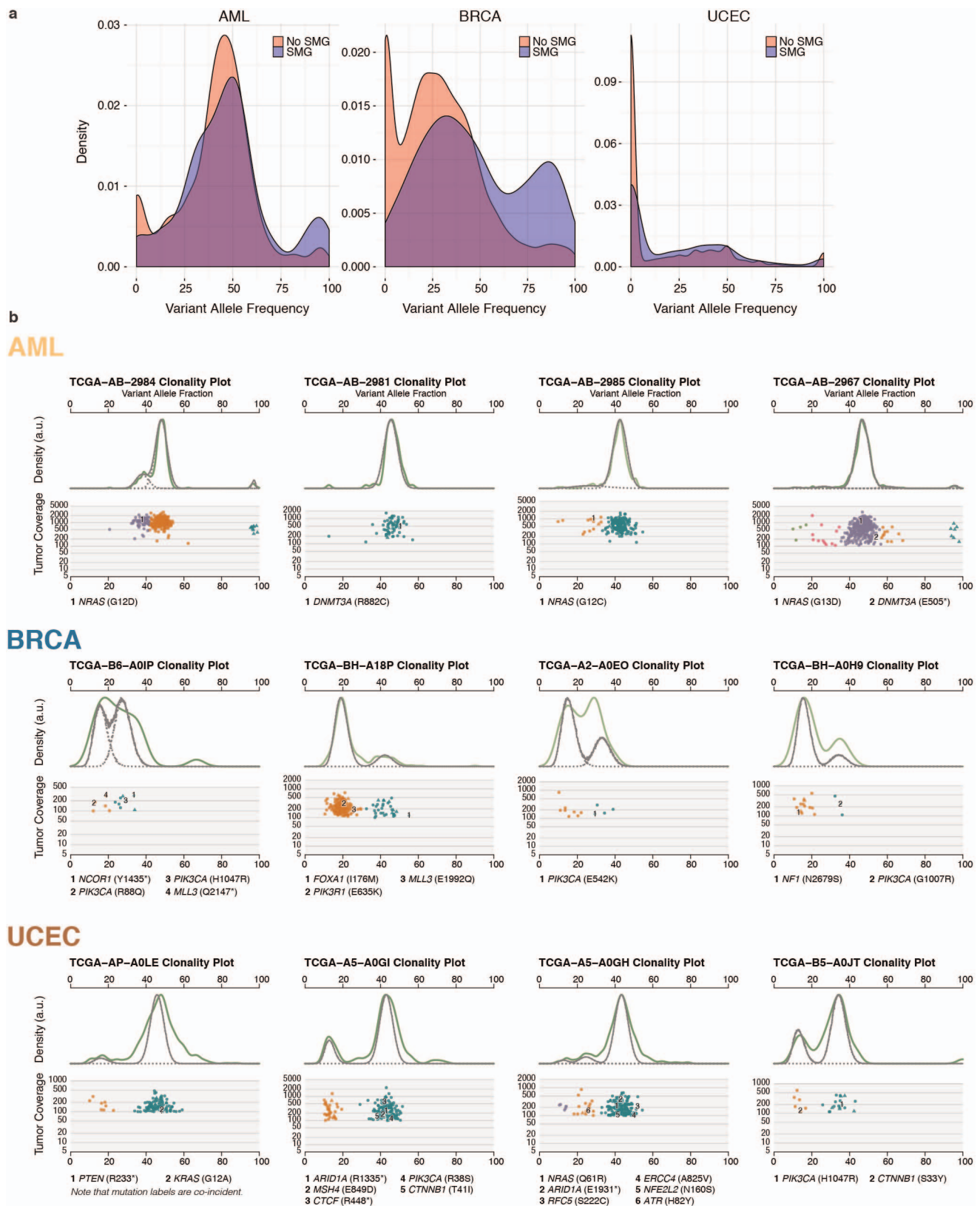
Extended Data Figure 6 | Kaplan–Meier plots for genes significantly associated with survival. Plots are shown for 24 genes showing significant ($P \leq 0.05$) association in individual cancer types. Although *NPM1* mutations in patients with AML having intermediate cytogenetic risk are relatively benign in the absence of internal tandem duplications in *FLT3*, we did not stratify patients

based on cytogenetics or *FLT3* internal tandem duplication status in this analysis, and cannot discern this effect. Because most patients with OV (95%) have *TP53* mutations, we could not obtain sufficient non-*TP53* mutant controls for confidently dissecting the relationship between *TP53* status and survival in OV.



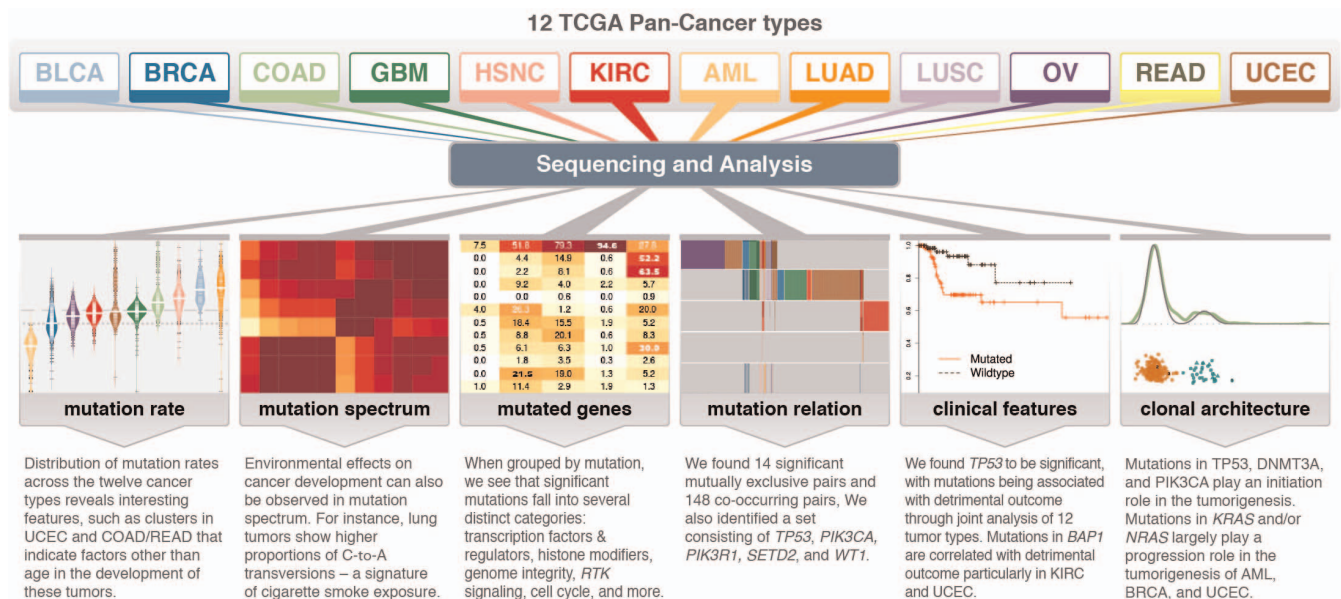
Extended Data Figure 7 | VAF distribution of mutations in SMGs across tumours from BLCA, KIRC, HNSC, LUAD, LUSC, COAD/READ, OV and GBM. To minimize the effect of copy number alterations on VAFs, only

mutations residing in copy number neutral segments were used for this analysis. Only mutation sites with $\geq 20\times$ coverage were used for analysis and plotting. SMGs with at least five data points were included in the plot.



Extended Data Figure 8 | Mutation expression and tumour clonal architecture in AML, BRCA and UCEC. **a**, Density plots of expressed VAFs for mutations in SMGs (blue) and non-SMGs (red). **b**, SciClone clonality example plots for AML (validation data), BRCA and UCEC. Two plots are

shown for each case: kernel density (top), followed by the plot of tumour VAF by sequence depth for sites from selected copy number neutral regions. Mutations (with annotations) in SMGs were shown.



Extended Data Figure 9 | Summary of major findings in Pan-Cancer 12. Systematic analysis of the TCGA Pan-Cancer mutation dataset identifies

SMGs, cancer-related cellular processes, and genes associated with clinical features and tumour progression.

Extended Data Table 1 | Clinical correlation and survival analysis for genes mutated at $\geq 2\%$ frequency in at least 2 tumour types

CROSS-CANCER INPUTS				INDIVIDUAL CANCER COMPONENT INPUTS AND RESULTS					OVERALL CROSS-CANCER RESULTS	
GENE	NUMBER OF CANCER TYPES	TOTAL TUMORS	MUTATED TUMORS	CANCER TYPE	TOTAL TUMORS	MUTATED TUMORS	HAZARD RATIO (95% CI)	P-VALUE	HAZARD RATIO (95% CI)	P-VALUE
BAP1	4	888	53	BLCA	92	3	3.57 (0.43:29.71)	0.24	2.2 (1.47:3.29)	0.00013
				KIRC	416	42	2.17 (1.38:3.41)	0.00079		
				LUAD	150	3	2.13 (0.49:9.21)	0.31		
				UCEC	230	5	4.16 (0.91:18.97)	0.066		
DNMT3A	3	507	60	LAML	186	47	1.45 (0.97:2.16)	0.07	1.59 (1.11:2.27)	0.011
				LUAD	150	6	0.86 (0.19:3.76)	0.84		
				LUSC	171	7	1.62 (0.56:4.68)	0.37		
HGF	3	621	32	HNSC	300	8	0.69 (0.22:2.19)	0.53	0.47 (0.23:0.96)	0.038
				LUAD	150	14	0.52 (0.16:1.74)	0.29		
				LUSC	171	10	0.39 (0.1:1.62)	0.2		
KDM5C	4	967	44	KIRC	416	27	1.72 (0.95:3.11)	0.073	1.63 (1.02:2.6)	0.04
				LUAD	150	7	0.9 (0.28:2.97)	0.87		
				LUSC	171	5	2.44 (0.74:7.99)	0.14		
				UCEC	230	5	7.78 (0.92:65.6)	0.059		
FBXW7	6	986	82	BLCA	92	9	1.56 (0.5:4.8)	0.44	1.57 (1.02:2.44)	0.042
				COAD/READ	193	22	2.18 (0.62:7.6)	0.22		
				HNSC	300	15	0.81 (0.35:1.88)	0.62		
				LUSC	171	9	2.37 (1.06:5.28)	0.036		
				UCEC	230	27	1.93 (0.55:6.84)	0.31		
BRCA2	6	1250	54	BLCA	92	6	0.98 (0.13:7.51)	0.99	0.62 (0.38:0.99)	0.047
				HNSC	300	11	0.93 (0.41:2.15)	0.87		
				LUAD	150	7	0.88 (0.27:2.92)	0.84		
				LUSC	171	10	0.69 (0.25:1.94)	0.49		
				OV	307	10	0.31 (0.12:0.85)	0.022		
				UCEC	230	10	4e-8 (0:inf)	1		
TP53	12	3083	1290	BLCA	92	47	0.98 (0.45:2.17)	0.97	1.19 (1.0:1.41)	0.049
				BRCA	763	251	1.36 (0.87:2.14)	0.18		
				COAD/READ	193	113	0.63 (0.22:1.77)	0.38		
				GBM	275	80	0.78 (0.55:1.1)	0.16		
				HNSC	300	209	2.58 (1.62:4.13)	7.00E-05		
				KIRC	416	9	3.16 (1.28:7.78)	0.012		
				LAML	186	14	2.76 (1.54:4.96)	0.0007		
				LUAD	150	78	1.13 (0.63:2.0)	0.68		
				LUSC	171	135	0.73 (0.43:1.24)	0.25		
				OV	307	290	0.53 (0.30:0.92)	0.025		
				UCEC	230	64	1.72 (0.61:4.87)	0.31		

Clinical correlation and survival analysis for genes mutated at $\geq 2\%$ frequency in at least 2 tumor types.

Reprogramming *in vivo* produces teratomas and iPS cells with totipotency features

María Abad¹, Lluç Mosteiro¹, Cristina Pantoja¹, Marta Cañamero², Teresa Rayon³, Inmaculada Ors³, Osvaldo Graña⁴, Diego Megías⁵, Orlando Domínguez⁶, Dolores Martínez⁷, Miguel Manzanera³, Sagrario Ortega⁸ & Manuel Serrano¹

Reprogramming of adult cells to generate induced pluripotent stem cells (iPS cells) has opened new therapeutic opportunities; however, little is known about the possibility of *in vivo* reprogramming within tissues. Here we show that transitory induction of the four factors *Oct4*, *Sox2*, *Klf4* and *c-Myc* in mice results in teratomas emerging from multiple organs, implying that full reprogramming can occur *in vivo*. Analyses of the stomach, intestine, pancreas and kidney reveal groups of dedifferentiated cells that express the pluripotency marker NANOG, indicative of *in situ* reprogramming. By bone marrow transplantation, we demonstrate that haematopoietic cells can also be reprogrammed *in vivo*. Notably, reprogrammable mice present circulating iPS cells in the blood and, at the transcriptome level, these *in vivo* generated iPS cells are closer to embryonic stem cells (ES cells) than standard *in vitro* generated iPS cells. Moreover, *in vivo* iPS cells efficiently contribute to the trophectoderm lineage, suggesting that they achieve a more plastic or primitive state than ES cells. Finally, intraperitoneal injection of *in vivo* iPS cells generates embryo-like structures that express embryonic and extraembryonic markers. We conclude that reprogramming *in vivo* is feasible and confers totipotency features absent in standard iPS or ES cells. These discoveries could be relevant for future applications of reprogramming in regenerative medicine.

Reprogramming into pluripotency remains an intense field of investigation that is providing many insights about cellular plasticity^{1,2}. Cellular reprogramming has been achieved under carefully controlled *in vitro* culture conditions³, whereas the *in vivo* tissue microenvironment is, in principle, conducive to cellular differentiation and opposed to reprogramming. However, we took note of remarkable examples in mice in which the normally irreversible state of cellular differentiation has been altered, inducing direct conversions *in vivo* from one cell type into a different one^{4–10}. Encouraged by these precedents, we have attempted to achieve reprogramming *in vivo*.

Generation of reprogrammable mice

We have generated reprogrammable mice similar, but not identical, to others previously described^{11–13}. A total of four transgenic mouse lines were obtained, each one carrying the transcriptional activator (rtTA) within the ubiquitously-expressed *Rosa26* locus¹⁴ and a single copy of a lentiviral doxycycline-inducible polycistronic cassette encoding the four murine factors *Oct4* (also known as *Pou5f1*), *Sox2*, *Klf4* and *c-Myc*¹⁵ (Fig. 1a; Extended Data Fig. 1a). In two of the four transgenic lines, the cassette was highly induced in most tissues (Extended Data Fig. 1b) and mouse embryonic fibroblasts (MEFs) from these lines were efficiently reprogrammed *in vitro* upon addition of doxycycline (Extended Data Fig. 1c, d). The other two transgenic lines did not express the cassette and their derived MEFs did not reprogram upon doxycycline addition. We have named the two functional transgenic lines as i4F-A and i4F-B, i4F standing for ‘inducible four factors’. We determined the integration sites of the transgenes, which in the case of line i4F-A is within an intron of the *Neto2* gene, and in the case of line i4F-B is within an intron of the *Pparg* gene (Extended Data Fig. 2a). Transcription of these two genes remained unaltered in a number of tissues, either with or without doxycycline (Extended Data Fig. 2b). We

conclude that transgenic lines i4F-A and i4F-B contain a functional inducible reprogramming transgene that is expressed in most tissues without affecting the resident endogenous genes.

Reprogrammable mice generate teratomas

To test the possibility of *in vivo* reprogramming, we first treated i4F-A and i4F-B mice continuously with a high dose of doxycycline (1 mg ml^{−1}) in the drinking water. This treatment resulted in weight loss and severe morbidity in both transgenic lines after 1 week. Histological examination of the mice revealed alterations in many tissues, particularly profound in the intestine and pancreas. The intestinal epithelium showed a generalized cytological and architectural dysplasia (Extended Data Fig. 3a), probably responsible for the weight loss. A similar phenotype has been reported for mice with transgenic expression of *Oct4* or *c-Myc*^{14,16}. In the case of the pancreas, mice presented multifocal dysplasia (Extended Data Fig. 3b). Taking into account these observations, we tested two milder induction protocols that turned out to be compatible with the long-term survival of the mice. In particular, 2.5-week treatment with low doxycycline (0.2 mg ml^{−1}) or 1-week treatment with high doxycycline (1 mg ml^{−1}), both followed by doxycycline withdrawal. Remarkably, after a variable period of time, treated mice succumbed to the presence of tumoral masses (Fig. 1b; Extended Data Fig. 4a), most of which consisted of teratomas (Fig. 1c; Extended Data Fig. 4b). Teratomas are a particular class of tumours that originate from pluripotent cells after a process of expansion and disorganized differentiation. Most of the teratomas (32/45, 71%) were well differentiated and presented abundant examples of the three embryonic germ layers (Fig. 1d). Therefore, the presence of teratomas in our reprogrammable mice is indicative of reprogramming into full pluripotency. Mice treated with the long-induction/low-doxycycline protocol developed teratomas faster and at a higher incidence rate than those treated with the short-induction/

¹Tumour Suppression Group, Spanish National Cancer Research Centre (CNIO), Madrid E-28029, Spain. ²Histopathology Unit, Spanish National Cancer Research Centre (CNIO), Madrid E-28029, Spain.

³Cardiovascular Development and Repair Department, Spanish National Cardiovascular Research Centre (CNIC), Madrid E-28029, Spain. ⁴Bioinformatics Unit, Spanish National Cancer Research Centre (CNIO), Madrid E-28029, Spain. ⁵Confocal Microscopy Unit, Spanish National Cancer Research Centre (CNIO), Madrid E-28029, Spain. ⁶Genomics Unit, Spanish National Cancer Research Centre (CNIO), Madrid E-28029, Spain. ⁷Flow Cytometry Unit, Spanish National Cancer Research Centre (CNIO), Madrid E-28029, Spain. ⁸Transgenic Mice Unit, Spanish National Cancer Research Centre (CNIO), Madrid E-28029, Spain.

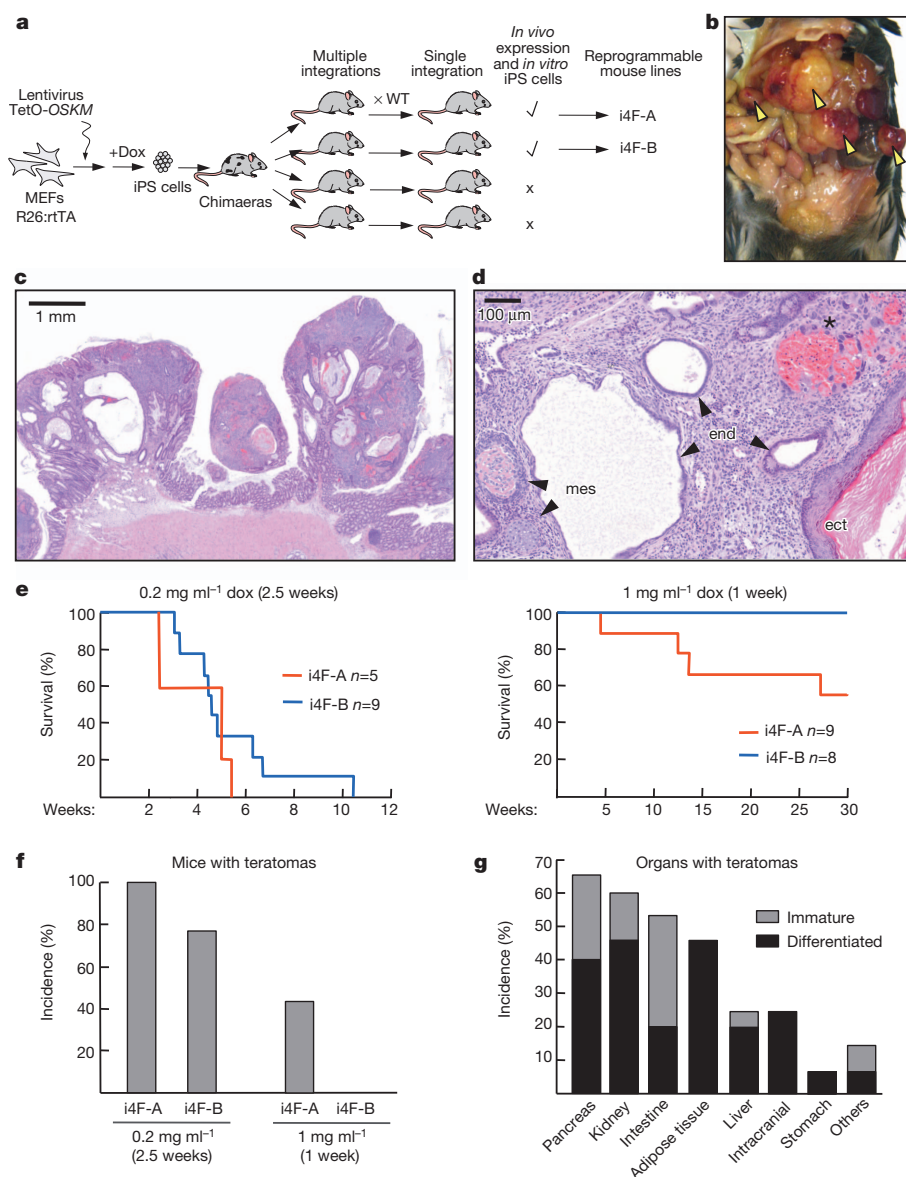


Figure 1 | Generation of teratomas upon *in vivo* induction of the four factors *Oct4*, *Sox2*, *Klf4* and *c-Myc*.

a, Reprogrammable mouse generation. **b**, Reprogrammable mouse with multiple teratomas (arrowheads). **c**, Teratomas in the intestine of a reprogrammable mouse. **d**, Histological section of a teratoma with mesoderm (mes), endoderm (end) and ectoderm (ect). Asterisk indicates giant trophoblast cells and haemorrhages. **e**, Survival of reprogrammable mice after the indicated doxycycline treatments. Time refers to the initiation of the treatments. **f**, Incidence of teratomas. Data corresponds to their time of death or week 30. **g**, Localization of teratomas in mice with teratomas.

high-doxycycline protocol (Fig. 1e). The incidence of teratomas was higher in line i4F-A than in i4F-B (Fig. 1f), and in both lines and protocols, teratomas appeared in a variety of organs (Fig. 1g). Reprogrammable mice that were not treated with doxycycline remained healthy at least during 2 years of observation, indicating the absence of leaky expression of the reprogramming cassette. The presence of multiples teratomas in both lines implies that reprogramming into pluripotency is feasible within *in vivo* conditions.

***In vivo* reprogramming occurs in multiple tissues**

Previous work has shown that haematopoietic progenitors can reprogram with high efficiency¹⁷. This, together with the broad distribution of haematopoietic cells within the organism, led us to consider that teratomas in our reprogrammable mice could originate from cells of the haematopoietic lineage. To address this, we performed bone marrow transplants into lethally irradiated hosts. In one setting, bone marrow (BM) from reprogrammable mice (i4F-BM) was transplanted into wild-type hosts and, in the reciprocal transplantation, wild-type bone marrow was transplanted into reprogrammable mice. Interestingly, both types of bone marrow reconstituted mice developed multiple teratomas upon induction (Fig. 2a, b). These results suggest that haematopoietic and non-haematopoietic cells can both be reprogrammed

in vivo. Of note, the teratomas present in i4F-BM transplanted mice were not emerging from organs, but outgrew attached to the serous membranes of the thoracic and abdominal cavities, whereas reprogrammable mice (either whole-body or transplanted with wild-type bone marrow) presented teratomas within multiple organs, as previously mentioned (Fig. 1g).

The above results prompted us to look for early reprogramming events in non-haematopoietic cells. In particular, we focused on the stomach, intestine, pancreas and kidney of whole-body reprogrammable mice. We performed double immunohistochemistry against the epithelial marker cytokeratin 19 (CK19, also known as KRT19) and the pluripotency marker NANOG. We found aberrant individual gastric glands and intestinal crypts (in the small and large intestine) that had lost or decreased CK19 and expressed NANOG (Fig. 2c, d). In some cases the entire gland or crypt was aberrant, whereas in others intermediate situations were found. In the pancreas, we observed both acinar-like (CK19-negative) and ductal-like (CK19-positive) structures with NANOG-positive cells (Fig. 2e). In the kidney, which does not undergo major detectable morphological changes upon doxycycline induction but has a high incidence of teratomas (Fig. 1g), we found isolated kidney tubules expressing NANOG (Extended Data Fig. 4c). In general, the number of reprogramming events evidenced

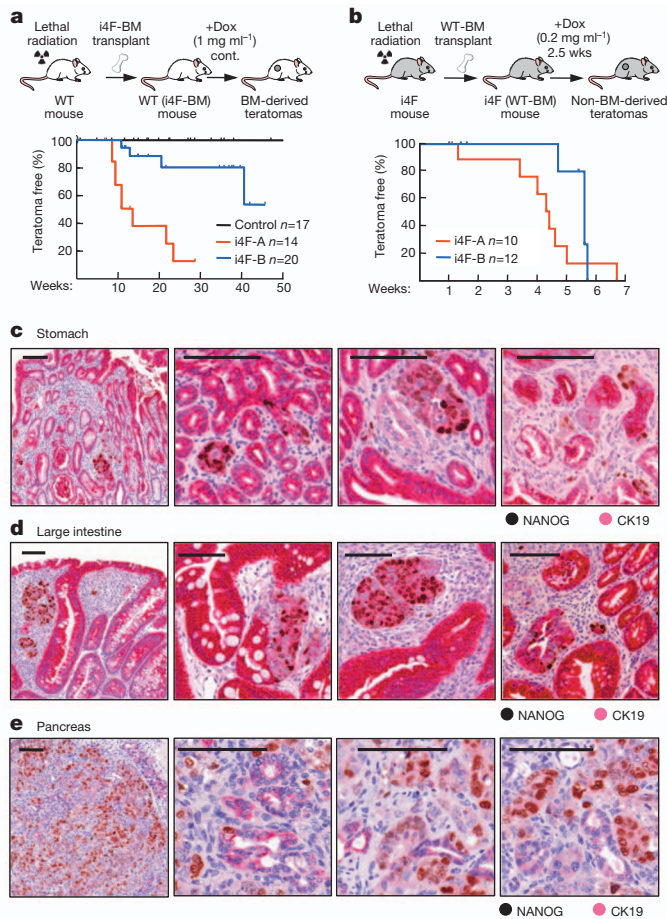


Figure 2 | Many cell types are reprogrammed *in vivo*. **a**, Incidence of teratomas in wild-type mice transplanted with reprogrammable bone marrow (BM). Time refers to the initiation of the treatment. **b**, Same as **a** in reprogrammable mice transplanted with wild-type BM. Ticks indicate censored mice dead without teratomas due to pulmonary oedema secondary to irradiation (**a**) or systemic i4F induction (**b**). **c**, Double immunohistochemistry of NANOG (dark brown) and cytokeratin 19 (CK19, magenta) in the stomach of whole-body reprogrammable mice. **d**, Same staining as **c** in the large intestine. **e**, Same staining as **c** in the pancreas. All scale bars correspond to 100 μ m.

by NANOG (Fig. 2d) was clearly lower than the number of cells expressing the reprogramming cassette (Extended Data Fig. 3a), implying that reprogramming *in vivo* is a low efficiency process that likely involves stochastic events, similar to what happens during *in vitro* reprogramming^{18,19}. The presence of isolated NANOG-positive structures, such as intestinal crypts or kidney tubules, probably reflects the clonal expansion of an individual reprogramming event. These observations support the concept that reprogramming occurs *in situ*, at least in the case of the epithelial cells of the stomach, intestine, pancreas and kidney.

Reprogrammable mice present iPS cells in the blood

Given the feasibility of *in vivo* reprogramming, we wondered whether it was possible to detect circulating iPS cells in the bloodstream. To address this, the cellular fraction of the blood from induced reprogrammable mice ($\sim 10^6$ leukocytes) was seeded into plates with feeder fibroblasts and iPS cell culture medium (all procedures after blood extraction were performed in the absence of doxycycline). Remarkably, after a variable period of time (1–2 weeks), colonies with iPS cell morphology were visible (Fig. 3a). These colonies were expanded (Fig. 3b) and were found to express pluripotency markers (Fig. 3c, d; Extended Data Fig. 5a) and to have silenced the lentiviral reprogramming cassette (Extended Data Fig. 5b). Moreover, *in vivo* iPS cells generated subcutaneous teratomas with representation of the three germ layers

(Fig. 3e), produced mouse chimaeras (Fig. 3f) and contributed to the germ lineage (Extended Data Fig. 5c). Therefore, we conclude that bona fide iPS cells can be isolated from the blood of reprogrammable mice. Of note, colonies of iPS cells were obtained from whole-body reprogrammable mice, as well as from wild-type mice with reprogrammable bone marrow and from reprogrammable mice with wild-type bone marrow (Extended Data Fig. 5d). Therefore, both haematopoietic and non-haematopoietic cells can generate *in vivo* circulating iPS cells. The overall frequency of mice with colony-forming iPS cells was 6.5% (5/77) (Fig. 3g), and this frequency was similar in the two transgenic lines (Extended Data Fig. 5d). In those blood samples that were positive for iPS cells colony formation, the number of colonies obtained was variable (9 ± 5) (Extended Data Fig. 5d). We will refer to the circulating iPS cells as *in vivo* iPS cells to distinguish them from the standard *in vitro* generated ones.

Transcriptomic analysis of *in vivo* iPS cells

To further characterize the *in vivo* iPS cells, we performed messenger RNA deep sequencing. We sequenced *in vivo* iPS cells ($n = 6$ independent clones), *in vitro* iPS cells ($n = 5$ independent clones derived from i4F-MEFs) and ES cells (JM8.F6 (ref. 20), Bruce4 (ref. 21) and CNIO in-house made C57BL6.10). The homogeneity of the samples of each cell type was confirmed by the high intra-group correlation coefficients (Extended Data Fig. 6a). Furthermore, all of the 14 transcriptomes analysed were highly similar regardless of their origin (the lowest pairwise correlation coefficient was $r = 0.93$) (Extended Data Fig. 6a). Interestingly, inter-group comparisons by scatter plots, volcano plots and Pearson coefficient correlations indicated a higher degree of similarity between *in vivo* iPS and ES cells ($r = 0.997$), than between the other two possible combinations (*in vivo* iPS cells vs *in vitro* iPS cells, $r = 0.971$; ES cells vs *in vitro* iPS cells, $r = 0.966$) (Extended Data Fig. 6c). Moreover, unsupervised hierarchical clustering of the 14 transcriptomes classified together *in vivo* iPS cells and ES cells, and separated them from *in vitro* iPS cells (Fig. 3h). The same classification was obtained using principal component analysis, which is another unbiased method to quantify the degree of similarity between large data sets (Extended Data Fig. 6b). The lists of differentially expressed genes were obtained for further analyses (Supplementary Tables 1–3). Interestingly, among the genes commonly upregulated in *in vivo* iPS and ES cells compared to *in vitro* iPS cells (a total of 51 genes; Supplementary Table 4) there were several pluripotency genes, including *Gbx2*, *Lin28a*, *Utf1* and others associated with pluripotency, such as *Epcam* and *Ccne1*. The upregulation of these genes in *in vivo* iPS and ES cells was validated by quantitative PCR with reverse transcription (qRT-PCR) (Extended Data Fig. 7a). Having established that *in vivo* iPS cells are extremely similar to ES cells, we focused on those few genes that were differentially expressed in *in vivo* iPS cells relative to ES cells and *in vitro* iPS cells (Fig. 3i; Supplementary Table 5). Among these genes, we validated the upregulation of *Nlrp4f* (known to be enriched at the morula state)²², *Etv4* (a transcription factor of the *Ets* family expressed during early development)²³, *Ppm1j* (a protein phosphatase transcriptionally upregulated upon GSK3 β inhibition)²⁴, *8430410A17Rik* (a gene consistently found associated with stemness)²⁵ and *Tgm1* (Fig. 3j; Extended Data Fig. 7b), and the downregulation of *Mmp12* and *Tnc* (both encoding components or regulators of the extracellular matrix) (Fig. 3j). Importantly, the pattern of expression of these genes was similar in *in vivo* iPS cells and in morulas (Fig. 3j; Extended Data Fig. 7b), thus suggesting that *in vivo* iPS cells and morulas share transcriptional features that are absent in ES cells or in *in vitro* iPS cells. We conclude that *in vivo* iPS cells are extremely similar to ES cells, but present differentially expressed genes that could conceivably confer additional properties to the *in vivo* iPS cells.

In vivo iPS cells contribute to the trophectoderm

We noted that the teratomas that appeared in reprogrammable mice often presented areas with large cells that resemble trophoblast giant

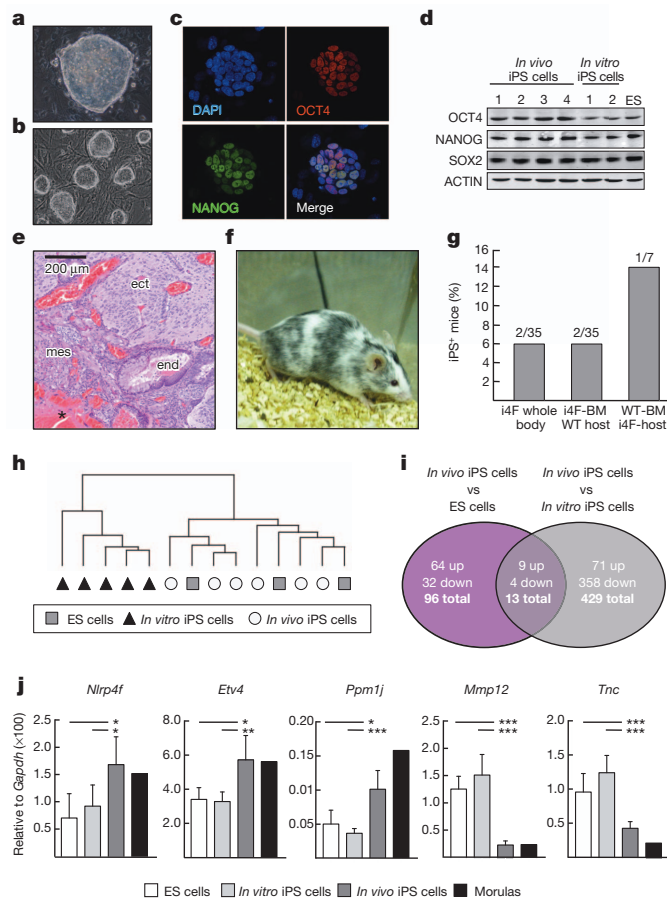


Figure 3 | Isolation and characterization of *in vivo* iPS cells. **a**, *In vivo* iPS cell colony 10 days after blood plating. **b**, Expansion of *in vivo* iPS cells. **c**, Immunofluorescence of *in vivo* iPS cell colony. **d**, Immunoblot of *in vivo* iPS cells, *in vitro* iPS cells (no. 1 from i4F MEFs; no. 2 from MEFs infected with lenti-OSKM) and C57BL/6.10 ES cells. **e**, Subcutaneous teratoma from *in vivo* iPS cells injection. Asterisk indicates giant trophoblast cells and haemorrhages. **f**, *In vivo* iPS cells derived chimaera. **g**, Frequency of *in vivo* iPS cells isolation. **h**, Unsupervised hierarchical clustering of *in vivo* iPS cells, *in vitro* iPS cells and ES cells (6, 5 and 3 clones respectively). **i**, Venn diagram of differentially expressed genes. **j**, qPCR analysis of differentially expressed genes in the same clones as in **h**. Average \pm s.d. and unpaired two-tailed Student's *t*-test are shown. **P* < 0.05; ***P* < 0.01; ****P* < 0.001.

cells associated with internal haemorrhages, altogether characteristic of placental tissue (Fig. 4a; see also examples in Figs 1d and 3e). Indeed, this was confirmed by the expression of PL-1 (placental lactogen 1) or chorionic somatomammotropin hormone 1) and CK8 (cytokeratin 8 or KRT8), which are both markers of trophoblast giant cells (Fig. 4a). We were intrigued by this observation because trophoblast differentiation is rare in teratomas produced by ES cells²⁶. To further explore this, we subjected ES cells, *in vitro* iPS cells and *in vivo* iPS cells to culture conditions that favour differentiation into trophoblast stem cells (namely, removal of LIF and addition of FGF4 and heparin)^{26–28}. After 5 days, *in vivo* iPS cells formed abundant colonies with a flattened morphology characteristic of trophoblast stem cells. In contrast, *in vitro* iPS and ES cells produced a lower number of colonies and only few of them showed trophoblast stem cell like morphology (Fig. 4b). Furthermore, *in vivo* iPS cells upregulated markers of trophoblast lineage (*Cdx2*, *Fgfr2* and *Eomes*) to a larger extent than equally treated *in vitro* iPS or ES cells (Fig. 4c; Extended Data Fig. 8a). The upregulation of *Cdx2* in *in vivo* iPS cells was confirmed by immunofluorescence (Fig. 4d). As a control, markers of ectoderm (*Sox1*), mesoderm (*T*) and endoderm (*Gata6*) lineages showed similar levels of expression among all the cell types examined (Extended Data Fig. 8a). Moreover, upon removal of

FGF4 and heparin, trophoblast stem cell differentiated *in vivo* iPS cells generated trophoblast giant cells (Fig. 4e).

Based on the above observations, we tested the capacity of *in vivo* iPS cells to contribute to the trophoblast lineage. For this, GFP-expressing *in vivo* iPS and ES cells were aggregated or microinjected into morulas (either wild type or carrying a Katushka red fluorescent transgene²⁹) and the resulting blastocysts were examined. As expected, both cell types, *in vivo* iPS and ES cells, efficiently contributed (100%) to the inner cell mass (ICM). Interestingly, *in vivo* iPS cells also contributed to the polar trophoblast (surrounding the ICM) and to the mural trophoblast (Fig. 4f; Extended Data Fig. 8b). Altogether, *in vivo* iPS cells contributed to the trophoblast with a remarkable efficiency (56%), which was in contrast to ES cells (0%) (Fig. 4g)³⁰. To test whether the *in vivo* iPS cells actually contribute to the formation of the placenta, we examined chimaeric E14.5 embryos generated with GFP-expressing *in vivo* iPS cells and we observed a high degree of chimaerism both in the embryo proper as well as in the placenta (Fig. 4h, i; Extended Data Fig. 8c). Previous investigators have reported that ES cells and standard iPS cells can transiently access a totipotency-like state similar to the 2-cell blastomeres (2C state)³¹. We wondered whether *in vivo* iPS cells are enriched in the 2C state, however, we could not see upregulation of the 2C markers *Zscan4*, *MuERV-L* and *IAP* (Extended Data Fig. 9). Therefore, *in vivo* iPS cells do not seem to be enriched in the 2C state, although, as shown above (Fig. 3j), they share transcriptional features with morulas. Together, we conclude that *in vivo* reprogramming confers a pluripotency state that, in contrast to ES cells or standard *in vitro* iPS cells, can readily access the trophoblast lineage.

In vivo iPS cells generate embryo-like structures

During the course of the above analyses we observed the presence of small cysts in the thoracic and abdominal cavities of two reprogrammable mice (from a total of 77 induced reprogrammable mice) (Fig. 5a). These cysts were often detached from the surrounding organs and from the lining of the abdominal and thoracic cavities (Fig. 5a). The cysts were formed by membranous structures and, based on their detailed characterization (see below), we refer to them as embryo-like structures. We wondered whether *in vivo* iPS cells could also form embryo-like structures when injected intraperitoneally into wild-type mice. Remarkably, in addition to the expected teratomas, a fraction of mice injected with *in vivo* iPS cells contained embryo-like structures, in contrast to the mice injected with *in vitro* iPS or ES cells (Fig. 5b). Immunohistological analyses of the embryo-like structures indicated the presence of cell layers and cellular areas expressing lineage markers SOX2 (ectoderm), T/BRACHYURY (mesoderm), or GATA4 (endoderm) (Fig. 5c; Extended Data Fig. 10). In addition, these embryo-like structures also expressed CDX2 (Fig. 5c; Extended Data Fig. 10), indicative of trophoblast lineage³², and presented cell layers with the typical border morphology of the yolk sac endoderm which co-expressed α -fetoprotein (AFP) and cytokeratin 8 (CK8) (Fig. 5c; Extended Data Fig. 10), both characteristic of the visceral endoderm of the yolk sac³³. Finally, embryo-like structures presented regions resembling blood islands, internally lined by the endothelial cell surface marker LYVE-1 (ref. 34) and with associated nucleated erythrocytes positive for the TER-119 marker (Fig. 5d), highly suggestive of yolk sac associated erythropoiesis. We conclude that *in vivo* iPS cells possess an unprecedented cell-autonomous capacity to produce embryo-like structures containing the three embryonic germ layers together with structures reminiscent of the extraembryonic ectoderm and the yolk sac. This reinforces the concept that *in vivo* reprogramming allows the acquisition of totipotency features that are absent in ES cells or in standard *in vitro* reprogrammed iPS cells.

Conclusion

In this work, we demonstrate that the four factors *Oct4*, *Sox2*, *Klf4* and *c-Myc* can induce dedifferentiation and pluripotency in a variety of cell types *in vivo*, including cells from the haematopoietic lineage, as

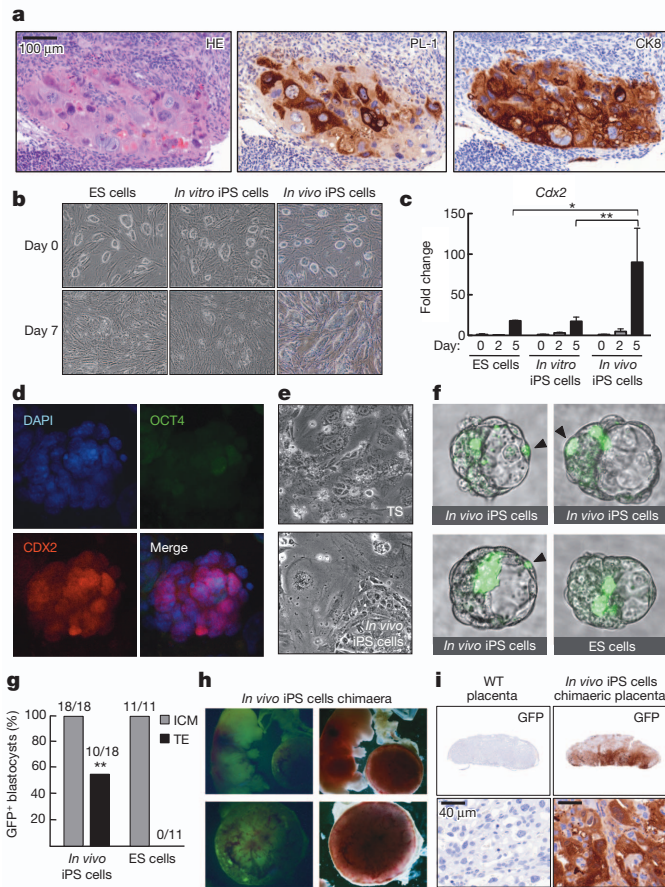


Figure 4 | *In vivo* iPS cells efficiently contribute to the trophoblast.

a, Teratomas with trophoblast giant cells. **b**, Trophoblast stem cell differentiation of the indicated cells. **c**, *Cdx2* expression in *in vivo* iPS cells, *in vitro* iPS cells and ES cells (6, 5 and 3 clones, respectively) during TS differentiation, relative to day 0. Average \pm s.d. and unpaired, two-tailed Student's *t*-test are shown: * $P < 0.05$, ** $P < 0.01$. **d**, Immunofluorescence of *in vivo* iPS cells derived trophoblast stem cells. **e**, Giant cells differentiated from trophoblast stem cells and *in vivo* iPS cells derived trophoblast stem cells. **f**, Chimaeric blastocysts from GFP *in vivo* iPS cells and GFP-ES cells. Arrowheads mark GFP⁺ trophoblast cells. **g**, Frequency of blastocysts with GFP⁺ trophoblast cells from *in vivo* iPS cells ($n = 2$ clones) and ES cells (JM8.F6). Fisher's exact test: ** $P < 0.01$. **h**, GFP *in vivo* iPS cells chimaeric embryo and placenta. **i**, Immunostaining against GFP.

well as epithelial cells from the stomach, intestine, pancreas and kidney. In the context of previous examples of *in vivo* cellular conversions^{4–10}, our results notably extend the concept of *in vivo* plasticity to many tissues and to the extreme case of generating embryonic pluripotent cells, a cell type that is absent in the adult organism. Previous investigators have shown that intentionally incomplete *in vitro* reprogramming with the four factors triggers a dedifferentiated cellular state that can have advantageous differentiation properties^{35,36}. In this regard, partial or transient activation of the four factors *in vivo* is an attractive approach for regenerative purposes.

Another important aspect of our work is the recovery of circulating iPS cells from the blood of induced reprogrammable mice, which can derive from both haematopoietic and non-haematopoietic cells. Notably, *in vivo* iPS and ES cells are extremely similar, and clearly separated from *in vitro* iPS cells. Despite the high similarity between *in vivo* iPS and ES cells, it is possible to detect differentially expressed genes among the two cell types. These differences may originate from differential epigenetic marks and/or self-sustained transcriptional networks, both of which are prominent regulators of pluripotency^{37,38}. *In vivo* iPS cells present a remarkable capacity to undergo trophoblast lineage differentiation, a property that is largely absent in ES cells (or *in vitro*

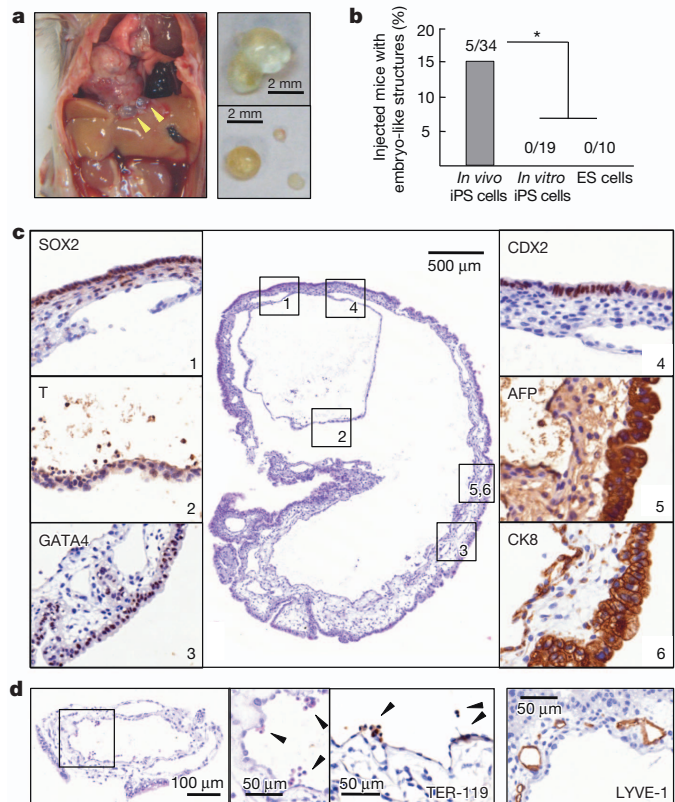


Figure 5 | *In vivo* reprogramming and *in vivo* iPS cells generate embryo-like structures. **a**, Cysts in the abdominal cavity of a reprogrammable mouse.

b, Frequency of embryo-like structures after intraperitoneal injection of *in vivo* iPS cells (3 clones), *in vitro* iPS cells (2 clones) and ES cells (JM8.F6). Fisher's exact test: * $P < 0.05$. **c**, Cyst generated by intraperitoneal injection. Left panels, germ layer markers: SOX2 (ectoderm), T/BRACHYURY (mesoderm) and GATA4 (endoderm). Right panels, extraembryonic markers: CDX2 (trophoblast), and AFP and CK8, both specific for visceral endoderm of the yolk sac. **d**, Cyst generated by intraperitoneal injection presenting TER-119⁺ nucleated erythrocytes and LYVE-1⁺ endothelial cells in structures resembling yolk sac blood islands.

iPS cells) under normal culture conditions. Finally, *in vivo* iPS cells have an unprecedented capacity to form embryo-like structures, including the three germ layers of the proper embryo and extraembryonic tissues, such as extraembryonic ectoderm and yolk sac like tissue with associated embryonic erythropoiesis. Together, we conclude that *in vivo* iPS cells represent a more primitive or plastic state than ES cells. Future work will explore the full capabilities of *in vivo* iPS cells.

METHODS SUMMARY

***In vivo* iPS cell isolation.** Peripheral blood (0.3–0.5 ml) was collected directly from the heart of doxycycline-induced i4F mice at the time of necropsy. After blood extraction, all procedures were performed in the absence of doxycycline. The recovered cells were plated on feeders and cultured in iPS cell medium.

Generation of embryo-like structures. Wild-type C57BL/6 mice were injected with 5×10^5 cells in 100 μ l of iPS cell medium. When teratomas were palpable, usually around 2 months post-injection, mice were euthanized.

Online Content Any additional Methods, Extended Data display items and Source Data are available in the online version of the paper; references unique to these sections appear only in the online paper.

Received 4 March; accepted 23 August 2013.

Published online 11 September; corrected online 16 October 2013 (see full-text HTML version for details).

1. Takahashi, K. & Yamanaka, S. Induction of pluripotent stem cells from mouse embryonic and adult fibroblast cultures by defined factors. *Cell* **126**, 663–676 (2006).

2. Robinton, D. A. & Daley, G. Q. The promise of induced pluripotent stem cells in research and therapy. *Nature* **481**, 295–305 (2012).
3. Maherali, N. & Hochedlinger, K. Guidelines and techniques for the generation of induced pluripotent stem cells. *Cell Stem Cell* **3**, 595–605 (2008).
4. Cobaleda, C., Jochum, W. & Busslinger, M. Conversion of mature B cells into T cells by dedifferentiation to uncommitted progenitors. *Nature* **449**, 473–477 (2007).
5. Zhou, Q., Brown, J., Kanarek, A., Rajagopal, J. & Melton, D. A. *In vivo* reprogramming of adult pancreatic exocrine cells to β -cells. *Nature* **455**, 627–632 (2008).
6. Qian, L. *et al.* *In vivo* reprogramming of murine cardiac fibroblasts into induced cardiomyocytes. *Nature* **485**, 593–598 (2012).
7. Song, K. *et al.* Heart repair by reprogramming non-myocytes with cardiac transcription factors. *Nature* **485**, 599–604 (2012).
8. Banga, A., Akinci, E., Greder, L. V., Dutton, J. R. & Slack, J. M. *In vivo* reprogramming of Sox9⁺ cells in the liver to insulin-secreting ducts. *Proc. Natl Acad. Sci. USA* **109**, 15336–15341 (2012).
9. Rouaux, C. & Arlotta, P. Direct lineage reprogramming of post-mitotic callosal neurons into corticofugal neurons *in vivo*. *Nature Cell Biol.* **15**, 214–221 (2013).
10. Torper, O. *et al.* Generation of induced neurons via direct conversion *in vivo*. *Proc. Natl Acad. Sci. USA* **110**, 7038–7043 (2013).
11. Stadtfeld, M., Maherali, N., Borkent, M. & Hochedlinger, K. A reprogrammable mouse strain from gene-targeted embryonic stem cells. *Nature Methods* **7**, 53–55 (2010).
12. Carey, B. W., Markoulaki, S., Beard, C., Hanna, J. & Jaenisch, R. Single-gene transgenic mouse strains for reprogramming adult somatic cells. *Nature Methods* **7**, 56–59 (2010).
13. Haenebalcke, L. *et al.* The ROSA26-iPSC mouse: a conditional, inducible, and exchangeable resource for studying cellular (de)differentiation. *Cell Rep.* **3**, 335–341 (2013).
14. Hochedlinger, K., Yamada, Y., Beard, C. & Jaenisch, R. Ectopic expression of Oct-4 blocks progenitor-cell differentiation and causes dysplasia in epithelial tissues. *Cell* **121**, 465–477 (2005).
15. Carey, B. W. *et al.* Reprogramming of murine and human somatic cells using a single polycistronic vector. *Proc. Natl Acad. Sci. USA* **106**, 157–162 (2009).
16. Finch, A. J., Soucek, L., Junttila, M. R., Swigart, L. B. & Evan, G. I. Acute overexpression of Myc in intestinal epithelium recapitulates some but not all the changes elicited by Wnt/ β -catenin pathway activation. *Mol. Cell. Biol.* **29**, 5306–5315 (2009).
17. Eminli, S. *et al.* Differentiation stage determines potential of hematopoietic cells for reprogramming into induced pluripotent stem cells. *Nature Genet.* **41**, 968–976 (2009).
18. Yamanaka, S. Elite and stochastic models for induced pluripotent stem cell generation. *Nature* **460**, 49–52 (2009).
19. Hanna, J. *et al.* Human embryonic stem cells with biological and epigenetic characteristics similar to those of mouse ESCs. *Proc. Natl Acad. Sci. USA* **107**, 9222–9227 (2010).
20. Pettitt, S. J. *et al.* Agouti C57BL/6N embryonic stem cells for mouse genetic resources. *Nature Methods* **6**, 493–495 (2009).
21. Hughes, E. D. *et al.* Genetic variation in C57BL/6 ES cell lines and genetic instability in the Bruce4 C57BL/6 ES cell line. *Mamm. Genome* **18**, 549–558 (2007).
22. Assou, S. *et al.* Transcriptome analysis during human trophectoderm specification suggests new roles of metabolic and epigenetic genes. *PLoS ONE* **7**, e39306 (2012).
23. Koo, T. B. *et al.* Differential expression of the PEA3 subfamily of ETS transcription factors in the mouse ovary and peri-implantation uterus. *Reproduction* **129**, 651–657 (2005).
24. Yao, X. Q. *et al.* Glycogen synthase kinase-3 β regulates leucine-309 demethylation of protein phosphatase-2A via PPMT1 and PME-1. *FEBS Lett.* **586**, 2522–2528 (2012).
25. Glover, C. H. *et al.* Meta-analysis of differentiating mouse embryonic stem cell gene expression kinetics reveals early change of a small gene set. *PLOS Comput. Biol.* **2**, e158 (2006).
26. Koh, K. P. *et al.* Tet1 and Tet2 regulate 5-hydroxymethylcytosine production and cell lineage specification in mouse embryonic stem cells. *Cell Stem Cell* **8**, 200–213 (2011).
27. Lu, C. W. *et al.* Ras-MAPK signaling promotes trophectoderm formation from embryonic stem cells and mouse embryos. *Nature Genet.* **40**, 921–926 (2008).
28. Ng, R. K. *et al.* Epigenetic restriction of embryonic cell lineage fate by methylation of Elf5. *Nature Cell Biol.* **10**, 1280–1290 (2008).
29. Diéguez-Hurtado, R. *et al.* A Cre-reporter transgenic mouse expressing the far-red fluorescent protein Katusha. *Genesis* **49**, 36–45 (2011).
30. Beddington, R. S. & Robertson, E. J. An assessment of the developmental potential of embryonic stem cells in the midgestation mouse embryo. *Development* **105**, 733–737 (1989).
31. Macfarlan, T. S. *et al.* Embryonic stem cell potency fluctuates with endogenous retrovirus activity. *Nature* **487**, 57–63 (2012).
32. Pfister, S., Steiner, K. A. & Tam, P. P. Gene expression pattern and progression of embryogenesis in the immediate post-implantation period of mouse development. *Gene Expr. Patterns* **7**, 558–573 (2007).
33. Conley, B. J., Trounson, A. O. & Mollard, R. Human embryonic stem cells form embryoid bodies containing visceral endoderm-like derivatives. *Fetal Diagn. Ther.* **19**, 218–223 (2004).
34. Gordon, E. J., Gale, N. W. & Harvey, N. L. Expression of the hyaluronan receptor LYVE-1 is not restricted to the lymphatic vasculature; LYVE-1 is also expressed on embryonic blood vessels. *Dev. Dyn.* **237**, 1901–1909 (2008).
35. Thier, M. *et al.* Direct conversion of fibroblasts into stably expandable neural stem cells. *Cell Stem Cell* **10**, 473–479 (2012).
36. Kurian, L. *et al.* Conversion of human fibroblasts to angioblast-like progenitor cells. *Nature Methods* **10**, 77–83 (2013).
37. Halley, J. D. *et al.* Self-organizing circuitry and emergent computation in mouse embryonic stem cells. *Stem Cell Res.* **8**, 324–333 (2012).
38. Marks, H. *et al.* The transcriptional and epigenomic foundations of ground state pluripotency. *Cell* **149**, 590–604 (2012).

Supplementary Information is available in the online version of the paper.

Acknowledgements We are grateful to M. Torres for advice, and to K. Hochedlinger and R. Jaenisch for reagents. We also thank F. Beier, R. Serrano and N. Soberón for technical support. Work in the laboratory of M.S. is funded by the CNIO and by grants from the Spanish Ministry of Economy (MINECO, SAF), the Regional Government of Madrid (ReCaRe), the European Union (RISK-IR), the European Research Council (ERC Advanced Grant), the Botin Foundation, the Ramon Areces Foundation and the AXA Foundation. Work in the laboratory of M.M. is funded by grants from the MINECO (BFU), the Regional Government of Madrid (Cell-DD) and the ProCNIC Foundation. The funders had no role in study design, data collection and analysis, decision to publish, or preparation of the manuscript.

Author Contributions M.A. performed most of the experiments, contributed to experimental design, data analysis, discussion and writing; L.M. performed a substantial amount of experimental work, contributed to experimental design, data analysis, discussion and writing; C.P. contributed to experimental work, data analysis, discussion and writing; M.C. performed all the histopathological and immunohistochemical analyses; T.R. and I.O. contributed to the trophoblast stem cell and giant cell differentiation assays; O.G. analysed the RNAseq data; D. Megías supervised and helped with the confocal microscopy; O.D. performed RNAseq and determined the lentiviral genomic insertion sites; D. Martínez performed cell sorting and contributed to the bone marrow and peripheral blood analyses; M.M. supervised trophoblast differentiation assays and gave advice; S.O. generated the transgenic mice, constructed chimeras, and performed morula and blastocyst assays; M.S. designed and supervised the study, secured funding, analysed the data, and wrote the manuscript. All authors discussed the results and commented on the manuscript.

Author Information The primary RNA-seq data has been deposited in the GEO repository under accession number GSE48364. Reprints and permissions information is available at www.nature.com/reprints. The authors declare no competing financial interests. Readers are welcome to comment on the online version of the paper. Correspondence and requests for materials should be addressed to M.S. (mserrano@cniio.es).

METHODS

Generation of i4F reprogrammable mice. To generate reprogrammable mice, we transduced C57BL/6 mouse embryonic fibroblasts (MEFs) carrying a doxycycline-inducible transcriptional activator (rtTA) within the *Rosa26* locus¹⁴ (generously provided by K. Hochedlinger) with a lentivirus carrying a doxycycline-inducible tetracistronic cassette with the four murine reprogramming factors (*Oct4*, *Sox2*, *Klf4*, *c-Myc*)¹⁵ (Tet-O-FUW-OSKM, obtained from Addgene #20321). After lentiviral transduction, MEFs were treated with $1 \mu\text{g ml}^{-1}$ of doxycycline and colonies of iPS cells appeared after 1 week. Several iPS cells colonies were picked, expanded and microinjected into albino C57BL/6J-*Tyr^{c-2J}/J* E3.5 blastocysts (5–7 iPS cells per blastocyst) to obtain chimaeras. Chimaeric mice were backcrossed with C57BL/6J mice until the lentiviral transgenes were transmitted at Mendelian proportions (indicative of single integration site). The resulting reprogrammable i4F mice used in this study are in a pure C57BL/6J genetic background.

Southern blotting. Genomic DNA (tail tip) was digested overnight with BamHI and hybridized with probes designed to recognize exonic sequences of *Sox2* and *Klf4*. The probes were generated by PCR of genomic DNA with the following primers: *Sox2*-F: 5'-TACAGCATGATGCAGGAGCA-3'; *Sox2*-R: 5'-CTGGG CCGATGTCAGTCTAC-3'; *Klf4*-F: 5'-CAGCTTCAGTATCCGATCC-3'; *Klf4*-R: 5'-CGCCTCTTGCTTAATCTTGG-3'.

Transgene insertion site determination. We performed gene walking as described³⁹. Insertion sites were confirmed by PCR using primers against genomic sequences around the insertion site (*Neto2* in the case of line i4F-A, primer 5'-GCGTCA GGCAATTATATACTCTGG-3'; and *Pparg* in the case of line i4F-B, primer 5'-CA GCATCAAATGGCTCGGTA-3') and against the lentiviral transgene (5'-GCAC CATCAAAGGTCAGTG-3').

Animal procedures. Animal experimentation at the CNIO, Madrid, was performed according to protocols approved by the CNIO-ISCIII Ethics Committee for Research and Animal Welfare (CElyBA). Doxycycline (Sigma) was administered in the drinking water supplemented with 7.5% of sucrose. Experiments were performed indistinguishably with mice of both sexes and from 2 to 6 months of age. For bone marrow (BM) transplant, groups of 8 wild-type mice (C57BL/6J, 8–10-weeks old) per donor mouse were irradiated with 12 Gy. The following day, the bone marrow of the donor mice was harvested from the femora and tibiae and 2×10^6 – 2.5×10^6 cells, suspended in Leibovitz medium (Sigma, L5520), were intravenously injected per recipient. Experiments on transplanted mice were performed after a latency of at least 30 days to ensure BM reconstitution. For the intraperitoneal injections, wild-type mice were injected with 5×10^5 cells suspended in 100 μl of iPS cell medium. For subcutaneous teratomas, iPS or ES cells were trypsinized and 2×10^6 cells were subcutaneously injected into the flanks of immunocompromised nude mice (Swiss nude from Charles River). Teratomas were isolated when the diameter reached >1.5 cm and processed for histological analysis.

Cell culture. Primary mouse embryonic fibroblasts (MEFs) were obtained from embryos at E13.5 and cultured in DMEM supplemented with 10% of FBS and penicillin-streptomycin. The following C57BL6 ES cell lines were used: JM8.F6 (ref. 20), Bruce4 (ref. 21), and CNIO in-house made C57BL6.10. Cultures were routinely tested for mycoplasma and were always negative. ES and iPS cells were cultured over mitomycin-C inactivated feeder cells on gelatin-coated plates and in 'iPS medium': high-glucose DMEM supplemented with KSR (15%, Invitrogen), LIF ($1,000 \text{ U ml}^{-1}$), non-essential amino acids, penicillin-streptomycin, glutamax and β -mercaptoethanol. For lentiviral transduction, we transfected HEK293T (5×10^6) cells with Tet-O-FUW-OSKM (Addgene #20321) and packaging vectors using Eugene HD (Roche). Viral supernatants were collected twice a day on two consecutive days starting 24 h after transfection and were used to infect ROSA26-rtTA MEFs, previously plated at a density of 2×10^5 cells per well in 6-well plates. Previous to infection, polybrene was added to the viral supernatants at a concentration of $8 \mu\text{g ml}^{-1}$. For *in vitro* i4F reprogramming, i4F MEFs were plated at a density of 5×10^5 cells per well in 6-well gelatin-coated plates, and at a density of 3×10^5 for the kinetics assay. Infected MEFs or i4F-MEFs were cultured in iPS cell medium with doxycycline ($1 \mu\text{g ml}^{-1}$). Medium was changed every 48 h until iPS cell colonies appeared (after ~7 days of treatment). Reprogramming plates were stained for alkaline phosphatase activity (AP detection kit, Sigma-Aldrich). When indicated, ES cells or *in vivo* iPS cells were retrovirally infected with a vector expressing GFP (pMSCV-PIG) and infected cells were sorted by FACS.

In vivo iPS cell isolation. Peripheral blood (0.3–0.5 ml) was collected directly from the heart of i4F mice at the time of necropsy, and was subjected to two rounds of erythrocyte lysis in ammonium chloride solution (Stem Cells). First round of lysis with 10 ml, for 15 min at room temperature, followed by centrifugation, and a second round of lysis with 3 ml, for 15 min at room temperature, followed by neutralization with 12 ml of iPS cell medium. Cells were pelleted and counted, recovering $\sim 10^6$ cells per mouse. Cells were resuspended, plated on feeders and cultured in iPS cell medium.

Immunofluorescence. Cells previously seeded in cover slips were fixed in 4% paraformaldehyde for 20 min, permeabilized (PBS 0.1% Triton X-100) for 15 min and blocked in FBS, for 1 h at room temperature. For the detection of OCT4 we used two antibodies with similar results, BD 611203, dilution 1:200, and Santa Cruz sc-5279, dilution 1:400; for NANOG, Novus NB100 58842, dilution 1:50; and for CDX2, Epitomics #2475-1, dilution 1:400. Cells were inspected under a Leica SP5 microscope equipped with white light laser and hybrid detection.

Chimera generation and germline contribution. For chimera generation, *in vivo* iPS cells (5–7 cells per embryo, ~10 passages) were microinjected into C57BL/6J-*Tyr^{c-2J}/J* blastocysts and transferred to Crj:CD1 (ICR) pseudopregnant females. To study the contribution to germline, GFP-infected *in vivo* iPS cells (~14 passages) were similarly microinjected into blastocysts and the gonads from chimaeric male E14.5 embryos were isolated, fixed in 4% paraformaldehyde, and analysed for GFP fluorescence in whole mount with laser scanning confocal microscope SP5 from Leica, equipped with white light laser and hybrid detection. Lens used for imaging were $\times 20$ (dry lens) 0.7 numerical aperture and $\times 63$ (water lens) with a 1.2 numerical aperture.

RNA-seq methods. Total RNA was extracted from ES cells (JM8.F6 (ref. 20), Bruce4 (ref. 21), and CNIO in-house made C57BL6.10), *in vitro* iPS cells (3 from i4F-A MEFs and 2 from i4F-B MEFs) and *in vivo* iPS cells (3 from i4F-A mice and 3 from i4F-B mice), all with ~10 passages. 1 μg of total RNA, with RIN (RNA integrity number) numbers in the range 9.8 to 10 (Agilent 2100 Bioanalyzer), was used. PolyA+ fractions were processed using TruSeq Stranded mRNA Sample Preparation Kit (Agilent). The resulting directional cDNA libraries were sequenced for 40 bases in a single-read format (Genome Analyzer IIx, Illumina). The complete set of reads have been deposited in the GEO repository (accession number GSE48364). Reads were aligned to the mouse genome (GRCm38/mm10) with TopHat-2.0.4 (ref. 40) (using Bowtie 0.12.7 (ref. 41) and Samtools 0.1.16 (ref. 42)), allowing two mismatches and five multihits. Transcripts assembly, estimation of their abundances and differential expression were calculated with Cufflinks 1.3.0 (ref. 40), using the mouse genome annotation data set GRCm38/mm10 from the UCSC Genome Browser.

Trophoblast stem cell differentiation. ES and iPS cells (all with ~10 passages) were plated on feeders (7×10^4 cells per well in 6-well plates) in iPS cells medium and 24 h later medium was changed into TS differentiation medium that contained the following components: 3 volumes of RPMI 1640 (with 20% FBS, 1 mM pyruvate, 2 mM L-glutamine, 100 μM β -mercaptoethanol), 7 volumes of conditioned medium from mitomycin-C-inactivated fibroblasts, 25 pg ml^{-1} of FGF4 (R&D Systems, 235-F4-025) and 1 $\mu\text{g ml}^{-1}$ of heparin (Sigma, H3149). Medium was changed every other day, and all cells were split once at day 2. For giant cell differentiation, trophoblast stem cell differentiated *in vivo* iPS cells and established trophoblast stem cells were plated on gelatin and cultured in RPMI 1640 (with 20% FBS, 1 mM pyruvate, 2 mM L-glutamine, 100 μM β -mercaptoethanol) in the absence of heparin and FGF4 for 3 days.

Analysis of trophoblast lineage contribution. GFP-labelled ES cells or *in vivo* iPS cells (5–7 cells, all with ~14 passages) were aggregated or microinjected into 8-cell stage embryos using standard techniques⁴³. Morulas were incubated overnight and observed under the confocal microscope in KSOM (Chemical International) microdrops under mineral oil. In some cases Tg.CAG-Katushka embryos²⁹ were used as recipients. To study the contribution of GFP-*in vivo* iPS cells to the placenta, blastocysts were transferred to pseudopregnant females and embryos (E14.5) with their placentas were collected in PBS and observed directly under a fluorescence-equipped stereomicroscope or fixed for immunostaining.

Analysis of mRNA levels. Total RNA was extracted from cell or tissue samples with Trizol (Invitrogen), following provider's recommendations and retrotranscribed into cDNA following the manufacturer's protocol (Maxima First Strand cDNA synthesis Kit for RT-qPCR, Fermentas). Quantitative real-time-PCR was performed using Syber Green Power PCR Master Mix (Applied Biosystems) in an ABI PRISM 7700 thermocycler (Applied Biosystem). For input normalization, we used the house-keeping genes *Actb* (β -actin) or *Gapdh*. The primers used were: *Actb* forward primer: 5'-GGCACCACACCTTCTACAATG-3', *Actb* reverse primer: 5'-GTGGTGGT GAAGCTGTAGCC-3'; *Ccne* forward primer: 5'-GTGGCTCCGACCTTTCAG TC-3', *Ccne* reverse primer: 5'-CAGAGTCTGTCAATCTTGGCA-3'; *Cdx2* forward primer: 5'-CAAGGACGTGAGCATGTATCC-3', *Cdx2* reverse primer: 5'-GTAACCACCGTAGTCCGGGA-3'; *E2A-c-Myc* forward primer, 5'-GGCTG GAGATGTTGAGAGCAA-3', *E2A-c-Myc* reverse primer 5'-AAAGGAAATCC AGTGGCGC-3'; *Eomes* forward primer 5'-TTCACCTTCTCAGAGACACAGT TCAT-3', *Eomes* reverse primer 5'-GAGTTAAGCTGTCATTCTCTGAAGCC-3'; *Epcam* forward primer 5'-GCGGCTCAGAGAGAGATGTC-3', *Epcam* reverse primer 5'-CCAAGCATTTAGACGCCAGTTT-3'; *Etv4* forward primer, 5'-TGGTGAT CAAACAGGAGCG-3', *Etv4* reverse primer, 5'-GGGTGGAGGTACATTGA TGC-3'; *Fgfr2* forward primer, 5'-GAGGAATACTTGGATCTCACC-3', *Fgfr2* reverse primer 5'-CTGGTGTCTGCTGTTTGGG-3'; *Gapdh* forward primer

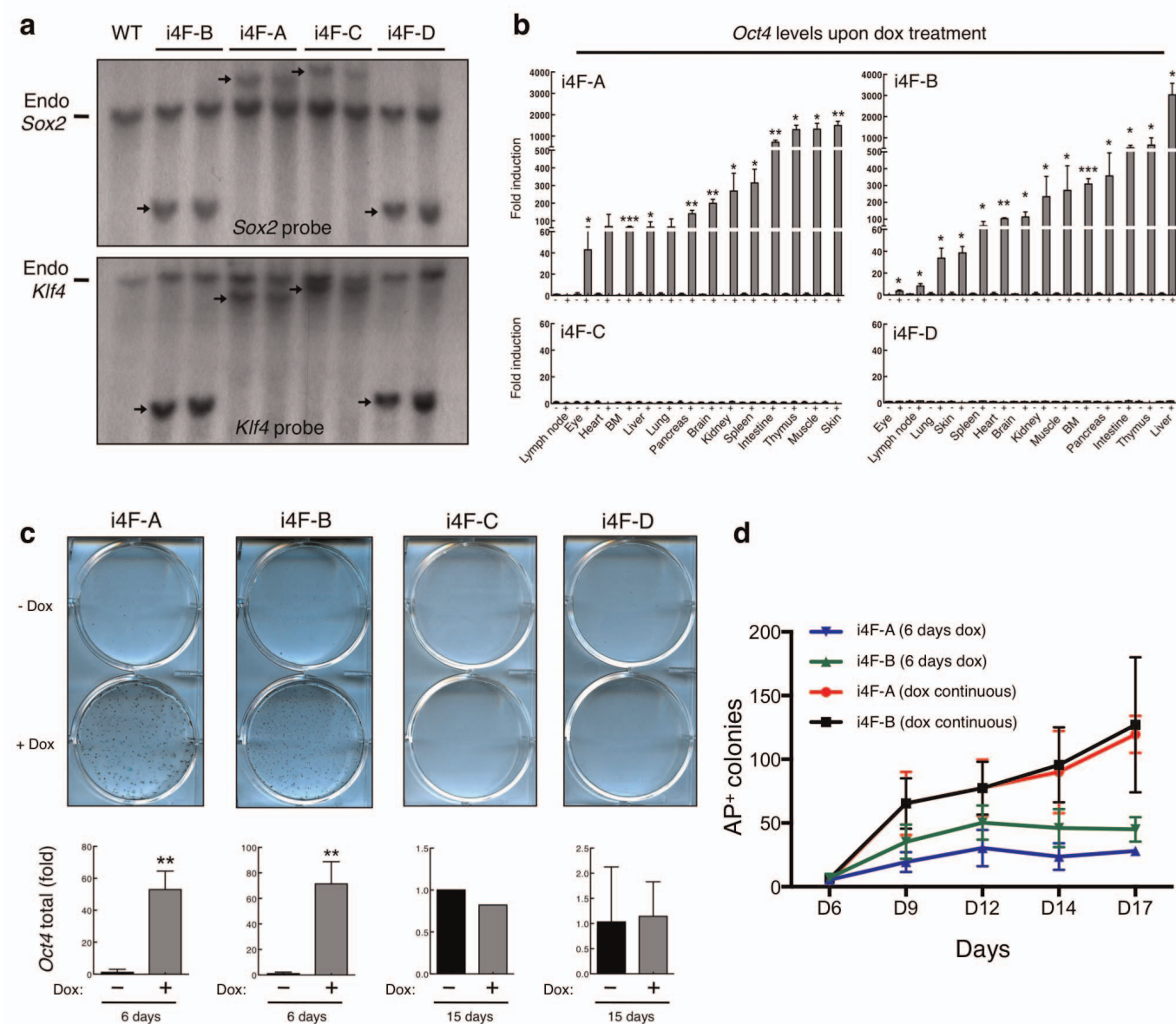
5'-TTCACCACCATGGAGAAGGC-3', *Gapdh* reverse primer 5'-CCCTTTTGGCTCCACCT-3'; *Gata6* forward primer 5'-TCATTACCTGTGCAATGCATGG-3', *Gata6* reverse primer 5'-ACGCCATAAGGTAGTGGTTGTGGT-3'; *Gbx2* forward primer 5'-CAACTTCGACAAAGCCGAGG-3', *Gbx2* reverse primer 5'-ACTCGTCTTCCCTTGCCCT-3'; *IAP* forward primer 5'-CAGACTGGGAGGAAGAAGCA-3', *IAP* reverse primer 5'-ATTGTTCCCTCACTGGCAAA-3'; *Lin28a* forward primer 5'-GAAGAACATGCAGAAGCGAAGA-3', *Lin28a* reverse primer 5'-CCGCAGTTGTAGCACCTGTCT-3'; *Mmp12* forward primer 5'-CTGCTCCCATGAATGACAGTG-3', *Mmp12* reverse primer 5'-AGTTGCTTCTAGCCAAAGAAC-3'; *MuERV-L* forward primer 5'-CCCATCATGAGCTGGGTACT-3', *MuERV-L* reverse primer 5'-CGTGCAGAGCCATCAGTAAA-3'; *Nanog* forward primer 5'-CAAGGGTCTGCTACTGAGATGCTCTG-3', *Nanog* reverse primer 5'-TTTGTGTTGGGACTGGTAGAAGAATCAG-3'; *Neto2* forward primer 5'-GTCGTGGAAGGGATTGCTGT-3', *Neto2* reverse primer 5'-AAGCAAATGACCTCCATTGC-3'; *Nlrp4* forward primer 5'-TGCTCTGAATGAAGGAGACCA-3', *Nlrp4* reverse primer 5'-TTACTCCTTACAAACACAGAGCA-3'; *Oct4* (total) forward primer 5'-GTTGGAGAAGGTGGAACCA-3', *Oct4* (total) reverse primer 5'-CCAAGGTGATCCTCTTCTGC-3'; *Pparg* forward primer 5'-GGCCGAGAAGGAGAAGCTGTTG-3', *Pparg* reverse primer 5'-TGGCCACCTCTTTGCTCTGCTC-3'; *Ppm1j* forward primer 5'-AGAGCAGGCACATGAGGAT-3', *Ppm1j* reverse primer 5'-CATCAAACAGGCCCCAGTAG-3'; *Sox1* forward primer, 5'-TGAACGCCTTCATGGTGTGGTC-3', *Sox1* reverse primer 5'-GCGCGGCCGGTACTTGTAAAT-3'; *Sox2* forward primer 5'-CGTAGATGGCCCAAGGAGAA-3', *Sox2* reverse primer 5'-GCTTCTCGGTCTCGGACAAA-3'; *Sox2-Klf4* forward primer 5'-ACTGCCCTGTGCGACAT-3', *Sox2-Klf4* reverse primer 5'-CATGTCTGAGCTCGCCAGGTG-3'; *T* forward primer 5'-GCTTCAAGGAGCTAACTAACGAG-3', *T* reverse primer 5'-CCAGCAAGAAAGAGTACATGGC-3'; *Tgm1* forward primer 5'-CAGATCTGCCCTCAGGCTT-3', *Tgm1* reverse primer 5'-CCATTCTTGACGGACTCCAC-3'; *Tnc* forward primer 5'-ACCATGGGTACAGGCTGTTG-3', *Tnc* reverse primer 5'-CCTTCTGCACTGAAGTTGCC-3'; *Utf1* forward primer 5'-TGTCCCGGTGACTACGTCT-3', *Utf1* reverse primer 5'-CCCAGAGTAGCTCCGTCTCT-3'; *Zscan4* forward primer 5'-GAGATTCATGGAGAGTCTGACTGATGAGTG-3', *Zscan4* reverse primer 5'-GCTGTGTGTTTCAAAAAGCTTGATGACTTC-3'; *8430410A17Rik* forward primer 5'-TGGATTCTACGAGTGGCAGC-3', *8430410A17Rik* reverse primer 5'-CTGTCTGAAGCATCGTTCCC-3'.

Protein analysis. Tissue samples (50–100 mg) were homogenized in medium-salt lysis buffer (150 mM NaCl, 50 mM Tris pH 8, 1% NP40 and protein inhibitors cocktail) using Precellys 24 homogenizer. A total protein amount of 30 µg was loaded per lane in a NuPAGE 4–12% Bis-Tris gel 1.0 mm (Invitrogen) and electrophoresed in MES SDS Running Buffer (Invitrogen). The following antibodies were used: for OCT4, Santa Cruz Biotechnology sc-9081, 1:500; for NANOG, Millipore AB 5731, 1:5,000; for SOX2, Santa Cruz sc-17320, 1:500; and for actin, Sigma-Aldrich AC-15, 1:5,000.

Immunohistochemistry. Tissue samples were fixed in 10% formaline, paraffine-embedded and cut in 3-µm sections, which were mounted in superfrostplus porta-objects and re-hydrated. For immunohistochemistry, paraffine sections underwent antigenic exposure process into the Discovery XT (Roche) system with CC1 buffer for standard antigen retrieval. The following primary antibodies were used: for NANOG, Cell Signalling Biotechnology, 8822; for cytokeratin 19 (CK19), CNIO Monoclonal Antibodies Core Unit, AM-TROMA III; for placental lactogen 1 (PL-1), Santa Cruz Biotechnology, sc34713; for cytokeratin 8 (CK8), CNIO Monoclonal Antibodies Core Unit, AM-TROMA I; for GFP, Roche, 11814460001; for SOX2, Cell Signalling Technology, 3728; for T/BRACHYURY, Santa Cruz Biotechnology, sc17743; for GATA4, Santa Cruz Biotechnology, sc1237; for CDX2, Biogenex, MU392A-UC; for α -fetoprotein (AFP), R&D Systems, AF5369; and for OCT4, Santa Cruz Biotechnology, sc-9081. Slides were then incubated with the corresponding secondary antibodies conjugated with peroxidase from Dako.

Statistical methods. Sample sizes for comparisons between cell types or between mouse genotypes followed Mead's recommendations⁴⁴. In particular, the accumulated n value (N) for a given comparison minus the number of groups or treatments (T) (for example, genotypes) was between 10 and 20, as recommended⁴⁴. Samples (cells or mice) were allocated to their experimental groups according to their pre-determined type (cell type or mouse genotype) and therefore there was no randomization. Investigators were not blinded to the experimental groups (cell types or mouse genotypes). In the case of Fig. 1e, no mice were censored. In the case of Fig. 2a, b, only mice that died with teratomas were considered, as indicated in the ordinate axes; mice that died due to other complications were censored and indicated with ticks in the Kaplan–Meier curves. Quantitative PCR data were obtained from independent biological replicates (n values indicated in the corresponding figure legends) and were tested for normal distribution using the Shapiro–Wilk test and for equal variance using the F -test. Normal distribution and equal variance was confirmed in the large majority of data and, therefore, we assumed normality and equal variance for all samples. Based on this, we used the Student's t -test (two-tailed, unpaired) to estimate statistical significance. For contingency tables, we used the Fisher's exact test.

39. Domínguez, O. & López-Larrea, C. Gene walking by unpredictably primed PCR. *Nucleic Acids Res.* **22**, 3247–3248 (1994).
40. Trapnell, C. *et al.* Differential gene and transcript expression analysis of RNA-seq experiments with TopHat and Cufflinks. *Nature Protocols* **7**, 562–578 (2012).
41. Langmead, B., Trapnell, C., Pop, M. & Salzberg, S. L. Ultrafast and memory-efficient alignment of short DNA sequences to the human genome. *Genome Biol.* **10**, R25 (2009).
42. Li, H. *et al.* The Sequence Alignment/Map format and SAMtools. *Bioinformatics* **25**, 2078–2079 (2009).
43. Pease, S. & Sounders, T. *Advanced Protocols for Animal Transgenesis, an ISTT Manual*. (Springer-Verlag, 2011).
44. Festing, M. F. W., Overend, P., Gaines Das, R., Cortina Borja, M. & Berdoy, M. *The design of animal experiments. Reducing the use of animals in research through better experimental design* (Royal Society of Medicine Press, 2002).

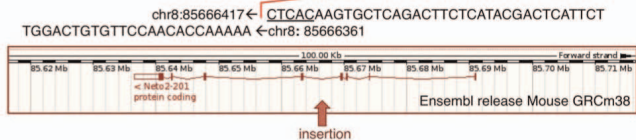


Extended Data Figure 1 | Characterization of four independent i4F transgenic mouse lines. **a**, Southern blot of tail tip genomic DNA digested with BamHI and hybridized with specific probes for *Sox2* and *Klf4*. **b**, Mice of the indicated transgenic lines carrying the reprogramming transgene (+) or without it (–) were treated with doxycycline (1 mg ml^{-1}) for 6 days. The mRNA levels of *Oct4* were determined by qRT-PCR. Values correspond to the average and s.d. ($n = 3$ mice per transgenic line) and are relative to the levels of wild-type mice treated with doxycycline. **c**, MEFs of the indicated mouse lines were treated with doxycycline ($1 \mu\text{g ml}^{-1}$). Colonies of iPS cells in the i4F-A and i4F-B plates were stained for alkaline phosphatase (AP) 10 days after induction. In the case of i4F-C and i4F-D, plates were stained after 15 days but no iPS cell

colonies were observed. In parallel, total *Oct4* mRNA levels were measured at the indicated times by qRT-PCR. Values correspond to the average and s.d. For i4F-A, i4F-B, and i4F-D, $n = 3$ MEF preparations; for i4F-C, $n = 1$. **d**, Comparison of the *in vitro* reprogramming kinetics and efficiency of MEFs from lines i4F-A and i4F-B. Reprogramming was induced with two different protocols: $1 \mu\text{g ml}^{-1}$ of doxycycline for 6 days, or continuous treatment with $1 \mu\text{g ml}^{-1}$ of doxycycline. AP⁺ colonies were counted at the indicated times. Values correspond to the average and s.d. ($n = 3$ independent MEF isolates per line). In **b** and **c**, statistical significance was evaluated by the Student's *t*-test (unpaired, two-tailed): * $P < 0.05$, ** $P < 0.01$, *** $P < 0.001$.

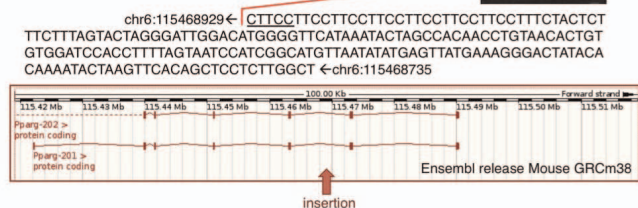
Lentiviral insertion in i4F-A: *Neto2* gene

TGGAAGGGCTAAT---[OSKM]---GGAAAATCTCTAGCA

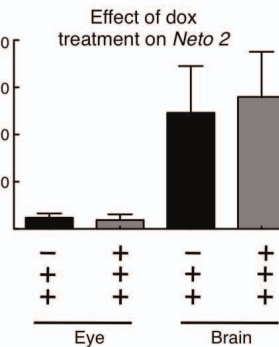
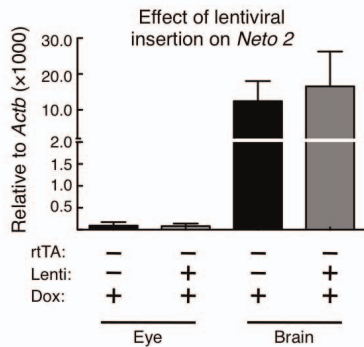


Lentiviral insertion in i4F-B: *Pparg* gene

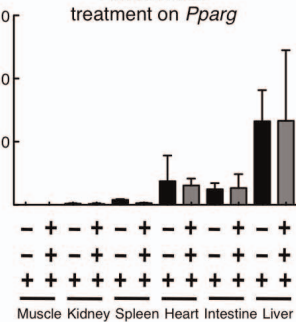
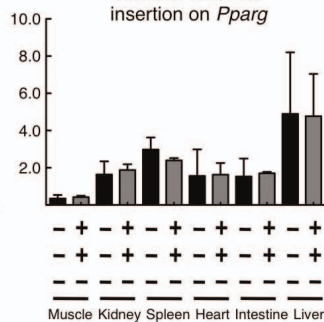
TGGAAGGGCTAAT---[OSKM]---GGAAAATCTCTAGCA



i4F-A mice

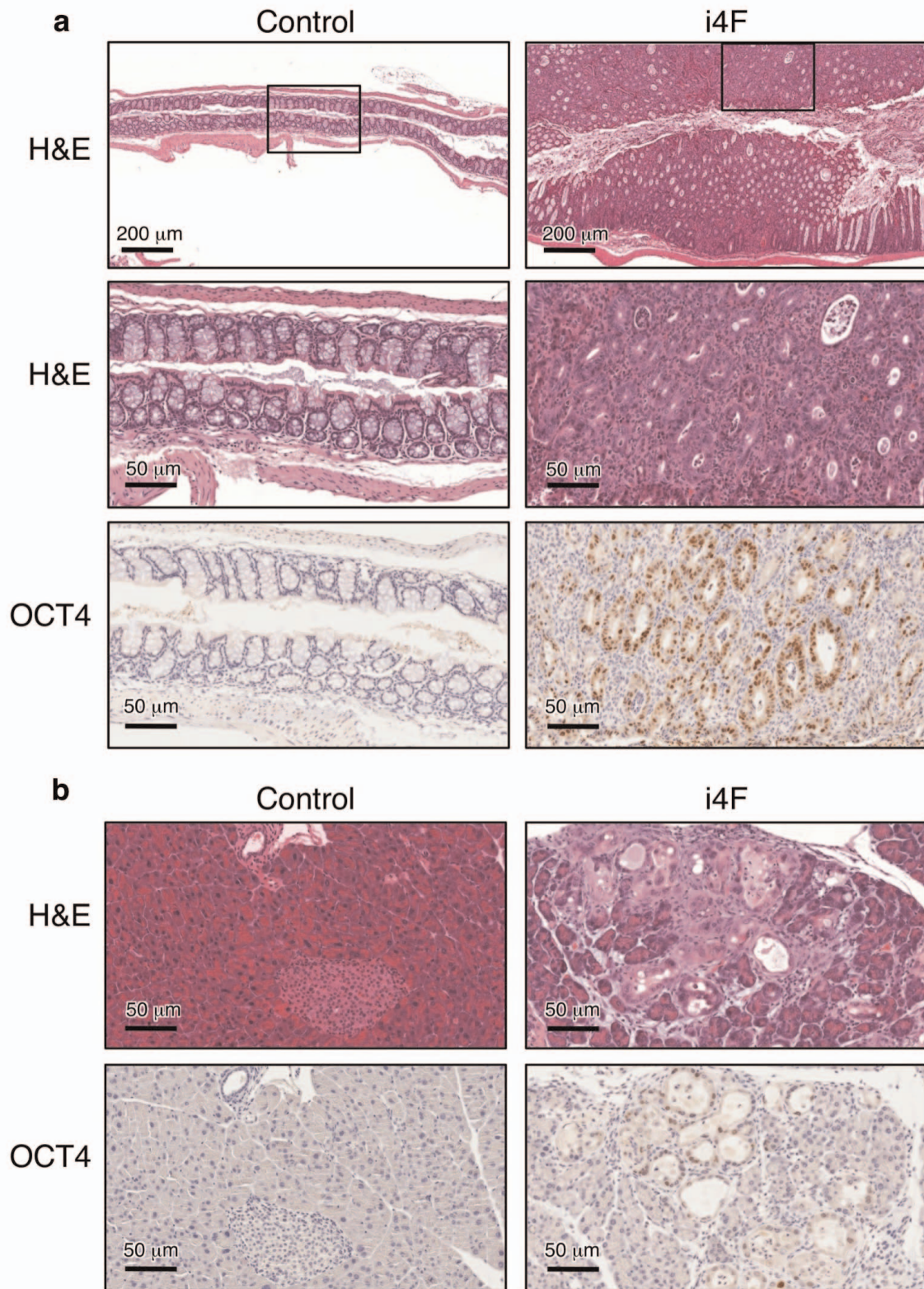


Effect of dox treatment on *Pparg*



Extended Data Figure 2 | Genomic insertion sites of lentiviral transgenes i4F-A and i4F-B and their effect on the host genes. **a.** Primers used for PCR to confirm insertion are shown in blue and underlined. These primers were used together with a common primer hybridizing to internal lentiviral sequences (see Methods). The 4 base pairs flanking the insertion site are duplicated upon lentiviral insertion and are underlined. A map of each gene is shown indicating with an arrow the approximate location of the lentiviral transgene. The pictures

of PCR agarose gels correspond to the PCR products obtained with the flanking primer (underlined sequence in blue) and the internal lentiviral primer (not shown) (see Methods). **b**, The indicated tissues were used to measure the levels of *Neto2* (host gene for the lentiviral transgene i4F-A) or *Pparg* (host gene for the lentiviral transgene i4F-B). Values correspond to the average and s.d. ($n = 3$ mice per condition). Statistical significance was evaluated by Student's *t*-test (unpaired, two-tailed). No significant differences were observed.



Extended Data Figure 3 | Histological alterations of the intestine and pancreas upon induction of i4F reprogrammable mice. Mice were treated with doxycycline (1 mg ml^{-1}) for 6 days. Haematoxylin and eosin (H&E)

staining and immunohistochemistry of OCT4 in the intestine (a) and pancreas (b). Similar alterations were found in both lines, i4F-A and i4F-B.

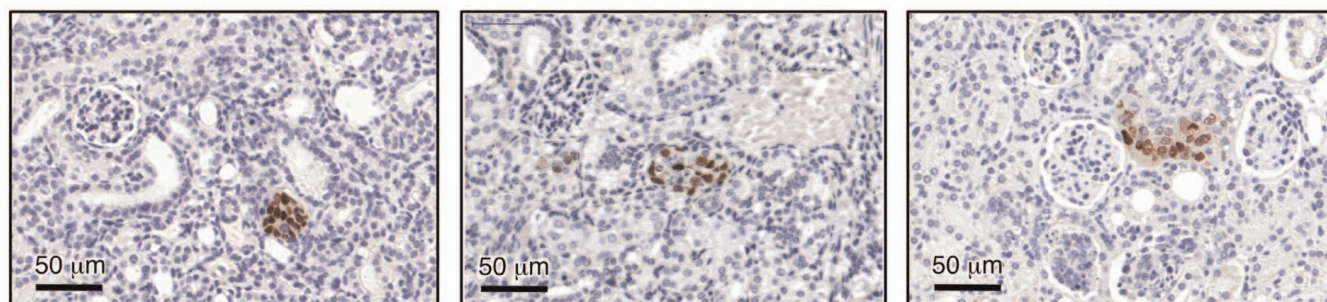
a



b

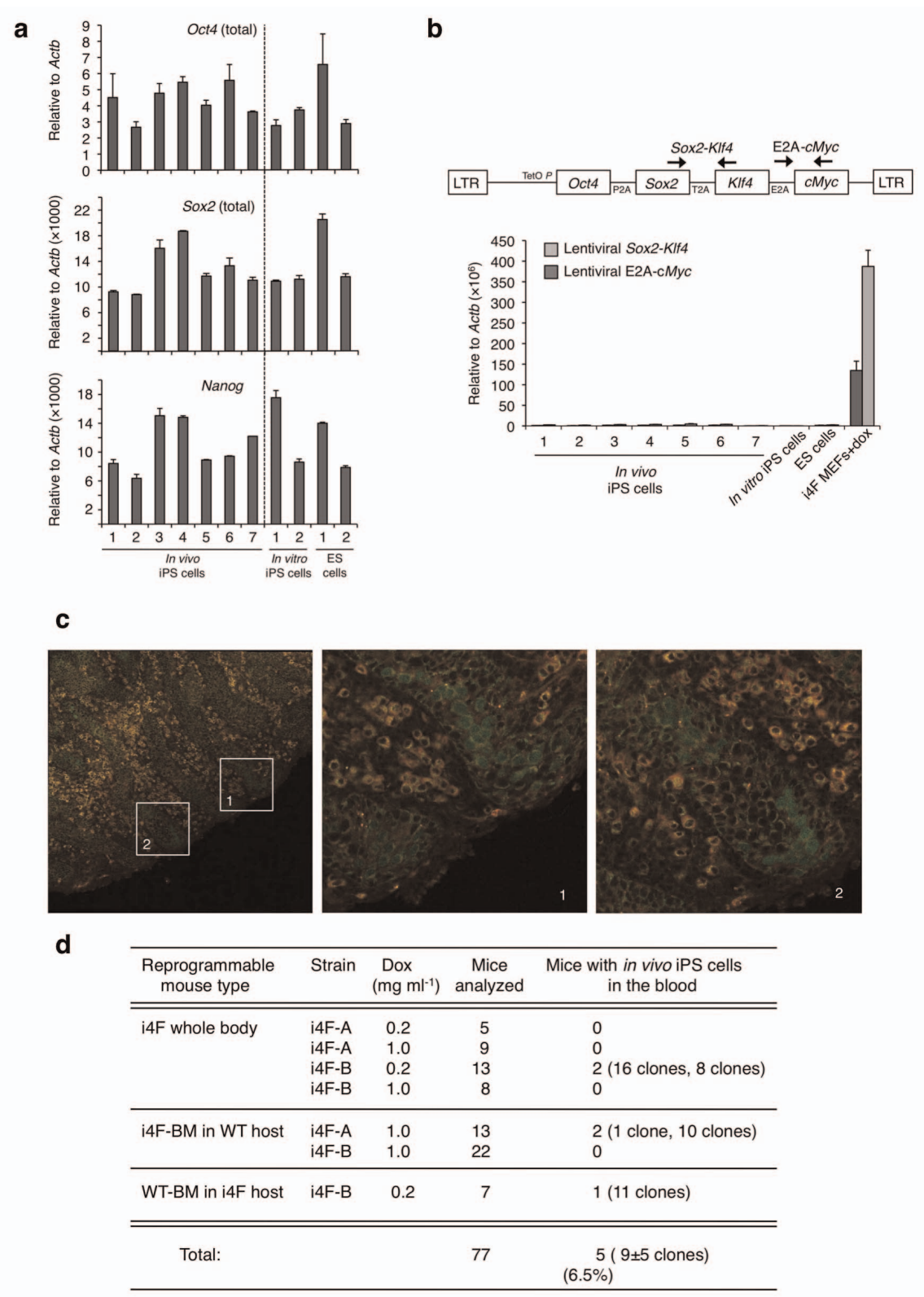
	Mice analyzed with teratomas	Teratomas	Other tumours in the same mice
i4F-A	8	Multiple per mouse	1 Wilm's tumour 1 skin papilloma 1 mouse with intestinal polyps
i4F-B	7	Multiple per mouse	1 urothelial carcinoma 1 mouse with intestinal polyps

c



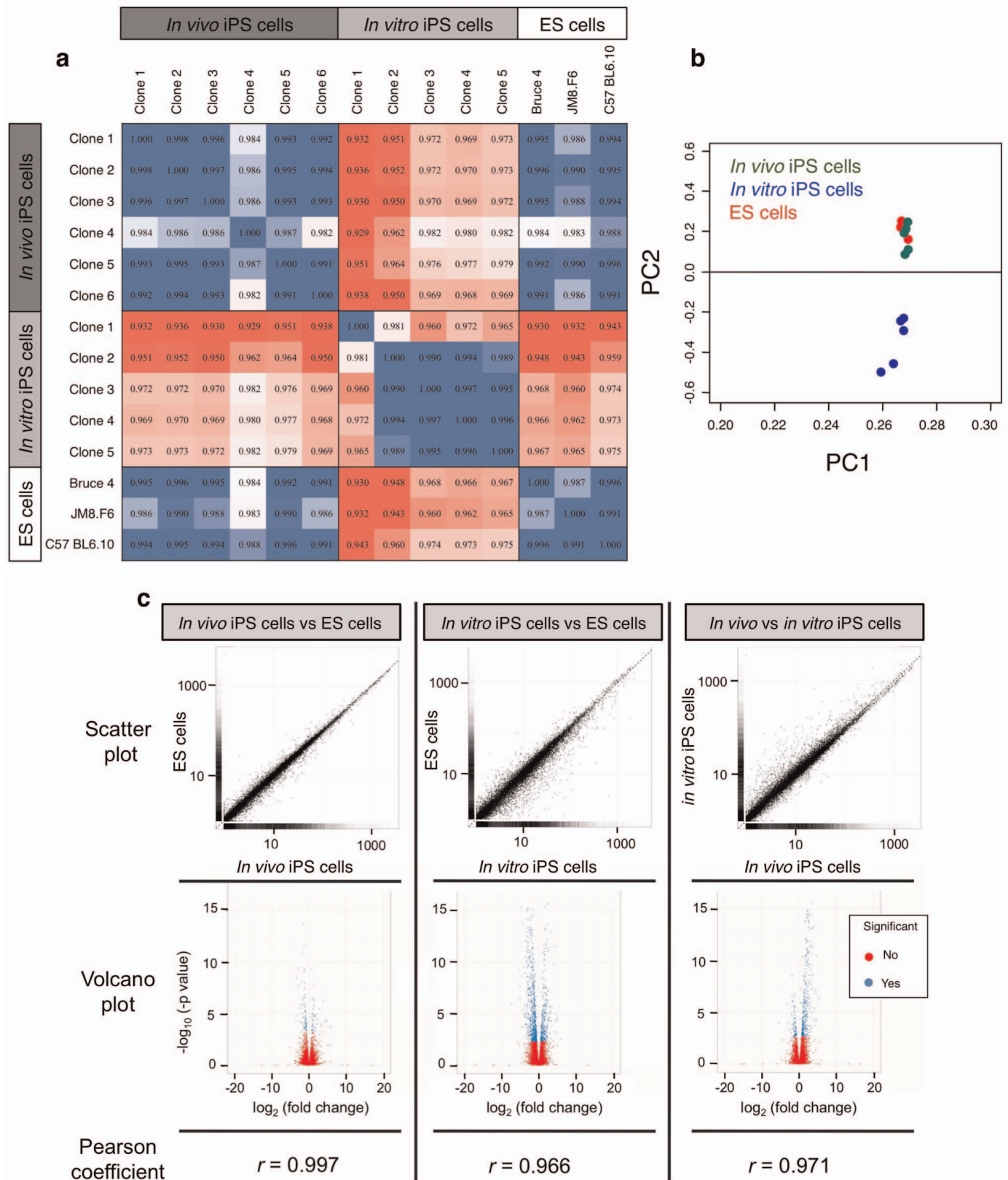
Extended Data Figure 4 | i4F induction leads to the appearance of tumoral masses and *in situ* reprogramming events. **a**, Reprogrammable mouse with multiple tumoral masses in the liver and kidneys (a representative example

is shown from 15 mice analysed with teratomas). **b**, Incidence of other tumours in reprogrammable mice with teratomas. **c**, Three examples of NANOG-positive tubules in different induced reprogrammable mice.



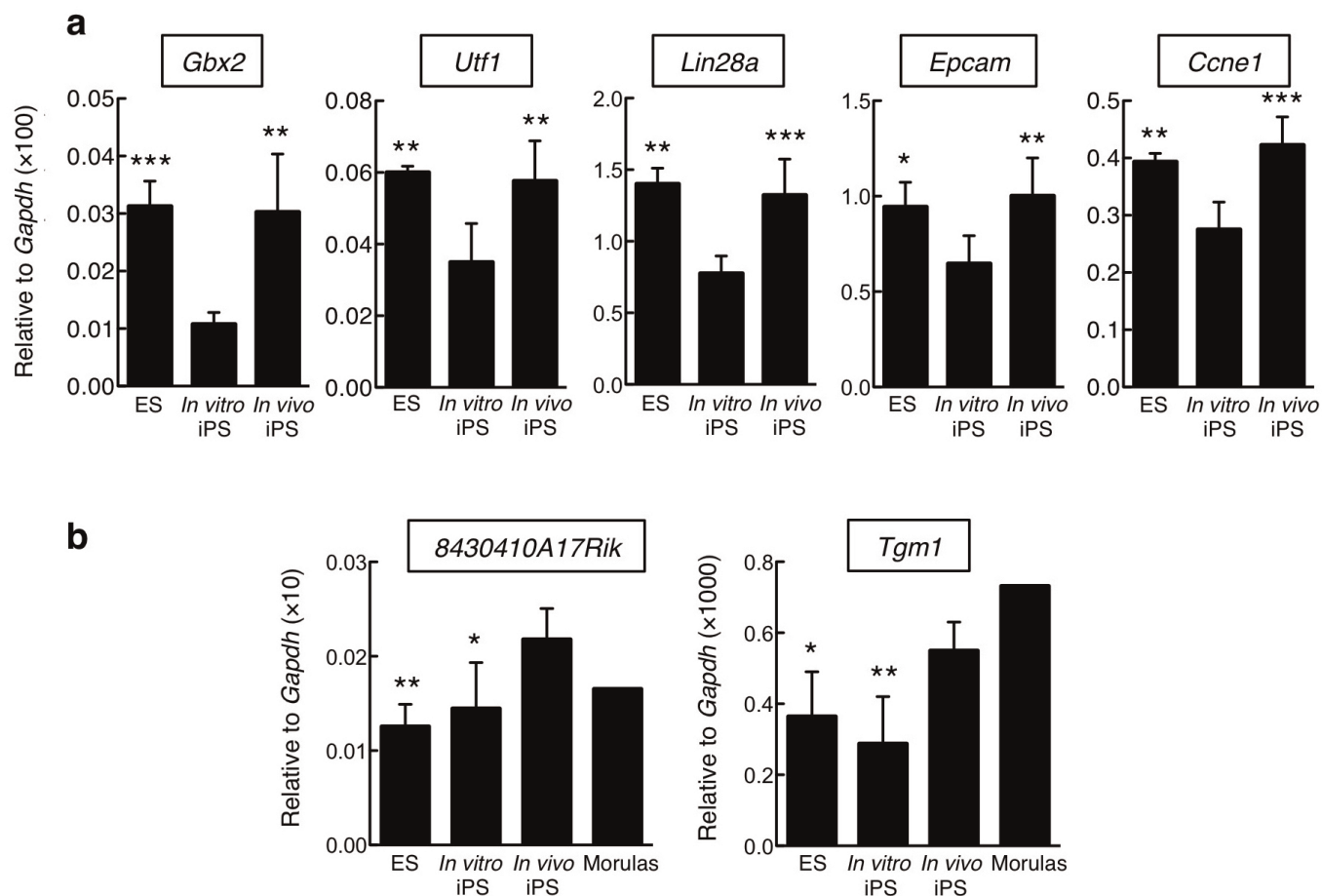
Extended Data Figure 5 | Characterization of *in vivo* iPS cells. **a**, Expression of pluripotency markers in the indicated cell types. Data correspond to qRT-PCR from seven independent *in vivo* iPS cell clones, two *in vitro* iPS cell clones (no. 1: *in vitro* reprogrammed i4F MEFs; no. 2: *in vitro* reprogrammed wild-type MEFs infected with lenti-OSKM), and two ES cell clones (no. 1: C57BL6.10; no. 2: G4). Values correspond to the average \pm s.d. of 3 technical replicates. **b**, Silencing of the lentiviral cassette in *in vivo* iPS cell clones. Upper

part, location of the PCR primers used. Lower part, lentiviral RNA levels in *in vivo* iPS cells (7 independent clones), in an *in vitro* iPS cell clone (*in vitro* reprogrammed i4F MEFs), in an ES cell line (C57BL6.10), and in i4F-MEFs induced with doxycycline for 3 days. Values correspond to the average \pm s.d. of 3 technical replicates. **c**, Chimaeric E14.5 testis generated with a GFP-labelled *in vivo* iPS cells. Magnifications show germ cells derived from *in vivo* iPS cells. **d**, Summary of the isolation of *in vivo* iPS cells from the bloodstream.



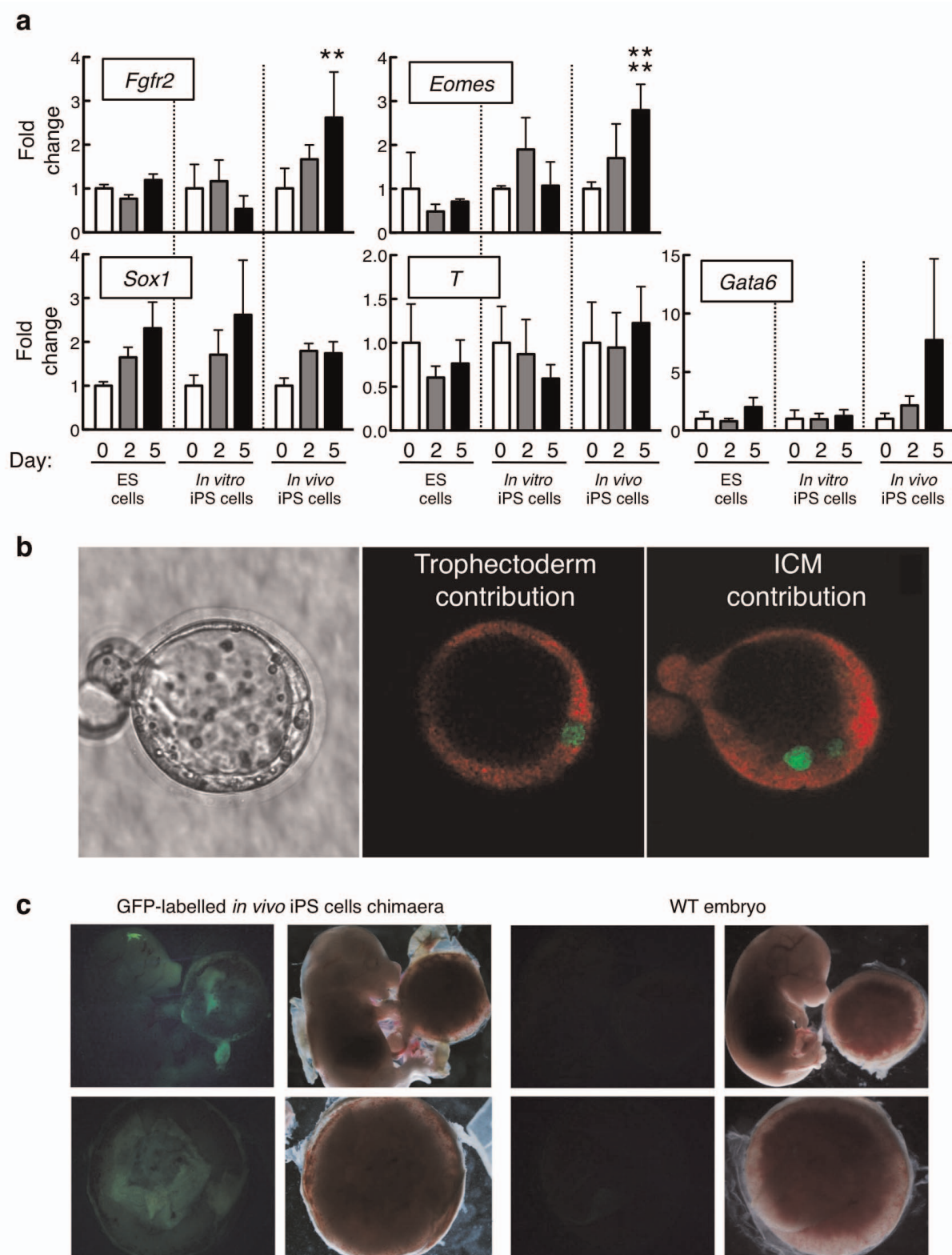
Extended Data Figure 6 | Transcriptomic profiles of *in vivo* iPS cells, *in vitro* iPS cells and ES cells. **a**, Pearson correlation coefficients among all sequenced samples. The highest and the lowest coefficients are coloured in a blue to red gradient. **b**, Principal component analysis of the transcriptomes of *in vivo* iPS cells, *in vitro* iPS cells and ES cells. Data correspond to 6 clones of *in vivo* iPS cells, 5 clones of *in vitro* iPS cells, and 3 lines of ES cells (C57BL6.10, JM8.F6 and Bruce4). **c**, Upper part, scatter plots representing the expression of each gene in

the indicated pairs of cell types. Middle part, volcano plots representing the P value of the differences in expression of each gene between the corresponding cell types. Significant P values are in blue (that is, indicating differentially expressed genes). Non-significant P values are in red (that is, indicating genes that are not differentially expressed). Lower part, Pearson coefficient correlation among samples. Data correspond to 6 clones of *in vivo* iPS cells, 5 clones of *in vitro* iPS cells, and 3 lines of ES cells (C57BL6.10, JM8.F6 and Bruce4).



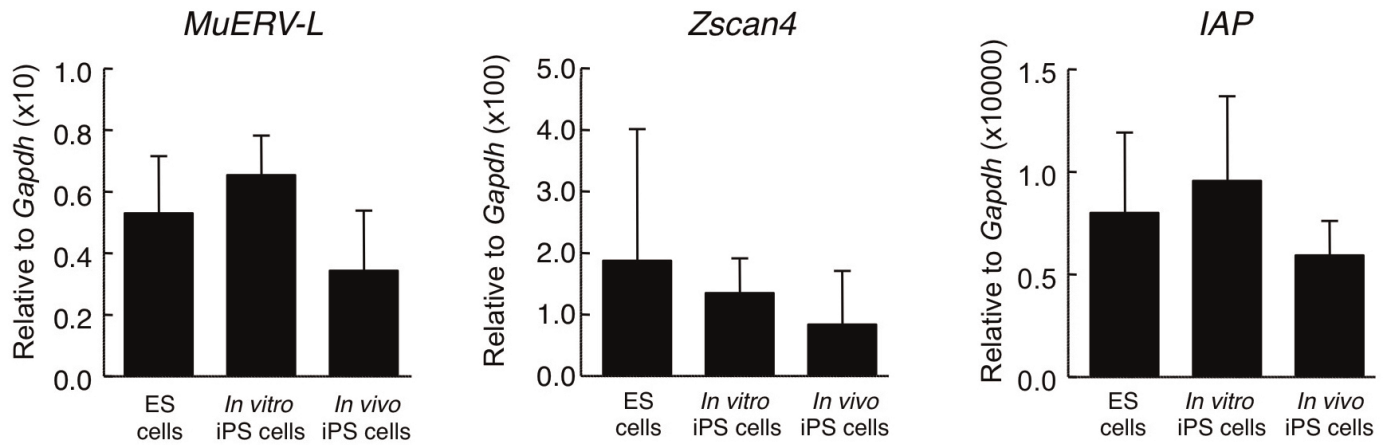
Extended Data Figure 7 | Validation of RNA-seq data. **a**, Genes upregulated in *in vivo* iPS and ES cells versus *in vitro* iPS cells. **b**, Genes upregulated in *in vivo* iPS cells versus ES cells and *in vitro* iPS cells. Expression levels of the indicated genes in *in vivo* iPS cells ($n = 6$ clones), *in vitro* iPS cells ($n = 5$ clones) and ES cells ($n = 3$ lines C57BL6.10, JM8.F6 and Bruce4). A sample of RNA

derived from a preparation of ~ 170 morulas was also included in **b**. Values correspond to the average \pm s.d. Statistical significance was evaluated relative to *in vitro* iPS cells (**a**) or relative to *in vivo* iPS cells (**b**) by the Student's *t*-test (unpaired, two-tailed): * $P < 0.05$, ** $P < 0.01$, *** $P < 0.001$.



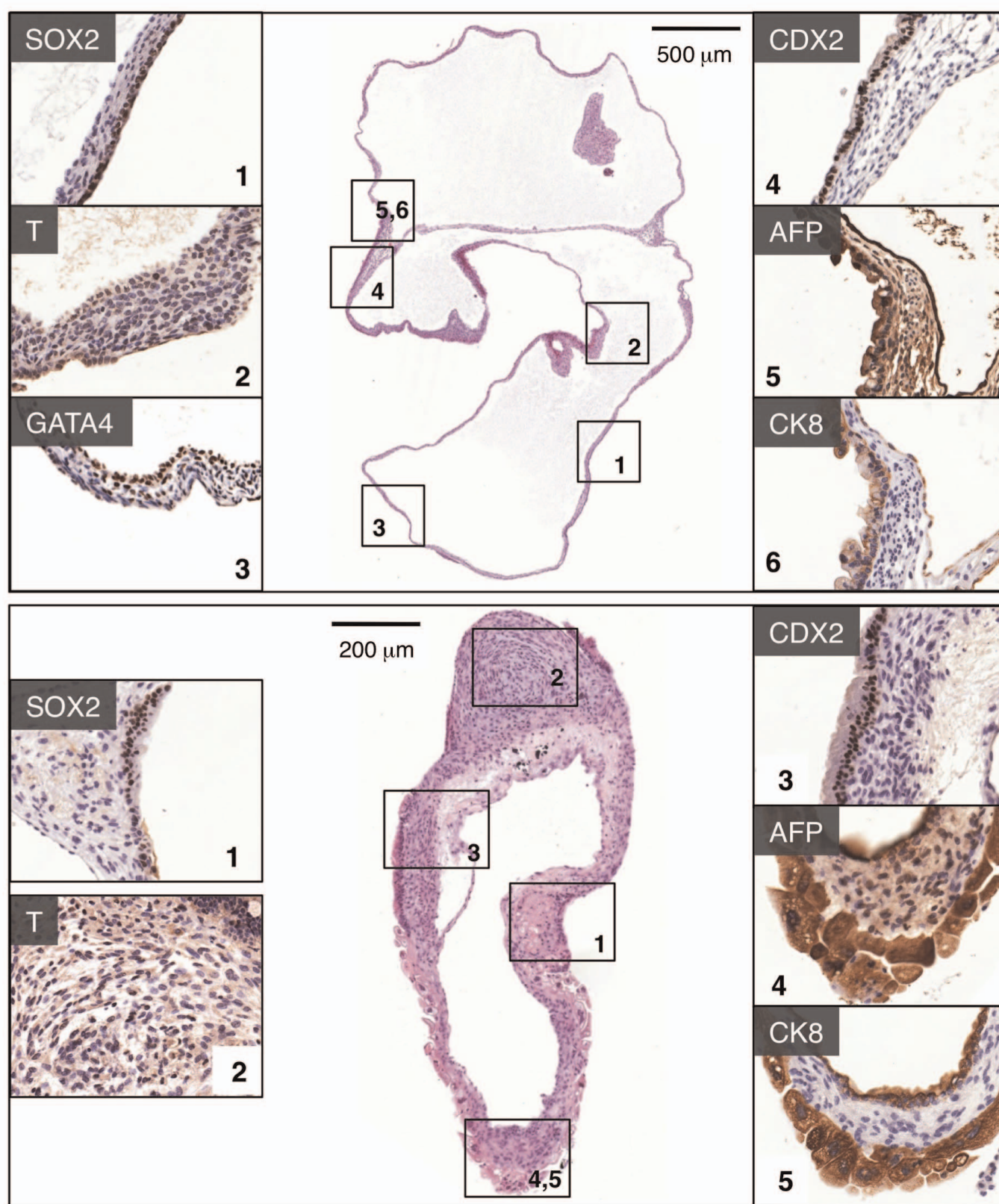
Extended Data Figure 8 | *In vivo* iPS cell contribution to the trophectoderm lineage. **a**, Induction of trophectoderm markers (*Fgfr2*, *Eomes*) in the indicated cell types after culture in TS differentiation medium (see Methods) during the indicated period of time. Other markers were used as controls: *Sox1* (ectoderm), *T* (mesoderm) and *Gata6* (endoderm). For each cell type, values are relative to the average levels at day 0. Values correspond to the average and s.d. For ES cells, $n = 3$ (lines C57BL6.10, JM8.F6 and Bruce4); for *in vitro* iPS cells, $n = 5$ clones; and for *in vivo* iPS cells, $n = 5$ clones. Statistical significance was determined using the Student's *t*-test (unpaired, two-tailed): * $P < 0.05$,

** $P < 0.01$. The lower line of asterisks refers to the comparison with *in vitro* iPS cells, and the upper line of asterisks to the comparison with ES cells. **b**, Example of a chimaeric blastocyst derived from a Katushka morula injected with GFP-labelled *in vivo* iPS cells. Two different confocal planes are shown containing GFP-labelled cells that have contributed to the trophectoderm and to the inner cell mass, as indicated. **c**, Chimaerism of GFP-labelled *in vivo* iPS cells in the proper embryo and placenta (E14.5). A wild-type embryo at the same stage of development is shown as a control. Fluorescence pictures were taken with the same settings.



Extended Data Figure 9 | Expression levels of 2C marker genes. Analysis of the expression of genes enriched in the 2C state: the retrotransposable elements *MuERV-L*, *Zscan4*, and intracisternal A particles (*IAP*) showed no differences between *in vivo* iPS cells compared to ES cells and *in vitro* iPS cells. For ES cells,

$n = 3$ (lines C57BL/6.10, JM8.F6 and Bruce4); for *in vitro* iPS cells, $n = 5$ clones; and for *in vivo* iPS cells, $n = 6$ clones. Values correspond to the average and s.d. Statistical significance was determined using the Student's *t*-test (unpaired, two-tailed). None of the differences was statistically significant.



Extended Data Figure 10 | Immunohistochemical characterization of embryo-like structures. Haematoxylin and eosin and immunostaining analysis of two examples of embryo-like structures generated upon *in vivo* iPS cells intraperitoneal injection. The following markers were used: SOX2

(ectoderm), T/BRACHYURY (mesoderm), GATA4 (endoderm), CDX2 (trophoblast), AFP and CK8 (visceral endoderm of the yolk sac). All lateral panels are at the same magnification.

Slowly fading super-luminous supernovae that are not pair-instability explosions

M. Nicholl¹, S. J. Smartt¹, A. Jerkstrand¹, C. Inserra¹, M. McCrum¹, R. Kotak¹, M. Fraser¹, D. Wright¹, T.-W. Chen¹, K. Smith¹, D. R. Young¹, S. A. Sim¹, S. Valenti^{2,3}, D. A. Howell^{2,3}, F. Bresolin⁴, R. P. Kudritzki⁴, J. L. Tonry⁴, M. E. Huber⁴, A. Rest⁵, A. Pastorello⁶, L. Tomasella⁶, E. Cappellaro⁶, S. Benetti⁶, S. Mattila^{7,8}, E. Kankare^{7,8}, T. Kangas⁸, G. Leloudas^{9,10}, J. Sollerman¹¹, F. Taddia¹¹, E. Berger¹², R. Chornock¹², G. Narayan¹², C. W. Stubbs¹², R. J. Foley¹², R. Lunnan¹², A. Soderberg¹², N. Sanders¹², D. Milisavljevic¹², R. Margutti¹², R. P. Kirshner^{12,13}, N. Elias-Rosa¹⁴, A. Morales-Garoffolo¹⁴, S. Taubenberger¹⁵, M. T. Botticella¹⁶, S. Gezari¹⁷, Y. Urata¹⁸, S. Rodney¹⁹, A. G. Riess¹⁹, D. Scolnic¹⁹, W. M. Wood-Vasey²⁰, W. S. Burgett⁴, K. Chambers⁴, H. A. Flewelling⁴, E. A. Magnier⁴, N. Kaiser⁴, N. Metcalfe²¹, J. Morgan⁴, P. A. Price²², W. Sweeney⁴ & C. Waters⁴

Super-luminous supernovae^{1–4} that radiate more than 10^{44} ergs per second at their peak luminosity have recently been discovered in faint galaxies at redshifts of 0.1–4. Some evolve slowly, resembling models of ‘pair-instability’ supernovae^{5,6}. Such models involve stars with original masses 140–260 times that of the Sun that now have carbon–oxygen cores of 65–130 solar masses. In these stars, the photons that prevent gravitational collapse are converted to electron–positron pairs, causing rapid contraction and thermonuclear explosions. Many solar masses of ^{56}Ni are synthesized; this isotope decays to ^{56}Fe via ^{56}Co , powering bright light curves^{7,8}. Such massive progenitors are expected to have formed from metal-poor gas in the early Universe⁹. Recently, supernova 2007bi in a galaxy at redshift 0.127 (about 12 billion years after the Big Bang) with a metallicity one-third that of the Sun was observed to look like a fading pair-instability supernova^{1,10}. Here we report observations of two slow-to-fade super-luminous supernovae that show relatively fast rise times and blue colours, which are incompatible with pair-instability models. Their late-time light-curve and spectral similarities to supernova 2007bi call the nature of that event into question. Our early spectra closely resemble typical fast-declining super-luminous supernovae^{2,11,12}, which are not powered by radioactivity. Modelling our observations with 10–16 solar masses of magnetar-energized^{13,14} ejecta demonstrates the possibility of a common explosion mechanism. The lack of unambiguous nearby pair-instability events suggests that their local rate of occurrence is less than 6×10^{-6} times that of the core-collapse rate.

The discovery of a luminous transient, PTF 12dam, was first reported¹⁵ by the Palomar Transient Factory on 23 May 2012. We recovered the transient in Pan-STARRS1 (Panoramic Survey Telescope and Rapid Response System) 3π survey data, between 13 and 29 April 2012, at right ascension (RA) 14 h 24 min 46.21 s and declination (dec.) $+46^\circ 13' 48.66''$. We triggered spectroscopic follow-up, beginning with Gran Telescopio Canarias and the William Herschel Telescope (23–25 May 2012). No traces of hydrogen or helium were visible, leading to a type Ic classification, and strong host galaxy lines provided a redshift measurement $z = 0.107$ (ref. 15). A second, similar transient, PS1-11ap, was discovered in the Pan-STARRS1 Medium Deep Survey on 2 January 2011 (RA 10 h 48 min 27.72 s, dec. $+57^\circ 09' 09.2''$). Early spectra showed host

galaxy emission lines at $z = 0.523$ (for details of the data, see Supplementary Information sections 1–3).

The high luminosity and slow decline of their light curves (Fig. 1, Extended Data Tables 1–3, Extended Data Fig. 1) marked out PTF 12dam and PS1-11ap as potential SN 2007bi-like events: that is, they could be pair-instability supernova (PISN) candidates discovered soon after explosion. SN 2007bi was discovered well after maximum light. Although the peak was recovered in the R band¹, the light-curve rise and early spectra were missed. Because of the long diffusion timescale associated with the very massive ejecta in PISN models, the time to reach maximum light (≥ 100 days) is a crucial observational test. The rise time for SN 2007bi was estimated at 77 days (ref. 1), but this was based on a parabolic fit to the data around the peak, and so was not well constrained. Our Pan-STARRS1 images reveal multiple early detections of PTF 12dam and PS1-11ap in g_{P1} , r_{P1} and i_{P1} bands at around 50 and 35 rest-frame days before peak brightness, respectively (Extended Data Fig. 2). PTF 12dam is not detected in z_{P1} images on 1 January 2012, 132 days before the peak. Although their light curves match the declining phases of SN 2007bi and the PISN models quite well, PTF 12dam and PS1-11ap rise to maximum light a factor of ~ 2 faster than these models.

The spectra of PTF 12dam and PS1-11ap show them to be similar supernovae. After 50 days from the respective light curve peaks, these spectra are almost identical to that of SN 2007bi at the same epoch (Fig. 2, Extended Data Table 4, Extended Data Fig. 3). The blue colours are in stark contrast to the predictions of PISN models^{7,8} (Fig. 3, Extended Data Fig. 4), which show much cooler continua below 5,000 Å and marked drop-offs in the ultraviolet. Particularly around and after maximum light, PISN colours are expected to evolve to the red owing to increasing blanketing by iron group elements^{7,8} abundant in their ejecta. We see no evidence of line blanketing in our spectra, even down to 2,000 Å (rest frame) in PS1-11ap, which suggests lower iron group abundances and a higher degree of ionization than in PISN models. Such conditions are fulfilled in models of ejecta reheated by magnetars—highly magnetic, rapidly rotating nascent pulsars^{13,16,17}. The pressure of the magnetar wind on the inner ejecta can form a dense shell^{13,14,17} at near-constant photospheric velocity. For PTF 12dam, the velocities of

¹Astrophysics Research Centre, School of Mathematics and Physics, Queen's University Belfast, Belfast BT7 1NN, UK. ²Las Cumbres Observatory Global Telescope Network, 6740 Cortona Drive, Suite 102, Goleta, California 93117, USA. ³Department of Physics, Broida Hall, University of California, Santa Barbara, California 93106, USA. ⁴Institute of Astronomy, University of Hawaii, 2680 Woodlawn Drive, Honolulu, Hawaii 96822, USA. ⁵Space Telescope Science Institute, 3700 San Martin Drive, Baltimore, Maryland 21218, USA. ⁶INAF, Osservatorio Astronomico di Padova, Vicolo dell'Osservatorio 5, 35122 Padova, Italy. ⁷Finnish Centre for Astronomy with ESO (FINCA), University of Turku, Väisäläntie 20, FI-21500 Piikkiö, Finland. ⁸Tuorla Observatory, Department of Physics and Astronomy, University of Turku, Väisäläntie 20, FI-21500 Piikkiö, Finland. ⁹The Oskar Klein Centre, Department of Physics, Stockholm University, 10691 Stockholm, Sweden. ¹⁰Dark Cosmology Centre, Niels Bohr Institute, University of Copenhagen, 2100 Copenhagen, Denmark. ¹¹The Oskar Klein Centre, Department of Astronomy, Stockholm University, 10691 Stockholm, Sweden. ¹²Harvard-Smithsonian Center for Astrophysics, 60 Garden Street, Cambridge, Massachusetts 02138, USA. ¹³Kavli Institute for Theoretical Physics, University of California Santa Barbara, Santa Barbara, California 93106, USA. ¹⁴Institut de Ciències de l'Espai (IEEC-CSIC), Facultat de Ciències, Campus UAB, 08193 Bellaterra, Spain. ¹⁵Max-Planck-Institut für Astrophysik, Karl-Schwarzschild-Strasse 1, 85741 Garching, Germany. ¹⁶INAF-Osservatorio Astronomico di Capodimonte, Salita Moiraiello 16, I-80131 Napoli, Italy. ¹⁷Department of Astronomy, University of Maryland, College Park, Maryland 20742-2421, USA. ¹⁸Institute of Astronomy, National Central University, Chung-Li 32054, Taiwan. ¹⁹Department of Physics and Astronomy, Johns Hopkins University, 3400 North Charles Street, Baltimore, Maryland 21218, USA. ²⁰Pittsburgh Particle Physics, Astrophysics, and Cosmology Center, Department of Physics and Astronomy, University of Pittsburgh, 3941 O'Hara Street, Pittsburgh, Pennsylvania 15260, USA. ²¹Department of Physics, Durham University, South Road, Durham DH1 3LE, UK. ²²Department of Astrophysical Sciences, Princeton University, Princeton, New Jersey 08544, USA.

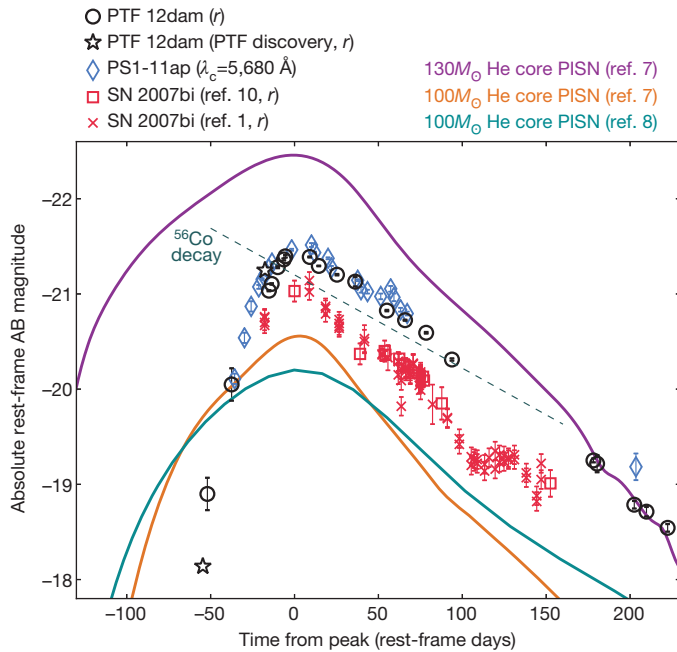


Figure 1 | Optical light curves of slow-fading super-luminous supernovae. Data for PTF 12dam (including discovery data announced¹⁵ by PTF) and SN 2007bi (from refs 1 and 10) are given in the SDSS (Sloan Digital Sky Survey) *r* band (central wavelength $\lambda_c = 6,230$ Å), while for PS1-11ap at $z = 0.523$, the PS1 z_{p1} filter corresponds to a rest-frame filter of $\lambda_c = 5,680$ Å (width of passband $\lambda_{\text{width}} \approx 1,350$ Å), similar to SDSS *r*. The first three PS1-11ap points were transformed from i_{p1} using the observed $i_{p1} - z_{p1}$ colour (see Supplementary Information sections 2 and 3 for details of the data, including *k*-corrections, colour transformations and extinction). The three supernovae (open symbols) display the same slow decline from maximum, matching the rate expected from ^{56}Co decay (dashed line) with close to full γ -ray trapping (although similar declines can be generated for ~ 100 days after peak from magnetar spin-down²¹). Powering these high luminosities radioactively requires at least $3\text{--}7M_{\odot}$ of ^{56}Ni (refs 1, 10, 18 and 20), suggesting an extremely massive progenitor and possible pair-instability explosion¹. Also shown are synthetic SDSS *r*-band light curves (solid lines) generated from published one-dimensional models^{7,8} of PISNs from $100\text{--}130M_{\odot}$ stripped helium cores. These fit the decline phase well, but do not match our early observations. The rise time of a PISN is necessarily long (rising 2.5 mag to peak in 95–130 days), because heating from $^{56}\text{Ni}/^{56}\text{Co}$ decay occurs in the inner regions, and the resultant radiation must then diffuse through the outer ejecta, which typically has mass $>80M_{\odot}$ (ref. 7). Models with higher-dimensional outward mixing of ^{56}Ni are likely to show even shallower gradients in the rising phase, while as-yet unexplored parameters such as rotation and magnetic fields will have little effect on the diffusion timescale, which is set by the mass, kinetic energy and opacity of the ejecta (see Supplementary Information section 5.2). The pre-peak photometry of PTF 12dam and PS1-11ap shows only a moderately slow rise over 50–60 days, which is therefore physically inconsistent with the PISN models. Error bars, $\pm 1\sigma$.

spectral lines are close to $10,000 \text{ km s}^{-1}$ at all times. Intriguingly, the early spectra of our objects are very similar to those of superluminous supernovae of type I (refs 2, 11, 12) and evolve in the same way, but on longer timescales and with lower line velocities (Fig. 2).

Nebular modelling of SN 2007bi spectra has been used to argue¹ for large ejected oxygen and magnesium masses of $8\text{--}15M_{\odot}$ and $0.07\text{--}0.13M_{\odot}$, respectively (where M_{\odot} is the solar mass). Such masses are actually closer to values in massive core-collapse models¹⁸ than in PISN models, which eject $\sim 40M_{\odot}$ oxygen and $\sim 4M_{\odot}$ magnesium^{1,8,9}. In the work reported in ref. 1, an additional $37M_{\odot}$ in total of Ne, Si, S, and Ar were added to the model, providing a total ejecta mass consistent with a PISN. However, this was not directly measured¹, because these elements lack any identified lines. These constraints are important, so we investigated line formation in this phase using our own non-local thermodynamic equilibrium code¹⁹ (Extended Data Fig. 5; Supplementary Information

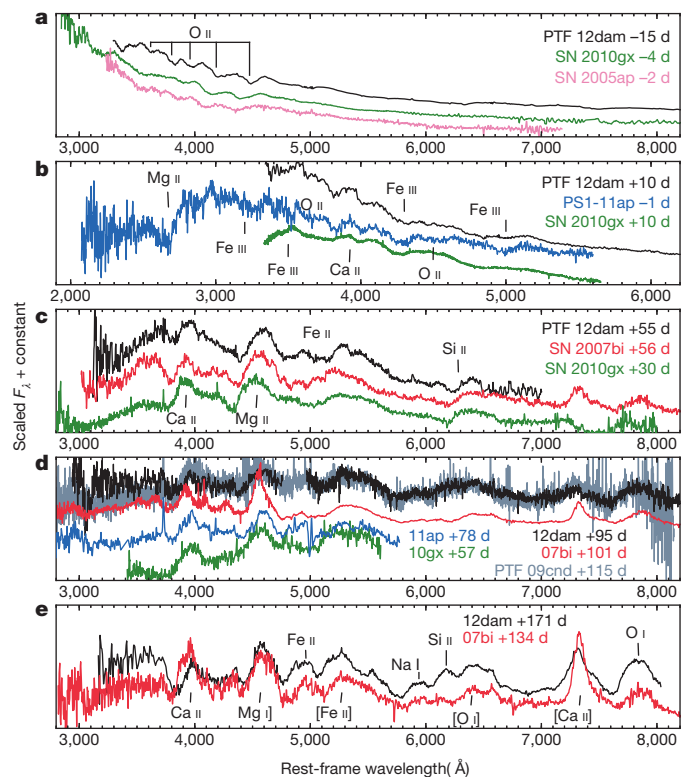


Figure 2 | Spectral evolution of PTF 12dam and PS1-11ap from super-luminous supernovae of type I to SN 2007bi-like. **a–e**, We show spectra of PTF 12dam, PS1-11ap, SN 2007bi, and the well-studied superluminous supernovae of type I, SN 2010gx¹¹, SN 2005ap² and PTF09cnd². Our spectra have been corrected for extinction and shifted to respective rest frames (details of reduction and analysis, including construction of model host continua for subtraction from **d** and **e**, in Supplementary Information section 3), and scaled to facilitate comparison. Phases are given in rest-frame days relative to maximum light. No hydrogen or helium are detected at any stage (near-infrared spectra of PTF 12dam, obtained at +13 days and +27 days, also show no He I; see Supplementary Information section 3). **a**, Before and around peak, our objects show the characteristic blue continua and O II absorptions common to super-luminous supernovae of type I/C^{21,22}, although the lines in the slowly evolving objects are at lower velocities than are typically seen in those events. **b**, Shortly after peak, Fe III features emerge, along with the Mg II and Ca II lines that dominate superluminous type I supernovae at this phase. **c**, By 55 days after peak, PTF 12dam is almost identical to SN 2007bi. We note that these objects still closely resemble SN 2010gx, but seem to be evolving on longer timescales (consistent with the slower light-curve evolution). **d**, At ~ 100 days, PTF 12dam also matches PTF09cnd², which faded slowly for a superluminous type I supernova after a 50-day rise. **e**, The spectra are now quasi-nebular, dominated by emission lines of Ca II H and K, Mg I, 4,571 Å, Mg I, 5,183 Å + [Fe II 5,200] Å blend, [O I] 6,300, 6,364 Å, [Ca II] 7,291, 7,323 Å, and O I 7,774 Å, but some continuum flux is still visible. We find that the emission line intensities can be reproduced by ejecta from a $15M_{\odot}$ type I supernova at a few thousand degrees, without requiring a large mass of iron (Supplementary Information section 4).

section 4). We found that the luminosities of [O I] 6,300, 6,364 Å, O I 7,774 Å and Mg I 4,571 Å, and the feature at 5,200 Å ([Fe II] + Mg I), can be reproduced with $10\text{--}20M_{\odot}$ of oxygen-dominated ejecta, containing $\sim 0.001\text{--}1M_{\odot}$ of iron, given reasonable physical conditions (singly ionized ejecta at a few thousand degrees). Thus, although the nebular modelling of SN 2007bi in ref. 1 provided a self-consistent solution for PISN ejecta, our calculations indicate that this solution is not unique, and has not ruled out lower-mass ejecta on the core-collapse scale ($10M_{\odot}$). Moreover, if the line at 5,200 Å is [Fe II], then both our model and the model of ref. 1 predict a dominant [Fe II] 7,155 Å line (at the low temperatures and high iron mass expected in PISN), which is not present in the observed spectra. To estimate the nickel mass needed to

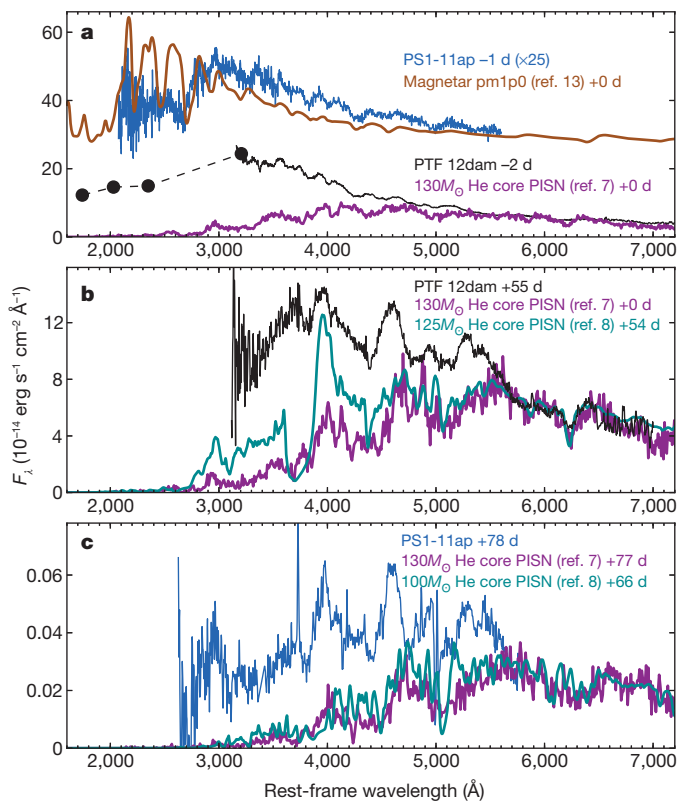


Figure 3 | Spectral comparison with pair-instability and magnetar-driven supernova models. **a–c.** We compare our ultraviolet and optical data to the predictions of PISN^{7,8,13} and magnetar models¹³ (lines in models are identified in refs 8 and 13). The absence of narrow lines and hydrogen/helium seems to make interaction-powered colliding-shell models unlikely (for example, the pulsational pair-instability; see Supplementary Information section 5.3). Model spectra are matched to the observed flux in the region 5,500–7,000 Å. **a.** We compare PS1-11ap to a Wolf–Rayet progenitor magnetar model (pm1p0¹³) at peak light (model spectra at later epochs do not currently exist in the literature). The magnetar energy input is equivalent to several solar masses of ⁵⁶Ni, in ejecta of only 6.94 M_{\odot} . The high internal-energy-to-ejecta-mass ratio keeps the ejecta hot and relatively highly ionized, resulting in a blue continuum to match our observations. Moreover, this energy source does not demand the high mass of metals intrinsic to the PISN scenario^{7,8}. Redward of the Mg II line at 2,800 Å, this model shows many of the same Fe III and O II lines dominating the observed spectra, although the strengths of the predicted Si III and C III lines in the near-ultraviolet are greater than those observed in PS1-11ap. We also compare PTF 12dam at peak to a 130 M_{\odot} He core PISN model⁷. The model spectrum has intrinsically red colours below 5,000 Å owing to many overlapping lines from the large mass of iron-group elements and intermediate-mass elements. Our rest-frame ultraviolet spectra of PS1-11ap, and ultraviolet photometry of PTF 12dam, show that the expected line blanketing/absorption is not observed. **b.** PTF 12dam compared to models of 125–130 M_{\odot} PISNs^{7,8} at 55 days. Although the observed spectrum has cooled, the models still greatly under-predict the flux blueward of 5,000 Å. **c.** PS1-11ap, at 78 days, compared to 100–130 M_{\odot} PISN models^{7,8} at similar epochs. Again, our observations are much bluer than PISN models. In particular, PS1-11ap probes the flux below 3,000 Å, where we see the greatest discrepancy.

power PTF 12dam radioactively, we constructed a bolometric light curve from our near-ultraviolet to near-infrared photometry (Fig. 4). PTF 12dam is brighter than SN 2007bi, and fitting it with radioactively powered diffusion models^{18,20} requires $\sim 15 M_{\odot}$ of ⁵⁶Ni in ~ 15 – $50 M_{\odot}$ of ejecta — combinations that are not produced in any physical model (Extended Data Fig. 6; Supplementary Information section 5.1). Furthermore, such large nickel fractions are clearly not supported by our spectra.

The combination of relatively fast rises and blue spectra, lacking ultraviolet line blanketing, shows that PTF 12dam, PS1-11ap and probably SN 2007bi are not pair-instability explosions. We suggest here one model that can consistently explain the data. A magnetar-powered supernova

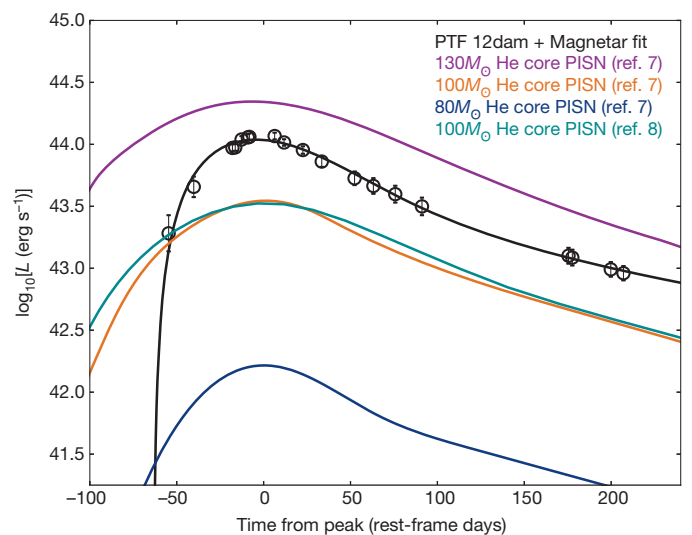


Figure 4 | Bolometric light curve and magnetar fit. Our PTF 12dam bolometric light curve (open circles), comprising Swift observations in the near-ultraviolet, extensive *griz* imaging, and multi-epoch near-infrared (*JHK*) data (Supplementary Information section 5), is well fitted by our semi-analytic magnetar model²¹ (black line) (see Supplementary Information section 5.4). This model, with magnetic field $B \approx 10^{14}$ G and spin period $P \approx 2.6$ ms, can fit both the rise and decay times of the light curve. A large ejecta mass of ~ 10 – $16 M_{\odot}$ is required—significantly higher than typically found for type Ibc supernovae²⁸, but similar to the highest estimates for SN 2011bm²⁹ and SN 2003lw³⁰ (though well below the $>80 M_{\odot}$ expected in PISNs). In the context of the magnetar model, the parameters of our fit are consistent with the observed spectroscopic relation to super-luminous supernovae of type I. Fits to a sample of such objects using the same model²¹ found uniformly lower ejected masses and higher magnetic fields than in PTF 12dam. The large ejecta mass here results in a slow light-curve rise and broad peak compared to other super-luminous supernovae of type Ic^{2,3,21}, and would explain the slower spectroscopic evolution, including why the spectrum is not fully nebular at 200 days. The weaker B field means that the magnetar radiates away its rotational energy less rapidly, so that more of the heating takes place at later times; this gives the impression of a radioactive tail. Higher ejected mass and weaker magnetar wind may account for the lower velocities in slowly declining events. Also shown for comparison are bolometric light curves of model PISNs^{7,8} from 80–130 M_{\odot} He cores (coloured lines). Although PISNs from less massive progenitors do show faster rise times, the rise of PTF 12dam is too steep to be consistent with the PISN explosion of a He core that is sufficiently massive to generate its observed luminosity. Errors bars, $\pm 1\sigma$ photometry, combined in quadrature.

can produce a light curve with the observed rise and decline rates as the neutron star spins down and reheats the ejecta^{13,14,16,17}. It has been suggested that $\sim 10\%$ of core-collapses may form magnetars¹⁴. Although their initial-spin distribution is unknown, periods $\gtrsim 1$ ms are physically plausible. This mechanism has already been proposed for SN 2007bi¹⁴, as well as for fast-declining superluminous type-I supernovae^{2,21}. We fitted a magnetar-powered diffusion model^{21,22} to the bolometric light curve of PTF 12dam (Fig. 4), and found a good fit for magnetic field $B \approx 10^{14}$ G and spin period $P \approx 2.6$ ms, with an ejecta mass of ~ 10 – $16 M_{\odot}$. At peak, the *r*-band luminosities of PTF 12dam and PS1-11ap are ~ 1.5 times that of SN 2007bi. Scaling our light curve by this factor, our model implies a similar ejected mass for SN 2007bi, with a slower-spinning magnetar ($P \approx 3.3$ ms), comparable to previous models¹⁴. If the magnetar theory is correct for normal superluminous type-I supernovae^{2,21}, our objects could be explained as a subset in which larger ejected masses and weaker magnetic fields result in slower photometric and spectroscopic evolution.

This leaves no unambiguous PISN candidates within redshift $z < 2$ (although possible examples exist at higher redshift⁴). We used the properties of the Pan-STARRS1 Medium Deep Survey (PS1 MDS, with a nightly detection limit of ~ 23.5 mag in *g,r,i*-like filters^{21,23,24}) to constrain

the local rate of stripped-envelope PISNs. We simulated PS1 MDS observations of 80, 100 and 130 M_{\odot} helium core PISN models⁷ using our own Monte Carlo code²⁵ (Supplementary Information section 6), requiring an apparent magnitude <21 in at least one bandpass and a continuous 100-day (observer-frame) window of PS1 monitoring before considering an event a candidate PISN detection. Initially assuming a rate of $10^{-5} R_{\text{CCSN}}$ (where R_{CCSN} is the rate of occurrence of core-collapse supernovae²⁶) for each model, we typically find five 100 M_{\odot} PISN candidates per year, at $z < 0.6$. The 130 M_{\odot} explosions have peak near-ultraviolet magnitudes of -22 , resulting in apparent r_{P1} and i_{P1} magnitudes <20 . PS1 should detect $>90\%$ of these within $z < 0.6$ (ten or more per year). Taking the 100 M_{\odot} result, the fact that we have not detected a single transient with these properties in the three years of PS1 is inconsistent with our assumed explosion rate at a level of 3.9σ (Poisson statistics). This implies a 3σ upper limit on their rate (within $z < 0.6$) of $<6 \times 10^{-6} R_{\text{CCSN}}$; even allowing another factor of ~ 2 to conservatively cover detection issues such as bad pixels or bright nearby stars, the rate of occurrence of super-luminous PISNs of type Ic must be at least a factor of ten lower than the overall rate of type-I superluminous supernovae¹². PS1-11ap was our best candidate for a PISN explosion, but it fails to match the models. However, our calculation suggests that almost all the lower-mass (80 M_{\odot}) PISNs would escape detection. Future searches for PISN candidates should target these fainter explosions at lower redshift (and larger volumes), or the more luminous candidates at $z > 1$.

We conclude that the classification of some slow-fading super-luminous supernovae¹² as radioactively driven is not supported observationally, and propose that these events can be united with virtually all known type-Ic super-luminous supernovae into a single class. Magnetar-powered models can explain their brightness and colours, and account for their diversity. The low upper limit we find for the rate of very massive PISNs reduces their potential impact on cosmic chemical evolution within $z \lesssim 1$. This relieves possible tension between their proposed existence in the nearby Universe, and the lack of detected chemical enrichment signatures in metal-poor stars and damped Lyman- α systems²⁷.

Online Content Any additional Methods, Extended Data display items and Source Data are available in the online version of the paper; references unique to these sections appear only in the online paper.

Received 10 May; accepted 9 August 2013.

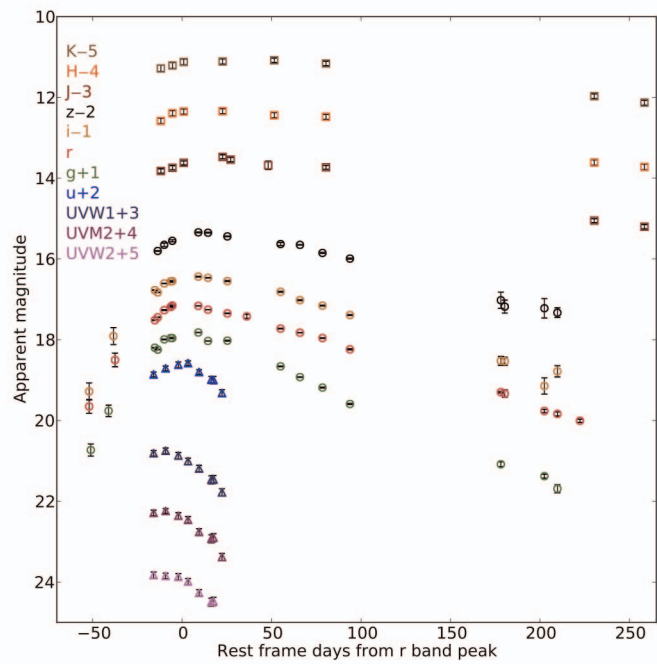
- Gal-Yam, A. *et al.* Supernova 2007bi as a pair-instability explosion. *Nature* **462**, 624–627 (2009).
- Quimby, R. M. *et al.* Hydrogen-poor super-luminous stellar explosions. *Nature* **474**, 487–489 (2011).
- Chomiuk, L. *et al.* Pan-STARRS1 discovery of two ultraluminous supernovae at $z \sim 0.9$. *Astrophys. J.* **743**, 114–132 (2011).
- Cooke, J. *et al.* Super-luminous supernovae at redshifts of 2.05 and 3.90. *Nature* **491**, 228–231 (2012).
- Barkat, Z., Rakavy, G. & Sack, N. Dynamics of supernova explosion resulting from pair formation. *Phys. Rev. Lett.* **18**, 379–381 (1967).
- Rakavy, G. & Shaviv, G. Instabilities in highly evolved stellar models. *Astrophys. J.* **148**, 803–816 (1967).
- Kasen, D., Woosley, S. E. & Heger, A. Pair instability supernovae: light curves, spectra, and shock breakout. *Astrophys. J.* **734**, 102 (2011).
- Dessart, L., Waldman, R., Livne, E., Hillier, D. J. & Blondin, S. Radiative properties of pair-instability supernova explosions. *Mon. Not. R. Astron. Soc.* **428**, 3227–3251 (2013).
- Heger, A. & Woosley, S. E. The nucleosynthetic signature of population III. *Astrophys. J.* **567**, 532–543 (2002).
- Young, D. R. *et al.* Two type Ic supernovae in low-metallicity, dwarf galaxies: diversity of explosions. *Astron. Astrophys.* **512**, A70 (2010).
- Pastorello, A. *et al.* Ultra-bright optical transients are linked with type Ic supernovae. *Astrophys. J.* **724**, L16–L21 (2010).
- Gal-Yam, A. Luminous supernovae. *Science* **337**, 927–932 (2012).
- Dessart, L., Hillier, D. J., Waldman, R., Livne, E. & Blondin, S. Super-luminous supernovae: ^{56}Ni power versus magnetar radiation. *Mon. Not. R. Astron. Soc.* **426**, L76–L80 (2012).
- Kasen, D. & Bildsten, L. Supernova light curves powered by young magnetars. *Astrophys. J.* **717**, 245–249 (2010).
- Quimby, R. M. *et al.* Discovery of a super-luminous supernova, PTF12dam. *Astron. Tel.* **4121** (2012).
- Thompson, T. A., Chang, P. & Quataert, E. Magnetar spin-down, hyperenergetic supernovae, and gamma-ray bursts. *Astrophys. J.* **611**, 380–393 (2004).
- Woosley, S. E. Bright supernovae from magnetar birth. *Astrophys. J.* **719**, L204–L207 (2010).
- Umeda, H. & Nomoto, K. How much ^{56}Ni can be produced in core-collapse supernovae? Evolution and explosion of 30–100 M_{\odot} stars. *Astrophys. J.* **673**, 1014–1022 (2008).
- Jerkstrand, A., Fransson, C. & Kozma, C. The ^{44}Ti -powered spectrum of SN 1987A. *Astron. Astrophys.* **530**, A45 (2011).
- Moriya, T. *et al.* A core-collapse model for the extremely luminous type Ic SN2007bi: an alternative to the pair-instability supernova model. *Astrophys. J.* **717**, L83–L86 (2010).
- Inserra, C. *et al.* Super-luminous Ic supernovae: catching a magnetar by the tail. *Astrophys. J.* **770**, 128 (2013).
- Arnett, W. D. Type I supernovae. I—Analytic solutions for the early part of the light curve. *Astrophys. J.* **253**, 785–797 (1982).
- Tonry, J. L. *et al.* First results from Pan-STARRS1: faint, high proper motion white dwarfs in the Medium-Deep fields. *Astrophys. J.* **745**, 42 (2011).
- Berger, E. *et al.* Ultraluminous supernovae as a new probe of the interstellar medium in distant galaxies. *Astrophys. J.* **755**, L29 (2012).
- Young, D. R. *et al.* Core-collapse supernovae in low-metallicity environments and future all-sky transient surveys. *Astron. Astrophys.* **489**, 359–375 (2008).
- Dahlen, T. *et al.* High-redshift supernova rates. *Astrophys. J.* **613**, 189–199 (2004).
- Kobayashi, C., Tominaga, N. & Nomoto, K. Chemical enrichment in the carbon enhanced damped Ly α system by population III supernovae. *Astrophys. J.* **730**, L14 (2011).
- Drout, M. R. *et al.* The first systematic study of type Ibc supernova multi-band light curves. *Astrophys. J.* **741**, 97 (2011).
- Valenti, S. *et al.* A spectroscopically normal type Ic supernova from a very massive progenitor. *Astrophys. J.* **749**, L28 (2012).
- Mazzali, P. A. *et al.* Models for the type Ic hypernova SN 2003lw associated with GRB 031203. *Astrophys. J.* **645**, 1323 (2006).

Supplementary Information is available in the online version of the paper.

Acknowledgements We thank D. Kasen and L. Dessart for sending us their model data. The Pan-STARRS1 Surveys (PS1) have been made possible through contributions of the Institute for Astronomy, the University of Hawaii, the Pan-STARRS Project Office, the Max Planck Society (and its participating institutes, the Max Planck Institute for Astronomy, Heidelberg, and the Max Planck Institute for Extraterrestrial Physics, Garching), The Johns Hopkins University, Durham University, the University of Edinburgh, Queen's University Belfast, the Harvard-Smithsonian Center for Astrophysics, the Las Cumbres Observatory Global Telescope Network Incorporated, the National Central University of Taiwan, the Space Telescope Science Institute, NASA grant no. NNX08AR22G issued through the Planetary Science Division of the NASA Science Mission Directorate, National Science Foundation grant no. AST-1238877, and the University of Maryland. S.J.S. acknowledges FP7/2007-2013/ERC Grant agreement no. 291222; J.L.T. and R. P. Kirshner acknowledge NSF grants AST-1009749, AST-121196; G.L. acknowledges Swedish Research Council grant no. 623-2011-7117; A.P., L.T., E.C., S.B. and M.T.B. acknowledge PRIN-INAF 2011. Work is based on observations made with the following telescopes: the William Herschel Telescope, Gran Telescopio Canarias, the Nordic Optical Telescope, Telescopio Nazionale Galileo, the Liverpool Telescope, the Gemini Observatory, the Faulkes North Telescope, the Asiago Copernico Telescope and the United Kingdom Infrared Telescope.

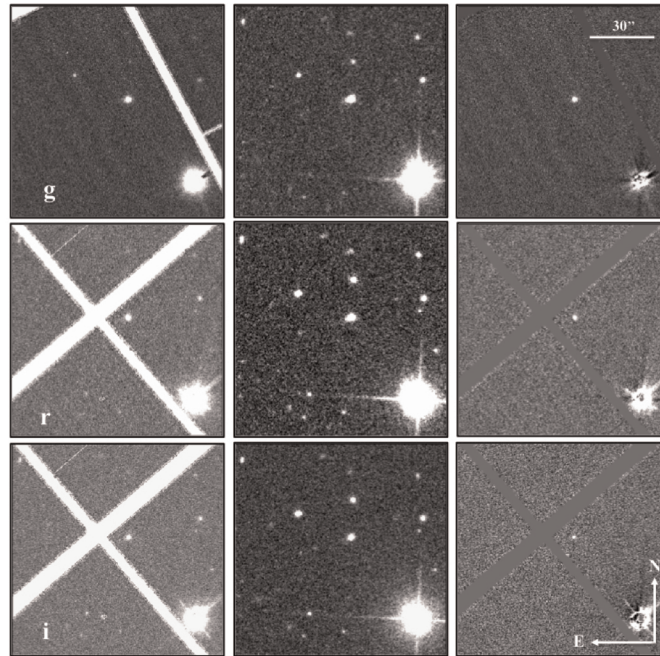
Author Contributions M.N. carried out the optical and near-infrared photometric and spectroscopic data analysis and wrote the manuscript. S.J.S. initiated, coordinated and managed the project, and contributed to manuscript preparation. A.J. carried out the theoretical modelling aspects, with contributions from S.A. C.I. reduced the ultraviolet data and assisted in all aspects of the analysis, including writing software to determine k -corrections and bolometric luminosity and running line identification routines. M.M.C. provided the PS1-11ap reduced data. M.F. and R.K. carried out observations and coordinated Liverpool Telescope and Faulkes Telescope data. D.W., T.-W.C., K.S., D.R.Y., S.V., M.T.B., M.F., R.K. and Y.U. worked on finding PS1 transients using manual searching and software development. D.R.Y. wrote and adapted the Monte Carlo code described. F.B. and R. P. Kudritzky provided Gemini data through joint programmes. D.A.H. provided data from Faulkes North Telescope. A.P., L.T., E.C. and S.B. undertook observations with the Asiago telescopes. S.M., E.K., T.K., G.L., J.S. and F.T. provided data and relevant reductions through their Nordic Optical Telescope programmes. E.B., R.C., G.N., R.J.F., A.R., S.R., A.G.R., D.S., S.G., S.R., W.M.W.-V., N.S., R.M., R.L., A.S., D.M. and R. P. Kirshner worked on PS1 data analysis including difference imaging for PS1-11ap through the photpipe software at CfA/JHU and ensuring difference images were photometrically calibrated, and manual searching and spectroscopic follow-up of PS1 transients. N.E.-R., A.M.-G. and S.T. provided and reduced the GTC spectral data. J.L.T., M.E.H., W.S.B., K.C., H.A.F., E.A.M., N.K., N.M., J.M., P.A.P., C.W.S., W.S. and C.W. worked on designing and operating the PS1 system, from hardware through to software and data reduction routines.

Author Information Reprints and permissions information is available at www.nature.com/reprints. The authors declare no competing financial interests. Readers are welcome to comment on the online version of the paper. Correspondence and requests for materials should be addressed to M.N. (mnichol03@qub.ac.uk).



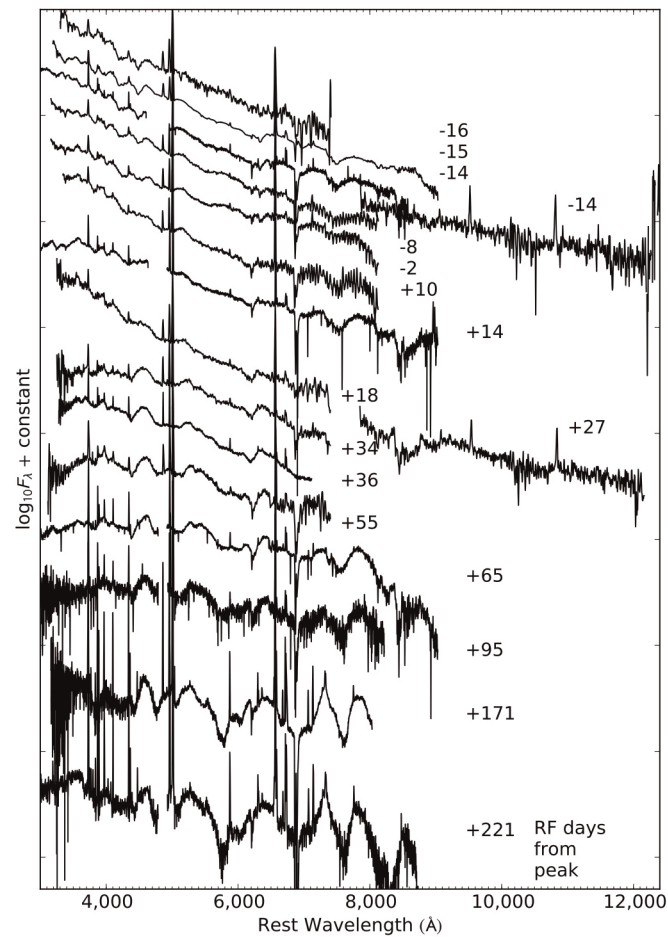
Extended Data Figure 1 | Multi-colour photometry of PTF 12dam.

Observed light curve of PTF 12dam in UVW2, UVM2, UVW1, u , g , r , i , z (AB magnitudes) and J , H , K (Vega magnitude system).



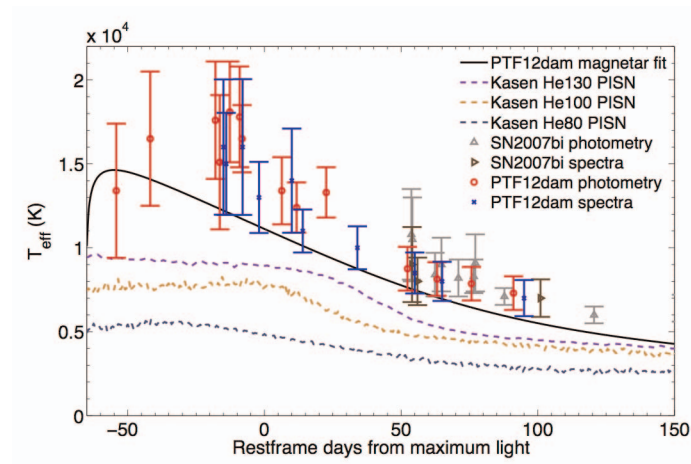
Extended Data Figure 2 | Image subtraction for the three earliest Pan-STARRS1 epochs of PTF 12dam in g_{P1} , r_{P1} and i_{P1} , using SDSS frames as reference images (taken on 11 February 2003). These illustrate reliable image subtraction, resulting in clear detections of PTF 12dam at early phases. The images on the left are our PS1 detections, those in the centre are the SDSS templates, and on the right are the differences between the two. The bright

star in the lower right was saturated and hence does not subtract cleanly. At each PS1 epoch there are two images, taken as transient time interval pairs. Photometry was carried out and determined in the SDSS photometric system to match the bulk of the follow-up *griz* imaging. The white areas are gaps between the 590×598 pixel cells in the PS1 chip arrays.



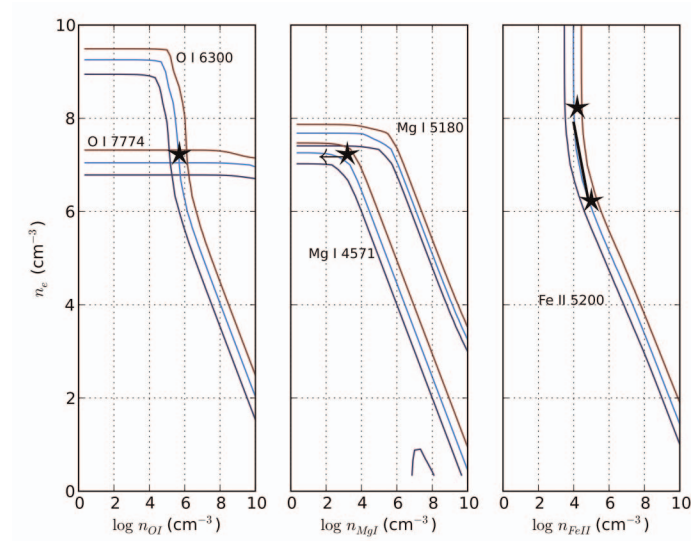
Extended Data Figure 3 | Spectral evolution of PTF 12dam. Full time-series optical and near-infrared spectroscopy of PTF 12dam, from two weeks before maximum light to an extended pseudo-nebular phase at 100 to >200 days afterwards. A Starburst99 model continuum spectral energy distribution

for the host galaxy has been calibrated against SDSS and GALEX (Galaxy Evolution Explorer) photometry and subtracted from the last three spectra. RF, rest-frame.



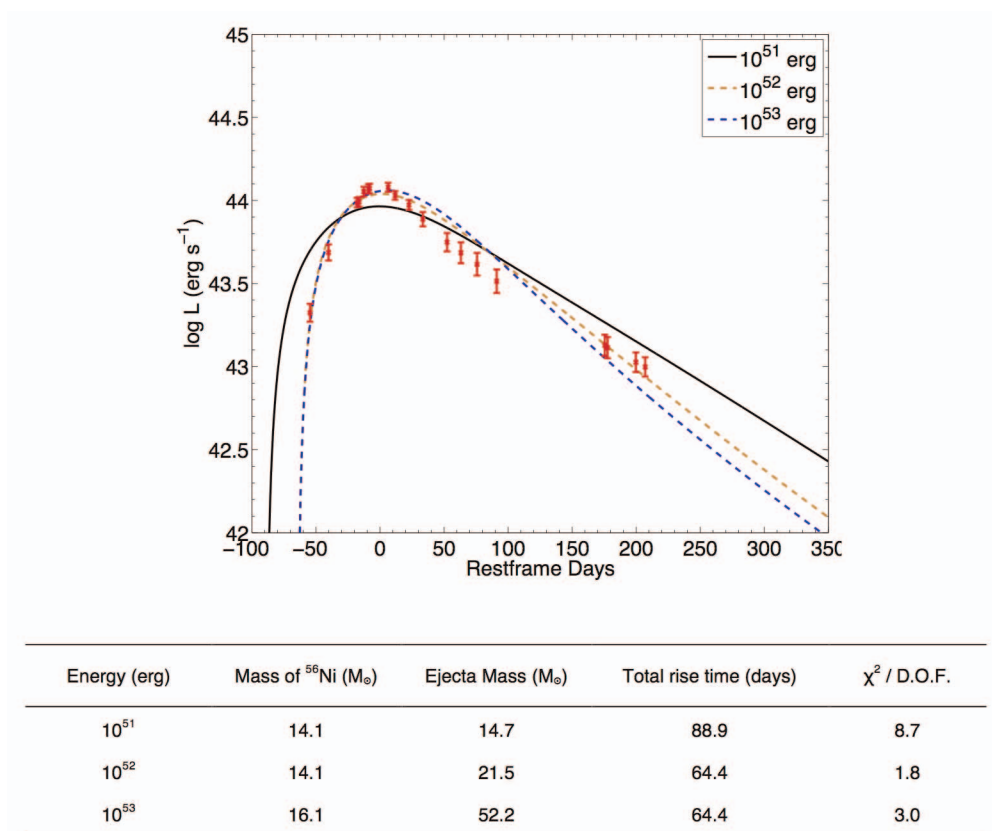
Extended Data Figure 4 | Effective temperature evolution of PTF 12dam and SN 2007bi, compared with magnetar-powered and pair-instability models. The magnetar model comes much closer to reproducing the high photospheric temperatures we observe, and matches the gradient of the decline

phase well. PISN models do not reach such high effective temperatures, and show an approximately 100-day temperature plateau as they rise, before declining after maximum light.



Extended Data Figure 5 | Modelling of the O I, Mg I and Fe II line fluxes in SN 2007bi at 367 days post-peak. We plot contours for oxygen, magnesium and iron line fluxes predicted by our model in units of $L = 10^{40} \text{ erg s}^{-1}$ (dark blue = $L/3$; light blue = L ; red = $3L$; where L is the approximate luminosity of the lines in the 367-day post-peak spectrum of SN 2007bi) as functions of the respective ion density, $\{n_{\text{OI}}, n_{\text{MgI}}, n_{\text{FeII}}\}$, and electron density, n_e , at 5,000 K (approximately the temperature derived for the iron zone from the relative strengths of iron lines). The panels for O I and Mg I show two lines (O I 6,300, 7,774 Å; Mg I 4,571, 5,180 Å), whereas Fe II shows only contours for the 5,200 Å blend. No blending is likely to occur for any of the oxygen lines;

the region where they intersect therefore gives the allowed densities, constraining n_e to about 10^7 cm^{-3} (this is quite insensitive to the temperature we assume). Blending is also unlikely for Mg I] 4,571 Å, and the allowed Mg I density is therefore the intersection of this contour with $n_e \approx 10^7 \text{ cm}^{-3}$, which can be seen to give $n_{\text{MgI}} \lesssim 10^3 \text{ cm}^{-3}$. At this magnesium density, we see that the Mg I 5,180 Å line makes some contribution to the 5,200 Å flux. Also shown is the allowed Fe II density at this temperature, for iron-zone electron densities spanning a factor of ten either side of that in the oxygen/magnesium zones.



Extended Data Figure 6 | Fits to the observed bolometric light curve of PTF 12dam with radioactive ^{56}Ni powered ejecta. The formal fits of the models with kinetic energies of 10^{52} and 10^{53} erg are good (see graph), but the required combinations of ^{56}Ni masses and ejecta masses (see data table) are not

produced in physical models; such large nickel fractions are only expected to be produced in thermonuclear explosions (supernova Ia or possibly PISN), whereas the total ejected mass corresponds to the core-collapse of a massive star below the pair-instability threshold.

Extended Data Table 1 | Optical photometry of PTF 12dam in SDSS *griz* bands, and *k*-corrections derived from our spectra.

Date	MJD	RF Phase (days)	Telescope	<i>g</i>	<i>K_g</i>	<i>r</i>	<i>K_r</i>	<i>i</i>	<i>K_i</i>	<i>z</i>	<i>K_z</i>
2012-04-13	56030.48	-51.9	PS1			19.45 (0.17) ^S	0.20	20.04 (0.21) ^S	0.24		
2012-04-14	56031.45	-51.0	PS1	19.62 (0.15) ^S	0.11						
2012-04-25	56042.47	-41.1	PS1	18.65 (0.14) ^S	0.11						
2012-04-28	56045.48	-38.4	PS1					18.67 (0.21) ^S	0.24		
2012-04-29	56046.50	-37.5	PS1			18.30 (0.17) ^S	0.20				
2012-05-23	56071.13	-15.2	GTC + OSIRIS	17.09 (0.01)	0.11	17.32 (0.01)	0.20	17.53 (0.01)	0.24		
2012-05-25	56072.92	-13.6	WHT + ACAM	17.13 (0.01)	0.11	17.26 (0.01)	0.19	17.59 (0.01)	0.24	17.52 (0.01)	0.14
2012-05-29	56076.95	-10.0	LT + RATCam	16.88 (0.01)	0.11	17.11 (0.01)	0.16	17.38 (0.01)	0.23	17.37 (0.04)	0.14
2012-06-02	56080.94	-6.4	LT + RATCam	16.84 (0.01)	0.12	17.05 (0.01)	0.14	17.34 (0.02)	0.22		
2012-06-03	56081.94	-5.5	LT + RATCam	16.84 (0.01)	0.12	17.02 (0.01)	0.13	17.33 (0.01)	0.22	17.27 (0.03)	0.14
2012-06-20	56098.03	9.1	TNG + LRS	16.76 (0.01)	0.06	16.97 (0.01)	0.19	17.24 (0.01)	0.20	17.12 (0.01)	0.11
2012-06-25	56104.02	14.5	WHT + ACAM	17.00 (0.01)	0.03	17.05 (0.01)	0.21	17.28 (0.01)	0.19	17.15 (0.01)	0.10
2012-07-07	56116.01	25.3	NOT+ALFOSC	17.05 (0.01)	-0.03	17.15 (0.01)	0.19	17.37 (0.01)	0.18	17.24 (0.01)	0.10
2012-07-17	56128.03	36.2	GTC + OSIRIS			17.25 (0.05)			0.17		
2012-08-09	56148.93	55.0	NOT+ALFOSC	17.76 (0.01)	-0.10	17.51 (0.01)	0.21	17.66 (0.01)	0.15	17.51 (0.04)	0.07
2012-08-21	56160.92	65.9	WHT + ACAM	17.99 (0.01)	-0.07	17.67 (0.01)	0.16	17.88 (0.01)	0.14	17.53 (0.01)	0.05
2012-09-04	56174.85	78.5	NOT+ALFOSC	18.22 (0.01)	-0.03	17.86 (0.01)	0.10	17.99 (0.01)	0.16	17.75 (0.02)	0.05
2012-09-21	56191.86	93.8	WHT + ACAM	18.58 (0.01)	0.01	18.21 (0.01)	0.03	18.20 (0.01)	0.19	17.95 (0.01)	0.02
2012-12-23	56285.21	178.1	LT + RATCam	19.84 (0.06) ^S	0.24	19.27 (0.02) ^S	0.03	19.47 (0.11) ^S	0.05	19.03 (0.20) ^S	0.01
2012-12-25	56287.63	180.3	FTN + FS02			19.30 (0.09) ^S	0.03	19.49 (0.01) ^S	0.05	19.12 (0.11) ^S	0.03
2013-01-19	56312.15	202.5	LT + RATCam	20.14 (0.05) ^S	0.24	19.72 (0.04) ^S	0.04	20.14 (0.20) ^S	0.01	19.23 (0.24) ^S	-0.03
2013-01-27	56320.21	209.8	LT + RATCam	20.45 (0.10) ^S	0.24	19.79 (0.05) ^S	0.04	19.78 (0.14) ^S	0.00	19.35 (0.12) ^S	-0.02
2013-02-10	56334.17	222.4	LT + RATCam			19.96 (0.04) ^S	0.04				
2003-02-11	52681.46		SDSS (host)	19.30 (0.01)		19.15 (0.01)		18.70 (0.01)		19.31 (0.07)	

Magnitudes have been corrected for host galaxy contamination; those labelled with a superscript 'S' were determined after image subtraction with SDSS templates (see Supplementary Information section 2.1).

Extended Data Table 2 | Photometry of PTF 12dam outside the optical range.

Date	MJD	Phase	Telescope	UVW2	UVM2	UVW1	SDSS u^*	J	H	K
2012-05-22	56070.38	-15.9	Swift+UVOT	18.83 (0.08)	18.29 (0.07)	17.81 (0.07)	16.86 (0.06)			
2012-05-26	56074.89	-11.8	TNG+NICS					16.82 (0.05)	16.58 (0.07)	16.28 (0.08)
2012-05-30	56077.80	-9.2	Swift+UVOT	18.85 (0.07)	18.24 (0.06)	17.75 (0.07)	16.71 (0.06)			
2012-06-03	56082.06	-5.4	TNG+NICS					16.74 (0.05)	16.39 (0.07)	16.21 (0.07)
2012-06-07	56085.69	-2.1	Swift+UVOT	18.87 (0.08)	18.36 (0.08)	17.87 (0.08)	16.62 (0.07)			
2012-06-10	56089.03	0.9	NOT+NOTCam					16.62 (0.05)	16.35 (0.07)	16.12 (0.06)
2012-06-13	56091.67	3.3	Swift+UVOT	18.99 (0.08)	18.46 (0.08)	18.01 (0.08)	16.58 (0.06)			
2012-06-20	56098.52	9.5	Swift+UVOT	19.27 (0.08)	18.76 (0.08)	18.19 (0.08)	16.80 (0.06)			
2012-06-27	56106.06	16.3	Swift+UVOT	19.50 (0.10)	18.93 (0.10)	18.47 (0.10)	16.99 (0.08)			
2012-06-28	56107.44	17.6	Swift+UVOT	19.48 (0.10)	18.90 (0.10)	18.46 (0.10)	17.00 (0.09)			
2012-07-04	56112.68	22.3	Swift+UVOT	20.16 (0.09)	19.38 (0.09)	18.78 (0.09)	17.32 (0.08)			
2012-07-04	56113.05	22.6	NOT+NOTCam					16.47 (0.05)	16.34 (0.07)	16.11 (0.06)
2012-07-09	56118.04	27.1	TNG+NICS					16.54 (0.05)		
2012-08-01	56141.25	48.1	UKIRT+WFCAM					16.68 (0.10)		
2012-08-05	56145.03	51.5	NOT+NOTCam						16.44 (0.07)	16.08 (0.06)
2012-09-07	56177.04	80.4	NOT+NOTCam					16.73 (0.05)	16.48 (0.06)	16.16 (0.06)
2013-02-20	56343.00	230.4	NOT+NOTCam					18.05 (0.05)	17.61 (0.07)	16.97 (0.06)
2013-03-22	56374.04	258.4	NOT+NOTCam					18.20 (0.06)	17.72 (0.07)	17.13 (0.06)
2013-04-25	56407.00	288.2	NOT+NOTCam					18.22 (0.07)	17.94 (0.08)	17.25 (0.07)

Ultraviolet photometry in Swift UVOT (Ultraviolet and Optical Telescope) bands, and near-infrared photometry in JHK (for details of the data, see Supplementary Information section 2.1).

* SDSS DR9 host magnitude: $u = 19.67$ (0.03).

Extended Data Table 3 | Pan-STARRS1 photometry of PS1-11ap used in this work.

Date	MJD	Telescope	i_{P1}	z_{P1}
2010-12-31	55561.6	PS1	21.49 (0.02)	
2011-01-09	55570.55	PS1	21.06 (0.02)	
2011-01-15	55576.62	PS1	20.74 (0.02)	
2011-01-22	55583.52	PS1		20.78 (0.04)
2011-01-24	55585.44	PS1	20.47 (0.01)	
2011-01-25	55586.61	PS1		20.70 (0.03)
2011-01-28	55589.56	PS1		20.63 (0.03)
2011-01-31	55592.58	PS1		20.58 (0.04)
2011-02-03	55595.53	PS1		20.54 (0.02)
2011-02-21	55613.44	PS1		20.38 (0.02)
2011-03-11	55631.38	PS1		20.35 (0.03)
2011-03-14	55634.32	PS1		20.41 (0.04)
2011-03-26	55646.43	PS1		20.52 (0.03)
2011-03-29	55649.50	PS1		20.56 (0.06)
2011-04-22	55673.34	PS1		20.73 (0.03)
2011-04-25	55676.34	PS1		20.81 (0.06)
2011-05-01	55682.25	PS1		20.82 (0.04)
2011-05-13	55694.28	PS1		20.90 (0.07)
2011-05-22	55703.28	PS1		20.83 (0.06)
2011-05-25	55706.26	PS1		20.99 (0.07)
2011-05-31	55712.26	PS1		21.02 (0.03)
2011-06-06	55718.26	PS1		21.08 (0.05)
2011-12-30	55925.90	PS1		22.60 (0.14)

The i_{P1} magnitudes are transformed to z_{P1} using the observed colour $i - z = -0.18$ at the earliest z point, MJD = 55583.52, with i linearly interpolated to this epoch (see Supplementary Information section 2.2).

Extended Data Table 4 | Log of spectra for PTF 12dam and the PS1-11ap spectra used in this work.

Date	MJD	RF phase (days)	Instrument	Grism/Grating	Range (Å)	Resolution (Å)
PS1-11ap						
2011-02-22	55614	-1	WHT + ISIS	R300B; R158R	3150-10500	12
2011-06-22	55734	+78	GN + GMOS	R150	4000-11000	23
PTF12dam						
2012-05-23	56070.99	-16	Asiago Copernico + AFOSC	Gr04	3400-8200	25
2012-05-24	56071.12	-15	GTC + OSIRIS	R300R	3500-10000	30
2012-05-25	56072.91	-14	WHT + ISIS	R300B; R158R	3250-5100; 5500-9500	3;5
2012-05-26	56073.95	-13	TNG + NICS	IJ	8700-14500	35
2012-06-01	56079.96	-8	NOT + ALFOSC	Gr04	3500-9000	15
2012-06-08	56086.95	-2	NOT + ALFOSC	Gr04	3500-9000	15
2012-06-21	56100.04	+10	NOT + ALFOSC	Gr04	3700-9000	15
2012-06-25	56103.99	+14	WHT + ISIS	R300B; R158R	3200-5200; 5450-10000	6;11
2012-06-29	56107.97	+18	Asiago Copernico + AFOSC	VPH6	3600-10000	15
2012-07-09	56117.99	+27	TNG + NICS	IJ	8700-13500	35
2012-07-17	56125.95	+34	Asiago Copernico + AFOSC	Gr04	3900-8140	13
2012-07-19	56128.03	+36	GTC + OSIRIS	R1000B	3600-7900	7
2012-08-09	56148.95	+55	NOT + ALFOSC	Gr04	3500-8200	20
2012-08-20	56159.92	+65	WHT + ISIS	R300B; R158R	3200-5300; 5450-10000	4;7
2012-09-22	56192.86	+95	WHT + ISIS	R300B; R158R	3200-5300; 5450-10000	6;11
2012-12-16	56277.5	+171	GN + GMOS	B600; R400	3500-8900	3;4
2013-02-10	56334.17	+221	WHT + ISIS	R300B; R158R	3200-5300; 5400-10000	5;10

Spectral evolution of PTF 12dam is plotted in Extended Data Fig. 3. Full PS1-11ap time-series are to be presented elsewhere³¹.

31. McCrum, M. *et al.* The super-luminous supernova PS1-11ap: bridging the gap between low and high redshift. *Mon. Not. R. Astron. Soc.* (submitted).

Deterministic entanglement of superconducting qubits by parity measurement and feedback

D. Ristè¹, M. Dukalski¹, C. A. Watson¹, G. de Lange¹, M. J. Tiggelman¹, Ya. M. Blanter¹, K. W. Lehnert², R. N. Schouten¹ & L. DiCarlo¹

The stochastic evolution of quantum systems during measurement is arguably the most enigmatic feature of quantum mechanics. Measuring a quantum system typically steers it towards a classical state, destroying the coherence of an initial quantum superposition and the entanglement with other quantum systems. Remarkably, the measurement of a shared property between non-interacting quantum systems can generate entanglement, starting from an uncorrelated state. Of special interest in quantum computing is the parity measurement¹, which projects the state of multiple qubits (quantum bits) to a state with an even or odd number of excited qubits. A parity meter must discern the two qubit-excitation parities with high fidelity while preserving coherence between same-parity states. Despite numerous proposals for atomic², semiconducting^{1,3–7} and superconducting qubits^{8,9}, realizing a parity meter that creates entanglement for both even and odd measurement results has remained an outstanding challenge. Here we perform a time-resolved, continuous parity measurement of two superconducting qubits using the cavity in a three-dimensional circuit quantum electrodynamics^{10,11} architecture and phase-sensitive parametric amplification¹². Using postselection, we produce entanglement by parity measurement reaching 88 per cent fidelity to the closest Bell state. Incorporating the parity meter in a feedback-control loop, we transform the entanglement generation from probabilistic to fully deterministic, achieving 66 per cent fidelity to a target Bell state on demand. These realizations of a parity meter and a feedback-enabled deterministic measurement protocol provide key ingredients for active quantum error correction in the solid state^{13–15}.

Recent advances in nearly quantum-limited amplification¹² and improved qubit coherence times in three-dimensional circuit quantum electrodynamics (3D cQED) architectures¹¹ have allowed investigations of the gradual collapse of single-qubit wavefunctions in the solid state^{16,17}, following previous fundamental studies in atomic systems¹⁸. The continuous measurement of a joint property extends this study to the multiqubit setting, resolving the projection to states which are inaccessible via individual qubit measurements. In a two-qubit system, the ideal parity measurement transforms an unentangled superposition state $|\psi^0\rangle = (|00\rangle + |01\rangle + |10\rangle + |11\rangle)/2$ into Bell states

$$|\Phi^+\rangle = \frac{1}{\sqrt{2}}(|01\rangle + |10\rangle) \text{ and } |\Psi^+\rangle = \frac{1}{\sqrt{2}}(|00\rangle + |11\rangle)$$

for odd and even outcome, respectively. Beyond generating entanglement between non-interacting qubits^{1,4–7}, parity measurements allow deterministic two-qubit gates^{3,19} and play a key role as syndrome detectors in quantum error correction^{13,14}. A heralded parity measurement has been recently realized for nuclear spins in diamond²⁰. By minimizing measurement-induced decoherence at the expense of single-shot fidelity, Pfaff *et al.*²⁰ generated highly entangled states with 3% success probability. Here we realize the first solid-state parity meter that produces entanglement with unity probability.

Our parity meter realization exploits the dispersive regime¹⁰ in two-qubit cQED. Qubit-state dependent shifts of a cavity resonance (here, the fundamental of a 3D cavity enclosing transmon qubits Q_A and Q_B) allow joint qubit readout by homodyne detection of an applied microwave pulse transmitted through the cavity (Fig. 1a). The temporal average V_{int} of the homodyne response $V_P(t)$ over the time interval $[t_i, t_f]$ constitutes the measurement needle, with expectation value

$$\langle V_{\text{int}} \rangle = \text{Tr}(\mathcal{O}\rho)$$

where ρ is the two-qubit density matrix and the observable \mathcal{O} has the general form

$$\mathcal{O} = \beta_0 + \beta_A \sigma_z^A + \beta_B \sigma_z^B + \beta_{BA} \sigma_z^A \sigma_z^B$$

where σ_z^q is the Pauli operator for qubit q . The coefficients β_0 , β_A , β_B and β_{BA} depend on the strength ε_p , frequency f_p and duration τ_p of the measurement pulse, and also on the cavity linewidth κ and the frequency shifts $2\chi_A$ and $2\chi_B$ of the fundamental mode when Q_A and Q_B are individually excited from $|0\rangle$ to $|1\rangle$. The necessary condition for realizing a parity meter is $\beta_A = \beta_B = 0$ (β_0 constitutes a trivial offset). A simple approach^{8,21}, pursued here, is to set f_p to the average of the resonance frequencies for the four computational basis states $|ij\rangle$ ($i, j \in \{0, 1\}$) and to match $\chi_A = \chi_B$. We engineer this matching by targeting specific qubit transition frequencies f_A and f_B below and above the fundamental mode during fabrication and using an external magnetic field to fine-tune f_B *in situ* (Extended Data Fig. 1). We align χ_A to χ_B to within $\sim 0.06\kappa = 2\pi \times 90$ kHz (Fig. 1b). The ensemble-average $\langle V_P \rangle$ confirms nearly identical high response for odd-parity computational states $|01\rangle$ and $|10\rangle$, and nearly identical low response for the even-parity $|00\rangle$ and $|11\rangle$ (Fig. 1c). The transients observed are consistent with the independently measured κ , χ_A and χ_B values, and the 4-MHz bandwidth of the Josephson parametric amplifier (JPA; Fig. 1a) at the front end of the output amplification chain (see Extended Data Fig. 2 for a detailed schematic of the set-up). Single-shot histograms (Fig. 1d) demonstrate the increasing ability of V_{int} to discern states of different parity as t_f grows (keeping $t_i = 0$), and its inability to discriminate between states of the same parity. The histogram separations at $t_f = 400$ ns give $|\beta_A|, |\beta_B| < 0.02 |\beta_{BA}|$ (Extended Data Fig. 3).

Moving beyond the description of the measurement needle, we now investigate the collapse of the two-qubit state during parity measurement. We prepare the qubits in the maximal superposition state $|\psi^0\rangle = \frac{1}{2}(|00\rangle + |01\rangle + |10\rangle + |11\rangle)$, apply a parity measurement pulse for τ_p , and perform tomography of the final two-qubit density matrix ρ with and without conditioning on V_{int} (Fig. 2a). We choose a weak parity measurement pulse exciting $\bar{n}_{\text{ss}} = 2.5$ intra-cavity photons on average in the steady-state, at resonance. A delay of $3.5/\kappa = 350$ ns is inserted to deplete the cavity of photons before performing tomography. The tomographic joint readout is also carried out at f_p , but with 14 dB higher power, at which the cavity response is weakly non-linear and sensitive to both single-qubit terms and two-qubit correlations ($\beta_A \approx \beta_B \approx \beta_{BA}$, see Extended Data Fig. 3), as required for tomographic reconstruction²².

¹Kavli Institute of Nanoscience, Delft University of Technology, PO Box 5046, 2600 GA Delft, The Netherlands. ²JILA, National Institute of Standards and Technology and Department of Physics, University of Colorado, Boulder, Colorado 80309, USA.

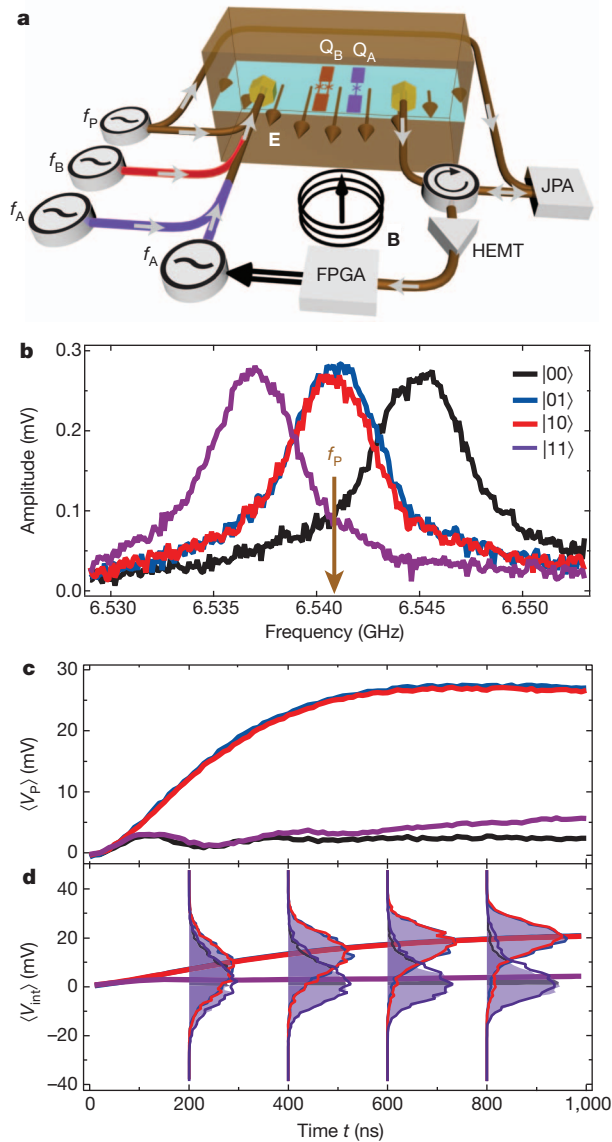


Figure 1 | Realization of cavity-based two-qubit parity readout in circuit QED. **a**, Simplified diagram of the experimental set-up. Single- and double-junction transmon qubits (Q_A and Q_B , respectively) dispersively couple to the fundamental mode E of a 3D copper cavity enclosing them. The transition frequency of Q_B is tuned by a static magnetic field B generated by an external coil. Parity measurement is performed by homodyne detection of the qubit state-dependent cavity response¹⁰ using phase-sensitive Josephson parametric amplification (JPA)¹². Following further amplification at 4 K by a low-noise semiconductor amplifier (HEMT) and room temperature, the signal is demodulated and integrated. A field-programmable-gate-array (FPGA) controller closes the feedback loop that achieves deterministic entanglement by parity measurement (Fig. 4). **b**, Matching of the dispersive cavity shifts realizing a parity measurement. Different colours correspond to qubits prepared in $|00\rangle$ (black), $|01\rangle$ (blue), $|10\rangle$ (red) and $|11\rangle$ (purple). **c**, Ensemble-averaged homodyne response $\langle V_p \rangle$ for qubits prepared in the four computational basis states (same colour code). **d**, Curves, corresponding ensemble averages of the running integral $\langle V_{\text{int}} \rangle$ of $\langle V_p \rangle$ between $t_i = 0$ and $t_f = t$. Single-shot histograms (5,000 counts each) of V_{int} are shown in 200-ns increments.

The ideal continuous parity measurement gradually suppresses the unconditioned density matrix elements $\rho_{ij,kl} = \langle ij|\rho|kl\rangle$ connecting states with different parity (either $i \neq k$ or $j \neq l$), and leaves all other coherences (off-diagonal terms) and all populations (diagonal terms) unchanged. The experimental tomography reveals the expected suppression of coherence between states of different parity (Fig. 2b, c). The temporal evolution of $|\rho_{11,10}|$, with near full suppression by $\tau_p = 400$ ns,

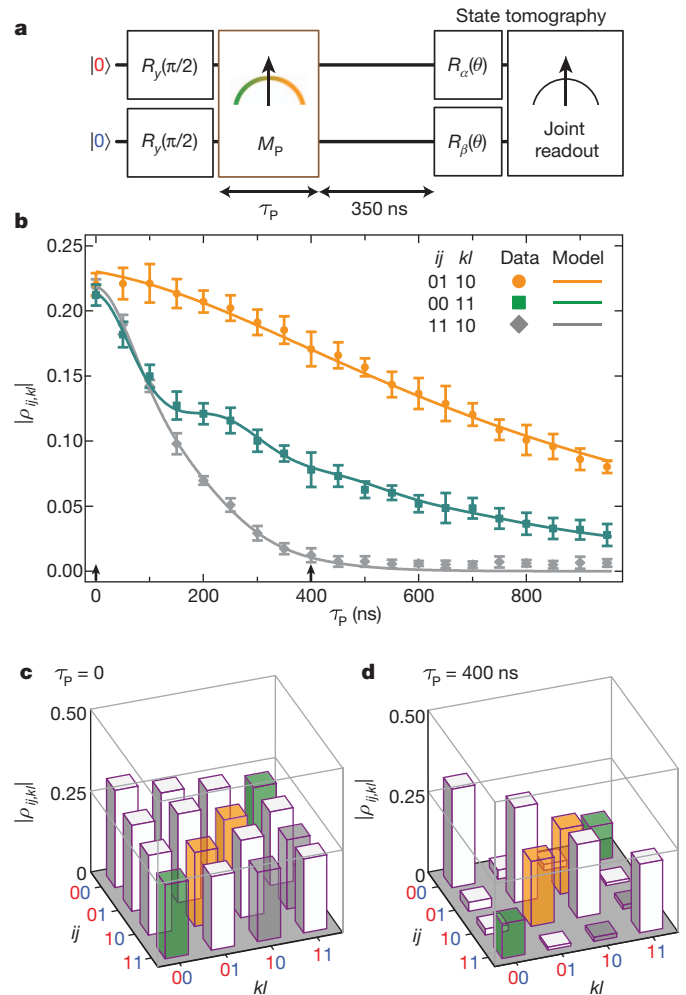


Figure 2 | Unconditioned two-qubit evolution under continuous parity measurement. **a**, Pulse sequence including preparation of the qubits in the maximal superposition state $\rho^{(0)} = |\psi^0\rangle\langle\psi^0|$, parity measurement and tomography of the final two-qubit state ρ using joint readout. **b**, Absolute coherences $|\rho_{11,10}|$, $|\rho_{01,10}|$, $|\rho_{00,11}|$ following a parity measurement with variable duration τ_p . Free parameters of the model are the steady-state photon number on resonance $\bar{n}_{ss} = 2.5 \pm 0.1$, the difference $(\chi_A - \chi_B)/\pi = 235 \pm 4$ kHz, and the absolute coherence values at $\tau_p = 0$ to account for few-percent pulse errors in state preparation and tomography pre-rotations. Note that the frequency mismatch differs from that in Fig. 1b owing to its sensitivity to measurement power. Error bars, standard deviation of 15 repetitions of tomography, with 22,500 averages per set of pre-rotations. **c**, **d**, Extracted density matrices for $\tau_p = 0$ (**c**) and $\tau_p = 400$ ns (**d**), by which time coherence across the parity subspaces (grey columns) is almost fully suppressed, while coherence persists within the odd-parity (orange columns) and even-parity (green columns) subspaces. See Extended Data Fig. 4 for the temporal evolution with parity measurement off and Extended Data Figs 5 and 6 for two-qubit tomography at other values of τ_p and \bar{n}_{ss} , respectively.

is quantitatively matched by a master-equation simulation of the two-qubit system (see Methods). Tomography also unveils a non-ideality: albeit more gradually, our parity measurement partially suppresses the absolute coherence between equal-parity states, $|\rho_{01,10}|$ and $|\rho_{00,11}|$. The effect is also quantitatively captured by the model. Although intrinsic qubit decoherence contributes (see Extended Data Fig. 4 for quantitative details), the dominant mechanism is the different a.c. Stark phase shift induced by intra-cavity photons on basis states of the same parity^{8,9,17}. This phase shift has both deterministic and stochastic components, and the latter suppresses absolute coherence under ensemble averaging. We emphasize that this imperfection is technical rather than fundamental. It can be mitigated in the odd subspace by perfecting the

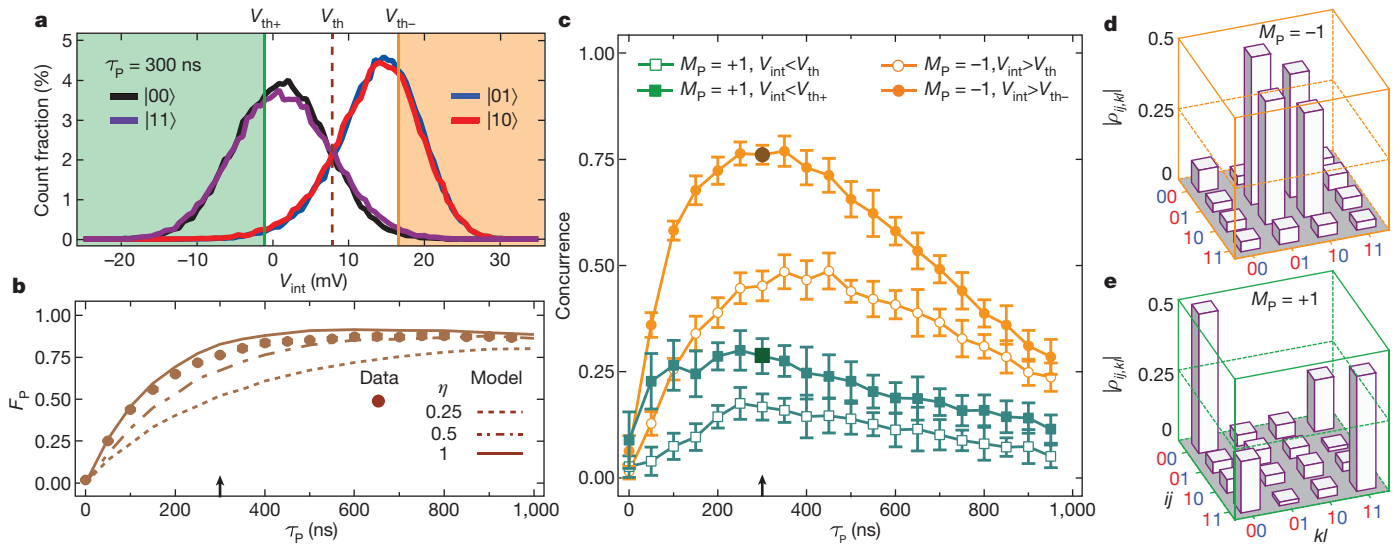


Figure 3 | Probabilistic entanglement generation by postselected parity measurement. **a**, Histograms of V_{int} ($\tau_P = 300$ ns) for the four computational states. The results are digitized into $M_P = +1(-1)$ for V_P below (above) a chosen threshold. Coloured areas indicate the choice of thresholds $V_{\text{th}+}$ and $V_{\text{th}-}$ for $M_P = +1$ (green) and $M_P = -1$ (orange), respectively. **b**, Parity readout fidelity F_P as a function of τ_P . We define $F_P = 1 - \varepsilon_e - \varepsilon_o$, with $\varepsilon_e = p(M_P = -1|\text{even})$ the readout error probability for a prepared even state, and similarly for ε_o , using the F_P -maximizing single threshold V_{th} (see also Extended Data Fig. 7). Data are corrected for residual qubit excitations (see Methods). Error bars (smaller than the dot size) are the standard deviation obtained from 15 sets of histograms, each with 22,500 counts per prepared state. Model curves are obtained from 5,000 quantum trajectories for each initial state and τ_P , with quantum efficiencies $\eta = 0.25, 0.5$ and 1 for the readout amplification chain (see Methods). No single value of η matches the dependence

matching of χ_B to χ_A , and in the even subspace by increasing $\chi_{A,B}/\kappa$ (~ 1.3 in this experiment).

The ability to discern parity subspaces while preserving coherence within each opens the door to generating entanglement by parity measurement on $|\psi^0\rangle$. For every run of the sequence in Fig. 2, we discriminate V_{int} using the threshold V_{th} that maximizes the parity measurement fidelity F_P (Fig. 3a). Assigning the parity measurement result $M_P = +1(-1)$ to V_{int} below (above) V_{th} , we bisect the tomographic measurements into two groups, and obtain the density matrix for each. We quantify the entanglement achieved in each case using concurrence \mathcal{C} as the metric²³, which ranges from 0% for an unentangled state to 100% for a Bell state. As τ_P grows (Fig. 3b), the optimal balance between increasing F_P at the cost of measurement-induced dephasing and intrinsic decoherence is reached at ~ 300 ns (Fig. 3c). Postselection on $M_P = \pm 1$ achieves $\mathcal{C}_{M_P = -1} = 45 \pm 3\%$ and $\mathcal{C}_{M_P = +1} = 17 \pm 3\%$, with each case occurring with probability $p_{\text{success}} \approx 50\%$. The higher performance for $M_P = -1$ results from lower measurement-induced dephasing in the odd subspace, consistent with Fig. 2.

The entanglement achieved by this probabilistic protocol can be increased with more stringent postselection. Setting a higher threshold $V_{\text{th}-}$ achieves $\mathcal{C}_{M_P = -1} = 77 \pm 2\%$ but keeps $p_{\text{success}} \approx 20\%$ of runs. Analogously, using $V_{\text{th}+}$ achieves $\mathcal{C}_{M_P = +1} = 29 \pm 4\%$ with similar p_{success} (Fig. 3d, e). However, increasing \mathcal{C} at the expense of reduced p_{success} is not evidently beneficial for quantum information processing. For the many tasks calling for maximally-entangled qubit pairs (ebits), one may use an optimized distillation protocol²³ to prepare one ebit from $N = 1/E_{\mathcal{N}}(\rho)$ pairs in a partially-entangled state ρ , where $E_{\mathcal{N}}$ is the logarithmic negativity²³. The efficiency \mathcal{E} of ebit generation would be $\mathcal{E} = p_{\text{success}} E_{\mathcal{N}}(\rho)$. For postselection on $M_P = -1$, we calculate $\mathcal{E} = 0.31$ ebits per run using V_{th} and $\mathcal{E} = 0.20$ using $V_{\text{th}-}$. Evidently, increasing entanglement at the expense of reducing p_{success} is counterproductive in this context.

of F_P on τ_P . We attribute this discrepancy to low-frequency fluctuations in the parametric amplifier bias point, not included in the model. **c**, Concurrence \mathcal{C} of the two-qubit entangled state obtained by postselection on $M_P = -1$ (orange) and on $M_P = +1$ (green squares). Open symbols correspond to the threshold V_{th} that maximizes F_P , binning $p_{\text{success}} \approx 50\%$ of the data (from Fig. 2) into each case. Filled symbols correspond to a threshold $V_{\text{th}-}$ ($V_{\text{th}+}$) for postselection on $M_P = -1$ ($+1$), at which $\varepsilon_o(\varepsilon_e) = 0.01$. Concurrence is optimized at $\tau_P \approx 300$ ns, where $p_{\text{success}} \approx 20\%$ in each case. We use maximum-likelihood estimation²² (MLE) to ensure physical density matrices, but concurrence values obtained with and without MLE differ by less than 3% over the full data set. Error bars, standard deviation of the concurrence obtained from 15 repetitions of tomography. **d**, **e**, State tomography conditioned on $V_P > V_{\text{th}-}$ (**d**) and $V_P < V_{\text{th}+}$ (**e**), with $\tau_P = 300$ ns, corresponding to the dark symbols in **c**. The fidelity of these states to the closest Bell state is 88% (**d**) and 64% (**e**).

Motivated by the above observation, we finally demonstrate the use of feedback control to transform entanglement by parity measurement from probabilistic to deterministic, that is, $p_{\text{success}} = 100\%$. Whereas initial proposals in cQED focused on analogue feedback schemes²⁴, here we adopt a digital strategy²⁵. Specifically, we use a custom-built programmable controller to apply a π pulse on Q_A conditional on measuring $M_P = +1$ (using V_{th} , Fig. 4). In addition to switching the two-qubit parity, this pulse lets us choose which odd-parity Bell state to target by selecting the phase φ of the conditional pulse. To optimize deterministic entanglement, we need to maximize overlap to the same odd-parity Bell state for $M_P = -1$ (Fig. 4b) as for $M_P = +1$ (Fig. 4c). For the targeted state $|\Phi^+\rangle$, this requires cancelling the deterministic a.c. Stark phase $\varphi_e = 0.73\pi$ accrued between $|00\rangle$ and $|11\rangle$ when $M_P = +1$. This is accomplished by choosing $\varphi = (\pi - \varphi_e)/2$, which clearly maximizes the entanglement obtained when no postselection on M_P is applied (Fig. 4c, d). The highest deterministic $\mathcal{C} = 34\%$ achieved is lower than for our best probabilistic scheme, but the boost to $p_{\text{success}} = 100\%$ achieves a higher $\mathcal{E} = 0.41$ ebits per run.

Our experiment extends the fundamental study of continuous measurement^{16,17} in superconducting circuits to the multiqubit scenario, providing a test-bed for the investigation of wavefunction projection and induced dephasing. Furthermore, the implemented parity meter generates entanglement for any measurement result, making it suitable for deterministic quantum information processing protocols. Specifically, the combination of parity measurement with digital feedback realizes a multiqubit measurement-based protocol in the solid state made deterministic through feedback, as achieved with photonic²⁶, ionic^{27,28} and atomic²⁹ systems. Future experiments will target the complementary use of analogue feedback control to combat measurement-induced dephasing^{9,30}. Integration of analogue feedback will refine the control over quantum measurement and feedback¹⁵ required to extend quantum coherence by active control methods.

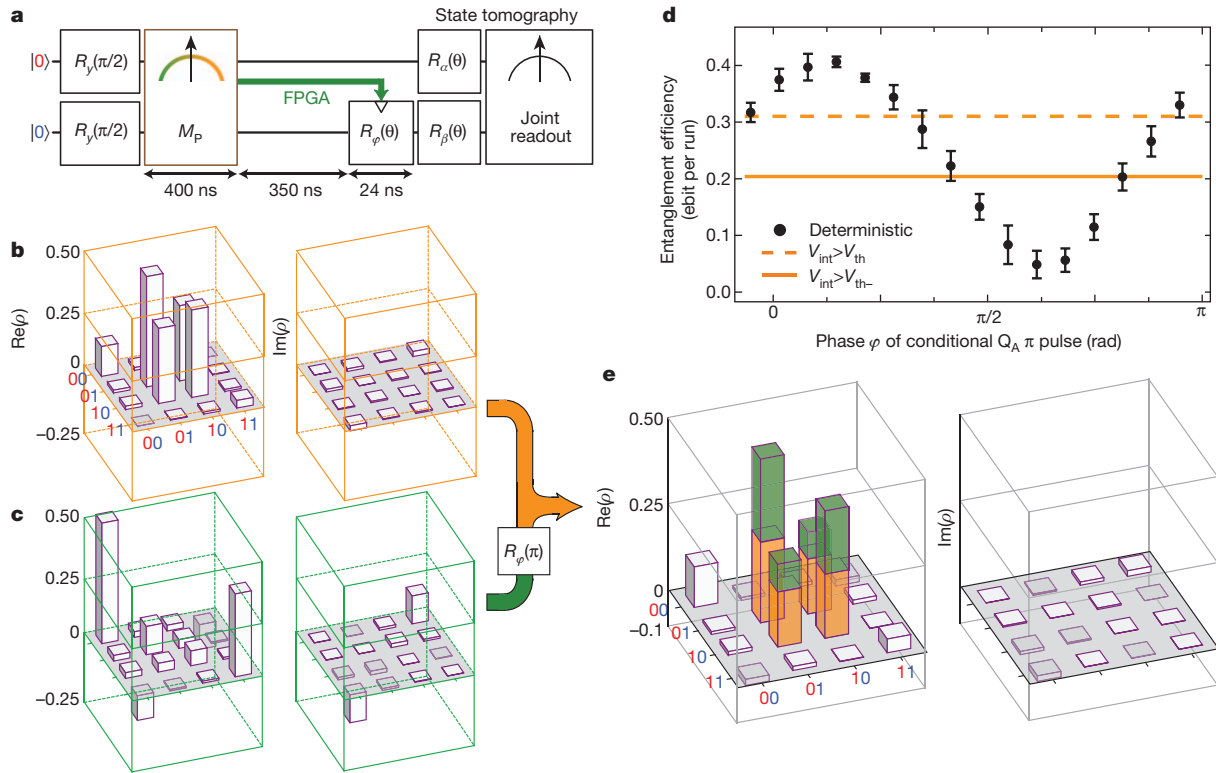


Figure 4 | Deterministic entanglement generation using feedback. **a**, We close a digital feedback loop by triggering (via the FPGA) a π pulse on Q_A conditional on the parity measurement result $M_P = +1$. This π pulse switches the two-qubit parity from even to odd, and allows the deterministic targeting of $|\Phi^+\rangle = (|01\rangle + |10\rangle)/\sqrt{2}$. **b, c**, Full state tomography (with real (imaginary) part of the density matrix on the left (right)) for parity measurement results $M_P = -1$ (**b**) and $M_P = +1$ (**c**), each occurring with $\sim 50\%$ probability. The deterministic a.c. Stark phase acquired between $|01\rangle$ and $|10\rangle$ during parity measurement (due to residual mismatch between χ_A and χ_B) is compensated by a global phase rotation in the tomography pulses. A different a.c. Stark phase is

acquired between $|00\rangle$ and $|11\rangle$, resulting in the state shown in **c**, with the maximal overlap with even Bell state $[|00\rangle + \exp(-i\varphi_e)|11\rangle]/\sqrt{2}$ at $\varphi_e = 0.73\pi$. **d**, Generation rate of entanglement using feedback, as a function of the phase φ of the π pulse. The deterministic entanglement generation efficiency outperforms the efficiencies obtained with postselection (Fig. 3). Error bars, standard deviation of seven repetitions of the experiment at each φ . **e**, Full state tomography for deterministic entanglement [$\varphi = (\pi - \varphi_e)/2$], achieving fidelity $\langle\Phi^+|\rho|\Phi^+\rangle = 66\%$ to the targeted $|\Phi^+\rangle$, and concurrence $C = 34\%$. Coloured bars highlight the contribution from cases $M_P = -1$ (orange) and $M_P = +1$ (green).

METHODS SUMMARY

Device parameters. Lorentzian best fits to cavity transmission (Fig. 1b) yield $\kappa = \kappa_{\text{out}} + \kappa_{\text{in}} = 2\pi \times (1.56 \pm 0.01 \text{ MHz})$ and $\{\chi_A, \chi_B\}/\pi = \{-4.03 \pm 0.02, -4.21 \pm 0.02\} \text{ MHz}$. From room-temperature characterization, we estimate asymmetric output/input couplings $\kappa_{\text{out}}/\kappa_{\text{in}} \approx 8$. The qubits have transition frequencies $\{f_A, f_B\} = \{5.52, 7.80\} \text{ GHz}$, relaxation times $\{T_1^A, T_1^B\} = \{22, 7\} \mu\text{s}$, and pure dephasing times $\{T_2^{\varphi, A}, T_2^{\varphi, B}\} = \{11, 8\} \mu\text{s}$ (see also Extended Data Fig. 8). Using the method detailed in ref. 31, we estimate a residual excitation of 1%(2%) for $Q_A(Q_B)$.

Readout signal processing. In Fig. 1b we probe the cavity with a pulse ($\bar{n}_{\text{ss}} \approx 1.4$) at variable frequency, after preparing the qubits in one of the four computational states. The cavity transmission is acquired with homodyne detection at 10 MHz intermediate frequency. In Fig. 1c and d the cavity response ($\bar{n}_{\text{ss}} = 2.5$), first amplified by the JPA, is demodulated with 0 intermediate frequency (measurement, local oscillator, and pump tones are provided by the same generator). For each shot, the average homodyne signal over a 2.5 μs window preceding state preparation is subtracted. This subtraction mitigates the infiltration of low-frequency fluctuations in the JPA bias. In Figs 2–4, $t_i = 100 \text{ ns}$ and $t_f = \tau_p + 150 \text{ ns}$, experimentally found to maximize F_p . Similarly, an offset integrated over 2.5 μs is subtracted from each V_{int} (Extended Data Fig. 9).

Model. The system is described by the dispersive Hamiltonian¹⁰:

$$H/\hbar = \left(\omega_r - \sum_{q=A,B} \chi_q \sigma_z^q \right) a^\dagger a - \sum_{q=A,B} \frac{1}{2} \omega_q \sigma_z^q + \varepsilon_p [a^\dagger e^{-i\omega_p t} + a e^{i\omega_p t}]$$

The cavity-mediated qubit-qubit interaction $J(\sigma_+^B \sigma_-^A + \sigma_-^B \sigma_+^A)$ is disregarded, as J vanishes for $\chi_A = \chi_B$. We model the evolution of ρ following the method of

quantum trajectories in refs 8, 9, 21 and 32. The stochastic master equation, valid for $t \ll T_1^A, T_1^B$, is:

$$\begin{aligned} d\rho = & \frac{1}{i\hbar} [H, \rho] dt \\ & + \sum_{q=A,B} \left(\frac{1}{T_1^q} \mathcal{D}[\sigma_z^q] \rho + \frac{1}{2T_2^{\varphi,q}} \mathcal{D}[\sigma_z^q] \rho \right) dt \\ & - \sum_{ijkl} \chi_{ij,kl} \left(\text{Im}[\alpha_{ij}^* \alpha_{kl}] + i \text{Re}[\alpha_{ij}^* \alpha_{kl}] \right) \Pi_{ij} \rho \Pi_{kl} dt \\ & + \sqrt{\kappa \eta} \mathcal{M}[\Pi_x e^{-i\phi}] \rho dW(t) \end{aligned} \quad (1)$$

with operators $\Pi_{ij} = |ij\rangle \langle ij|$ and $\Pi_x = \sum_{ij} \alpha_{ij} \Pi_{ij}$, super-operators $\mathcal{D}[\Theta] \rho = \Theta \rho \Theta^\dagger - \frac{1}{2} \{ \Theta^\dagger \Theta, \rho \}$ and $\mathcal{M}[\Theta] \rho = \Theta \rho + \rho \Theta^\dagger - \langle \Theta + \Theta^\dagger \rangle \rho$. Here, ϕ is the homodyne-detection phase set by the JPA pump, and $\chi_{ij,kl} = \chi_{ij} - \chi_{kl}$, where $\chi_{ij} = \langle ij | \sum_{q=A,B} \chi_q \sigma_z^q | ij \rangle$. The dynamics of α_{ij} in the frame rotating at ω_p is given by:

$$\dot{\alpha}_{ij} = -i\varepsilon_p(t) - i(\omega_r - \omega_p + \chi_{ij})\alpha_{ij} - \frac{\kappa}{2}\alpha_{ij}$$

dW is the noise in the homodyne record:

$$V_p(t) dt \propto \sqrt{\kappa \eta} \langle \Pi_x e^{-i\phi} + \Pi_x^\dagger e^{i\phi} \rangle dt + dW$$

Quantum trajectories are unravelled by numerically solving equation (1) with $dt = 1 \text{ ns}$ and a Wiener white-noise process dW (zero mean, variance dt) generated pseudo-randomly. For each trajectory, V_{int} is obtained using the same integration and offset-subtraction parameters as in the experiment. The unconditioned ρ is obtained by solving equation (1) without the last term.

Online Content Any additional Methods, Extended Data display items and Source Data are available in the online version of the paper; references unique to these sections appear only in the online paper.

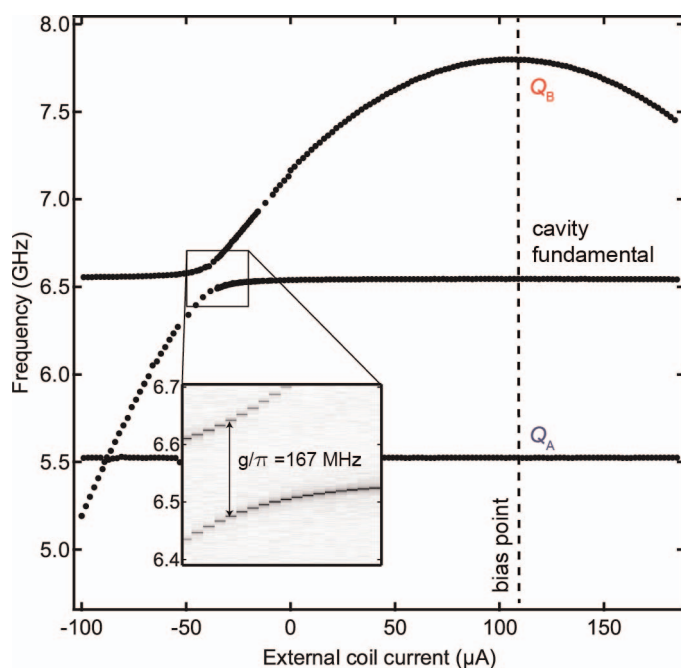
Received 12 June; accepted 24 July 2013.

1. Ruskov, R. & Korotkov, A. N. Entanglement of solid-state qubits by measurement. *Phys. Rev. B* **67**, 241305 (2003).
2. Kerckhoff, J., Bouten, L., Silberfarb, A. & Mabuchi, H. Physical model of continuous two-qubit parity measurement in a cavity-QED network. *Phys. Rev. A* **79**, 024305 (2009).
3. Engel, H.-A. & Loss, D. Fermionic Bell-state analyzer for spin qubits. *Science* **309**, 586–588 (2005).
4. Trauzettel, B., Jordan, A. N., Beenakker, C. W. J. & Büttiker, M. Parity meter for charge qubits: an efficient quantum entangler. *Phys. Rev. B* **73**, 235331 (2006).
5. Ionicioiu, R. Entangling spins by measuring charge: a parity-gate toolbox. *Phys. Rev. A* **75**, 032339 (2007).
6. Williams, N. S. & Jordan, A. N. Entanglement genesis under continuous parity measurement. *Phys. Rev. A* **78**, 062322 (2008).
7. Haack, G., Förster, H. & Büttiker, M. Parity detection and entanglement with a Mach-Zehnder interferometer. *Phys. Rev. B* **82**, 155303 (2010).
8. Lalmière, K., Gambetta, J. M. & Blais, A. Tunable joint measurements in the dispersive regime of cavity QED. *Phys. Rev. A* **81**, 040301 (2010).
9. Tornberg, L. & Johansson, G. High-fidelity feedback-assisted parity measurement in circuit QED. *Phys. Rev. A* **82**, 012329 (2010).
10. Blais, A., Huang, R.-S., Wallraff, A., Girvin, S. M. & Schoelkopf, R. J. Cavity quantum electrodynamics for superconducting electrical circuits: an architecture for quantum computation. *Phys. Rev. A* **69**, 062320 (2004).
11. Paik, H. *et al.* Observation of high coherence in Josephson junction qubits measured in a three-dimensional circuit QED architecture. *Phys. Rev. Lett.* **107**, 240501 (2011).
12. Castellanos-Beltrán, M. A., Irwin, K. D., Hilton, G. C., Vale, L. R. & Lehnert, K. W. Amplification and squeezing of quantum noise with a tunable Josephson metamaterial. *Nature Phys.* **4**, 929–931 (2008).
13. Nielsen, M. A. & Chuang, I. L. *Quantum Computation and Quantum Information* (Cambridge Univ. Press, 2000).
14. Ahn, C., Doherty, A. C. & Landahl, A. J. Continuous quantum error correction via quantum feedback control. *Phys. Rev. A* **65**, 042301 (2002).
15. Devoret, M. H. & Schoelkopf, R. J. Superconducting circuits for quantum information: an outlook. *Science* **339**, 1169–1174 (2013).
16. Hatridge, M. *et al.* Quantum back-action of an individual variable-strength measurement. *Science* **339**, 178–181 (2013).
17. Murch, K. W., Weber, S. J., Macklin, C. & Siddiqi, I. Observing single quantum trajectories of a superconducting qubit. Preprint at <http://arXiv.org/abs/1305.7270> (2013).
18. Guerlin, C. *et al.* Progressive field-state collapse and quantum non-demolition photon counting. *Nature* **448**, 889–893 (2007).
19. Beenakker, C. W. J., DiVincenzo, D. P., Emary, C. & Kindermann, M. Charge detection enables free-electron quantum computation. *Phys. Rev. Lett.* **93**, 020501 (2004).
20. Pfaff, W. *et al.* Demonstration of entanglement-by-measurement of solid-state qubits. *Nature Phys.* **9**, 29–33 (2013).
21. Hutchison, C. L., Gambetta, J. M., Blais, A. & Wilhelm, F. K. Quantum trajectory equation for multiple qubits in circuit QED: generating entanglement by measurement. *Can. J. Phys.* **87**, 225–231 (2009).
22. Filipp, S. *et al.* Two-qubit state tomography using a joint dispersive readout. *Phys. Rev. Lett.* **102**, 200402 (2009).
23. Horodecki, R., Horodecki, P., Horodecki, M. & Horodecki, K. Quantum entanglement. *Rev. Mod. Phys.* **81**, 865–942 (2009).
24. Sarovar, M., Goan, H.-S., Spiller, T. P. & Milburn, G. J. High-fidelity measurement and quantum feedback control in circuit QED. *Phys. Rev. A* **72**, 062327 (2005).
25. Ristè, D., Bultink, C. C., Lehnert, K. W. & DiCarlo, L. Feedback control of a solid-state qubit using high-fidelity projective measurement. *Phys. Rev. Lett.* **109**, 240502 (2012).
26. Furusawa, A. *et al.* Unconditional quantum teleportation. *Science* **282**, 706–709 (1998).
27. Barrett, M. D. *et al.* Deterministic quantum teleportation of atomic qubits. *Nature* **429**, 737–739 (2004).
28. Riebe, M. *et al.* Deterministic quantum teleportation with atoms. *Nature* **429**, 734–737 (2004).
29. Sherson, J. F. *et al.* Quantum teleportation between light and matter. *Nature* **443**, 557–560 (2006).
30. Frisk Kockum, A., Tornberg, L. & Johansson, G. Undoing measurement-induced dephasing in circuit QED. *Phys. Rev. A* **85**, 052318 (2012).
31. Ristè, D., van Leeuwen, J. G., Ku, H.-S., Lehnert, K. W. & DiCarlo, L. Initialization by measurement of a superconducting quantum bit circuit. *Phys. Rev. Lett.* **109**, 050507 (2012).
32. Gambetta, J. *et al.* Quantum trajectory approach to circuit QED: quantum jumps and the Zeno effect. *Phys. Rev. A* **77**, 012112 (2008).
33. Gambetta, J. *et al.* Qubit-photon interactions in a cavity: measurement induced dephasing and number splitting. *Phys. Rev. A* **74**, 042318 (2006).
34. Houck, A. A. *et al.* Controlling the spontaneous emission of a superconducting transmon qubit. *Phys. Rev. Lett.* **101**, 080502 (2008).
35. Koch, J. *et al.* Charge-insensitive qubit design derived from the Cooper pair box. *Phys. Rev. A* **76**, 042319 (2007).
36. Motzoi, F., Gambetta, J. M., Rebentrost, P. & Wilhelm, F. K. Simple pulses for elimination of leakage in weakly nonlinear qubits. *Phys. Rev. Lett.* **103**, 110501 (2009).

Acknowledgements We thank C. C. Bultink and H.-S. Ku for experimental assistance, and G. Haack, R. Hanson, G. Johansson, A. F. Kockum and L. Tornberg for discussions. We acknowledge funding from the Dutch Organization for Fundamental Research on Matter (FOM), the Netherlands Organization for Scientific Research (NWO, VIDI scheme), the EU FP7 integrated projects SOLID and SCALEQIT, and partial support from the DARPA QuEST programme.

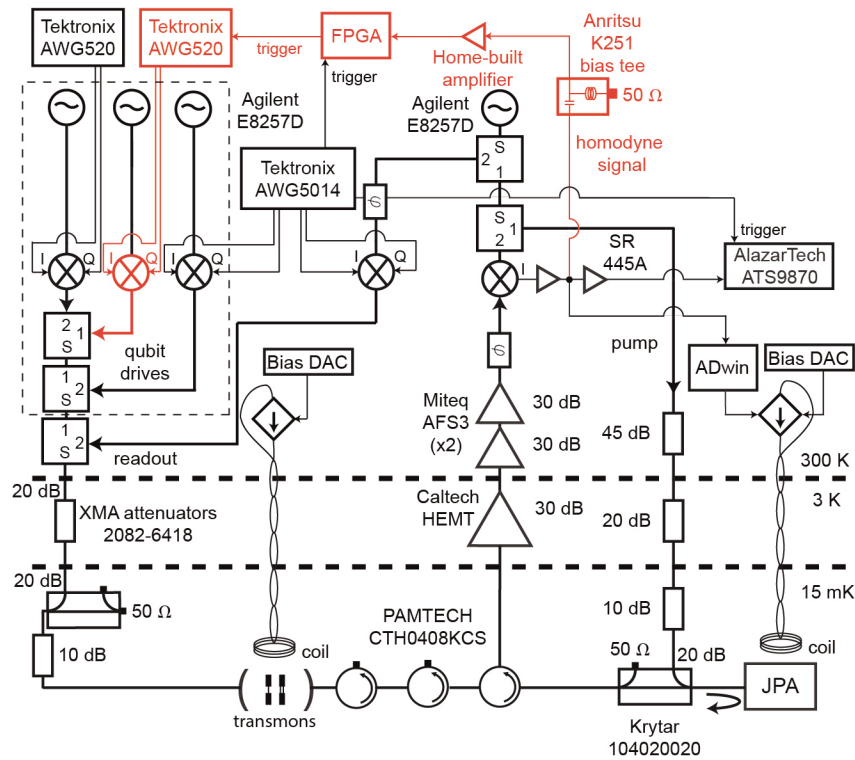
Author Contributions D.R. fabricated the device. D.R. and C.A.W. performed the measurements. D.R., C.A.W. and G.d.L. analysed the data. M.D., Ya.M.B. and L.D.C. provided theory support. M.J.T. and R.N.S. produced the feedback controller. K.W.L. designed the JPA. D.R., G.d.L. and L.D.C. wrote the manuscript with feedback from all authors. L.D.C. designed and supervised the project.

Author Information Reprints and permissions information is available at www.nature.com/reprints. The authors declare no competing financial interests. Readers are welcome to comment on the online version of the paper. Correspondence and requests for materials should be addressed to L.D.C. (ldcarlo@tudelft.nl).



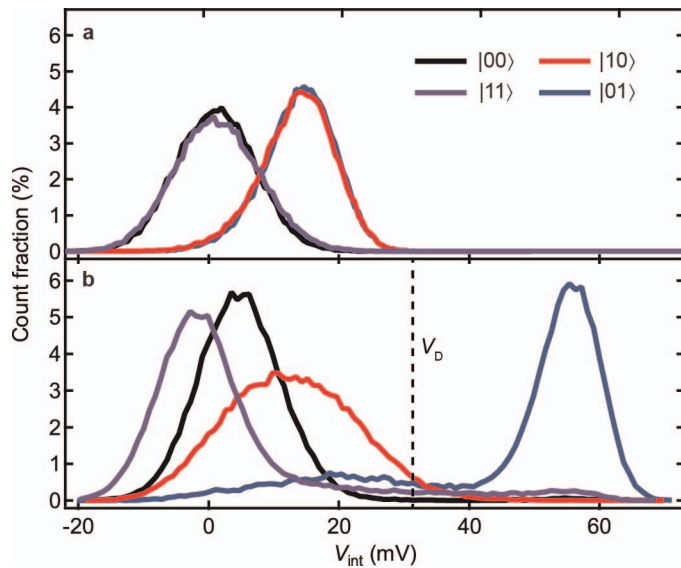
Extended Data Figure 1 | Spectroscopy of the two-qubit and cavity system.

The transition frequency of Q_B is tuned by applying magnetic flux through its SQUID loop with an external coil. Q_A ($f_A = 5.52$ GHz) is a single-junction transmon and thus not tunable. Q_B was designed tunable to allow trimming of the dispersive-shift matching condition. However, the maximal frequency of Q_B ($f_B = 7.80$ GHz) is still approximately 20 MHz lower than needed for a perfect match of dispersive shifts. Thus, we flux bias Q_B at this maximal frequency, which is also optimal for coherence. Inset, higher resolution spectroscopy of the avoided crossing of Q_B with the cavity fundamental mode ($f_c = 6.55$ GHz), revealing a minimum splitting of 167 MHz.

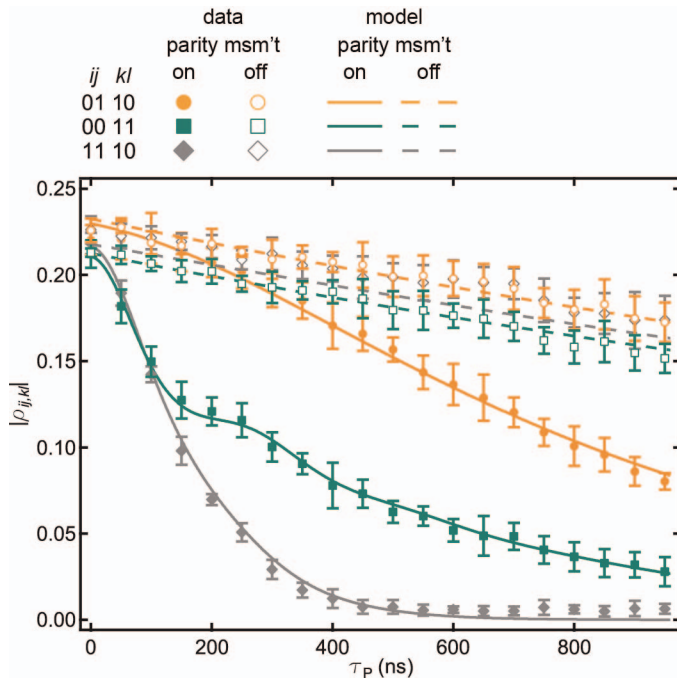


Extended Data Figure 2 | Detailed schematic of the experimental set-up. Complete wiring of electronic components outside and inside the $^3\text{He}/^4\text{He}$ dilution refrigerator (Leiden Cryogenics CF-650). Readout and qubit-drive pulses, shaped by a Tektronix AWG5014 and two Tektronix AWG520, enter the cavity via a single transmission line. The cavity output is reflected by the JPA, which is biased by a superconducting coil and a strong pump tone, bending its resonance down to f_p and providing parametric amplification¹². The signal is further amplified at the 3 K stage (Caltech Cryo1-12, 0.06 dB noise figure) and at room temperature (two Miteq AFS3-04000800-10-ULN amplifiers, 0.8 dB noise figure). Demodulation to baseband is provided by a

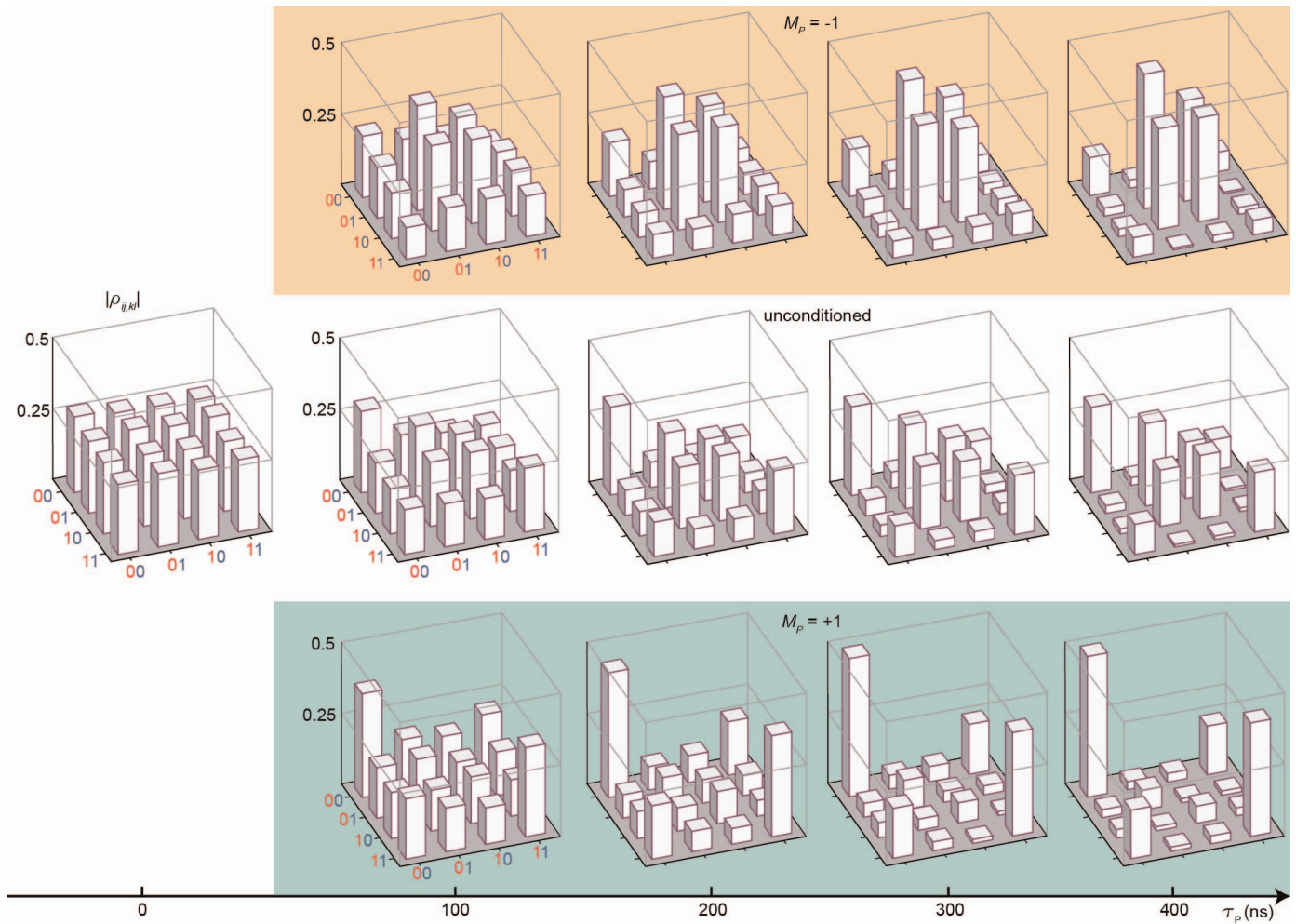
generator at f_p , also used for readout and pump. Two phase shifters allow adjusting the relative phase between the three tones at f_p . The demodulated signal is split into three separate arms after amplification by a Stanford Research Systems SR445A. One arm stabilizes the JPA flux bias via an ADwin-GOLD processor programmed as a PID controller³¹. In the second arm, the signal is filtered by a bias tee, amplified with a custom-built amplifier, and integrated and thresholded by the FPGA. The FPGA conditionally triggers a $Q_A \pi$ pulse from an AWG520 (Fig. 4). The third arm connects to an AlazarTech ATS9870 digitizer for data storage and processing after a second SR445A amplification stage. Red colour highlights the key components of the feedback loop.



Extended Data Figure 3 | Readout configuration for parity measurement and state tomography. **a**, Histograms for the computational basis for the parity measurement M_P ($\tau_P = 300$ ns, $\bar{n}_{ss} = 2.5$), as in Fig. 3a. At this measurement power, states within each parity subspace are largely indistinguishable (see also Fig. 1b and Extended Data Fig. 7). For an ideal parity measurement, $\beta_A = \beta_B = 0$. We extract $\beta_A = 0.0146$ mV, $\beta_B = -0.123$ mV, $\beta_{BA} = -6.25$ mV and $\beta_0 = 7.46$ mV. **b**, Histograms for the tomography measurement (integration time 850 ns, $\bar{n}_{ss} \approx 60$). At this power, the cavity response is nonlinear (critical photon number³³ $n_{\text{crit}} \approx 60$), causing the resonance for $|10\rangle$ to bend towards lower frequency. As the resonance for $|01\rangle$ is instead power-independent, this effect discriminates $|01\rangle$ from the other states. This gives the joint readout the sensitivity to single and two-qubit terms required to perform state tomography²². Averaging of raw tomography measurements yields $\beta_A = -8.10$ mV, $\beta_B = 9.10$ mV, $\beta_{BA} = -12.8$ mV and $\beta_0 = 17.1$ mV. Digitizing the single shots with threshold $V_D = 32$ mV gives $\beta_A = 0.424$, $\beta_B = -0.360$, $\beta_{BA} = 0.379$ and $\beta_0 = 0.540$.

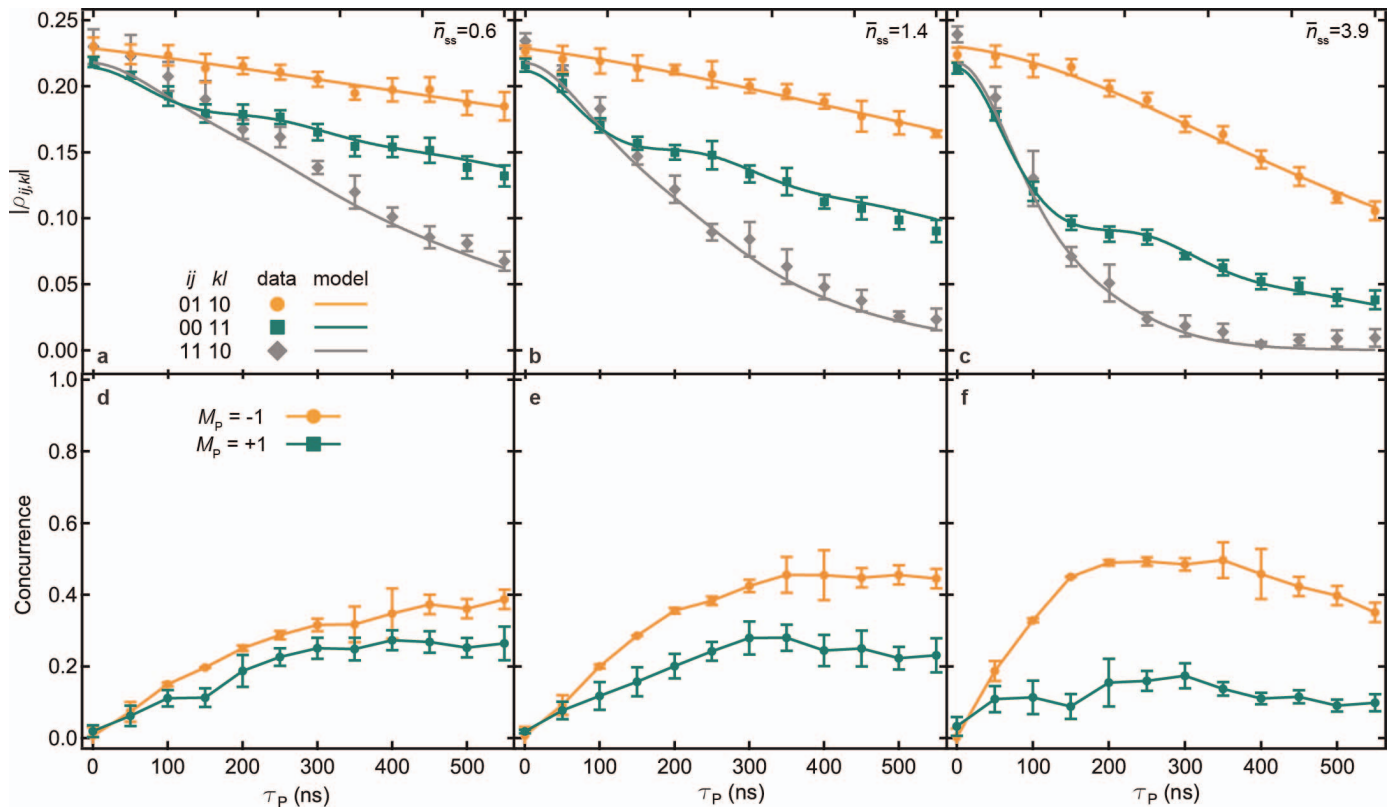


Extended Data Figure 4 | Temporal evolution of two-qubit superposition state with and without continuous parity measurement. Comparison of the unconditioned two-qubit evolution during parity measurement (filled symbols, same data as in Fig. 2b) and during a delay of the same duration τ_P (open symbols). In the latter case, the decay of $|\rho_{ij,kl}|$ is solely due to intrinsic qubit decoherence. Evidently, measurement-induced dephasing dominates over intrinsic qubit dephasing. For reference, we estimate that entanglement ($\mathcal{C} > 0$) would be achieved in the deterministic scheme provided the net qubit dephasing rate $1/T_2^{\varphi,A} + 1/T_2^{\varphi,B} < 1/0.4 \mu\text{s}^{-1}$, under the experimental conditions of Fig. 4.



Extended Data Figure 5 | Two-qubit evolution under continuous parity measurement. Unconditioned and conditioned state tomography of the final two-qubit state similar to Figs 2 and 3, but at more values of τ_p and using the threshold V_{th} optimizing parity readout fidelity ($\bar{n}_{\text{ss}} = 2.5$). Middle row, unconditioned evolution. For $\tau_p = 0$, there is only a 10 ns buffer between state

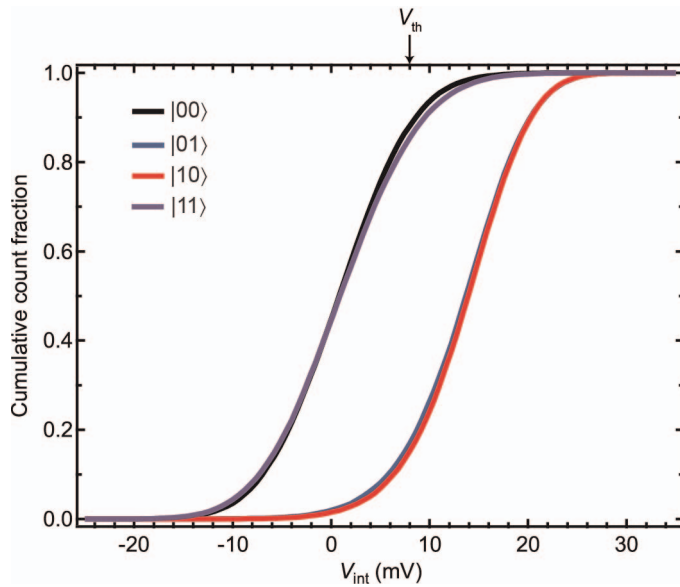
preparation and tomography, instead of the 350 ns used in Figs 2–4 and all other τ_p values here. The uniformity of $|\rho_{ij,kl}|$ for $\tau_p = 0$ (<4% relative difference) attests to the preparation fidelity of the initial maximal superposition state. Top row, evolution conditioned on $V_{\text{int}} > V_{\text{th}}$ ($M_P = -1$); bottom row, evolution conditioned on $V_{\text{int}} < V_{\text{th}}$ ($M_P = +1$).



Extended Data Figure 6 | Two-qubit unconditioned evolution and conditioned concurrence for different measurement strengths.

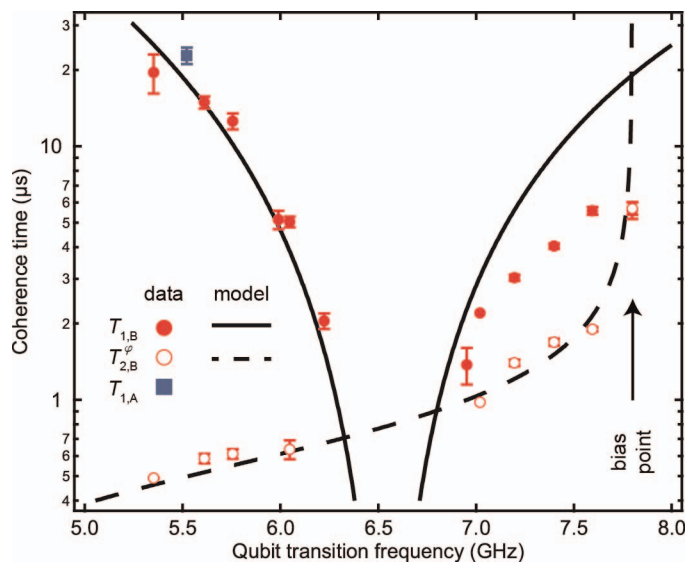
a–f, Experiment as in Figs 2 and 3 with measurement strength corresponding to $\bar{n}_{ss} = 0.6 \pm 0.1$ (a, d), 1.4 ± 0.1 (b, e) and 3.9 ± 0.1 (c, f). The best-fit frequency

mismatch $(\mathcal{X}_A - \mathcal{X}_B)/\pi$ (see also Extended Data Fig. 3) is 182 ± 32 kHz (a, d), 220 ± 18 kHz (b, e) and 275 ± 7 kHz (c, f). Concurrence is calculated after postselection on $V_{\text{int}} < V_{\text{th}}$ ($M_P = +1$) or $V_{\text{int}} > V_{\text{th}}$ ($M_P = -1$).



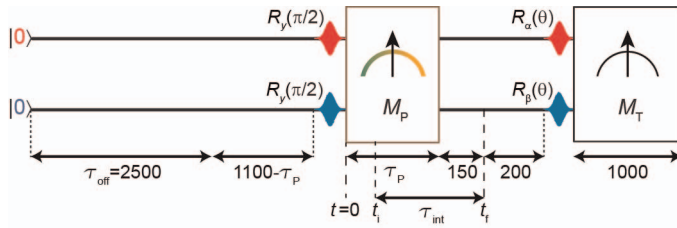
Extended Data Figure 7 | Cumulative histograms of parity measurements.

The four computational states are subjected to a parity measurement with $\tau_p = 300$ ns, $\bar{n}_{ss} = 2.5$, as in Fig. 3a. At the optimal threshold V_{th} (dashed line), the average errors in determining the parity are $\varepsilon_e = 0.13$, $\varepsilon_o = 0.11$, yielding a parity measurement fidelity of $F_p = 1 - \varepsilon_e - \varepsilon_o = 0.76$ (corrected for residual qubit excitations, see Methods). In a similar manner, we define the distinguishability within each parity subspace as the fidelity of the measurement discriminating between those states, yielding 0.03 for the even subspace and 0.02 for the odd.



Extended Data Figure 8 | Frequency-dependent coherence times of Q_B .

Energy relaxation times T_1^B (filled circles) and T_1^A (square) below the fundamental cavity resonance are consistent with the single-mode Purcell effect³⁴ and a coupling strength $g/\pi = 167$ MHz at the Q_B -cavity avoided crossing, as extracted from spectroscopy (Extended Data Fig. 1). We attribute the lower T_1^B above the fundamental resonance to the effect of higher cavity modes. Pure dephasing times $T_2^{\phi,B}$ (open circles) are in excellent agreement with the first-order approximation for flux noise³⁵ with spectral density $S_f(\omega) = A^2/|\omega|$ and best-fit $A = (1.9 \pm 0.1) \times 10^{-5} \Phi_0$ (dashed line), with Φ_0 the flux quantum.



Extended Data Figure 9 | Pulse timing and measurement integration windows. Extended view (not to scale) of the pulse sequence used in Figs 2–4, showing also the integration windows used for parity measurement (τ_{int} for signal and τ_{off} for offset) and tomographic joint readout. All specified time intervals are expressed in ns. Qubit control is performed with DRAG pulses³⁶ with Gaussian envelopes on the main quadrature ($\sigma = 6$ ns, 4σ total duration) and derivative-of-Gaussian envelopes of optimized amplitude on the other. Single-qubit pulses are applied sequentially (Q_B first), with 10 ns buffer between them. The tomography measurement pulse is 1 μ s long, and the homodyne response integrated for 850 ns starting after the first 100 ns.

Coherent Raman spectro–imaging with laser frequency combs

Takuro Ideguchi^{1*}, Simon Holzner^{1*}, Birgitta Bernhardt^{1,3}, Guy Guelachvili², Nathalie Picqué^{1,2,3} & Theodor W. Hänsch^{1,3}

Advances in optical spectroscopy and microscopy have had a profound impact throughout the physical, chemical and biological sciences. One example is coherent Raman spectroscopy, a versatile technique interrogating vibrational transitions in molecules. It offers high spatial resolution and three-dimensional sectioning capabilities that make it a label-free tool^{1,2} for the non-destructive and chemically selective probing of complex systems. Indeed, single-colour Raman bands have been imaged in biological tissue at video rates^{3,4} by using ultra-short-pulse lasers. However, identifying multiple, and possibly unknown, molecules requires broad spectral bandwidth and high resolution. Moderate spectral spans combined with high-speed acquisition are now within reach using multichannel detection⁵ or frequency-swept laser beams^{6–9}. Laser frequency combs¹⁰ are finding increasing use for broadband molecular linear absorption spectroscopy^{11–15}. Here we show, by exploring their potential for nonlinear spectroscopy¹⁶, that they can be harnessed for coherent anti-Stokes Raman spectroscopy and spectro-imaging. The method uses two combs and can simultaneously measure, on the microsecond timescale, all spectral elements over a wide bandwidth and with high resolution on a single photodetector. Although the overall measurement time in our proof-of-principle experiments is limited by the waiting times between successive spectral acquisitions, this limitation can be overcome with further system development. We therefore expect that our approach of using laser frequency combs will not only enable new applications for nonlinear microscopy but also benefit other nonlinear spectroscopic techniques.

Coherent anti-Stokes Raman spectroscopy (CARS) is a nonlinear four-wave mixing process, which is coherently driven when the energy difference between a pump laser and a Stokes laser is resonant with a Raman active molecular transition. Scattering off the probe beam generates the high-frequency-shifted anti-Stokes signal, which is enhanced by many orders of magnitude relative to spontaneous Raman scattering signals. In our technique of dual-comb CARS, we harness two femtosecond lasers with repetition frequencies $f + \delta f$ and f to irradiate a sample. In the time domain (Fig. 1a), a pulse from the first laser coherently excites a molecular vibration of period $1/f_{\text{vib}}$ that is longer than the pulse duration and the coherently vibrating molecules give rise¹⁷ to an oscillating refractive index modulated at the vibrational frequency (Fig. 1b). A pulse of the second laser probes the sample with a time separation Δt that increases linearly from pulse pair to pulse pair. If this second pulse (for simplicity also taken to be short compared with the molecular vibration period¹⁸) arrives after a full molecular period $1/f_{\text{vib}}$, the vibration amplitude is increased and the back-action on the probe pulse is a spectral shift towards lower frequencies. If it arrives after half a period, the vibration amplitude is damped and the pulse experiences a shift towards higher frequencies. As long as the pulse separation Δt remains shorter than the coherence time of the molecular oscillation, an intensity modulation of frequency $f_{\text{vib}}\delta f/f$ is thus observed in the transmitted probe radiation after a

spectral edge filter. The two femtosecond lasers have a symmetrical function: the sign of time separation Δt between the pulses changes every $1/(2\delta f)$. A theoretical description of such a time-resolved CARS signal can be found in ref. 19.

In the frequency domain (Fig. 1c, d), the two frequency comb generators produce an optical spectrum consisting of several hundred thousand perfectly evenly spaced spectral lines. Their frequencies may be described by

$$f^{(1)}_m = m(f + \delta f) + f_{\text{ceo}}$$

$$f^{(2)}_{m'} = m'f + f'_{\text{ceo}}$$

where m and m' are integers, and f_{ceo} and f'_{ceo} are the carrier-envelope offset frequencies.

The frequency differences within each comb form regular combs themselves with vanishing carrier-envelope offset frequencies and line spacings of $f + \delta f$ and f , respectively. For instance, for comb 1 all pairs of lines with $m - n = k$ contribute to the same difference frequency $k(f + \delta f)$. Each of the difference frequency combs resonantly excites a molecular level of frequency f_{vib} by means of Raman-like two-photon excitation whenever a difference frequency comes close to f_{vib} ; that is, when $k \approx f_{\text{vib}}/f$. The excitations by the two combs interfere and modulate the molecular vibration at a beat note frequency $k\delta f = f_{\text{vib}}\delta f/f$. The two-photon excitation leads to a resonant enhancement of the third-order nonlinear susceptibility observed by means of the anti-Stokes radiation. The intensity of the generated broadband anti-Stokes radiation is modulated at the beat note frequency $f_{\text{vib}}\delta f/f$. When several vibrational levels ($f_{\text{vib}1}, f_{\text{vib}2}, \dots$) are excited, the composite modulation contains all the beating frequencies ($f_{\text{vib}1}\delta f/f, f_{\text{vib}2}\delta f/f, \dots$) representative of the involved levels. The Raman excitation spectrum is revealed by Fourier transformation of the intensity recorded against time. The spectrum is mapped in the radiofrequency domain by the downconversion factor $\delta f/f$ (typically of the order of 10^{-7} to 10^{-6}). This permits rapid measurement time and efficient signal processing. Absolute calibration of the Raman shifts is achieved by dividing the radiofrequencies by the downconversion factor, which is easy to measure accurately. The carrier-envelope offsets cancel and do not have to be measured or controlled. This notably simplifies the experimental implementation and the calibration procedure. Similar modulation transfer phenomena have been exploited in experiments using a single femtosecond laser and a phase-modulation pulse shaper²⁰ or a Michelson interferometer^{21–23}, but measurement times were fundamentally limited either by the sweep period of the phase modulation or by the mechanical motion in the Michelson interferometer. Our motionless frequency-comb-based technique enables more than 1,000-fold shorter acquisition times (see also Supplementary Information), and a spectral

¹Max-Planck-Institut für Quantenoptik, Hans-Kopfermann-Strasse 1, 85748 Garching, Germany. ²Institut des Sciences Moléculaires d'Orsay, CNRS, Bâtiment 350, Université Paris-Sud, 91405 Orsay, France. ³Ludwig-Maximilians-Universität München, Fakultät für Physik, Schellingstrasse 4/III, 80799 München, Germany.

*These authors contributed equally to this work.

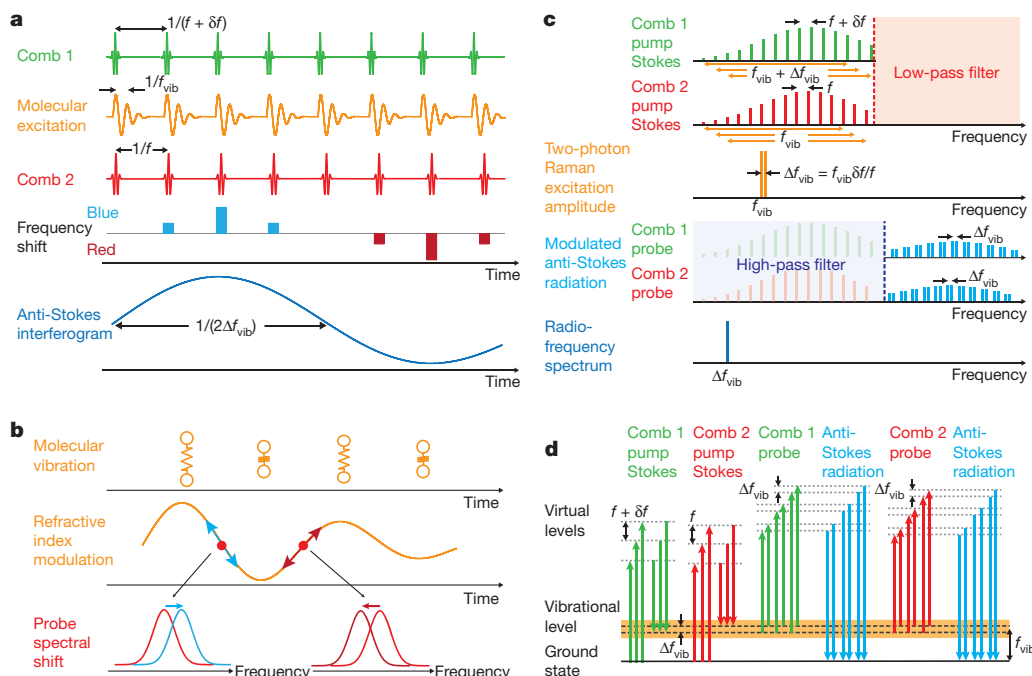


Figure 1 | Principle of dual-comb CARS. Δf_{vib} stands for $f_{\text{vib}}\delta f/f$. **a**, Time-domain representation in the limit of a molecular decoherence time that is shorter than the time interval between two laser pulses. The train of pulses of laser frequency comb 1 periodically excites the molecular vibration, which is probed by the pulses of laser frequency comb 2 with a linearly increasing time delay. The resulting filtered anti-Stokes radiation provides the interferogram. The two combs have a symmetric function. In the figure, only the situation in which the delay between the pulses of comb 2 and those of comb 1 is positive is displayed. **b**, When the probe pulse is short compared with the molecular oscillation (impulsive stimulated Raman scattering), the refractive index

resolution and spectral span only limited by the measurement time and the spectral bandwidth of the femtosecond lasers.

Figure 2 sketches the experimental setup (see Methods), which is similar to that used in dual-comb absorption spectroscopy^{11–13} except for dispersion management and spectral filtering to isolate the CARS signal from the comb beams. As the Raman-like two-photon excitation involves virtual energy levels, dispersion decreases both the spectral span and the excitation efficiency. The time-domain interference signal—the interferogram—is periodic. Every $1/\delta f$, a strong burst mostly contains the non-resonant four-wave mixing signal resulting from the interference between the overlapping pulses of the two combs. A reproducible modulation (Fig. 3a), due to the CARS signal only, follows the burst and has a duration proportional to the coherence time of the sample transitions. A time-windowed portion of the interferogram, which excludes the interferometric non-resonant contribution, is Fourier transformed. The width of the window is chosen according to the desired spectral resolution (see Methods for a detailed explanation of the recording parameters). The resulting spectra (Fig. 3b–d) span Raman shifts from

modulation of the sample—induced by the pump and Stokes beam—shifts the probe spectrum alternatively towards lower and higher frequencies.

c, Frequency-domain representation in the limit of a comb line spacing that is larger than the resonant Raman excitation bandwidth. The two frequency combs modulate the excitation amplitude of the molecular vibration with a frequency Δf_{vib} . This modulation is then transferred by the combs to the anti-Stokes radiation. For simplicity, the Raman excitations are represented as narrow lines. **d**, Energy-level diagram, illustrating the four-wave mixing that leads to intensity-modulated anti-Stokes radiation.

200 cm^{-1} to 1,400 cm^{-1} . The non-resonant background, which strongly lowers the sensitivity of CARS, is entirely suppressed, as in other specific CARS schemes^{20–23}.

We illustrate acquisition times with three spectra at an apodized resolution of 4 cm^{-1} and recorded with $\delta f = 100$ Hz (Fig. 3b) or 5 Hz (Fig. 3c, d) for a mixture of hexafluorobenzene, nitrobenzene, nitromethane and toluene in a cuvette 5 mm long. The spectra involve no averaging and were measured in 14.8 μs (Fig. 3b) and 295.5 μs (Fig. 3c, d); the number of individual spectral elements (defined as the spectral span divided by the resolution) for all three spectra is 300. The signal-to-noise ratio culminates at 1,000 for the most intense blended line of toluene and nitrobenzene in Fig. 3c. Recorded under different experimental conditions, the three spectra show great similarities in line position and relative intensity.

Imaging capabilities are illustrated with a capillary plate (25- μm diameter holes, thickness 500 μm) filled with a mixture of hexafluorobenzene, nitromethane and toluene. For each pixel, we measure an interferogram within 12 μs to obtain a spectrum at an apodized resolution of

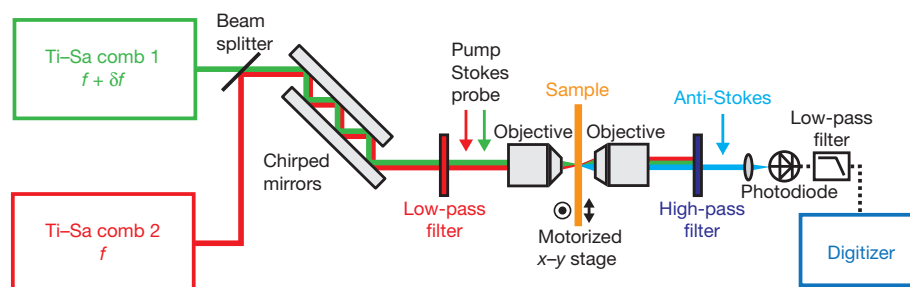


Figure 2 | Experimental setup for dual-comb CARS spectro-imaging. See Methods for details. The colour code is consistent with that of Fig. 1. Ti-Sa, titanium-sapphire.

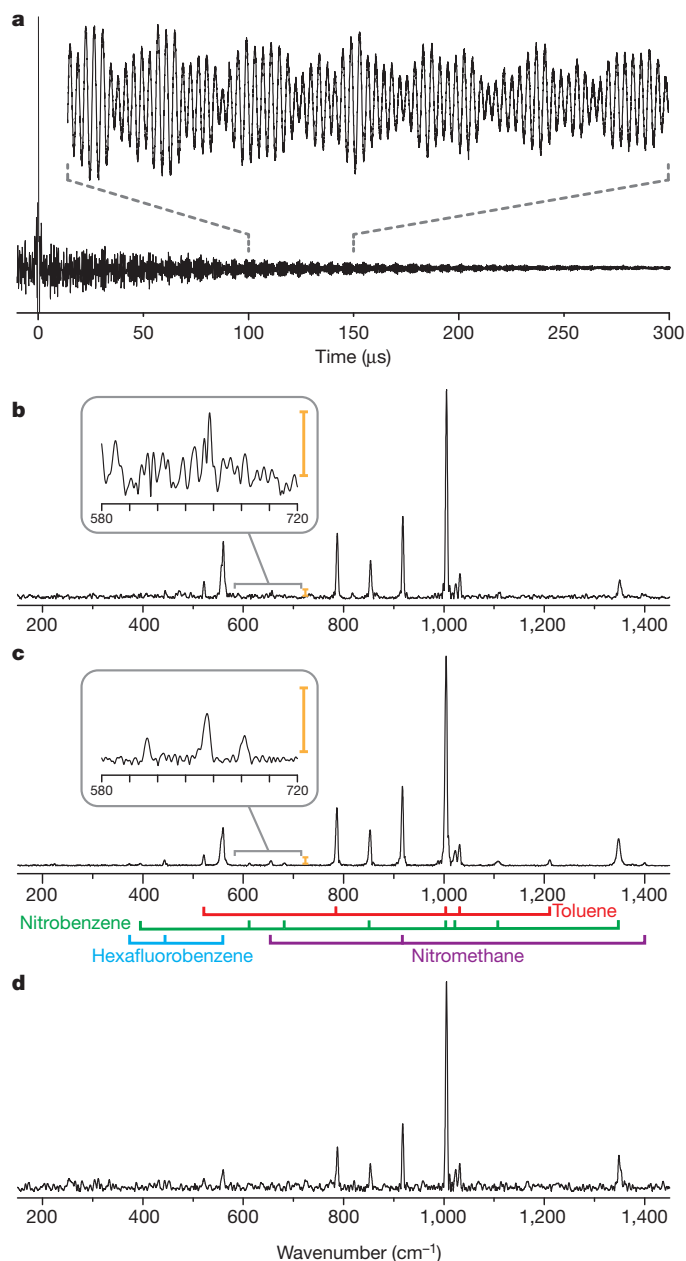


Figure 3 | High-resolution dual-comb CARS of a mixture of liquid chemicals. **a**, Unaveraged interferogram showing the non-resonant interference signal around the zero time delay and the interferometric modulation of the vibrational transitions shown in **c** ($\delta f = 5$ Hz; energy per pulse 3 nJ). **b**, Dual-comb CARS unaveraged spectrum ($\delta f = 100$ Hz; measurement time 14.8 μ s; apodized resolution 4 cm^{-1} ; energy per pulse 3 nJ). **c**, Dual-comb CARS unaveraged spectrum ($\delta f = 5$ Hz; measurement time 295.5 μ s; apodized resolution 4 cm^{-1} ; energy per pulse 3 nJ). **d**, Dual-comb CARS unaveraged spectrum ($\delta f = 5$ Hz; measurement time 295.5 μ s; apodized resolution 4 cm^{-1} ; energy per pulse 0.5 nJ). The insets in **b** and **c** magnify the vertical scale tenfold.

10 cm^{-1} . The total measurement time of 40.5 s for the $45 \times 45 \mu\text{m}^2$ hyperspectral image corresponds to an acquisition rate of 50 pixels s^{-1} ; it is limited by the refresh rate of the interferograms, although the entire sampling time of the interferograms—which are Fourier transformed to give the spectral hypercube in Fig. 4—lasts only 24.3 ms.

Taken together, the above proof-of-principle experiments demonstrate the potential of our method for the rapid acquisition of both high-resolution spectra spanning a broad bandwidth and hyperspectral images of vibrational transitions. A unique feature of our technique is its multiplex nature: all the spectral elements are measured at

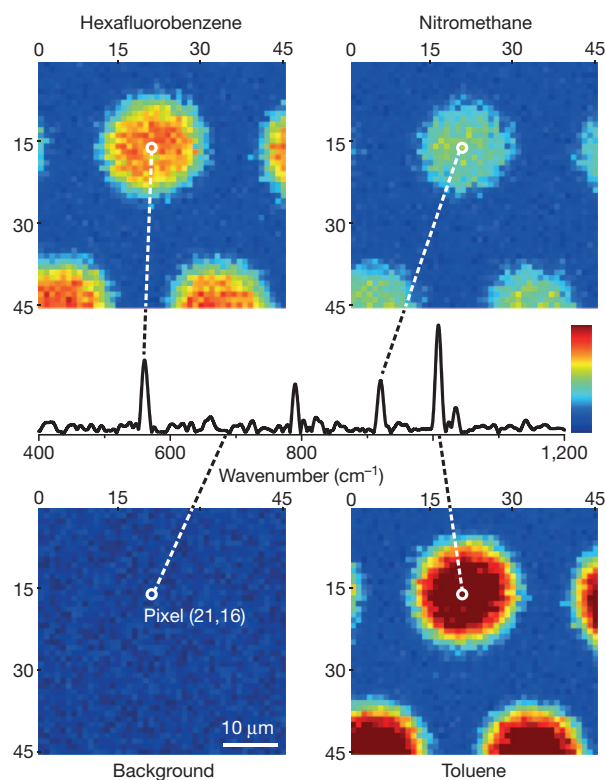


Figure 4 | Hyperspectral image of a capillary plate with holes filled with a chemical mixture. Each of the 2,025 pixels of the hyperspectral cube corresponds to a spectrum at 10 cm^{-1} apodized resolution measured within 12 μ s at a fixed spatial location and provides the spectral signature of compounds present in this part of the sample. Scale numbers on the images indicate pixels; the spectrum shown in the centre corresponds to pixel (21,16). Each spectral element of the cube may be plotted as an image (that is, intensity for all pixels at a fixed wavenumber) similar to the four that are shown and provides the spatial quantitative distribution of a given compound with a distinguishable spectral signature at that wavenumber.

the same time on a single photodetector, which ensures consistency of the spectra. Moreover, the frequency combs guarantee the reproducibility and accuracy of the wavenumber scale. However, a major limitation in the present proof-of-principle experiments is the low duty cycle (the ratio between the time it takes to measure an interferogram and the time before the next interferogram is measured), which for the spectro-imaging experiments shown in Fig. 4 is only 6×10^{-4} . The interferogram refresh time is the inverse of the difference of the laser repetition frequencies $1/\delta f$, whereas the spectral information is only collected when the delay between the pairs of pulses is shorter than the coherent molecular ringing time (see Supplementary Information for more detailed discussion). One solution would be to use combs with a larger line spacing, which could allow the duty cycle of interferogram acquisition to approach unity while keeping measurement times and signal-to-noise ratios similar to those in Figs 3 and 4. Frequency comb generators based on solid-state lasers with a short cavity²⁴ or on chip-scale microresonators²⁵ might offer a route towards realizing such high duty cycle experiments. For microscopy experiments, scanning the laser beam with a galvanometric mirror rather than the sample stage provides a straightforward way to speed up the mapping process. High-speed cameras (more than 10^6 frames s^{-1}) could even allow real-time hyperspectral dual-comb CARS imaging. There is also scope for improvements that would affect the signal itself. For example, a more sophisticated dispersion management, particularly of third-order dispersion, would enhance the signal-to-noise ratio. This could be complemented with fast synchronous or differential detection schemes that might further decrease the noise level. Finally, few-cycle oscillators or spectral broadening with nonlinear fibres will expand the spectral span of the setup.

Several schemes exploiting coherent Raman scattering for novel spectroscopy and microscopy applications have recently emerged, and we expect that their combination with our method will deliver techniques with improved performance and utility. For example, our dual-comb approach could benefit surface-enhanced^{26,27} CARS measurements or studies of Raman optical activity²⁸. Moreover, exciting imaging capabilities might arise when extending our method to exploit either near-field effects (for example at a metal tip²⁹) or far-field effects (for example state depletion³⁰) to achieve sub-wavelength spatial resolution.

METHODS SUMMARY

Two titanium-sapphire lasers (Synergy20 UHP; Femtolasers) emit 20-fs pulses centred at $12,580\text{ cm}^{-1}$ with energies up to 13 nJ. Both have adjustable repetition frequencies of about 100 MHz. The beams of the two lasers (Fig. 2) are combined on a beamsplitter, and a chirped mirror compressor (Layertec) compensates for the second-order dispersion induced by the optical components of the setup. Spectral filtering is applied to improve the signal-to-background ratio. A low-frequency-pass filter (ET750LP, cutoff $13,330\text{ cm}^{-1}$; Chroma Technology) before the sample and a high-frequency-pass filter (3RD740SP, cutoff $13,510\text{ cm}^{-1}$; Omega Optical Inc.) after the sample isolate the CARS signal that is generated by the sample after proper focusing with a lens or a microscope objective. The spectral span is thus limited on the low-energy side by the optical filters and on the high-energy side by the spectral bandwidth of the femtosecond lasers. The anti-Stokes radiation is forward-collected and focused on a silicon photodiode with a frequency bandwidth of the order of 100 MHz. The electric signal is low-pass filtered to 50 MHz to avoid aliasing. It is then amplified and digitized with a 16-bit data acquisition board ($1.8 \times 10^8\text{ samples s}^{-1}$, ATS9462; Alazartech).

Online Content Any additional Methods, Extended Data display items and Source Data are available in the online version of the paper; references unique to these sections appear only in the online paper.

Received 9 February; accepted 27 August 2013.

- Nafie, L. A. Recent advances in linear and nonlinear Raman spectroscopy. Part VI. *J. Raman Spectrosc.* **43**, 1845–1863 (2012).
- Cheng, J. X. & Xie, X. S. (eds). *Coherent Raman Scattering Microscopy* (CRC Press, 2012).
- Evans, C. L. *et al.* Chemical imaging of tissue *in vivo* with video-rate coherent anti-Stokes Raman scattering microscopy. *Proc. Natl Acad. Sci. USA* **102**, 16807–16812 (2005).
- Saar, B. G. *et al.* Video-rate molecular imaging *in vivo* with stimulated Raman scattering. *Science* **330**, 1368–1370 (2010).
- Knutsen, K. P., Messer, B. M., Onorato, R. M. & Saykally, R. J. Chirped coherent anti-Stokes Raman scattering for high spectral resolution spectroscopy and chemically selective imaging. *J. Phys. Chem. B* **110**, 5854–5864 (2006).
- Ozeki, Y. *et al.* High-speed molecular spectral imaging of tissue with stimulated Raman scattering. *Nature Photon.* **6**, 845–851 (2012).
- Kong, L. *et al.* Multicolor stimulated Raman scattering microscopy with a rapidly tunable optical parametric oscillator. *Opt. Lett.* **38**, 145–147 (2013).
- Pegoraro, A. F. *et al.* Optimally chirped multimodal CARS microscopy based on a single Ti:sapphire oscillator. *Opt. Express* **17**, 2985–2996 (2009).
- Fu, D., Holtom, G., Freudiger, C., Zhang, X. & Xie, X. S. Hyperspectral imaging with stimulated Raman scattering by chirped femtosecond lasers. *J. Phys. Chem. B* **117**, 4634–4640 (2013).
- Hänsch, T. W. Nobel Lecture. Passion for precision. *Rev. Mod. Phys.* **78**, 1297–1309 (2006).
- Schliesser, A., Picqué, N. & Hänsch, T. W. Mid-infrared frequency combs. *Nature Photon.* **6**, 440–449 (2012).
- Bernhardt, B. *et al.* Cavity-enhanced dual-comb spectroscopy. *Nature Photon.* **4**, 55–57 (2010).
- Coddington, I., Swann, W. C. & Newbury, N. R. Coherent multiheterodyne spectroscopy using stabilized optical frequency combs. *Phys. Rev. Lett.* **100**, 013902 (2008).
- Diddams, S. A., Hollberg, L. & Mbele, V. Molecular fingerprinting with the resolved modes of a femtosecond laser frequency comb. *Nature* **445**, 627–630 (2007).
- Thorpe, M. J. *et al.* Broadband cavity ringdown spectroscopy for sensitive and rapid molecular detection. *Science* **311**, 1595–1599 (2006).
- Ideguchi, T., Bernhardt, B., Guelachvili, G., Hänsch, T. W. & Picqué, N. Raman-induced Kerr effect dual-comb spectroscopy. *Opt. Lett.* **37**, 4498–4500 (2012).
- Boyd, R. W. *Nonlinear Optics* 3rd edn, Ch. 10.3 (Academic, 2008).
- Yan, Y., Gamble, E. B. & Nelson, K. A. Impulsive stimulated scattering: general importance in femtosecond laser pulse interaction with matter, and spectroscopy applications. *J. Chem. Phys.* **83**, 5391–5399 (1985).
- Mukamel, S. *Principles of Nonlinear Optical Spectroscopy* (Oxford Univ. Press, 1995).
- Dudovich, N., Oron, D. & Silberberg, Y. Single-pulse coherently controlled nonlinear Raman spectroscopy and microscopy. *Nature* **418**, 512–514 (2002).
- Weiner, A. M., Leaird, D. E., Wiederrecht, G. P. & Nelson, K. A. Femtosecond multiple-pulse impulsive stimulated Raman scattering spectroscopy. *J. Opt. Soc. Am. B* **8**, 1264–1275 (1991).
- Volkmer, A., Book, L. D. & Xie, X. S. Time-resolved coherent anti-Stokes Raman scattering microscopy: imaging based on Raman free induction decay. *Appl. Phys. Lett.* **80**, 1505–1507 (2002).
- Ogilvie, J. P., Beaurepaire, E., Alexandrou, A. & Joffe, M. Fourier-transform coherent anti-Stokes Raman scattering microscopy. *Opt. Lett.* **31**, 480–482 (2006).
- Bartels, A., Heinecke, D. & Diddams, S. A. 10-GHz self-referenced optical frequency comb. *Science* **326**, 681 (2009).
- Kippenberg, T. J., Holzwarth, R. & Diddams, S. A. Microresonator-based optical frequency combs. *Science* **332**, 555–559 (2011).
- Steuwe, C., Kaminski, C. F., Baumberg, J. J. & Mahajan, S. Surface enhanced coherent anti-Stokes Raman scattering on nanostructured gold surfaces. *Nano Lett.* **11**, 5339–5343 (2011).
- Frontiera, R. R., Henry, A. I., Gruenke, N. L. & Van Duyne, R. P. Surface-enhanced femtosecond stimulated Raman spectroscopy. *J. Phys. Chem. Lett.* **2**, 1199–1203 (2011).
- Hiramatsu, K. *et al.* Observation of Raman optical activity by heterodyne-detected polarization-resolved coherent anti-Stokes Raman scattering. *Phys. Rev. Lett.* **109**, 083901 (2012).
- Ichimura, T., Hayazawa, N., Hashimoto, M., Inouye, Y. & Kawata, S. Tip-enhanced coherent anti-Stokes Raman scattering for vibrational nanoimaging. *Phys. Rev. Lett.* **92**, 220801 (2004).
- Cleff, C. *et al.* Ground-state depletion for subdiffraction-limited spatial resolution in coherent anti-Stokes Raman scattering microscopy. *Phys. Rev. A* **86**, 023825 (2012).

Supplementary Information is available in the online version of the paper.

Acknowledgements We thank P. Hommelhoff, M. Schultze and W. Schweinberger for the loan of optical components, and A. Hipke for experimental support. Research was conducted in the scope of the European Laboratory for Frequency Comb Spectroscopy. We acknowledge support from the Max Planck Foundation, the Munich Center for Advanced Photonics, Eurostars and the European Research Council (Advanced Investigator grant no. 267854).

Author Contributions T.I. and S.H. contributed equally to the experimental work. All authors contributed extensively to the work presented in this paper.

Author Information Reprints and permissions information is available at www.nature.com/reprints. The authors declare no competing financial interests. Readers are welcome to comment on the online version of the paper. Correspondence and requests for materials should be addressed to N.P. (nathalie.picque@mpq.mpg.de).

METHODS

Detailed experimental setup. Two titanium–sapphire lasers (Synergy20 UHP; Femtolasers) emit 20-fs pulses centred at $12,580\text{ cm}^{-1}$ with energies up to 13 nJ. Titanium–sapphire lasers are chosen because of their capabilities to generate ultra-short pulses in a spectral region where most samples have no or only weak absorption and where advanced photonics tools are available. Both oscillators have repetition frequencies of about 100 MHz, which can be adjusted by moving a cavity mirror mounted on a motorized translation stage and a piezoelectric transducer. The repetition frequencies are monitored with fast silicon photodiodes connected to frequency counters (53131A; Agilent). To prevent long-term drifts, the repetition frequency of each laser comb is stabilized against a radiofrequency clock by means of a mirror of the laser's cavity mounted on a piezoelectric transducer. This does not affect the quality of an individual spectrum but improves the reproducibility of the wavenumber scale of a sequence of spectra. The laser beams are linearly polarized. The pulse energy available for the spectroscopy experiments is adjusted for each laser beam individually with a combination of a half-wave plate and a polarizer. The beams of the two lasers are combined (Fig. 2) on a pellicle beamsplitter, and a chirped mirror compressor (Layertec) compensates for the second-order dispersion induced by the optical components of the setup. Spectral filtering is applied to improve the signal-to-background ratio. A low-frequency-pass optical filter (ET750LP, cutoff $13,330\text{ cm}^{-1}$; Chroma Technology) before the sample and a high-frequency-pass optical filter (3RD740SP, cutoff $13,510\text{ cm}^{-1}$; Omega Optical Inc.) after the sample isolate the CARS signal that is generated by the sample after proper focusing with a lens or a microscope objective. The spectral span is thus limited on the low-energy side by the optical filters and on the high-energy side by the spectral bandwidth of the femtosecond lasers. The anti-Stokes radiation is forward-collected and focused on a single silicon photodiode with a frequency bandwidth of the order of 100 MHz. The electric signal is low-pass filtered to 50 MHz to avoid aliasing. The non-interferometric signal, which occurs at the pulse repetition frequency, is also filtered out. This non-interferometric signal (CARS and non-resonant signal within a single laser pulse) is the main source of undesired background. The interferometric signal is then amplified with a wideband variable-gain voltage amplifier (DHPVA-100; FEMTO Messtechnik GmbH) and digitized with a 16-bit data acquisition board (1.8×10^8 samples s^{-1} , ATS9462; AlazarTech). Apodization and Fourier transformation may be accomplished in real time with the use of field-programmable gate arrays or a posteriori with a basic desktop computer.

The data of Fig. 3 were recorded with orthogonal linear polarizations of the two laser beams. This decreased the interferometric non-resonant background, while the fast depolarization of the sample maintained the strength of the anti-Stokes signal. For the spectra of Fig. 3b, c, the focusing optics consisted of lenses with a focal length of 20 mm and required an amount of dispersion compensation of -600 fs^2 . The pulse energy at the sample was 3 nJ. The spectrum of Fig. 3d was measured with a focusing lens with a focal length of 8 mm, a pulse energy of 0.5 nJ and an avalanche photodetector (APD Module C4777; Hamamatsu).

To record the hyperspectral images (Fig. 4), the difference in repetition frequencies of the two combs was set to 50 Hz and a microscope objective (LCPLN20XIR; Olympus) focused the beams on the sample, with a beam diameter of $1.9\text{ }\mu\text{m}$ and a Rayleigh length of $3.4\text{ }\mu\text{m}$. The pulse energy at the sample was 3.8 nJ and a second-order dispersion of $-3,000\text{ fs}^2$ was compensated for. The sample was mounted on a motorized x–y platform (MLS203, Thorlabs) to raster scans across the sample in $1\text{-}\mu\text{m}$ steps.

Choice of recording parameters. In our experiments of coherent anti-Stokes Raman spectroscopy with two laser frequency combs, the vibrational levels that are excited in a Raman two-photon process have an energy f_{vib} that matches a

frequency difference between pairs of lines of one comb. The vibration is modulated by the interference between the excitation by the two combs and is thus downconverted to the frequency $f_{\text{vib}}\delta f/f$.

The energy $f_{\text{vib,max}}$ (in hertz) of the higher-lying vibrational level that can be observed is about the spectral bandwidth of the combs ΔF (in hertz), roughly twice the full width at half-maximum of the laser spectrum:

$$f_{\text{vib,max}} = \Delta F$$

The difference δf in repetition frequencies between the two lasers must be adjusted to image the domain $0-\Delta F$ into a radiofrequency free spectral range of $0-f/2$ at most. Thus, to avoid aliasing, one has to choose $\delta f \leq f^2/(2\Delta F)$. For the faster recording times, δf should be chosen equal to $f^2/(2\Delta F)$. However, for signal-to-noise ratio improvement, it may be advantageous to set δf to a lower value, as illustrated in Fig. 3.

The Fourier transform of the interferometric signal provides a radiofrequency spectrum with a free spectral range equal to $\Delta F\delta f/f$ (and less than or equal to $f/2$). The Raman-shift scale is retrieved by dividing the measured radiofrequency scale by the downconversion factor $\delta f/f$.

The resolution δv_{rf} (in hertz) in the radiofrequency domain, in a magnitude spectrum with triangular apodization, is given by the inverse of the measurement time T :

$$\delta v_{\text{rf}} = 1.8/T$$

The optical resolution δv_{opt} (in hertz) of the Raman spectrum is retrieved by dividing the radiofrequency resolution δv_{rf} by the downconversion factor $\delta f/f$:

$$\delta v_{\text{opt}} = 1.8f/(\delta f T)$$

The instrumental resolution is fundamentally limited by the line spacing f of the comb. For most mode-locked lasers the line spacing is within the range 50 MHz to 1 GHz. Thus this limitation is not an issue in most liquid-phase studies, because the width of the vibrational bands is generally broader than 100 GHz (3.3 cm^{-1}). It is, however, possible to improve the resolution by interleaving successively acquired spectra recorded with slightly different radiofrequency line spacings.

The difference δf in repetition frequencies between the two lasers also determines the interferogram refresh rate. Every $1/\delta f$ the pulse train of one laser scans the entire pulse period of the second laser comb to generate a single interferogram, which is afterwards time-windowed to provide the desired resolution. This refresh rate limits the speed of successive acquisitions and thus is currently the main limitation for fast hyperspectral imaging experiments. A detailed discussion in Supplementary Information elaborates on this difficulty and shows that frequency combs of a relatively large line spacing (1 GHz) hold promise to overcome it.

In our experiment we use lasers with a repetition frequency of about $f = 100\text{ MHz}$. When the difference of repetition frequencies of the two lasers is set to $\delta f = 100\text{ Hz}$, the downconversion factor $\delta f/f$ is 10^{-6} . The radiofrequency free-spectral range is 50 MHz and the optical free spectral range ΔF is 50 THz ($1,668\text{ cm}^{-1}$). A recording time of $15\text{ }\mu\text{s}$ leads to a radiofrequency resolution δv_{rf} of 120 kHz, which converts to an optical resolution δv_{opt} of 120 GHz (4 cm^{-1}). The refresh time of the interferograms is 10 ms.

Molecular understanding of sulphuric acid–amine particle nucleation in the atmosphere

João Almeida^{1,2}, Siegfried Schobesberger³, Andreas Kürten¹, Ismael K. Ortega³, Oona Kupiainen-Määttä³, Arnaud P. Praplan⁴, Alexey Adamov³, Antonio Amorim⁵, Federico Bianchi⁴, Martin Breitenlechner⁶, André David², Josef Dommen⁴, Neil M. Donahue⁷, Andrew Downard⁸, Eimear Dunne⁹, Jonathan Duplissy³, Sebastian Ehrhart¹, Richard C. Flagan⁸, Alessandro Franchin³, Roberto Guida², Jani Hakala³, Armin Hansel⁶, Martin Heinritzi⁶, Henning Henschel³, Tuija Jokinen³, Heikki Junninen³, Maija Kajos³, Juha Kangasluoma³, Helmi Keskinen¹⁰, Agnieszka Kupc¹¹, Theo Kurtén¹², Alexander N. Kvashin¹³, Ari Laaksonen^{10,14}, Katrianne Lehtipalo³, Markus Leiminger¹, Johannes Leppä¹⁴, Ville Loukonen³, Vladimir Makhmutov¹³, Serge Mathot², Matthew J. McGrath¹⁵, Tuomo Nieminen^{3,16}, Tinja Olenius³, Antti Onnela², Tuukka Petäjä³, Francesco Riccobono⁴, Ilona Riipinen¹⁷, Matti Rissanen³, Linda Rondo¹, Taina Ruuskanen³, Filipe D. Santos⁵, Nina Sarnela³, Simon Schallhart³, Ralf Schnitzhofer⁶, John H. Seinfeld⁸, Mario Simon¹, Mikko Sipilä^{3,16}, Yuri Stozhkov¹³, Frank Stratmann¹⁸, Antonio Tomé⁵, Jasmin Tröstl⁴, Georgios Tsagkogeorgas¹⁸, Petri Vaattovaara¹⁰, Yrjö Viisanen¹⁴, Annele Virtanen¹⁰, Aron Vrtala¹¹, Paul E. Wagner¹¹, Ernest Weingartner⁴, Heike Wex¹⁸, Christina Williamson¹, Daniela Wimmer^{1,3}, Penglin Ye⁷, Taina Yli-Juuti³, Kenneth S. Carslaw⁹, Markku Kulmala^{3,16}, Joachim Curtius¹, Urs Baltensperger⁴, Douglas R. Worsnop^{3,10,14,19}, Hanna Vehkamäki³ & Jasper Kirkby^{1,2}

Nucleation of aerosol particles from trace atmospheric vapours is thought to provide up to half of global cloud condensation nuclei¹. Aerosols can cause a net cooling of climate by scattering sunlight and by leading to smaller but more numerous cloud droplets, which makes clouds brighter and extends their lifetimes². Atmospheric aerosols derived from human activities are thought to have compensated for a large fraction of the warming caused by greenhouse gases². However, despite its importance for climate, atmospheric nucleation is poorly understood. Recently, it has been shown that sulphuric acid and ammonia cannot explain particle formation rates observed in the lower atmosphere³. It is thought that amines may enhance nucleation^{4–16}, but until now there has been no direct evidence for amine ternary nucleation under atmospheric conditions. Here we use the CLOUD (Cosmics Leaving Outdoor Droplets) chamber at CERN and find that dimethylamine above three parts per trillion by volume can enhance particle formation rates more than 1,000-fold compared with ammonia, sufficient to account for the particle formation rates observed in the atmosphere. Molecular analysis of the clusters reveals that the faster nucleation is explained by a base-stabilization mechanism involving acid–amine pairs, which strongly decrease evaporation. The ion-induced contribution is generally small, reflecting the high stability of sulphuric acid–dimethylamine clusters and indicating that galactic cosmic rays exert only a small influence on their formation, except at low overall formation rates. Our experimental measurements are well reproduced by a dynamical model based on quantum chemical calculations of binding energies of molecular clusters, without any fitted parameters. These results show that, in regions of the atmosphere near amine sources, both amines and sulphur dioxide should be considered when assessing the impact of anthropogenic activities on particle formation.

The primary vapour responsible for atmospheric nucleation is thought to be sulphuric acid (H₂SO₄), derived from the oxidation of sulphur dioxide. However, peak daytime H₂SO₄ concentrations in the

atmospheric boundary layer are about 10⁶ to 3 × 10⁷ cm^{−3} (0.04–1.2 parts per trillion by volume (p.p.t.v.)), which results in negligible binary homogeneous nucleation of H₂SO₄–H₂O (ref. 3). Additional species such as ammonia or amines^{4,5} are therefore necessary to stabilize the embryonic clusters and decrease evaporation. However, ammonia cannot account for particle formation rates observed in the boundary layer³ and, despite numerous field and laboratory studies^{6–16}, amine ternary nucleation has not yet been observed under atmospheric conditions. Amine emissions are dominated by anthropogenic activities (mainly animal husbandry), but about 30% of emissions are thought to arise from the breakdown of organic matter in the oceans, and 20% from biomass burning and soil¹⁷. Atmospheric measurements of gas-phase amines are sparse, but typical values range between negligible and a few tens of p.p.t.v. per amine species^{17–20}.

Here we report results from the CLOUD experiment at CERN (for experimental details see Methods, Extended Data Fig. 1 and Supplementary Information). The data were obtained during three campaigns at the CERN Proton Synchrotron between October 2010 and November 2012, and comprise measurements of sulphuric acid–amine nucleation at atmospheric concentrations. Dimethylamine (DMA; C₂H₇N) was selected for this study because it is expected to have cluster binding energies representative of other light alkyl amines⁴.

Nucleation rates *J* were measured under neutral (*J*_n), galactic cosmic ray (*J*_{gcr}) and π⁺ beam (*J*_π) conditions, corresponding to ion-pair concentrations of about 0, 650 and 3,000 cm^{−3}, respectively. Both *J*_{gcr} and *J*_π comprise the sum of neutral and ion-induced nucleation rates, whereas *J*_n measures the neutral rate alone. Figure 1 shows the nucleation rates at 1.7 nm mobility diameter (1.4 nm mass diameter) as a function of [H₂SO₄] for ‘binary’ (H₂SO₄–H₂O), ammonia ternary (H₂SO₄–NH₃–H₂O) and amine ternary (H₂SO₄–DMA–H₂O) nucleation at 278 K and 38% relative humidity (RH). Here ‘binary’ includes previous measurements made in the presence of NH₃ and DMA contaminants³, estimated from later campaigns to be <2 p.p.t.v. and <0.1 p.p.t.v., respectively, for the conditions of ref. 3. Nucleation

¹Goethe-University of Frankfurt, Institute for Atmospheric and Environmental Sciences, 60438 Frankfurt am Main, Germany. ²CERN, CH-1211 Geneva, Switzerland. ³University of Helsinki, Department of Physics, FI-00014 Helsinki, Finland. ⁴Paul Scherrer Institute, Laboratory of Atmospheric Chemistry, CH-5232 Villigen, Switzerland. ⁵SIM, University of Lisbon and University of Beira Interior, 1749-016 Lisbon, Portugal. ⁶Ionicon Analytik GmbH and University of Innsbruck, Institute for Ion and Applied Physics, 6020 Innsbruck, Austria. ⁷Carnegie Mellon University, Center for Atmospheric Particle Studies, Pittsburgh, Pennsylvania 15213, USA. ⁸California Institute of Technology, Division of Chemistry and Chemical Engineering, Pasadena, California 91125, USA. ⁹University of Leeds, School of Earth and Environment, Leeds LS2 9JT, UK. ¹⁰University of Eastern Finland, FI-70211 Kuopio, Finland. ¹¹University of Vienna, Faculty of Physics, 1090 Vienna, Austria. ¹²University of Helsinki, Department of Chemistry, FI-00014 Helsinki, Finland. ¹³Lebedev Physical Institute, Solar and Cosmic Ray Research Laboratory, 119991 Moscow, Russia. ¹⁴Finnish Meteorological Institute, FI-00101 Helsinki, Finland. ¹⁵Department of Biophysics, Graduate School of Science, Kyoto University, 606-8502 Kyoto, Japan. ¹⁶Helsinki Institute of Physics, University of Helsinki, FI-00014 Helsinki, Finland. ¹⁷University of Stockholm, Department of Applied Environmental Science, SE-10961 Stockholm, Sweden. ¹⁸Leibniz Institute for Tropospheric Research, 04318 Leipzig, Germany. ¹⁹Aerodyne Research Inc., Billerica, Massachusetts 01821, USA.

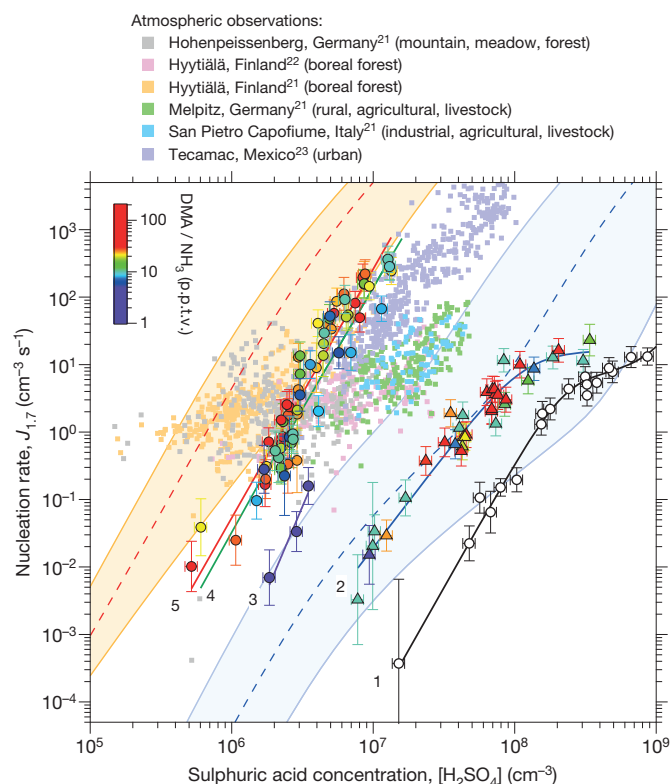


Figure 1 | Plot of experimental, atmospheric and theoretical nucleation rates against H_2SO_4 concentration. Observations in the atmospheric boundary layer are indicated by small coloured squares^{21–23}. The CLOUD data, recorded at 38% RH and 278 K, show J_{GCR} with only H_2SO_4 , water and contaminants (<0.1 p.p.t.v. DMA and <2 p.p.t.v. NH_3) in the chamber (open black circles, curve 1); J_{GCR} with <0.1 p.p.t.v. DMA and 2–250 p.p.t.v. NH_3 (coloured triangles, curve 2); and J_{n} , J_{GCR} and J_{π} with 10 p.p.t.v. NH_3 and 3–5 p.p.t.v. DMA (coloured circles, curve 3), 5–13 p.p.t.v. DMA (coloured circles, curve 4) and 13–140 p.p.t.v. DMA (coloured circles, curve 5). The mixing ratios of NH_3 or DMA are indicated by a colour scale. The curves are drawn to guide the eye; the straight sections follow power laws, $J \propto [\text{H}_2\text{SO}_4]^n$, with fitted slopes n of 3.6 ± 0.5 (curve 1), 2.7 ± 0.1 (curve 2), 5.0 ± 0.8 (curve 3), 3.6 ± 0.2 (curve 4) and 3.7 ± 0.1 (curve 5). The flattening of curves 1 and 2 at higher $[\text{H}_2\text{SO}_4]$ results from saturation of the ion production rate and also a decreasing contribution of ammonia ternary nucleation. The bars indicate 1σ total errors, although the overall factor 2 systematic scale uncertainty on $[\text{H}_2\text{SO}_4]$ is not shown. Theoretical expectations (ACDC model) are indicated for H_2SO_4 nucleation with 10 p.p.t.v. NH_3 (dashed blue line and blue band) and for 10 p.p.t.v. DMA plus 10 p.p.t.v. NH_3 (dashed red line and orange band, assuming a sticking probability of 0.5 for neutral–neutral collisions and 1.0 for charged–neutral collisions). The bands correspond to the uncertainty range of the theory: $+1$ and -1 kcal mol⁻¹ binding energy (blue band) and sticking probabilities for neutral–neutral collisions between 0.1 and 1.0 (orange band), for the lower and upper limits, respectively.

rates with 5 p.p.t.v. DMA are enhanced more than 1,000-fold compared with 250 p.p.t.v. ammonia (Fig. 1). Additional DMA up to 140 p.p.t.v. results in a less than threefold further rate increase, indicating that amine levels of about 5 p.p.t.v. are sufficient to reach the rate limit for amine ternary nucleation under atmospheric conditions ($[\text{H}_2\text{SO}_4] \leq 3 \times 10^7$ cm⁻³, or 1.2 p.p.t.v.).

The amine ternary nucleation rates pass through the band of atmospheric observations (Fig. 1). However, the latter reveal distinct regional differences, with some environments showing nucleation rates both above and below the amine limit (boreal forest and mountain^{21,22}), whereas others are only below the limit (agricultural, livestock, industrial and urban^{21,23}). This suggests that nucleation in different regions of the boundary layer may be controlled by different ternary vapours. In regions where amines are likely to be present (livestock farming and urban), the atmospheric rates are compatible

with amine nucleation. However, the atmospheric data show considerable variability, probably resulting from variations in ternary vapour concentrations and particle coagulation sinks. When growth rates are low, the measured nucleation rates are highly sensitive to particle coagulation sinks, which influence particle losses both above and below the quoted formation threshold sizes. Losses below the threshold size are uncorrected, implying higher variability in the atmosphere, where conditions are less well defined than in the laboratory.

Figure 1 shows the theoretical expectations for NH_3 (blue band) and DMA ternary nucleation (orange band), obtained with the Atmospheric Cluster Dynamics Code model (ACDC)²⁴ (see Methods and Supplementary Information for further details). The model uses cluster evaporation and fragmentation rates calculated from quantum chemistry, with no fitted parameters²⁵. The agreement is quite good, although the model predicts somewhat higher DMA ternary nucleation rates than measured experimentally. Part of this discrepancy is due to the smaller size—and hence higher formation rate—of the modelled clusters (up to four acid and four base molecules per cluster, corresponding to mobility diameters of 1.2–1.4 nm). Computational studies (see Supplementary Information and Extended Data Figs 2 and 3) indicate that DMA ternary nucleation is rather insensitive to RH or temperature, reflecting the strong acid–base binding. The experimental measurements obtained at 38% RH and 278 K may therefore be considered representative of a wide range of boundary layer conditions.

Plots of the nucleation rates J_{n} , J_{GCR} and J_{π} against DMA mixing ratio are shown in Fig. 2a. Here, all measurements have been scaled to $[\text{H}_2\text{SO}_4] = 2.0 \times 10^6$ cm⁻³ using the fitted slopes, n , from Fig. 1. The addition of only 5 p.p.t.v. DMA enhances the nucleation rate of sulphuric acid particles by more than six orders of magnitude, but the addition of further DMA up to 140 p.p.t.v. produces a negligible further increase. The measured neutral, galactic cosmic ray (GCR) and beam nucleation rates are indistinguishable, within experimental uncertainties. However, a more sensitive determination of the ion-induced nucleation rate, $J_{\text{ion}} = J_{\text{ion}}^+ + J_{\text{ion}}^-$, is obtained from direct ion measurements with the neutral cluster and air ion spectrometer. The ion-induced fractions, $J_{\text{ion}}/J_{\text{GCR}}$ or J_{ion}/J_{π} (Fig. 2b), are found to average about 20% at 0.5 cm⁻³ s⁻¹ but grow in relative importance as the total nucleation rate decreases. This indicates that the influence of galactic cosmic rays on the nucleation of sulphuric acid–amine particles is only significant at low overall formation rates. No difference is measured for the ion-induced fraction under GCR or beam conditions (Fig. 2b). This follows, because the ion–ion recombination lifetimes are below 10 min and are comparable to the monomer arrival rate on the cluster (one molecule per 12 min for $\text{H}_2\text{SO}_4 \cdot \text{HSO}_4^-$ at 10^6 cm⁻³ $[\text{H}_2\text{SO}_4]$). Consequently, although the ion pair concentration is larger for beam conditions, it is compensated for by a shorter ion lifetime, which decreases the time available for nucleation before the ion cluster is neutralized.

Figure 3 shows the molecular composition of nucleating charged clusters in the presence of DMA for negative ions (Fig. 3a) and positive ions (Fig. 3b), measured with atmospheric-pressure interface time-of-flight mass spectrometers (APi-TOFs). The predominant negatively charged clusters include an HSO_4^- or HSO_5^- ion. The latter is deprotonated peroxysulphuric acid, whose presence varies with the ozone concentration in the chamber (it is absent when no ozone is present). We found no indication that the nucleation rates are sensitive to the relative contribution of these ion species. Contaminant NO_3^- ions are also detected, but at much lower concentrations. The predominant positively charged clusters contain a protonated DMA ion, $\text{DMA} \cdot \text{H}^+$ ($\text{C}_2\text{H}_7\text{N} \cdot \text{H}^+$), in association with H_2SO_4 and DMA. The remaining positive ions are largely protonated light organic contaminants, mostly also nitrogen-containing.

Amine ternary nucleation is observed to proceed by the same base-stabilization mechanism as that found previously for ammonia ternary nucleation³. We will use the label (n, m) to indicate the number of sulphuric acid ($n\text{SA}$) and DMA ($m\text{DMA}$) molecules in pure

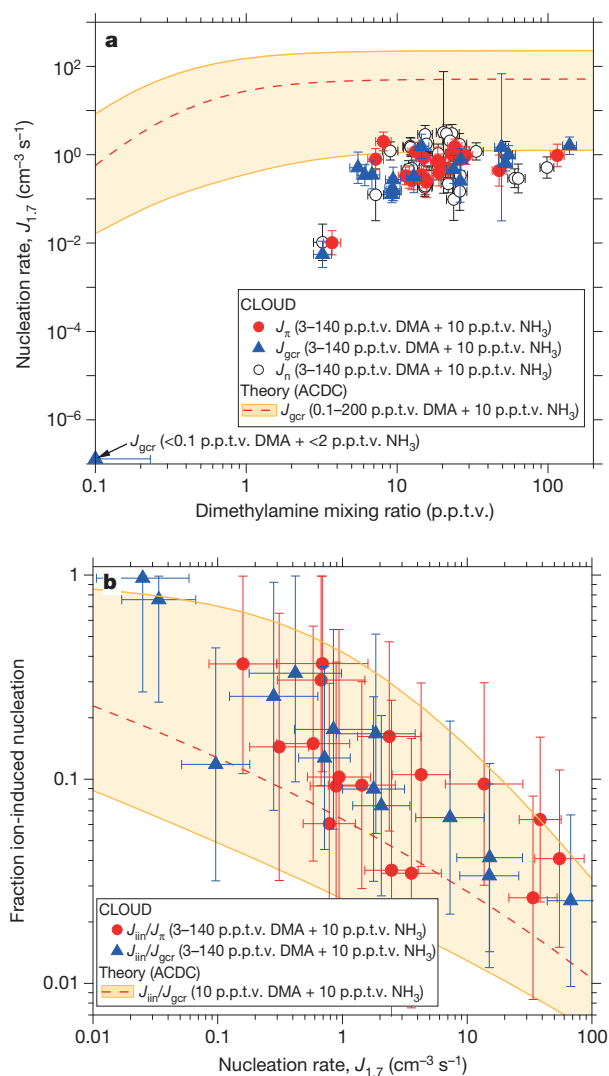


Figure 2 | Contribution of DMA and ions to amine ternary nucleation. Measurements recorded at 38% RH and 278 K. **a**, Nucleation rates, J_{gr} , $J_{\text{gr}}/J_{\text{gr}}^{\text{theor}}$ and $J_{\text{gr}}/J_{\text{gr}}^{\text{theor}}$, as a function of DMA mixing ratio. **b**, Ion-induced fractions, $J_{\text{gr}}/J_{\text{gr}}^{\text{theor}}$ and $J_{\text{gr}}/J_{\text{gr}}^{\text{theor}}$, as a function of J_{gr} or $J_{\text{gr}}/J_{\text{gr}}^{\text{theor}}$ at DMA = 3–140 p.p.t.v. In **a**, all nucleation rates are scaled to $[\text{H}_2\text{SO}_4] = 2.0 \times 10^6 \text{ cm}^{-3}$ (0.08 p.p.t.v.) using the fitted slopes in Fig. 1. The point at 0.1 p.p.t.v. DMA shows the mean projected J_{gr} measurement at contaminant-level DMA and NH_3 . The bars indicate 1σ total errors and include correlated systematic contributions. Theoretical expectations are shown by dashed red lines (sticking probability of 0.5 for neutral–neutral collisions and 1.0 for charged–neutral collisions) and uncertainties by orange bands (sticking probabilities for neutral–neutral collisions between 0.1 and 1.0).

$\text{SA} \cdot \text{DMA}$ clusters, where n and m include both neutral and charged species. Negatively charged nucleation (Fig. 3a) proceeds as follows. The first step is dimer (2, 0) formation: $\text{HSO}_4^- \cdot \text{H}_2\text{SO}_4$ (for simplicity the ‘ HSO_4^- ’ ion implies either HSO_4^- or HSO_5^-). This constitutes an acid–base pair because HSO_4^- is a Lewis base (an electron pair donor). Consequently the first negatively charged cluster to which DMA can bind to form an acid–base pair is the acid trimer. The most abundant acid trimer contains two DMA molecules (3, 2). Thereafter, each additional acid molecule is stabilized by one additional DMA molecule, following a sequence of acid–base pairs: (3, 2) \rightarrow (4, 3) \rightarrow (5, 4) \rightarrow (n , $n - 1$). Our calculations suggest that the process involves mainly the accretion of $\text{SA} \cdot \text{DMA}$ (dimethylaminium bisulphate) clusters, but it may also involve the stepwise addition of an SA molecule followed by a DMA molecule. Beyond (7, 6) clusters, there is evidence for further neutralization of the acid by additional DMA (partial formation of

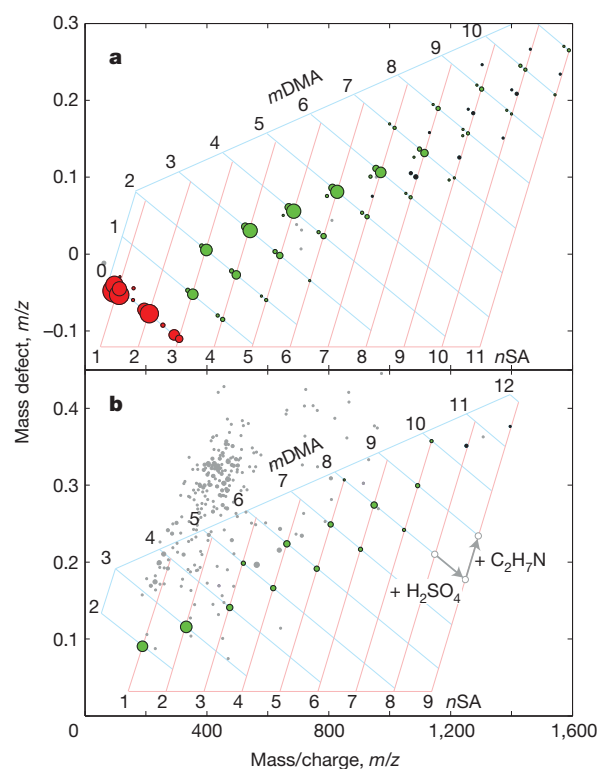


Figure 3 | Mass and molecular composition of charged clusters during a nucleation event with DMA. Molecular composition of charged clusters measured by the API-TOF for $J_{\text{gr}} = 1.2 \text{ cm}^{-3} \text{s}^{-1}$, $4.0 \times 10^6 \text{ cm}^{-3}$ [H_2SO_4], 11 p.p.t.v. NH_3 , 9.4 p.p.t.v. DMA, 38% RH and 278 K. **a**, Negative particles. **b**, Positive particles. Cluster mass/charge, m/z , defect (difference from integer m/z) is plotted against m/z ; each circle represents a distinct molecular composition and its area represents counts s^{-1} . The labels (n , m) indicate the number of sulphuric acid ($n\text{SA}$) and DMA ($m\text{DMA}$) molecules in pure clusters of SA and DMA, including both neutral and charged species. The addition of a single SA (H_2SO_4) or DMA ($\text{C}_2\text{H}_7\text{N}$) molecule to any cluster displaces it on the plot by a vector distance indicated by the grey arrows in **b**. Red circles represent pure SA clusters; green circles are clusters containing SA and DMA alone; black circles contain ammonia in addition (only appearing in some clusters above $m/z = 900$); other clusters (mostly containing light organic contaminants) are grey circles. Water molecules evaporate rapidly in the API-TOF and are not detected (see Supplementary Information).

dimethylaminium sulphate). Positively charged nucleation (Fig. 3b) proceeds similarly. Here $\text{DMA} \cdot \text{H}^+$ is a Lewis acid and so binds only weakly with H_2SO_4 . Hence the first positively charged cluster is a $\text{DMA} \cdot \text{H}^+$ ion together with a single $\text{SA} \cdot \text{DMA}$ acid–base pair (1, 2). Thereafter, the cluster grows by the accretion of $\text{SA} \cdot \text{DMA}$ pairs, exactly as seen for negatively charged clusters. No $\text{DMA} \cdot \text{H}^+$ monomer is detected because its mass-to-charge ratio (m/z), 46, is below the API-TOF cutoff, as configured for these experiments.

Because both HSO_4^- and DMA are Lewis bases, each can form an acid–base pair with H_2SO_4 . In fact HSO_4^- is the stronger base, as demonstrated by its much stronger binding energy with H_2SO_4 (Supplementary Table 1)⁴. The only fundamental difference is that not more than one HSO_4^- ion can be present in the cluster because of electrostatic repulsion. So, although the API-TOF measures only charged clusters in the CLOUD chamber, this suggests that neutral nucleation proceeds by the same mechanism, namely the initial formation of an acid–base pair ($\text{SA} \cdot \text{DMA}$)—equivalent to the acid–base pair ($\text{SA} \cdot \text{HSO}_4^-$) seen in charged nucleation (Fig. 3a)—and subsequently the accretion of additional $\text{SA} \cdot \text{DMA}$ pairs. This is also indicated by the Atmospheric Cluster Dynamics Code (ACDC) model (see Supplementary Information and Extended Data Fig. 4).

There is direct experimental evidence to support this picture of the neutral nucleation mechanism. Figure 4 shows a plot of the concentration

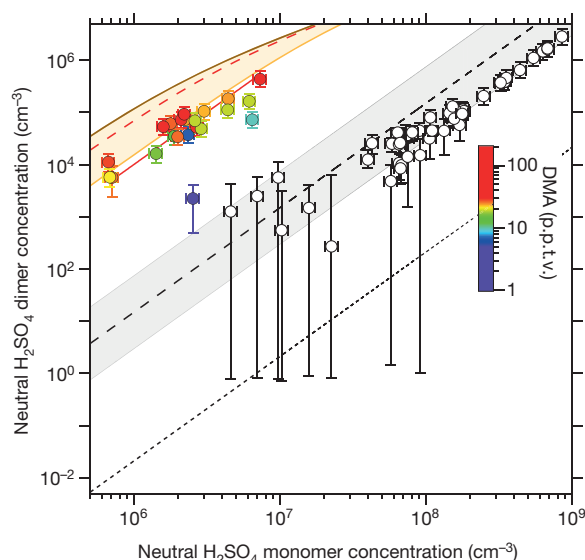


Figure 4 | Plot of neutral H_2SO_4 dimer against monomer concentrations before and after the addition of DMA. Concentrations were measured by the CIMS in CLOUD without DMA (open circles) and with 3–140 p.p.t.v. DMA and 10 p.p.t.v. NH_3 (coloured circles), at 38% RH and 278 K. Ions are absent from the CLOUD chamber (the clearing field is on). The bars indicate 1σ counting errors. The fitted red curve through the DMA data shows a quadratic dependence on monomer concentration. The other curves show the expected neutral dimer concentrations for the binary H_2SO_4 – H_2O system (short-dashed black line)²⁶, for production in the CIMS ion source (dashed black line and grey uncertainty band) and for 10 p.p.t.v. DMA in the ACDC model, assuming 0.5 sticking probability (dashed red line). The orange band shows the model uncertainty range (sticking probabilities between 0.1 and 1.0). The brown curve indicates the upper limit of the dimer concentration calculated with the ACDC model, which is close to the kinetic limit (unit sticking probability and negligible evaporation).

of the neutral acid dimer against that of the neutral acid monomer, measured with the chemical ionization mass spectrometer (CIMS) before and after the addition of DMA, when the clearing field was present (implying that there were only neutral clusters in the CLOUD chamber). We infer from the observed absence of DMA on the negatively charged monomer or dimer (Fig. 3a) that, after charging in the CIMS, clusters containing one H_2SO_4 molecule will be detected as DMA-free charged monomers, and clusters containing two H_2SO_4 molecules will be detected as DMA-free charged dimers—regardless of whether or not they were originally clustered with DMA. Before adding any DMA, the dimer concentrations are consistent with the expected production in the CIMS ion source. However, with 5 p.p.t.v. DMA or more, the dimer concentrations are about six orders of magnitude higher than those expected for a pure binary system²⁶. The concentration of neutral acid dimer with DMA approaches the kinetic limit, indicating highly stable clusters with negligible evaporation, and supporting the neutral nucleation mechanism inferred above.

A previous experiment²⁷ measured unexpectedly high dimer concentrations in a laminar flow tube and concluded that a stabilizing contaminant must be present, although none was measured. This was proposed²⁷ to explain the high ‘binary’ nucleation rates previously measured in ref. 28 in the same flow tube. Another experiment¹⁵ measured high dimer formation rates linked to amine mixing ratios of about 1 part per billion by volume and above. Our results directly link high concentrations of neutral H_2SO_4 dimer with amines at atmospheric levels.

The results reported here show that nucleation in the atmospheric boundary layer is highly sensitive to trace amine levels of only a few p.p.t.v. Sulphuric acid–amine nucleation is found to proceed by the same base-stabilization mechanism as that previously observed for ammonia, in which each additional acid molecule in the cluster is

stabilized by one (or occasionally, two) base molecules³. However, the acid–base pairs that sulphuric acid forms with amines are more tightly bound than with ammonia, resulting in cluster formation rates that approach the kinetic limit. Little increase is seen above 5 p.p.t.v. DMA, indicating that nucleation at atmospheric H_2SO_4 concentrations (below $3 \times 10^7 \text{ cm}^{-3}$ or 1.2 p.p.t.v.) is then limited by the availability of H_2SO_4 and not that of DMA. Our experimental rate and molecular measurements are well reproduced by a dynamical model based on quantum chemical calculations of binding energies of molecular clusters.

Although measurements of ambient gas-phase amines are rare, mixing ratios of a few p.p.t.v. in the continental boundary layer have been reported^{17,19,20}, suggesting that sulphuric acid–amine nucleation is likely to be an important atmospheric process. However, atmospheric observations indicate both the presence^{10,11,16} and the absence²² of a significant amine fraction in newly formed particles, which suggests considerable variability of ambient amine levels. Although amines are volatile vapours, our measurements show that sulphate particles constitute an almost perfect sink (negligible evaporation). However, unlike H_2SO_4 , amine vapours are directly emitted from sources in their chemically active form and so they will be localized to source regions, with highly variable concentrations that depend on ambient sulphate particle sinks and OH radical levels (the DMA oxidation lifetime is about 4 h at 10^6 cm^{-3} [OH]). Amines can therefore explain only a part of atmospheric nucleation. Indeed, our measurements leave open the possibility that nucleation may also proceed with other atmospheric vapours, such as highly oxidized organic species of very low volatility. In such cases, extremely low amine concentrations may still enhance nucleation by forming stable acid–base pairs with some fraction of the sulphuric acid molecules in an embryonic cluster (constituting at least four-component nucleation).

The ion-induced contribution to amine ternary nucleation is generally small, except at low overall formation rates. Ions can enhance nucleation either by an increased collision rate between a charged cluster and polar molecules (such as H_2SO_4 or $\text{H}_2\text{SO}_4 \cdot \text{DMA}$) or by an increased cluster binding energy (and hence decreased evaporation rate). Because neutral clusters of H_2SO_4 and DMA are highly stable, charge offers little competitive advantage. Taken together with previous CLOUD measurements³, this suggests that ions can be significant in atmospheric particle formation provided that the associated neutral particles have appreciable evaporation and provided that the overall nucleation rates are low and below the ion-pair production rate.

The Intergovernmental Panel on Climate Change (IPCC) considers that the increased amount of aerosol in the atmosphere from human activities constitutes the largest present uncertainty in climate radiative forcing² and projected climate change this century²⁹. The results reported here show that the uncertainty is even greater than previously thought, because extremely low amine emissions—which have substantial anthropogenic sources and have not hitherto been considered by the IPCC—have a large influence on the nucleation of sulphuric acid particles. Moreover, amine scrubbing is likely to become the dominant technology for CO_2 capture from fossil-fuelled power plants, so anthropogenic amine emissions are expected to increase in the future³⁰. If amine emissions were to spread into pristine regions of the boundary layer where they could switch on nucleation, substantial increases in regional and global cloud condensation nuclei could occur. This underscores the importance of monitoring amine emissions—as well as those of sulphur dioxide—when assessing the impact of anthropogenic activities on the radiative forcing of regional and global climate by aerosols.

METHODS SUMMARY

CLOUD is designed to study the effects of cosmic rays on aerosols, cloud droplets and ice particles, under precisely controlled laboratory conditions. The CLOUD chamber and gas system have been built to the highest technical standards of cleanliness and performance. Owing to its large volume (26 m^3) and highly stable

operating conditions, the chamber allows nucleation rates to be measured reliably over a wide range from $0.001 \text{ cm}^{-3} \text{ s}^{-1}$ to well above $100 \text{ cm}^{-3} \text{ s}^{-1}$. The loss rate of condensable vapours onto the walls of the chamber is comparable to the condensation sink rate onto ambient aerosols under pristine atmospheric boundary layer conditions. The experiment has several unique aspects, including precise control of the 'cosmic ray' beam intensity from the CERN Proton Synchrotron, the capability to create an ion-free environment with an internal electric clearing field, precise and uniform adjustment of the H_2SO_4 concentration by means of ultraviolet illumination from a fibre-optic system, and highly stable operation at any temperature between 203 and 300 K. The contents of the chamber are continuously analysed by a suite of instruments connected to sampling probes that project into the chamber.

The experimental measurements are compared with theoretical expectations based on a dynamical model in which collision and coagulation rates are computed from kinetic gas theory. Equilibrium constants are computed from quantum chemical calculations of binding energies of molecular clusters, and evaporation and cluster fission rates are then obtained from detailed balance. All possible cluster-cluster processes are included. The electrostatic enhancement of ion-molecule collisions is calculated by using dipole moments and polarizabilities obtained from quantum chemistry. The model has no fitted parameters.

Online Content Any additional Methods, Extended Data display items and Source Data are available in the online version of the paper; references unique to these sections appear only in the online paper.

Received 4 March; accepted 17 September 2013.

Published online 6 October 2013.

- Merikanto, J., Spracklen, D. V., Mann, G. W., Pickering, S. J. & Carslaw, K. S. Impact of nucleation on global CCN. *Atmos. Chem. Phys.* **9**, 8601–8616 (2009).
- IPCC. *Climate Change 2007: the Physical Science Basis. Contribution of Working Group I to the Fourth Assessment Report of the Intergovernmental Panel on Climate Change* (Cambridge Univ. Press, 2007).
- Kirkby, J. *et al.* Role of sulphuric acid, ammonia and galactic cosmic rays in atmospheric aerosol nucleation. *Nature* **476**, 429–433 (2011).
- Kurtén, T., Loukonen, V., Vehkamäki, H. & Kulmala, M. Amines are likely to enhance neutral and ion-induced sulphuric acid-water nucleation in the atmosphere more effectively than ammonia. *Atmos. Chem. Phys.* **8**, 4095–4103 (2008).
- Loukonen, V. *et al.* Enhancing effect of dimethylamine in sulphuric acid nucleation in the presence of water—a computational study. *Atmos. Chem. Phys.* **10**, 4961–4974 (2010).
- Mäkelä, J. M. *et al.* Chemical composition of aerosol during particle formation events in boreal forest. *Tellus* **53B**, 380–393 (2001).
- Murphy, S. M. *et al.* Secondary aerosol formation from atmospheric reactions of aliphatic amines. *Atmos. Chem. Phys.* **7**, 2313–2337 (2007).
- Facchini, M. C. *et al.* Important source of marine secondary organic aerosol from biogenic amines. *Environ. Sci. Technol.* **42**, 9116–9121 (2008).
- Berndt, T. *et al.* Laboratory study on new particle formation from the reaction $\text{OH} + \text{SO}_2$: influence of experimental conditions, H_2O vapour, NH_3 and the amine tert-butylamine on the overall process. *Atmos. Chem. Phys.* **10**, 7101–7116 (2010).
- Smith, J. N. *et al.* Observations of ammonium salts in atmospheric nanoparticles and possible climatic implications. *Proc. Natl Acad. Sci. USA* **107**, 6634–6639 (2010).
- Zhao, J. *et al.* Observation of neutral sulphuric acid-amine containing clusters in laboratory and ambient measurements. *Atmos. Chem. Phys.* **11**, 10,823–10,836 (2011).
- Erupe, M. E., Viggiano, A. A. & Lee, S.-H. The effect of trimethylamine on atmospheric nucleation involving H_2SO_4 . *Atmos. Chem. Phys.* **11**, 4767–4775 (2011).
- Yu, H., McGraw, R. & Lee, S.-H. Effects of amines on formation of sub-3 nm particles and their subsequent growth. *Geophys. Res. Lett.* **39**, L02807 (2012).
- Zollner, J. H. *et al.* sulphuric acid nucleation: power dependencies, variation with relative humidity, and effect of bases. *Atmos. Chem. Phys.* **12**, 4399–4411 (2012).
- Chen, M. *et al.* Acid-base chemical reaction model for nucleation rates in the polluted atmospheric boundary layer. *Proc. Natl Acad. Sci. USA* **109**, 18713–18718 (2012).
- Creamean, J. M. *et al.* Measurements of aerosol chemistry during new particle formation events at a remote rural mountain site. *Environ. Sci. Technol.* **45**, 8208–8216 (2011).
- Ge, X., Wexler, A. S. & Clegg, S. L. Atmospheric amines—Part I. A review. *Atmos. Environ.* **45**, 524–546 (2011).
- Grönberg, L., Lövkist, P. & Jönsson, J. A. Measurement of aliphatic-amines in ambient air and rainwater. *Chemosphere* **24**, 1533–1540 (1992).
- Hanson, D. R., McMurry, P. H., Jiang, J., Tanner, D. & Huey, L. G. Ambient pressure proton transfer mass spectrometry: detection of amines and ammonia. *Environ. Sci. Technol.* **45**, 8881–8888 (2011).
- Yu, H. & Lee, S.-H. Chemical ionisation mass spectrometry for the measurement of atmospheric amines. *Environ. Chem.* **9**, 190–201 (2012).
- Paasonen, P. *et al.* On the roles of sulphuric acid and low-volatility organic vapours in the initial steps of atmospheric new particle formation. *Atmos. Chem. Phys.* **10**, 11223–11242 (2010).
- Kulmala, M. *et al.* Direct observations of atmospheric aerosol nucleation. *Science* **339**, 943–946 (2013).
- Kuang, C., McMurry, P. H., McCormick, A. V. & Eisele, F. L. Dependence of nucleation rates on sulphuric acid vapour concentration in diverse atmospheric locations. *J. Geophys. Res.* **113**, D10209 10.1029/2007JD009253 (2008).
- McGrath, M. J. *et al.* Atmospheric Cluster Dynamics Code: a flexible method for solution of the birth-death equations. *Atmos. Chem. Phys.* **12**, 2345–2355 (2012).
- Ortega, I. K. *et al.* From quantum chemical formation free energies to evaporation rates. *Atmos. Chem. Phys.* **12**, 225–235 (2012).
- Hanson, D. R. & Lovejoy, E. R. Measurement of the thermodynamics of the hydrated dimer and trimer of sulphuric acid. *J. Phys. Chem. A* **110**, 9525–9528 (2006).
- Petäjä, T. *et al.* Experimental observation of strongly bound dimers of sulphuric acid: application to nucleation in the atmosphere. *Phys. Rev. Lett.* **106**, 228302 (2011).
- Sipilä, M. *et al.* The role of sulphuric acid in atmospheric nucleation. *Science* **327**, 1243–1246 (2010).
- Andreae, M. O., Jones, C. D. & Cox, P. M. Strong present-day aerosol cooling implies a hot future. *Nature* **435**, 1187–1190 (2005).
- Nielsen, C. J., Herrmann, H. & Weller, C. Atmospheric chemistry and environmental impact of the use of amines in carbon capture and storage (CCS). *Chem. Soc. Rev.* **41**, 6684–6704 (2012).

Supplementary Information is available in the online version of the paper.

Acknowledgements We thank J.-L. Agostini, P. Carrie, L.-P. De Menezes, F. Josa, I. Krasin, R. Kristic, O.S. Maksumov, S.V. Mizin, R. Sitals, A. Wasem and M. Wilhelmsson for their contributions to the experiment, and D. Hanson and P. McMurry for discussions on their unpublished measurements of ambient gas-phase amines. We thank the CSC Centre for Scientific Computing in Espoo, Finland, for computer time, and J. Pierce and P. Paasonen for discussions. We thank CERN for supporting CLOUD with technical and financial resources, and for providing a particle beam from the CERN Proton Synchrotron. This research received funding from the EC Seventh Framework Programme (Marie Curie Initial Training Network 'CLOUD-ITN' no. 215072, MC-ITN 'CLOUD-TRAIN' no. 316662, ERC-Starting 'MOCAPAF' grant 57360 and ERC-Advanced 'ATMNUCLE' grant 227463), the German Federal Ministry of Education and Research (projects 01LK0902A and 01LK1222A), the Swiss National Science Foundation (projects 200020_135307 and 206620_130527), the Academy of Finland (Center of Excellence project 1118615), the Academy of Finland (135054, 133872, 251427, 139656, 139995, 137749, 141217 and 141451), the Finnish Funding Agency for Technology and Innovation, the Väisälä Foundation, the Nessling Foundation, the Austrian Science Fund (FWF; projects P19546 and L593), the Portuguese Foundation for Science and Technology (project CERN/FP/116387/2010), the Swedish Research Council, Vetenskapsrådet (grant 2011-5120), the Presidium of the Russian Academy of Sciences and Russian Foundation for Basic Research (grants 08-02-91006-CERN and 12-02-91522-CERN), and the US National Science Foundation (grants AGS1136479 and CHE1012293).

Author Contributions J.A. performed nucleation rate analysis. S.S. conducted API-TOF charged-cluster analysis. A.K. performed CIMS neutral cluster analysis. O.K.-M. and I.O. were responsible for ACDC analysis and for ACDC Supplementary Information text. A.A., J.A., A.A., F.B., M.B., J.Do., A.Do., E.D., J.Du., S.E., A.F., J.H., M.H., T.J., H.J., M.K., H.K., J.K., J.Ka., A.Kü., A.Ku., A.N.K., K.L., M.L., V.M., S.M., T.N., T.P., A.P., F.R., L.R., M.R., N.S., R.S., S.S., M.Sim., M.Sip., A.T., J.T., G.T., A.V., C.W., D.W. and P.Y. conducted data collection and analysis. K.S.C., E.D., S.E., H.H., O.K.-M., T.K., J.L., V.L., M.M., T.O., I.O., I.R., H.V. and T.Y. performed modelling. J.K. wrote the manuscript. J.A., U.B., K.S.C., J.C., N.D., R.F., J.K., A.Kü., M.K., T.K., J.H.S., H.V. and D.R.W. interpreted the data and edited the manuscript. All authors contributed to development of the CLOUD facility and analysis instruments, and commented on the manuscript.

Author Information Reprints and permissions information is available at www.nature.com/reprints. The authors declare no competing financial interests. Readers are welcome to comment on the online version of the paper. Correspondence and requests for materials should be addressed to J.K. (jasper.kirkby@cern.ch).



This work is licensed under a Creative Commons Attribution-NonCommercial-Share Alike 3.0 Unported licence. To view a copy of this licence, visit <http://creativecommons.org/licenses/by-nc-sa/3.0>

METHODS

The key features of the CLOUD experiment (Extended Data Fig. 1) are a large-volume (26 m³) stainless steel chamber; precise (± 0.01 K) temperature control at any tropospheric temperature; precise delivery of selected trace gases and ultra-pure humidified synthetic air; precise and uniform adjustment of the H₂SO₄ concentration by means of ultraviolet illumination from a fibre-optic system; suppression of contaminant vapours at the technological limit; an adjustable π^+ beam from the CERN Proton Synchrotron to simulate cosmic rays; and the ability to simulate an ion-free environment by applying an electric field to sweep ions from the chamber.

A comprehensive array of state-of-the-art instruments continuously samples and analyses the contents of the chamber. For the results reported here, the instruments included a chemical ionization mass spectrometer for H₂SO₄ concentration³¹, two API-TOFs (TOFWERK AG and Aerodyne Research, Inc.)³² for the molecular composition of positive and negative charged clusters, several condensation particle counters (CPCs) with 50% detection efficiency thresholds near 2 nm (two Airmodus A09 particle size magnifiers (PSMs)³³, two diethylene glycol CPCs (DEG-CPCs)^{34,35}, a TSI 3776 CPC and a TSI 3786 CPC), a scanning mobility particle sizer (SMPS), a neutral cluster and air ion spectrometer (NAIS)³⁶, a proton transfer reaction time-of-flight mass spectrometer for organic vapours³⁷, and an ion chromatograph for measurements of NH₃ and DMA concentrations³⁸.

Two particle counters were operated in a continuously stepped scanning mode to provide measurements of particle growth rates at small sizes: first, a PSM whose detection threshold was varied between about 1 and 2.5 nm, and second, the TSI 3786 with a variable laminar flow rate through its sampling probe, leading to a cutoff size between about 2.5 and 5 nm. The H₂SO₄ concentration is derived from channels 97 (HSO₄⁻) and 160 (HNO₃·HSO₄⁻) of the CIMS, which measure the sulphuric acid monomer signal after charging in the CIMS ion source. The sulphuric acid dimer concentration measured by the CIMS is derived assuming the same calibration factor as for monomers.

Nucleation rates J_n , J_{GCR} and J_π (cm⁻³ s⁻¹) were measured as follows. Neutral nucleation rates are measured with no ion beam and with the field cage electrodes set to ± 30 kV, which establishes an electric field of about 20 kV m⁻¹ in the chamber. This completely suppresses ion-induced nucleation because, under these conditions, small ions or molecular clusters are swept from the chamber in about 1 s. Because all of the nucleation processes under consideration take place on substantially longer time scales, neutral nucleation rates can be measured with zero background from ion-induced nucleation. For GCR and beam conditions, the electric field was set to zero, leading to ion pair concentrations of about 650 cm⁻³ for J_{GCR} , representative of the boundary layer, and about 3,000 cm⁻³ for J_π , representative of the top of the troposphere. Both J_{GCR} and J_π comprise the sum of neutral and ion-induced nucleation rates, at their respective ion concentrations, whereas J_n measures the neutral rate alone.

The nucleation rates are obtained from the formation rates, $dN_{d_{\text{th}}}/dt$ (where the subscript d_{th} refers to the detection threshold diameter of the particle counter). The nucleation rates, $J_{1.7}$, are determined at 1.7 nm mobility diameter (1.4 nm mass diameter) after correcting for losses between 1.7 nm and the detection size threshold^{39,40}. A diameter of 1.7 nm corresponds to a cluster considered to be above the critical size and therefore thermodynamically stable. The critical size, which corresponds to equal evaporation and growth rates of the cluster, varies with temperature, chemical species and concentrations, and may even be absent when evaporation rates are highly suppressed as in the case of sulphuric acid–DMA clusters. Because the loss rate of freshly nucleated particles to the chamber walls is comparable to the rate at which they are lost in the atmosphere to pre-existing aerosols under pristine boundary-layer conditions, the reported formation rates at 1.7 nm size should correspond reasonably well to atmospheric observations of new particle formation.

Before $J_{1.7}$ is calculated, the measured particle number concentrations versus time are corrected^{39,40} in two sequential steps for the loss of particles due to the chamber walls, dilution and coagulation: first, particle losses above d_{th} , and second, particle losses during growth from 1.7 nm to d_{th} . The wall loss rate is 1.7×10^{-3} s⁻¹ for H₂SO₄ monomers and decreases with increasing cluster diameter as $1/d$. The dilution lifetime is 3–5 h, depending on the total sampling rate of all instruments attached to the chamber. Correction 2 above requires knowledge of the particle growth rate. This is determined experimentally from the different rise times measured in a scanning PSM, which detects particles over a range of threshold diameters between 1 and 2.5 nm. The growth rates were verified with several other instruments, including a fixed-threshold PSM, two DEG-CPCs, a TSI 3776, two API-TOFs, a NAIS and a SMPS. Because instrumentally determined growth rates were not available for all runs, a parameterization was derived to allow the growth rate to be calculated for every run.

The detection thresholds of the particle counters do not represent perfect step functions, so particles with smaller diameters are detected to some extent. This

leads to over-counting, which becomes a more important—and more uncertain—correction as the CPC threshold approaches 1.7 nm. For this reason, the nucleation rates reported here are based on a TSI 3776 CPC with $d_{\text{th}} = 3.2$ nm since—although requiring the largest corrections for losses between 1.7 nm and the detection threshold—it has negligible sensitivity to clusters below 1.7 nm. To confirm the nucleation rates obtained with the 3.2 nm CPC, they were derived independently from the other CPCs with lower detection thresholds and verified to agree within systematic uncertainties.

The ion-induced nucleation rate, J_{ion} , for positive and negative particles is measured with the NAIS. This provides the most sensitive determination of the ion-induced fraction, $J_{\text{ion}}/J_{\text{total}}$, because the NAIS measures only charged clusters. Loss corrections are applied to the charged cluster spectra to account for wall losses, dilution and ion-ion recombination. In addition a source correction is applied to account for diffusion charging of neutral clusters by small ions. The latter correction requires knowledge of the number concentrations of small ions and of neutral clusters versus particle diameter. The neutral cluster concentrations are measured with the 3.2 nm TSI 3776 CPC and their size spectra are measured with the SMPS. The small-ion concentrations are measured with the AIS⁺ and AIS⁻. The charging (collision) probabilities are determined using the collision kernels versus diameter from ref. 41.

The error on $J_{1.7}$ has three components that are added together in quadrature to estimate the total error indicated in Figs 1 and 2a. The first is a statistical measurement error derived from the scatter of the particle counter measurements, evaluated separately for each nucleation event; the second is an estimated $+50\%/ -33\%$ uncertainty on the calculated correction factor, $J_{1.7}/J_{d_{\text{th}}}$, where $J_{d_{\text{th}}}$ is the nucleation rate at size d_{th} , obtained after correcting $dN_{d_{\text{th}}}/dt$ for detection losses. The third is a $\pm 30\%$ systematic uncertainty on $J_{d_{\text{th}}}$ estimated from the run-to-run reproducibility of $dN_{d_{\text{th}}}/dt$ under nominally identical chamber conditions.

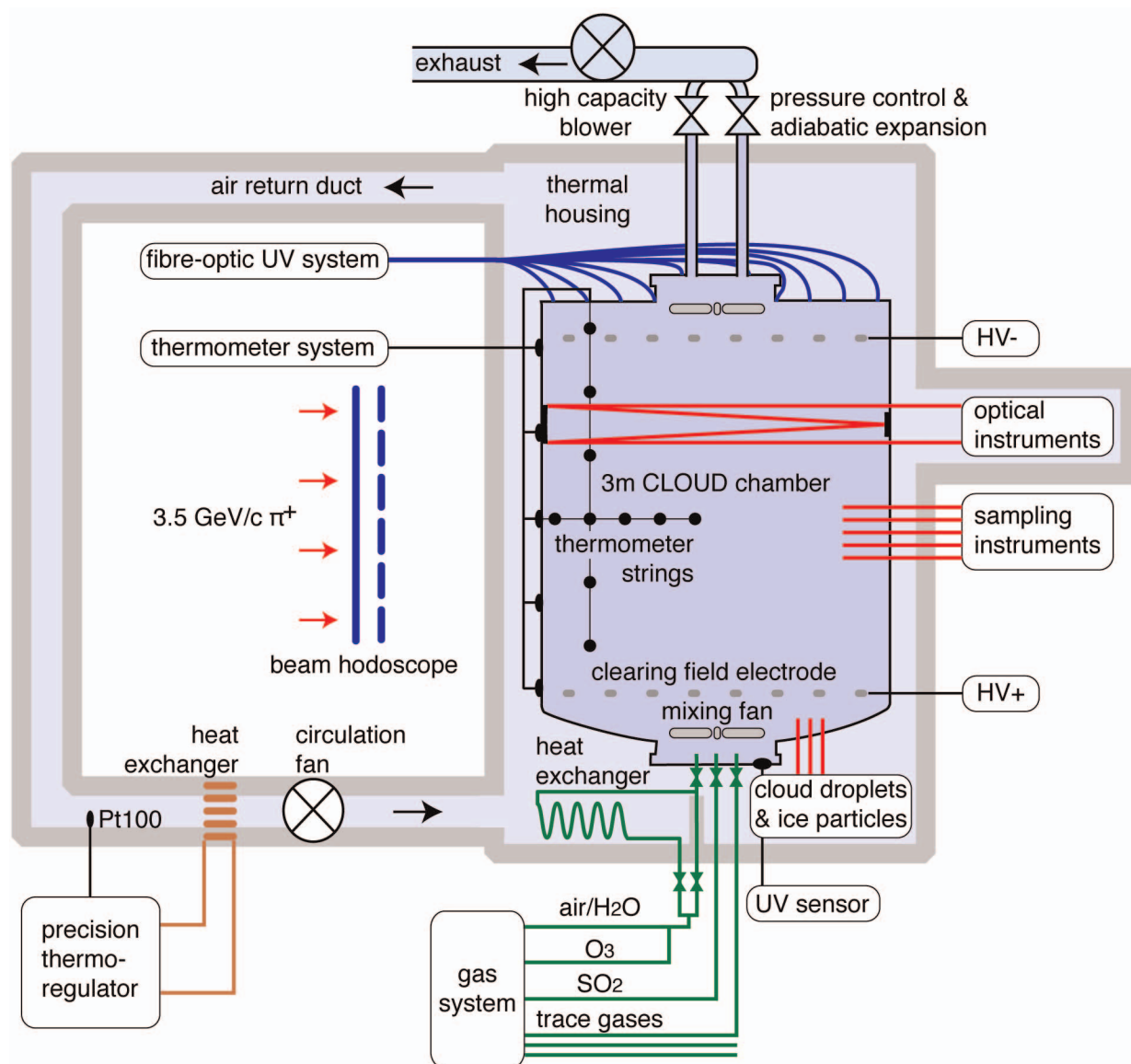
The error on J_{ion} has two main components. The first is a statistical measurement error derived from the scatter of the NAIS measurements, evaluated separately for each nucleation event. The second is an estimated $\pm 50\%$ error to account for the uncertainty in the correction for diffusion charging of neutral clusters by small ions. These errors are added together in quadrature with the error on $J_{1.7}$ to estimate the error on the ion-induced fraction, $J_{\text{ion}}/J_{1.7}$, shown in Fig. 2b.

The overall experimental uncertainty on [H₂SO₄] measured by the CIMS is estimated to be $+100\%/ -50\%$, on the basis of three independent measurements: particle growth rate under binary nucleation conditions, the depletion rate of [SO₂] by photo-oxidation, and an external calibration source⁴². However, the run-to-run relative experimental uncertainty on [H₂SO₄] is smaller, typically $\pm 10\%$. In deriving the sulphuric acid dimer concentrations measured by the CIMS (Fig. 4), we assumed the same charging efficiency by the ion source as for monomers. The concentrations of SO₂ and O₃ are measured with calibrated instruments and are known to $\pm 10\%$. The overall uncertainty on the NH₃ mixing ratio is estimated to be $+100\%/ -50\%$. The point-to-point uncertainty on the DMA mixing ratio is estimated to be $\pm(11\% + 12\%/[\text{DMA}])$ (p.p.t.v.), with an overall scale uncertainty of $+50\%/ -33\%$. The minimum directly measurable values are 2 p.p.t.v. for NH₃ and 0.2 p.p.t.v. for DMA. However, lower values can be estimated from precise calibration of the trace gas delivery systems together with molecular analysis of the nucleating clusters in the API-TOFs.

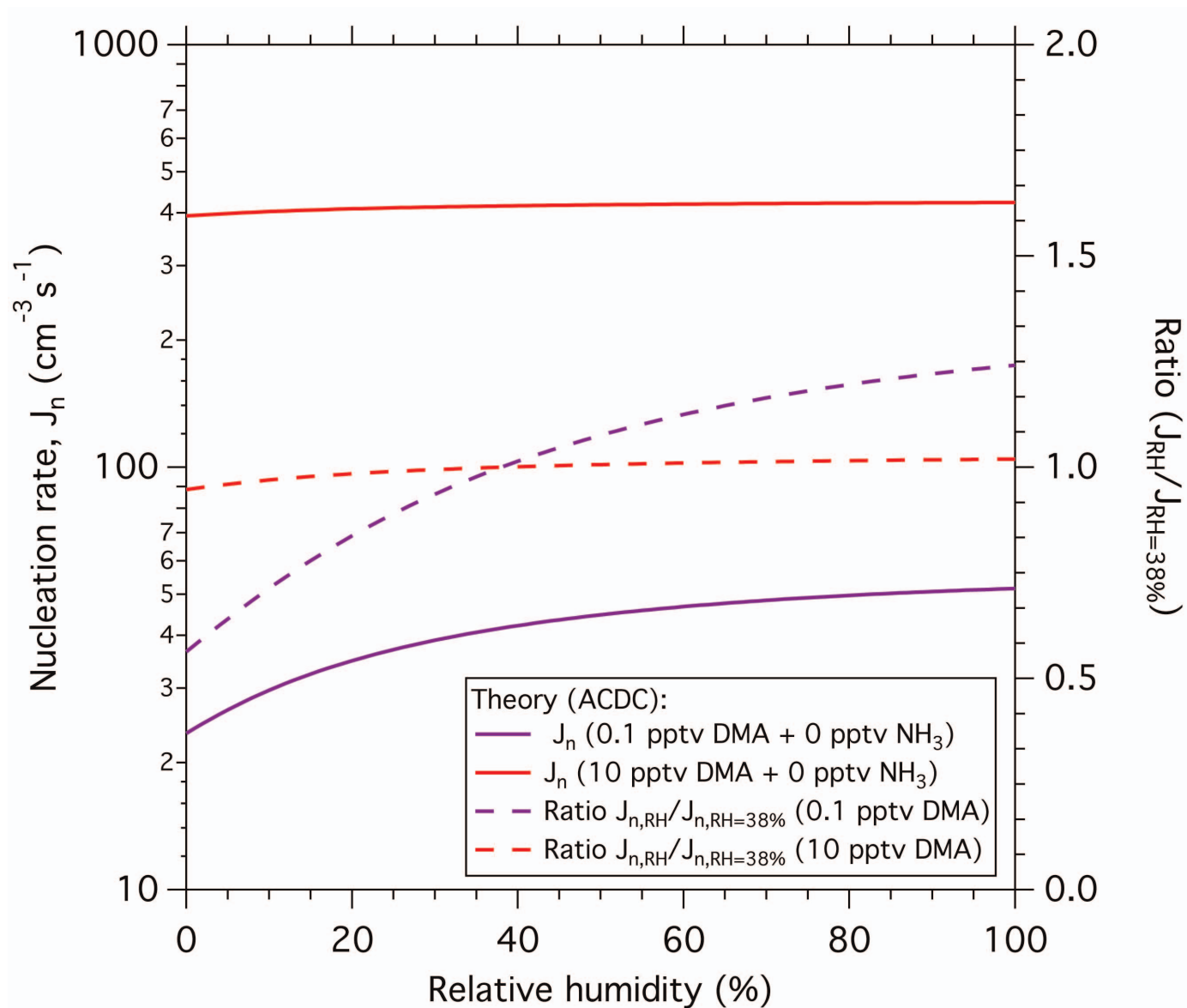
To compare the CLOUD measurements with theoretical expectations, all possible collision, coagulation, evaporation and fragmentation reactions have been explicitly simulated for a certain set of clusters. Collision and coagulation rates are computed from kinetic gas theory, while evaporation and fragmentation rates are obtained from quantum chemistry²⁵. Dynamical simulations were performed with the ACDC model²⁴ to calculate the formation of neutral, positively charged and negatively charged clusters containing sulphuric acid, ammonia and DMA. The electrostatic enhancement of ion–molecule collisions is calculated using dipole moments and polarizabilities obtained from quantum chemistry. The model has no fitted parameters. As a result of computing limitations, the formation and evaporation of clusters containing up to four sulphuric acid and four base molecules (mobility diameters 1.2–1.4 nm) have been modelled so far. The diameters of the largest computed clusters are smaller than the 1.7 nm size at which the experimental formation rates ($J_{1.7}$) are determined. The modelled formation rates can therefore be expected to overestimate the CLOUD measurements somewhat. Further description of the ACDC model is provided in Supplementary Information.

- Kürten, A., Rondo, L., Ehrhart, S. & Curtius, J. Performance of a corona ion source for measurement of sulphuric acid by chemical ionisation mass spectrometry. *Atmos. Meas. Tech.* **4**, 437–443 (2011).
- Junninen, H. et al. A high-resolution mass spectrometer to measure atmospheric ion composition. *Atmos. Meas. Tech.* **3**, 1039–1053 (2010).
- Vanhänen, J. et al. Particle size magnifier for nano-CN detection. *Aerosol Sci. Technol.* **45**, 533–542 (2011).
- Iida, K., Stolzenburg, M. R. & McMurry, P. H. Effect of working fluid on sub-2 nm particle detection with a laminar flow ultrafine condensation particle counter. *Aerosol Sci. Technol.* **43**, 81–96 (2009).

35. Wimmer, D. *et al.* Performance of diethylene glycol based particle counters in the sub 3 nm size range. *Atmos. Meas. Tech. Discuss.* **6**, 2151–2181 (2013).
36. Kulmala, M. *et al.* Towards direct measurement of atmospheric nucleation. *Science* **318**, 89–92 (2007).
37. Graus, M., Müller, M. & Hansel, A. High resolution PTR-TOF: quantification and formula confirmation of VOC in real time. *J. Am. Soc. Mass Spectrom.* **21**, 1037–1044 (2010).
38. Praplan, A. P., Bianchi, F., Dommen, J. & Baltensperger, U. Dimethylamine and ammonia measurements with ion chromatography during the CLOUD4 campaign. *Atmos. Meas. Tech.* **5**, 2161–2167 (2012).
39. Kerminen, V.-M. & Kulmala, M. Analytical formulae connecting the ‘real’ and the ‘apparent’ nucleation rate and the nuclei number concentration for atmospheric nucleation events. *J. Aerosol Sci.* **33**, 609–622 (2002).
40. Kulmala, M. & Kerminen, V.-M. On the formation and growth of atmospheric nanoparticles. *Atmos. Res.* **90**, 132–150 (2008).
41. Laakso, L. *et al.* Kinetic nucleation and ions in boreal forest particle formation events. *Atmos. Chem. Phys.* **4**, 2353–2366 (2004).
42. Kürten, A., Rondo, L., Ehrhart, S. & Curtius, J. Calibration of a chemical ionization mass spectrometer for the measurement of gaseous sulphuric acid. *J. Phys. Chem. A* **116**, 6375–6386 (2012).

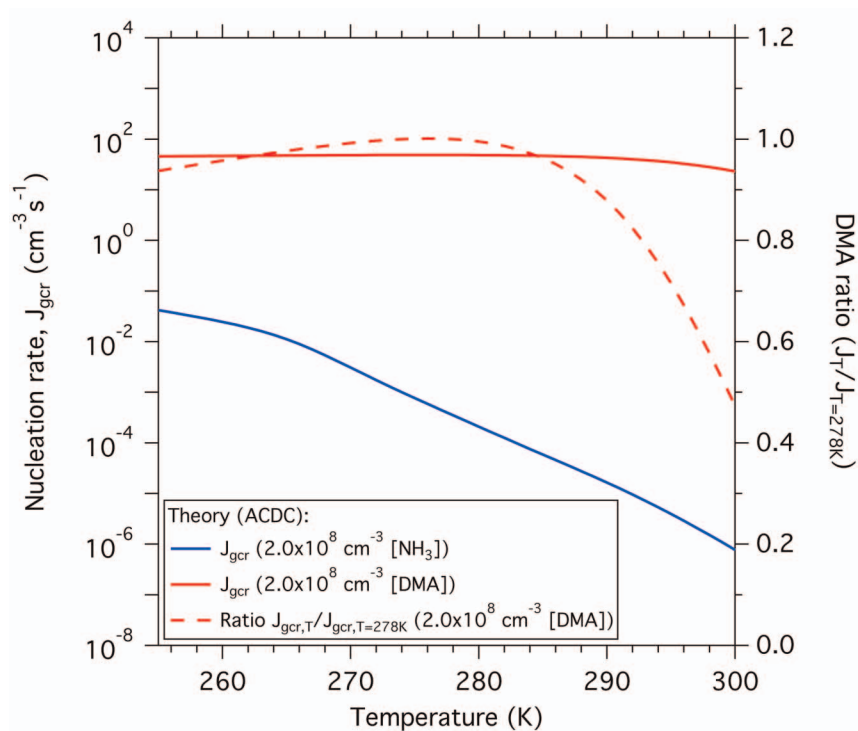


Extended Data Figure 1 | Schematic diagram of the CLOUD experiment at the CERN Proton Synchrotron.



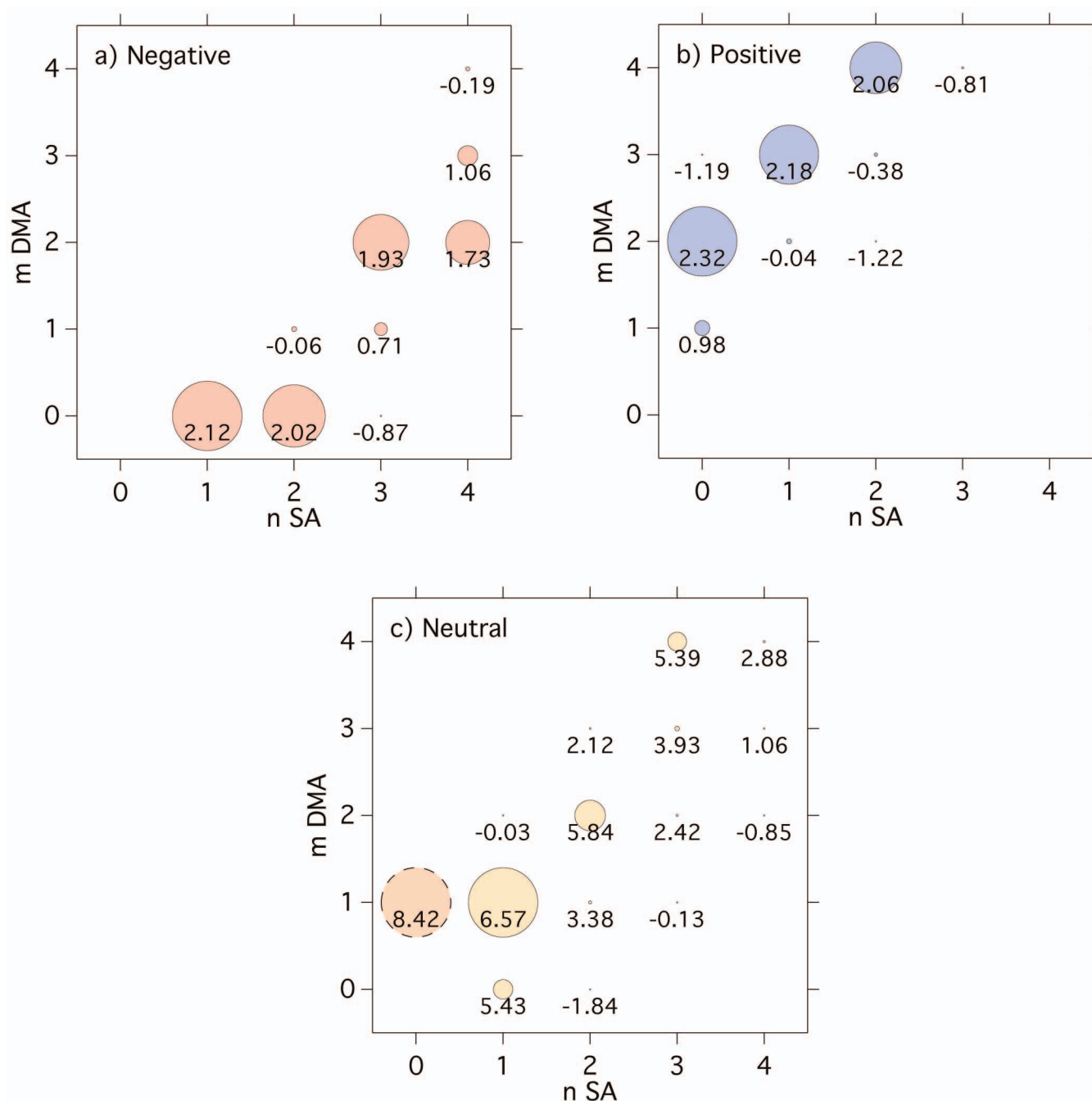
Extended Data Figure 2 | Theoretical dependence of amine ternary nucleation rates on RH. Modelled neutral nucleation rates as a function of RH (left-hand scale) at $2.0 \times 10^6 \text{ cm}^{-3}$ [H_2SO_4] and 278 K, and either 0.1 p.p.t.v.

DMA (purple curve) or 10 p.p.t.v. DMA (red curve). The nucleation rates relative to their value at 38% RH are shown on the right-hand scale (dashed purple and red curves).



Extended Data Figure 3 | Theoretical dependence of ammonia ternary and amine ternary nucleation rates on temperature. Modelled GCR nucleation rates as a function of temperature (left-hand scale) at $2.0 \times 10^6 \text{ cm}^{-3}$ [H_2SO_4] and either $2.0 \times 10^8 \text{ cm}^{-3}$ [NH_3] (blue curve) or $2.0 \times 10^8 \text{ cm}^{-3}$ [DMA] (red curve). (A concentration of $2.0 \times 10^8 \text{ cm}^{-3}$ is equivalent to mixing ratios

between 7.0 p.p.t.v. at 255 K and 8.2 p.p.t.v. at 300 K.) The sulphuric acid–DMA nucleation rate relative to the value at $T = 278 \text{ K}$ is shown on the right-hand scale (dashed red line). In the sulphuric acid–DMA system a sticking probability of 0.5 is assumed for all neutral–neutral collisions, and 1.0 for all charged–neutral collisions.



Extended Data Figure 4 | Theoretical concentrations of negative, positive and neutral clusters during DMA ternary nucleation. Modelled steady-state concentrations (m DMA versus n SA) at $4.0 \times 10^6 \text{ cm}^{-3}$ [H_2SO_4], 10 p.p.t.v. DMA, 4 ion pairs $\text{cm}^{-3} \text{ s}^{-1}$ and 278 K. **a**, Negative clusters. **b**, Positive clusters. **c**, Neutral clusters. A sticking probability of 0.5 is assumed for all

neutral–neutral collisions and 1.0 for all charged–neutral collisions. The numbers below the centre of each circle show $\log_{10} C$, where $C \text{ (cm}^{-3}\text{)}$ is the cluster concentration (the threshold is 0.01 cm^{-3}). The circle areas within each panel are proportional to C (with the exception of the DMA monomer in **c**).

Chelicerate neural ground pattern in a Cambrian great appendage arthropod

Gengo Tanaka¹, Xianguang Hou², Xiaoya Ma^{2,3}, Gregory D. Edgecombe³ & Nicholas J. Strausfeld⁴

Preservation of neural tissue in early Cambrian arthropods has recently been demonstrated¹, to a degree that segmental structures of the head can be associated with individual brain neuromeres. This association provides novel data for addressing long-standing controversies about the segmental identities of specialized head appendages in fossil taxa^{2,3}. Here we document neuroanatomy in the head and trunk of a 'great appendage' arthropod, *Alalcomenaeus* sp., from the Chengjiang biota, southwest China, providing the most complete neuroanatomical profile known from a Cambrian animal. Micro-computed tomography reveals a configuration of one optic neuropil separate from a protocerebrum contiguous with four head ganglia, succeeded by eight contiguous ganglia in an eleven-segment trunk. Arrangements of optic neuropils, the brain and ganglia correspond most closely to the nervous system of Chelicerata of all extant arthropods, supporting the assignment of 'great appendage' arthropods to the chelicerate total group^{4,5}. The position of the deutocerebral neuromere aligns with the insertion of the great appendage, indicating its deutocerebral innervation and corroborating a homology between the 'great appendage' and chelicera indicated by morphological similarities^{4,6,7}. *Alalcomenaeus* and *Fuxianhuia protensa*¹ demonstrate that the two main configurations of the brain observed in modern arthropods, those of Chelicerata and Mandibulata, respectively⁸, had evolved by the early Cambrian.

Cambrian 'great appendage' arthropods, collectively known as Megacheira⁹, are variously regarded as mono-, para- or polyphyletic

and variously interpreted as stem-group chelicerates^{4–7} or as stem-group arthropods^{2,10}. They are characterized by raptorial cephalic appendages with an 'elbow joint' between a proximal pedunculate part and a distal part bearing an elongate spine on each article⁷. Morphologically and taxonomically best understood are Leancoiliidae, which have three long spine-bearing or spiniform articles on the great appendage, each with a flagellate distal part^{11,12}.

YKLP 11075 is a leancoiliid from the early Cambrian Chengjiang biota (Yu'an-shan Member, Heilinpu Formation), Yunnan Province, southwest China¹³. It is preserved as part and counterpart in dorso-ventral aspect, exhibiting the cephalic shield and 11 complete trunk segments (Figs 1a and 2a). It is assigned to *Alalcomenaeus* (Fig. 3a, b) rather than the closely allied *Leancoilia* (Fig. 3c), abundantly represented in the Chengjiang biota by *Leancoilia illecebrosa*. Distinction from *Leancoilia* is based on the straight (rather than pointed) anterior margin of the cephalic shield and rounded, paddle-shaped (rather than lanceolate) telson¹⁴ (Fig. 3a). Studied specimens are similar to *Alalcomenaeus cambricus* from the Burgess Shale, Canada, having four rather than three pairs of cephalic appendages, as described for *A. cambricus*¹⁵. We describe them in open nomenclature, that is, *Alalcomenaeus* sp., because most of the *Alalcomenaeus* material from the Chengjiang biota has not been studied in detail.

Paired eyes, well separated by exoskeleton, are preserved each side of the midline at the anterior margin of the cephalic shield (Fig. 2a). Each eye is approximately 0.75 mm wide, composed of approximately

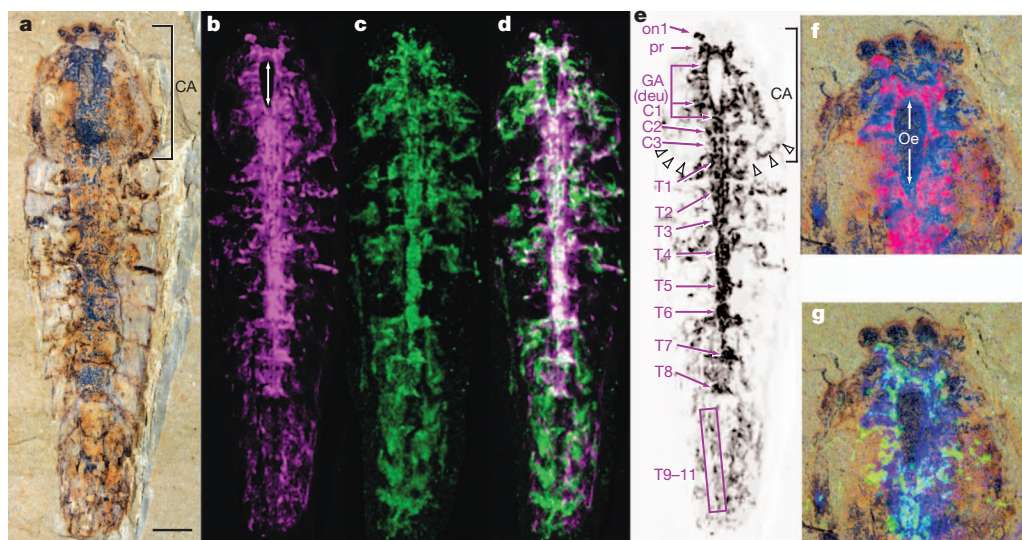


Figure 1 | *Alalcomenaeus* sp. from the Chengjiang Lagerstätte. **a**, Incident light photograph, dorsal view of mounted part and counterpart YKLP 11075. **b**, Energy-dispersive X-ray fluorescence (EDXRF) Fe profile. Double-headed arrow indicates rostro-caudal extent of oesophageal foramen. **c**, MicroCT scan. **d**, Overlay of EDXRF Fe and microCT. **e**, Inverted white coincidence signal after isolated magenta (**b**) and green (**c**) removal. Arrowheads mark posterior margin of

cephalic shield. **f**, Cephalon with superimposed EDXRF Cu (blue) and EDXRF Fe (red) profiles. **g**, Cephalon with superimposed EDXRF Cu (blue) and CT (green) profiles. C1, tritocerebrum; C2, C3, cephalic biramous segment neuropils; CA, cephalic segments; GA, great appendage neuropil = deutocerebrum (deu); Oe, oesophageal foramen; on1, first-order visual neuropil; pr, protocerebrum; T1–T8, trunk segment neuropils; T9–11, trunk segments lacking ganglia. Scale bar, 2 mm.

¹Japan Agency for Marine–Earth Science and Technology, Yokosuka 2370061, Japan. ²Yunnan Key Laboratory for Palaeobiology, Yunnan University, Kunming 650091, China. ³Department of Earth Sciences, The Natural History Museum, Cromwell Road, London SW7 5BD, UK. ⁴Department of Neuroscience and Center for Insect Science, University of Arizona, Tucson, Arizona 85721, USA.

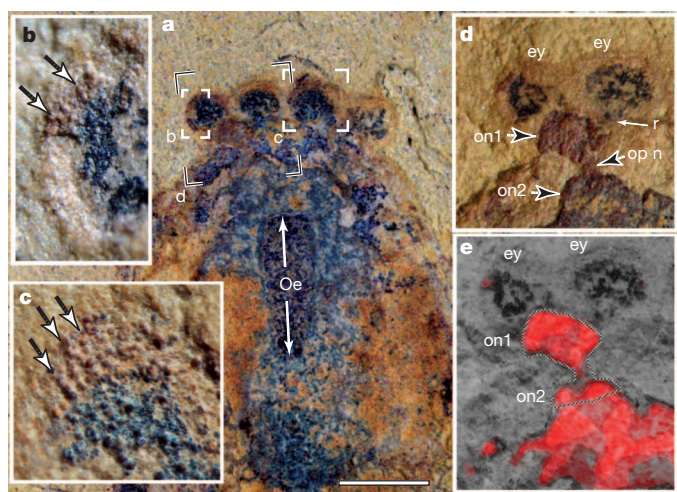


Figure 2 | Details of eye pairs and visual neuropils in *Alalcomenaeus* sp. YKLP 11075. **a**, Cephalic region; boxed areas refer to panels **b–d**. **b**, Left cornea of left eye pair showing lenses (arrowed) surmounting pigmented area. **c**, Lens rows (arrowed: left eye of right pair). **d**, Enlargement of left eye (ey) pair showing trace of retinula axon bundle (r) extending to rust-coloured first-order optic neuropil (on1) separate from the brain, but connected to it by an optic nerve (op n) terminating in a similarly coloured domain (on2) integrated in the protocerebrum. **e**, Superimposition of EDXRF Fe (red) showing strict coincidence of detected iron at the first-order optic neuropil (on1) and underlying protocerebral areas. Outlines of on1 and on2 are superimposed. Scale bar, 2 mm.

15 μ m diameter facets (Fig. 2b, c) spaced as 20–25 rows. Each comprises 8–10 vertically arranged elements, equipping each eye with 160–250 facets. Facets surmount a dark zone contiguous with centrally extending traces of the retinula nerve from each eye (Fig. 2d). Nerves from a lateral pair of eyes converge to an obcordate rust-brown area identified as the first visual neuropil (Fig. 2d, left). A single optic nerve connects it to a similarly rust-brown strip interpreted as the second optic neuropil integrated in the rostral volume of the protocerebrum (Fig. 2d). The extent of these neuropils is resolved by superimposition of iron distribution detected by energy-dispersive X-ray fluorescence (EDXRF Fe) over the relevant region (Figs 1f and Fig. 2e, and Extended Data Fig. 1).

Outlines of contiguous cerebral and thoracic neuromeres were resolved by combining EDXRF Fe with computed tomography (CT). The EDXRF copper (blue) signal (Extended Data Fig. 1) corresponds to much of the internal volume of the specimen. Overlaying the EDXRF Fe (magenta) signal demonstrates a highly constrained distribution of iron to the putative nervous system (Fig. 1f). Overlaying the CT signal (Fig. 1c, green) and EDXRF Fe (Fig. 1b, magenta) signal in Fig. 1d, then subtracting isolated greens and magentas and inverting the white coincidence signal, resolves highly constrained segmental neuromeres (Fig. 1e). In the head, EDXRF Fe and CT overlie the protocerebrum and first-order visual neuropil (Fig. 1f, g), which receives its input from the two eyes (Fig. 2a, d, e), followed by an elongated neuromere corresponding to the deutocerebral origin of the great appendage (Fig. 1e–g, GA; Extended Data Fig. 1). Two smaller swellings indicate fused neuromeres corresponding to the segmental origins of the first and second pairs of biramous cephalic appendages (C1, C2) (Fig. 1e). These three neuromeres (GA, C1, C2) flank the extended oesophageal foramen reaching rostrally to the caudal margin of the protocerebrum (Fig. 1e). Neuropils lateral to the foramen converge between the second (C2) and third post-GA neuromere (C3), which is at the midline (Fig. 1e). Each neuromere aligns with the segment of the head defined by the attachment points of the corresponding member of the first four appendage pairs. All are resolved anterior to the posterior margin of the head shield (open arrowheads in Figs 1e and 3a–c).

In contrast to discrete ganglia linked by elongated connectives³, the robust post-cephalic neuromeres T1–T8 are effectively contiguous, without intervening connectives. Segments 9–11 show no detectable signal indicative of ganglia. These most caudal segments are equipped with successively smaller appendages until the broad, ovoid telson (Fig. 3a), which is attached to the eleventh segment. Telson flexion, such as would elicit reflex escape behaviours, requires power from longitudinal muscles within the last few trunk segments. These were probably specialized in segments 8–11, driven by motor neurons in ganglion T8, a similar arrangement existing in the extant crustacean order Mystacocarida in which the last four trunk segments lack ganglia but are innervated from post-cephalic segment T8 (ref. 16).

Reconstruction of neuromeric topology shows critical correspondences with the nervous systems of chelicerates, exemplified by the horseshoe crab *Limulus polyphemus* and scorpion *Centruroides sculpturatus*

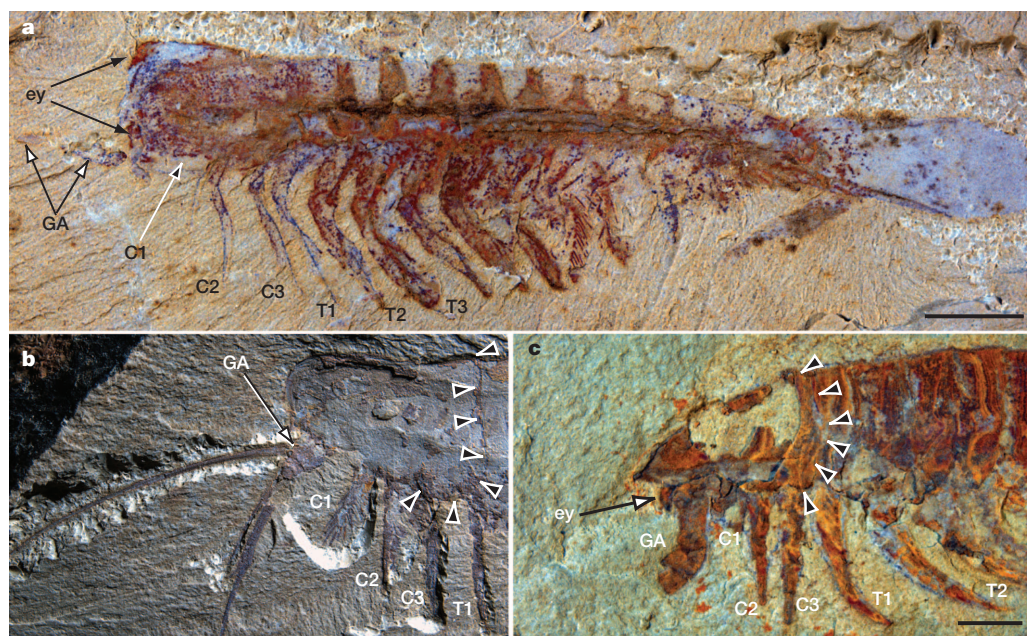


Figure 3 | Leancoiliid megacheiran arthropods from the Chengjiang Lagerstätte. Lateral views. Arrowheads mark posterior margin of cephalic shield. **a**, **b**, *Alalcomenaeus* sp. **a**, YKLP 11076. **b**, YKLP 11077. **c**, *Leancoilia*

illecebrosa. YKLP 11078. C1–C3, biramous cephalic appendages 1–3; ey, eye; GA, great appendage; T1–T3, biramous limbs of trunk segments 1–3. Scale bars, 2 mm.

(Fig. 4). In all three taxa a single optic neuropil, which is separate from the brain, serves each eye (Fig. 2a, d), and all taxa have an extended oesophageal foramen flanked by the fused proto-, deuto- and tritocerebral neuromeres (Fig. 1e). As in *Limulus*, the fourth rostral neuromere also participates in this flanking arrangement. Although distinct entities, the ganglia in the trunk of *Alalcomenaeus* show partial fusion, as in *Limulus*.

The great appendage of *Megacheira* has variously been regarded as proto-, deuto-³ or tritocerebral⁴. A deutocerebral identity is consistent with a structural homology between the great appendage and chelicera with respect to the elbow joint and arrangement of fixed and movable fingers^{4,7}. Chelicerae are demonstrably deutocerebral based on Hox gene expression domains¹⁷. The arrangement of neural structures in *Alalcomenaeus* favours a deutocerebral innervation of the great appendage. The position of its ventral point of origin corresponds to that of the second largest neuromere, immediately posterior to the protocerebrum, itself defined by its connection with the separate optic neuropil. Although the great appendage is incomplete in YKLP 11075, its attachment point in other specimens of *Alalcomenaeus* (Fig. 3b) and in *Leancoilia* (Fig. 3c) best corresponds to the position of the prominent deutocerebral neuromere in YKLP 11075.

The distribution of neuromeres in the head of YKLP 11075 conforms to the presence of three pairs of biramous limbs posterior to the great appendage, although only two pairs have been described from the Burgess Shale *Alalcomenaeus cambricus*¹⁵. Two pairs had likewise been documented in *Leancoilia superlata*¹⁸, but a small first pair was subsequently identified in that species¹². The presence of three pairs in the present Chengjiang *Alalcomenaeus* (Fig. 3a, b) suggests that this is a diagnostic feature of leancoiliids generally, and brings this group into

line with the ground pattern of crown-group euarthropods as well as trilobites, which possess paired uniramous antennae and three biramous post-antennal head segments¹⁹.

Descriptions of the *Leancoilia* midgut show a uniformly broad, contiguous and segmentally convoluted organ system of associated glands distinct from segmental ganglia³, originating at the level of C3 and terminating at trunk segment T8 (ref. 20), whereas a more tubular gut tract is seen in *Alalcomenaeus cambricus*¹⁵. A gut identity can be ruled out for the nerve cord in *Alalcomenaeus* because of its continuity with the brain and the obvious intersegmental constrictions between segmental ganglia (Fig. 1e). In *Alalcomenaeus* the oesophageal foramen reaches forward to the caudal margin of the protocerebral neuromere (Figs 1e and 2a), demonstrating that in this taxon only the protocerebrum is supraoesophageal, a condition typifying *Limulus* and *Centruroides* and suggested as ancestral for chelicerates⁸. Chelicerate brains differ from those of mandibulates in that only the first-order visual neuropil of each eye lies separate from the brain, connected by relays to second- and third-order visual centres integrated within the protocerebrum. This organization, shared by pycnogonids²¹, xiphosurans²² and arachnids²³, contrasts with mandibulates, in which three (Malacostraca, Insecta) or two (Scutigromorpha) nested optic neuropils reside separate from, but connected to, the mid-brain proper^{1,8}. Furthermore, other than in pycnogonids, all extant chelicerates, including *Limulus*, show fusion of cerebral and trunk ganglia. *Alalcomenaeus* shares these crucial elements of the chelicerate central nervous system ground pattern. Phylogenetic analysis of a comprehensive data set of neural characters²⁴ (Supplementary Tables 1 and 2) resolves fusion of cerebral and trunk ganglia, and the single optic neuropil outside the protocerebrum, as apomorphies of Chelicerata s.l. (sensu lato; Pycnogonida and Euchelicerata),

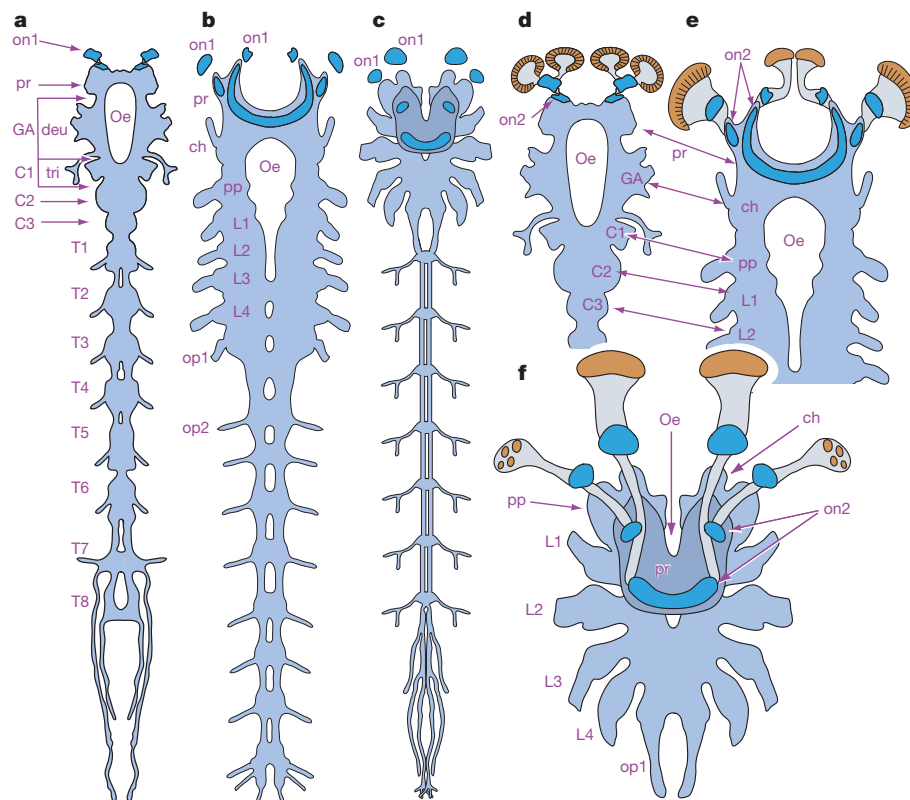


Figure 4 | Nervous systems of Chelicerata. a–c, Reconstruction of ‘great appendage’ arthropod and Chelicerata nervous systems. a, *Alalcomenaeus* sp. b, Larval *Limulus polyphemus* (Xiphosura). c, *Centruroides sculpturatus* (Scorpiones). d–f, Enlargements of corresponding segmental neuromeres and optic neuropils (shown in navy blue). Each eye supplies its first optic neuropil (on1) outside the protocerebral mass; second order optic neuropils (on2) are integrated within the protocerebrum (pr). The oesophageal foramen (Oe) reaches the caudal margin of the protocerebrum; second and third neuromeres

flank the foramen. In *Centruroides*, the protocerebrum is recurved over the cheliceral (ch) and pedipalp (pp) neuromeres (homologues of *Alalcomenaeus* great appendage neuromere (GA) and first cephalic appendage neuromere (C1), and *Limulus* cheliceral and pedipalp neuromeres). C1–C3, first–third cephalic neuromeres; deu, deutocerebrum; L1–L4, first to fourth leg ganglia; op1, op2, first and second opisthosomal neuromeres; T1–T8, trunk ganglia 1–8; tri, tritocerebrum. Eyes shown in brown, faceted eyes indicated by radial divisions.

including *Alalcomenaeus*. The only arthropod outside the chelicerates known to possess a nervous system condensed into a single mass is the hemipteran water strider (Gerridae), but as in other mandibulates the three nested optic lobes extend laterally from the protocerebrum⁸. Segmentation of the postoral nervous system in *Alalcomenaeus* is a shared derived character of Euarthropoda rather than an indicator of affinity to a particular euarthropod clade.

Mandibulate arthropods possess just one pair of compound eyes, except where the upper and ventral halves are specialized to serve different perceptual functions, as in Bibionidae and Gyrinidae^{25,26}. Multiple pairs of eyes typifies chelicerates. Possession of paired eyes disposed laterally and relaying to their optic neuropils fits the cladogram (Extended Data Fig. 2) as a derived character of Chelicerata s.l. including *Alalcomenaeus*. We infer this character to also apply to *Leanchoilia* where four visual units (as in *Alalcomenaeus* sp.) have been unambiguously described for *L. superlata* and *L. persephone*^{12,18}. Structures in *Leanchoilia* interpreted as paired pendulous eyes 'structured like a bunch of grapes'²⁷ are likely cuticular features of the great appendages¹².

The utility of computed synchrotron and phase-contrast radiation X-ray tomography for resolving soft tissue preservation has precedents in studies of ancient soft tissue from Cambrian Orsten trilobites²⁸ and crustaceans²⁹, including data on the gut, connective tissue and possible segmental muscle. For this account, computed tomography was achieved on a specimen that, unlike most Chengjiang specimens, showed considerable preservation in depth. Resolving nervous tissue resulted from scanning conjoined part and counterpart and subtracting contaminants of other tissue fragments (see Methods). Such combinatorial approaches should yield comparable internal details for other Burgess-Shale-type fossils that show appropriate dimensionality.

METHODS SUMMARY

Part and counterpart of the specimen (YKLP 11075) were precisely aligned for X-ray computed tomography (see Methods, Supplementary Information). Elemental distribution analyses were obtained using energy-dispersive X-ray fluorescence (EDXRF) microscopy. Light microscopy images were processed with Adobe Photoshop Elements 10 (Adobe Systems) using enhance functions for colour correction, balance, overlays, subtractions and inversions (see Methods, Supplementary Information and Figs 1d–g, 2e and Extended Data, Fig. 1).

Online Content Any additional Methods, Extended Data display items and Source Data are available in the online version of the paper; references unique to these sections appear only in the online paper.

Received 10 June; accepted 1 August 2013.

- Ma, X., Hou, X., Edgecombe, G. D. & Strausfeld, N. J. Complex brain and optic lobes in an early Cambrian arthropod. *Nature* **490**, 258–261 (2012).
- Budd, G. E. A palaeontological solution to the arthropod head problem. *Nature* **417**, 271–275 (2002).
- Yang, J., Ortega-Hernández, J., Butterfield, N. J. & Zhang, X. Specialized appendages in fuxianhuiids and the head organization of early arthropods. *Nature* **494**, 468–471 (2013).
- Cotton, T. J. & Braddy, S. J. The phylogeny of arachnomorph arthropods and the origin of the Chelicerata. *Trans. R. Soc. Edinb. Earth Sci.* **94**, 169–193 (2003).
- Stein, M., Budd, G. E., Peel, J. S. & Harper, D. A. T. *Arthroaspis* n. gen., a common element of the Sirius Passet Lagerstätte (Cambrian, North Greenland), sheds light on trilobite ancestry. *BMC Evol. Biol.* **13**, 99 (2013).
- Chen, J., Waloszek, D. & Maas, A. A new 'great-appendage' arthropod from the Lower Cambrian of China and homology of chelicerate chelicerae and raptorial antero-ventral appendages. *Lethaia* **37**, 3–20 (2004).
- Haug, J. T., Waloszek, D., Maas, A., Liu, Y. & Haug, C. Functional morphology, ontogeny and evolution of mantis shrimp-like predators in the Cambrian. *Palaeontology* **55**, 369–399 (2012).
- Strausfeld, N. J. *Arthropod Brains: Evolution, Functional Elegance, and Historical Significance* (Harvard Univ. Press, 2012).

- Hou, X. & Bergström, J. Arthropods of the Lower Cambrian Chengjiang fauna, southwest China. *Fossils and Strata* **45**, 1–116 (1997).
- Legg, D. A., Sutton, M. D., Edgecombe, G. D. & Caron, J.-B. Cambrian bivalved arthropod reveals origins of arthrodisation. *Proc. R. Soc. Lond. B* **279**, 4699–4704 (2012).
- Edgecombe, G. D., García-Bellido, D. C. & Paterson, J. R. A new leanchioid megacheiran arthropod from the lower Cambrian Emu Bay Shale, South Australia. *Acta Palaeontol. Pol.* **56**, 385–400 (2011).
- Haug, J. T., Briggs, D. E. G. & Haug, C. Morphology and function in the Cambrian Burgess Shale megacheiran arthropod *Leanchoilia superlata* and the application of a descriptive matrix. *BMC Evol. Biol.* **12**, 162 (2012).
- Hou, X.-G. et al. *The Cambrian Fossils of Chengjiang, China: The Flowering of Early Animal Life* (Blackwell, 2004).
- Liu, Y., Hou, X. & Bergström, J. Chengjiang arthropod *Leanchoilia illecebrosa* (Hou, 1987) reconsidered. *GFF* **129**, 263–272 (2007).
- Briggs, D. E. G. & Collins, D. The arthropod *Alalcomenaeus cambricus* Simonetta, from the Middle Cambrian Burgess Shale of British Columbia. *Palaeontology* **42**, 953–977 (1999).
- Brenneis, G. & Richter, S. Architecture of the nervous system in Mystacocarida (Arthropoda, Crustacea)—an immunohistochemical study and 3D reconstruction. *J. Morphol.* **271**, 169–189 (2010).
- Damen, W. G., Hausdorf, M., Seyfarth, E. A. & Tautz, D. A conserved mode of head segmentation in arthropods revealed by the expression pattern of Hox genes in a spider. *Proc. Natl Acad. Sci. USA* **95**, 10665–10670 (1998).
- García-Bellido, D. C. & Collins, D. Reassessment of the genus *Leanchoilia* (Arthropoda, Arachnomorpha) from the Middle Cambrian Burgess Shale, British Columbia, Canada. *Palaeontology* **50**, 693–709 (2007).
- Richter, S., Stein, M., Frase, T. & Szucsich, N. U. In *Arthropod Biology and Evolution* (eds Minelli A., Boxshall G. & Fusco G.) The Arthropod Head 223–240 (Springer, 2013).
- Butterfield, N. J. *Leanchoilia* guts and the interpretation of three-dimensional structures in Burgess Shale-type fossils. *Paleobiology* **28**, 155–171 (2002).
- Lehmann, T., Hess, M. & Melzer, R. R. Wiring a periscope - ocelli, retinula axons, visual neuropils and the ancestry of sea spiders. *PLoS ONE* **7**, e30474 (2012).
- Harzsch, S. et al. Evolution of arthropod visual systems: development of the eyes and central visual pathways in the horseshoe crab *Limulus polyphemus* Linnaeus, 1758 (Chelicerata, Xiphosura). *Dev. Dyn.* **235**, 2641–2655 (2006).
- Strausfeld, N. J., Weltzien, P. & Barth, F. G. Two visual systems in one brain: neuropil serving the principal eyes of the spider *Cupiennius salei*. *J. Comp. Neurol.* **328**, 63–75 (1993).
- Strausfeld, N. J. & Andrew, D. R. A new view of insect-crustacean relationships. I. Inferences from neural cladistics and comparative neuroanatomy. *Arthropod Struct. Dev.* **40**, 276–288 (2011).
- Zeil, J. Sexual dimorphism in the visual system of flies: the divided brain of male Bibionidae (Diptera). *Cell Tissue Res.* **229**, 591–610 (1983).
- Lin, C. & Strausfeld, N. J. A precocious adult visual center in the larva defines the unique optic lobe of the split-eyed whirligig beetle *Dineutus sublineatus*. *Front. Zool.* **10**, 7 (2013).
- Schoenemann, B. & Clarkson, E. N. K. The eyes of *Leanchoilia*. *Lethaia* **45**, 524–531 (2012).
- Eriksson, M. E. & Terfelt, F. Exceptionally preserved Cambrian trilobite digestive system revealed in 3D by synchrotron-radiation X-ray tomographic microscopy. *PLoS ONE* **7**, e35625 (2012).
- Eriksson, M. E., Terfelt, F., Eloffson, R. & Marone, F. Internal soft-tissue anatomy of Cambrian 'Orsten' arthropods as revealed by synchrotron X-ray tomographic microscopy. *PLoS ONE* **7**, e42582 (2012).

Supplementary Information is available in the online version of the paper.

Acknowledgements We thank N. Shimobayashi, H. Maeda, and T. Kogiso for arranging and performing EDXRF analyses, and D. Andrew for advice on cladistics. This work was supported by grants from the Natural Science Foundation of China (no. 40730211), Research in Education and Science from the Government of Japan (no. 21740370), a Leverhulme Trust Research Project Grant (F/00 696/T), by the Center for Insect Science, University of Arizona, and a grant from the Air Force Research Laboratories (FA8651-10-1-0001) to N.J.S.

Author Contributions The project was conceived by G.T. Fossil data were analysed by all authors. G.D.E., N.J.S. and X.M. composed the text.

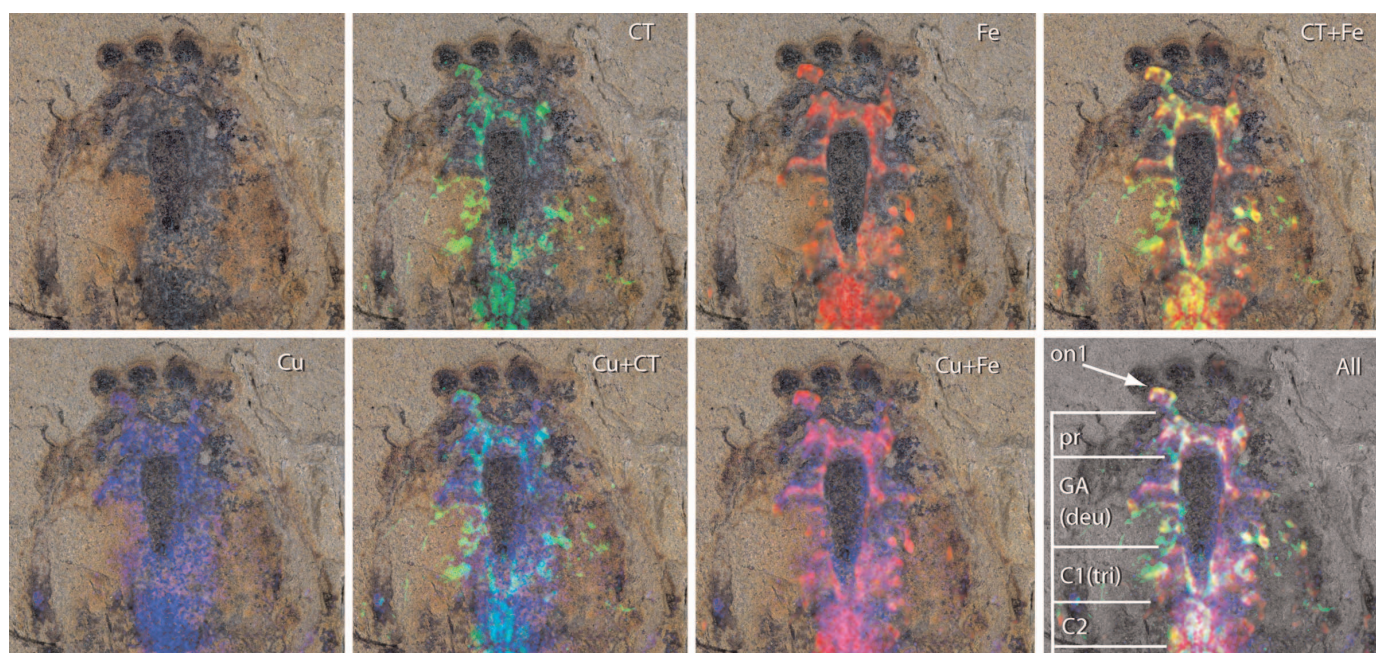
Author Information Reprints and permissions information is available at www.nature.com/reprints. The authors declare no competing financial interests. Readers are welcome to comment on the online version of the paper. Correspondence and requests for materials should be addressed to X.H. (xghou@ynu.edu.cn) or N.J.S. (flybrain@email.arizona.edu).

METHODS

Matrix obscuring parts of the fossil was removed with a fine needle under a binocular microscope. Part and counterpart of the specimen (YKLP 11075; stored at the Yunnan Key Laboratory for Palaeobiology, Yunnan University) were precisely aligned, wrapped in cotton wool for stability and placed into a film case. For X-ray computed tomography (CT) the encased specimen was scanned using a ScanXmate-L system (Comscantecno) at 151 kV with a resolution of 28.8 μm (Fig. 1c) or 14.4 μm (Fig. 1g and Extended Data Fig. 1). Molcer Plus software (White Rabbit) was used to convert the two-dimensional CT image stacks into a three-dimensional (3D) image. For Fig. 1c, volume rendering was performed on a 1332 TIFF image stack (28.8 μm stack intervals). For Fig. 1g and Extended Data Fig. 1, volume rendering was performed on a 1264 TIFF image stack (14.4 μm stack intervals). Contrast and brightness of the 3D images were processed with Molcer Plus software. Elemental distribution analyses were obtained using energy-dispersive X-ray fluorescence

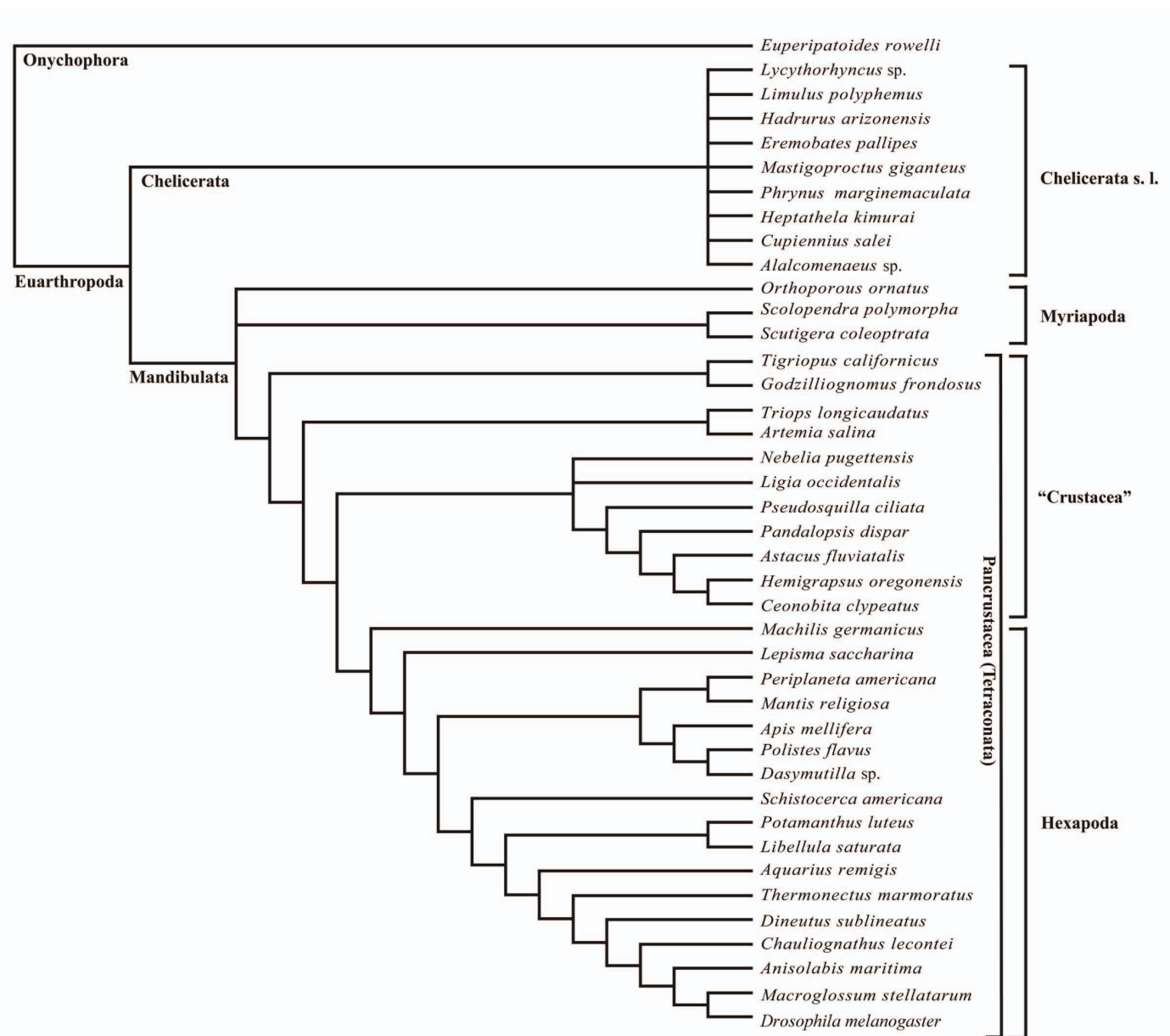
(EDXRF) microscopy. HORIBA XGT-7000V (HORIBA) at 50 kV accelerated voltage and 1 mA probe current, using mono-capillary primary optics to focus the X-ray beam to a diameter of 100 μm . YKLP 11075 was attached to an aluminium stage using conductive carbon tape, its position in the vacuum chamber adjusted using a motorised xyz platform, and viewed using three integrated colour video cameras. An area of 25.6 mm \times 7.2 mm was analysed under full vacuum using 50 μm steps and 200 \times 74 frames to provide two-dimensional distribution maps of Fe and Cu recorded as high-resolution TIFF images. Light microscopy photographs were taken with a Leica DFC 500 digital camera attached to a Leica M205C microscope. Images were processed with Adobe Photoshop Elements 10 (Adobe Systems) using enhance functions for colour correction, balance, overlays, subtractions and inversions (Figs 1d–g, 2e and Extended Data Fig. 1).

Each reconstruction in Fig. 4 has been scaled up or down to aid comparison. Figure 4b is based on published immunocytochemical data²¹. Figure 4c is adapted from histological observations of scorpion central nervous system⁸.



Extended Data Figure 1 | Cephalic region of *Alalcomenaeus* sp. YKLP 11075 All in dorsal view, composites of part and counterpart (upper left). Second left to right: CT scan (green); EDXRF Fe (red); superimposition of CT and EDXRF Fe. Lower row, left to right: EDXRF Cu (blue); superimposition of

CT and EDXRF Cu; superimposition of EDXRF Fe and EDXRF Cu; superimposition of all scans. C1, first post-GA neuropil = tritocerebrum (tri); C2, second post-GA neuropil; GA, great appendage neuropil = deutocerebrum (deu); on1, first optic neuropil; pr, protocerebrum.



Extended Data Figure 2 | Arthropod relationships based on neuroanatomical characters. Strict consensus of 34 shortest cladograms based on 145 characters in Supplementary Information Table 2.

A juvenile mouse pheromone inhibits sexual behaviour through the vomeronasal system

David M. Ferrero¹, Lisa M. Moeller², Takuya Osakada³, Nao Horio³, Qian Li¹, Dheeraj S. Roy¹, Annika Cichy², Marc Spehr², Kazushige Touhara^{3,4} & Stephen D. Liberles¹

Animals display a repertoire of different social behaviours. Appropriate behavioural responses depend on sensory input received during social interactions. In mice, social behaviour is driven by pheromones, chemical signals that encode information related to age, sex and physiological state¹. However, although mice show different social behaviours towards adults, juveniles and neonates, sensory cues that enable specific recognition of juvenile mice are unknown. Here we describe a juvenile pheromone produced by young mice before puberty, termed exocrine-gland secreting peptide 22 (ESP22). ESP22 is secreted from the lacrimal gland and released into tears of 2- to 3-week-old mice. Upon detection, ESP22 activates high-affinity sensory neurons in the vomeronasal organ, and downstream limbic neurons in the medial amygdala. Recombinant ESP22, painted on mice, exerts a powerful inhibitory effect on adult male mating behaviour, which is abolished in knockout mice lacking TRPC2, a key signalling component of the vomeronasal organ^{2,3}. Furthermore, knockout of TRPC2 or loss of ESP22 production results in increased sexual behaviour of adult males towards juveniles, and sexual responses towards ESP22-deficient juveniles are suppressed by ESP22 painting. Thus, we describe a pheromone of sexually immature mice that controls an innate social behaviour, a response pathway through the accessory olfactory system and a new role for vomeronasal organ signalling in inhibiting sexual behaviour towards young. These findings provide a molecular framework for understanding how a sensory system can regulate behaviour.

We developed a genome-based strategy for identifying additional mouse pheromones (Fig. 1a). Chemicals that function as pheromones include urinary volatiles, steroid derivatives and proteins secreted into bodily fluids such as urine, tears and saliva^{4–7}. Several protein pheromones are encoded by large, rapidly evolving gene families, but most pheromone homologues encoded by the mouse genome are of unknown function^{8–10}. We constructed quantitative PCR (qPCR) primers to detect expression of protein pheromones and their homologues, including exocrine gland-secreting peptides (ESPs), androgen-binding proteins (ABPs), major urinary proteins and other lipocalins. Expression levels were quantified in complementary DNA (cDNA) derived from various pheromone-producing tissues obtained from mice of different sexes, ages and physiological states.

Using this strategy, we identified several peptides with striking age-dependent production in the extraorbital lacrimal gland, including ESP22 produced by juveniles, ESP15 and ESP16 produced by adults of both sexes and ABP27 produced by neonates (Fig. 1b and Extended Data Fig. 1a). We also identified male-enriched peptides of unknown function, including ESP24 and various ABPs. Interestingly, sexually dimorphic production of ESP24 and the male pheromone ESP1 was similar (~500-fold male-enriched), but occurred in different mouse strains (Extended Data Fig. 2b).

Because juvenile pheromones are unknown, we performed additional studies of ESP22. ESP22 was maximally expressed in lacrimal

gland between 2 and 3 weeks of age, and decreased sharply after 4 weeks of age, near puberty (Fig. 1b). Quantitative analysis indicated ESP22 expression in lacrimal gland to be similar in male and female juveniles, and approximately 50-fold higher in juveniles than adults (Extended Data Fig. 2d). ESP22 expression was not detected in cDNA derived from 16 other mouse tissues, including other exocrine glands, internal organs and sensory epithelia (Fig. 1c and Extended Data Fig. 2f). In contrast, ABP27 expression was detected in adult salivary gland as well as neonatal lacrimal gland (Extended Data Fig. 2e).

Next, we identified lacrimal gland cell types that expressed ESP22 and other pheromone homologues using RNA *in situ* hybridization. We found that ESP22 is produced by a subset of lacrimal secretory cells, termed acinar cells (Extended Data Fig. 1c), which release contents into tears, a source of mouse pheromones⁹. ESP22 expression was detected in juvenile but not adult acinar cells, whereas ESP24 expression was detected only in adult male acinar cells (Fig. 1d). Furthermore, *Esp22* was not expressed in castrated and ovariectomized adults, suggesting sex-hormone-independent *Esp22* gene regulation (Extended Data Fig. 1b).

To test whether ESP22 protein was secreted into tears by acinar cells, we generated and affinity-purified a polyclonal anti-ESP22 antibody. Western blot analysis using this antibody identified a protein of expected mass (approximately 10 kDa) that was enriched in juvenile tears (Fig. 1e). Concentrations of this protein (3–5 ng μl^{-1} in juvenile tears, or 300–500 nM) were determined using a standard curve of recombinant ESP22 (Extended Data Fig. 3). Mass spectrometry identified ESP22-derived tryptic peptides in tears of juveniles but not adults, indicating greater than 100-fold enrichment (Fig. 1f), and showed the primary structure of mature ESP22 (amino acids 23–111, Extended Data Fig. 4). Together, these findings indicate that ESP22 is a lacrimal peptide secreted into tears of juvenile mice.

Next, we asked whether ESP22 was detected by the mouse olfactory system. Other protein pheromones, including ESP1, activate basal vomeronasal organ (VNO) sensory neurons¹¹, so we examined electrophysiological responses to ESP22 in the VNO. Recombinant ESP22 was prepared as a fusion protein with maltose binding protein (MBP), which enhanced solubility¹². Electrovomerogram (EVG) recordings indicated that recombinant ESP22 (200 nM) evoked a negative field potential in the VNO (Fig. 2a), with a sensitivity matching ESP1 responses previously reported with this technique^{13,14}. MBP was not similarly detected, although small EVG responses to MBP were observed at higher concentrations (data not shown). High-affinity responses to ESP22 in the VNO required the ion channel TRPC2 (Fig. 2a), and were not observed in electroolfactogram (EOG) recordings of the main olfactory epithelium (Fig. 2b), which is also important for pheromone-driven social behaviours^{15–17}.

Next, we used extracellular loose-seal recordings to examine ESP22 responses in individual VNO sensory neurons. ESP22 evoked robust and repetitive discharge patterns in 1.3% of basal VNO sensory neurons (5/383), consistent with detection by one or a few VNO receptors

¹Department of Cell Biology, Harvard Medical School, Boston, Massachusetts 02115, USA. ²Department of Chemosensation, Institute for Biology II, RWTH Aachen University, Aachen, Germany.

³Department of Applied Biological Chemistry, Graduate School of Agricultural and Life Sciences, The University of Tokyo, Tokyo 113-8657, Japan. ⁴ERATO Touhara Chemosensory Signal Project, Japan Science and Technology Agency, The University of Tokyo, Tokyo 113-8657, Japan.

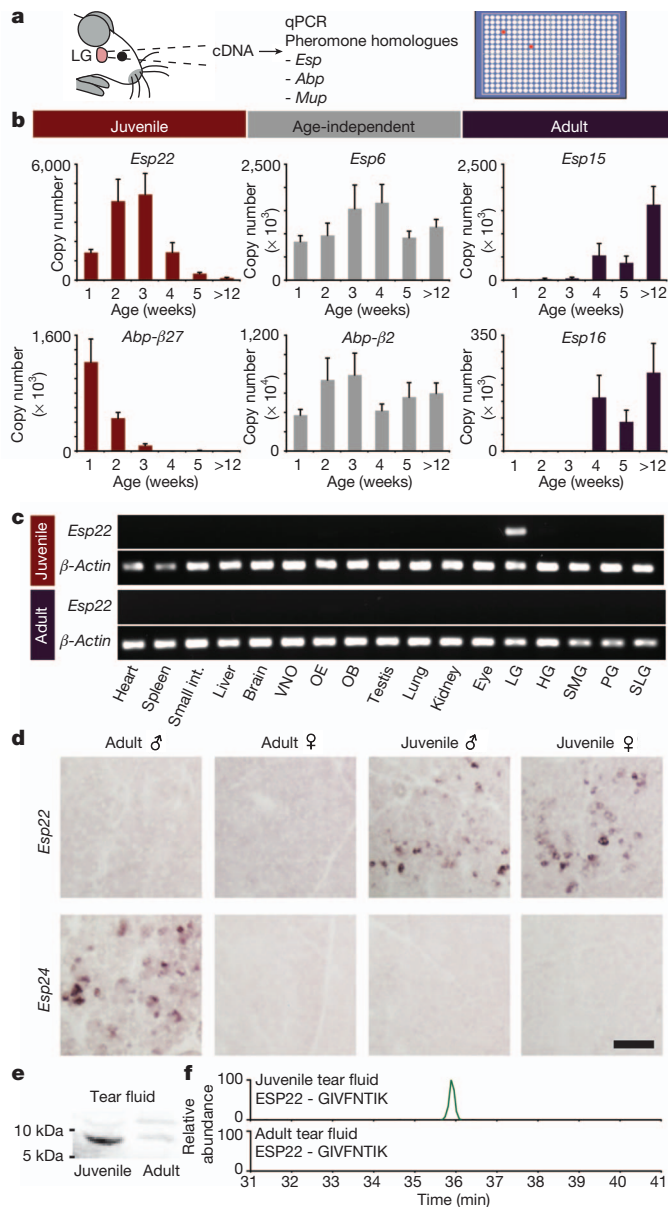


Figure 1 | ESP22 is secreted into juvenile tear fluid. **a**, Strategy to identify mouse pheromones. *Abp-β27* is also known as *Scgb2b27*; *Abp-β2* is also known as *Scgb2b2*. **b**, Age-dependent gene expression in lacrimal gland (LG) determined by qPCR ($n = 4-12$, mean \pm s.e.m.). **c**, *Esp22* expression in juvenile and adult tissues determined by PCR with reverse transcription (RT-PCR); olfactory epithelium (OE), olfactory bulb (OB), harderian gland (HG), submaxillary gland (SMG), parotid gland (PG), sublingual gland (SLG). **d**, Age- and sex-dependent *Esp* expression in lacrimal gland determined by *in situ* hybridization. Scale bar, 100 μ m. **e**, Western blot analysis of tears using anti-ESP22 antibody. **f**, Mass spectrometry analysis of an ESP22-derived tryptic peptide (GIVFNTIK) from tears.

(Fig. 2c, Extended Data Fig. 5 for higher [ESP22]). Threshold ESP22 responses observed by single unit extracellular recordings (Fig. 2d) occurred at similar concentrations (20 pM) to threshold ESP1 responses previously measured using genetically encoded calcium indicators¹⁸. Most neurons responsive to ESP22 were activated by juvenile tears but not by MBP or adult tears (6/11, Fig. 2e and Extended Data Fig. 5), with neuron viability verified by K^+ -mediated depolarization. High-affinity ESP22 responses were also recorded in 1–2% of VNO sensory neurons using current-clamp recording techniques and single-neuron calcium imaging (data not shown).

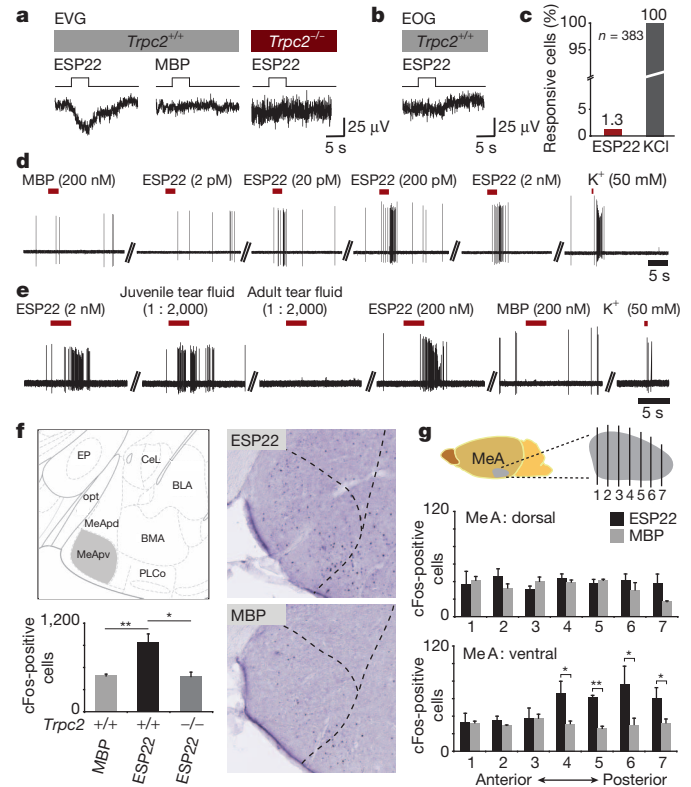


Figure 2 | ESP22 activates the vomeronasal system. **a**, **b**, EVG (**a**) and EOG (**b**) recordings in *Trpc2*^{-/-} and *Trpc2*^{+/+} mice exposed to ESP22 (200 nM) and MBP (450 nM). **c**, The percentage of basal VNO sensory neurons ($n = 383$) responsive to ESP22 (20 pM) and KCl (50 mM) determined by single-unit extracellular loose-seal recordings. **d**, **e**, Responses of single VNO sensory neurons. **f**, **g**, Visualization and quantification of cFos-expressing neurons in MeA, determined by immunohistochemistry in coronal brain sections from ESP22- and MBP-exposed male mice (mean \pm s.e.m., $n = 3$, $*P < 0.05$, $**P < 0.01$, Student's one-tailed *t*-test).

We next identified limbic neurons activated by ESP22 exposure using immunohistochemistry for the neural activity marker cFos in cryosections of adult male mouse brains. ESP22 and juvenile tears (Fig. 2f and Extended Data Fig. 6) induced cFos expression in the medial amygdala (MeA), a region that receives VNO input by way of the accessory olfactory bulb^{13,19}. cFos responses were not observed in *Trpc2*^{-/-} mice (Fig. 2f), or in other amygdala regions that receive olfactory input (Extended Data Fig. 6). cFos responses were enriched in the postero-ventral MeA (Fig. 2g), which sends projections to hypothalamic areas that control defensive and reproductive responses^{20,21}.

These findings indicate ESP22 to be a juvenile chemosignal that activates a VNO response pathway. However, a role for the VNO in regulating adult–juvenile social interactions is unknown. *Trpc2*^{-/-} mice provide a valuable tool for VNO loss-of-function studies, and show severe deficits in sex recognition²³. Here, we introduced *Trpc2*^{+/-} or *Trpc2*^{-/-} males to juveniles and monitored social behaviour.

Surprisingly, we observed that *Trpc2*^{-/-} mice displayed a striking increase in sexual behaviour towards prepubescent females (Supplementary Videos 1 and 2). Although *Trpc2*^{+/-} mice showed rare mounting attempts towards juvenile females, *Trpc2*^{-/-} mice showed vigorous mounting behaviour quantified as increases in mean mounting attempts and the percentage of animals mounting in 3 and 10 min, as well as decreases in mounting latency and intermount interval (Fig. 3 and Extended Data Fig. 7a). A similar percentage of *Trpc2*^{+/-} males showed mounting behaviour by 30 min, but these mounts were rare and did not increase in frequency during the trial duration (Fig. 3d and Extended Data Fig. 7b). In contrast, the sexual behaviour of *Trpc2*^{-/-} and *Trpc2*^{+/-} males towards adult females was similar, as reported previously²³. *Trpc2*^{-/-}

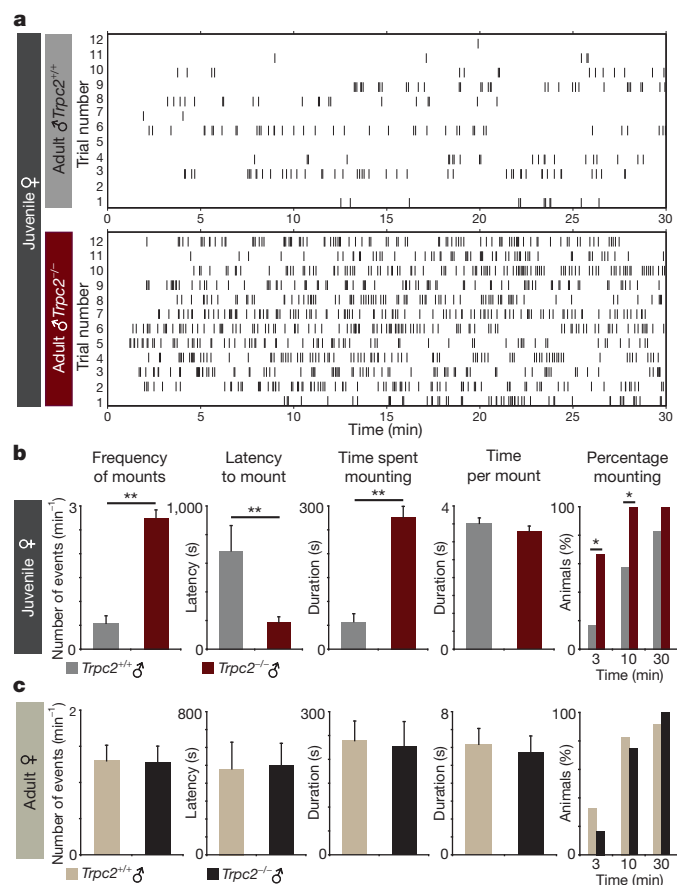


Figure 3 | *Trpc2*^{-/-} males display increased sexual behaviour towards juveniles. **a**, Raster plots depicting individual mounting displays of adult *Trpc2*^{+/+} and *Trpc2*^{-/-} males ($n = 12$) towards female juveniles (C57BL/6, 2–3 weeks old) during behavioural testing (30 min). Each tick indicates onset of one mount. **b**, **c**, Quantitative analysis of parameters associated with sexual behaviour towards juvenile and adult females shown by *Trpc2*^{+/+} and *Trpc2*^{-/-} males (mean \pm s.e.m., * $P < 0.05$, ** $P < 0.01$, Mann–Whitney U -test).

mice showed sexual behaviour towards juvenile females even when presented simultaneously with adult oestrous females (Extended Data Fig. 7c), and also showed increased sexual behaviour towards juvenile males (Extended Data Fig. 8). On the basis of these findings, VNO signalling normally prevents mating advances towards young, and one mechanism probably involves detection of chemosignals released from juvenile animals.

We reasoned that ESP22 is an excellent candidate to function as such a mating inhibitor based on the timing of its expression, the role of another ESP as a pheromone¹³ and the ability of ESP22 to activate both VNO sensory neurons and central limbic regions. ESP22 is juvenile-enriched in several strains of mice, but we identified two strains (C3H and CBA) that lacked juvenile ESP22 expression (Fig. 4a). These mouse strains provided valuable tools for controlling ESP22 levels during social interactions, and we observed increased sexual behaviour of wild-type males towards C3H and CBA juveniles (Fig. 4b).

We asked whether painting recombinant ESP22 onto C3H juveniles blocked male sexual approaches. We observed that males displayed similar levels of sexual behaviour towards unpainted, ESP6-painted and MBP-painted C3H juveniles (Fig. 4d). However, males showed a significant reduction in mounting attempts and an increase in mounting latency towards C3H juveniles painted with ESP22 (1 ng). Higher ESP22 amounts (10 μ g) caused a striking 70-fold reduction in mounting attempts towards C3H juveniles, with most animals (10/11) failing to show a single mating attempt during the entire 30 min trial (Fig. 4c, d). A dose-dependent analysis indicated that amounts of ESP22 derived from

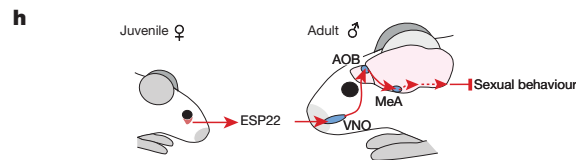
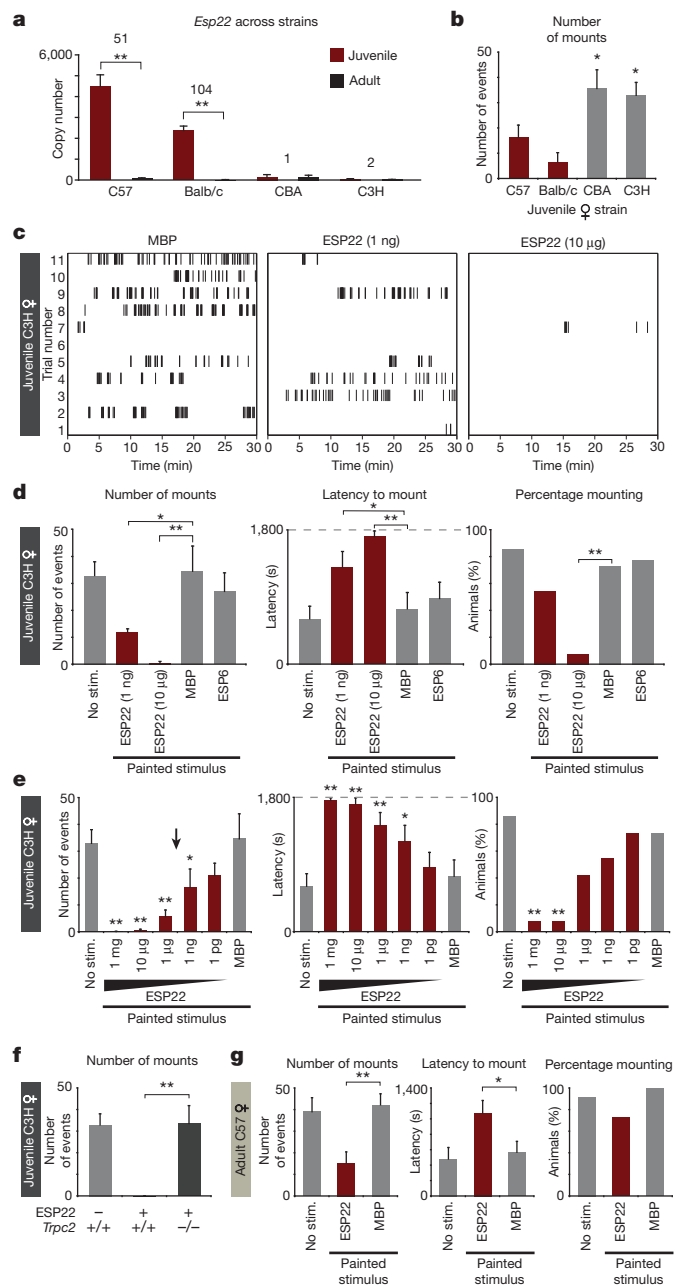


Figure 4 | **ESP22 inhibits male sexual behaviour.** **a**, ESP22 levels in lacrimal gland from mouse strains and ages indicated ($n = 5$ –12, averages \pm s.e.m.). **b**, Sexual behaviour of wild-type males towards juveniles from strains indicated ($n = 11$ or 12, mean \pm s.e.m.). **c**–**g**, Raster plots and quantification of sexual behaviour shown by wild-type males (**d**–**f**) or *Trpc2*^{-/-} males (**f**) towards C3H juveniles (**d**–**f**) or C57BL/6 oestrous females (**g**) painted with ESP6 (10 μ g), ESP22 (10 μ g or indicated) or MBP (4 mg) ($n = 9$ –12, averages \pm s.e.m.). Arrow depicts ESP22 concentration in C57BL/6 juvenile tears. **h**, Model for ESP22 signalling. * $P < 0.05$, ** $P < 0.01$, Student's one-tailed t -test (**a**), one-way (**b**, **d**, **e**, **g**) or two-way (**f**) analysis of variance (ANOVA) followed by Tukey's honestly significant difference (HSD) post hoc tests.

small quantities of juvenile tears (<200–333 nl) were sufficient for inhibition of adult male sexual behaviour (Fig. 4e). ESP22 was not aversive, as ESP22 painting did not affect social interaction time (Extended

Data Fig. 9). ESP22 also did not inhibit sexual behaviour of *Trpc2*^{-/-} males, consistent with a role for vomeronasal circuits in mediating ESP22 responses (Fig. 4f). Interestingly, *Trpc2*^{-/-} males did not show further increases in sexual behaviour towards C3H juveniles (Fig. 4f), suggesting that C3H juveniles do not release other VNO-dependent mating inhibitors. However, ESP22 did inhibit the sexual behaviour of C3H adult males, which presumably have encountered little or no ESP22 previously (Extended Data Fig. 10). Finally, recombinant ESP22 also decreased sexual behaviour towards adult females in oestrous (Fig. 4g). Lower levels of sexual behaviour persisted towards ESP22-painted oestrous females, suggesting that oestrous females release other signals that counteract ESP22. On the basis of these findings, ESP22 is a juvenile pheromone that blocks sexual behaviour through the vomeronasal system (Fig. 4h).

Behavioural responses to ESP22 differ from responses to other VNO activators, such as pheromones and predator odours that trigger mating, aggression and fear^{12,13,22,23}. These findings are consistent with the existence of parallel subcircuits of the accessory olfactory system, which selectively channel sensory inputs to enable proper selection of a behavioural display²⁰. Identifying a collection of VNO activators that regulate different instinctive behaviours provides a valuable toolbox to understand how a sensory system controls behaviour.

METHODS SUMMARY

All animal procedures were in compliance with institutional animal care and use committee guidelines. Full details of experimental procedures for qPCR analysis, RNA *in situ* hybridization, western blot analysis, mass spectrometry, recombinant proteins, electrophysiology, cFos staining, behaviour analysis and statistical analysis are provided in Methods.

Online Content Any additional Methods, Extended Data display items and Source Data are available in the online version of the paper; references unique to these sections appear only in the online paper.

Received 7 December 2012; accepted 16 August 2013.

Published online 2 October 2013.

1. Tirindelli, R., Dibattista, M., Pifferi, S. & Menini, A. From pheromones to behavior. *Physiol. Rev.* **89**, 921–956 (2009).
2. Leypold, B. G. *et al.* Altered sexual and social behaviors in *trp2* mutant mice. *Proc. Natl Acad. Sci. USA* **99**, 6376–6381 (2002).
3. Stowers, L., Holy, T. E., Meister, M., Dulac, C. & Koentges, G. Loss of sex discrimination and male-male aggression in mice deficient for TRP2. *Science* **295**, 1493–1500 (2002).
4. Ferrero, D. M. & Liberles, S. D. The secret codes of mammalian scents. *Wiley Interdiscip. Rev. Syst. Biol. Med.* **2**, 23–33 (2010).
5. Nodari, F. *et al.* Sulfated steroids as natural ligands of mouse pheromone-sensing neurons. *J. Neurosci.* **28**, 6407–6418 (2008).
6. Novotny, M. V. Pheromones, binding proteins and receptor responses in rodents. *Biochem. Soc. Trans.* **31**, 117–122 (2003).
7. Touhara, K. Sexual communication via peptide and protein pheromones. *Curr. Opin. Pharmacol.* **8**, 759–764 (2008).

8. Karn, R. C. & Laukaitis, C. M. The roles of gene duplication, gene conversion and positive selection in rodent esp and mup pheromone gene families with comparison to the *abp* family. *PLoS ONE* **7**, e47697 (2012).
9. Kimoto, H., Haga, S., Sato, K. & Touhara, K. Sex-specific peptides from exocrine glands stimulate mouse vomeronasal sensory neurons. *Nature* **437**, 898–901 (2005).
10. Logan, D. W., Marton, T. F. & Stowers, L. Species specificity in major urinary proteins by parallel evolution. *PLoS ONE* **3**, e3280 (2008).
11. Chamero, P. *et al.* G protein G α o is essential for vomeronasal function and aggressive behavior in mice. *Proc. Natl Acad. Sci. USA* **108**, 12898–12903 (2011).
12. Papes, F., Logan, D. W. & Stowers, L. The vomeronasal organ mediates interspecies defensive behaviors through detection of protein pheromone homologs. *Cell* **141**, 692–703 (2010).
13. Haga, S. *et al.* The male mouse pheromone ESP1 enhances female sexual receptive behaviour through a specific vomeronasal receptor. *Nature* **466**, 118–122 (2010).
14. Kimoto, H. *et al.* Sex- and strain-specific expression and vomeronasal activity of mouse ESP family peptides. *Curr. Biol.* **17**, 1879–1884 (2007).
15. Li, Q. *et al.* Synchronous evolution of an odor biosynthesis pathway and behavioral response. *Curr. Biol.* **23**, 11–20 (2013).
16. Mandiyan, V. S., Coats, J. K. & Shah, N. M. Deficits in sexual and aggressive behaviors in *Cnga2* mutant mice. *Nature Neurosci.* **8**, 1660–1662 (2005).
17. Wang, Z. *et al.* Pheromone detection in male mice depends on signaling through the type 3 adenylyl cyclase in the main olfactory epithelium. *J. Neurosci.* **26**, 7375–7379 (2006).
18. He, J. *et al.* Distinct signals conveyed by pheromone concentrations to the mouse vomeronasal organ. *J. Neurosci.* **30**, 7473–7483 (2010).
19. Dulac, C. & Wagner, S. Genetic analysis of brain circuits underlying pheromone signaling. *Annu. Rev. Genet.* **40**, 449–467 (2006).
20. Choi, G. B. *et al.* Lhx6 delineates a pathway mediating innate reproductive behaviors from the amygdala to the hypothalamus. *Neuron* **46**, 647–660 (2005).
21. Yang, C. F. *et al.* Sexually dimorphic neurons in the ventromedial hypothalamus govern mating in both sexes and aggression in males. *Cell* **153**, 896–909 (2013).
22. Chamero, P. *et al.* Identification of protein pheromones that promote aggressive behaviour. *Nature* **450**, 899–902 (2007).
23. Novotny, M., Harvey, S., Jemiolo, B. & Alberts, J. Synthetic pheromones that promote inter-male aggression in mice. *Proc. Natl Acad. Sci. USA* **82**, 2059–2061 (1985).

Supplementary Information is available in the online version of the paper.

Acknowledgements We thank M. Albers and S. R. Datta for reading the manuscript, J. Yang, C. Mark Fletcher and Y. Tachibana-Baffour for experimental assistance, and the Taplin Mass Spectrometry Facility for mass spectrometry analysis. This work was supported by a grant from the National Institutes of Health (to S.D.L., award number R01 DC010155) and in part by a Grant-in-Aid for Young Scientists (S) from the Japan Society for the Promotion of Science, and by ERATO Touhara Chemosensory Signal Project from the Japan Science and Technology Agency (to K.T.). N.H. is supported by a Grant-in-Aid for JSPS Fellows, M.S. is a Lichtenberg-Professor of the Volkswagen Foundation and D.M.F. is supported by a Boehringer Ingelheim Fonds PhD Fellowship.

Author Contributions D.M.F., S.D.L., M.S. and K.T. conceived the project, designed the experiments and wrote the manuscript. D.M.F. performed molecular biology, biochemistry and behaviour experiments. D.S.R. and Q.L. performed *in situ* hybridization analysis. L.M.M., A.C., T.O. and N.H. performed electrophysiological analysis. T.O. performed cFos analysis.

Author Information Reprints and permissions information is available at www.nature.com/reprints. The authors declare no competing financial interests. Readers are welcome to comment on the online version of the paper. Correspondence and requests for materials should be addressed to S.D.L. (Stephen_Liberles@hms.harvard.edu).

METHODS

Animals. All animal procedures were in compliance with institutional animal care and use committee guidelines. Mice from various strains, as well as castrated and ovariectomized animals, were obtained from Jackson Laboratory and Charles River Laboratories unless otherwise noted. *Trpc2*^{-/-} mice were provided by R. Axel. C3H mice refer to the strain C3H/He. Oestrous was induced in ovariectomized adult females (C57BL/6, 10–12 weeks) by timed injection of oestradiol benzoate (Sigma-Aldrich, 10 µg sesame seed oil, subcutaneous injection) 48 and 24 h before testing, and progesterone (Sigma-Aldrich, 500 µg in sesame seed oil, subcutaneous injection) 3 h before testing.

qPCR analysis. cDNAs from the extraorbital lacrimal gland and other tissues were prepared from animals of ages and sexes indicated using published protocols²⁴. Copy number, unless otherwise indicated, refers to abundance in cDNA derived from 50 ng of RNA, with absolute values determined in control PCR reactions involving plasmid titrations. qPCR primers were verified not to cross react with closely related ESPs and ABPs (>60% identity) based on control reactions involving ESP- and ABP-encoding plasmids (Extended Data Fig. 2a). (*Esp22* forward: 5'-GTCCCGGAATCTGTTATCCA-3'; *Esp22* reverse: 5'-CAGCAATGCTCAC TGAAGGA-3'. *Esp15* forward: 5'-AACAGGAGCTGCTCTGAATTA-3'; *Esp15* reverse: 5'-GCCTATGACAGAGCCACTTA-3'. *Esp16* forward: 5'-TCTGTGTC TCATGCACTGCTTCCT-3'; *Esp16* reverse: 5'-GGAAGTATTGTTGGAACA CCAGAAA-3'. *Esp6* forward: 5'-TCCTTGGTCTGAGATTGCT-3'; *Esp6* reverse: 5'-TTTGCTCACCACCAACCA-3'. *Abp-β27* forward: 5'-GGTGGAAA TAGGCTAGCTCTGA-3'; *Abp-β27* reverse: 5'-GGTTCCAGAAAGTATATTTT TTATA-3'. *Abp-β2* forward: 5'-AGCATGCATACCTTTCTTCGCGTA-3'; *Abp-β2* reverse: 5'-TGCATTCTGAGCTGAAGAGTATAGTTGT-3'.) Different primers were used in PCR reactions described in Fig. 1c (*Esp22* forward: 5'-ATGAATTCT GTCCAGTCATG-3'; *Esp22* reverse: 5'-TCAAGTATTTGTCAAAGGCGT-3'), and specific amplification of the *Esp22* gene was verified by DNA sequencing.

RNA *in situ* hybridization. *In situ* hybridization analysis of lacrimal gland tissue was performed using established techniques involving colorimetric visualization²⁵ or multicolour fluorescence²⁶. cRNA riboprobes were used for *Esp22* (full coding sequence plus 500 base pairs of the 3' untranslated region), *Esp24* and *Esp15* (full coding sequence), and *Rab3D* (926 base-pair sequence amplified by primers TTCCGCTATGCCGATGACTC and TGACAACTTCAGCCAGCGAT). The *Esp22* riboprobe shares less than 75% identity with other *Esp* genes, a level of identity below what typically results in cross-hybridization under high stringency conditions used. Furthermore, *Esp22* is most closely related to *Esp24*, and we did not observe cross-hybridization between these genes (Fig. 1d). Images were taken on a Nikon 80i upright microscope for colorimetric images, and on a Leica TCS SP5 II confocal microscope for fluorescent images.

Western blot analysis. Anesthetized mice were injected with pilocarpine (Sigma-Aldrich, 0.5 µg per g body weight, intraperitoneally) and tear fluid was collected using microcapillary pipettes. Proteins in tear fluid were separated by electrophoresis using 16.5% Tris-Tricine Gels (Biorad), transferred to PVDF membranes (Immobilin) and incubated with a rabbit polyclonal antibody raised against ESP22 (amino acids 51–63: CRRLRDVPESVIH, New England Peptide, 1:500, 24–48 h, 4 °C). Bound antibody was detected with a donkey anti-rabbit 800 Infrared Dye (Odyssey, 5,000:1, 45 min, room temperature). Blots were analysed using a Quantitative IR Western Blot Detection LI-COR (Odyssey) and the Li-COR Quantitative Gel Documentation and Blot Detection Software (Odyssey).

Mass spectrometry. Tear fluid was collected and separated by gel electrophoresis as described above. Excised gel bands containing approximately 3–14 kDa proteins were then subjected to a modified in-gel trypsin digestion procedure²⁷. Samples were loaded by a Famos auto sampler (LC Packings) onto a nano-scale reverse-phase high-performance liquid chromatography capillary column²⁸, and eluted using a gradient of increasing acetonitrile containing 0.1% formic acid. Eluted peptides were subjected to electrospray ionization and analysed by an LTQ-Orbitrap mass spectrometer (Thermo Fisher). Eluted peptides were isolated, including those corresponding to *m/z* 612.4 and 446.3 (the +2 charge states of the ESP22 tryptic peptides DVPESVIHISK and GIVFNTIK), and fragmented to produce a tandem mass spectrum of specific fragment ions for each peptide. Peptide sequences were determined using Sequest (ThermoFinnigan)²⁹.

Recombinant proteins. A gene encoding the secreted form of ESP22 (Ala23-End) was cloned into pMAL-c5x bacterial expression vector (New England Biolabs) using SacI and BamHI restriction sites. ESP22 was expressed and purified as a fusion protein with maltose-binding protein (MBP) in BL21(DE3) cells following the manufacturer's protocols (pMAL Protein Fusion & Purification System, New England Biolabs). Protein was eluted from an amylose affinity resin using maltose and concentrated using a centrifugal filter unit (Millipore). The ESP6 coding sequence was subcloned into the expression vector pET-28a (Novagen) and purified as described previously¹⁴.

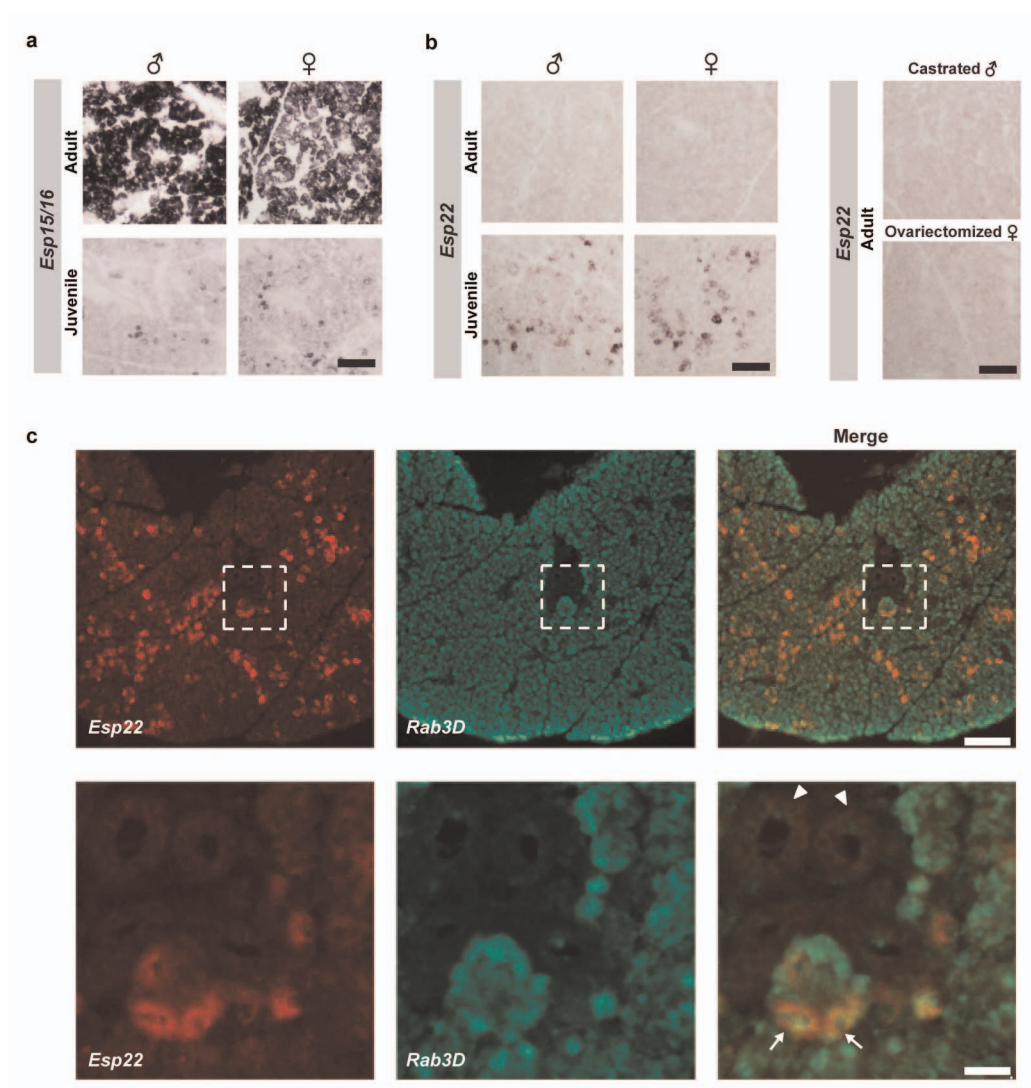
Electrophysiology. EVG, EOG and extracellular recordings were performed as described previously with minor modifications^{14,30,31}. To prevent dialysis of intracellular components, action-potential-driven capacitive currents were recorded in 'loose-seal' cell-attached configuration (seal resistance 30–150 MΩ) from vomeronasal sensory neuron somata located deep in the sensory epithelium's basal layer close to the basement membrane. Spikes were analysed using Igor Pro functions (SpAcAn, G. Dugué and C. Rousseau). Inter-stimulus intervals were 30 s. Neuronal responses were classified according to the following criteria: (1) discharge was time-locked to stimulus presentation (responses occurred during and/or up to 3 s after stimulation onset); (2) spike patterns clearly deviated from previous baseline activity (frequency histograms (1 s bin width) were calculated over repeated trials and responses were evaluated according to a $\Delta f \geq 2\sigma f_{\text{baseline}}$ criterion). MBP and ESP22 evoked TRPC2-independent EVG and EOG responses at approximately 100-fold higher concentrations (data not shown).

cFos staining. Sexually naive males (Japan SLC, C57BL/6, 9–11 weeks old) were housed individually (17 cm × 25 cm Plexiglas test chambers, 12 h light/12 h dark cycle). Stimuli included ESP22 (250 µg), tear fluid (containing 50 µg protein) or MBP (200 µg) in 20 mM Tris-HCl (pH 7.5, 100 µl) transfused onto a piece of cotton (30 mg) and dried in a Speed Vac (3 h). High concentrations of ESP22 were necessarily used for cFos studies, as this non-volatile stimulus is poorly investigated when presented in isolation. Stimuli were placed on bedding during the dark phase (90 min), and all mice were observed to investigate the stimulus during testing. Mice were then anaesthetized with pentobarbital sodium and perfused quickly. Brains were removed and post-fixed in 4% paraformaldehyde in PBS (3 h, 4 °C) and cryoprotected in 15 and 30% sucrose solutions in PBS (4 °C). Immunohistochemistry and quantification of cFos-positive nuclei were performed as described previously²³. MeA regions were defined using established anatomical landmarks (Extended Data Fig. 6), comparison with a reference image (Bregma -1.58 mm)³² and Lhx9 staining³⁰ (data not shown).

Behaviour. Before experiments, sexually naive adult males (2–4 months old, C57BL/6 *Trpc2*^{+/+} or *Trpc2*^{-/-}) were maintained under a reverse light cycle for 2 weeks and individually housed for at least 24 h. Behavioural testing occurred in the home cage with the food tray removed more than 3 h after onset of dark phase. A sexually naive male or female (17- to 18-day-old juvenile or adult in oestrous) was introduced to the male, and interaction behaviour was recorded for 30 min using a digital camcorder compatible with low light conditions (Sony). For some experiments, females were painted by swabbing stimulus (100 µl) on the back (50 µl), head (25 µl) and anogenital region (25 µl) before testing. Mounting behaviour was defined when males used both forepaws to climb onto a female for copulation, and parameters associated with mounting behaviour were analysed using Matlab (Mathworks). In rare cases (<5%), juvenile pups showed stimulus-independent escape behaviour and were excluded from analysis. Animals were randomly assigned to different testing conditions. For Fig. 4c–e, quantification was performed blind to experimental conditions.

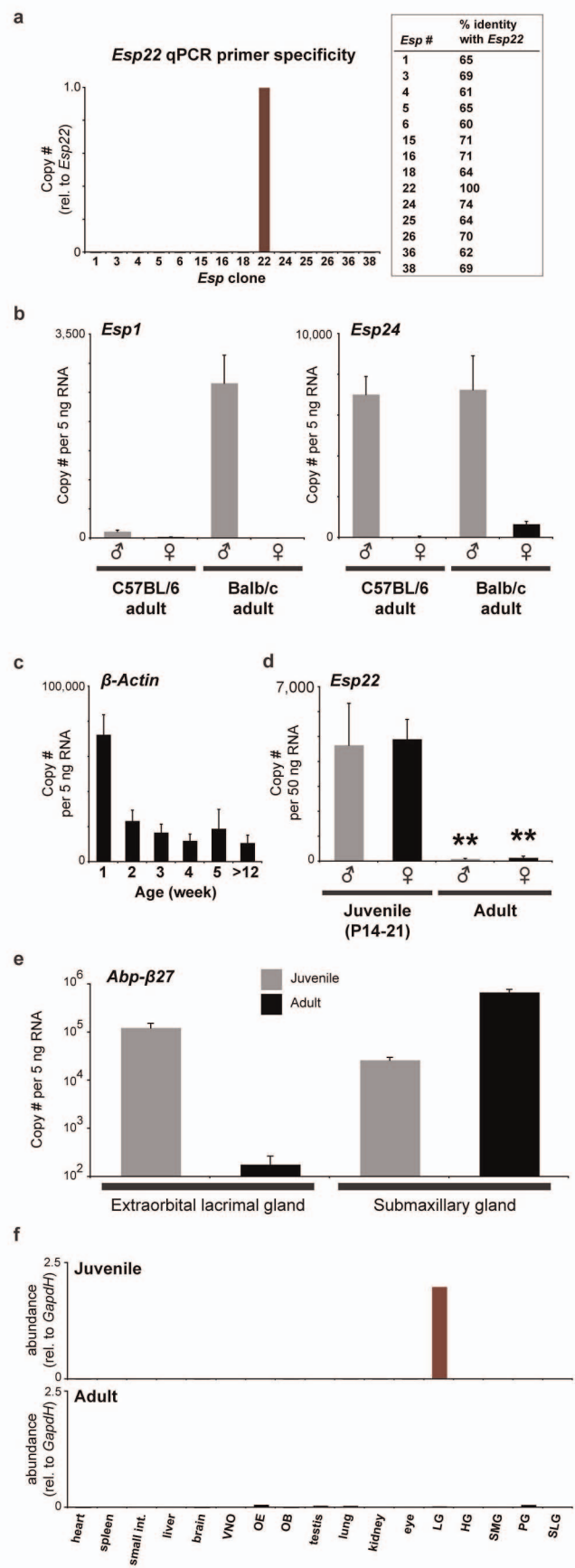
Statistical analyses. All samples represent biological replicates. Sample sizes for biochemistry, electrophysiology, cFos and behaviour met or exceeded the standards in the field. In Fig. 1b, sample sizes (*n*) for data points reading left to right are as follows: 12, 7, 7, 8, 6, 13 for *Esp22*; 12, 7, 8, 8, 6, 12 for *Esp6*; 8, 5, 5, 7, 6, 12 for *Esp15*; 8, 10, 8, 4, 8 for *Abp-β27*; 11, 8, 10, 8, 6, 10 for *Abp-β2*; and 5, 5, 6, 5, 10 for *Esp16*. In Fig. 4a, sample sizes reading left to right are 13, 10, 6, 6, 5, 7 and 8. In Fig. 4b, sample sizes reading left to right are 12, 9, 9 and 14. In Fig. 4d, sample sizes reading left to right are 14, 12, 11 and 9. In Fig. 4e, sample sizes reading left to right are 14, 12, 12, 11, 11 and 11. In Fig. 4f, sample sizes reading left to right are 12, 12 and 11. In Fig. 4g, sample sizes reading left to right are 12, 11 and 11. Categorical data were analysed by a Fisher's exact test. Other reported *P* values were calculated using a one-tailed Student's *t*-test (qPCR, cFos), Mann-Whitney *U*-tests (mouse behaviour) or one- or two-way ANOVA followed by Tukey's HSD post hoc tests (mouse behaviour), as indicated in the figure legends.

24. Liberles, S. D. & Buck, L. B. A second class of chemosensory receptors in the olfactory epithelium. *Nature* **442**, 645–650 (2006).
25. Montmayeur, J. P., Liberles, S. D., Matsunami, H. & Buck, L. B. A candidate taste receptor gene near a sweet taste locus. *Nature Neurosci.* **4**, 492–498 (2001).
26. Liberles, S. D. *et al.* Formyl peptide receptors are candidate chemosensory receptors in the vomeronasal organ. *Proc. Natl Acad. Sci. USA* **106**, 9842–9847 (2009).
27. Shevchenko, A., Wilm, M., Vorm, O. & Mann, M. Mass spectrometric sequencing of proteins silver-stained polyacrylamide gels. *Anal. Chem.* **68**, 850–858 (1996).
28. Peng, J. & Gygi, S. P. Proteomics: the move to mixtures. *J. Mass Spectrom.* **36**, 1083–1091 (2001).
29. Eng, J. K., McCormack, A. L. & Yates, J. R. An approach to correlate tandem mass-spectral data of peptides with amino-acid-sequences in a protein database. *J. Am. Soc. Mass Spectrom.* **5**, 976–989 (1994).
30. Hagedorff, S., Flügge, D., Engelhardt, C. & Spehr, M. Homeostatic control of sensory output in basal vomeronasal neurons: activity-dependent expression of ether-a-go-go-related gene potassium channels. *J. Neurosci.* **29**, 206–221 (2009).
31. Spehr, J. *et al.* Ca²⁺-calmodulin feedback mediates sensory adaptation and inhibits pheromone-sensitive ion channels in the vomeronasal organ. *J. Neurosci.* **29**, 2125–2135 (2009).
32. Franklin, K. & Paxinos, G. *The Mouse Brain in Stereotaxic Coordinates* Fig. 44 (Academic, 2008).

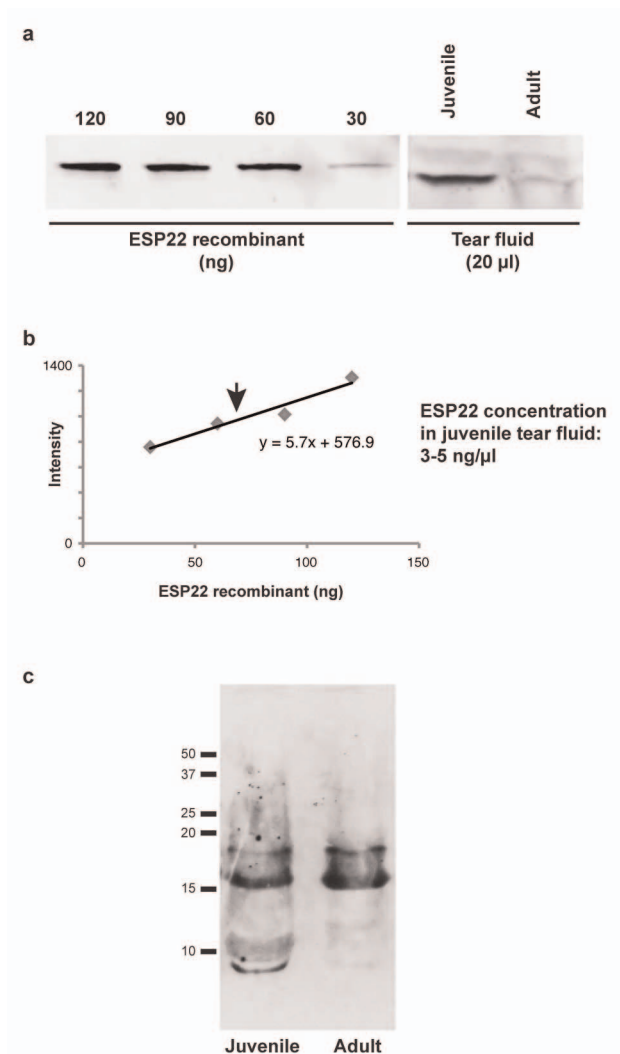


Extended Data Figure 1 | RNA *in situ* hybridization to characterize expression of *Esp* genes in the lacrimal gland. a–c, Colorimetric analysis in tissue from animals indicated using cRNA riboprobes for (a) *Esp15* and (b) *Esp22*, and two-colour fluorescence analysis (c) in juvenile lacrimal gland with cRNA riboprobes for *Esp22* (red) and a marker for acinar secretory cells,

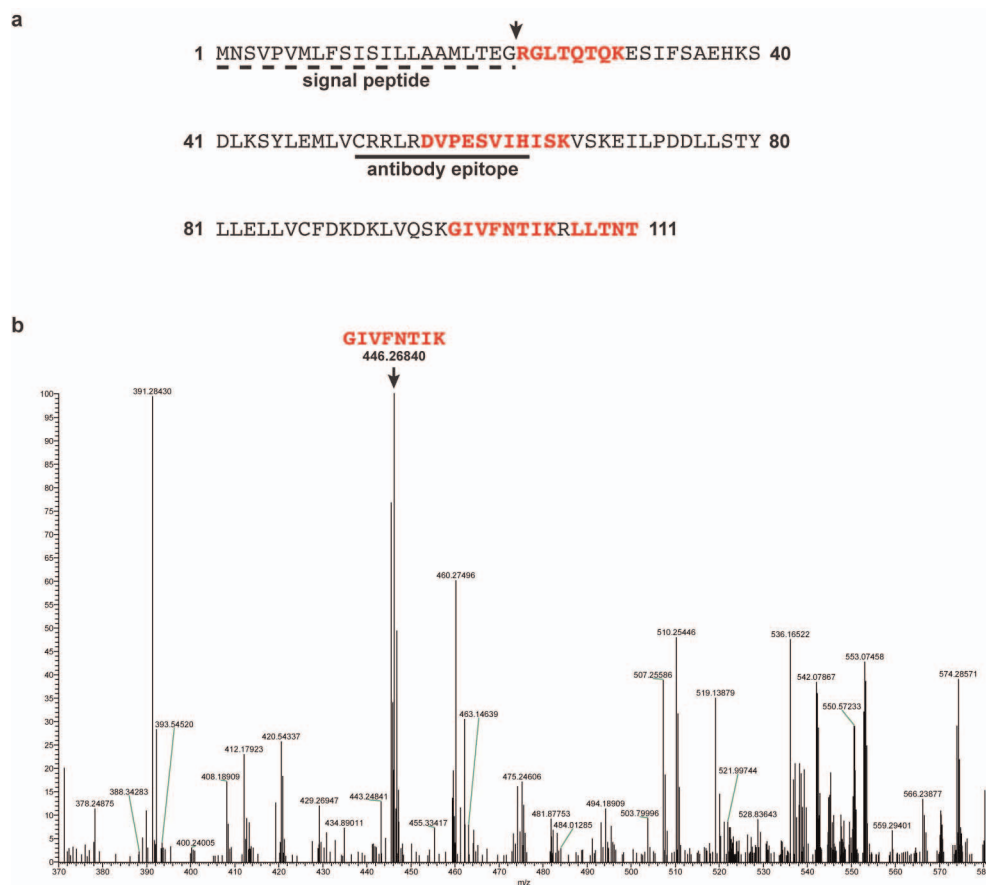
Rab3D (green). cRNA riboprobes for *Esp15* are expected to cross-hybridize with *Esp16* mRNA. Some images used in b are identical to panels in Fig. 1d, and are included for reference. Dashed boxes (c) indicate regions magnified below. Arrows, acinar cells; arrowheads, ductal cells; scale bars, 100 μ m (a, b, c top), 20 μ m (c bottom).



Extended Data Figure 2 | qPCR analysis of gene expression. **a**, *Esp22* qPCR primers specifically detect a plasmid containing cloned *Esp22*, but not plasmids containing other *Esp*s with greater than 60% identity to *Esp22*. **b–f**, cDNA was derived from lacrimal gland (**b–e**), submaxillary gland (**e**) or other tissues (**f**) of animals indicated. In **f**, abundance is calculated by normalization to amounts of *Gapdh*. C57BL/6 mice were used (**b–d**) unless otherwise indicated (**b**). Experiments where sex is not indicated involved equal numbers of males and females; olfactory epithelium (OE), olfactory bulb (OB), harderian gland (HG), submaxillary gland (SMG), parotid gland (PG), sublingual gland (SLG) ($n = 6–12$, averages \pm s.e.m., $**P < 0.01$, two-way ANOVA followed by Tukey's HSD post hoc tests).

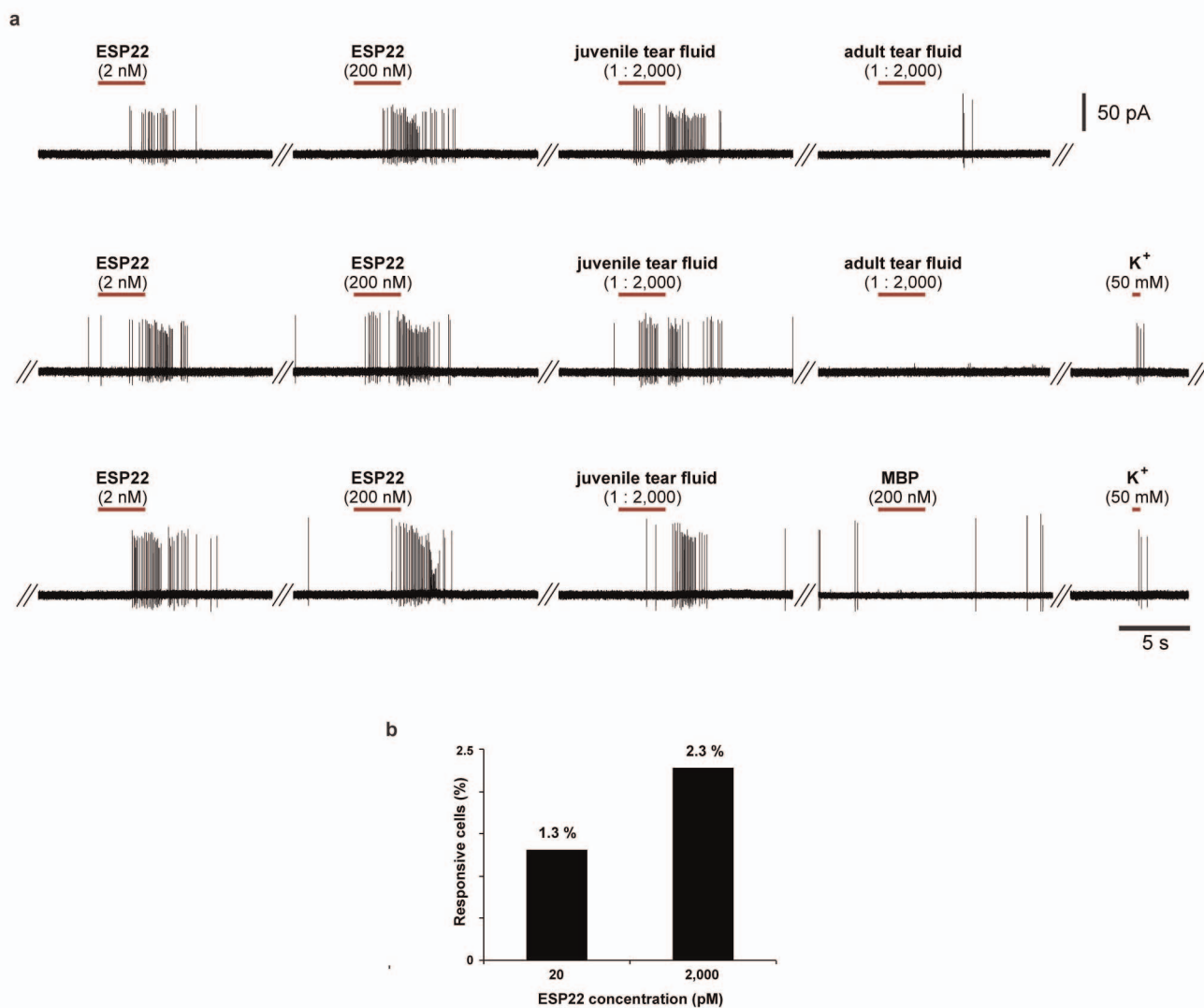


Extended Data Figure 3 | Quantification of protein concentrations in tear fluid by western blot analysis using an anti-ESP22 antibody. **a, b,** A standard curve based on signal intensity was generated using different concentrations of recombinant ESP22 (**a**, left panel; **b**). The arrow indicates the intensity level of the band in the juvenile tear sample (**a**, right panel). **c,** Entire western blot analysis of tear fluid using anti-ESP22 antibody.



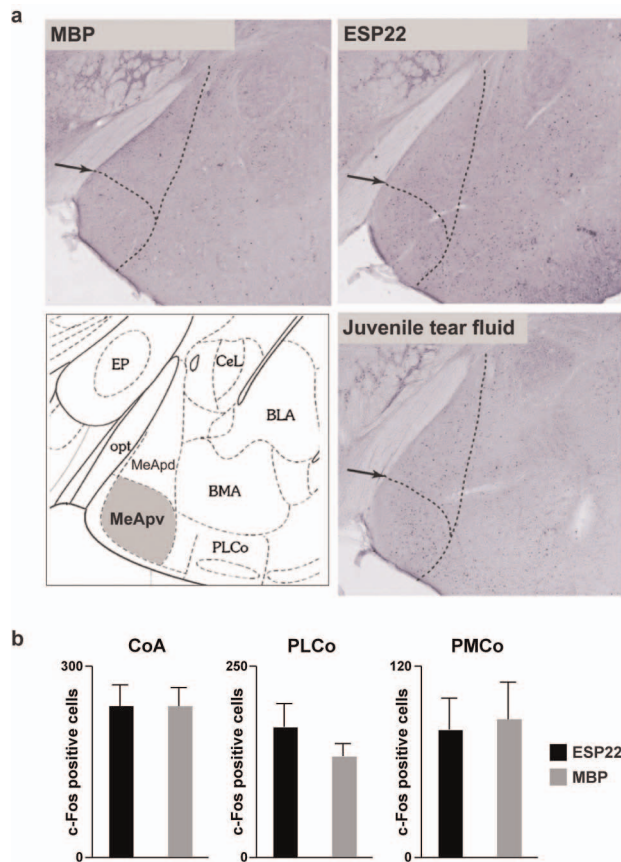
Extended Data Figure 4 | ESP22-derived tryptic peptides identified by mass spectrometry. **a**, The amino-acid sequence of immature ESP22 is depicted, along with a predicted signal peptide and the epitope used for antibody generation. Four tryptic peptides were identified by mass spectrometry (highlighted in red), including one peptide containing the first amino acid after the predicted signal sequence and another containing the encoded carboxy

(C)-terminal residue. Trypsin does not efficiently cleave amino (N)-terminal lysines or arginines, consistent with R23 being the first amino acid in mature ESP22. **b**, Mass spectrum of an high-performance liquid chromatography fraction of juvenile tear fluid showing the ESP22-derived tryptic peptide GIVFNTIK, with sequence identity confirmed by tandem mass spectrometry analysis.



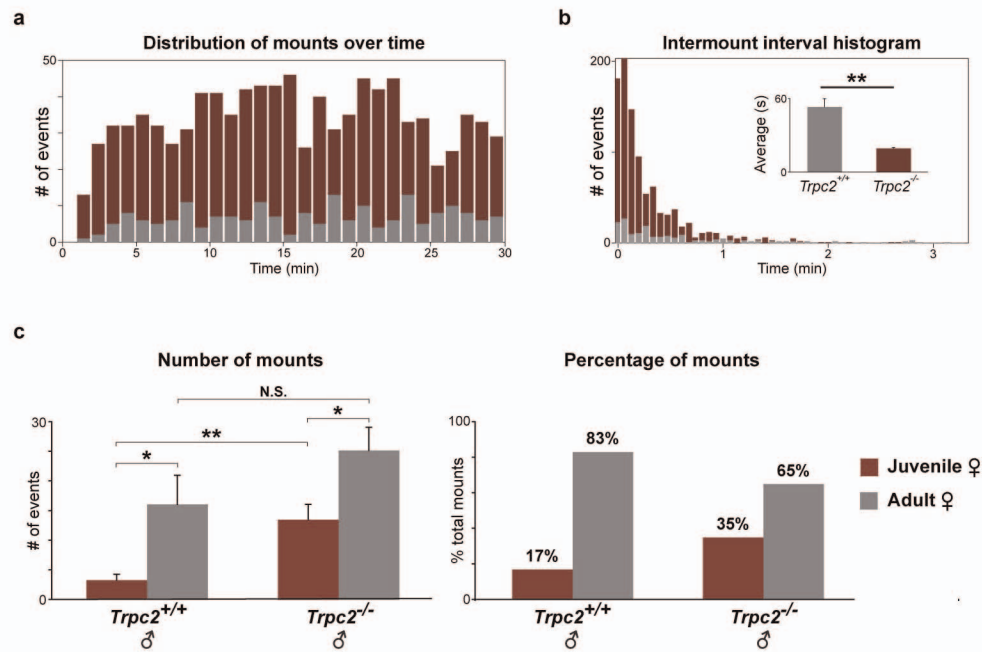
Extended Data Figure 5 | Electrophysiological responses to ESP22 in VNO sensory neurons. **a**, Single-unit extracellular loose-seal recording from a single VNO sensory neuron repeatedly exposed to different stimuli indicates

reproducibility of responses. **b**, The percentage of basal VNO sensory neurons responsive to 20 pM ($n = 383$) and 2 nM ($n = 749$) ESP22.



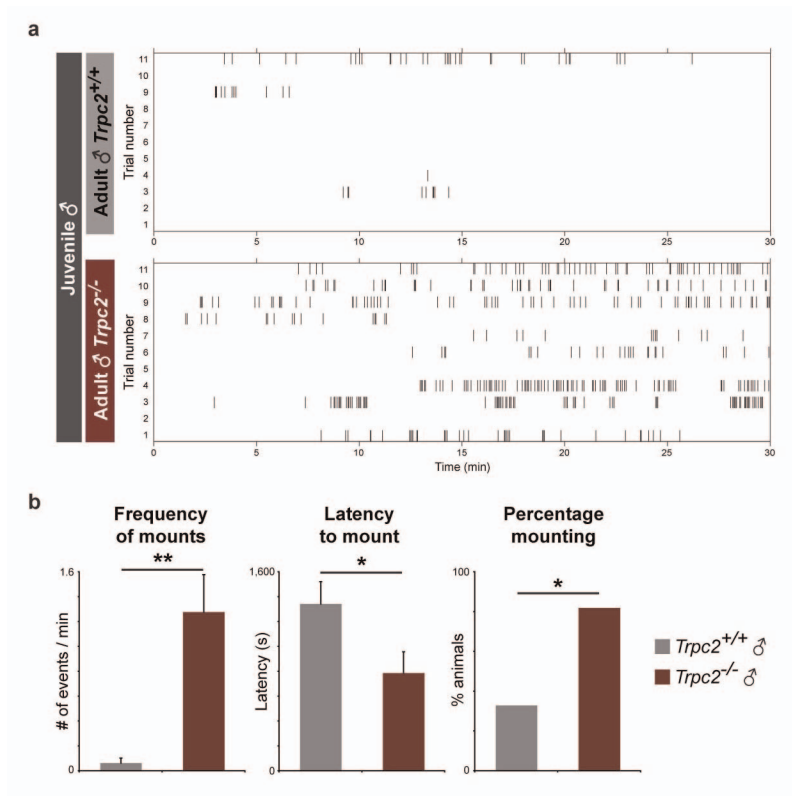
Extended Data Figure 6 | cFos responses to ESP22 in the amygdala.

a, ESP22 and juvenile tear fluid, but not MBP, induce cFos expression in the postero-ventral MeA. Dashed lines and arrows indicate boundaries of MeA regions. **b**, Similar responses were not observed in other amygdala nuclei that receive olfactory input, including the postero-medial cortical amygdala (PMCo), anterior cortical amygdala (CoA) and postero-lateral cortical amygdala (PLCo) (mean \pm s.e.m., $n = 3$).



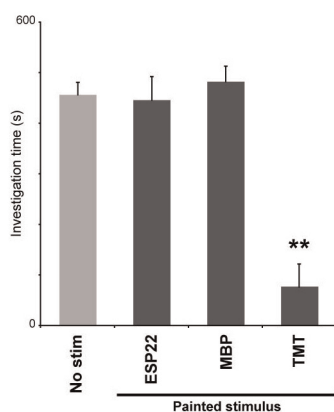
Extended Data Figure 7 | *Trpc2*^{-/-} males show increased sexual behaviour towards wild-type juveniles. **a, b,** Histograms of mounts by minute of social interaction and intermount intervals shown towards juveniles by *Trpc2*^{+/+} and *Trpc2*^{-/-} males (sum, $n = 12$). Inset depicts average intermount intervals (mean \pm s.e.m., * $P < 0.05$, ** $P < 0.01$, Mann-Whitney U -test). **c,** Analysis of

adult male sexual behaviour during simultaneous interaction with juvenile and adult oestrous females. *Trpc2*^{+/+} and *Trpc2*^{-/-} males show similar amounts of sexual behaviour towards adult oestrous females, but *Trpc2*^{-/-} males show increased sexual behaviour towards juveniles ($n = 10$, averages \pm s.e.m., * $P < 0.05$, ** $P < 0.01$, one-way multivariate ANOVA).



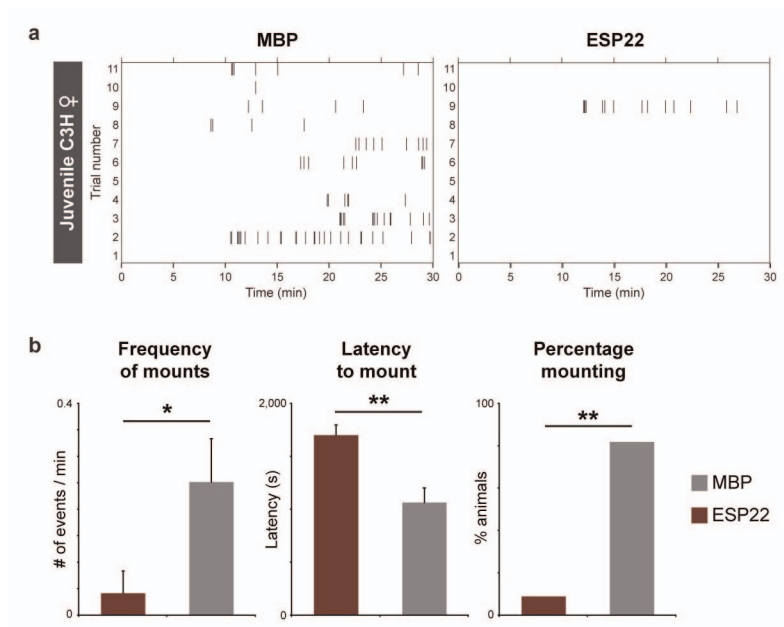
Extended Data Figure 8 | *Trpc2*^{-/-} males show sexual behaviour towards juvenile males. **a**, Raster plots depicting individual mounting displays of adult *Trpc2*^{+/+} and *Trpc2*^{-/-} males towards juvenile males (C57BL/6, postnatal day 17) during social interaction (30 min). Each tick indicates onset of one mount.

b, Quantitative analysis of parameters associated with sexual behaviour towards juvenile males shown by *Trpc2*^{+/+} and *Trpc2*^{-/-} males (*n* = 11 or 12, averages ± s.e.m., **P* < 0.05, ***P* < 0.01, Mann-Whitney *U*-test).



Extended Data Figure 9 | ESP22 did not decrease social investigation time.

Wild-type C57BL/6 males were introduced to C3H juvenile females painted with stimuli indicated. Social investigation time of the male was recorded as time spent with the nose in direct contact with the female. These data were extracted from the same experiments reported in Fig. 4c, d, with additional experiments involving TMT (100 μ l, 155 mM, $n = 11$ or 12, averages \pm s.e.m., ** $P < 0.01$, one-way ANOVA followed by Tukey's HSD post hoc tests).



Extended Data Figure 10 | ESP22 (10 µg) inhibits sexual behaviour of C3H males. **a**, Raster plots of sexual behaviour shown by C3H males towards C3H juvenile females (postnatal day 17) painted with indicated stimuli (30 min social interaction). Each tick indicates onset of one mount. **b**, Quantitative

analysis of parameters associated with sexual behaviour towards juvenile females shown by C3H males ($n = 11$, averages \pm s.e.m., $*P < 0.05$, $**P < 0.01$, one-way ANOVA followed by Tukey's HSD post hoc tests).

Diabetic hyperglycaemia activates CaMKII and arrhythmias by O-linked glycosylation

Jeffrey R. Erickson^{1,2}, Laetitia Pereira¹, Lianguo Wang¹, Guanghui Han³, Amanda Ferguson¹, Khanhha Dao¹, Ronald J. Copeland³, Florin Despa^{1,4}, Gerald W. Hart³, Crystal M. Ripplinger¹ & Donald M. Bers¹

Ca²⁺/calmodulin-dependent protein kinase II (CaMKII) is an enzyme with important regulatory functions in the heart and brain, and its chronic activation can be pathological. CaMKII activation is seen in heart failure, and can directly induce pathological changes in ion channels, Ca²⁺ handling and gene transcription¹. Here, in human, rat and mouse, we identify a novel mechanism linking CaMKII and hyperglycaemic signalling in diabetes mellitus, which is a key risk factor for heart² and neurodegenerative diseases^{3,4}. Acute hyperglycaemia causes covalent modification of CaMKII by O-linked N-acetylglucosamine (O-GlcNAc). O-GlcNAc modification of CaMKII at Ser 279 activates CaMKII autonomously, creating molecular memory even after Ca²⁺ concentration declines. O-GlcNAc-modified CaMKII is increased in the heart and brain of diabetic humans and rats. In cardiomyocytes, increased glucose concentration significantly enhances CaMKII-dependent activation of spontaneous sarcoplasmic reticulum Ca²⁺ release events that can contribute to cardiac mechanical dysfunction and arrhythmias¹. These effects were prevented by pharmacological inhibition of O-GlcNAc signalling or genetic ablation of CaMKII δ . In intact perfused hearts, arrhythmias were aggravated by increased glucose concentration through O-GlcNAc- and CaMKII-dependent pathways. In diabetic animals, acute blockade of O-GlcNAc inhibited arrhythmogenesis. Thus, O-GlcNAc modification of CaMKII is a novel signalling event in pathways that may contribute critically to cardiac and neuronal pathophysiology in diabetes and other diseases.

Under basal conditions, CaMKII is autoinhibited by an interaction between the regulatory and catalytic subunits of each CaMKII monomer (Fig. 1a). Ca²⁺/calmodulin (Ca²⁺/CaM) binding to the regulatory domain disrupts autoinhibition, opening the structure to allow the catalytic domain to phosphorylate targets⁵. This conformational change is also the basis for fluorescence resonance energy transfer (FRET) changes in a CaMKII activity reporter called Camui, which uses full-length CaMKII and attached green fluorescent proteins^{6,7} (Fig. 1a). Open-state CaMKII is subject to post-translational modifications, including phosphorylation at T286 (ref. 8) and oxidation at the MM280/281 pair⁹, which stabilize CaMKII in the open state even when Ca²⁺/CaM dissociates, creating molecular memory but also having potentially pathological effects¹. We tested whether diabetic hyperglycaemia might alter CaMKII activity.

Using Camui as a direct CaMKII activity reporter, cells exposed to glucose-free or low-glucose (100 mg dl⁻¹; 5.5 mmol l⁻¹) conditions did not exhibit autonomous CaMKII activity (in lysates plus Ca²⁺/CaM and EGTA buffer) (Fig. 1b, white bars). However, glucose levels corresponding to borderline or severe diabetes (240–500 mg dl⁻¹) induced robust autonomous CaMKII activation. The non-metabolizable sugar mannitol did not activate autonomous CaMKII activity (Extended Data Fig. 1a). Glucose-dependent CaMKII activation was still present in CaMKII mutants lacking critical autophosphorylation and oxidation sites (Extended Data Fig. 1b, c), ruling out involvement of those pathways.

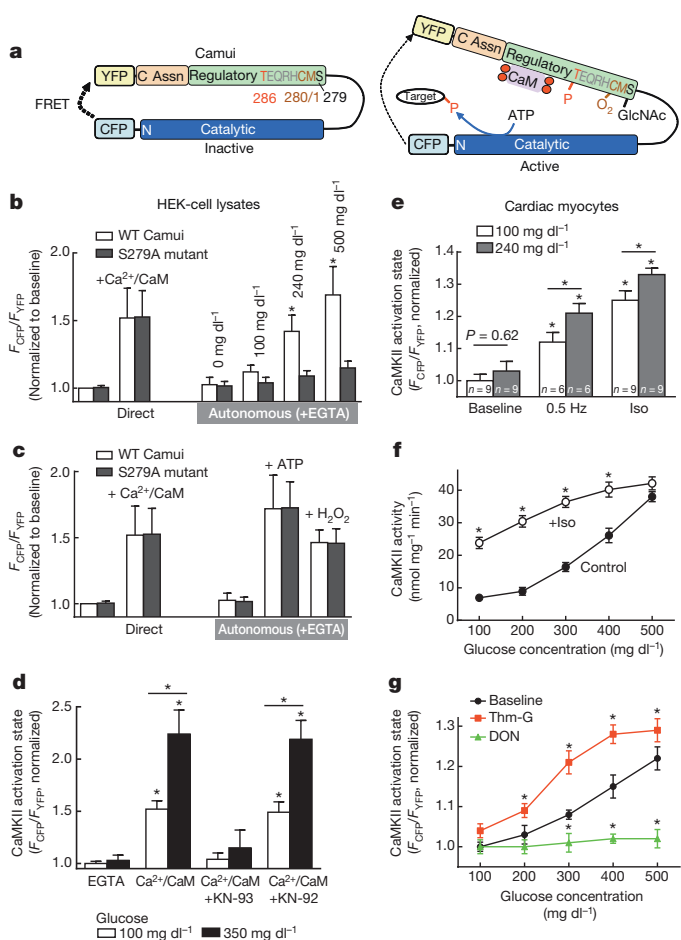


Figure 1 | Glucose-induced CaMKII activity is O-GlcNAc dependent.

a, Schematic of Camui CaMKII sensor (numbers are amino acid sequence numbers; Assn is the association domain of CaMKII). **b**, Direct (Ca²⁺/CaM) or autonomous (+EGTA) activation of Camui measured in lysates after HEK-cell exposure to indicated glucose concentration. F_{CFP}/F_{YFP} , ratio of fluorescence of cyan fluorescent protein (CFP) to fluorescence of yellow fluorescent protein (YFP). WT, wild type. **c**, S279 mutation does not affect Ca²⁺/CaM, phosphorylation, or oxidation-dependent activity. **d**, Glucose-dependent Camui activation is ablated by KN-93 or Ca²⁺ chelation (+EGTA). **e**, Increased glucose concentration enhances pacing- or Iso-induced CaMKII activity. **f**, Glucose-dependent CaMKII activity measured by ³²P incorporation. **g**, Glucose-dependent Camui activation is enhanced by Thm-G and ablated by O-GlcNAc inhibition (+DON) ($n = 3$ for all data points). Data show mean \pm standard error of the mean (s.e.m.); experiments are with three preparations done in triplicate, unless indicated. * $P < 0.05$ versus control.

¹Department of Pharmacology, University of California, Davis, 451 Health Sciences Drive, Davis, California 95616, USA. ²Department of Physiology, University of Otago, Dunedin 9054, New Zealand.

³Department of Biological Chemistry, Johns Hopkins University School of Medicine, 725 North Wolfe Street, Baltimore, Maryland 21205, USA. ⁴Department of Molecular and Biomedical Pharmacology, University of Kentucky, 900 S. Limestone, Lexington, Kentucky 40536, USA.

Post-translational modification by *O*-GlcNAc ('*O*-GlcNAcylation') can alter protein function¹⁰, and such regulation is seen in heart^{11,12} and brain proteins^{13–15}. *O*-GlcNAcylation is enhanced by elevated glucose concentration, which raises levels of the direct substrate (uridine diphosphate (UDP)-*N*-acetylglucosamine) of the enzyme *O*-GlcNAc transferase (OGT). *O*-GlcNAc groups are removed by the enzyme *O*-GlcNAcase. We tested whether direct *O*-GlcNAcylation might mediate glucose-induced autonomous CaMKII activation, analogous to autophosphorylation in the conserved CaMKII regulatory domain (Extended Data Fig. 1e). Two consensus *O*-GlcNAcylation sites are T286 and S279. T286A-mutant Camui only slightly limited glucose-induced autonomous activation (Extended Data Fig. 1b), but that could be indirect, through synergy between *O*-GlcNAcylation at another site enhancing T286 autophosphorylation.

Remarkably, S279A-mutant Camui abolished glucose-induced autonomous CaMKII activation (Fig. 1b, black bars). Importantly, S279A had no effect on either direct CaMKII activation or on autonomous activity induced by autophosphorylation or oxidation (Fig. 1c). Thus, S279 may be a specific target for *O*-GlcNAc-mediated CaMKII activity during hyperglycaemia.

High glucose did not alter the CaMKII activation state in cells kept in Ca^{2+} -free, EGTA-containing conditions (Fig. 1d). When cells were exposed to elevated glucose (and normal Ca^{2+}), the subsequently measured maximal Ca^{2+} /CaM-dependent activity was enhanced (Fig. 1d, middle bars). Pre-treatment with the CaMKII inhibitor KN-93 (which locks CaMKII in the closed high-FRET state) prevented autonomous activation by high glucose, even in the presence of Ca^{2+} /CaM. Rat cardiomyocytes expressing Camui and exposed to high glucose (without stimulation) for 24 h showed no significant change in baseline CaMKII activation versus low-glucose myocytes (Fig. 1e). However, increasing intracellular $[\text{Ca}^{2+}]$, either by pacing (0.5 Hz for 30 s) or isoprenaline (Iso; 100 nM for 20 min) yielded significantly greater CaMKII activation at higher glucose concentrations. These observations suggest that *O*-GlcNAcylation of CaMKII is analogous to autophosphorylation and oxidation, requiring initial opening via Ca^{2+} /CaM.

To confirm our Camui observations, we cultured rat myocytes for 24 h in varying glucose concentrations and measured autonomous CaMKII activity (\pm Iso) using a standard assay (^{32}P incorporation into a CaMKII substrate; Fig. 1f). CaMKII activity was increased by glucose $>200 \text{ mg dl}^{-1}$, and by combined Iso and high glucose. *O*-GlcNAcylation is dynamic in cells and limited by glucose availability¹⁰ and the enzymatic functions of OGT¹⁶ and *O*-GlcNAcase¹⁷. Specific inhibition of glutamine–fructose amidotransferase by 50 μM diazo-5-oxonorleucine (DON) to prevent production of the OGT substrate (Fig. 4g), and hence *O*-GlcNAcylation, abolished glucose-induced autonomous CaMKII activation (Fig. 1g). Conversely, inhibition of *O*-GlcNAcase with 100 nM thiamet-G (Thm-G) promotes *O*-GlcNAc modification and enhanced myocyte CaMKII activity in conditions of elevated glucose concentration. Mutant-S279A Camui was not appreciably activated by high glucose in intact cells (Extended Data Fig. 1d). Thus, glucose-induced CaMKII activity involves S279 and an *O*-GlcNAc-dependent pathway.

To determine the extent of CaMKII *O*-GlcNAcylation in heart and brain, we used a custom-designed antibody that specifically recognizes this modification¹⁵. The fraction of CaMKII that was *O*-GlcNAc-modified and autophosphorylated was increased in rat myocytes cultured in high relative to normal glucose (350 versus 150 mg dl^{-1} , Fig. 2a), confirming that high glucose induces *O*-GlcNAc modification and increased activation of CaMKII. *O*-GlcNAc modification of CaMKII was blocked by KN-93 and in the S279A mutant (Fig. 2a), whereas it was enhanced by treating myocytes with 100 nM Iso 20 min before lysis (Extended Data Fig. 2a). We verified that the antibody reacted specifically to *O*-GlcNAc by immunoblots before and after β -elimination reactions that specifically cleaved *O*-linked glycans without degrading proteins (Extended Data Fig. 2b). The *O*-GlcNAc antibody no longer recognized high-glucose-treated CaMKII after β -elimination, but CaMKII levels were unaltered. *O*-GlcNAc modification of CaMKII was also disrupted by 50 μM DON and enhanced by 100 nM Thm-G (Extended Data Fig. 2c). We subjected peptides encoding the regulatory domain of CaMKII to *in vitro* labelling with *O*-GlcNAc transferase and confirmed

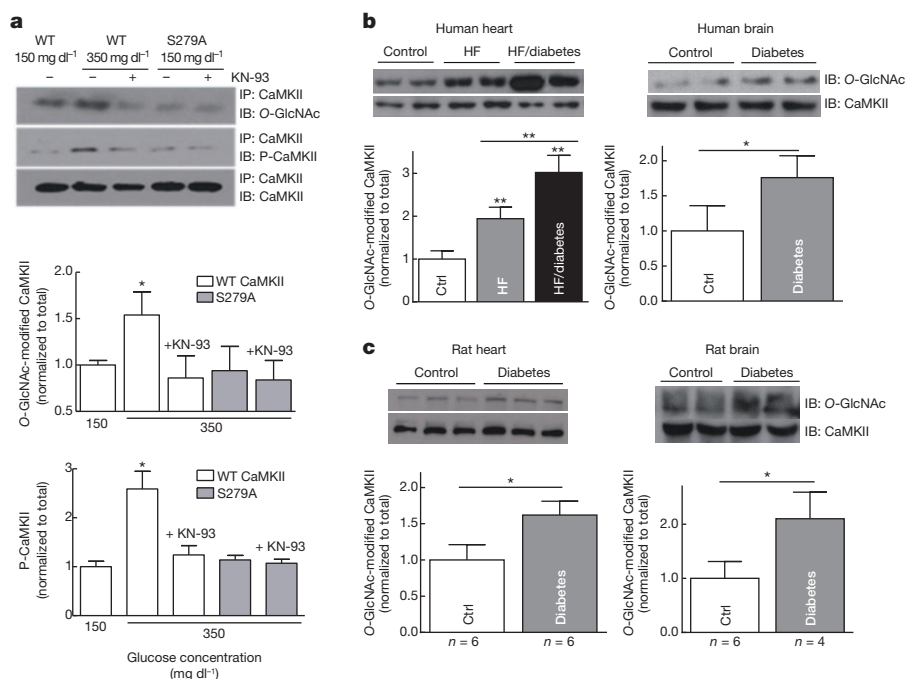


Figure 2 | *O*-GlcNAcylation of CaMKII occurs *in vivo*. **a**, Immunoblot (IB) with *O*-GlcNAc-specific and CaMKII-phospho-T286-specific (P-T286) antibodies show that high glucose concentration (350 mg dl^{-1}) increases *O*-GlcNAcylation and activation of CaMKII, but not in S279A-mutant CaMKII or after KN-93 treatment ($n = 3$ myocyte preparations). IP, immunoprecipitate. **b**, The ratio of *O*-GlcNAc-modified to total CaMKII is

increased in heart ($n = 6$ hearts per group) and brain ($n = 3$ brains per group) from diabetic versus control non-diabetic human patients. Ctrl, control. HF, heart failure. **c**, *O*-GlcNAc modification of CaMKII is also increased in heart and brain from diabetic rats compared with wild-type controls (number of rats indicated). Data are shown as mean \pm s.e.m. * $P < 0.05$, ** $P < 0.01$ versus control.

the S279 site as a target for O-GlcNAc modification using electron-transfer-dissociation mass spectrometry (ETD-MS; Extended Data Fig. 3).

CaMKII expression is increased in patients with heart failure¹⁸, and elevated CaMKII expression and activity have been implicated in the transition to heart failure^{19,20}. Using the O-GlcNAc-specific antibody, we probed cardiac samples (holding total CaMKII constant) from patients with heart failure and diabetes (blood glucose >400 mg dl⁻¹), alongside failing and non-failing non-diabetic hearts (blood glucose <200 mg dl⁻¹). The fraction of CaMKII that was O-GlcNAc modified was doubled in heart failure patients and nearly tripled in heart failure patients with diabetes versus those with non-failing, non-diabetic hearts (Fig. 2b). Similarly, brain samples from people with diabetes had significantly increased O-GlcNAc-modified CaMKII relative to those from non-diabetic people. In a diabetic rat model with reduced insulin secretion and blood glucose >600 mg dl⁻¹ (ref. 21), CaMKII O-GlcNAcylation was greatly elevated in heart and brain samples versus in control rats (Fig. 2c). Interestingly, CaMKII autophosphorylation was also enhanced in cardiac tissue from diabetic rats (Extended Data Fig. 2d), consistent with synergistic CaMKII activation through these mechanisms. Taken together, our data demonstrate that CaMKII O-GlcNAcylation and activation occur in the heart and brain of diabetic subjects.

Ryanodine receptor (RyR) phosphorylation by CaMKII enhances cardiac sarcoplasmic reticulum Ca²⁺ release events (Ca²⁺ sparks and waves)^{22–24}. In intact isolated myocytes, GlcNAcase inhibition with Thm-G or elevated glucose concentration alone increased Ca²⁺ spark and wave frequency (Fig. 3a–c). The Thm-G-induced Ca²⁺ spark increase occurred without altered sarcoplasmic reticulum Ca²⁺ content (Extended Data Fig. 4a) and was prevented by the CaMKII inhibitor KN-93, but not its inactive analogue KN-92. Combining Thm-G treatment with increased glucose concentration (350 mg dl⁻¹) markedly increased Ca²⁺ sparks and waves, consequently depleting sarcoplasmic reticulum Ca²⁺ (Extended Data Fig. 5). Thus, hyperglycaemia and reduced GlcNAcase activity synergize in activating sarcoplasmic reticulum Ca²⁺ release. Acute blockade of either CaMKII (+KN-93) or O-GlcNAcylation (+DON) prevented glucose-dependent Ca²⁺ sparks (Fig. 3c), but did not alter sarcoplasmic reticulum Ca²⁺ load (Extended Data Fig. 4b). Ca²⁺ spark frequency versus control was neither altered by DON (Fig. 3c) nor the

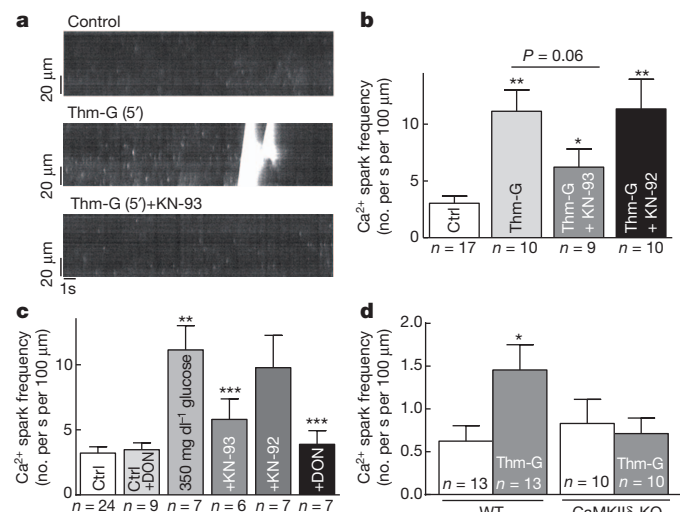


Figure 3 | Glucose-induced cardiac Ca²⁺ sparks are O-GlcNAc and CaMKII dependent. **a**, Ca²⁺ sparks and waves are increased by GlcNAcase inhibitor Thm-G. **b**, Thm-G-induced Ca²⁺ sparks are prevented by CaMKII inhibitor KN-93 (but not the inactive analogue KN-92). **c**, Glucose-induced Ca²⁺ sparks are ablated by CaMKII inhibitor KN-93 and the O-GlcNAc inhibitor DON. **d**, Thm-G induces Ca²⁺ sparks in wild-type (WT) mice, but not mice lacking CaMKIIδ (CaMKIIδ-KO; baseline Ca²⁺ spark frequency differs in rat versus mouse myocytes). Data are shown as mean \pm s.e.m. The number of myocytes is indicated. * $P < 0.05$, ** $P < 0.01$ versus control, *** $P < 0.05$ versus 350 mg dl⁻¹ glucose.

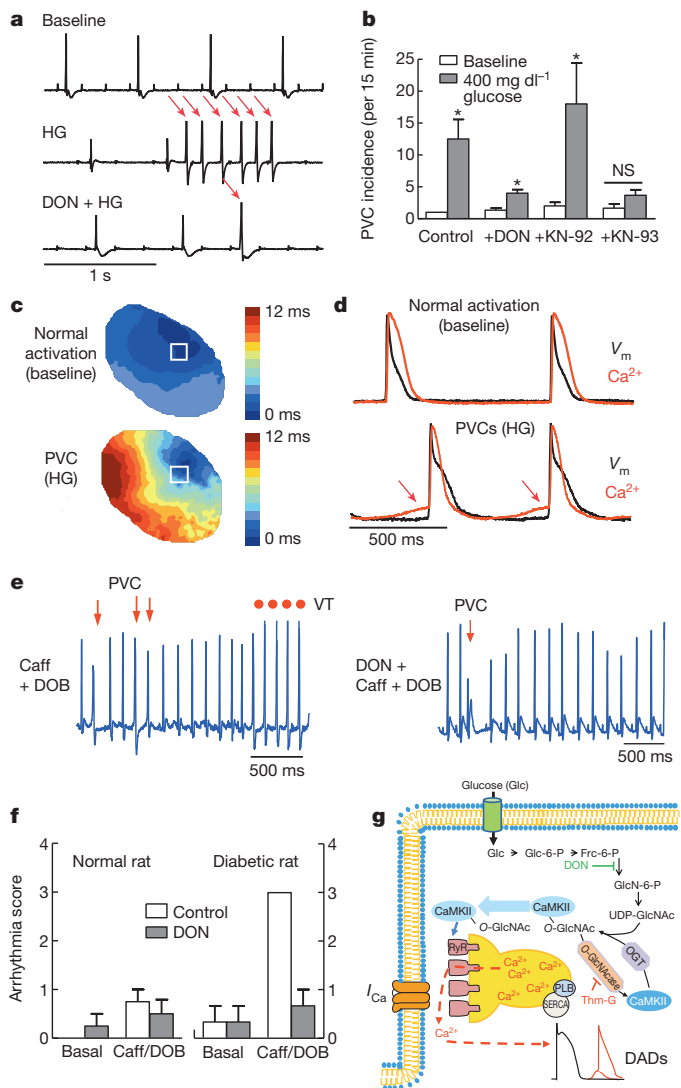


Figure 4 | Glucose-induced arrhythmias are suppressed by DON and KN-93. **a**, Electrocardiograms (ECGs) during baseline conditions (top), high glucose concentrations (HG), and DON pre-treatment plus high glucose. **b**, PVCs (per 15 min) increased after glucose concentration was raised (versus baseline). DON or KN-93 pre-treatment reduced glucose-induced PVCs, but had no effect under baseline conditions. **c**, Activation maps for normal activation (top) and high-glucose-induced PVC (bottom). **d**, Action potentials (black) and Ca²⁺ transients (red) from area indicated by white boxes in **c**. **e**, **f**, Caffeine- (Caff) and dobutamine- (DOB) induced PVCs and ventricular tachycardia (VT) were inhibited by DON in diabetic rats *in vivo*. **g**, Working model of O-GlcNAc-induced and CaMKII-dependent arrhythmic events. DADs, delayed afterdepolarizations; Frc-6-P, fructose-6-phosphate; I_{Ca} , Ca current; PLB, phospholamban. Data show mean \pm s.e.m.; $n = 3$ hearts (**a–d**) or animals (**e, f**). * $P < 0.05$ versus control. NS, not significant.

non-metabolizable sugar mannitol (Extended Data Fig. 4c). Thus, glucose-induced arrhythmogenic Ca²⁺ waves occur through a CaMKII- and O-GlcNAc-dependent mechanism.

To test whether CaMKIIδ (the dominant cardiac isoform) is required for O-GlcNAc-dependent effects on sarcoplasmic reticulum Ca²⁺ release, we used myocytes from CaMKIIδ-knockout mice. Neither Ca²⁺ transient amplitude nor sarcoplasmic reticulum Ca²⁺ load (Extended Data Fig. 4d, e) were altered by acute Thm-G exposure in wild-type or CaMKIIδ-knockout mouse cells. Ca²⁺ spark frequency was significantly enhanced by Thm-G in wild-type but not in CaMKIIδ-knockout myocytes (Fig. 3d).

Using optical mapping in Langendorff-perfused rat hearts exposed to 400 mg dl⁻¹ glucose, we observed a significant increase in premature ventricular complexes (PVCs) compared with baseline (Fig. 4a),

consistent with observations of enhanced PVCs in human diabetic patients²⁵. This effect was attenuated by inhibiting either CaMKII (using KN-93) or O-GlcNAc (using DON) (Fig. 4b). We also mapped intracellular $[Ca^{2+}]_i$ and voltage simultaneously. Epicardial activation during PVCs was typified by markedly slowed conduction and activation times compared with normal activation (Fig. 4c). Additionally, spontaneous diastolic $[Ca^{2+}]_i$ elevation preceded the action potential upstroke in high glucose conditions (Fig. 4d), an effect prevented by blocking OGT using DON pre-treatment (Extended Data Fig. 6a, b).

We also found higher *in vivo* arrhythmia susceptibility in normal and diabetic rats during challenge with caffeine and dobutamine (Fig. 4e, f). DON pre-treatment ablated arrhythmias induced by caffeine and dobutamine in diabetics, but had no effect on baseline or caffeine/dobutamine-induced arrhythmia in non-diabetic rats. We also confirmed that CaMKII activity is elevated in diabetic rat hearts, and that this effect is blunted by pre-treatment of rats with DON (Extended Data Fig. 6c), consistent with O-GlcNAc- and CaMKII-dependent hyperglycaemia-induced arrhythmogenesis.

We identified a novel mechanism for autonomous CaMKII activation by O-GlcNAc modification at CaMKII S279 (Fig. 4g). Acute extracellular glucose elevation, to levels that mimic those in diabetic patients, suffices to activate CaMKII through this pathway in intact cardiac myocytes and leads to arrhythmic events in intact hearts and animals. In diabetic hearts and brains CaMKII O-GlcNAcylation is elevated and this may contribute to pathological alterations in cardiac myocytes and neurons. Indeed, this pathway may synergize with autonomous CaMKII activation by phosphorylation⁸ and oxidation²⁶, which are important in signalling in many cell types. CaMKIV, related to CaMKII, is O-GlcNAcylated at S189, which inhibits its activation by CaM kinase kinase¹⁵. O-GlcNAc-mediated activation in CaMKII is not analogous to the inhibition seen for CaMKIV.

The S279 site is highly conserved in all mammalian CaMKII isoforms (Extended Data Fig. 1e), and the robust functional effects in cardiomyocytes suggest that hyperglycaemia can readily activate CaMKII in both heart and brain, and alter phosphorylation of multiple CaMKII targets (including CaMKII itself) to exert both acute (for example, altered Ca^{2+} handling/arrhythmias) and chronic (for example, transcriptional regulation) effects in many tissues. CaMKII is an important nodal point in both acute and chronic modulation of ion channels in both heart and brain. Overactivation of CaMKII caused by hyperglycaemia during diabetes may lead to widespread and as yet unappreciated pathological consequences that merit exploration. It is already known that overactivation of CaMKII occurs in heart failure and neuronal excitotoxicity, and that this activated CaMKII can contribute to major dysfunction at the level of acute ion channel modulation that contributes to cardiac arrhythmias^{1,24}, reduced contractility, neuronal damage²⁷ and altered gene transcription¹. In diabetes, these powerful CaMKII signalling pathways are likely to be activated by hyperglycaemia-induced O-GlcNAc modification of CaMKII, and this should be considered in future therapeutic strategies. This could also broaden the impact of CaMKII inhibitors in therapeutics in heart disease and beyond.

METHODS SUMMARY

Camui constructs were generated as previously described⁷. HEK293 cells were kept in culture for 24 h and transiently transfected with expression plasmids encoding Camui. Cells were cultured for an additional 24 h after transfection. Fluorescence measurements were performed using fluorescence spectrophotometry, excited at 440 nm with emission recorded at 477 nm for cyan fluorescent protein (CFP) (F_{CFP}) and 527 nm for yellow fluorescent protein (YFP) (F_{YFP}). Camui fluorescence and ratio (F_{CFP}/F_{YFP}) was measured with 10 μ M CaM plus 200 μ M Ca^{2+} for maximal activity and with 1 mM EGTA to chelate Ca^{2+} for assessing deactivated or autonomous CaMKII activation. CaMKII activity was directly measured as incorporation of ^{32}P from ATP- γ - ^{32}P into an artificial substrate as previously described⁸. Ca^{2+} transients and sparks were recorded using confocal microscopy. Pooled data are represented as mean \pm s.e.m. Statistical comparisons were made with repeated two-way analysis of variance and paired Student's *t*-test where applicable. $P < 0.05$ was considered significant.

Online Content Any additional Methods, Extended Data display items and Source Data are available in the online version of the paper; references unique to these sections appear only in the online paper.

Received 5 July 2012; accepted 12 August 2013.

Published online 29 September 2013.

- Anderson, M. E., Brown, J. H. & Bers, D. M. CaMKII in myocardial hypertrophy and heart failure. *J. Mol. Cell. Cardiol.* **51**, 468–473 (2011).
- Roger, V. L. *et al.* Heart disease and stroke statistics—2011 update: a report from the American Heart Association. *Circulation* **123**, e18–e209 (2011).
- Haan, M. N. Therapy Insight: type 2 diabetes mellitus and the risk of late-onset Alzheimer's disease. *Nature Clin. Pract. Neurol.* **2**, 159–166 (2006).
- Biessels, G. J., Staekenborg, S., Brunner, E., Brayne, C. & Scheltens, P. Risk of dementia in diabetes mellitus: a systematic review. *Lancet Neurol.* **5**, 64–74 (2006).
- Rosenberg, O. S., Deindl, S., Sung, R. J., Nairn, A. C. & Kuriyan, J. Structure of the autoinhibited kinase domain of CaMKII and SAXS analysis of the holoenzyme. *Cell* **123**, 849–860 (2005).
- Takao, K. *et al.* Visualization of synaptic Ca^{2+} /calmodulin-dependent protein kinase II activity in living neurons. *J. Neurosci.* **25**, 3107–3112 (2005).
- Erickson, J. R., Patel, R., Ferguson, A., Bossuyt, J. & Bers, D. M. Fluorescence resonance energy transfer-based sensor Camui provides new insight into mechanisms of calcium/calmodulin-dependent protein kinase II activation in intact cardiomyocytes. *Circ. Res.* **109**, 729–738 (2011).
- Hudmon, A. & Schulman, H. Structure—function of the multifunctional Ca^{2+} /calmodulin-dependent protein kinase II. *Biochem. J.* **364**, 593–611 (2002).
- Erickson, J. R. *et al.* A dynamic pathway for calcium-independent activation of CaMKII by methionine oxidation. *Cell* **133**, 462–474 (2008).
- Hart, G. W., Housley, M. P. & Slawson, C. Cycling of O-linked β -N-acetylglucosamine on nucleocytoplasmic proteins. *Nature* **446**, 1017–1022 (2007).
- Chatham, J. C. & Marchase, R. B. The role of protein O-linked β -N-acetylglucosamine in mediating cardiac stress responses. *Biochim Biophys Acta* **1800**, 57–66 (2010).
- Zhu-Mauldin, X., Marsh, S. A., Zou, L., Marchase, R. B. & Chatham, J. C. Modification of STIM1 by O-linked N-acetylglucosamine (O-GlcNAc) attenuates store-operated calcium entry in neonatal cardiomyocytes. *J. Biol. Chem.* **287**, 39094–39106 (2012).
- Rengifo, J., Gibson, C. J., Winkler, E., Collin, T. & Ehrlich, B. E. Regulation of the inositol 1,4,5-trisphosphate receptor type I by O-GlcNAc glycosylation. *J. Neurosci.* **27**, 13813–13821 (2007).
- Bimboese, P., Gibson, C. J., Schmidt, S., Xiang, W. & Ehrlich, B. E. Isoform-specific regulation of the inositol 1,4,5-trisphosphate receptor by O-linked glycosylation. *J. Biol. Chem.* **286**, 15688–15697 (2011).
- Dias, W. B., Cheung, W. D., Wang, Z. & Hart, G. W. Regulation of calcium/calmodulin-dependent kinase IV by O-GlcNAc modification. *J. Biol. Chem.* **284**, 21327–21337 (2009).
- Kreppel, L. K., Blomberg, M. A. & Hart, G. W. Dynamic glycosylation of nuclear and cytosolic proteins. Cloning and characterization of a unique O-GlcNAc transferase with multiple tetratricopeptide repeats. *J. Biol. Chem.* **272**, 9308–9315 (1997).
- Gao, Y., Wells, L., Comer, F. I., Parker, G. J. & Hart, G. W. Dynamic O-glycosylation of nuclear and cytosolic proteins: cloning and characterization of a neutral, cytosolic β -N-acetylglucosaminidase from human brain. *J. Biol. Chem.* **276**, 9838–9845 (2001).
- Hoch, B., Meyer, R., Hetzer, R., Krause, E. G. & Karczewski, P. Identification and expression of δ -isoforms of the multifunctional Ca^{2+} /calmodulin-dependent protein kinase in failing and nonfailing human myocardium. *Circ. Res.* **84**, 713–721 (1999).
- Zhang, T. *et al.* The δ C isoform of CaMKII is activated in cardiac hypertrophy and induces dilated cardiomyopathy and heart failure. *Circ. Res.* **92**, 912–919 (2003).
- Ling, H. *et al.* Requirement for Ca^{2+} /calmodulin-dependent kinase II in the transition from pressure overload-induced cardiac hypertrophy to heart failure in mice. *J. Clin. Invest.* **119**, 1230–1240 (2009).
- Butler, A. E. *et al.* Diabetes due to a progressive defect in β -cell mass in rats transgenic for human islet amyloid polypeptide (HIP Rat): a new model for type 2 diabetes. *Diabetes* **53**, 1509–1516 (2004).
- Kohlhaas, M. *et al.* Increased sarcoplasmic reticulum calcium leak but unaltered contractility by acute CaMKII overexpression in isolated rabbit cardiac myocytes. *Circ. Res.* **98**, 235–244 (2006).
- Guo, T., Zhang, T., Mestral, R. & Bers, D. M. Ca^{2+} /calmodulin-dependent protein kinase II phosphorylation of ryanodine receptor does affect calcium sparks in mouse ventricular myocytes. *Circ. Res.* **99**, 398–406 (2006).
- Zhao, Z. *et al.* Angiotensin II induces afterdepolarizations via reactive oxygen species and calmodulin kinase II signaling. *J. Mol. Cell. Cardiol.* **50**, 128–136 (2011).
- Del Gobbo, L. C. *et al.* Low serum magnesium concentrations are associated with a high prevalence of premature ventricular complexes in obese adults with type 2 diabetes. *Cardiovasc. Diabetol.* **11**, 23 (2012).
- Luo, M. *et al.* Diabetes increases mortality after myocardial infarction by oxidizing CaMKII. *J. Clin. Invest.* **123**, 1262–1274 (2013).
- Ashpole, N. M. & Hudmon, A. Excitotoxic neuroprotection and vulnerability with CaMKII inhibition. *Mol. Cell. Neurosci.* **46**, 720–730 (2011).

Acknowledgements We thank Y. Hayashi for providing initial Camui samples, H. Schulman for helpful discussions, K. Margulies for human heart samples, L.-W. Jin, M. Melara and the University of California, Davis Alzheimer's Disease Center (NIH-P30AG010129) for human brain samples, and J. H. Brown for providing CaMKII δ -knockout mice. We thank Pfizer, Inc. for the gift of a breeding pair of HIP rats to F.D. This work was supported by American Heart Association 13SDG14680072 and National Institutes of Health (NIH) T32HL86350 (J.R.E.); NIH 1R01HL118474-01A1, NSF CBET 1133339, ADA 1-13-IN-70 and AHA 13GRNT16470034 (F.D.); NIH R01DK61671 and P01HL107153 (G.W.H.); NIH R01HL111600 (C.M.R.); NIH P01HL080101, R37HL30077 and Fondation Leducq Transatlantic CaMKII Alliance (D.M.B.). G.W.H. receives a share of royalty on sales of the CTD 110.6 antibody, which are managed by Johns Hopkins University.

Author Contributions J.R.E. and D.M.B. conceived the project. J.R.E. and L.P. carried out most of the experiments. L.W. and C.M.R. conducted optical mapping and *in vivo* ECG experiments and analysis. G.H., R.J.C. and G.W.H. conducted ETD-MS analysis. A.F. and K.D. generated constructs, performed animal surgeries, and participated in data analysis. F.D. contributed diabetic rats and some analysis therewith. J.R.E. and D.M.B. wrote the manuscript, with assistance from the other authors.

Author Information Reprints and permissions information is available at www.nature.com/reprints. The authors declare no competing financial interests. Readers are welcome to comment on the online version of the paper. Correspondence and requests for materials should be addressed to D.M.B. (dmbbers@ucdavis.edu).

METHODS

Construction of adenoviral vectors encoding biosensors. The Camui construct⁷ was incorporated in adenoviruses using the AdEasy adenoviral vector system (Qbiogene) to ensure high infection efficiency in terminally differentiated adult ventricular myocytes. Mutant variants of Camui (T286A, CM280/281VV and S279A) were generated using the commercially available QuickChange site-directed mutagenesis kit (Stratagene), and likewise incorporated into adenovirus.

HEK293-cell transfection. HEK293 cells (mycoplasma free at the time of this study) were cultured in DMEM (Invitrogen) with 5% FBS and penicillin/streptomycin for 24 h, and then transiently transfected with expression plasmids encoding Camui using a mammalian transfection kit (Stratagene). Cells were cultured for an additional 36 h after transfection. Camui expression was checked by fluorescence microscopy before experiments.

Human and rat models of diabetes. Failing hearts from type 2 diabetic and non-diabetic patients were obtained at the time of orthotopic heart transplantation as a gift from K. Margulies (University of Pennsylvania). Brain samples from human temporal cortex were obtained as a gift from L.-W. Jin and M. Melara (University of California, Davis). All human specimens, including failing heart tissues and brain samples, were obtained in accordance with Institutional Review Board approval at the respective institutions where samples were collected. All tissue was obtained with informed consent before transplantation surgery. Inclusion in tissue-based studies was not restricted on the basis of age, sex, race or ethnic status. Human cardiac tissue samples were divided into three groups: a non-failing and non-diabetic group (Fig. 2b control: 3 males, 3 females; ages 42–60), a heart failure group not under treatment for diabetes and with blood glucose $< 200 \text{ mg dl}^{-1}$ (Fig. 2b) heart failure: 3 males, 3 females; ages 41–63), and a heart failure group with diagnosed diabetes and blood glucose $> 200 \text{ mg dl}^{-1}$ (Fig. 2b heart failure/diabetes: 4 males, 2 females; ages 38–66). Human brain tissue samples were divided into two groups: a non-diabetic group (Fig. 2b control: 3 females; ages 79–89), and a diabetic group with blood glucose $> 200 \text{ mg dl}^{-1}$ (Fig. 2b diabetes: 3 females; ages 65–82). Male Sprague–Dawley (SD) rats transgenic for human amylin in the pancreatic β -cells (HIP rats) were used at age 10–12 months as previously described²⁸. Animal studies were not randomized or blinded for this study. Sample sizes were determined by power analysis or based on previous studies with the selected models²⁸. Blood glucose levels in rats were measured 1 day before experiments were conducted using a OneTouch Ultra glucose meter (LifeScan; model no. AW 060-213-01A). All diabetic HIP rats had a blood glucose concentration of over 600 mg dl^{-1} at the time of death.

In vitro fluorescence and CaMKII activity assays. Fluorescence measurements were performed using an MS SpectraMax plate reader spectrophotometer (Molecular Devices). Excitation and emission slits were set at 4 nm. An excitation wavelength of 440 nm was used, and dual photon counting emission detectors were set at 477 nm (F_{CFP}) and 527 nm (F_{YFP}), respectively. HEK cells or rat ventricular myocytes expressing Camui were treated with $10 \mu\text{M}$ CaM and $200 \mu\text{M}$ Ca^{2+} , then lysed in a buffer containing 50 mM Tris-HCl (pH 7.5), 5 mM MgCl_2 , and protease inhibitors to measure 'direct' activation (for example, see Fig. 1b). For autonomous Camui fluorescence measurements, Ca^{2+} /CaM treatment was performed in the presence of $100\text{--}500 \text{ mg dl}^{-1}$ glucose (Fig. 1b, d, e, g), $100 \mu\text{M}$ ATP (Fig. 1c) or $1 \mu\text{M}$ H_2O_2 (Fig. 1c). Cell lysis was then performed in a buffer containing 1 mM EGTA to chelate Ca^{2+} and isolate the kinase activity attributed to autonomous (rather than direct) activation. In Fig. 1d, cells were pretreated with 1 mM EGTA or $10 \mu\text{M}$ KN-92/KN-93. In Fig. 1e, myocytes were not directly treated with Ca^{2+} /CaM, but instead were subjected to pacing (0.5 Hz) or treated with Iso (100 nM) in the presence of 100 or 240 mg dl^{-1} glucose. In Fig. 1g, cells were treated with Ca^{2+} /CaM and increasing glucose concentration in the presence of either $50 \mu\text{M}$ DON or 100 nM Thm-G. In Fig. 1f, CaMKII kinase activity was determined at increasing glucose concentrations and in the presence (and absence) of Iso using a kinase assay that measures incorporation of ^{32}P -ATP into an artificial substrate, syntide-2, as previously described⁹ (Fig. 1f).

ETD-MS analysis. The peptide was analysed using an LTQ-Orbitrap XL mass spectrometer (Thermo Fisher Scientific) with ETD. The synthetic peptide was O-GlcNAcylated by *in vitro* labelling with OGT overnight at 4°C . After the O-GlcNAcylation reaction, the pH was adjusted to approximately 3 using 10% formic acid, and the sample was desalted with a C18 spin column (The Nest Group). The desalted sample was lyophilized to dryness using a Speed Vac concentrator and reconstituted in 50% methanol, 0.2% acetic acid to a final concentration of $10 \text{ pmol } \mu\text{l}^{-1}$. The sample was directly infused into the LTQ-Orbitrap XL mass spectrometer at a flow rate of $1 \mu\text{l min}^{-1}$ using a spray voltage of 1.9 kV. The full MS scans were acquired in the FT analyser with the following parameters: resolution 100,000; mass scan range mass-to-charge ratio (m/z) 300–800; and microscans 1. The ETD-MS2 scans were acquired in the ion-trap analyser with the following parameters: reagent AGC target 4×10^5 ; mass scan range m/z 250–2,000; microscans 1; isolation width m/z 1; and ETD activation time 80 ms.

Myocyte isolation and adenoviral infection. All protocols involving animals were performed in accordance with the Guide for the Care and Use of Laboratory Animals and approved by the University of California, Davis Institutional Animal Care and Use Committee. Adult rat ventricular myocytes were isolated as previously described²². Myocytes were seeded on laminin-coated coverslips in serum-free PC-1 medium (Lonza) supplemented with penicillin/streptomycin. Myocytes were infected for 2 h at a multiplicity of infection of 10–100 with adenovirus encoding Camui, followed by replacement with fresh medium. Infected cells were kept in culture for 36 h with one final replacement of fresh medium 1 h before experiments.

Confocal microscopy imaging. Coverslips were mounted on the stage of an inverted microscope (Zeiss, LSM5 Pascal) equipped with a $40 \times 1.4 \text{ NA}$ water immersion objective lens. Argon laser excitation wavelengths were 458 nm for CFP and 514 nm for YFP. CFP emission fluorescence was measured by confocal microscopy at $485 \pm 15 \text{ nm}$, and YFP emission fluorescence was measured at $\geq 535 \text{ nm}$. Camui imaging experiments were performed as previously described⁷. ImageJ software was used for image analysis.

Spark measurements. Intact ventricular myocytes were loaded with Fluo-3 AM ($5 \mu\text{M}$; Molecular Probes) and transients were recorded as previously described²⁹. Ca^{2+} transients were obtained by field stimulation at 1 Hz. Sarcoplasmic reticulum Ca^{2+} load was evaluated by the Ca^{2+} transient upon rapid caffeine application (10 mM). Experiments were performed with confocal microscopy (BioRad, Radiance 2100, $\times 40$ objective) using line scan mode with argon 4 laser (excitation at 488 nm, emission at $> 505 \text{ nm}$). Image analysis used ImageJ software and home-made routines in interactive data language (IDL).

Langendorff-perfused rat hearts. All procedures involving animals were approved by the Animal Care and Use Committee of the University of California, Davis and adhered to the Guide for the Care and Use of Laboratory Animals published by the National Institutes of Health. Adult male Sprague–Dawley rats (250–300 g) were anaesthetized with pentobarbital sodium (150 mg kg^{-1} , intraperitoneal (IP)) containing 500 IU kg^{-1} of heparin. After a midsternal incision, hearts were rapidly excised and Langendorff perfused at 37°C with oxygenated (95% O_2 , 5% CO_2) modified Tyrode's solution of the following composition (in mmol l^{-1}): NaCl 128.2, CaCl_2 1.3, KCl 4.7, MgCl_2 1.05, NaH_2PO_4 1.19, NaHCO_3 20 and glucose 11.1 (pH 7.4). Flow rate ($6\text{--}15 \text{ ml min}^{-1}$) was adjusted to maintain a perfusion pressure of 60–70 mm Hg. One leaflet of the mitral valve was carefully damaged with sharp forceps inserted through the pulmonary vein to prevent solution congestion in the left ventricular cavity after suppression of ventricular contraction. This also prevented acidification of the perfusate and the development of ischaemia in the left ventricle. Two Ag/AgCl disc electrodes were positioned in the bath to record an ECG analogous to a lead I configuration. ECG was continuously recorded throughout the duration of the experiment. A bipolar pacing electrode was positioned on the base of the left ventricular epicardium for pacing, which was performed at a basic cycle length (BCL) of 200 ms using a 2 ms pulse width at twice the diastolic threshold.

Dual optical mapping of V_m and Ca^{2+} . Hearts were loaded with the fluorescent intracellular Ca^{2+} indicator Rhod-2 AM (Molecular Probes; $250 \mu\text{l}$ of 1 mg ml^{-1} in dimethylsulphoxide (DMSO) containing 10% pluronic acid) and were subsequently stained with the voltage-sensitive dye RH237 (Molecular Probes; $25 \mu\text{l}$ of 1 mg ml^{-1} in DMSO). Blebbistatin (Tocris Bioscience; $10\text{--}20 \mu\text{M}$) was added to the perfusate to eliminate motion artefact during optical recordings. The anterior epicardial surface was excited using LED light sources centred at 530 nm and band-pass filtered from 511–551 nm (LEX-2; SciMedia) and focused directly on the surface of the preparation. The emitted fluorescence was collected through a 50 mm objective (Nikon) and split with a dichroic mirror at 630 nm (Omega). The longer wavelength moiety, containing the V_m signal, was long-pass filtered at 700 nm, and the shorter wavelength moiety, containing the Ca^{2+} signal, was band-pass filtered between 574–606 nm. The emitted fluorescence signals were recorded using two CMOS cameras (MiCam Ultima-L; SciMedia) with a sampling rate of 1 kHz and 100×100 pixels with a $20 \times 20 \text{ mm}$ field of view. The atrioventricular node was ablated using a fine-tip thermal cautery (Acuderm) to produce a slow intrinsic rhythm which allowed for ectopic activity and PVCs to escape. After loading the dyes, baseline electrophysiological parameters were recorded during normal rhythm as well as left ventricular epicardial pacing at a BCL of 200 ms. Hearts were then subjected to hyperglycaemia (400 mg dl^{-1}) with ($n = 3$) or without ($n = 5$) pre-treatment (10 min) with the O-GlcNAc inhibitor DON ($50 \mu\text{M}$). Optical recordings were taken every 5 min after treatment and ECG was continuously recorded.

In vivo ECG recordings. *In vivo* experiments were performed in anaesthetized diabetic rats (blood glucose $> 500 \text{ mg dl}^{-1}$). Rats received an injection of caffeine (IP; 120 mg kg^{-1}) and dobutamine (intravenous; $50 \mu\text{g kg}^{-1}$) during *in vivo* experiments. The same individuals were pre-treated (30 min before caffeine/dobutamine challenge) with an IP injection of DON (5 mg kg^{-1}). Experiments were

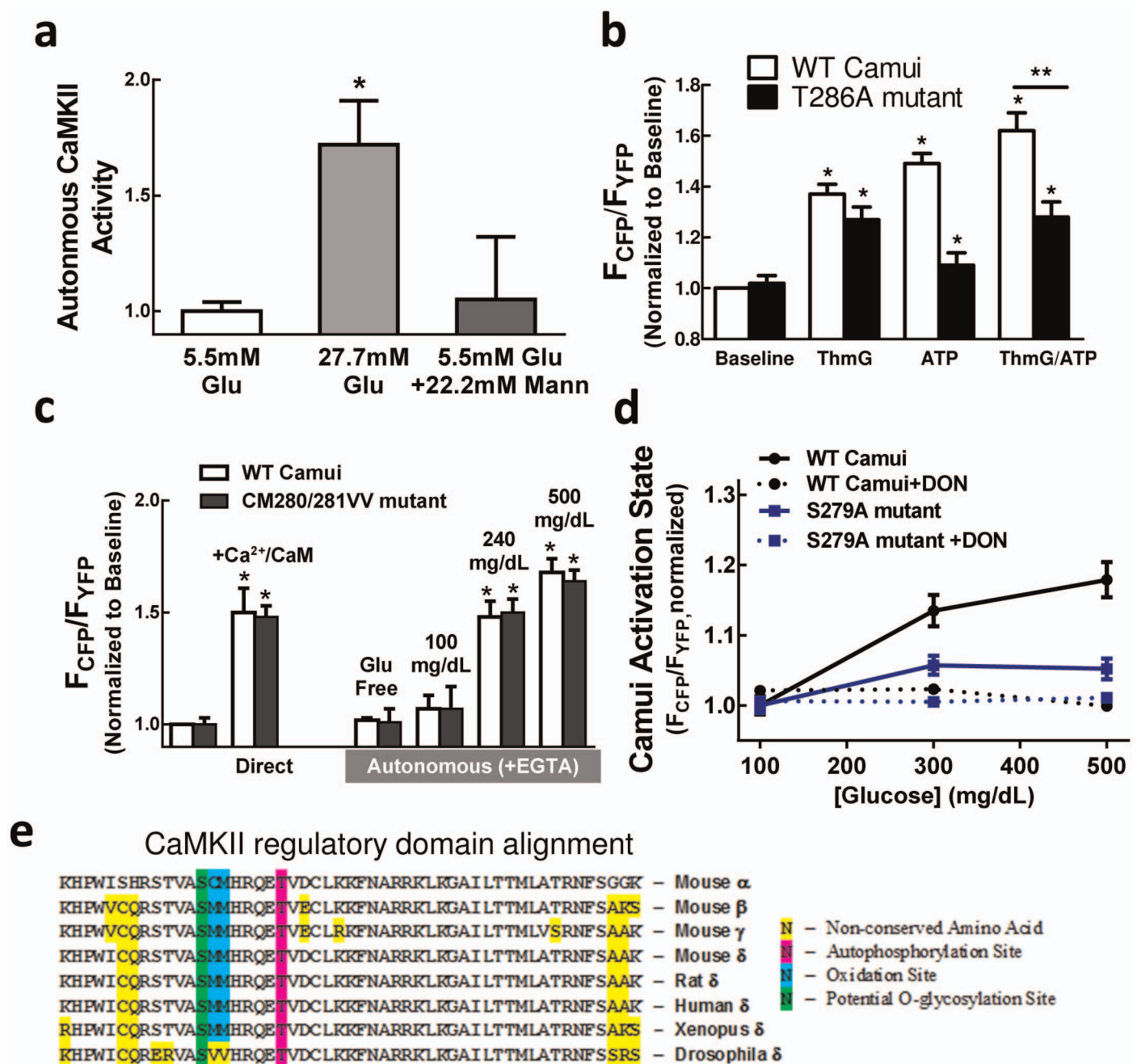
done 1 week apart, and some individuals received the reverse of the described procedure (+DON in first trial, −DON in second trial) to control for compensation effects between trials. For quantification of arrhythmia scores, the severity of arrhythmias was quantified using a previously published scoring system³⁰. Each individual heart was evaluated by means of a 5-point arrhythmia score, where single PVCs were given a score of 1, bigeminy/salvos a score of 2, ventricular tachycardia a score of 3, ventricular fibrillation a score of 4, spontaneous ventricular fibrillation a score of 5, and an assigned number corresponded to the most severe type of arrhythmia observed in that heart. Scores were used for group analysis of severity of arrhythmias.

Optical mapping data analysis and statistics. Optical mapping data analysis was performed using two different commercially available analysis programs (BV_Analyze, Brainvision; and Optiq, Cairn). V_m and Ca^{2+} data sets were spatially aligned and processed with a Gaussian spatial filter (radius 3 pixels). For both action potentials and Ca^{2+} transients (CaTs), activation time was determined as the time at 50% between diastolic and peak amplitude. Diastolic Ca^{2+} elevation was measured as the percentage of diastolic Ca^{2+} increase relative to the following CaT amplitude at baseline and 30 min post-treatment. The average diastolic Ca^{2+} elevation was calculated for each heart by averaging all Ca^{2+} signals from the entire anterior surface of

the heart within the optical mapping field of view. PVC incidence was determined from the continuous ECG recording as the number of PVCs that occurred during a 15 min period of baseline activity (before initiation of treatment) and during the first 15 min of treatment.

All values are presented as mean \pm s.e.m.; n values are generally biological replicates (hearts, brains, animals, myocytes, cell preparations) as indicated in legends. In addition, three technical replicates (triplicates) from three biological replicates were used for some cellular Camui experiments in Fig. 1. Comparisons between two groups of data were made using a Student's t -test, paired where appropriate or with repeated two-way analysis of variance. $P < 0.05$ was considered statistically significant.

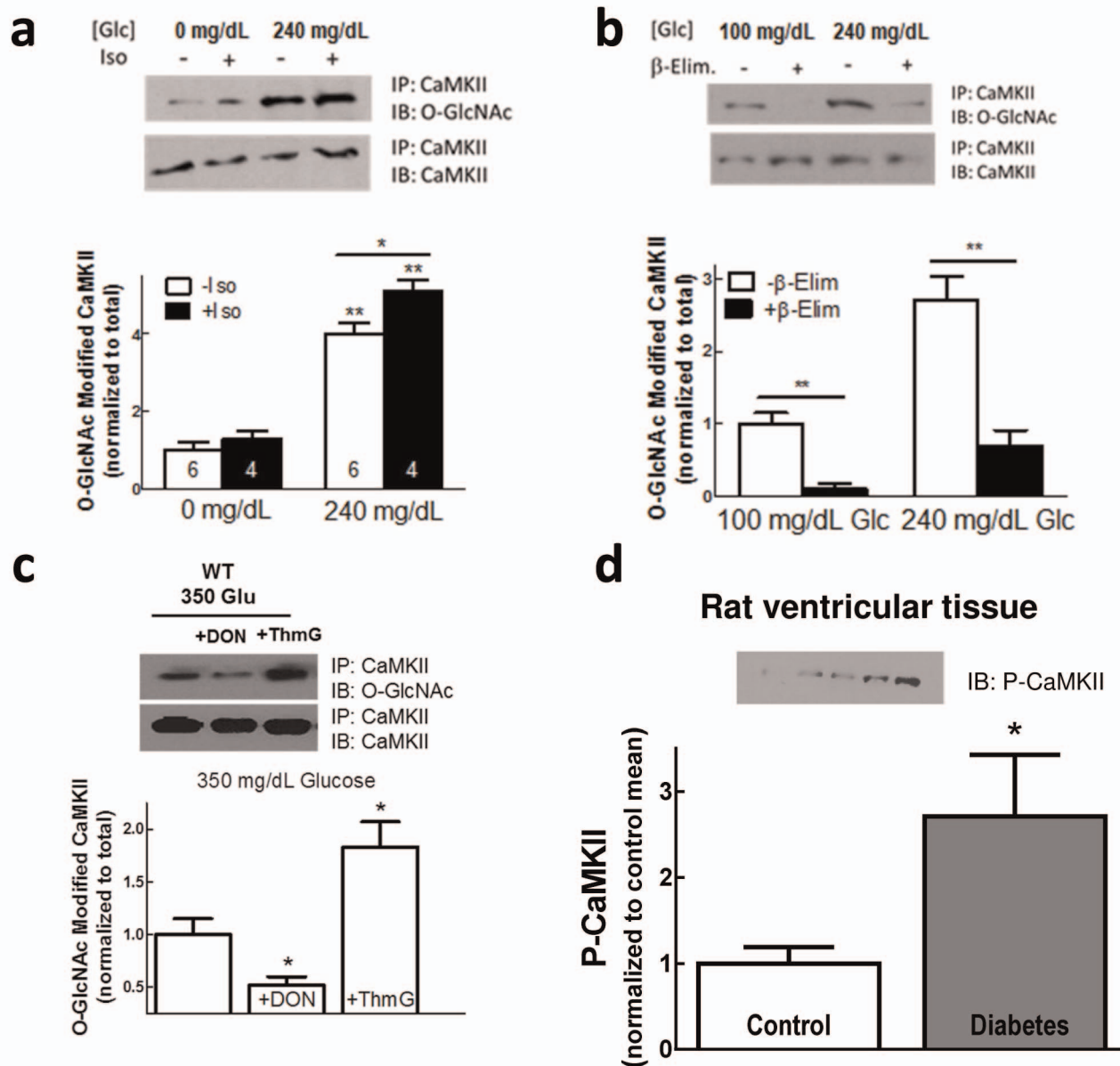
28. Despa, S. *et al.* Hyperamylinemia contributes to cardiac dysfunction in obesity and diabetes: a study in humans and rats. *Circ. Res.* **110**, 598–608 (2012).
29. van Oort, R. J. *et al.* Ryanodine receptor phosphorylation by calcium/calmodulin-dependent protein kinase II promotes life-threatening ventricular arrhythmias in mice with heart failure. *Circulation* **122**, 2669–2679 (2010).
30. Curtis, M. J. & Walker, M. J. Quantification of arrhythmias using scoring systems: an examination of seven scores in an in vivo model of regional myocardial ischaemia. *Cardiovasc. Res.* **22**, 656–665 (1988).



Extended Data Figure 1 | O-GlcNAc effect is not abolished by T286A or CM280/1VV mutation and CaMKII regulatory domain contains consensus O-GlcNAc modification sites. **a**, Increased glucose concentration, but not osmolarity-matched mannitol, activates CaMKII in HEK cells ($n = 9$). **b**, O-GlcNAc-dependent CaMKII activation is reduced but still present in T286A-mutant Camui ($n = 9$). WT, wild type. **c**, Glucose-dependent CaMKII activation is preserved in CM280/281VV-mutant Camui expressed in

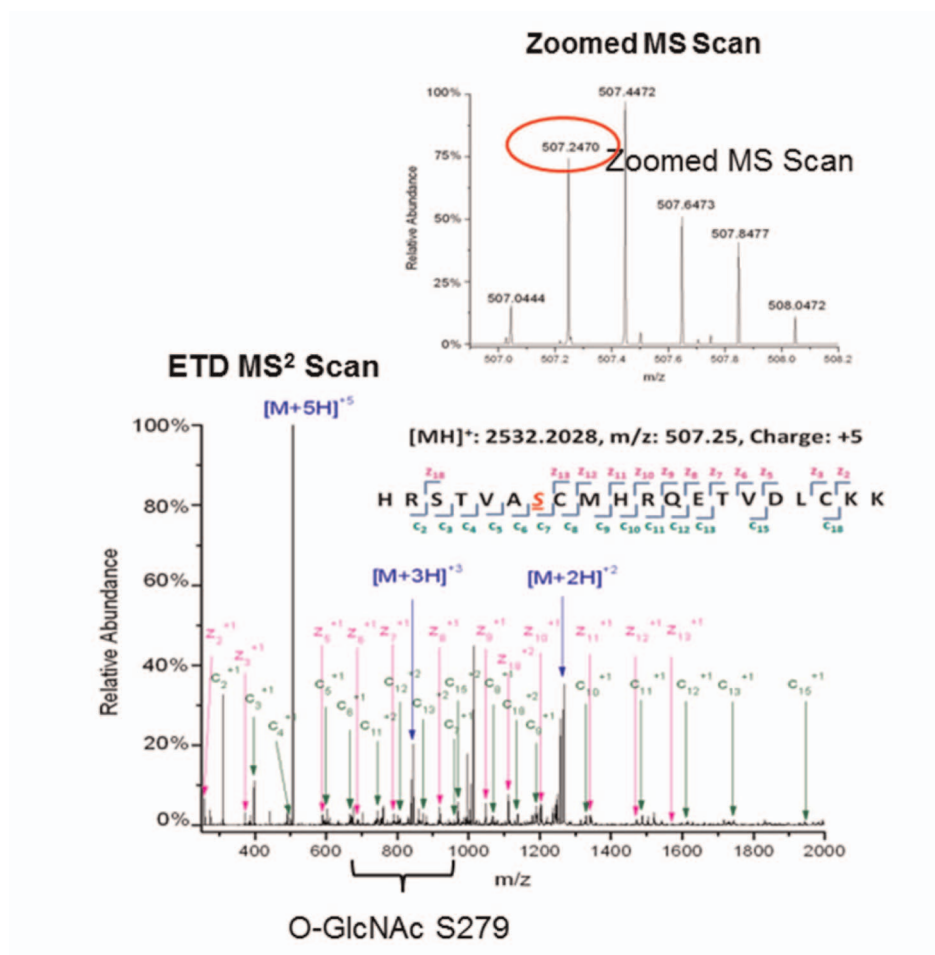
HEK-cell lysates ($n = 9$). **d**, Activation of Camui by increased glucose is blunted in the S279A mutant and ablated entirely by DON (n values: wild type = 100, wild type + DON = 72, S279A = 57, S279A + DON = 44 cells).

e, These sites are conserved in all known isoforms of CaMKII and in a wide variety of mammalian species. Data are mean \pm s.e.m. * $P < 0.05$, ** $P < 0.01$ versus control.



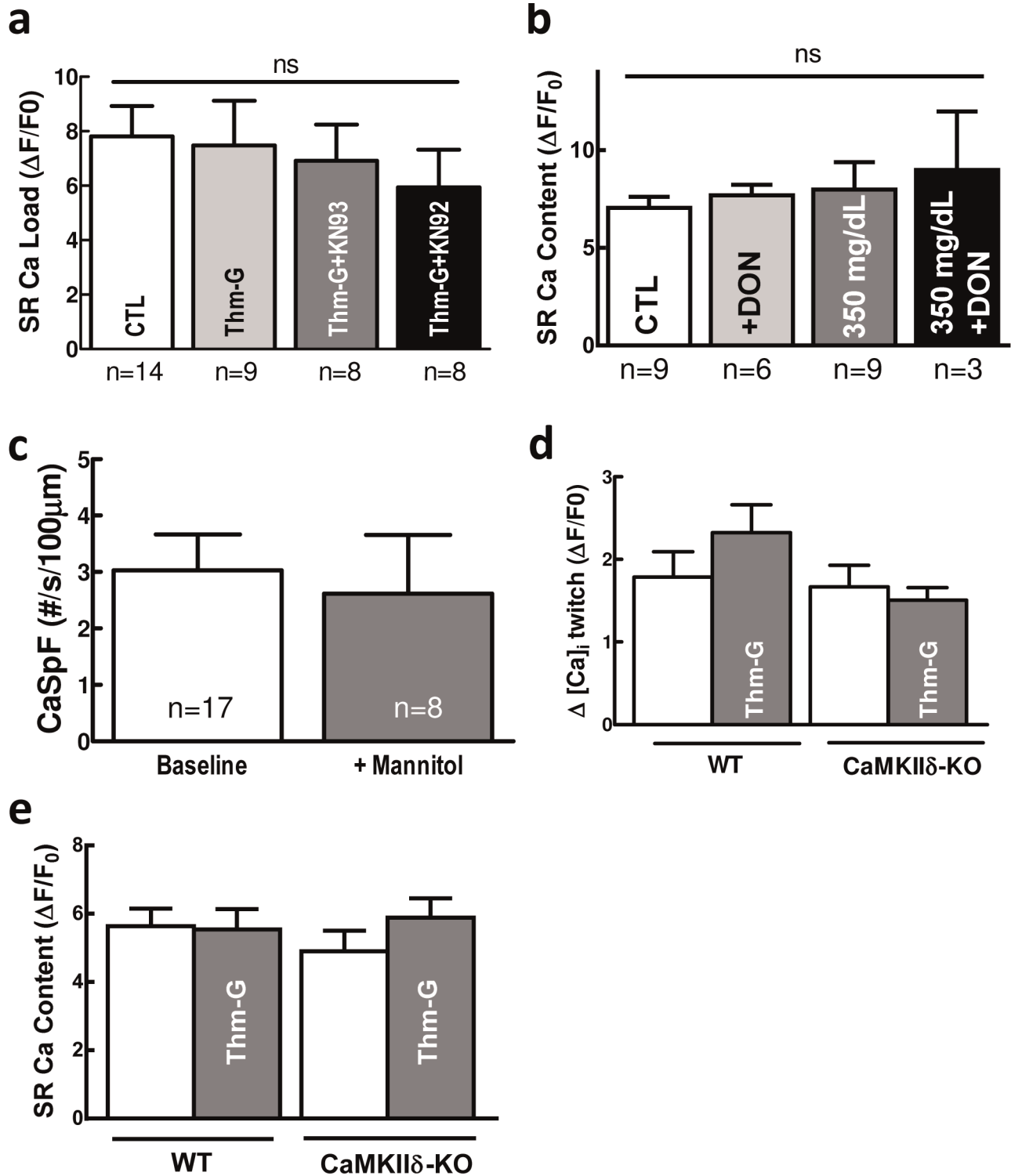
Extended Data Figure 2 | O-GlcNAc modification of CaMKII is enhanced in hyperglycaemic conditions. **a**, Immunoblot with an O-GlcNAc-specific antibody shows O-GlcNAc modification of CaMKII is inducible by increased glucose availability and is enhanced by Iso treatment (*n* values indicated). **b**, O-GlcNAc modification of CaMKII is reversed by β -elimination reaction

before immunoblot. **c**, O-GlcNAc modification of CaMKII is ablated by DON and enhanced by Thm-G. **d**, Autophosphorylation of cardiac CaMKII is significantly increased in a rat model of diabetes. *n* = 3 for all immunoblots except where indicated. Data are mean \pm s.e.m. **P* < 0.05, ***P* < 0.01 versus control.



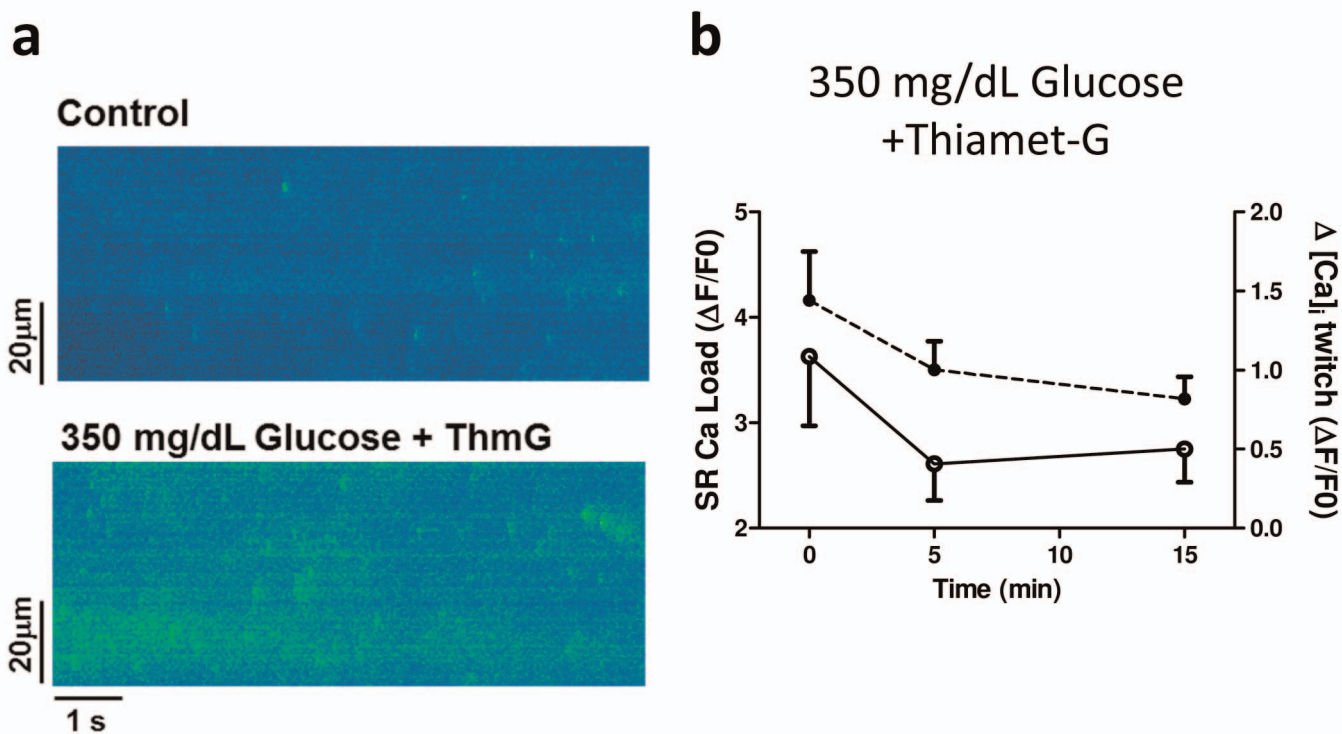
Extended Data Figure 3 | ETD-MS analysis confirms O-GlcNAc modification at S279A. A synthetic peptide encoding the regulatory domain of CaMKII was subjected to *in vitro* O-GlcNAc labelling followed by ETD-MS

analysis. Examination of the 507.25 m/z peptide fragment (top right inset) indicates the presence of an O-GlcNAc modification at S279 (c_6 to c_7 fragmentation).



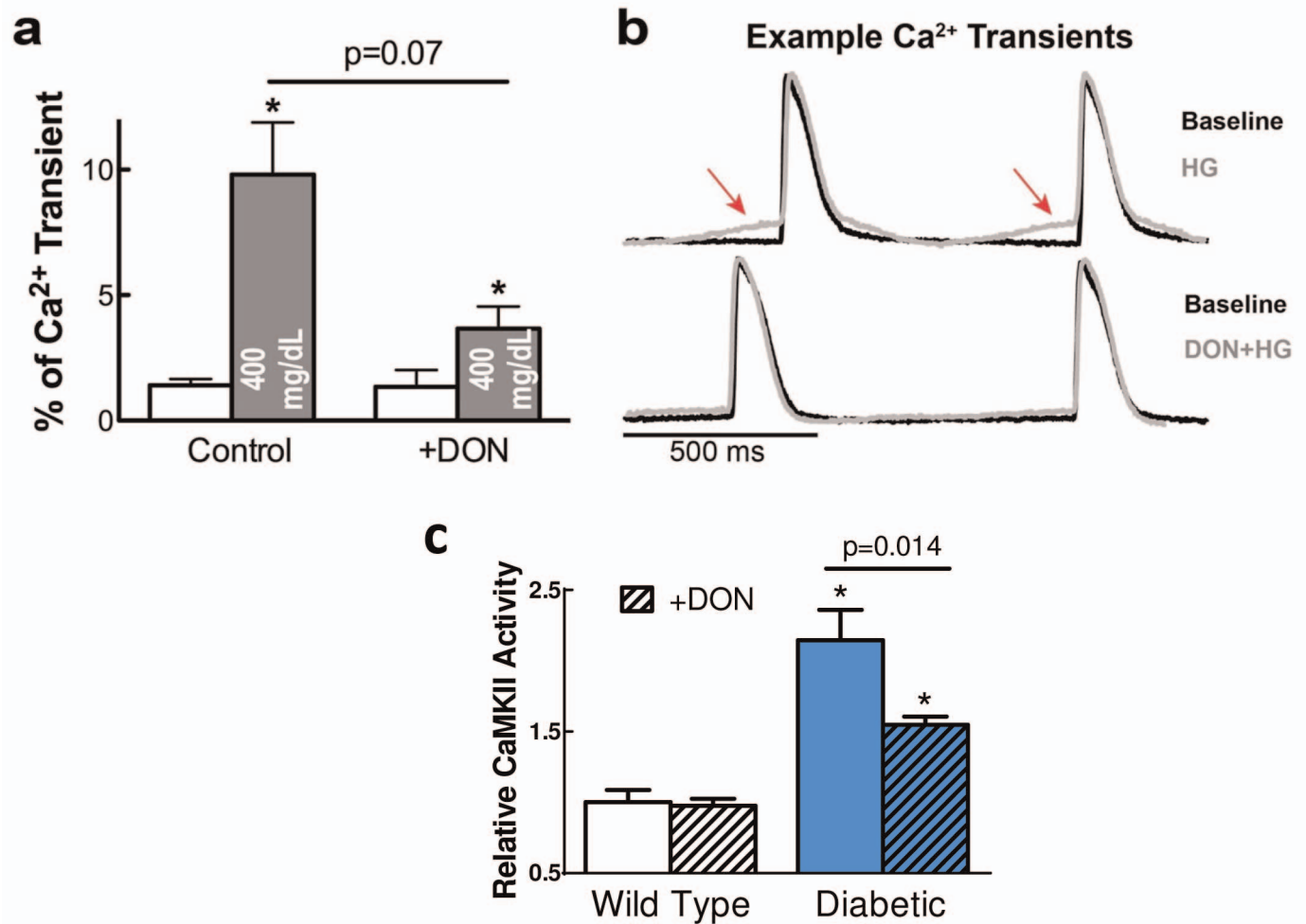
Extended Data Figure 4 | Sarcoplasmic reticulum Ca^{2+} content, sparks and twitch Ca^{2+} transients. a, b, Sarcoplasmic reticulum (SR) content is unaffected by Thm-G (a) or DON (b) in isolated rat myocytes (*n* values indicated). c, Mannitol does not enhance calcium spark frequency in isolated

rat myocytes. d, e, Ca^{2+} transient amplitude (d, *n* = 13) and SR content (e, *n* = 13) are unaffected by Thm-G treatment in isolated myocytes from wild-type (WT) or CaMKII δ -knockout mice. Data are mean \pm s.e.m. NS, no significant difference.



Extended Data Figure 5 | Ca^{2+} sparks induced by glucose and Thm-G.
a, b, Simultaneous treatment with 3,500 mg dl^{-1} glucose and Thm-G greatly

enhances spark frequency (a) and SR Ca^{2+} depletion (b) in isolated rat myocytes ($n = 6$). Data are mean \pm s.e.m.



Extended Data Figure 6 | Diastolic calcium elevation under high glucose is suppressed by pre-treatment with 50 mM DON. **a**, Average diastolic calcium elevation at baseline and following treatment with either high glucose (HG) or DON plus high glucose. Calcium elevation was measured as the percentage increase in the diastolic calcium signal relative to the amplitude of the following transient ($n = 3$). **b**, Example transients during baseline conditions (black) and

after treatment with either high glucose or DON plus high glucose (grey). Minimal diastolic calcium elevation occurs after pre-treatment with DON. $n = 3-4$ rats for all data points. **c**, CaMKII activity is enhanced in heart lysate from diabetic rats ($n = 3$), and this effect is blunted by treatment with DON. Data are mean \pm s.e.m. * $P < 0.05$ versus control.

A statin-dependent QTL for *GATM* expression is associated with statin-induced myopathy

Lara M. Mangravite^{1*}, Barbara E. Engelhardt^{2*†}, Marisa W. Medina³, Joshua D. Smith⁴, Christopher D. Brown⁵, Daniel I. Chasman⁶, Brigham H. Mecham¹, Bryan Howie², Heejung Shim², Devesh Naidoo³, QiPing Feng⁷, Mark J. Rieder^{4†}, Yii.-Der I. Chen⁸, Jerome I. Rotter⁸, Paul M Ridker⁶, Jemma C. Hopewell⁹, Sarah Parish⁹, Jane Armitage⁹, Rory Collins⁹, Russell A. Wilke⁷, Deborah A. Nickerson⁴, Matthew Stephens^{2,10} & Ronald M. Krauss³

Statins are prescribed widely to lower plasma low-density lipoprotein (LDL) concentrations and cardiovascular disease risk¹ and have been shown to have beneficial effects in a broad range of patients^{2,3}. However, statins are associated with an increased risk, albeit small, of clinical myopathy⁴ and type 2 diabetes⁵. Despite evidence for substantial genetic influence on LDL concentrations⁶, pharmacogenomic trials have failed to identify genetic variations with large effects on either statin efficacy^{7–9} or toxicity¹⁰, and have produced little information regarding mechanisms that modulate statin response. Here we identify a downstream target of statin treatment by screening for the effects of *in vitro* statin exposure on genetic associations with gene expression levels in lymphoblastoid cell lines derived from 480 participants of a clinical trial of simvastatin treatment⁷. This analysis identified six expression quantitative trait loci (eQTLs) that interacted with simvastatin exposure, including rs9806699, a *cis*-eQTL for the gene glycine amidinotransferase (*GATM*) that encodes the rate-limiting enzyme in creatine synthesis. We found this locus to be associated with incidence of statin-induced myotoxicity in two separate populations (meta-analysis odds ratio = 0.60). Furthermore, we found that *GATM* knockdown in hepatocyte-derived cell lines attenuated transcriptional response to sterol depletion, demonstrating that *GATM* may act as a functional link between statin-mediated lowering of cholesterol and susceptibility to statin-induced myopathy.

Analysis of individual variation in transcriptional response to drug treatment has successfully identified regulatory genetic variants that interact with treatment in model organisms¹¹ and human tissues^{12–15}. Cellular transcriptional analysis may be particularly useful for investigating genetic influences on statin efficacy, as statin-induced plasma LDL lowering is controlled through sterol-response element binding protein (SREBP)-mediated transcriptional regulation¹⁶. Therefore, to identify novel regulatory variants that interact with statin exposure, we conducted a genome-wide eQTL analysis based on comparing simvastatin exposure versus control exposure of 480 lymphoblastoid cell lines (LCLs) derived from European American participants in the Cholesterol and Pharmacogenetics (CAP) trial (<http://www.clinicaltrials.gov/ct2/show/NCT00451828>). LCLs have proven to be a useful model system for the study of genetic regulation of gene expression^{17,18}. Although non-genetic sources of variation, if uncontrolled, may limit the utility of LCLs for transcriptional perturbation analyses^{19,20}, there has been increasing use of these cells to screen for genetic variants associated with molecular response to drug intervention²⁰. Furthermore, many features of statin-mediated regulation of cholesterol metabolism are operative in LCLs²¹.

Simvastatin exposure had a significant effect on gene expression levels for 5,509 of 10,195 expressed genes (54%, false discovery rate (FDR) < 0.0001). The magnitude of change in expression across all responsive genes was small (0.12 ± 0.08 mean absolute log₂ change \pm s.d., Fig. 1) with 1,952 genes exhibiting $\geq 10\%$ change in expression and only 21 genes exhibiting $\geq 50\%$ change in expression. Among the strongest responders were 3-hydroxy-3-methylglutaryl-CoA reductase (*HMGCR*), which encodes the direct target of simvastatin inhibition (0.49 ± 0.29 mean log₂ change \pm s.d., $P < 0.0001$, $n = 480$), and low density lipoprotein receptor (*LDLR*), which encodes the receptor responsible for internalization of LDL particles (0.50 ± 0.35 mean log₂ change \pm s.d., $P < 0.0001$). As expected, surface expression of the LDLR protein was also increased following simvastatin exposure (1.6 ± 0.11 mean log₂ change \pm s.d., $P < 0.0001$, $n = 474$). Gene-set enrichment analysis showed a treatment-dependent increase in expression of genes involved in

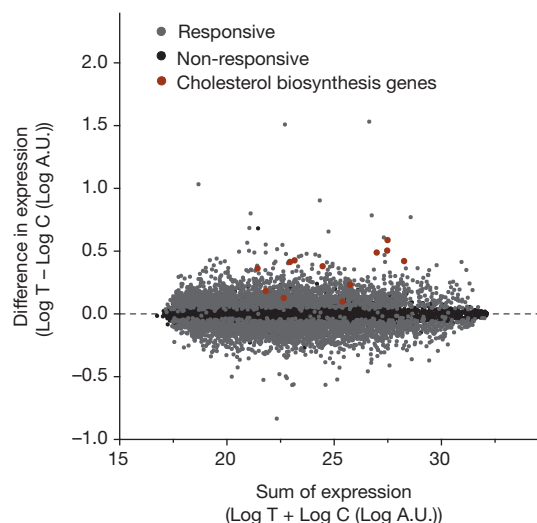


Figure 1 | Simvastatin treatment alters transcript expression in LCLs. Log change in expression following simvastatin- and control-exposed lymphoblastoid cell lines ($n = 480$) displayed as a function of the log sum of expression traits. Grey, genes for which expression was significantly changed in response to simvastatin exposure ($n = 5,509$ genes, 0.12 ± 0.08 mean absolute log₂ change \pm s.d., $q < 0.0001$); black, genes for which expression was not significantly changed ($n = 4,686$); red, genes in the cholesterol biosynthesis pathway, all of which exhibited significant changes in expression. A.U., arbitrary units.

¹Sage Bionetworks, 1100 Fairview Avenue North, Seattle, Washington 98109, USA. ²Department of Human Genetics, University of Chicago, 920 East 58th Street, Chicago, Illinois 60637, USA. ³Children's Hospital Oakland Research Institute, 5700 Martin Luther King Jr Way, Oakland, California 94609, USA. ⁴Department of Genome Sciences, University of Washington, 3720 15th Avenue Northeast, Seattle, Washington 98195, USA. ⁵Department of Genetics, University of Pennsylvania, 415 Curie Boulevard, Philadelphia, Pennsylvania 19103, USA. ⁶Center for Cardiovascular Disease Prevention, Division of Preventative Medicine, Brigham and Women's Hospital, 900 Commonwealth Drive, Boston, Massachusetts 02115, USA. ⁷Department of Medicine, Division of Clinical Pharmacology, Vanderbilt University Medical Center, 23rd Avenue South, Nashville, Tennessee 37232, USA. ⁸Institute for Translational Genomics and Population Sciences, Los Angeles BioMedical Research Institute at Harbor-UCLA Medical Center, 1124 West Carson Street, Torrance, California 90502, USA. ⁹Clinical Trial Service Unit and Epidemiological Studies Unit, University of Oxford, Richard Doll Building, Old Road Campus, Roosevelt Drive, Oxford OX3 7LF, UK. ¹⁰Department of Statistics, Eckhart Hall, 5734 South University Avenue, University of Chicago, Chicago, Illinois 60637, USA. [†]Present addresses: Biostatistics and Bioinformatics Department and Department of Statistical Science, Duke University, Durham, North Carolina, USA (B.E.E.); Adaptive Biotechnologies, Seattle, Washington, USA (M.J.R.).

*These authors contributed equally to this work.

steroid biosynthesis, consistent with the mechanism responsible for the lipid-lowering response to statin, and a decrease in expression of genes involved in RNA splicing, consistent with evidence for statin regulation of alternative splicing of genes involved in cellular cholesterol homeostasis²² (Supplementary Fig. 1).

We first identified eQTLs without considering whether they interact with simvastatin exposure. We computed Bayes factors²³ to quantify evidence for the association between every single-nucleotide polymorphism (SNP) and the expression level of each gene, and we used permutations to estimate FDRs (see Methods). This analysis identified 4,590 genes with *cis*-eQTLs, defined as eQTLs within 1 megabase (Mb) of the gene's transcription start or end site (FDR = 1%, \log_{10} Bayes factor ≥ 3.24 , Supplementary Table 1). Statistical power to detect eQTLs was substantially increased by controlling for known covariates and unknown confounders (represented by principal components of the gene expression data^{24,25}) and by testing for association with expression traits averaged across paired simvastatin- and control-exposed samples to reduce measurement error (Supplementary Table 2 and Supplementary Fig. 2). Our analysis also identified 98 *trans*-eQTLs at the same stringent FDR (FDR = 1%, \log_{10} Bayes factor ≥ 7.20 , Supplementary Table 3).

To identify eQTLs that interact with simvastatin exposure (that is, eQTLs with different effects in control- versus simvastatin-exposed samples, or differential eQTLs), we used two approaches¹⁴: first, univariate association mapping of log fold expression change between paired control- and simvastatin-exposed samples; and second, bivariate association mapping of paired control- and simvastatin-exposed samples. This bivariate approach aims to improve power and interpretability by explicitly distinguishing among different modes of interaction (see

Methods), which the univariate approach does not distinguish. The univariate approach identified differential *cis*-eQTLs for four genes: *GATM*, *RSRC1*, *VPS37D* and *OR11L1* (FDR = 20%, \log_{10} Bayes factor ≥ 4.9 , Supplementary Tables 4 and 5). No differential *trans*-eQTLs were identified at an FDR of 20%, so *trans* analyses were not pursued further (see Supplementary Table 6 for top differential *trans*-eQTLs). The bivariate approach identified differential *cis*-eQTLs for six genes (FDR = 20%, \log_{10} Bayes factor ≥ 5.1 ; Supplementary Tables 4 and 7, Supplementary Fig. 3 and Supplementary Data), including two genes that were not identified in the univariate analysis: *ATP5SL* and *ITFG2*. Both *GATM* and *VPS37D* had significantly stronger eQTL associations under simvastatin-exposed conditions in comparison to control, whereas the other four genes had significantly stronger eQTL associations under control-exposed conditions (Fig. 2a, Supplementary Table 4 and Supplementary Fig. 3). As in similar studies^{12–14,17}, we found many fewer differential eQTLs than stable eQTLs, or SNPs with similar effects across both conditions. The finding of relatively few gene by exposure interactions, and of relatively modest effect sizes of those interactions, seems remarkably consistent across studies regardless of method (including family-based comparisons), exposure, sample size, sample source, or the number of stable eQTLs detected. We focus further analysis on our most significant differential association from the bivariate model, the *GATM* locus, for which we observed stronger evidence for eQTL association after statin exposure and for which there was evidence for biological relevance to pathways involved in lipoprotein metabolism and myopathy (see Supplementary data).

GATM encodes glycine amidinotransferase, an enzyme that is required for the synthesis of creatine. We observed evidence for differential eQTL

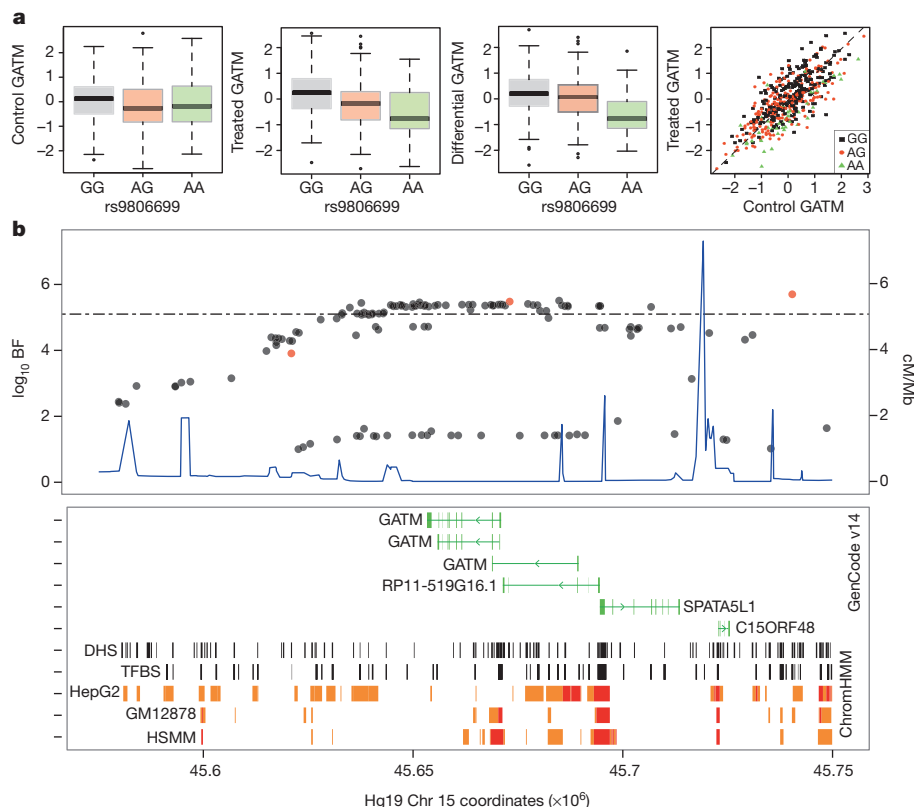


Figure 2 | Treatment-specific QTL associated with *GATM* expression. **a**, Association of rs9806699 with quantile normalized *GATM* expression levels following control exposure (left panel, not significant); simvastatin exposure (middle left panel, \log_{10} Bayes factor (BF) = 5.1, effect size = -0.43); fold change (middle right panel, \log_{10} BF = 5.7, effect size = -0.40); control versus simvastatin-exposed *GATM* expression (right panel; black, GG, $n = 225$; red, GA, $n = 207$; green, AA, $n = 48$). Box height and whiskers are described in Supplementary Methods. **b**, Top panel, SNPs associated with *GATM*

expression (\log_{10} BF, left y axis); SNPs associated with statin-induced myopathy (red); significance threshold (dotted line) recombination rates in centimorgans (cM) per megabase (Mb) (blue, right y axis). Bottom panel, transcribed genes (green); DNase I hypersensitive (DHS) sites and transcription factor binding sites (TFBS; black); predicted chromosomal enhancers (orange) and promoters (red) as identified in hepatocyte (HepG2), lymphoblastoid (GM12878), and myocyte (HSM) cell lines, using ChromHMM software (see Methods).

Table 1 | Associations of SNPs at the *GATM* locus with statin-induced myopathy.

	Cases (n)	Controls (n)	SNP	Position	LD (r^2)	MAF (cases)	MAF (controls)	Effect size	P value
Marshfield	72	220	rs9806699	Chr 15: 43,527,684	1.0	0.21	0.30	0.61 (0.39–0.95)	3.2×10^{-2}
	72	220	rs1719247	Chr 15: 43,408,027	0.76	0.19	0.29	0.59 (0.36–0.93)	2.4×10^{-2}
	72	220	rs1346268	Chr 15: 43,460,321	0.80	0.21	0.29	0.66 (0.41–1.02)	6.4×10^{-2}
SEARCH	100	4,021	rs1719247	Chr 15: 43,408,027	0.70	0.17	0.25	0.61 (0.42–0.88)	1.0×10^{-2}
	100	4,029	rs1346268	Chr 15: 43,460,321	0.74	0.18	0.26	0.62 (0.43–0.90)	1.0×10^{-2}
Meta-analysis			rs1719247	Chr 15: 43,408,027		0.18	0.25	0.60 (0.45–0.81)	7.0×10^{-4}
			rs1346268	Chr 15: 43,460,321		0.19	0.26	0.63 (0.48–0.84)	1.8×10^{-3}

Differential eQTL associations with *GATM* expression in CAP were: \log_{10} Bayes factor = 6.22 (rs9806699), \log_{10} Bayes factor = 4.35 (rs1719247), and \log_{10} Bayes factor = 5.96 (rs1346268). All SNPs were in Hardy–Weinberg equilibrium in these populations. Effect size reported as odds ratio with 95% confidence interval in parentheses. Chr, chromosome; LD, linkage disequilibrium with respect to the top differential eQTL SNP, rs9806699 based on Pearson correlation (r^2).

association with *GATM* (\log_{10} Bayes factor > 5.1) across a group of 51 SNPs within the *GATM* locus that are in linkage disequilibrium (chromosome 15: 45627979–45740392, hg19, $r^2 = 0.85–0.99$, $n = 587$). The most significant differential eQTL association was observed with SNP rs9806699 (minor allele frequency (MAF) = 0.32), for which we observed stronger evidence for an association with *GATM* expression following simvastatin exposure (\log_{10} Bayes factor = 5.1, effect size = -0.43) than following control exposure (\log_{10} Bayes factor = 0.52, effect size = -0.17 , Fig. 2a). SNPs at this locus also had a stable association with expression of a neighbouring gene, *SPATA5L1* (differential eQTL rs9806699 \log_{10} Bayes factor = -0.33 , stable eQTL rs9806699 \log_{10} Bayes factor = 21.75, Supplementary Fig. 4). This locus has been shown previously to be associated with reduced glomerular filtration rate (GFR)²⁶ with a small effect size (<1%). This association was specific to GFR as estimated from plasma creatinine but not from cystatin C, a second biomarker of renal function, suggesting that the association was related to variation in creatinine production rather than renal elimination. We found evidence for SNP differential association with *GATM* that spans the *GATM* coding region and includes multiple SNPs located within DNase I hypersensitive sites, active promoters and several alternative *GATM* transcription start sites (Fig. 2b).

Phosphorylation of creatine, the primary downstream product of *GATM* activity, is a major mechanism for energy storage in muscle and is mediated by creatine kinase, the primary plasma biomarker of statin-induced myopathy. To test the relationship of this locus with statin-induced myopathy, we examined the association of the *GATM* differential eQTL locus with statin-induced myopathy in a population-based cohort comprised of 72 cases of myopathy and 220 matched controls (Marshfield cohort)²⁷. In this cohort, we observed that the minor allele at the *GATM* differential eQTL locus was associated with reduced incidence of statin-induced myopathy (odds ratio = 0.61, 95% confidence interval = 0.39–0.95, $P = 0.03$; Table 1). This association was replicated in a second cohort consisting of 100 cases of myopathy identified within the Study of Effectiveness of Additional Reductions in Cholesterol and Homocysteine (SEARCH; <http://clinicaltrials.gov/ct2/show/NCT00124072>)¹⁰ (odds ratio for rs1719247 = 0.61, confidence interval = 0.42–0.88, $P = 0.01$; $r^2 = 0.70$ to rs9806699; Table 1). Meta-analysis of these two cohorts showed an overall odds ratio of 0.60 (confidence interval = 0.45–0.81, $P = 6 \times 10^{-4}$, \log_{10} Bayes factor = 1.5, Table 1). As myopathy is defined in part through elevation in plasma creatine kinase concentrations, we also tested for a direct association of this locus with this enzyme in statin-treated populations in which myopathy was not observed. Within CAP (40 mg per day simvastatin exposure for 6 weeks), no association of rs9806699 was observed with plasma creatine kinase either before simvastatin exposure ($n = 575$, $P = 0.83$) or following exposure ($n = 574$, $P = 0.48$). This lack of association was confirmed in a second statin study (Justification for the Use of Statins in Prevention: an Intervention Trial Evaluating Rosuvastatin (JUPITER) trial, 20 mg per day rosuvastatin, median follow-up = 1.9 years; <http://clinicaltrials.gov/show/NCT00239681>) both before rosuvastatin exposure ($n = 8,504$, $P = 0.54$) and after treatment ($n = 3,052$, $P = 0.83$)³. These findings suggest that the observed association of the *GATM* locus with risk for statin-induced myopathy is independent of an association with plasma creatine kinase. Although the present studies do not address

the mechanism for the link between reduced *GATM* expression and protection from statin-induced myopathy, it is thought that diminished capacity for phosphocreatine storage modifies cellular energy storage and adenosine monophosphate-activated protein kinase (AMPK) signalling^{28,29} in a manner that is protective against cellular stress as induced by glucose deprivation²⁹ or, potentially, by cholesterol depletion. Given that myocellular creatine stores are predominantly derived from renal and hepatic creatine biosynthesis, these results raise the possibility that statins may predispose to muscle toxicity in part through metabolic effects in the liver, the major site of statin's pharmacologic actions (Supplementary Fig. 5). Conversely, the finding of severe myopathy in two cases of extreme genetic *GATM* deficiency³⁰ suggests that this protective effect may be overcome if creatine synthesis is insufficient to support myocellular energy needs.

Given the influence of statin exposure on regulation of *GATM* expression, we next tested whether *GATM* may modulate sterol-mediated changes in cholesterol homeostasis. Knockdown of *GATM* in hepatocyte-derived cell lines (HepG2 and Huh7) resulted in reduced upregulation of SREBP-responsive genes (*HMGCR*, *LDLR* and *SREBF2*) by sterol depletion (Fig. 3a). Moreover, *GATM* knockdown decreased media accumulation of apolipoprotein B (apoB), the major structural protein of LDL, in both cell lines ($P < 0.05$; Fig. 3b), but did not alter levels of apoAI, the major structural protein in high density lipoproteins (HDLs),

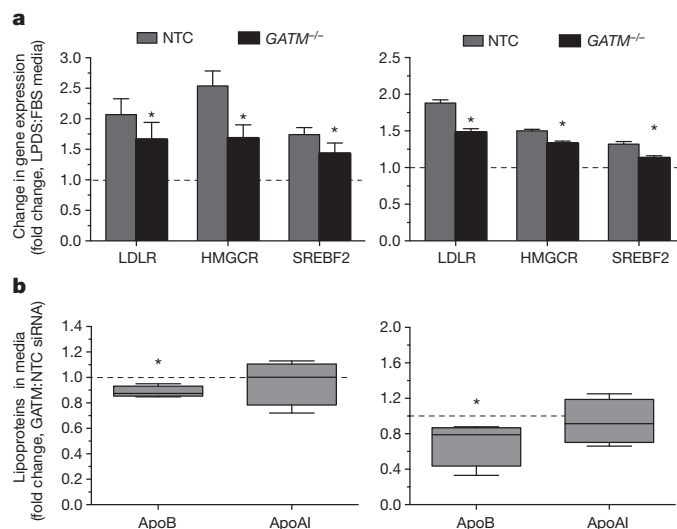


Figure 3 | *GATM* knockdown attenuated sterol-mediated induction of expression of SREBP-responsive genes. **a**, Changes in transcript concentrations following sterol depletion through 24 h exposure to lipoprotein deficient serum (LPDS)-containing media versus standard FBS-containing media in hepatocyte-derived HepG2 (left, $n = 12$) and Huh7 (right, $n = 12$) cell lines. Asterisk indicates $P < 0.05$ for the comparison of *GATM* versus non-targeting control (NTC) siRNA treated cells. **b**, Fold changes in accumulation of apolipoprotein B (ApoB) and apolipoprotein AI (ApoAI) in media after gene knockdown with *GATM* versus (NTC) siRNA in HepG2 cells (left, $n = 6–10$) or Huh7 cells (right, $n = 4–6$) under standard culture conditions. Experiments repeated 2–3 times with 2–8 biological replicates each. Data presented as average values. Error bars, s.e.m.

Fig. 3b). An effect of *GATM* deficiency on cholesterol and lipoprotein metabolism is supported further by a recent study describing reduced plasma cholesterol concentrations in *GATM* knockout mice²⁸.

In summary, this study has provided evidence that functionally significant genetic effects can be discovered using a novel cell-based screen for gene-by-treatment effects on transcriptional expression. This approach has led to the identification of *GATM* as a genetic locus associated with statin-induced myopathy, and as a potential link between cellular cholesterol homeostasis and energy metabolism.

METHODS SUMMARY

Gene expression levels were measured using the Illumina Human-Ref8v3 beadarray in 480 lymphoblastoid cell lines derived from European American participants in CAP, a 6-week trial of simvastatin (40 mg per day), after 24 h exposure to 2 μ M activated simvastatin or control buffer. Treatment-specific effects were modelled after adjustment for known covariates and unknown confounding variables using linear regression, and eQTLs were identified using the BIMBAM software after imputing the available genotypes. Differential eQTLs were identified using the BIMBAM software (univariate test) as well as linear models of differential association (bivariate tests). Associations with myopathy were tested in two cohorts containing cases of statin-induced myopathy (definitions of myopathy in Marshfield and SEARCH are described in the Supplementary Methods), and associations with plasma creatine kinase were tested in two statin trials that did not contain myopathy cases (CAP and JUPITER). Media accumulation of apolipoproteins was measured by enzyme-linked immunosorbent assay (ELISA) and gene expression was measured by quantitative PCR in hepatoma cell lines (HepG2 and Huh7) after *GATM* knockdown as achieved by 48 h transfection of Ambion Silence Select short interfering RNA (siRNA) or non-targeting control. See full Methods for complete details.

Full Methods and any associated references are available in the online version of the paper.

Received 11 April; accepted 26 July 2013.

Published online 28 August 2013.

1. Cholesterol Treatment Trialists' (CTT) Collaborators. Efficacy and safety of cholesterol-lowering treatment: prospective meta-analysis of data from 90,056 participants in 14 randomised trials of statins. *Lancet* **366**, 1267–1278 (2005).
2. Simon, J. A. *et al.* Phenotypic predictors of response to simvastatin therapy among African-Americans and Caucasians: the Cholesterol and Pharmacogenetics (CAP) Study. *Am. J. Cardiol.* **97**, 843–850 (2006).
3. Ridker, P. M. *et al.* Rosuvastatin to prevent vascular events in men and women with elevated C-reactive protein. *N. Engl. J. Med.* **359**, 2195–2207 (2008).
4. Fernandez, G., Spatz, E. S., Jablecki, C. & Phillips, P. S. Statin myopathy: a common dilemma not reflected in clinical trials. *Cleve. Clin. J. Med.* **78**, 393–403 (2011).
5. Rajpathak, S. N. *et al.* Statin therapy and risk of developing type 2 diabetes: a meta-analysis. *Diabetes Care* **32**, 1924–1929 (2009).
6. Teslovich, T. M. *et al.* Biological, clinical and population relevance of 95 loci for blood lipids. *Nature* **466**, 707–713 (2010).
7. Barber, M. J. *et al.* Genome-wide association of lipid-lowering response to statins in combined study populations. *PLoS ONE* **5**, e9763 (2010).
8. Chasman, D. I. *et al.* Pharmacogenetic study of statin therapy and cholesterol reduction. *J. Am. Med. Assoc.* **291**, 2821–2827 (2004).
9. Trompet, S. *et al.* Replication of LDL GWAS hits in PROSPER/PHASE as validation for future (pharmacogenetic) analyses. *BMC Med. Genet.* **12**, 131 (2011).
10. The SEARCH Collaborative Group. SLCO1B1 variants and statin-induced myopathy—a genomewide study. *N. Engl. J. Med.* **359**, 789–799 (2008).
11. Brem, R. B., Storey, J. D., Whittle, J. & Kruglyak, L. Genetic interactions between polymorphisms that affect gene expression in yeast. *Nature* **436**, 701–703 (2005).
12. Grundberg, E. *et al.* Global analysis of the impact of environmental perturbation on cis-regulation of gene expression. *PLoS Genet.* **7**, e1001279 (2011).
13. Romanoski, C. E. *et al.* Systems genetics analysis of gene-by-environment interactions in human cells. *Am. J. Hum. Genet.* **86**, 399–410 (2010).
14. Maranville, J. C. *et al.* Interactions between glucocorticoid treatment and cis-regulatory polymorphisms contribute to cellular response phenotypes. *PLoS Genet.* **7**, e1002162 (2011).
15. Smirnov, D. A. *et al.* Genetic variation in radiation-induced cell death. *Genome Res.* **21**, 332–339 (2011).

16. Brown, M. S. & Goldstein, J. L. The SREBP pathway: regulation of cholesterol metabolism by proteolysis of a membrane-bound transcription factor. *Cell* **89**, 331–340 (1997).
17. Morley, M. *et al.* Genetic analysis of genome-wide variation in human gene expression. *Nature* **430**, 743–747 (2004).
18. Stranger, B. E. *et al.* Population genomics of human gene expression. *Nature Genet.* **39**, 1217–1224 (2007).
19. Caliskan, M., Cusanovich, D. A., Ober, C. & Gilad, Y. The effects of EBV transformation on gene expression levels and methylation profiles. *Hum. Mol. Genet.* **20**, 1643–1652 (2011).
20. Choy, E. *et al.* Genetic analysis of human traits *in vitro*: drug response and gene expression in lymphoblastoid cell lines. *PLoS Genet.* **4**, e1000287 (2008).
21. Mangravite, L. M. *et al.* Combined influence of LDLR and HMGCR sequence variation on lipid-lowering response to simvastatin. *Arterioscler. Thromb. Vasc. Biol.* **30**, 1485–1492 (2010).
22. Medina, M. W. *et al.* Coordinately regulated alternative splicing of genes involved in cholesterol biosynthesis and uptake. *PLoS ONE* **6**, e19420 (2011).
23. Stephens, M. & Balding, D. J. Bayesian statistical methods for genetic association studies. *Nature Rev. Genet.* **10**, 681–690 (2009).
24. Leek, J. T. & Storey, J. D. Capturing heterogeneity in gene expression studies by surrogate variable analysis. *PLoS Genet.* **3**, e161 (2007).
25. Innocenti, F. *et al.* Identification, replication, and functional fine-mapping of expression quantitative trait loci in primary human liver tissue. *PLoS Genet.* **7**, e1002078 (2011).
26. Köttgen, A. *et al.* Multiple loci associated with indices of renal function and chronic kidney disease. *Nature Genet.* **41**, 712–717 (2009).
27. Mareedu, R. K. *et al.* Use of an electronic medical record to characterize cases of intermediate statin-induced muscle toxicity. *Prev. Cardiol.* **12**, 88–94 (2009).
28. Choe, C. U. *et al.* L-arginine:glycine amidinotransferase deficiency protects from metabolic syndrome. *Hum. Mol. Genet.* **22**, 110–123 (2013).
29. Ide, T. *et al.* GAMT, a p53-inducible modulator of apoptosis, is critical for the adaptive response to nutrient stress. *Mol. Cell* **36**, 379–392 (2009).
30. Edvardson, S. *et al.* L-arginine:glycine amidinotransferase (AGAT) deficiency: clinical presentation and response to treatment in two patients with a novel mutation. *Mol. Genet. Metab.* **101**, 228–232 (2010).

Supplementary Information is available in the online version of the paper.

Acknowledgements This project was funded by a grant from the US National Institutes of Health (NIH), U01 HL69757. B.E.E. was funded through the Bioinformatics Research Development Fund, supported by K. and G. Gould and NIH grant K99/R00 HG006265. M.S. was funded by NIH grant HG002585. We acknowledge the efforts of T. Kitchner and R. Mareedu for case validation in the Marshfield cohort. SEARCH was supported by the Medical Research Council, British Heart Foundation, National Health Service Genetic Knowledge Park, Centre National de Génotypage and Merck. The Heart Protection Study was funded by grants from the Medical Research Council, British Heart Foundation, Roche Vitamins and Merck. J.C.H. acknowledges support from the BHF Centre of Research Excellence, Oxford, UK. Genetic analysis in JUPITER was funded by a grant from AstraZeneca to D.I.C. and P.M.R.

Author Contributions L.M.M. designed experiment and analyses, generated samples, performed analyses, and wrote the manuscript. B.E.E. designed and performed analyses and wrote the manuscript. C.D.B. performed analyses of ENCODE data. B.H.M. designed and performed correlation analyses. J.D.S., M.J.R. and D.A.N. generated expression and genotype data. M.W.M. and D.N. designed, performed and analysed functional experiments. B.H. and H.S. developed and performed the imputation methodology. R.A.W., Q.F., J.D.S., M.J.R. and D.A.N. collected and genotyped the myopathy cohort from the Marshfield clinic and performed association analyses. J.C.H., S.P., J.A. and R.C. collected and genotyped myopathy cohort from the SEARCH trial and performed association analyses in that cohort along with the Heart Protection Study. J.I.R. and Y.-D.I.C. measured creatine kinase in CAP. D.I.C. and P.M.R. measured creatine kinase and performed related analyses in JUPITER. M.S. supervised, designed and contributed to analyses, and participated in manuscript development. R.M.K. supervised the project and participated in experimental design and manuscript development. M.S. and R.M.K. co-directed this project.

Author Information The gene expression data have been deposited in the Gene Expression Omnibus (GEO) under accession number GSE36868 and in Synapse (<https://www.synapse.org/>) under accession number syn299510. Code and analytical output complementary to this analysis are also provided through Synapse (<https://www.synapse.org/#!Synapse:syn299510>). The genotype data have been deposited in the database for genotypes and phenotypes (dbGaP, <http://www.ncbi.nlm.nih.gov/gap>) under accession number phs000481. The full set of eQTLs identified in our study is available at <http://eqtl.uchicago.edu>. Reprints and permissions information is available at www.nature.com/reprints. The authors declare no competing financial interests. Readers are welcome to comment on the online version of the paper. Correspondence and requests for materials should be addressed to L.M.M. (lara.mangravite@sagebase.org), M.S. (mstephens@uchicago.edu) or R.M.K. ([rakrauss@chori.org](mailto:rkrauss@chori.org)).

METHODS

In vitro simvastatin exposure of lymphoblastoid cell lines. Lymphoblastoid cell lines (LCLs), immortalized by Epstein–Barr virus transformation of lymphocytes isolated from whole blood³¹, were derived from European American participants in the CAP trial, a 6-week simvastatin trial of 40 mg per day (Supplementary Table 8)². Simvastatin was provided by Merck, converted to active form (beta-hydroxy simvastatin acid, SVA) and quantified by liquid chromatography–tandem mass spectrometry as described previously²¹. LCLs were normalized to a uniform cell density and exposed to 2 μ M SVA (simvastatin-exposed) or control buffer (control-exposed) for 24 h as described previously²¹. This concentration was selected by assessing dose–response effects on expression profiles ($n = 8$ LCLs, 4 doses), wherein a more robust change in expression profiles was observed with 2 μ M simvastatin exposure (7.8% of genes, $q = 0.001$) than lower doses ($<0.1\%$ of genes for 0.02 μ M or 0.2 μ M, $q = 0.001$, data not shown). Pre-experiment cell density was recorded as a surrogate for cell growth rate. After exposure, cells were lysed in RNeasy lysis buffer (Qiagen), and RNA was isolated using the Qiagen miniprep RNA isolation kit with column DNase treatment.

Expression profiling and differential expression analysis. RNA quality and quantity were assessed using a Nanodrop ND-1000 spectrophotometer and an Agilent Bioanalyzer, respectively. Paired RNA samples, selected based on RNA quality and quantity, were amplified and labelled with biotin using the Illumina TotalPrep-96 RNA amplification kit, hybridized to Illumina HumanRef-8v3 beadarrays (Illumina), and scanned using an Illumina BeadXpress reader. Data were read into GenomeStudio and samples were selected for inclusion based on quality-control criteria: signal to noise ratio (95th:5th percentiles); matched gender between sample and data; and average correlation of expression profiles within three standard deviations of the within-group mean ($r = 0.99 \pm 0.0093$ for control-exposed and $r = 0.98 \pm 0.0071$ for simvastatin-exposed beadarrays). In total, viable expression data were obtained from 1,040 beadarrays including 480 sets of paired samples for 10,195 genes. Genes were annotated through biomaRt from ensembl Build 54 (<http://may2009.archive.ensembl.org/biomart/martview>). Treatment-specific effects were modelled from the data following adjustment for known covariates using linear regression³². False discovery rates were calculated for differentially expressed transcripts using the qvalue package³³. Ontological enrichment in differentially expressed gene sets was measured using GSEA (1,000 permutations by phenotype) using gene sets representing Gene Ontology biological processes as described in the Molecular Signatures v3.0 C5 Database (10–500 genes per set)³⁴.

Expression QTL mapping. For association mapping, we use a Bayesian approach²³ implemented using the software package BIMBAM³⁵ that is robust to poor imputation and small minor-allele frequencies³⁶. Gene expression data were normalized as described in the Supplementary Methods for the control-treated (C480) and simvastatin-treated (T480) data and used to compute $D480 = T480 - C480$ and $S480 = T480 + C480$, where T480 represents the adjusted simvastatin-treated data and C480 represents the adjusted control-treated data. SNPs were imputed as described in the Supplementary Methods. To identify eQTLs and differential eQTLs, we measured the strength of association between each SNP and gene in each analysis (control-treated, simvastatin-treated, averaged, and difference) using BIMBAM with default parameters³⁵. BIMBAM computes the Bayes factor for an additive or dominant response in expression data as compared with the null, which is that there is no correlation between that gene and that SNP. BIMBAM averages the Bayes factor over four plausible prior distributions on the effect sizes of additive and dominant models. We used a permutation analysis (see Supplementary Methods) to determine cutoffs for eQTLs in the averaged analysis (S480) at an FDR of 1% for *cis*-eQTLs (\log_{10} Bayes factor > 3.24) and *trans*-eQTLs (\log_{10} Bayes factor > 7.20). For *cis*-eQTLs, we considered the largest \log_{10} Bayes factor above the *cis*-cutoff for any SNP within 1 Mb of the transcription start site or the transcription end site of the gene under consideration. For *trans*-eQTLs, we considered the largest \log_{10} Bayes factor above the *trans*-cutoff for any SNP, and if that SNP was in the *cis*-neighbourhood of the gene being tested, we ignored any potential *trans*-associations; there were 6,130 genes for which the SNP with the largest \log_{10} Bayes factor was not in *cis* with the associated gene. Correspondingly, we only considered those 6,130 genes when computing the permutation-based FDR for the *trans*-associations.

Differential expression QTL mapping. We define *cis*-SNPs as being within 1 Mb of the transcription start site or end site of that gene. To identify differential eQTLs, we first computed associations between all SNPs and the log fold change using BIMBAM as above.

We then considered a larger set of models for differential eQTLs. The associations for the genes in Supplementary Fig. 3 indicate that there are a few possible patterns of differential association. Although these patterns may have different mechanistic or phenotypic interpretations, they are not distinguished by a test of log fold change. We used the interaction models introduced in another paper¹⁴ to compute the statistical support (assessed with Bayes factors) for the four alternative eQTL models described above versus the null model (no association with genotype).

These methods are based on a bivariate normal model for the treated data (T) and control-treated data (U). Note that simply quantile transforming T and U to a standard normal distribution is not sufficient to ensure that they are jointly bivariate normal, and so we used the following more extensive normalization procedure. Let $D = qT - qU$ and $S = qT + qU$, where q indicates that the vector following it has been quantile normalized. We then quantile normalize and scale D and S to produce $S = (\sigma_S qS)$ and $D = (\sigma_D qD)$, where σ_S , σ_D are robust estimates of the standard deviations of S and D , respectively (specifically, they are the median absolute deviation multiplied by 1.4826). Note that this transformation ensures that S and D are univariate normal. Furthermore, they are approximately independent, which ensures that they are also bivariate normal. Finally, let $U = 0.5(S - D)$ and $T = 0.5(S + D)$.

The Bayes factor when the eQTL effect is identical in the two conditions (model 1) uses the linear model $L(S \sim D + g)$, where g is the vector of genotypes at a single SNP. The Bayes factor when the eQTL is only present in the control-treated samples (model 2) uses the model $L(U \sim T + g)$. The Bayes factor when the eQTL is only present in the simvastatin-treated samples (model 3) uses the model $L(T \sim U + g)$. The Bayes factor when the eQTL effect is in the same direction but unequal in strength (model 4) uses the model $L(D \sim S + g)$. We averaged each Bayes factor for each gene and each *cis*-SNP over four plausible effect size priors (0.05, 0.1, 0.2 and 0.4).

To find eQTLs that interact with treatment (that is, those that conform best to one of the differential models 2–4, rather than the null model or the stable model) we defined an interaction Bayes factor (IBF) = $2(\text{Bayes factor}_2 + \text{Bayes factor}_3 + \text{Bayes factor}_4) / (3(\text{Bayes factor}_1 + 1))$, where Bayes factor_i denotes the Bayes factor for model i compared with the null model (the 1 in the denominator represents the null model Bayes factor). Large values of the IBF represent strong support for at least one interaction model (2–4) compared with the two non-interacting models (0–1), and hence strong support for a differential association.

Association with statin-induced myopathy. For the Marshfield Cohort³⁷, cases of myopathy were identified from electronic medical records of patients treated at the Marshfield Clinic (Wisconsin, USA) using a combination of automated natural language processing and manual review as described previously³⁷. Seventy-two cases of incipient myopathy (creatinine kinase concentrations greater than 3-fold normal concentrations, with evidence in the charts of muscle complaints) were identified for which patients were not also undergoing treatment with concomitant drugs known to increase incidence of statin-induced myopathy (fibrates or niacin). Controls were matched based on statin exposure, age and gender. This study was approved by the Marshfield Clinic institutional review board. The study population included residents living in Central and Northern Wisconsin, served by the Marshfield Clinic, a large multi-specialty group practice³⁷. For the SEARCH and Heart Protection Study Collaborative Groups^{10,38}, a total of 100 myopathy cases were identified from participants with genotyping data in the SEARCH trial, including 39 definite myopathy cases (creatinine kinase $> 10 \times$ upper limit of normal (ULN) with muscle symptoms) and 61 incipient myopathy cases (defined as creatinine kinase ≥ 5 times baseline value and alanine transaminase ≥ 1.7 times baseline value and creatinine kinase $> 3 \times$ ULN). Genotypes were available from the Illumina Human610-Quad Beadchip for 25 myopathy cases (12% of which had definite myopathy) and from the Illumina HumanHap300-Duo BeadChip for 75 myopathy cases (48% of which had definite myopathy). Genotypes for rs9806699 were only available for the 25 cases genotyped on the Illumina Human610-Quad Beadchip, so proxy SNPs were used for analyses in Table 1. Analyses of rs9806699 are provided in Supplementary Table 9. All myopathy cases were compliant with statin therapy (95 myopathy cases occurred while the patient was taking simvastatin 80 mg daily, and 5 cases while taking simvastatin 20 mg daily). Controls were identified from the SEARCH Study as well as from the Heart Protection Study (where considerably more participants had been genotyped). Controls from the Heart Protection Study had similar baseline characteristics to those in the SEARCH Study and inclusion of this large number of additional controls improved statistical power. Multi-centre ethics approval was obtained from the South East Research Ethics Committee for the SEARCH study, and from the local ethics committees covering each of the 69 UK hospitals involved in the Heart Protection Study. Genetic associations were determined by chi-squared analysis using an additive model. A meta-analysis was performed using a random effects model and, for the Bayesian analysis, we used an expected effect size of 0.2. Associations of rs9806699 with plasma creatinine kinase in the CAP² and JUPITER³ trials were also assessed using linear regression. The CAP trial (ClinicalTrials.gov number NCT00451828) was approved by the institutional review boards located at Children's Hospital Oakland Research Institute (Oakland, California) and all enrollment sites. The JUPITER trial (ClinicalTrials.gov number NCT00239681) was approved by the Institutional Review Board of Brigham and Women's Hospital. Informed consent was obtained from all participants in all trials.

Genomic characterization of GATM locus. *Cis*-regulatory elements were downloaded from the ChromHMM (ref. 39) track of the UCSC Genome Browser (ref. 40) and aggregated manually.

Functional analysis of candidate genes. *GATM* knockdown was achieved by 48 h transfection of Ambion Silence Select siRNA or non-targeting control into 80,000 HepG2 or Huh7 cells per well in 12-well plates. To assess the influence of sterol depletion, cell culture medium was replaced with medium containing 10% lipoprotein deficient serum (Hyclone) or fetal bovine serum (Omega Scientific) at 24 h after transfection. All samples were harvested 48 h post transfection. Transcript levels were quantified by quantitative PCR and normalized to *CLPTM*. Cell culture medium was taken from all samples at the time of collection, and ApoB (MP Biomedicals) and ApoAI (Meridian Life Sciences) were quantified in triplicate by sandwich-style ELISA. Samples with a coefficient of variation greater than 15% were subjected to repeat measurement.

31. Pressman, S. & Rotter, J. I. Epstein-Barr virus transformation of cryopreserved lymphocytes: prolonged experience with technique. *Am. J. Hum. Genet.* **49**, 467 (1991).
32. Meacham, B. H., Nelson, P. S. & Storey, J. D. Supervised normalization of microarrays. *Bioinformatics* **26**, 1308–1315 (2010).
33. Storey, J. D. A direct approach to false discovery rates. *J. R. Stat. Soc.* **64**, 479–498 (2002).
34. Subramanian, A., Kuehn, H., Gould, J., Tamayo, P. & Mesirov, J. P. GSEA-P: a desktop application for Gene Set Enrichment Analysis. *Bioinformatics* **23**, 3251–3253 (2007).
35. Servin, B. & Stephens, M. Imputation-based analysis of association studies: candidate regions and quantitative traits. *PLoS Genet.* **3**, e114 (2007).
36. Guan, Y. & Stephens, M. Practical issues in imputation-based association mapping. *PLoS Genet.* **4**, e1000279 (2008).
37. Wilke, R. A. *et al.* Identifying genetic risk factors for serious adverse drug reactions: current progress and challenges. *Nature Rev. Drug Discov.* **6**, 904–916 (2007).
38. Hopewell, J. C. *et al.* Impact of common genetic variation on response to simvastatin therapy among 18 705 participants in the Heart Protection Study. *Eur. Heart J.* **34**, 982–992 (2013).
39. Ernst, J. & Kellis, M. ChromHMM: automating chromatin-state discovery and characterization. *Nature Methods* **9**, 215–216 (2012).
40. Kent, W. J. *et al.* The human genome browser at UCSC. *Genome Res.* **12**, 996–1006 (2002).

HELQ promotes RAD51 paralogue-dependent repair to avert germ cell loss and tumorigenesis

Carrie A. Adelman¹, Rafal L. Lolo¹, Nicolai J. Birkbak², Olga Murina³, Kenichiro Matsuzaki¹, Zuzana Horejsi¹, Kalindi Parmar⁴, Valérie Borel¹, J. Mark Skehel⁵†, Gordon Stamp⁶, Alan D'Andrea⁴, Alessandro A. Sartori³, Charles Swanton^{7,8} & Simon J. Boulton¹

Repair of interstrand crosslinks (ICLs) requires the coordinated action of the intra-S-phase checkpoint and the Fanconi anaemia pathway, which promote ICL incision, translesion synthesis and homologous recombination (reviewed in refs 1, 2). Previous studies have implicated the 3'–5' superfamily 2 helicase HELQ in ICL repair in *Drosophila melanogaster* (MUS301 (ref. 3)) and *Caenorhabditis elegans* (HELQ-1 (ref. 4)). Although *in vitro* analysis suggests that HELQ preferentially unwinds synthetic replication fork substrates with 3' single-stranded DNA overhangs and also disrupts protein–DNA interactions while translocating along DNA^{5,6}, little is known regarding its functions in mammalian organisms. Here we report that HELQ helicase-deficient mice exhibit subfertility, germ cell attrition, ICL sensitivity and tumour predisposition, with *Helq* heterozygous mice exhibiting a similar, albeit less severe, phenotype than the null, indicative of haploinsufficiency. We establish that HELQ interacts directly with the RAD51 paralogue complex BCDX2 and functions in parallel to the Fanconi anaemia pathway to promote efficient homologous recombination at damaged replication forks. Thus, our results reveal a critical role for HELQ in replication-coupled DNA repair, germ cell maintenance and tumour suppression in mammals.

To examine the effect of HELQ deficiency in vertebrates, we generated a *Helq*^{ΔC}-deficient mouse strain that is truncated at the carboxy terminus of HELQ (Fig. 1a, b and Extended Data Fig. 1a, b) and results in loss of detectable HELQ protein (Fig. 1d and Extended Data Fig. 1c). Although *Helq*^{ΔC/ΔC} mice are viable (Fig. 1c), are born in normal Mendelian ratios and lack growth or developmental abnormalities (Extended Data Fig. 1d, e), breeding experiments with *Helq*^{ΔC/ΔC} mutant pairs revealed a fertility defect. Eight heterozygous and 8 homozygous pairs were mated continuously for 5–6 months, resulting in 320 offspring in the case of heterozygotes (an average of 6.1 litters and 40 pups each) but only 38 pups in the case of homozygotes (1.4 litters and 4.7 pups per pair). Mating of mutants to control animals revealed that females contribute more to this phenotype than males (Fig. 1e).

Consistent with a fertility defect, *Helq*^{ΔC/ΔC} testes were smaller than those of wild-type males (0.58% of body weight for wild type versus 0.38% for mutants (Fig. 1f)). Histological analysis of testes revealed many normal tubules but also regions of atrophy in the mutants (Fig. 1g and Extended Data Fig. 1g–l). Dysgenesis/atrophy was even more pronounced in *Helq*^{ΔC/ΔC} ovaries (Fig. 1g and Extended Data Fig. 1f). A possible stem cell origin was investigated as no particular subset of spermatocytes appeared affected (Extended Data Fig. 1g–l). Indeed, *Helq*^{ΔC/ΔC} adults had significantly fewer c-KIT (also known as KIT)⁺ spermatogonia than controls (Extended Data Fig. 2a, b). As atrophy was not linked to ageing (Extended Data Fig. 2c), a developmental origin was examined; tubules from 5-day-old wild-type mice contained sixfold more spermatogonia than mutants (Fig. 1h), indicating that atrophic

tubules in mutant adults may primarily arise from reduced spermatogonial stem cell pools during development.

The effect of HELQ deficiency during organismal ageing revealed that tumour-free survival was significantly reduced in *Helq* mutants (Fig. 1i and Extended Data Fig. 2d), with twice as many *Helq*^{ΔC/ΔC} mice developing two or more primary tumours in comparison to controls (Fig. 1j). Ovarian tumours (resembling granulosa and other sex cord stromal tumours; Extended Data Fig. 3b–f) and pituitary adenomas (Extended Data Fig. 3g–j) were the most prominent tumour types in female mice, with incidences of 40% in the case of ovarian tumours and 30% in the case of pituitary tumours (Fig. 1k). Unexpectedly, *Helq*^{+/ΔC} heterozygous females also presented with ovarian pathology similar to that of younger mutant females (Extended Data Fig. 2d). Pathology included cystic (4 out of 7 mice) and dysgenic/atrophic (5 out of 7) ovaries with few or no maturing follicles (7 out of 7) and luteinized stroma (2 out of 7). *Helq*^{+/ΔC} heterozygous females also frequently displayed pituitary (5 out of 7 mice), Harderian gland (3 out of 7) and gastrointestinal (3 out of 7) adenomas, polyps and hyperplasias. Although these phenotypes are less severe than observed in the *Helq*^{ΔC/ΔC} homozygous mice, the data reveal that loss of a single allele of *Helq* confers haploinsufficiency in mice.

The phenotype of *Helq*^{ΔC/ΔC} mice is similar to that observed in mouse models of Fanconi anaemia⁷. Haematopoietic stem and progenitor cell (HSPC) defects and sensitivity to ICLs are also hallmarks of Fanconi anaemia and were therefore examined in *Helq* mutants. Although bone marrow HSPCs from *Helq*^{ΔC/ΔC} mice exhibit hypersensitivity to the ICL agent mitomycin C (MMC; Extended Data Fig. 4a), *Helq*^{ΔC/ΔC} HSPCs were not compromised in numbers (Extended Data Fig. 4b, c), proliferative capacity (Extended Data Fig. 4d, e) or engraftment (Extended Data Fig. 4f–i). HELQ-deficient cells exhibited hypersensitivity to replication blocking agents such as MMC and camptothecin (CPT; Fig. 2a, b), but not to ionizing radiation or ultraviolet radiation (Fig. 2c, d). *Helq*^{ΔC/ΔC} cells also exhibited significantly more chromatid breaks and radial chromosomes than control cells upon treatment with mitomycin C (MMC; Fig. 2e, j). Silencing of *HELQ* by short interfering RNA (siRNA) in human cells resulted in similar phenotypes (Extended Data Fig. 4j).

To examine the phenotypic relationship between HELQ and the Fanconi anaemia pathway we generated *Helq*^{ΔC/ΔC} *Fancd2*^{−/−} double-mutant mice (the *Fancd2* strain is described in ref. 8). Double mutants were born in Mendelian ratios (Extended Data Fig. 4k) and growth and appearance were normal. Surprisingly, testes from double mutants were significantly smaller than single mutants and all tubules were atrophic, containing only Sertoli cells (Fig. 2f, g). Similarly, double-mutant cells exhibited greater sensitivity to MMC and CPT than either single-mutant (Fig. 2h, i) and spontaneous and MMC-induced chromosomal aberrations were significantly increased over the *Helq* single mutant

¹DNA Damage Response Laboratory, London Research Institute, Cancer Research UK, Clare Hall, South Mimms EN6 3LD, UK. ²Center for Biological Sequence Analysis, Technical University of Denmark, Lyngby 2800, Denmark. ³Institute of Molecular Cancer Research, University of Zurich, Winterthurerstrasse 190, CH-8057 Zurich, Switzerland. ⁴Department of Radiation Oncology, Dana Farber Cancer Institute, Boston, Massachusetts 02215, USA. ⁵Protein Analysis and Proteomics Laboratory, London Research Institute, Cancer Research UK, Clare Hall, South Mimms EN6 3LD, UK. ⁶Experimental Histopathology Laboratory, London Research Institute, Cancer Research UK, 44 Lincoln's Inn Fields, London WC2A 3LY, UK. ⁷Translational Cancer Therapeutics Laboratory, London Research Institute, Cancer Research UK, 44 Lincoln's Inn Fields, London WC2A 3LY, UK. ⁸UCL Cancer Institute, Huntley Street, London WC1E 6DD, UK. †Present address: Mass Spectrometry, Medical Research Council Laboratory of Molecular Biology, Hills Road, Cambridge CB2 0QH, UK.

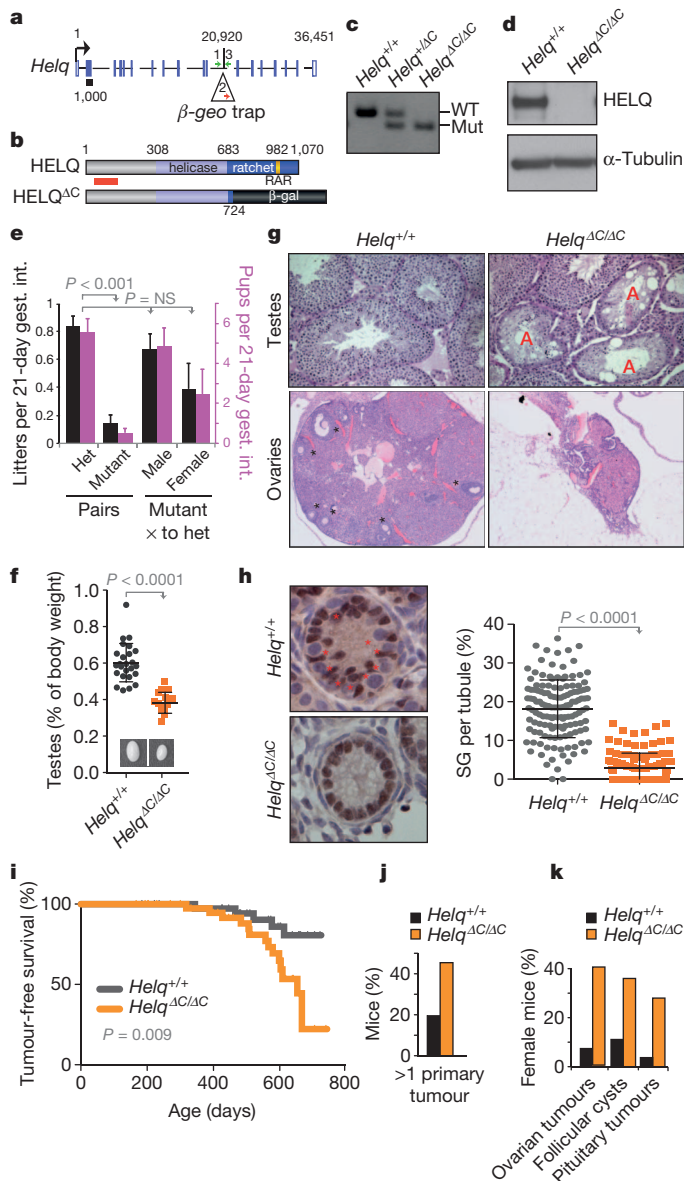


Figure 1 | A mouse model of HELQ deficiency. **a**, *Helq* genomic locus. Base pairs are indicated above. Introns are not to scale; exons are roughly to scale with black bar indicating 1 kilobase. Location of the β -geo gene trap and genotyping primers are shown. **b**, HELQ domain architecture: amino acids are indicated, red bar spans epitope recognized by the HELQ antibody used for western blotting. **c**, *Helq* genotype PCR. **d**, Lysates from ear fibroblasts of *Helq* mice probed for HELQ. **e**, The number of litters (black) and pups (pink) generated per 21-day gestational interval. **f**, *Helq* testis images and weights. **g**, Histological sections of *Helq* gonads. 'A' denotes atrophic tubules; asterisks denote developing ovarian follicles. **h**, Left, 5-day-old neonatal testes labelled with the Sertoli marker WT1 (brown) and haematoxylin (blue), to reveal spermatogonia (asterisks). Right, quantification of spermatogonia (SG). **i**, Epithelial and stromal tumour-free survival of *Helq* mice. **j**, **k**, Frequency of mice with two or more primary tumours (j) and female-specific pathology (k).

(Fig. 2j). These results suggest that HELQ and FANCD2 act in parallel ICL repair pathways.

To gain insight into the function of HELQ during DNA repair, we performed proteomic analysis of proteins co-precipitated with Flag-tagged HELQ. Mass spectrometry revealed several checkpoint and DNA repair proteins, including the replication checkpoint kinase ATR, the single-stranded DNA binding protein RPA70 (also known as RPA1), the four components of the BCDX2 complex required for homologous recombination, and the FANCD2–FANCI heterodimer that functions

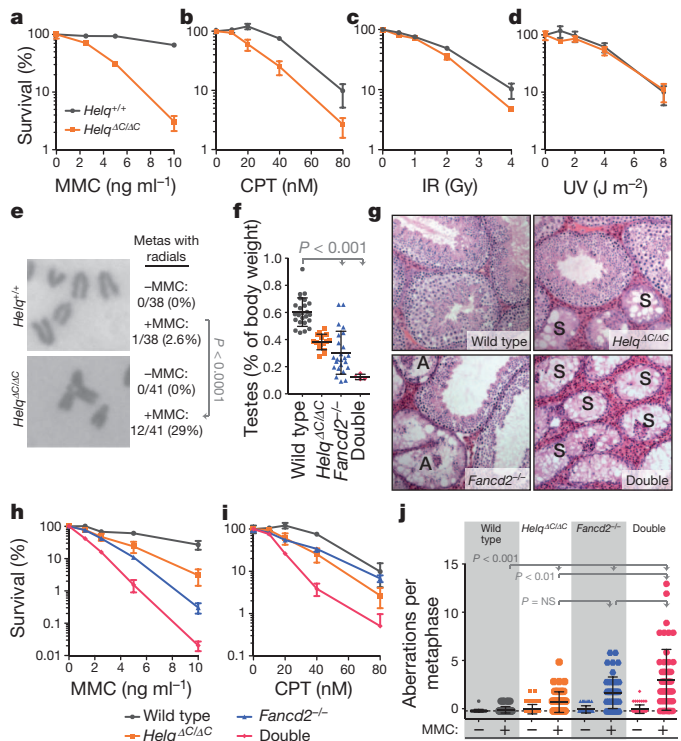
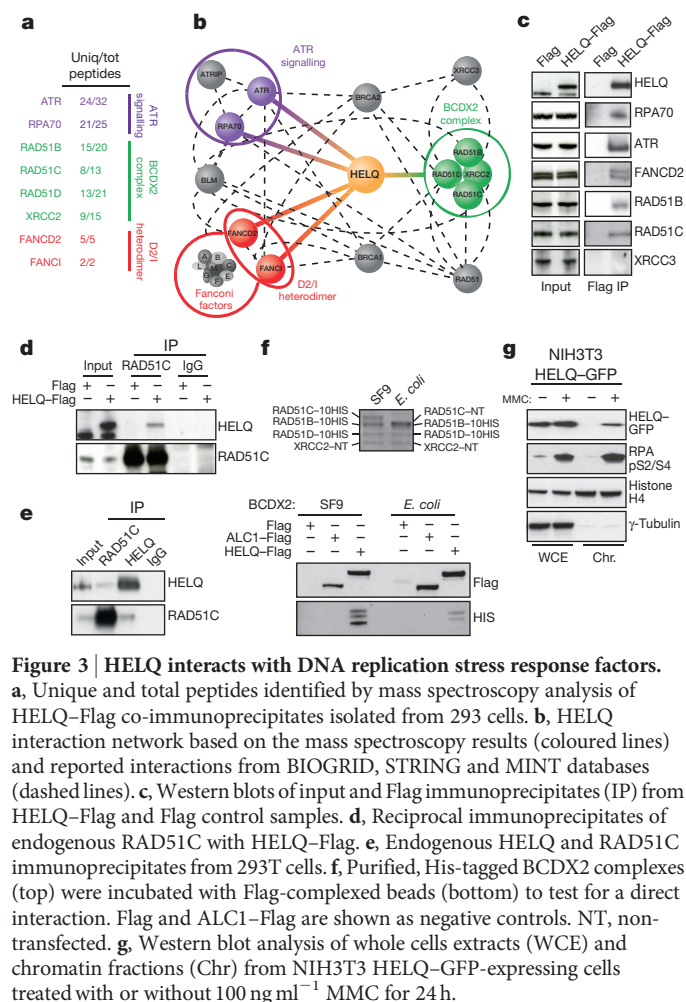


Figure 2 | *Helq* damage sensitivity and *Helq* *Fancd2* double-mutant phenotypes. **a–d**, Clonogenic survival assays of immortalized cells exposed to the indicated damaging agents. **e**, Metaphase chromosomes (metas) from immortalized cells treated with 5 ng ml⁻¹ MMC for 16 h; frequency of metaphases with radials \pm MMC are indicated. **f**, Testis weights of wild-type, *Helq* single- and *Helq* *Fancd2* double-mutant mice. **g**, Histological sections of testes. A, atrophic; S, Sertoli cell only. **h**, **i**, Clonogenic survival assays as in **a**, **j**, Metaphase aberrations from immortalized cells treated with or without 10 ng ml⁻¹ MMC for 16 h.

in the Fanconi anaemia pathway (Fig. 3a, b and Extended Data Fig. 5a). Interaction partners identified by mass spectrometry were confirmed via immunoprecipitation/western blot (Fig. 3c). Reciprocal immunoprecipitation of RAD51C confirmed its association with Flag–HELQ (Fig. 3d), and endogenous HELQ was detected in RAD51C immunoprecipitates from 293T cells and vice versa (Fig. 3e). Recombinant BCDX2 proteins purified from either insect cells or bacteria also bound to purified Flag–HELQ but not to ALC1–Flag or Flag controls (Fig. 3f). Intriguingly, XRCC3, a component of the RAD51C–XRCC3 (CX3) RAD51 paralogue complex, was not detected by either mass spectrometry or western blotting of Flag–HELQ immunoprecipitates (Fig. 3c). Furthermore, HELQ was not found in reciprocal immunoprecipitates with endogenous XRCC3 (Extended Data Fig. 5c). These data indicate that HELQ interacts directly with the BCDX2 complex but not with the CX3 complex.

As ATR, RPA70, the BCDX2 complex and FANCD2–FANCI all respond to stalled replication forks, we examined the localization of green fluorescent protein-tagged HELQ (HELQ–GFP) expressed in NIH 3T3 cells⁹. Subcellular fractionation revealed that HELQ–GFP is enriched on chromatin in response to replication fork stalling with either MMC or aphidicolin, and this is compromised by ATR inhibition (Fig. 3g and Extended Data Fig. 5e–g).

To determine the possible underlying cause of the defect in HELQ-deficient cells we examined replication dynamics, indices of checkpoint activation, Fanconi anaemia pathway activation, double-strand break (DSB) formation, and the integrity of homologous recombination. Replication fork extension rates in *Helq*^{ΔC/ΔC} cells were significantly lower than in wild-type cells (Extended Data Fig. 6d, e) and this was exacerbated by treatment with CPT (Extended Data Fig. 6d). Replication



fork tract asymmetry was also evident in mutants relative to controls indicative of increased fork stalling/collapse (Extended Data Fig. 6f, g).

Checkpoint activation as measured by phosphorylation of ATM, CHK1 and CHK2 (also known as CHEK1 and CHEK2, respectively) and γ H2AX in response to DNA damage was unaffected by loss of HELQ in either mouse or human cells (Extended Data Fig. 7a–d). Furthermore, HELQ-deficient cells exhibited constitutive FANCD2 monoubiquitination, indicating that HELQ is dispensable for this modification (Fig. 4a). Assessment of RAD51 recruitment to damaged replication forks revealed that RAD51 is enriched on chromatin in response to MMC treatment in HELQ-deficient mouse and human cells (Fig. 4b and Extended Data Fig. 7e, 8a) and RAD51, RPA (also known as RPA1) and γ H2AX accumulate in repair foci (Fig. 4c and Extended Data Fig. 7e–g). However, RAD51 and γ H2AX persisted on chromatin and remained present in repair foci at later time points in HELQ-deficient mouse and human cells (Fig. 4b, c and Extended Data Fig. 7e, f), suggesting that the defect in the absence of HELQ occurs at a step downstream of RAD51 recruitment to damaged replication forks. Pulsed field gel electrophoresis revealed that DSBs form in *Helq* and *Fancd2* single and double mutant cells after MMC treatment, but that these lesions persist at later time points, indicating that DSBs induced at ICLs are not efficiently repaired (Fig. 4d). siRNA-induced depletion of HELQ resulted in a two- to threefold decrease in homologous recombination efficiency, implicating HELQ in promoting homologous recombination (Fig. 4e and Extended Data Fig. 8b). Furthermore, clonogenic survival of HELQ-deficient mouse and human cells were significantly compromised in response to poly-ADP ribose polymerase (PARP) inhibition, which is a hallmark of homologous recombination-deficient cells¹⁰ (Fig. 4f and

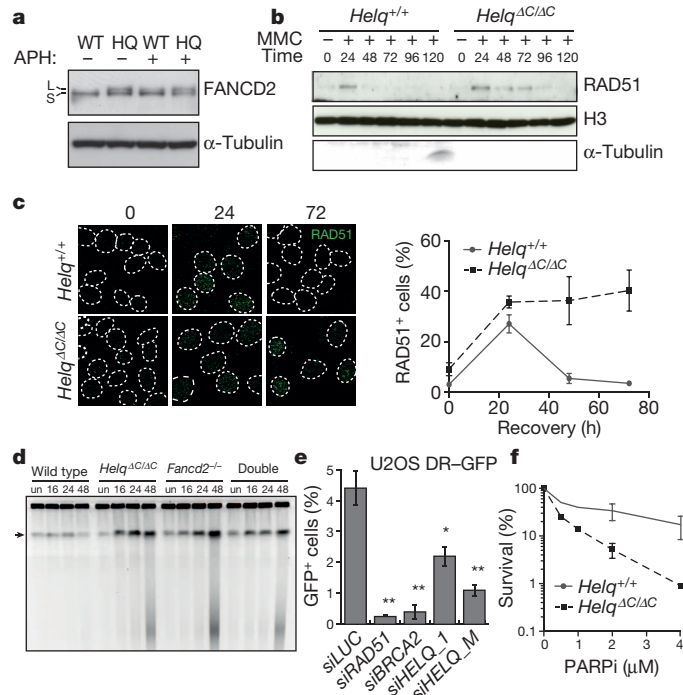


Figure 4 | HELQ influences DNA repair and homologous recombination efficiency.

a, Lysates from immortalized mouse cells, grown under physiological O₂ and treated with or without 3 μ M aphidicolin (APH) for 6 h, were probed for FANCD2. Wild-type (WT), HELQ-deficient (HQ), unmodified (S) and ubiquitinated (L) forms of FANCD2 were used. **b**, Chromatin fractions from immortalized mouse cells, probed for RAD51, histone H3 and α -tubulin at the indicated time points (hours) following treatment with or without 100 ng ml⁻¹ MMC. **c**, Left, representative images of RAD51 focus formation in immortalized mouse cells at the indicated time points (hours) following treatment with 1 μ M MMC. Right, quantification of RAD51 foci at the indicated time points. **d**, Pulsed field gel electrophoresis of genomic DNA from immortalized cells treated with or without 1 μ M MMC for 1 h and recovered for the indicated number of hours. un, undamaged. Wells, intact DNA; arrow, band containing large chromosomal fragments (10–0.45 megabases); below the arrow, smaller fragments resolved by size. **e**, Homologous recombination frequencies in direct repeat (DR)-GFP reporter cells treated with the indicated siRNAs. *LUC*, luciferase. * $P < 0.05$; ** $P < 0.001$. **f**, Clonogenic survival assays of immortalized mouse cells exposed to PARP inhibitor (PARPi). Error bars represent s.e.m.

Extended Data Fig. 8c). It is notable that the HELQ interacting protein and BCDX2 complex factor, RAD51D, is also required for PARP inhibitor resistance¹¹.

In summary, our results uncover a critical role for HELQ in germ cell maintenance and tumour suppression in mammals, which we attribute to a role in replication-coupled DNA repair. The interaction between HELQ and the RAD51 paralogue BCDX2 complex may provide molecular insight into the HELQ phenotype and its role in tumorigenesis, as the BCDX2 complex functions to promote replication-coupled homologous recombination, RAD51C has been implicated in a Fanconi anaemia-like disorder¹², and mutations in RAD51B and RAD51D are associated with hereditary ovarian cancer in humans^{11,13–18}. These findings suggest *HELQ* as a strong candidate for screening in human cancers and also explain why mutations in *D. melanogaster* homologues of HELQ, RAD51, and the two RAD51 paralogues (MUS301 (also known as SPN-C), SPN-A, SPN-B and SPN-D, respectively) confer a very similar phenotype¹⁹. Finally, our findings help to explain the prevalence of non-synonymous variants in *HELQ*, which are significantly associated with upper aerodigestive tract cancers, particularly amongst smokers²⁰; and variants in *HELQ* associated with early menopause²¹, which may reflect the germ cell defects and ovarian dysgenesis observed in HELQ-deficient mice.

METHODS SUMMARY

HELQ-deficient mice were generated from a commercially available embryonic stem cell clone (clone ID: RRF112, Bay Genomics, University of California, Davis). All strains were maintained on a mixed B6/129 background. Testes for histology were fixed in Bouin's solution and periodic acid-Schiff/haematoxylin stained; all other tissues were fixed in neutral buffered formalin and stained with haematoxylin and eosin. Bone marrow cells were collected and analysed by FACS, colony formation and transplantation as described previously^{8,22,23}. HELQ-Flag, Flag, and ALC1-Flag cell lines were generated using the HEK293 Flp-In system according to the manufacturer's protocol (Invitrogen). HELQ-GFP-expressing NIH3T3 cells were generated according to the bacterial artificial chromosome recombineering method described previously⁹. Pulse field gel electrophoresis was carried out similar to the method described in ref. 24. Isolation of HELQ-Flag immunocomplexes entailed lysis of cells in the presence of benzonase to prevent non-specific DNA-bridging of proteins. Flag immunoprecipitates for mass spectrometry analysis were eluted by boiling in SDS-PAGE sample buffer and processed using standard methods. The Biological General Repository for Interaction Data sets (BioGRID, <http://thebiogrid.org/>), the Molecular Interaction database (MINT, <http://mint.bio.uniroma2.it/mint>) and Search Tool for the Retrieval of Interacting Genes/Proteins database (STRING, <http://string-db.org/>) were used to compile the interaction network. For assays of *in vitro* binding to purified His-tagged BCDX2, Flag-tagged proteins were purified by washing immune-complexed beads four times with buffer containing 1 M NaCl. Purified Flag proteins were then incubated with recombinant BCDX2 complex, washed and eluted for analysis. Chromatin fractionation was carried out using modified versions of previously established methods^{25,26}. For siRNA transfections of U2OS cells, cells were subjected to two rounds of reverse transfections using siGENOME siRNA and Dharmafect1 (ThermoFisher) according to the manufacturer's protocol. Histology/immunohistochemistry, primary cell line derivation and immortalization, immunofluorescence, assays for clonogenic survival, metaphase aberrations, micronuclei and DNA combing were carried out using standard procedures.

Online Content Any additional Methods, Extended Data display items and Source Data are available in the online version of the paper; references unique to these sections appear only in the online paper.

Received 26 March; accepted 15 August 2013.

Published online 4 September 2013.

- Kim, H. & D'Andrea, A. D. Regulation of DNA cross-link repair by the Fanconi anemia/BRCA pathway. *Genes Dev.* **26**, 1393–1408 (2012).
- Kottmann, M. C. & Smogorzewska, A. Fanconi anaemia and the repair of Watson and Crick DNA crosslinks. *Nature* **493**, 356–363 (2013).
- Boyd, J. B., Golino, M. D., Shaw, K. E., Osgood, C. J. & Green, M. M. Third-chromosome mutagen-sensitive mutants of *Drosophila melanogaster*. *Genetics* **97**, 607–623 (1981).
- Muzzini, D. M., Plevani, P., Boulton, S. J., Cassata, G. & Marini, F. *Caenorhabditis elegans* POLQ-1 and HEL-308 function in two distinct DNA interstrand cross-link repair pathways. *DNA Repair* **7**, 941–950 (2008).
- Richards, J. D. *et al.* Structure of the DNA repair helicase hel308 reveals DNA binding and autoinhibitory domains. *J. Biol. Chem.* **283**, 5118–5126 (2008).
- Ward, J. D. *et al.* Overlapping mechanisms promote postsynaptic RAD-51 filament disassembly during meiotic double-strand break repair. *Mol. Cell* **37**, 157–158 (2010).
- Parmar, K., D'Andrea, A. & Niedernhofer, L. J. Mouse models of Fanconi anemia. *Mutat. Res.* **668**, 133–140 (2009).
- Parmar, K. *et al.* Hematopoietic stem cell defects in mice with deficiency of Fancd2 or Usp1. *Stem Cells* **28**, 1186–1195 (2010).
- Poser, I. *et al.* BAC TransgeneOmics: a high-throughput method for exploration of protein function in mammals. *Nature Methods* **5**, 409–415 (2008).
- Huehls, A. M., Wagner, J. M., Huntoon, C. J. & Karnitz, L. M. Identification of DNA repair pathways that affect the survival of ovarian cancer cells treated with a poly(ADP-ribose) polymerase inhibitor in a novel drug combination. *Mol. Pharmacol.* **82**, 767–776 (2012).
- Loveday, C. *et al.* Germline mutations in *RAD51D* confer susceptibility to ovarian cancer. *Nature Genet.* **43**, 879–882 (2011).
- Vaz, F. *et al.* Mutation of the *RAD51C* gene in a Fanconi anemia-like disorder. *Nature Genet.* **42**, 406–409 (2010).
- Meindl, A. *et al.* Germline mutations in breast and ovarian cancer pedigrees establish *RAD51C* as a human cancer susceptibility gene. *Nature Genet.* **42**, 410–414 (2010).
- Loveday, C. *et al.* Germline *RAD51C* mutations confer susceptibility to ovarian cancer. *Nature Genet.* **44**, 475–476 (2012).
- Vuorela, M. *et al.* Further evidence for the contribution of the *RAD51C* gene in hereditary breast and ovarian cancer susceptibility. *Breast Cancer Res. Treat.* **130**, 1003–1010 (2011).
- Peltari, L. M. *et al.* *RAD51C* is a susceptibility gene for ovarian cancer. *Hum. Mol. Genet.* **20**, 3278–3288 (2011).
- Wickramanyake, A. *et al.* Loss of function germline mutations in *RAD51D* in women with ovarian carcinoma. *Gynecol. Oncol.* **127**, 552–555 (2012).
- Osher, D. J. *et al.* Mutation analysis of *RAD51D* in non-BRCA1/2 ovarian and breast cancer families. *Br. J. Cancer* **106**, 1460–1463 (2012).
- González-Reyes, A., Elliott, H. & St Johnston, D. Oocyte determination and the origin of polarity in *Drosophila*: the role of the spindle genes. *Development* **124**, 4927–4937 (1997).
- McKay, J. D. *et al.* A genome-wide association study of upper aerodigestive tract cancers conducted within the INHANCE consortium. *PLoS Genet.* **7**, e1001333 (2011).
- Stolk, L. *et al.* Meta-analyses identify 13 loci associated with age at menopause and highlight DNA repair and immune pathways. *Nature Genet.* **44**, 260–268 (2012).
- Ceccaldi, R. *et al.* Bone marrow failure in Fanconi anemia is triggered by an exacerbated p53/p21 DNA damage response that impairs hematopoietic stem and progenitor cells. *Cell Stem Cell* **11**, 36–49 (2012).
- Ploemacher, R. E., van der Sluijs, J. P., van Beurden, C. A., Baert, M. R. & Chan, P. L. Use of limiting-dilution type long-term marrow cultures in frequency analysis of marrow-repopulating and spleen colony-forming hematopoietic stem cells in the mouse. *Blood* **78**, 2527–2533 (1991).
- Hanada, K. *et al.* The structure-specific endonuclease Mus81–Eme1 promotes conversion of interstrand DNA crosslinks into double-strands breaks. *EMBO J.* **25**, 4921–4932 (2006).
- Aygün, O., Svejstrup, J. & Liu, Y. A. RECQ5–RNA polymerase II association identified by targeted proteomic analysis of human chromatin. *Proc. Natl Acad. Sci. USA* **105**, 8580–8584 (2008).
- Mirzoeva, O. K. & Petrini, J. H. DNA replication-dependent nuclear dynamics of the Mre11 complex. *Mol. Cancer Res.* **1**, 207–218 (2003).

Acknowledgements We wish to thank S. West for purified BCDX2 complexes and antibody reagents; Ó. Fernández-Capetillo for ATR inhibitors; D. Cox, G. Martin and H. Chapman for assistance with mouse breeding and maintenance; E. Nye, T. Bunting and B. Spencer-Dene for histopathology services; I. Rosewell for transgenic services; H. Flynn for mass spectrometry services; and M. Petalcorin for assistance with BAC recombineering. O.M. and A.A.S. are supported by grants of the Swiss National Science Foundation (PDFMP3_127523) and the Vontobel Foundation. The laboratory of A.D. is supported by National Institutes of Health grant R01-DK43889. The laboratories of S.J.B. and C.S. are funded by Cancer Research UK. The S.J.B. laboratory is also funded by a European Research Council advanced investigator grant (RecMitMei). S.J.B. is a Royal Society Wolfson Research Merit Award holder.

Author Contributions C.A.A., R.L.L. and S.J.B. designed the study, performed experiments and wrote the manuscript unless otherwise stated. G.S. performed mouse post-mortem analyses and advised on histopathology. O.M. and A.A.S. performed and supervised DR-GFP homologous recombination assays. K.M. performed RAD51 foci experiments. Z.H. performed human clonogenic survival assays. K.P. and A.D. performed and supervised mouse bone marrow experiments. V.B. assisted with mouse tumour watch monitoring. J.M.S. supervised mass spectrometry. N.J.B. and C.S. advised on experiments and manuscript revisions, and all authors contributed to revision of the manuscript.

Author Information Reprints and permissions information is available at www.nature.com/reprints. The authors declare no competing financial interests. Readers are welcome to comment on the online version of the paper. Correspondence and requests for materials should be addressed to S.J.B. (simon.boulton@cancer.org.uk).

METHODS

Mouse strains, maintenance, localization of genetrap, genotyping. All mice were housed and maintained according to the Home Office guidance outlined in the Animals Scientific Procedures Act. All strains were maintained on a mixed B6/129 background.

A commercially available embryonic stem cell clone (clone ID: RRF112, Bay Genomics, University of California, Davis) harbouring the trapped allele of *Helq* was obtained. The position of the β -geo gene trap cassette from the pGT0Lx vector was determined via splinkerette PCR²⁷ using a modified version of the method described in ref. 28. In brief, 3 μ g genomic DNA from *Helq* gene-trapped embryonic stem cells was digested overnight at 37 °C with BfaI. Splinkerette primers were annealed in SuRE Buffer M (Roche) by heating to 95 °C, followed by cooling by 1 °C increments for 15 s each. A total of 40 pmol of the annealed splinkerette adaptor was ligated to 600 ng of BfaI-digested genomic DNA, followed by passage over a PCR purification column (Qiagen). The splinkerette-adapted genomic DNA was re-digested with BfaI for 1 h (eliminating potential background due to splinkerette ligation to partially digested genomic DNA fragments) and re-purified. Primary and nested PCRs were performed using genetrap- and splinkerette-specific primers, with 0.4% of the primary PCR used in the nested round. Nested PCR products were gel purified and sequenced using standard methods.

The *Helq*^{AC} mouse strain was generated using standard transgenic technology. For more background and discussion pertaining to this and other aspects of the manuscript, see elsewhere in the Methods and Extended Data. *FANCD2*-deficient mice were described previously⁸. Mice were identified using standard ear snip methods, and snips were used for genomic DNA preparation using the HotSHOT method²⁹ for use in genotype PCR. *Helq* wild-type, heterozygous and mutant mice were genotyped in a single reaction using the following primers: pGT0Lx_F2-CA GGGTTTCCCAGTCACGAC (genetrap-specific primer), mHELQint11_F8-GT CCTGTGCCCCAAGTACAG (wild-type-specific primer), mHELQint11_R5-CC TAGTGTGGCTTATCTCCTCTTTC (common primer). *Fancd2* mice were genotyped according to the previously described method⁸.

Breedings to establish Mendelian ratios and fertility consisted of continuously mated, individually housed pairs. The *Helq Fancd2* double-mutant strain was established from mating of double heterozygous *Helq*^{+/AC} *Fancd2*^{+/-} mice. Weights of *Helq* mice were measured weekly starting at 10 days post-partum. The tumour watch cohort was established using littermate controls wherever possible and mice were regularly monitored for signs of deterioration using a scoring system that will be described in a separate publication. Mice were euthanized before terminal end points were reached.

Statistics. For survival study, sample size was estimated using standard power calculation methods in order to measure a difference of 3–4 months in survival between mutant and control groups. For *Helq* and *Helq Fancd2* matings, deviations from expected Mendelian ratios were tested by Chi-squared analysis ($P > 0.25$ for both strains). For fertility analysis, the number of litters and pups were tested using Kruskal–Wallace analysis of variance. The Gaussian approximation of P values indicated that medians varied significantly between the groups ($P = 0.0019$ for litters, $P = 0.0014$ for pups). Dunn's multiple comparison post-test was used to compare specific sample pairs. Results of P value calculations for both litters and pups were the same, and are the values indicated on the graph ($P < 0.001$ for control versus mutant pairs, $P =$ not significant for control versus male or female mutant pairs). For wild-type versus *Helq* mutant testes weights, the Mann–Whitney test was used to analyse whether the weights differed between the two groups. Gaussian approximation was used for calculation of the indicated P value ($P < 0.0001$). For wild-type and *Helq* mutant testes weights versus age, linear regression was used to generate slopes of best-fit lines which were tested for deviation of slope from zero. R^2 and P values indicated on the graph demonstrate that although there is a correlation between reduced testes weight and age in wild-type mice ($P = 0.0091$), there is no correlation between testes weight and age for *Helq* mutants ($P = 0.78$). For spermatogonia numbers in wild-type versus *Helq* mutant neonatal testes, the Mann–Whitney test was used to analyse whether spermatogonia differed between the two groups. Gaussian approximation was used for calculation of the indicated P value ($P < 0.0001$). For MMC-induced metaphase aberrations in wild-type versus *Helq* mutant cell lines, the Mann–Whitney test was used to analyse whether radial chromosomes per metaphase differed between the two groups ($P < 0.0001$). For wild-type versus *Helq* and *Fancd2* single- and double-mutant testes weights, the Kruskal–Wallace analysis of variance test was used. Gaussian approximation of the P value indicated that medians varied significantly between the groups ($P < 0.0001$). Dunn's multiple comparison post-test was used to compare specific sample pairs. Results of P value calculations are indicated on the graph ($P < 0.001$ for both wild-type versus *Fancd2* single mutant and wild type versus *Helq Fancd2* double mutant). For MMC-induced metaphase aberrations in wild-type versus *Helq* and *Fancd2* single mutants and *Helq Fancd2* double mutants, the Kruskal–Wallace analysis of variance test

was used. Gaussian approximation of the P value indicated medians varied significantly between the groups ($P < 0.0001$). Dunn's multiple comparison post-test was used to compare specific sample pairs. Results of P value calculations for MMC-damaged samples are indicated on the graph ($P < 0.001$ for wild-type versus single and double mutants, $P < 0.01$ for *Helq* mutants versus double mutants, and $P =$ not significant for *Helq* versus *Fancd2* single mutants and for *Fancd2* mutants versus double mutants). For HELQ–GFP chromatin recruitment upon ATR inhibitor treatment, Student's t -test was performed to determine whether the observed differences were statistically significant. For DNA combing of replication tracts from wild-type versus *Helq* mutant cells at atmospheric O₂, and tracts from wild-type, *Helq* and *Fancd2* single, and *Helq Fancd2* double mutants at physiological O₂, the Kruskal–Wallace analysis of variance test was used. Gaussian approximation of the P values indicated that medians varied significantly between the groups ($P < 0.0001$ for both experiments). Dunn's multiple comparison post-test was used to compare specific sample pairs. Results of P value calculations are indicated on the graphs ($P < 0.01$ for wild type versus *Helq* mutants and for undamaged versus CPT damaged *Helq* mutant cells; $P < 0.001$ for wild type versus single and double mutants). For wild type versus *Helq* mutant tumour watch, the Kaplan–Meier epithelial and stromal tumour-free survival curve was analysed with Mantel–Cox log-rank test for P value calculation ($P = 0.009$).

Histology, immunohistochemistry sample preparation and reagents. For all histology, samples were paraffin embedded and sectioned at 4 μ m. Testes for histology were fixed in Bouin's solution, Periodic acid–Schiff stained and haematoxylin counter-stained; all other tissues, including post-mortem tissues for analysis of tumour watch cohort, were fixed in 10% neutral buffered formalin (NBF) and stained with haematoxylin and eosin.

Immunohistochemistry was carried out using standard methods. In brief, testes for immunohistochemistry were NBF fixed and sections from adult mice were processed for c-KIT staining by microwaving in 0.01 M citrate buffer, pH 6, to unmask antigens. After incubation with c-KIT primary antibodies (Dako A4502, 1:600), samples were incubated with biotinylated secondary antibody (Vector) followed by incubation with Avidin Biotin Complex (Vector); slides were developed in 3,3'-diaminobenzidine (DAB) substrate (Vector) and counterstained in haematoxylin. Neonatal testis sections were similarly processed and labelled with antibodies against WT1 (Santa Cruz sc-192, 1:450).

Cell line derivation. Ear fibroblasts for primary and SV40 immortalized cultures were generated as follows: mice were euthanized and ear tissue was collected using sterile scissors, ear fragments were rinsed twice in 70% ethanol followed by two rinses in PBS supplemented with 100 μ g ml⁻¹ kanamycin. Tissue was transferred into 0.3 ml of protease solution (4 mg ml⁻¹ each of collagenase D and dispase in DMEM; filter sterilized), and incubated at 37 °C for 45 min. In total, 1.5 ml DMEM containing 10% FBS, 1 \times glutamine and 5 \times antibiotic–antimycotic solution were added to protease solution containing ear fragments, and samples were incubated at 37 °C overnight. Cells were dissociated by pipetting, passed through a 40- μ m mesh cell strainer, and plated in DMEM as above except using 1 \times antibiotic–antimycotic solution. Cells were passaged upon reaching confluence to five dishes, and upon reaching confluence, cells were frozen at passage 1 or used immediately for immortalization or experiments.

Fibroblasts were immortalized via transfection with a vector expressing SV40 large T antigen. Constitutively expressed HELQ–Flag, Flag, and ALC1–Flag cell lines were generated using the 293 Flp-In system according to the manufacturer's protocol (Invitrogen). NIH3T3 cells stably expressing GFP-tagged mouse HELQ (consisting of a bacterial artificial chromosome (BAC) containing the entire *Helq* promoter and genomic locus) were generated according to the BAC recombineering method described previously⁹. These and all other cell lines used in this study (293T, HeLa, NIH3T3 and U2OS) were grown in DMEM supplemented with 10% FBS and L-glutamine. Cells were grown in 5% CO₂ incubators at atmospheric O₂ concentrations (~21%) with noted exceptions where samples were cultured at physiological O₂ concentrations (~5%).

For HELQ–GFP transient transfections in HeLa cells (Extended Data Fig. 3d), human *HELQ* was cloned into the pcDNA6.2/C-EmGFP-DEST vector using Gateway technology (Invitrogen). The vector was transfected into HeLa cells with Lipofectamine 2000 using the manufacturer's protocol (Invitrogen). Live or para-formaldehyde (PFA)-fixed cells (fixed cells were counterstained with DAPI (4',6-diamidino-2-phenylindole)) were visualized 48–96 h after transfection under epifluorescence using a Zeiss Axio Imager M1 microscope with an ORCA-ER camera (Hamamatsu), and images were acquired using the Volocity software (Improvision, Perkin Elmer).

Clonogenic survival, metaphase spreads, growth and micronuclei analyses. For all experiments, fibroblast lines established from littermates or siblings were used wherever possible. Experiments involving primary cells were conducted in physiological O₂ using cell lines of similar passage number.

For clonogenic survival assays, SV40 immortalized mouse ear fibroblasts and siRNA-treated U2OS cells were plated in triplicate on 10-cm dishes at clonal density, allowed to adhere for 8–16 h, and damage treatments administered (CPT medium was changed after 24 h). After 8–10 days of growth, plates were rinsed, fixed/stained in 20% ethanol/4% crystal violet (w/v), rinsed in distilled water and colonies tabulated. All results were normalized to untreated to adjust for plating efficiency and determine percentage survival. Survival experiments were carried out on at least two independent sets of mutant and control mouse cell lines, and in most cases cell lines were tested in at least two independent experiments. Similar results were obtained across all experiments and sets of cell lines.

For analysis of metaphase aberrations, SV40 immortalized cells were damaged as indicated and treated with colcemid (2×10^{-7} M) for 30 min, collected, swelled in hypotonic solution (0.075 M KCl) for 7 min at 37 °C, fixed and washed in ice-cold methanol-acetic acid (3:1), dropped on humid slides and briefly steamed over a 65 °C bath. Slides were dried, stained with Giemsa (Sigma) for 10 min, rinsed with distilled water, and coverslips were mounted (Permount, Fisher). For each sample ≥ 40 spreads were scored.

Growth kinetics of primary cells were determined using a modified 3T3 protocol to calculate cumulative population doublings. In brief, primary cells were collected, counted and 150,000 cells reseeded in triplicate 10-cm dishes every third day. Cumulative population doublings were calculated using the formula: $\log_{10}(n/n_0) \times 3.32$, in which n = number of cells collected after growth and n_0 = number of cells seeded. Similar growth kinetics were obtained for three different mutant and control mouse embryonic fibroblasts and embryonic fibroblast cell line pairs.

Micronuclei were examined by seeding SV40 immortalized embryonic fibroblasts in 6-well dishes containing glass coverslips. The following day, cells were fixed in 4% PFA and stained with DAPI. For each sample ≥ 100 cells were scored. **Bone marrow protocols, antibodies/reagents, analysis.** Bone marrow cells were collected from 3–4-month-old control and *Helq*^{AC/AC} mice and analysed for haematopoietic stem and progenitor cells (HSPCs) as described previously^{8,22}. For LSK (lineage[−] Sca-1⁺ c-Kit⁺) staining, cells were stained in Hank's balanced salt solution containing 2% FBS and 10 mM HEPES buffer (Gibco) using biotinylated anti-lineage antibody cocktail (anti-Mac1 α , Gr-1, Ter119, CD3e, CD4 and CD8a), phycoerythrin (PE)-Cy-7-anti-Sca-1 antibody (clone E13-161.7), and APC-anti-c-Kit antibody (clone 2B8), followed by staining with PE-streptavidin secondary antibody (all primary and secondary antibodies from BD Biosciences). The samples were acquired using a BD FACSAria high-speed sorter.

For c.f.u.-c assays, bone marrow cells were seeded in 12-well plates at a density of 7×10^4 cells per well in mouse MethoCult medium M3434 (StemCell Technologies) and haematopoietic colonies (c.f.u.-c) were counted at 7–10 days after culture. c.f.u.-c assays were used to determine the survival of bone marrow in presence of MMC. To determine the *ex vivo* clonal growth of murine HSPCs, a cobblestone area-forming cell (CAFC) assay was performed by a limiting dilution analysis of bone marrow in micro-cultures using the bone marrow stromal cell line FBMD-1 (refs 8, 23). This assay quantifies a spectrum of haematopoietic cells that is well-validated to compare with other functional assays. Specifically, day-7 and day-14 CAFC correspond to early progenitor cells and to c.f.u.-spleen-day-12 cells, whereas the more primitive haematopoietic stem cells with long-term repopulating ability correspond to day-28 CAFC²³.

Bone marrow transplantation was performed as described previously⁸. In brief, bone marrow cells (5×10^5) from control or *Helq*^{AC/AC} mice (CD45.2⁺) were mixed with 2.5×10^5 bone marrow supporting cells from CD45.1⁺ congenic mice and transplanted into lethally irradiated CD45.1⁺ congenic recipient mice. The donor cell engraftment efficiency in the recipient mice, after 17 weeks post-transplant, was determined by staining peripheral blood leukocytes with FITC-labelled anti-CD45.2 (clone 104) antibody. The percentage of donor-derived T cells, B cells and myeloid cells was determined by co-staining with PE-labelled anti-CD3e (clone 145-2C11), anti-B220 (clone RA3-6B2) and anti-Mac-1/Gr-1 antibodies (clones M1/70 and RB6-8C5), respectively, and analysed on a FACScan instrument (Becton Dickinson). All antibodies were from BD Biosciences.

Mass spectrometry and proteomics. HELQ-Flag and Flag control cells were collected and lysed in benzonase lysis buffer (20 mM Tris-Cl, pH 7.5, 75 mM NaCl, 10% glycerol, 2 mM MgCl₂, 0.5% NP40, 30 U ml^{−1} benzonase, protease inhibitors). NaCl concentration was adjusted to 150 mM, EDTA to 3 mM and lysates were cleared by centrifugation. Supernatants were pre-cleared with Protein G agarose beads for 30 min at 4 °C. Pre-cleared lysates were incubated with anti-Flag affinity agarose resin (Sigma) for 4 h at 4 °C. Beads were washed five times with wash buffer (20 mM Tris-Cl, pH 7.5, 150 mM NaCl, 3 mM EDTA, 0.5% NP40) and once with PBS. Bound proteins were eluted by boiling in SDS-PAGE sample buffer and eluates were resolved on NuPAGE Bis-Tris gels (Invitrogen) and stained with Sypro Ruby (Invitrogen). Gel slices were excised and processed for mass spectrometry using the Janus automated liquid handling system (PerkinElmer). Peptides were analysed by nanoscale capillary liquid chromatography–electrospray

ionization/multi-stage mass spectrometry (LC–ESI MS/MS), data were processed using Mascot Distiller (Matrix Science) and exported to Scaffold for viewing (Proteome Software).

The Biological General Repository for Interaction Data sets (BioGRID, <http://thebiogrid.org/>), the Molecular Interaction database (MINT, <http://mint.bio.uniroma2.it/mint/>), and Search Tool for the Retrieval of Interacting Genes/Proteins database (STRING, <http://string-db.org/>) were used to compile the protein interaction network.

Cell lysates, *in vitro* binding assay and fractionation for western blot analyses. All cell lines used in this study were short tandem repeat-profiled and tested for mycoplasma infection before use. All lysis buffers were supplemented with protease inhibitor cocktail (Roche) and phosphatase inhibitors (Sigma).

For validation of mass spectrometry data, HELQ-Flag- and Flag-expressing cells were used. (This was due to our inability to validate these interactions using endogenous HELQ, stemming from the fact that it is expressed at very low levels in most human cell lines, and no antibodies were found to reliably immunoprecipitate the human version. Validation using endogenous mouse HELQ was similarly hindered by a lack of reagents available for detection of the mouse RAD51 paralogs.) Cells were lysed in the presence of benzonase and 2 mg of total protein were immunoprecipitated with anti-Flag affinity resin as above. Beads were washed, bound proteins eluted with 1 \times NuPAGE LDS sample buffer and analysed by western blot. Similar methods were employed using lysates prepared from 293T cells to examine endogenous HELQ or RAD51C coimmunoprecipitates.

For *in vitro* binding assays, HELQ-Flag, ALC1-Flag and Flag cells were lysed in the presence of benzonase and pre-cleared lysate was used for Flag immunoprecipitate as described above. Flag-immunocomplexed beads were then washed four times with a modified wash buffer containing 1 M NaCl to remove bound co-precipitates, and once with *in vitro* binding buffer (20 mM Tris-Cl, pH 7.5, 280 mM NaCl, 3 mM EDTA, 0.5% NP40). Washed beads were incubated with recombinant RAD51 paralogue BCDX2 complex (gift of S. West's laboratory) in binding buffer for 4 h at 4 °C and washed four times with the same buffer. Eluates were analysed by western blot.

GFP-tagged HELQ was stably expressed in NIH3T3 cells using a BAC recombineering method to C-terminally Flag/GFP-tag the BAC-containing full-length genomic *Helq*, which included the endogenous promoter. This allowed HELQ-GFP to be expressed at physiological levels.

For chromatin fractionation of embryonic fibroblasts and siRNA-treated U2OS cells, cells were treated with or without 3 μ M aphidicolin for 6 h or with or without 1 mM MMC for 24 h, collected and fractionated using a modified version of the method described in ref. 26: pellets were re-suspended in CSK buffer (10 mM PIPES, pH 6.8, 100 mM NaCl, 300 mM sucrose, 3 mM MgCl₂, 1 mM EGTA, pH 7, 0.5% Triton X-100), incubated for 10 min on ice (a small fraction of this was removed and SDS-PAGE sample buffer was added to obtain WCEs), pelleted at low speed and supernatants reserved as soluble fraction. Pellets were washed in CSK buffer, and re-pelleted. Pellets were re-suspended in benzonase CSK buffer (10 mM PIPES, pH 7.5, 100 mM NaCl, 300 mM sucrose, 3 mM MgCl₂, 0.5% Triton X-100, 0.1 U μ l^{−1} benzonase), lysates were incubated for 30 min at 37 °C, pelleted and supernatants reserved for chromatin fraction. Pellets were re-suspended in high-salt CSK (recipe as above except NaCl was added to 500 mM), lysates were incubated for 10 min on ice, cleared at high speed and supernatants pooled with benzonase CSK lysates to yield chromatin extracts²⁵. In total, 25 μ g of soluble and 10 μ g of chromatin proteins were analysed by western blotting.

Western blot, immunoprecipitated antibodies/reagents and siRNA oligonucleotides. Precast NuPAGE Bis-Tris or Tris-acetate gels and electrophoresis system were by Invitrogen. Western blotting transfers were carried out in BioRad transblot chambers and all blots were blocked and probed in 5% milk-phosphate buffer saline triton X100 (PBST) with the exception of p-CHK1 blots, which were processed in 3% BSA-Tris buffered saline triton X100 (TBST). Mouse and rabbit horseradish peroxidase-conjugated secondary antibodies were from ThermoFisher, and signals were visualized with ECL western blotting detection reagent (Amersham) or SuperSignal West Femto reagent (Thermoscientific).

Antibodies used for western blot analysis: Flag (Sigma F1804, 1:2,000), HELQ (Santa Cruz 81095, 1:200), His (Clontech 631212, 1:2,000), PARP1 (Trevigen 4338-ML-50, 1:1,000), CHK1 (Sigma C9358, 1:500), S345-P-CHK1 (Cell Signalling 2348, 1:500), CHK2/p-CHK2 (Upstate 05-649, 1:400), ATM (Sigma A1106, 1:2,000), S1981-p-ATM (Cell signalling 4526, 1:1,000), histone H3 (Abcam 10799, 1:2,000), α -tubulin (Sigma T6199, 1:2,000), RAD51 (Santa Cruz 8349, 1:200), FANCD2 (Epitomics 2986-1, 1:1,000), γ H2AX (Cell Signalling 2577, 1:1,000), RPA32 (Abcam 12F3.3, 1:1,000), BRCA2 (Santa Cruz 8326, 1:200), TFIIB p89 (Santa Cruz 293, 1:200). All RAD51 paralogue antibodies were a kind gift from S. West's laboratory, as described in ref. 30: RAD51B (IH3 mouse monoclonal antibody, 1:500), RAD51C (2H11 mouse monoclonal antibody, 1:500), RAD51D (5B3 mouse monoclonal

antibody, 1:400), XRCC2 (7B7 mouse monoclonal antibody, 1:400), XRCC3 (10F1 mouse monoclonal antibody, 1:400).

Antibodies used for immunoprecipitation: RAD51C (R68 rabbit antibody), XRCC3 (10F1 mouse monoclonal antibody), mouse IgG (Abcam 18413) and rabbit IgG (Abcam 46540) were used where appropriate as negative control immunoprecipitates.

siRNA oligonucleotides: RAD51 (ref. 31) 5'-AAGGGAAUAGUGAAGCCAA-3', BRCA2 (ref. 32) 5'-AACACAAUACGAACCAA-3'. siRNA oligonucleotides used in DR-GFP and in *HELQ_1* (this study): 5'-GAAGGUCCAAUAAU-3', *HELQ_3* (this study): 5'-AAUGUGAGGUGAUUAAGAA-3', *HELQ_M33*: 5'-CAAAGGAAGATTTCCTCCAACTAA-3', *HELQ-01*: 5'-GUUU GAAGAUUGCAACGAA-3', *HELQ-03*: 5'-AAUGUGAGGUGAUUAAGAA-3', *HELQ-04*: 5'-GGUAGAAGAGUUAACUAAGA-3', *HELQ-17*: 5'-GUUUGAAGA UUGCAACGAA-3', XRCC2: 5'-CAGGGTACTACGCAAGCCT-3', XRCC3: 5'-CAGAATTATTGCTGCAATT-3', RAD51C: 5'-AAGAGAATGTCTCACAAT-3', RAD51D: 5'-CTGGGTGGAAATAAGCTTA-3'.

siRNA transfection and ATR inhibition. U2OS cells were subjected to two rounds of reverse transfections using siGENOME siRNA and Dharmafect1 (ThermoFisher) according to the manufacturer's protocol. Thirty-six hours after the second transfection, cells were treated for 14 h with 3 μ M aphidicolin. For ATR inhibition, 3 μ M ATR inhibitor was added to cultures 30 min before aphidicolin treatment.

Immunofluorescence. Cells were first washed in PBS and then fixed with 2% PFA at room temperature (18 °C) for 15 min, and then washed three times in PBS. The fixed cells were further permeabilized with 3% BSA in PBS plus 0.1% Triton X-100 for 30 min at room temperature. Primary antibodies (RAD51; 1:500, RPA; 1:1,000, γ H2AX) were added and incubated at 37 °C for 1 h. After washing with PBS plus 0.1% Triton X-100, secondary antibodies (provided by Jackson ImmunoResearch) were applied and incubated for 1 h in the dark. The stained coverslips were mounted with prolong Gold Antifade reagent (Invitrogen). Imaging was carried out using Axio Imager (Zeiss) or Axioplan 2 Imaging (Zeiss) microscope and analysed by Axiovision software (Zeiss).

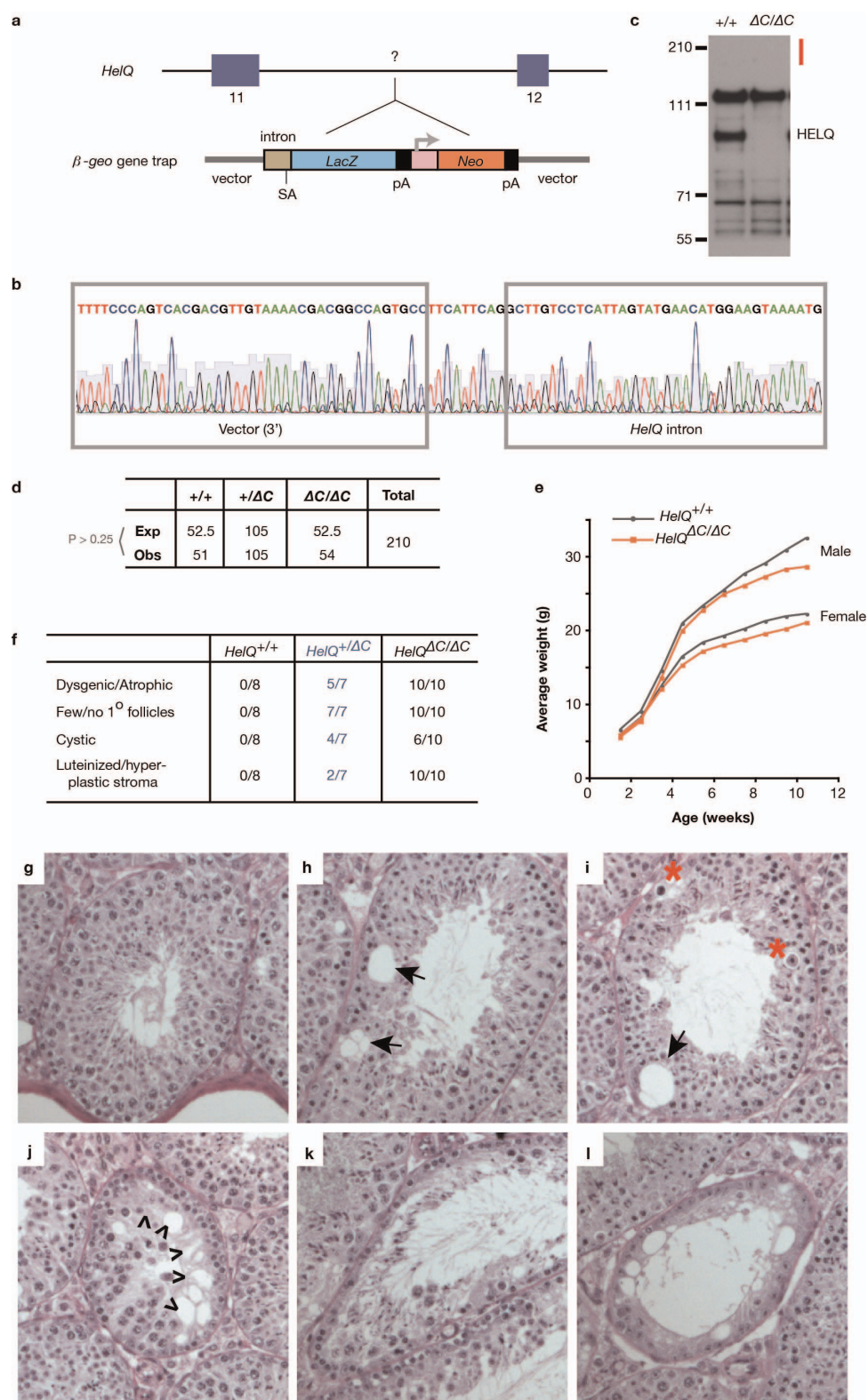
Homologous recombination reporter assays. DSB repair efficiency by homologous recombination was measured in DR-GFP U2OS cells as described previously³⁴. In brief, 48 h after the first round of siRNA transfection (40 nM) using Lipofectamine RNAiMAX (Invitrogen), cells were either mock-transfected (pcDNA3.1) or transfected with 0.6 μ g of an I-SceI expression plasmid (pCBASce) together with siRNA (20 nM) using 3.6 μ l of Lipofectamine 2000 (Invitrogen). The media was replaced 3 h after I-SceI transfection and cells were analysed for GFP expression by flow cytometry on a Cyan ADP (Dako) 72 h after I-SceI transfection. To confirm siRNA efficiency, western blotting was carried out on 50 μ g of NP-40 lysates plus sonication run on 4–15% Precast SDS-PAGE gels (Bio-Rad).

DNA combing. Replication tracts were labelled for 20 min with 20 μ M iododeoxyuridine (IdU) (in atmospheric O₂ experiments, cells were treated with or without 2.5 μ M CPT for the final 15 min of IdU labelling to test replication fork stalling/restart), washed three times with PBS and labelled for 20 min with 200 μ M

chlorodeoxyuridine (CldU). Cells were washed, collected on ice, counted and embedded in agarose. Cells were digested in 2–3 changes of proteinase K buffer for 24 h at 50 °C. Plugs were washed for 5 \times 10 min in Tris-EDTA followed by β -agarase digestion overnight at 42 °C. Genomic DNA was combed onto silanized coverslips (Genomic Vision) using a Molecular Combing System instrument (Genomic Vision), dried and stained using previously described methods³⁵. Experiments were conducted on two separate sets of mutant and control cell lines with similar results obtained for both experiments.

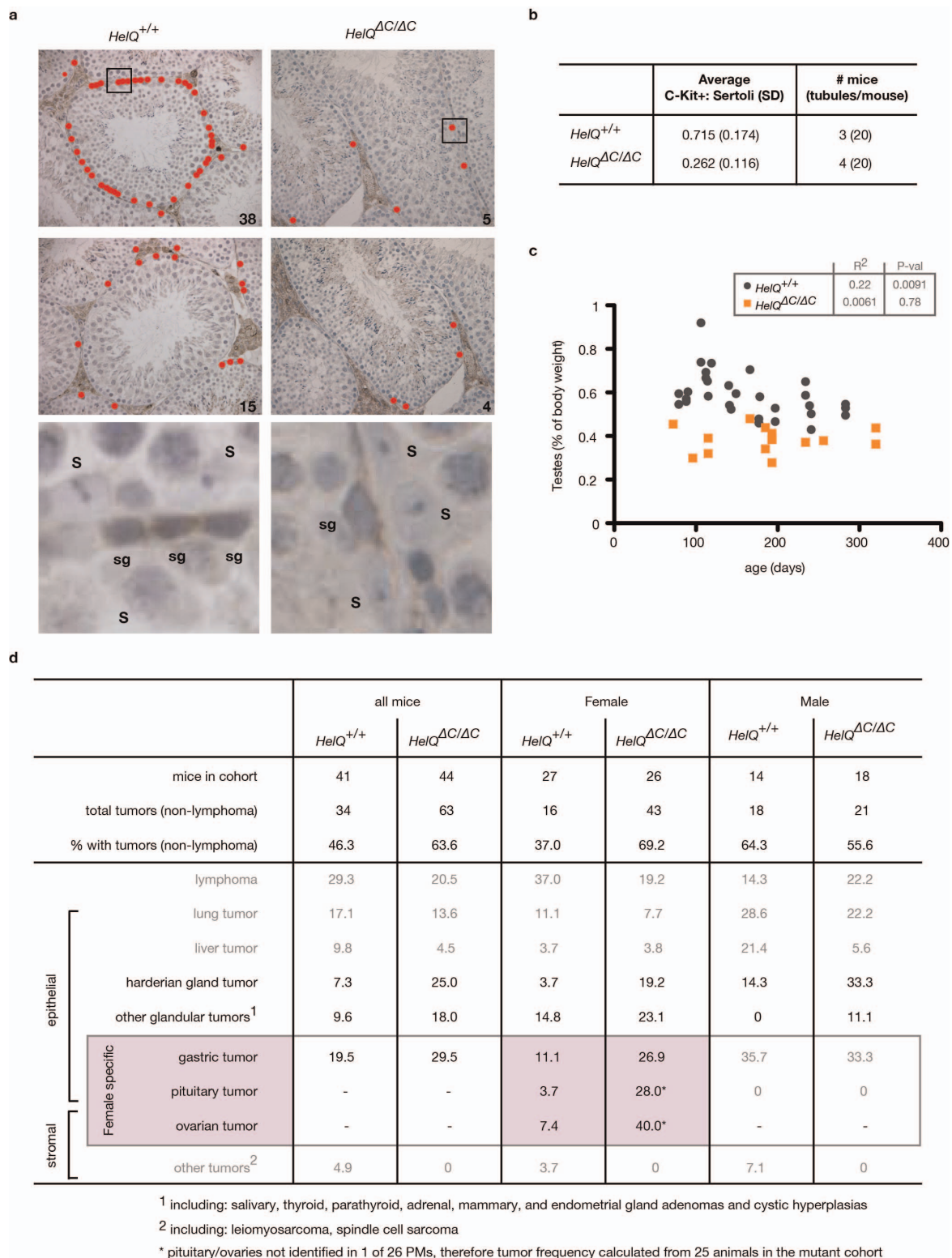
Pulsed field gel electrophoresis analysis. Immortalized embryonic fibroblasts were treated with or without MMC for 1 h and then allowed to recover for 16–48 h. Cells were collected and processed for pulsed field gel electrophoresis (PFGE) analysis similar to previously described methods²⁴. In brief, cell suspensions were placed on ice, cell numbers counted and equivalent cell numbers of each genotype were embedded in agarose plugs in duplicate. Cells were digested by incubating plugs in proteinase K overnight at 50 °C, plugs were washed 4 \times 1 h, sealed with low-melting-point agarose into the well of a 1% agarose/0.5 \times Tris/borate/EDTA (TBE) pulsed field gel, and run for 24 h on a Gene Navigator PFGE apparatus (Amersham) using the following conditions: running temperature: 13 °C; running angle: 120° (hex electrode); connection setup: interpolation (phase 1 of 2: N/S 30 s, E/W 30 s, phase time 23 h; phase 2 of 2: N/S 5 s, E/W 5 s); power program: 180 V 15 min, 170 V 30 min, 160 V 1 h, 150 V 2 h, 140 V 4 h, 130 V 8 h, 120 V 7 h. Gels were post-stained with ethidium bromide and washed in 0.5 \times TBE. PFGE was carried out on two independent sets of mutant and control cell lines and results were repeated two or more times for each set of cell lines. Similar results were obtained across all experiments and sets of cell lines.

27. Horn, C. *et al.* Splinkerette PCR for more efficient characterization of gene trap events. *Nature Genet.* **39**, 933–934 (2007).
28. Dupuy, A. J., Fritz, S. & Largaespada, D. A. Transposition and gene disruption in the male germline of the mouse. *Genesis* **30**, 82–88 (2001).
29. Truett, G. E. *et al.* Preparation of PCR-quality mouse genomic DNA with hot sodium hydroxide and tris (HotSHOT). *Biotechniques* **29**, 52–54 (2000).
30. Masson, J. Y., Stasiak, A. Z., Stasiak, A., Benson, F. E. & West, S. C. Complex formation by the human RAD51C and XRCC3 recombination repair proteins. *Proc. Natl Acad. Sci. USA* **98**, 8440–8446 (2001).
31. Kratz, K. *et al.* Deficiency of FANCD2-associated nuclease KIAA1018/FANL1 sensitizes cells to interstrand crosslinking agents. *Cell* **142**, 77–88 (2010).
32. Bruun, D. *et al.* siRNA depletion of BRCA1, but not BRCA2, causes increased genome instability in Fanconi anemia cells. *DNA Repair* **2**, 1007–1013 (2003).
33. Moldovan, G. L. *et al.* DNA polymerase POLN participates in cross-link repair and homologous recombination. *Mol. Cell. Biol.* **30**, 1088–1096 (2010).
34. Gunn, A. & Stark, J. M. I-SceI-based assays to examine distinct repair outcomes of mammalian chromosomal double strand breaks. *Methods Mol. Biol.* **920**, 379–391 (2012).
35. Seiler, J. A., Conti, C., Syed, A., Aladjem, M. I. & Pommier, Y. The intra-S-phase checkpoint affects both DNA replication initiation and elongation: single-cell and -DNA fiber analyses. *Mol. Cell. Biol.* **27**, 5806–5818 (2007).



Extended Data Figure 1 | Allele and subfertility of HELQ deficiency. **a**, Schematic of the β -geo gene trap and its approximate location within the *Helq* genomic locus. **b**, Sequence and traces showing the exact location of the gene trap insertion as determined by sequencing of splinkerette PCR products. **c**, HELQ western blot from wild-type (+/+) and *Helq* mutant ($\Delta C/\Delta C$) mouse cells, showing loss of HELQ and absence of a HELQ- β gal fusion protein (which, if present, would be evident in the region of the blot marked with the red bar). **d**, Table of observed and expected Mendelian ratios calculated from heterozygous matings. Chi-squared analysis was used to test for deviation of observed from expected. **e**, Average weights of *Helq* mice tracked between 2 and

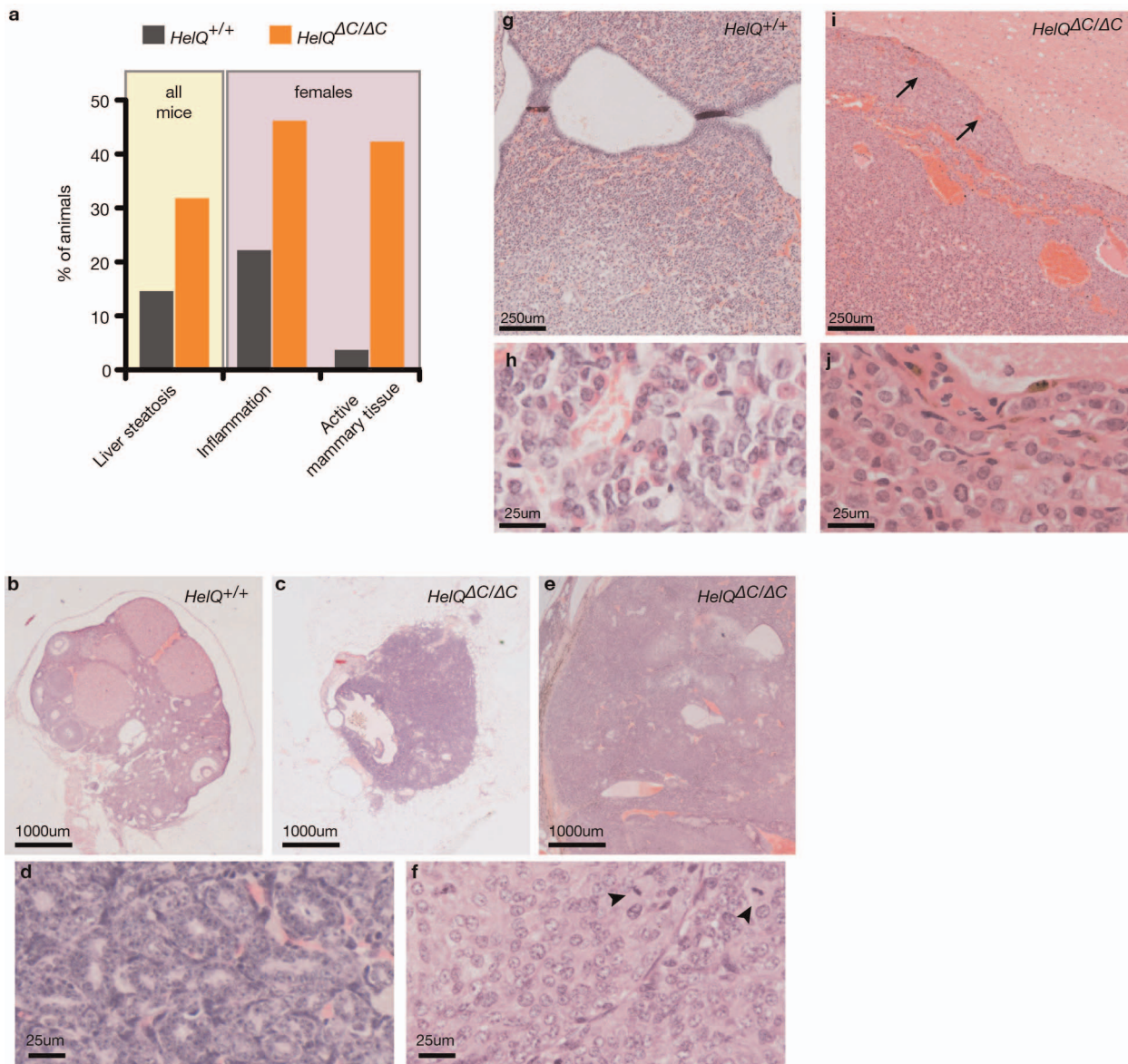
12 weeks of age. Means of 5–13 mice for each group are shown, and for clarity, s.d. is not plotted. Differences are not significant. **f**, Table of ovarian pathology in 30-week-old *Helq* control and mutant females (black text) and heterozygous females within the tumour watch study (blue text, 17–21 months old). **g–l**, Histological sections of testes from *Helq* ^{$\Delta C/\Delta C$} males showing various degrees of atrophy, including: normal tubules (**g**), mild atrophy (**h**, **i**), pockets of atrophy (arrows), pyknotic nuclei (asterisks); moderate atrophy (**j**, **k**), missing spermatogenic layer (arrowheads) and severe atrophy (**l**), with only Sertoli cells present.



Extended Data Figure 2 | *HELQ*-deficient germ cell and tumour phenotypes.

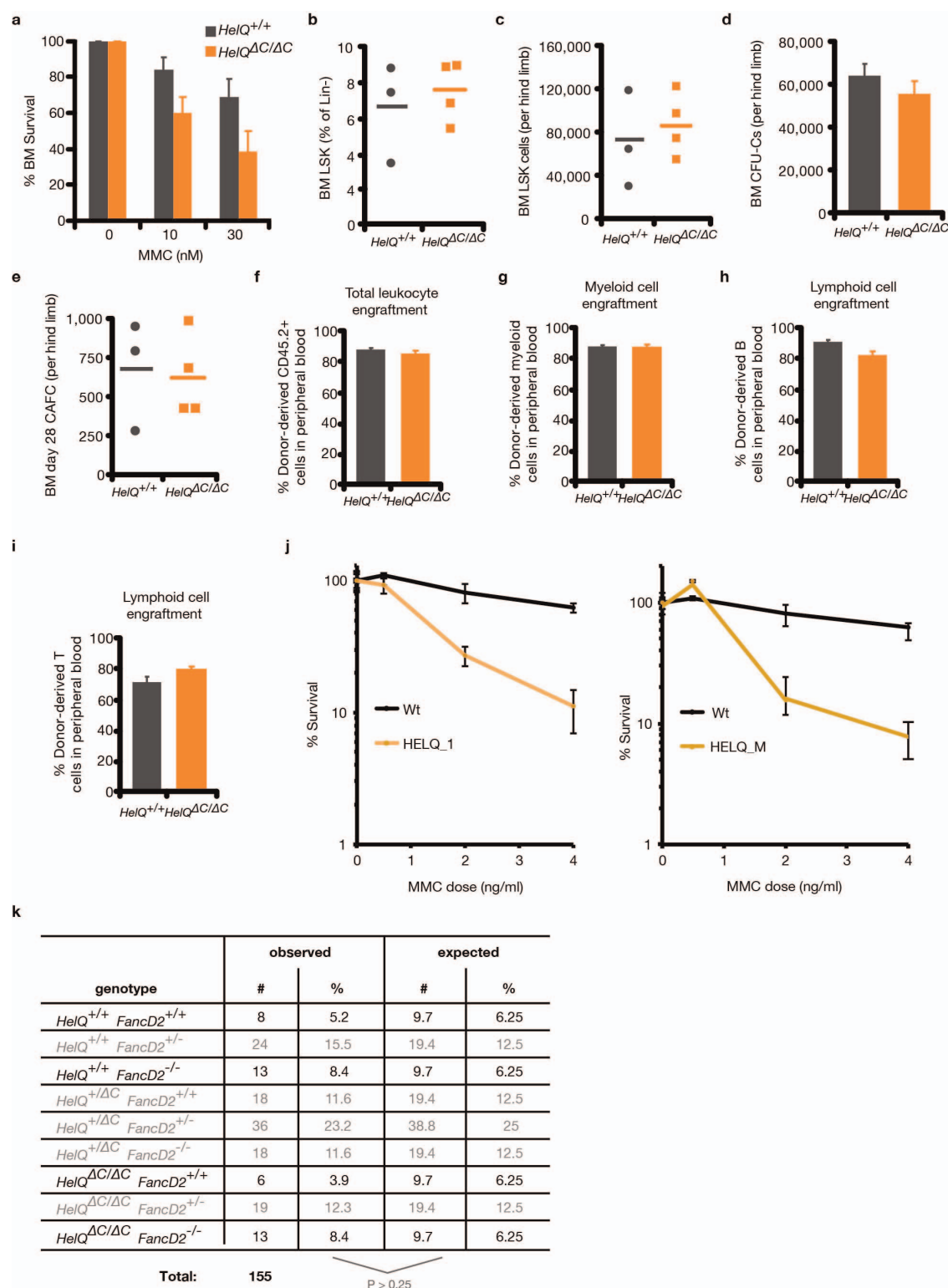
a, Immunohistochemical analysis of adult testes labelled with the stem cell marker c-KIT⁺ (brown) to highlight spermatogonia, and counterstained with haematoxylin to visualize remaining cells in the tubule (blue). Two representative images from wild-type (left) and mutant (right) mice are shown, with red circles indicating c-KIT⁺ cells. The number of c-KIT⁺ cells for each panel is indicated in the bottom right corner. Boxed regions in top panels are magnified in bottom panels to demonstrate staining. S, Sertoli cells; SG, c-KIT⁺ spermatogonia. **b**, Tabulation of average c-KIT⁺ cells per tubule

normalized to the number of Sertoli cells. **c**, Testis weights plotted by mouse age in days. Linear regression used to generate slope of best-fit line; tested best-fit line for deviation of slope from 0: *R*² and *P* values are indicated, revealing no correlation between age and testes weight for *Helq* mutants. **d**, Table of tumour frequency and tumour spectrum of *Helq* mutant and control mice showing data for all mice, females, and males in the tumour watch cohort. 129/B6 background phenomena are coloured in grey text, *Helq* mutant-specific effects are in black, and female-specific pathology is highlighted in pink.



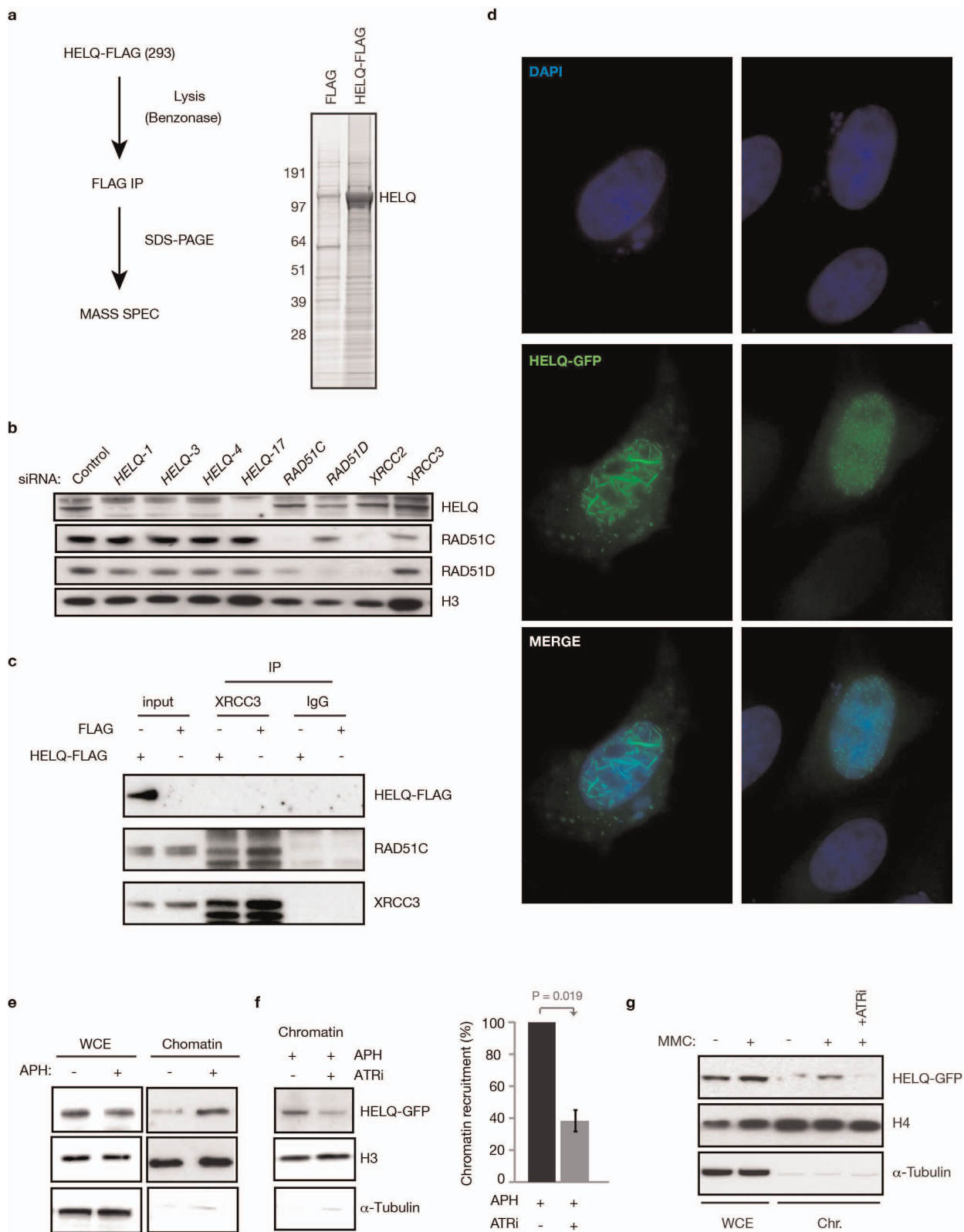
Extended Data Figure 3 | Tumour histology of HELQ deficiency. **a**, The frequency of liver steatosis in all mice, and inflammation and activated mammary tissue in female mice. **b–f**, Ovary sections showing normal wild-type ovary (**b**) and common ovarian pathology in mutant animals (**c–f**). Low-magnification (**c**) and high-magnification (**d**) images of dysgenic ovary from a *Helq* mutant exhibiting a sex cord stromal tumour containing tubular-like structures. Low-magnification (**e**) and high-magnification (**f**) images of large

nodular granulosa cell tumour from a *Helq* mutant. Arrowheads indicate mitotic figures (**f**). **g–j**, Pituitary sections showing low-magnification (**g**) and high-magnification (**h**) images of normal wild-type pituitary. Low-magnification (**i**) and high-magnification (**j**) images of pituitary tumour from a *Helq* mutant mouse. Arrows indicate boundary where large, haemorrhagic pituitary adenoma compresses overlying brain (**h**).



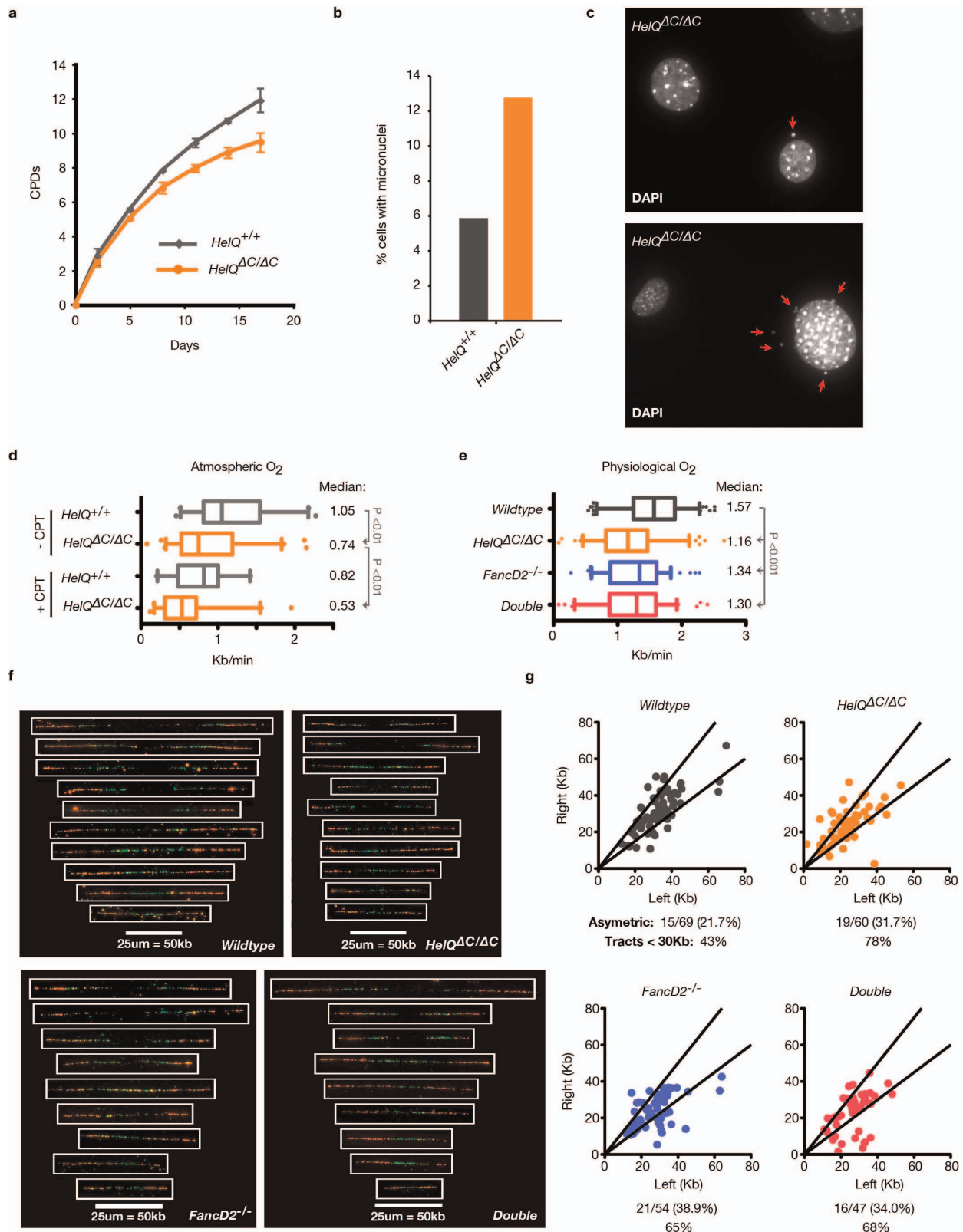
Extended Data Figure 4 | Characterization of *Helq*^{ΔC/ΔC} bone marrow and generation of *Helq Fancd2* double-mutant offspring. **a**, *Helq*^{ΔC/ΔC} and control bone marrow cells were isolated and exposed to MMC at the indicated doses and clonogenic survival of haematopoietic progenitors was plotted as percentage of surviving cells relative to untreated. Means ± s.e.m. for three mice per genotype are shown. **b–i**, Bone marrow (BM) from mutant and control mice was isolated and subjected to various haematopoietic stem and progenitor cell analyses: tabulation of bone marrow LSK (lineage⁻ Sca-1⁺ c-Kit⁺) cell populations (**b**, **c**); bone marrow c.f.u.-c (colony-forming units in culture) assays (**d**); bone marrow day-28 cobblestone area-forming cells

(CAFCs; **e**); and total donor-derived leukocyte (**f**), myeloid (**g**) and lymphoid (**h**, **i**) engraftment upon bone marrow transplantation. Raw data (symbols) and means (horizontal lines) from three mice are plotted (**b**, **c**, **e**); means ± s.e.m. for three mice per genotype (**d**); and means ± s.e.m. for 6–10 recipients for each genotype (**f–i**). **j**, siRNA-treated U2OS cells were plated for clonogenic survival and treated with the indicated reagents. **k**, Observed and expected Mendelian ratios calculated from *Helq*^{+ΔC} *Fancd2*^{+/-} double heterozygous matings. Chi-square analysis was used to test for deviation of observed from expected.



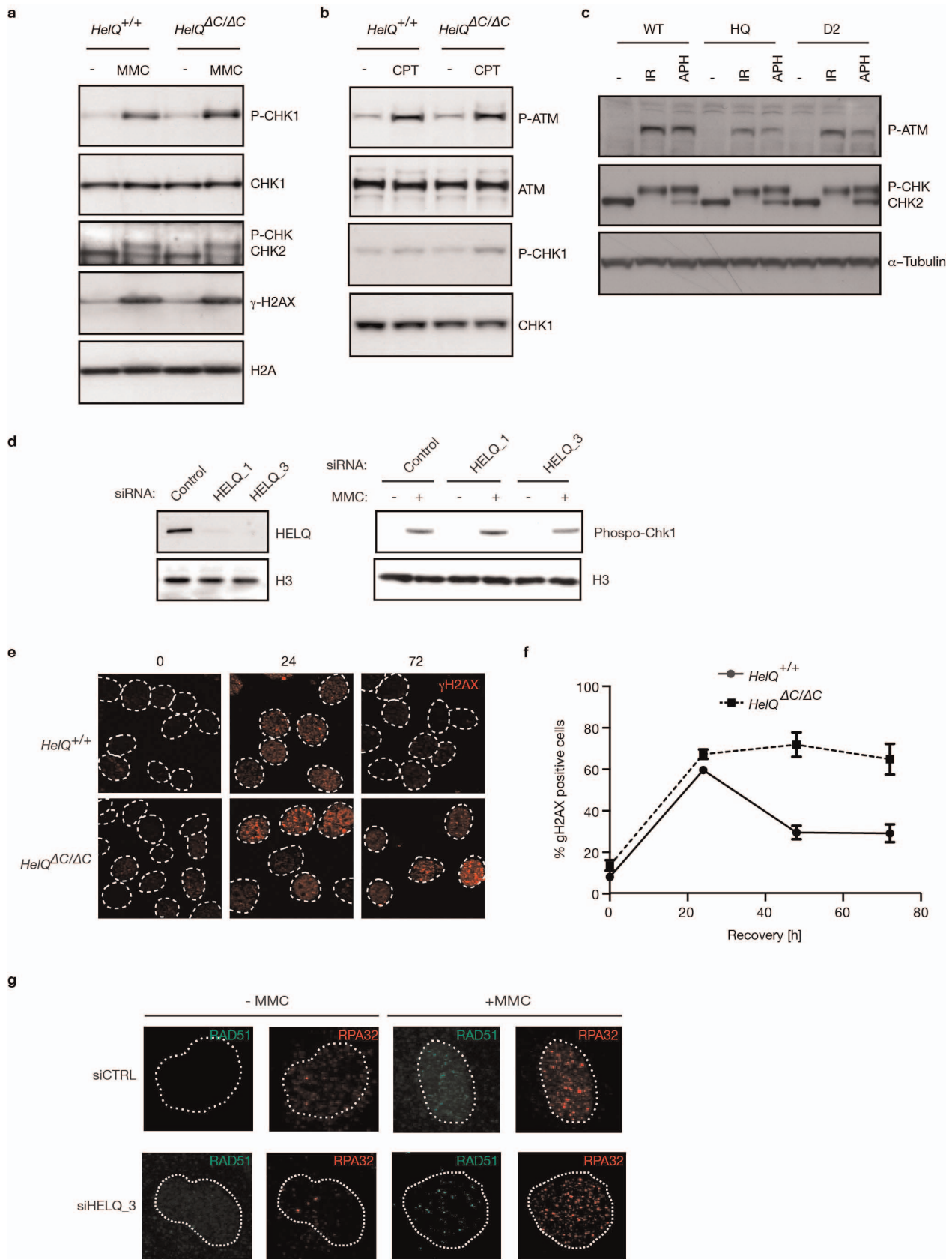
Extended Data Figure 5 | HELQ mass spectrometry, its relationship with the RAD51 paralogues, ATR, and overexpression. **a**, HELQ purification scheme and SDS-PAGE gel showing proteins co-purified with HELQ-Flag and control Flag immunoprecipitates. **b**, Cells treated with the indicated siRNAs were collected and probed for HELQ and the RAD51 paralogues. **c**, XRCC3 immunoprecipitated from HELQ-Flag and Flag control cell lysates and probed for Flag, XRCC3 and RAD51C (positive XRCC3 interacting protein control). IgG was used as a negative control. **d**, HeLa cells transiently expressing

recombinant HELQ-GFP (green panels) fixed and stained with DAPI (blue panels) to identify nuclei. Two examples of spontaneous nuclear aggregation patterns are shown: small focal aggregates (right) and large filamentous aggregates (left). **e**, Chromatin fractions of HELQ-GFP cells treated with or without 2 μ M APH for 24 h. **f**, Cells treated as in **e**, with or without 3 mM ATR inhibitor (ATRi). Quantification of HELQ in chromatin fractions normalized to H3 (right). **g**, Cells treated with or without 100 ng ml⁻¹ MMC for 24 h and fractionated as in **e**.



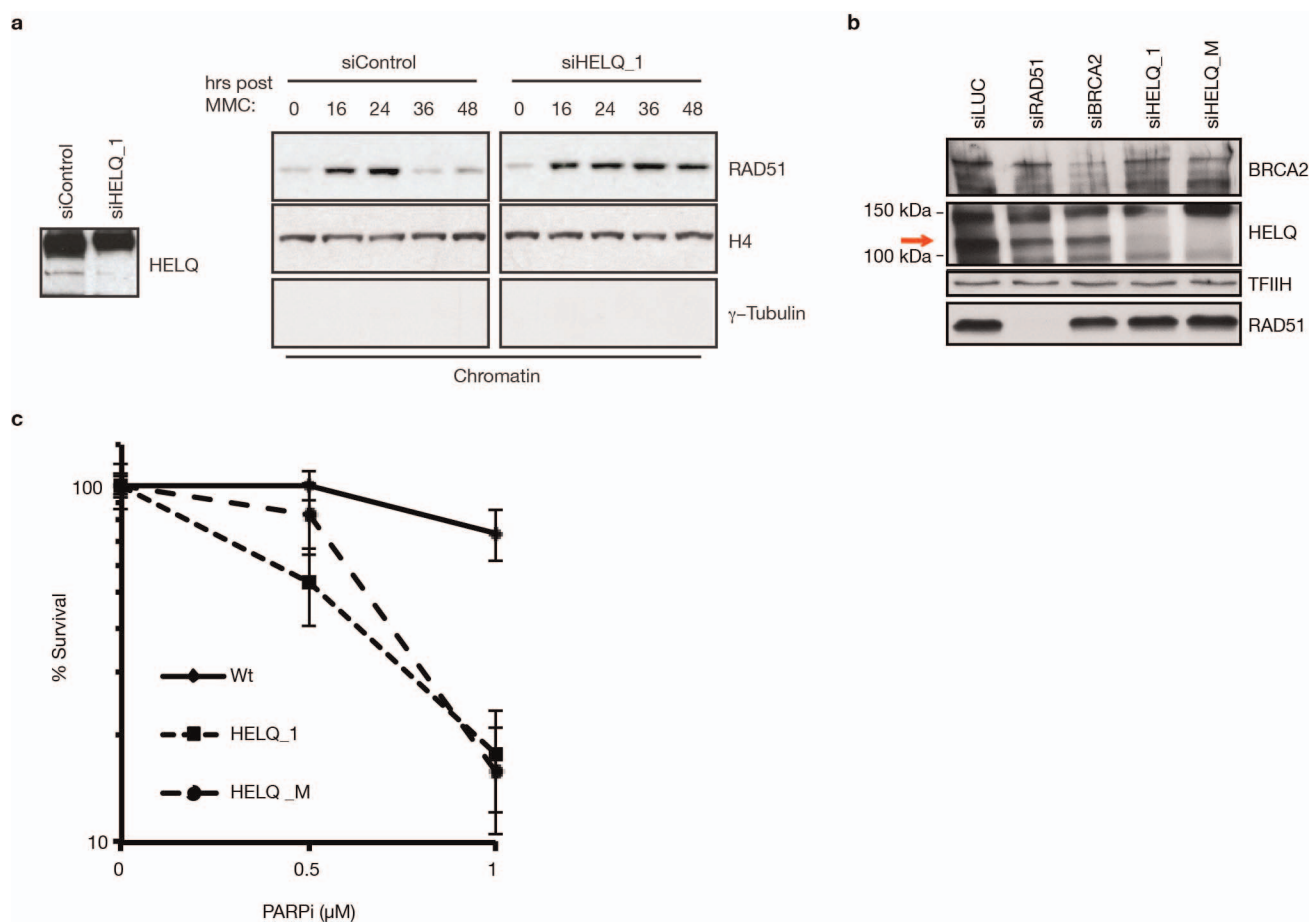
Extended Data Figure 6 | Spontaneous defects, checkpoint indices, damage foci and clonogenic survival of HELQ-deficient cells. **a**, Primary *Helq* mutant and control cell lines were grown in physiological O_2 for the indicated number of days and passaged regularly to generate a cumulative population doubling (CPD) curve. Means \pm s.d. of triplicate replicas are shown. **b**, **c**, *Helq* mutant and control cells grown on coverslips were formaldehyde fixed and DAPI stained to determine levels of spontaneous micronuclei formation: percentage

of 100 cells exhibiting 1 or more micronucleus (**b**); representative images (**c**), micronuclei (arrows). **d**, **e**, DNA combing used to calculate replication fork rates of primary cells grown under atmospheric (**d**) or physiological (**e**) O_2 . Cells in **d** were treated with or without 2.5 μM CPT for 15 min during labelling. **f**, Examples of origin containing IdU (green)- and CldU (red)-labelled fibres. **g**, Right versus left replication tract lengths to determine fork asymmetry (defined as tracts falling outside the interquartile lines).



Extended Data Figure 7 | Checkpoint and double-strand break repair function. **a, b**, Immortalized *HelQ*^{ΔC/ΔC} and *HelQ*^{+/+} cells treated with or without 500 ng ml⁻¹ MMC (**a**) or 50 nM CPT (**b**) for 20 h and probed for the indicated checkpoint indices. **c**, Primary wild-type (WT), HELQ-deficient (HQ) and FANCD2-deficient (D2) cells were left untreated (-), or exposed to 5 Gy irradiation and collected 30 min later, or 3 μM APH for 16 h and harvested 10 min

later, and lysates were probed for the indicated checkpoint indices. **d**, Phospho-Ser 345 CHK1 levels in U2OS cells subjected to 1 μM MMC for 24 h. **e**, Immortalized mouse cells were treated with 1 μM MMC for 24 h, allowed to recover for the indicated times (in hours), and stained for γH2AX. **f**, Quantification of percentage of positive cells from **e**. **g**, RPA32 and RAD51 foci formation in U2OS cells ± 1 μM MMC for 24 h subjected to control and *HELQ* siRNA.



Extended Data Figure 8 | Homologous recombination dynamics and PARP inhibitor sensitivity. **a**, U2OS cells treated with or without 100 ng ml^{-1} MMC for 24 h, allowed to recover for the indicated times (in hours), fractionated and probed for RAD51. H4 and α -tubulin are shown as controls for chromatin

fractionation. **b**, DR-GFP reporter cells treated with the indicated siRNAs were probed for BRCA2, HELQ and RAD51; transcription factor IIH (TFIIH) is shown as a loading control. **c**, siRNA-treated U2OS cells were plated for clonogenic survival and treated with the indicated reagents.

Hidden specificity in an apparently nonspecific RNA-binding protein

Ulf-Peter Guenther^{1,2}, Lindsay E. Yandek², Courtney N. Niland², Frank E. Campbell¹, David Anderson³, Vernon E. Anderson², Michael E. Harris² & Eckhard Jankowsky^{1,2}

Nucleic-acid-binding proteins are generally viewed as either specific or nonspecific, depending on characteristics of their binding sites in DNA or RNA^{1,2}. Most studies have focused on specific proteins, which identify cognate sites by binding with highest affinities to regions with defined signatures in sequence, structure or both^{1–4}. Proteins that bind to sites devoid of defined sequence or structure signatures are considered nonspecific^{1,2,5}. Substrate binding by these proteins is poorly understood, and it is not known to what extent seemingly nonspecific proteins discriminate between different binding sites, aside from those sequestered by nucleic acid structures⁶. Here we systematically examine substrate binding by the apparently nonspecific RNA-binding protein C5, and find clear discrimination between different binding site variants. C5 is the protein subunit of the transfer RNA processing ribonucleoprotein enzyme RNase P from *Escherichia coli*. The protein binds 5' leaders of precursor tRNAs at a site without sequence or structure signatures. We measure functional binding of C5 to all possible sequence variants in its substrate binding site, using a high-throughput sequencing kinetics approach (HITS-KIN) that simultaneously follows processing of thousands of RNA species. C5 binds different substrate variants with affinities varying by orders of magnitude. The distribution of functional affinities of C5 for all substrate variants resembles affinity distributions of highly specific nucleic acid binding proteins. Unlike these specific proteins, C5 does not bind its physiological RNA targets with the highest affinity, but with affinities near the median of the

distribution, a region that is not associated with a sequence signature. We delineate defined rules governing substrate recognition by C5, which reveal specificity that is hidden in cellular substrates for RNase P. Our findings suggest that apparently nonspecific and specific RNA-binding modes may not differ fundamentally, but represent distinct parts of common affinity distributions.

The term 'nonspecific' is widely used to describe proteins that bind DNA or RNA substrates at sites without apparent sequence or structure signatures^{1,2,5}. Although nonspecific proteins are numerous and have many important biological roles, a key open question is whether the absence of defined recognition elements in nucleic-acid-binding sites reflects largely indiscriminate substrate binding, or whether and how nonspecific proteins discriminate between different binding sites. To answer this question, we systematically examined substrate binding for the apparently nonspecific RNA-binding protein C5, the protein subunit of RNase P from *E. coli*. RNase P is a ribonucleoprotein enzyme that removes 5' leader sequences from precursor tRNA (ptRNA) in bacteria⁷ (Fig. 1a). The C5 protein promotes ptRNA processing by RNase P⁸, and contributes to ptRNA binding by associating with six consecutive nucleotides in the 5' ptRNA leaders^{9,10} (Fig. 1a, b). This binding site displays no apparent sequence or structure signatures in the 87 genomically encoded *E. coli* ptRNA leaders (Extended Data Fig. 1).

To determine whether and how C5 discriminates between different binding sites, we measured functional binding of C5 to all sequence variants in its cognate ptRNA site. Here, functional binding reflects

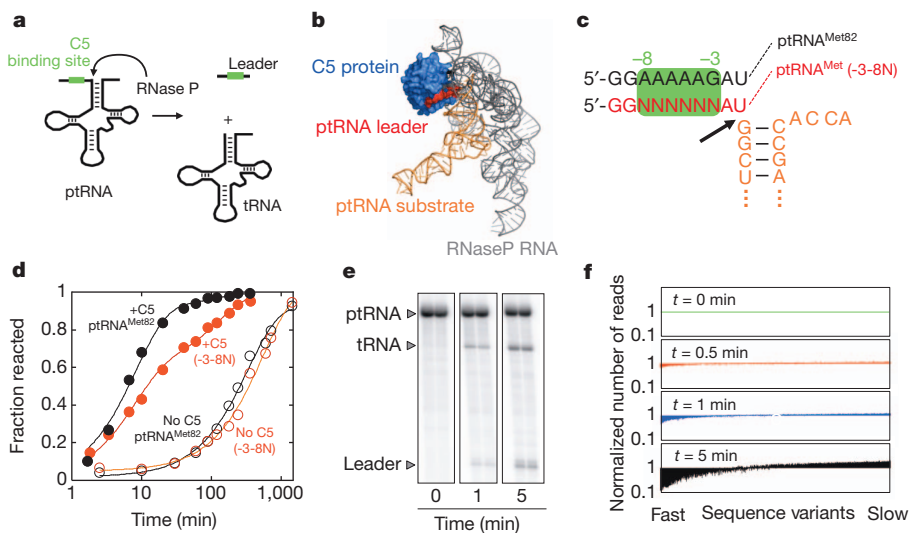


Figure 1 | Processing of precursor tRNA with randomized leader sequences. **a**, ptRNA processing reaction by RNase P. **b**, Structure of the RNase P holoenzyme⁹. **c**, Sequences of non-initiator ptRNA^{Met82} leaders (reference, black; randomized, red). The tRNA body is omitted for clarity. The arrow indicates the cleavage site. **d**, Time courses of RNase P processing of ptRNA^{Met82} (black) and ptRNA^{Met(-3-8N)} (red), in the presence (filled circles), and in the absence (open

circles) of C5. The solid lines are fits to the integrated rate equation for a biphasic first order reaction. **e**, Polyacrylamide gel electrophoresis (PAGE) of reactions processed for Illumina sequencing. **f**, Distributions of species for individual time points, ranked from fastest to slowest. The y axis marks the change in read numbers for each substrate species at the reaction time indicated, normalized to the number of reads at $t = 0$. Colours emphasize the different reaction times.

¹Center for RNA Molecular Biology, Case Western Reserve University, Cleveland, Ohio 44106, USA. ²Department of Biochemistry, School of Medicine, Case Western Reserve University, Cleveland, Ohio 44106, USA. ³Department of Management, Zicklin School of Business, Baruch College, The City University of New York, New York 10010, USA.

productive substrate association in an ongoing enzymatic reaction. It is expressed by the specificity constant (k_{cat}/K_m , the ratio of turnover number and Michaelis constant) for a given substrate variant, which measures biologically relevant specificity^{11,12}. To determine functional binding of C5 to all substrate variants simultaneously, we generated non-initiator precursor tRNA^{Met} with a randomized C5-binding site (ptRNA^{Met(-3-8N)}, Fig. 1c), and followed the processing reaction of this substrate population (Fig. 1d). Reactions were conducted with excess ptRNA^{Met(-3-8N)}. Under these multiple turnover conditions all sequence variants compete for C5 association, and the relative reaction rate for each variant reflects functional binding¹³.

The time course for the reaction of the randomized ptRNA^{Met(-3-8N)} population differed markedly from the time course of ptRNA^{Met82} with a genomically encoded leader (Fig. 1d). This difference indicates that sequence variation affects functional binding by C5. Removal of C5 slowed the reaction rate as expected and greatly diminished the kinetic differences between the substrates with the genomically encoded and the randomized leaders (Fig. 1d).

To determine reaction rate constants for the individual substrate variants, we isolated remaining substrates at various reaction times and measured the distribution of the RNA species by Illumina sequencing (Fig. 1e, f, Extended Data Fig. 2 and Extended Data Table 1). We used primers with degenerate barcodes to detect biased amplification of sequences during the PCR (Extended Data Fig. 2 and Extended Data Table 1). Of the 4,096 sequence variants, 2,900 showed unbiased amplification and were retained for further analysis. The distribution of sequence variants changed over the reaction time, revealing distinct fast- and slow-reacting species (Fig. 1f). These data demonstrate that C5 discriminates between different sequence variants, despite the lack of sequence signatures in genomically encoded *E. coli* ptRNA leaders.

We calculated a relative processing rate constant (k^{rel}) for each RNA variant, using internal competition analysis, developed for the evaluation of kinetic isotope effects (Extended Data Fig. 3)^{13–15}. The k^{rel} value is the ratio between the k_{cat}/K_m values for the given sequence variant and our reference sequence, the physiological leader AAAAAG. The relative rate constants for all sequence variants describe C5 binding to the entire sequence space of the six-nucleotide recognition site. Our approach to measure functional binding of large numbers of substrates during an ongoing reaction adds a kinetic dimension to the scope of high-throughput sequencing experiments with randomized RNA populations^{3,4,16,17}. We therefore propose to term our method high-throughput sequencing kinetics (HITS-KIN). The approach is applicable to other systems for kinetic analysis of next generation sequencing data.

For the ptRNA processing reaction with C5, the HITS-KIN method revealed a range of relative rate constants spanning several orders of magnitude (Fig. 2a). Obtained relative rate constants were highly reproducible in independent experiments (Fig. 2b). We also validated rate constants by direct kinetic measurements of selected sequence variants (Fig. 2c and Extended Data Fig. 4). Together, these data show that the HITS-KIN approach provides reproducible and accurate relative rate constants.

We next plotted the number of sequence variants processed at a given range of relative rate constants (Fig. 2d). The resulting histogram revealed that a significant number of sequence variants reacted faster than the physiological leader reference ($k^{\text{rel}} > 1$). Numerous sequence variants reacted slower ($k^{\text{rel}} < 1$). These observations indicate that physiological leader sequences of non-initiator ptRNA^{Met} are not preferentially bound by C5. Removal of C5 greatly contracted the range of relative rate constants, highlighting the impact of C5 on functional substrate binding and on the characteristic affinity distribution (Extended Data Fig. 5).

Most notably, the shape of the distribution of functional C5 affinities closely resembled affinity distributions of highly specific DNA-binding proteins, for which large numbers of sequence variants had been examined^{18–21} (Fig. 2d). This degree of similarity between the non-specific C5 and specific proteins was unexpected, given the absence of sequence signatures in the C5 binding site. For specific proteins, the

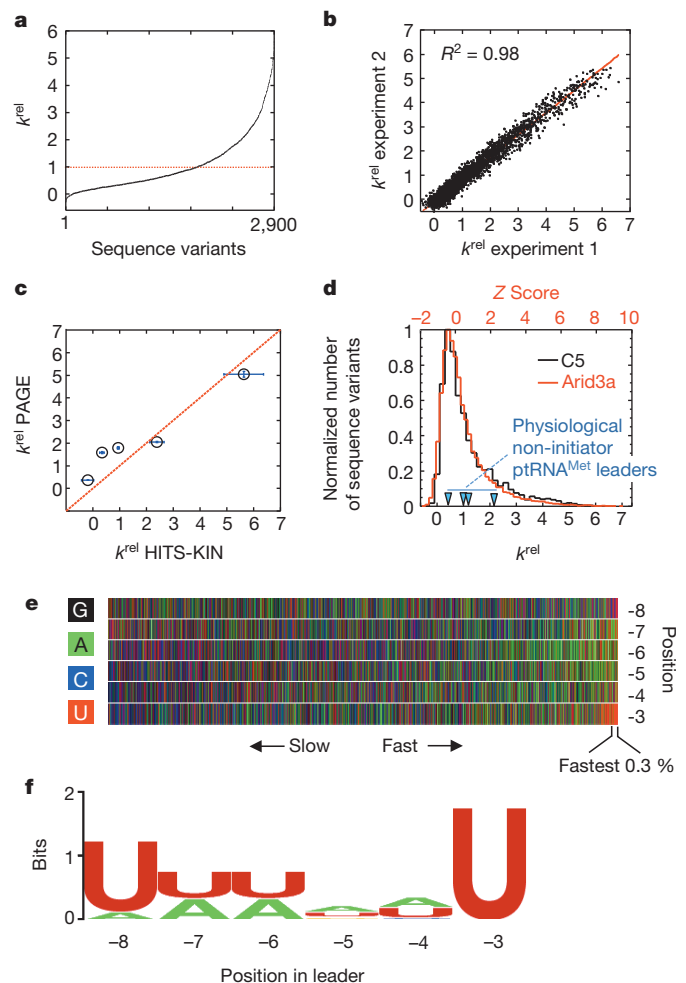


Figure 2 | Discrimination of C5 between different precursor tRNA^{Met} leader sequences. **a**, Relative rate constants (k^{rel}) for processing of all ptRNA leader sequence variants, ranked from slow to fast. Relative rate constants are averaged from four values (two time points of two experiments) and shown for only sequences where data from all four measurements passed quality control criteria (Extended Data Table 1). The line at $k^{\text{rel}} = 1$ marks the reference sequence. **b**, Correlation of relative rate constants from two independent biological replicates (red line, linear fit through the data; R^2 , correlation coefficient). **c**, Correlation between relative rate constants obtained by PAGE and by the HITS-KIN approach for selected sequence variants. Error bars represent the s.d. of three or more individual measurements. **d**, Distribution of relative rate constants for processing of ptRNA^{Met(-3-8N)} sequence variants by C5 (black) and apparent affinities for DNA binding by the transcription factor Arid3a, indicated as Z-scores based on published microarray data¹⁸. The Z-score is not identical to k^{rel} values, but accurately reflects affinity-based ranking of all sequences¹⁸ (triangles, k^{rel} values for genomic leader sequences of ptRNA^{Met}). **e**, Plot of all sequence variants ranked from slowest to fastest processed. The bracket marks 0.3% of sequence variants with the largest relative rate constants. **f**, Sequence logo for this fraction.

cellular substrates that define binding site signatures are found at the high-affinity tail of the distribution^{18,19} (Extended Data Fig. 6a, b). Remarkably, this high-affinity region for C5 also shows a clear sequence signature (Fig. 2e, f), as seen for specific proteins. In stark contrast to specific proteins, the C5 sequence signature does not correspond to the physiological binding sites on the non-initiator ptRNA^{Met}. None of the genomically encoded non-initiator ptRNA^{Met} leader sequences falls into this fastest-reacting fraction (Fig. 2d). For both C5 and specific proteins, no sequence signatures were detected for other regions of the sequence spectrum (Extended Data Fig. 6). Our results therefore reveal remarkable similarities between sequence discrimination by the apparently nonspecific C5 and by specific DNA-binding proteins. At the same time, our data

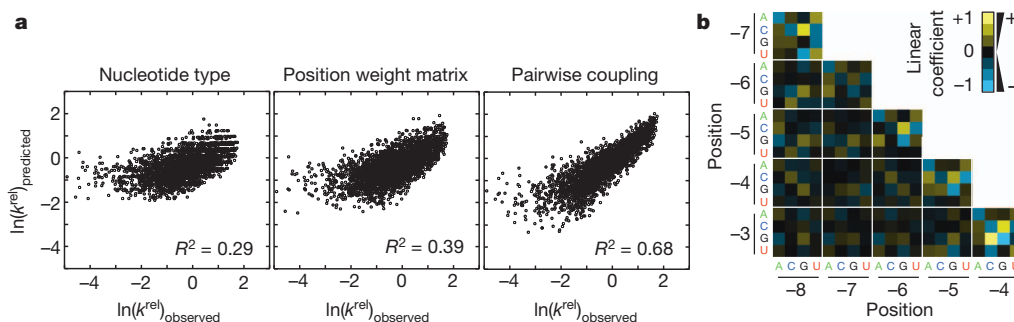


Figure 3 | Rules for sequence discrimination by C5. **a**, Correlation between observed k^{rel} and values calculated with the best fit of the data to models of increasing complexity. Logarithmic k^{rel} values are used because of their correspondence to differences in binding energies³⁰. R^2 expresses the

correlation of each model with measured processing rate constants.

b, Functional coupling between two base positions. Yellow squares show promotion of processing (high linear coefficients), black squares indicate small or no effects, blue squares mark inhibition of processing.

highlight a major difference: sequences bound with the highest affinity do not represent physiological substrates for C5, but for specific DNA-binding proteins with known affinity distributions.

To delineate sequence determinants that govern substrate recognition by C5, we fit the distribution of rate constants to models of increasing complexity and determined which percentage of the measured variance in the rate constants was explained by the respective model. Our simplest model considered only the number of a given nucleotide in the binding site, regardless of position. This model explained 29% of the variance in the measured rate constants (Fig. 3a, left). The model suggested favourable binding of sequences rich in adenine and uracil (Extended Data Fig. 7a). As A–U base pairs are thermodynamically less stable than G–C base pairs, we speculate that the variance explained by this model reflects in part the propensity of the leader to form transient structures with other parts of the ptRNA²², which potentially compete with C5 binding. Although competing structures are generally expected in RNAs with more than two dozen nucleotides²³, the relatively low correlation of the model with measured rate constants suggests that competing RNA structures have only limited impact on C5 binding for the majority of sequences.

We next considered both base identity and position in the binding site. This model, a traditional position weight matrix²¹, explained 39% of the variance in measured rate constants (Fig. 3a, middle, and Extended Data Fig. 7b). This modest improvement over the previous model indicated that the position of individual bases in the binding site impacted C5 binding only to a limited extent. However, the position weight matrix assesses the bases independently of each other²¹. To probe inter-dependence of the bases in the binding site, we used a model accounting for functional coupling between two bases. This model explained 68% of the variance in measured rate constants (Fig. 3a, right). The strongest couplings were detected between neighbouring bases (Fig. 3b).

The observed strength of the couplings between adjacent bases did not scale with energies expected to overcome stacking of the respective bases²². This finding suggests that the couplings result from interactions of the RNA with C5, not primarily from inherent RNA conformations. Functional couplings between more than two base positions, assessed by neural network analysis, only modestly improved correlation between predicted and measured data, and explained 76% of the variance (Extended Data Fig. 8). Thus, functional couplings between adjacent bases exert the largest influence on C5 binding. The limited resolution of the structural model of RNase P protein bound to RNA⁹ currently precludes structural interpretation of these effects. However, we note that functional coupling between neighbouring bases also contributes markedly to the binding of several specific transcription factors to DNA^{21,24,25}.

Taken together, the examination of the functional binding data with models of increasing complexity reveals defined rules for substrate binding by C5. The data demonstrate that discrimination between different substrates, and thus specificity, is an inherent property of C5. However,

this specificity is ‘hidden’ in the cellular RNA targets. This observation raises the question of why the specificity in C5 has not led to selection of ptRNA leaders with high-affinity sequence signatures, as seen in proteins with canonical specificity^{18–21}. Our data suggest a further-reaching utility of specificity. C5 uses its inherent specificity, as reflected in the rules for substrate recognition, to enable binding of diverse substrate variants with similar functional affinity. This enables RNase P to process these diverse substrates at a similar rate, which may be required for cellular tRNA homeostasis²⁶.

The marked similarities between affinity distributions of C5 and those of highly specific transcription factors also raise questions about the concept of ‘nonspecific’ RNA-binding proteins. Given that RNA binding requires a protein interface to establish interactions with the RNA, certain RNA sequence or structure variants conceivably fit this interface better than others. Genuine nonspecificity may therefore be difficult to accomplish, even for proteins binding exclusively to the RNA backbone, because sequence differences impact backbone geometry²⁷. Differences between substrate variants may become smaller for proteins that bind to the backbone of RNA duplexes, which show less structural heterogeneity, but are nevertheless dynamic²⁸.

Preferences of apparently nonspecific proteins for certain binding-site variants are thus likely to impact substrate selection, unless compensation for these preferences exist. Compensation may arise from varying concentrations of RNA species, rate-determining metabolic steps other than substrate binding, or a combination of these. Alternatively, a single protein could bind multiple distinct substrate regions while thermodynamically compensating for the preferences at each region, as shown for uniform binding of diverse aminoacyl-tRNAs to elongation factor Tu²⁹.

Although hidden specificity remains to be revealed for other proteins, the findings for C5 indicate that absence of sequence or structure signatures in cellular binding sites does not reflect an inability to discriminate between different RNA binding sites. At the same time, the data highlight the key difference between the hidden specificity of C5 and proteins that are specific in a canonical sense. For proteins with canonical specificity, cellular substrates seem to fall mainly into the high-affinity region of the sequence distribution. This region is associated with sequence signatures, even for C5. Biological substrates for C5 bind near the median of the affinity distribution, which does not produce a sequence signature. These findings suggest that specific and nonspecific binding modes may not fundamentally differ, but represent distinct parts of similar affinity distributions. Our data therefore have potentially broad implications for RNA binding by proteins thought to be nonspecific, including many RNases, RNA helicases or the La-protein.

METHODS SUMMARY

ptRNAs and ptRNA^{Met} with randomized leader sequences were produced by *in vitro* transcription from PCR-generated templates. RNase P processing reactions were carried out with 1 μM ptRNA and 5 nM RNase P holoenzyme (equimolar RNase P RNA and C5). Product and unreacted ptRNA were separated by PAGE. Complementary

DNA libraries for Illumina sequencing were prepared from unreacted pRNA at each given time point. Primers with degenerate barcodes were used to detect biased PCR amplification of certain sequences. Sequencing was performed on an Illumina GA2. Relative rate constants k^{rel} for individual substrate variants were calculated from changes in the distribution of substrates over time, using a multiple turnover reaction scheme for competitive substrate kinetics, which was extended to several thousand substrates. Computational modelling for the rules of substrate discrimination was performed by ordinary least squares regression of the matrix of values for $\ln(k^{\text{rel}})$ for each sequence variant according to four models of increasing complexity. The quality of the different models was judged by the correlation coefficient between a data set calculated from values obtained from the regression analysis and the set of experimentally obtained values for $\ln(k^{\text{rel}})$.

Online Content Any additional Methods, Extended Data display items and Source Data are available in the online version of the paper; references unique to these sections appear only in the online paper.

Received 15 May; accepted 14 August 2013.

Published online 22 September 2013.

- Gupta, A. & Gribskov, M. The role of RNA sequence and structure in RNA-protein interactions. *J. Mol. Biol.* **409**, 574–587 (2011).
- von Hippel, P. H. & Berg, O. G. On the specificity of DNA-protein interactions. *Proc. Natl Acad. Sci. USA* **83**, 1608–1612 (1986).
- Ray, D. *et al.* Rapid and systematic analysis of the RNA recognition specificities of RNA-binding proteins. *Nature Biotechnol.* **27**, 667–670 (2009).
- Campbell, Z. T. *et al.* Cooperativity in RNA-protein interactions: global analysis of RNA binding specificity. *Cell Rep.* **1**, 570–581 (2012).
- Singh, R. & Valcárcel, J. Building specificity with nonspecific RNA-binding proteins. *Nature Struct. Mol. Biol.* **12**, 645–653 (2005).
- Zhuang, F., Fuchs, R. T., Sun, Z., Zheng, Y. & Robb, G. B. Structural bias in T4 RNA ligase-mediated 3'-adapter ligation. *Nucleic Acids Res.* **40**, e54 (2012).
- Kurz, J. C. & Fierke, C. A. Ribonuclease P: a ribonucleoprotein enzyme. *Curr. Opin. Chem. Biol.* **4**, 553–558 (2000).
- Smith, J. K., Hsieh, J. & Fierke, C. A. Importance of RNA-protein interactions in bacterial ribonuclease P structure and catalysis. *Biopolymers* **87**, 329–338 (2007).
- Reiter, N. J. *et al.* Structure of a bacterial ribonuclease P holoenzyme in complex with tRNA. *Nature* **468**, 784–789 (2010).
- Rueda, D., Hsieh, J., Day-Storms, J. J., Fierke, C. A. & Walter, N. G. The 5' leader of precursor tRNA^{Asp} bound to the *Bacillus subtilis* RNase P holoenzyme has an extended conformation. *Biochemistry* **44**, 16130–16139 (2005).
- Herschlag, D. The role of induced fit and conformational changes of enzymes in specificity and catalysis. *Bioorg. Chem.* **16**, 62–96 (1988).
- Fersht, A. R. *Enzyme Structure and Mechanism* (Freeman, 1985).
- Cornish-Bowden, A. Enzyme specificity: its meaning in the general case. *J. Theor. Biol.* **108**, 451–457 (1984).
- Cleland, W. W. in *Isotope Effects in Chemistry and Biology* (eds Kohen, A. & Limbach, H. H.) 915–930 (CRC Press, 2006).
- Schellenberger, V., Siegel, R. A. & Rutter, W. J. Analysis of enzyme specificity by multiple substrate kinetics. *Biochemistry* **32**, 4344–4348 (1993).
- Lorenz, C. *et al.* Genomic SELEX for Hfq-binding RNAs identifies genomic aptamers predominantly in antisense transcripts. *Nucleic Acids Res.* **38**, 3794–3808 (2010).
- Pitt, J. N. & Ferré-D'Amaré, A. R. Rapid construction of empirical RNA fitness landscapes. *Science* **330**, 376–379 (2010).
- Badis, G. *et al.* Diversity and complexity in DNA recognition by transcription factors. *Science* **324**, 1720–1723 (2009).
- Rowe, W. *et al.* Analysis of a complete DNA-protein affinity landscape. *J. R. Soc. Interface* **7**, 397–408 (2010).
- Nutiu, R. *et al.* Direct measurement of DNA affinity landscapes on a high-throughput sequencing instrument. *Nature Biotechnol.* **29**, 659–664 (2011).
- Stormo, G. D. & Zhao, Y. Determining the specificity of protein-DNA interactions. *Nature Rev. Genet.* **11**, 751–760 (2010).
- Santalucia J. Jr & Turner, D. H. Measuring the thermodynamics of RNA secondary structure formation. *Biopolymers* **44**, 309–319 (1997).
- Forsdyke, D. R. Calculation of folding energies of single-stranded nucleic acid sequences: conceptual issues. *J. Theor. Biol.* **248**, 745–753 (2007).
- Maerkl, S. J. & Quake, S. R. A systems approach to measuring the binding energy landscapes of transcription factors. *Science* **315**, 233–237 (2007).
- Zhao, Y. & Stormo, G. Quantitative analysis demonstrates most transcription factors require only simple models of specificity. *Nature Biotechnol.* **29**, 480–483 (2011).
- Sun, L., Campbell, F. E., Yandek, L. E. & Harris, M. E. Binding of C5 protein to P RNA enhances the rate constant for catalysis for P RNA processing of pre-tRNAs lacking a consensus (+1)/C(+72) pair. *J. Mol. Biol.* **395**, 1019–1037 (2010).
- Leontis, N. B., Lescoute, A. & Westhof, E. The building blocks and motifs of RNA architecture. *Curr. Opin. Struct. Biol.* **16**, 279–287 (2006).
- Snoussi, K. & Leroy, J. L. Imino proton exchange and base-pair kinetics in RNA duplexes. *Biochemistry* **40**, 8898–8904 (2001).
- LaRivière, F. J., Wolfson, A. D. & Uhlenbeck, O. C. Uniform binding of aminoacyl-tRNAs to elongation factor Tu by thermodynamic compensation. *Science* **294**, 165–168 (2001).
- Stormo, G. D., Schneider, T. D. & Gold, L. Quantitative analysis of the relationship between nucleotide sequence and functional activity. *Nucleic Acids Res.* **14**, 6661–6679 (1986).

Supplementary Information is available in the online version of the paper.

Acknowledgements We particularly thank T. Nilsen for comments on the manuscript. We are grateful to G. Stormo for discussion, M. Adams for support with the Illumina sequencing, and H.-C. Lin for technical assistance. This work was supported by the US National Institutes of Health (NIH) (GM067700, GM099720 and CSTA UL1R024989 to E.J.; GM056740 and GM096000 to M.E.H.; T32 GM08056 to C.N.N.). U.-P.G. received a DFG fellowship.

Author Contributions U.-P.G., M.E.H. and E.J. designed the study. U.-P.G., L.E.Y., C.N.N. and F.E.C. performed the experiments. V.E.A. contributed to the development of the data analysis framework. D.A. developed and performed the modelling for binding models. U.-P.G., D.A., M.E.H. and E.J. analysed the data. U.-P.G., M.E.H. and E.J. wrote the paper.

Author Information Reprints and permissions information is available at www.nature.com/reprints. The authors declare no competing financial interests. Readers are welcome to comment on the online version of the paper. Correspondence and requests for materials should be addressed to M.E.H. (meh2@case.edu) or E.J. (exj13@case.edu).

METHODS

E. coli RNase P holoenzyme and RNase P RNA were prepared and tested for integrity as described previously^{31,32}. The non-initiator ptRNA^{Met} substrates contain 8 nucleotides of the genomically encoded leader (Fig. 1c), and 21 nucleotides at the 5' end for Illumina sequencing (Extended Data Fig. 2). These RNAs were generated by *in vitro* transcription from DNA generated by PCR amplification of the ptRNA^{Met82} gene (PMET82). The forward primer introduced the T7 promoter sequence and the additional 21 nucleotides (Extended Data Fig. 4). The ptRNA^{Met(-3-8N)} substrate population with randomized leader sequence N(-3) to N(-8) was generated using a primer with this region randomized (NNNNNN).

The following PCR primers were used (C5 binding site is underlined):

ptRNA^{Met82F}, 5'-TAATACGACTCACTATAGGGAGACCGGAATTCAGATTGATGAAAAAGATGGCTACGTAGCTCAGTTGG-3'; ptRNA^{Met82F_{Eco}}, 5'-GGGTAAACCTAATACGACTCACTATAGGGAGACCGGAATTCAGATTGATGAAAAAGATGGCTACGTAGCTCAGTTGG-3'; ptRNA^{Met82F_{Randomized}}, 5'-TAATACGACTCACTATAGGGAGACCGGAATTCAGATTGATGNNNNNNATGGCTACGTAGCTCAGTTGG-3'; ptRNA^{Met82R}, 5'-TGGTGGCTACGACGGGATTC-3'; ptRNA^{Met82R_{Bbs}}, 5'-CGGGATCCGAAGACAGTGGTGGCTACGACGGGATTC-3'. DNA templates for substrates L1 to L5 (Fig. 2c) contained the following C5-binding sites: L1, TTATAT; L2, TCAGAC; L3, ATTCAG; L4, CGTCAG; L5, CTCCTG.

PCR protocol: 95 °C, 2 min; 30 cycles (95 °C, 30 s at 55 °C, 45 s at 72 °C), final extension at 72 °C for 5 min.

The PCR products (142 base pairs (bp)) were extracted with phenol and chloroform and recovered by ethanol precipitation. PCR products for the ptRNA^{Met82} DNA were amplified with the ptRNA^{Met82F_{Eco}} and ptRNA^{Met82R_{Bbs}} primers, which include BamHI and EcoRI restriction sites. The PCR product was digested with these enzymes and cloned into pUC19. The resulting plasmid, pPTRNAmT(+21), was digested with BbsI to yield the template for *in vitro* transcription with the correct ptRNA^{Met82} 3' end.

In vitro transcription was performed in a volume of 400 µl with 15–20 µg of PCR template or cloned plasmid DNA template, 400 enzyme units of T7 RNA polymerase (Ambion), 0.01 unit yeast pyrophosphatase, 0.5 mM NTP, and the reaction buffer supplied by the polymerase manufacturer was supplemented with 2.5 mM MgCl₂. Reactions were incubated overnight at 37 °C. The full-length RNA was purified on 8% denaturing PAGE, as described previously^{31,32}.

Recovered ptRNAs were dephosphorylated using calf intestinal phosphatase and 5' end labelled with ³²P using ³²P-ATP and T4 polynucleotide kinase according to standard methods. For the HITS-KIN experiments, the RNA was uniformly labelled with ³²P-GTP in the *in vitro* transcription (NTPs 100 µM).

RNase P processing reactions. Multiple turnover reactions were performed in buffer containing 50 mM Tris-HCl, pH 8.0, 100 mM NaCl, 17.5 mM MgCl₂, 0.005% Triton X-100, with 1 µM ptRNA and 5 nM *E. coli* RNase P holoenzyme (1:1 ratio of P RNA and C5 protein). Equal volumes (40 µl) of enzyme and radiolabelled substrate at two times their final concentrations were prepared in reaction buffer and combined to initiate the reaction. Aliquots (5 µl) were removed at the times indicated for 5% to 30% substrate conversion. The reactions were quenched by addition of a solution (5 µl) containing formamide and 100 mM EDTA. ptRNA and reaction products were resolved on 10% denaturing PAGE (Fig. 1e). The fraction substrate converted to product was determined with a PhosphorImager (GE) and the ImageQuant software. Subsequently, precursor bands in the gel were located by exposure to X-ray film. The bands were excised and eluted as described previously³². Eluted RNA was extracted with phenol and chloroform, and recovered by ethanol precipitation.

Relative rate constants for individual non-initiator ptRNA^{Met} substrates (L1–L5, Fig. 2c, for defined sequences of C5 binding site, see above) were determined in reactions containing 1 µM of the pool of randomized ptRNA^{Met(-3-8N)}, spiked with trace amounts (<0.1 nM) of the respective radiolabelled L1–L5 substrate. Time courses of the reactions were followed as described above and apparent rate constants were determined from plots of product accumulation over time³². As outlined below, the ratio of the observed rate constants is k^{rel} because in competition kinetics the substrates at the concentrations used behave as V/K systems. V/K is proportional to k_{cat}/K_m at a given substrate concentration.

DNA library preparation. Complementary DNA libraries for Illumina sequencing were prepared from unreacted ptRNA, recovered from PAGE as described above. RNA was resuspended in 25 µl H₂O, and concentration was determined with a Beckman ultraviolet spectrophotometer. First-strand synthesis was performed with 4 pmol of this RNA in a 20-µl standard reaction containing 1 µM reverse transcription primer (Extended Data Fig. 2a) and 0.5 µl Superscript III (Invitrogen) for 10 min at 42 °C, 40 min at 50 °C and 20 min at 55 °C. The reaction was stopped by incubation at 95 °C for 5 min. The generated cDNA was diluted (1:300). One microlitre of this solution was used in PCR reactions with 1.25 enzyme units Herculase polymerase

(Stratagene), reverse transcription primer (0.5 µM) and indexed forward primer (0.5 µM) for 2 min at 98 °C, followed by 19 cycles (15 s at 98 °C, 20 s at 59 °C, 20 s at 72 °C), and incubation for 10 min at 72 °C. PCR products were purified with P6 microcentrifuge columns (Bio-Rad) and analysed by agarose gel electrophoresis (Extended Data Fig. 2b). The solutions were pooled in an equimolar fashion and sequenced in a single lane of an Illumina GA2, according to the manufacturer's protocols. Primer sequences were as follows: reverse transcription primer, 5'-CAAGCAGAAGACGGCATACGATGGTGGCTACGACGGGAT-3'; indexed forward primers (NN, degenerate barcode; underlined letters, index barcode), 5'-AATGATACGGCGACCAACCGAGATCTACACTCTTTCCCTACACGACGCTCTTCCGATCTNNATCGGGAGACCGGAATTCAGATTG-3'; 5'-AATGATACGGCGACCAACCGAGATCTACACTCTTTCCCTACACGACGCTCTTCCGATCTNNATCGGGAGACCGGAATTCAGATTG-3'; 5'-AATGATACGGCGACCAACCGAGATCTACACTCTTTCCCTACACGACGCTCTTCCGATCTNNATCGGGAGACCGGAATTCAGATTG-3'; 5'-AATGATACGGCGACCAACCGAGATCTACACTCTTTCCCTACACGACGCTCTTCCGATCTNNATCGGGAGACCGGAATTCAGATTG-3'.

Processing of Illumina sequencing data. All reads were aligned to the sequence of nucleotides 6–29 of the read (Extended Data Fig. 2c), permitting one mismatch but no gaps, using the basic local alignment search tool (BLAST). Aligned reads were then sorted according to their index tag, and separated into different files. For corresponding statistics, see Extended Data Table 1.

We probed possible over- or under-amplification of certain sequences during the PCR using the two-nucleotide degenerate barcode (positions 1 and 2, Extended Data Fig. 2c). Correctly amplified sequences show a distribution of degenerated barcode nucleotide combinations that is identical, within error, for all leader species. Both over- and under-amplification cause deviations from this distribution. We determined the distribution of all nucleotide combinations at positions 1 and 2 for each leader sequence. The expected distribution of the two-nucleotide degenerate barcode was calculated from all 4,096 leader sequence variants. Then, chi-squared tests were performed for each leader variant. Sequences for which the threshold exceeded $\alpha > 0.05$ were excluded from further analysis (between 4% and 10% of the sequence variants, Extended Data Table 1).

Determination of relative rate constants k^{rel} from Illumina sequencing data. Rate constants for individual substrate variants were calculated from time-dependent changes of the distribution of substrate variants (Fig. 1f), using a multiple turnover reaction scheme for competitive alternative substrate kinetics^{15,33} (Extended Data Fig. 3).

The observed rate constant ($v_{1,i}$) for processing of one individual substrate (S_i) is proportional to the fraction of total enzyme that binds this substrate to form a complex (ES_i) that further reacts to form product and regenerates free enzyme according to:

$$v_1 = V_1 E f_{ES1} \quad (1)$$

Here, V_1 is the first order rate constant for the reaction of ES_1 to yield free product (Extended Data Fig. 3), f_{ES1} is the fraction of total (active) enzyme (E) in the ES_1 complex. Additional substrates act essentially as competitive inhibitors of the multiple turnover reaction. Accordingly, v_1 is:

$$v_1 = \frac{V_1 E \frac{S_1}{K_1}}{\left(1 + \sum_{i=1}^n \frac{S_i}{K_i}\right)} \quad (2)$$

Variables are defined in Extended Data Fig. 3. By extension, v_2 is:

$$v_2 = \frac{V_2 E \frac{S_2}{K_2}}{\left(1 + \sum_{i=1}^n \frac{S_i}{K_i}\right)} \quad (3)$$

As the denominators of equations (2) and (3) are the same, the ratio of two observed rate constants (v_1/v_2) therefore becomes:

$$\frac{v_2}{v_1} = \frac{\left(\frac{V}{K}\right)_2}{\left(\frac{V}{K}\right)_1} \left(\frac{S_2}{S_1}\right) \quad (4)$$

We define the parameter k^{rel} as the ratio of the V/K values of a given substrate (S_2) to a reference substrate (S_1):

$$\frac{\left(\frac{V}{K}\right)_2}{\left(\frac{V}{K}\right)_1} = k^{\text{rel}} \quad (5)$$

and thus:

$$\frac{v_2}{v_1} = k^{\text{rel}} \left(\frac{S_2}{S_1} \right) \quad (6)$$

The reference substrate S_1 is the genomically encoded leader sequence for the ptRNA^{Met82} (AAAAAG)³⁴. Thus, $k^{\text{rel}} > 1$ for a ptRNA variant that reacts faster than the reference substrate ($V_i/K_i > V_1/K_1$), whereas $k^{\text{rel}} < 1$ indicates a slower reaction ($V_i/K_i < V_1/K_1$).

Equations (4) to (6) highlight three important points regarding the use of internal competition kinetics for the analysis of deep sequencing data. First, both substrates will behave as V/K systems^{35,36} regardless of the substrate concentrations. This is true even if one or both concentrations are greater than the respective values for K_m , because both substrates compete for free enzyme^{13,15}. Second, the ratio of observed rate constants and the ratio of V/K values are independent of enzyme concentration, provided the steady state conditions are maintained. Third, the reaction step that limits V/K does not have to be the same for both substrates.

Integration of equation (5) over time ensures validity of the expression for any reaction interval¹³, and we obtain:

$$k^{\text{rel}} = \frac{\ln \left(\frac{S_2}{S_{2,0}} \right)}{\ln \left(\frac{S_1}{S_{1,0}} \right)} \quad (7)$$

Here, $S_{1,0}$ and $S_{2,0}$ are the initial concentrations of the two substrates. S_1 (reference substrate) and S_2 (the specific sequence variant) are the respective concentrations at a defined time interval. The quantities that can be measured are the relative concentrations of S_2 and S_1 ; that is, S_2/S_1 and $S_{2,0}/S_{1,0}$. We define these quantities as the ratios (R) between substrates:

$$R_i = \frac{S_i}{S_1} \quad (8)$$

$$R_{i,0} = \frac{S_{i,0}}{S_{1,0}} \quad (9)$$

The initial mole fractions (X_i) of S_i are defined as:

$$X_i = \frac{S_i}{\sum_{i=1}^n S_{i,0}} \quad (10)$$

$S_{1,0}$ is the concentration of a given substrate at the reaction start, S_1 is the concentration at a time point where the overall reaction amplitude for the entire substrate population has reached the value f . We obtain:

$$f = 1 - \sum_{i=1}^n X_i \quad (11)$$

Analogous to the treatment of kinetic isotope effects using internal competition in a previous publication¹⁴, we insert the defined mole fractions and substrate ratios (equations (8) to (11)) into equation (11). This is rearranged, and the result is the following equation:

$$\frac{S_i}{S_{i,0}} = \frac{(1-f)}{R_i \sum_{i=1}^n \left(\frac{R_i}{R_{i,0}} X_i \right)} \quad (12)$$

We substitute this term in equation (7), and consider that substrate ratios at time zero equal one.

$$\frac{R_1}{R_{1,0}} = 1 \quad (13)$$

We obtain the following expression for the relative rate constant for any substrate, S_i :

$$k_i^{\text{rel}} = \frac{\ln \left(\frac{R_{i,0}}{R_i} \left(\sum_{i=1}^n \frac{R_i}{R_{i,0}} X_i \right) \right)}{\ln \left(\frac{(1-f)}{\sum_{i=1}^n \frac{R_i}{R_{i,0}} X_i} \right)} \quad (14)$$

Here, R is the ratio of each sequence (including S_1) to S_1 , R_0 is the ratio of each variant to $S_{1,0}$ at the reaction start, and X is the mole fraction for a given sequence variant. The method outlined above is applicable to any technique capable of determining substrate ratios (for example, mass spectrometry, isotopic counting, chromatography).

We computed R and X values for each substrate using the filtered number of counts for each variant, obtained from Illumina sequencing (Supplementary Table 2). The overall fraction of reacted product was determined by PhosphorImager analysis of the PAGE (Fig. 1e).

In principle, values for k^{rel} can be computed at any value of f . However, there is little relative change in the number of sequencing reads at early time points. However, at early time points the highest resolution is seen for the fastest reacting variants, while k^{rel} values for slower sequences are optimally measured at greater values of f . Values of $f = 0.1$ to 0.3 provided reliable measurements for most sequence variants. Nevertheless, for slow-reacting variants small changes in the number of sequencing reads at early time points are occasionally exceeded by sampling error in the number of reads, resulting in negative values for k^{rel} .

Computational modelling of rules for substrate discrimination. With regard to nucleotide type, this model considers the number of each nucleobase in the binding site, regardless of its position. For each sequence variant the corresponding value of $\ln(k^{\text{rel}})$ (Fig. 3a) is described by a set of linear coefficients (β), according to the equation:

$$\ln(k^{\text{rel}}) = \beta_0 + \beta_A \bullet A + \beta_C \bullet C + \beta_G \bullet G \quad (15)$$

A , C and G are the number of the respective nucleobases (explanatory value). The number of U follows from these variables and is therefore not included ($\beta_U = 0$). Equation (15) describes the average increase in $\ln(k^{\text{rel}})$ corresponding to a one-unit increase in the explanatory variable. For example, for each additional C in the sequence, the $\ln(k^{\text{rel}})$ increases by β_C .

Linear coefficients for the entire data set were computed by ordinary least squares (OLS) regression, using the open-source statistical package R (<http://www.r-project.org/>) and the exact equation:

$$\beta_N = (X^T X)^{-1} X^T Y \quad (16)$$

Here, Y is the vector of outcomes $\ln(k^{\text{rel}})$ and X is the matrix of explanatory variables (A, C, G). X^T is X transposed, and X^{-1} is the inverse of X .

To compare predicted and measured $\ln(k^{\text{rel}})$ values for all sequence variants (Fig. 3a), we calculated predicted values using equation (15), plotted these versus the corresponding measured value, and determined the correlation between measured and calculated data set. The coefficient of correlation (R^2) was computed according to³⁷:

$$R^2 = 1 - \frac{S_{\text{error}}^2}{S_{\text{total}}^2} \quad (17)$$

S_{error}^2 is the sum of squared errors and measures the error, or unexplained variance, in the regression. The error is the distance from each point to the regression line, and is calculated for each data point, squared, and summed, according to:

$$S_{\text{error}}^2 = \sum_i (y_i - f_i)^2 \quad (18)$$

S_{total}^2 is the sample variance, which is calculated according to:

$$S_{\text{total}}^2 = \sum_i (y - \bar{y})^2 \quad (19)$$

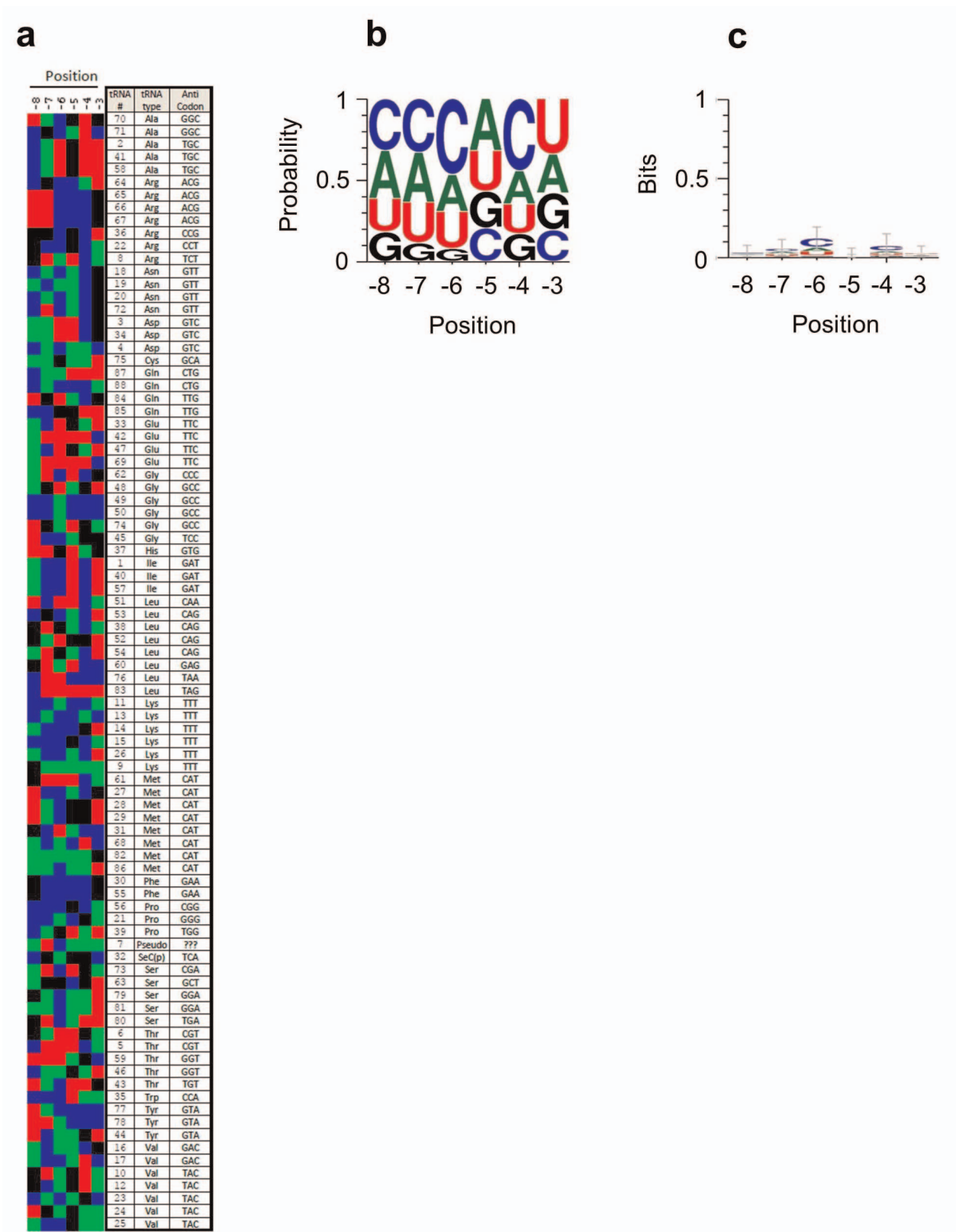
Position weight matrix. To examine how the position of different nucleobases in the binding site affects the reaction rate, we included the position of each base in the regression model. This model has 18 explanatory variables, three for each of the six positions, as explained above. Each variable is 1 if the respective base is at a given position, and 0 otherwise. For example, G4 will be 1 if the fourth base is a G, and 0 otherwise. We used the reference sequence as baseline, and did therefore not include these variables in the regression. Calculations of linear coefficients (Extended Data Fig. 7b), and the comparison between predicted and measured values for individual $\ln(k^{\text{rel}})$ values (Fig. 3a) were performed as described above.

Functional couplings between bases. We created interaction variables of the same form as in the two-dimensional model 2, but these interaction terms were composed of two bases. For example, A1G4 is 1 if the first base is A and the fourth base is G, and will be 0 otherwise. We then performed calculations with the two-dimensional model 240 times, each time adding a separate interaction term. Interactions whose effect was statistically significant ($P < 10^{-5}$) were retained, other interactions were not considered further. Next, we included all statistically significant interactions in one model, which was further pared using stepwise regression³⁸. This approach yielded a model similar to the position weight matrix augmented with the 44 most significant interaction terms. Calculations of linear coefficients (Fig. 3b), and the comparison between predicted and measured values for individual $\ln(k^{\text{rel}})$ values (Fig. 3a) were performed as described above.

Neural network analysis. Analysis was performed with the MATLAB Neural Networks Toolbox (v. 3.0). Data input was identical to the two-dimensional model above. Data were fit to a three-layer feed-forward network with 13 hidden nodes.

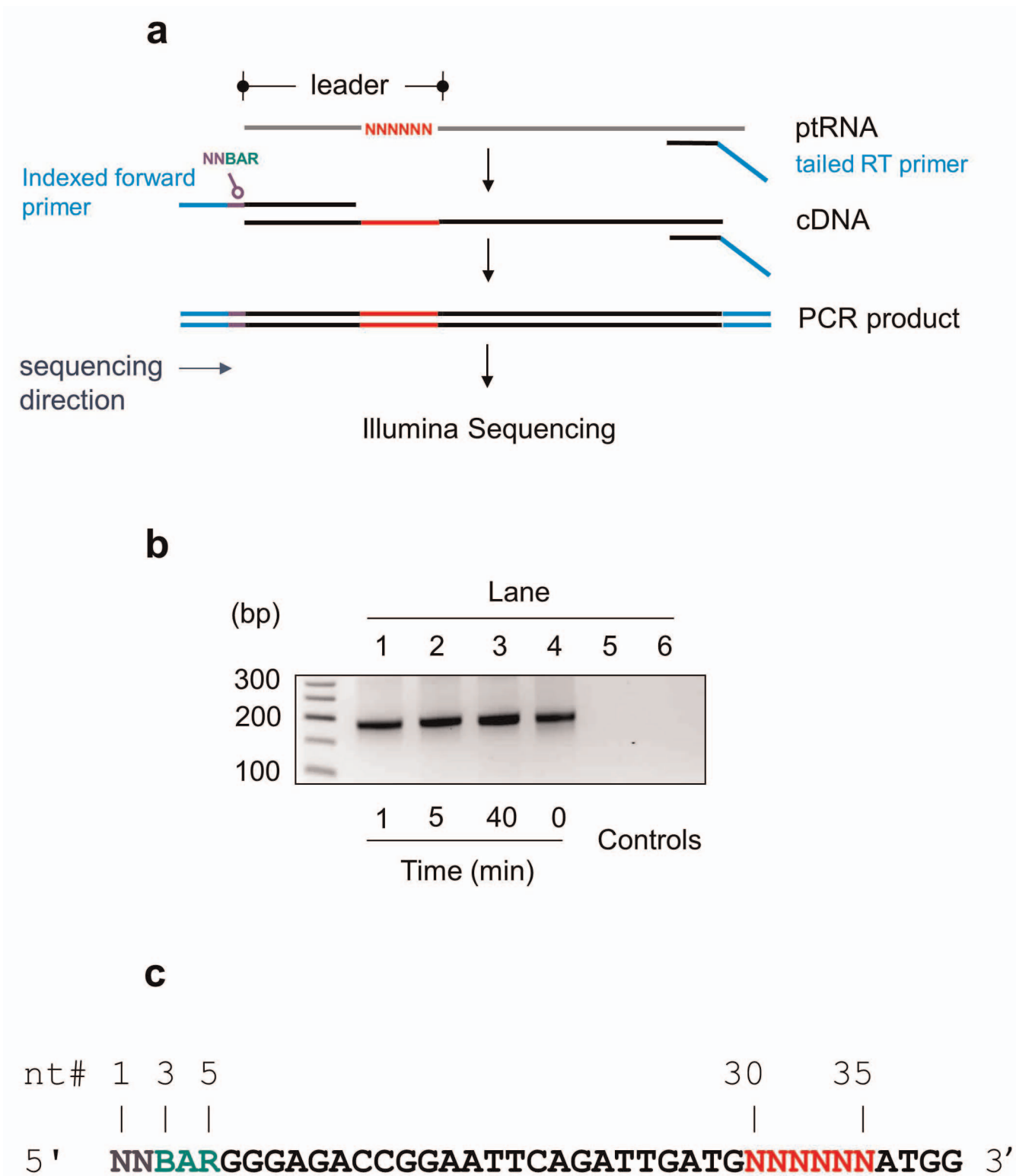
Interaction terms are not necessary in this model, because the neural network learns the interaction patterns from the raw sequence data. The resulting network was used to generate estimates for the reaction rate for each base sequence. Neural nets were trained on 60% of the data, validated on 20% of the data and tested on the remaining 20%. Almost identical R^2 values were obtained for both the 20% hold-out sample, and the entire data set.

31. Guo, X. *et al.* RNA-dependent folding and stabilization of C5 protein during assembly of the *E. coli* RNase P holoenzyme. *J. Mol. Biol.* **360**, 190–203 (2006).
32. Christian, E. L., McPheeters, D. S. & Harris, M. E. Identification of individual nucleotides in the bacterial ribonuclease P ribozyme adjacent to the pre-tRNA cleavage site by short-range photo-cross-linking. *Biochemistry* **37**, 17618–17628 (1998).
33. Cha, S. Kinetics of enzyme reactions with competing alternative substrates. *Mol. Pharmacol.* **4**, 621–629 (1968).
34. Chan, P. P. & Lowe, T. M. GtRNAdb: a database of transfer RNA genes detected in genomic sequence. *Nucleic Acids Res.* **37**, D93–D97 (2009).
35. Northrop, D. B. Fitting enzyme-kinetic data to V/K . *Anal. Biochem.* **132**, 457–461 (1983).
36. Northrop, D. B. Rethinking fundamentals of enzyme action. *Adv. Enzymol.* **73**, 25–55 (1999).
37. Theil, H. *Economic Forecasts and Policy* (North Holland Publishing, 1961).
38. Bendel, R. B. & Afifi, A. A. Comparison of stopping rules in forward “stepwise” regression. *J. Am. Stat. Assoc.* **72**, 46–53 (1977).



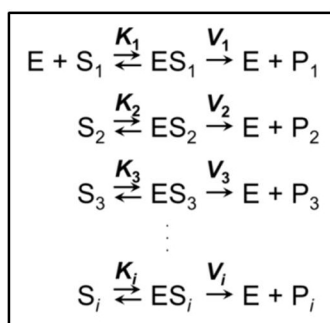
Extended Data Figure 1 | C5 binding site in the 87 ptRNA leaders in *E. coli*. **a–c**, Alignment and sequence logos for the C5 binding site in all 87 ptRNA leaders encoded by *E. coli*. Binding of C5 to the consecutive ptRNA positions –3 to –8 is well established, based on a crystal structure⁹ and biochemical evidence¹⁰; that is, looping of bases seen for certain RNA- and DNA-binding proteins, does not occur with C5. Consistent with this idea, we did not detect any sequence motif with the MEME software, when including positions –1 to

–10. **a**, Sequence alignment. Sequences were aligned with CLUSTAL. Coloured squares indicate the bases (C, blue; A, green; U, red; G, black). Anticodon, the anticodon recognized by the tRNA; tRNA#, the tRNA identification number; tRNA type, the amino acid. **b**, Sequence logo depicting the probability of any base at a given position, based on the alignment in **a**. The logo was generated with Weblogo. **c**, Sequence logo for the information content of the alignment in **a**. The logo was generated with Weblogo.

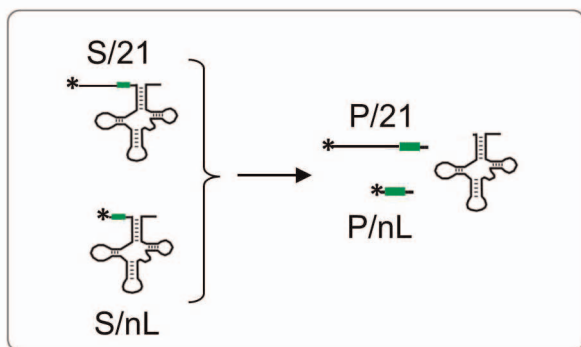
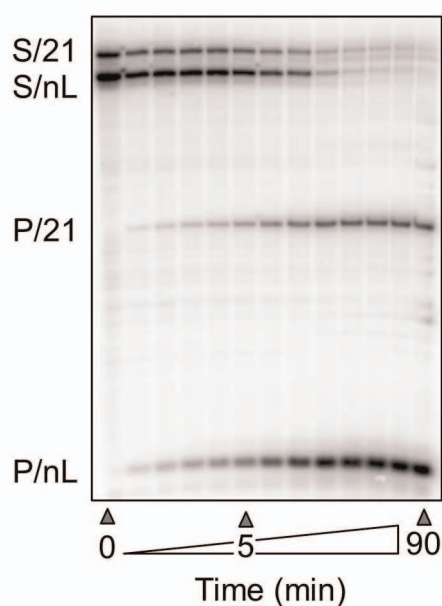
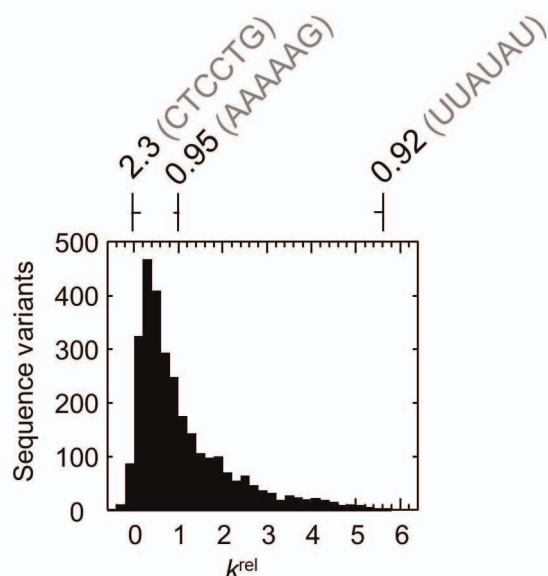


Extended Data Figure 2 | Preparation of DNA libraries for Illumina sequencing. **a**, BAR, the indexing barcode; NN, the degenerated barcode. For primer sequences see Methods. RT, reverse transcription. **b**, DNA libraries (PCR products, **a**) for samples at the time points indicated. Controls: lane 5, no

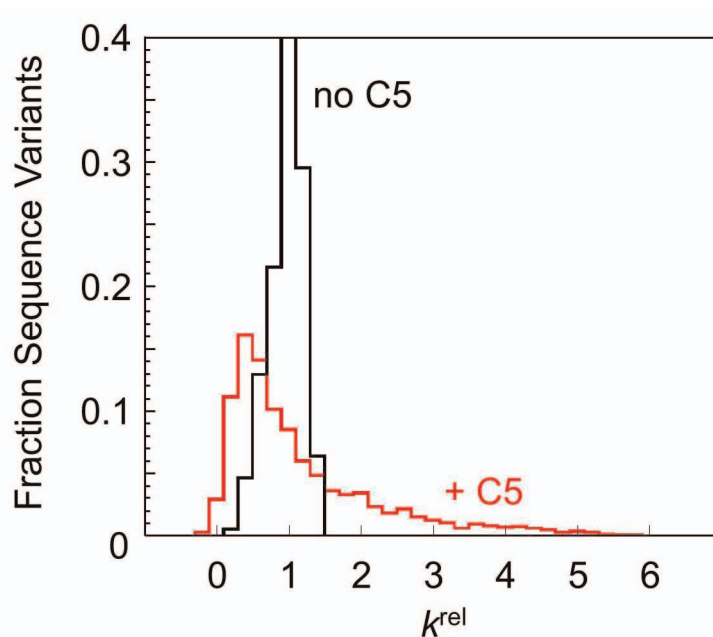
RNA; lane 6, no reverse transcriptase. **c**, Read structure. Nucleotides 1 and 2 are degenerated barcode; nucleotides 3–5 are sample barcode (index tag); nucleotides 6–29 are additional leader sequence, nucleotides 30–35 are randomized leader sequence; nucleotides 38 onwards are tRNA.



Extended Data Figure 3 | Multiple turnover reaction scheme. E, enzyme; $ES_{1...i}$, individual enzyme substrate complexes; $K_{1...i}$, individual functional binding constants; $S_{1...i}$, individual substrate variants; $V_{1...i}$, individual reaction rate constants.

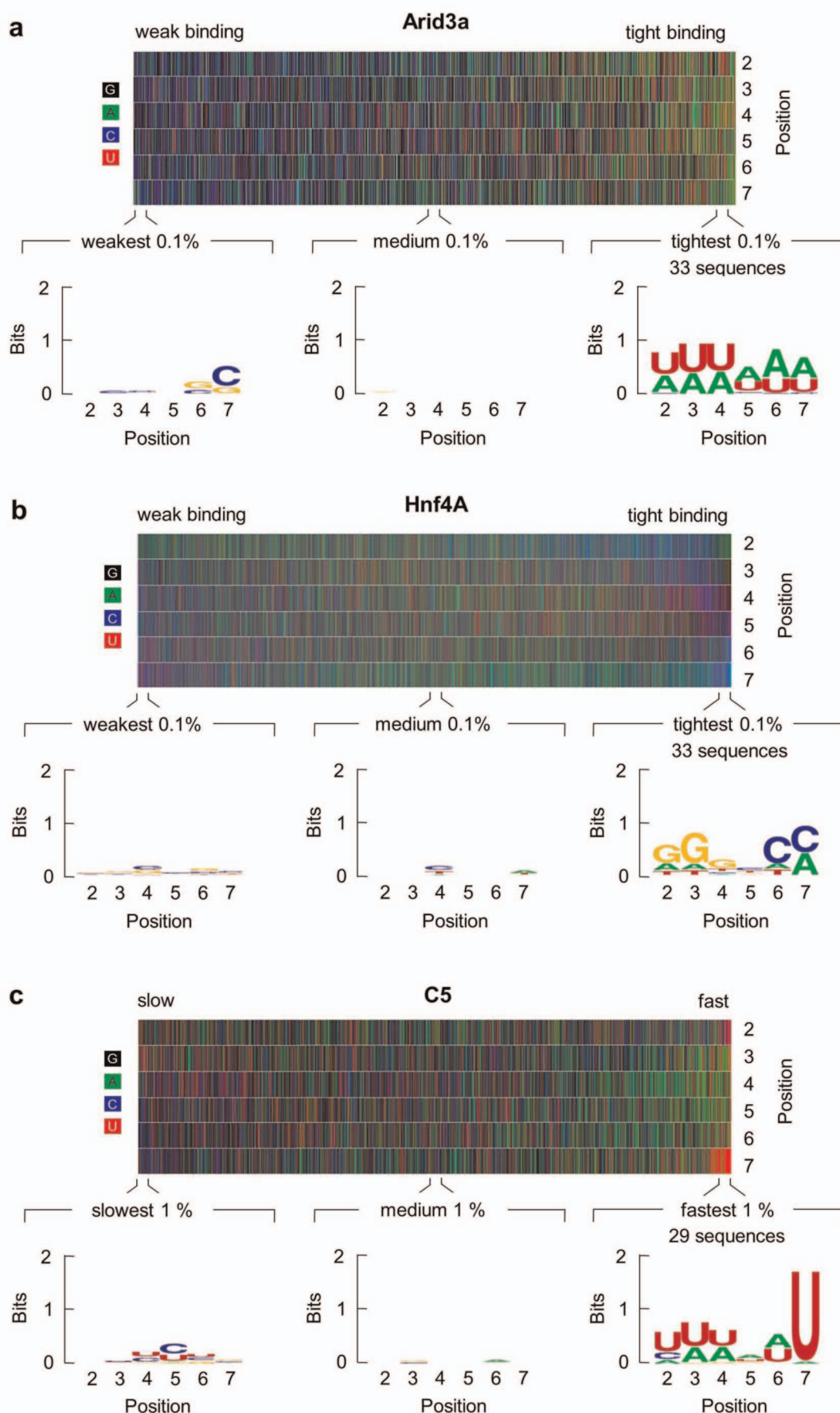
a**b****c**

Extended Data Figure 4 | Effect of the 21 nucleotide extension on ptRNA processing by RNase P. **a**, Relative processing rate constants were measured for three sequence variants from different parts of the affinity distribution by PAGE. Reactions for each sequence variant were conducted in the presence of the randomized population (unlabelled) with equal amounts of substrate with (S/21) and without the 21-nucleotide extension (S/nL). The asterisk marks the position of the radiolabel at the 5' end of the substrate. Reactions were conducted under the conditions described in the Methods. **b**, PAGE for the reaction of the reference sequence variant. The time point at 5 min is marked for reference. **c**, The effects of the 21-nucleotide extension on relative processing rate constants of the three indicated sequence variants. The position of each sequence variant in the affinity distribution of all sequence variants (Fig. 2d) is given for reference by the vertical line above the plot. The number indicates the factor (S/nL)/(S/21) by which the 21-nucleotide extension decreases the relative rate constant of the given sequence variant, given as average from three independent experiments. The horizontal line approximates the degree of the relative change. The 21-nucleotide extension decreases the observed for sequence variant (CTCCTG) by a factor of 2.3. For the genomically encoded leader sequence AAAAAG, the 21-nucleotide extension decreases k^{rel} for by a factor of 0.95; that is, the substrate with the extension reacts slightly faster than the substrate without extension. The fast reacting substrate (TTATAT) is also only minimally affected by the extension (0.92). Together, the data show only minor effects of the 21-nucleotide extension on the position of a given sequence variant in the affinity distribution.



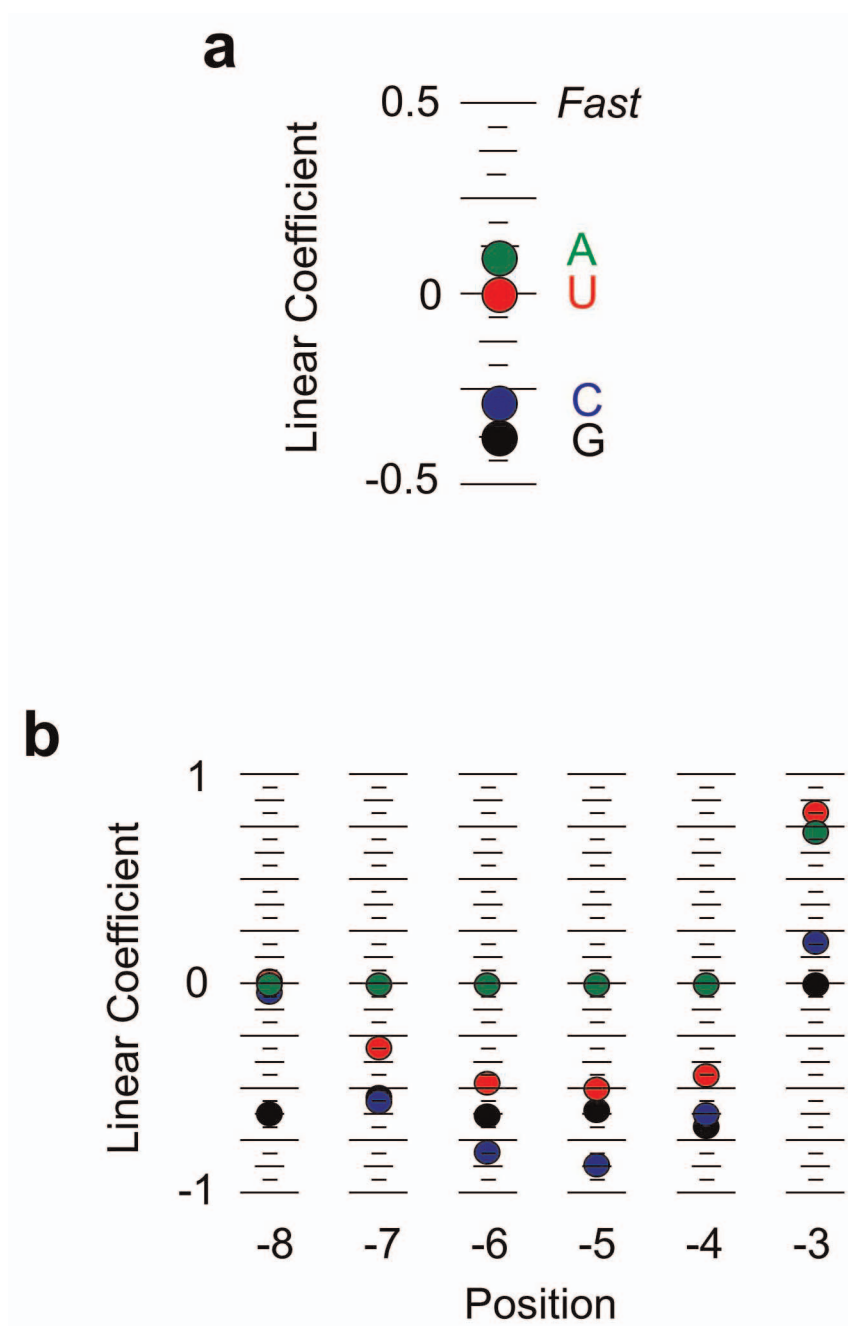
Extended Data Figure 5 | Processing of $\text{ptRNA}^{\text{Met}(-3-8)}$ by RNase P without C5. Distribution of k^{rel} values for processing of $\text{ptRNA}^{\text{Met}(-3-8)}$ by RNase P

without C5 (black line). Data were obtained analogously to those with C5. For comparison, the distribution of k^{rel} values with C5 is shown (red line).



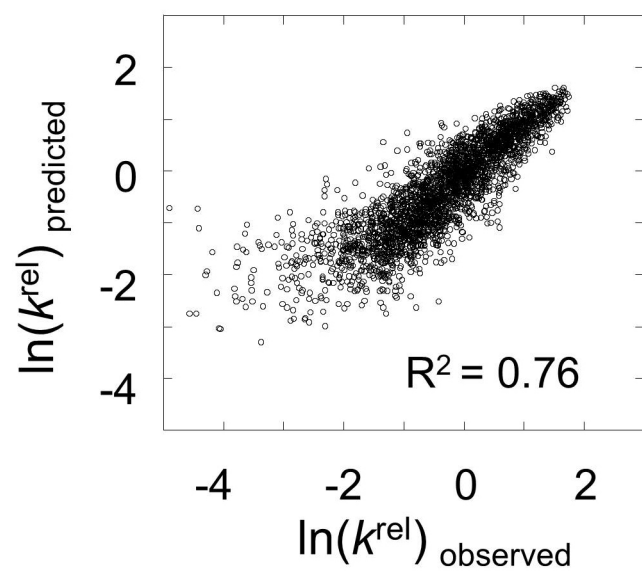
Extended Data Figure 6 | Sequence logos are only associated with the high-affinity tail of the distribution. **a**, Plot of sequence variants ranked from weakest to tightest binder to the specific transcription factor Arid3a (Fig. 2d), based on data published previously¹⁸. To facilitate direct comparison to the six-nucleotide binding site of C5, only approximately half of all sequences are shown in the plot, and only six positions (positions two to seven, as indicated) of the eight-nucleotide binding site are shown. The position in the binding site is marked on the right. The brackets mark 0.1% of sequence variants (33 sequences) that bind tightest, fall into the medium, and bind weakest. Sequence logos show the information content in these sequences. The logos were generated with Weblogo. Sequence signatures of the tightest binding

variants are highly enriched in physiological substrates of Arid3a¹⁸. **b**, Plot of sequence variants ranked from weakest to tightest binder to another specific transcription factor, Hnf4a, based on data published previously¹⁸. Approximately half of all sequences are shown in the plot, and six positions (positions two to seven, as indicated) of the eight-nucleotide binding site. Sequence signatures of the tightest binding variants are highly enriched in physiological substrates of Hnf4a¹⁸. **c**, Plot of sequence variants ranked from slowest to fastest reacting for C5 (Fig. 2e). The brackets mark 1% of sequence variants that react fastest, fall into the medium and react slowest. Sequence logos were generated as in **a**.



Extended Data Figure 7 | Sequence determinants for substrate recognition by C5. **a**, Model considering identity, but not position of a given base in the C5 binding site. Ranking of the four bases according to their potential to promote (positive linear coefficient) or decrease (negative linear coefficient) functional C5 binding. For calculation of linear coefficients, see the Methods. **b**, Position weight matrix (PWM) model considering both base identity and

position in the binding site, but assuming independent contributions of each position. The plot shows the ranking of the bases according to their potential to promote (positive linear coefficient) or decrease (negative linear coefficient) functional C5 binding, relative to the reference sequence (AAAAAG, Fig. 1c). Bases are coloured as in **a**. For the calculation of linear coefficients, see the Methods.



Extended Data Figure 8 | Neural network analysis. Correlation between observed k^{rel} and values calculated with the best model obtained by neural network analysis (Methods).

Extended Data Table 1 | Sequencing data.

Replicate 1				
Timepoint	0	T 1	T 5	T 40
(min:sec)	0:00	1:19	5:28	40:00
Fraction ptRNA processed *	0	0.14	0.28	0.55
Total sequence reads (number)	2,828,358	4,212,150	4,603,710	4,882,095
Reads passed quality threshold †	2,646,624	3,849,190	4,391,105	4,676,773
Fract. reads below quality threshold	0.064	0.086	0.0462	0.042
Replicate 2				
Timepoint	0	T 0.5	T 1	T 5
(min:sec)	0:00	0:37	1:15	5:15
Fraction ptRNA processed *	0	0.08	0.12	0.28
Total sequence reads (number)	6,434,248	8,172,493	11,054,769	11,604,173
Reads passed quality threshold †	5,800,933	7,476,616	10,341,132	10,421,304
Fract. reads below quality threshold	0.098	0.085	0.064	0.101

The overall number of reads obtained for the respective time points in the independent replicate experiments 1 and 2, and the number of reads that passed the quality control. *The fraction of processed ptRNA was determined from PAGE data (Fig. 1e and Methods). †Read numbers after filtering for potential PCR artefacts for each sequence variant (Methods).

Migrating bubble during break-induced replication drives conservative DNA synthesis

Natalie Saini^{1*}, Sreejith Ramakrishnan^{2*}, Rajula Elango², Sandeep Ayyar², Yu Zhang¹, Angela Deem^{2†}, Grzegorz Ira³, James E. Haber⁴, Kirill S. Lobachev¹ & Anna Malkova^{2,5}

The repair of chromosomal double strand breaks (DSBs) is crucial for the maintenance of genomic integrity. However, the repair of DSBs can also destabilize the genome by causing mutations and chromosomal rearrangements, the driving forces for carcinogenesis and hereditary diseases. Break-induced replication (BIR) is one of the DSB repair pathways that is highly prone to genetic instability^{1–3}. BIR proceeds by invasion of one broken end into a homologous DNA sequence followed by replication that can copy hundreds of kilobases of DNA from a donor molecule all the way through its telomere^{4,5}. The resulting repaired chromosome comes at a great cost to the cell, as BIR promotes mutagenesis, loss of heterozygosity, translocations, and copy number variations, all hallmarks of carcinogenesis^{4–9}. BIR uses most known replication proteins to copy large portions of DNA, similar to S-phase replication^{10,11}. It has therefore been suggested that BIR proceeds by semiconservative replication; however, the model of a bona fide, stable replication fork contradicts the known instabilities associated with BIR such as a 1,000-fold increase in mutation rate compared to normal replication⁹. Here we demonstrate that in budding yeast the mechanism of replication during BIR is significantly different from S-phase replication, as it proceeds via an unusual bubble-like replication fork that results in conservative inheritance of the new genetic material. We provide evidence that this atypical mode of DNA replication, dependent on Pif1 helicase, is responsible for the marked increase in BIR-associated mutations. We propose that the BIR mode of synthesis presents a powerful mechanism that can initiate bursts of genetic instability in eukaryotes, including humans.

In theory, BIR may constitute a unidirectional, bona fide replication fork producing two semiconservatively replicated molecules^{4,11} (Fig. 1A, a). Alternatively, a D-loop (displacement loop) formed by invasion of the broken chromosome may persist throughout BIR, migrating down the length of the chromosome, creating an unusual condition of conservative inheritance of newly synthesized DNA^{1,12,13} (Fig. 1A, b–d).

To distinguish between these models, we used a disomic yeast system (Fig. 1B, a) containing a second, truncated copy of chromosome III, cleaved by HO endonuclease under control of a galactose-inducible promoter². The HO-induced DSB possesses only one efficiently repairable end that invades the second copy of chromosome III, and initiates BIR that copies over 100 kilobases (kb) of the distal part of the chromosome. Using this system, we recently demonstrated that BIR stimulates mutagenesis along the path of DNA synthesis at a series of *lys2* frameshift reporters⁹. Here we examined these *Lys*⁺ mutations to determine whether errors during BIR were acquired semiconservatively (inherited by either the donor or recipient molecule; Fig. 1B, b) or conservatively (inherited only by the recipient molecule; Fig. 1B, c). Pulse-field gel electrophoresis (PFGE) was used to separate donor and recipient molecules from *Lys*⁺ BIR outcomes resulting from mutations

in a *lys2* reporter located 16 or 36 kb distal to the site of BIR initiation (Fig. 2a, b). Sequencing of the polymerase chain reaction (PCR) products derived from the separated chromosomes revealed that the great majority of heterozygous frameshift mutations (58 of 58 and 68 of 77 from strains with reporters at 16 and 36 kb, respectively) were inherited by the recipient molecule, whereas the donor sequence remained unchanged (see also Supplementary Discussion). Overall, the mutation pattern supports a conservative replication mechanism for BIR. However, because

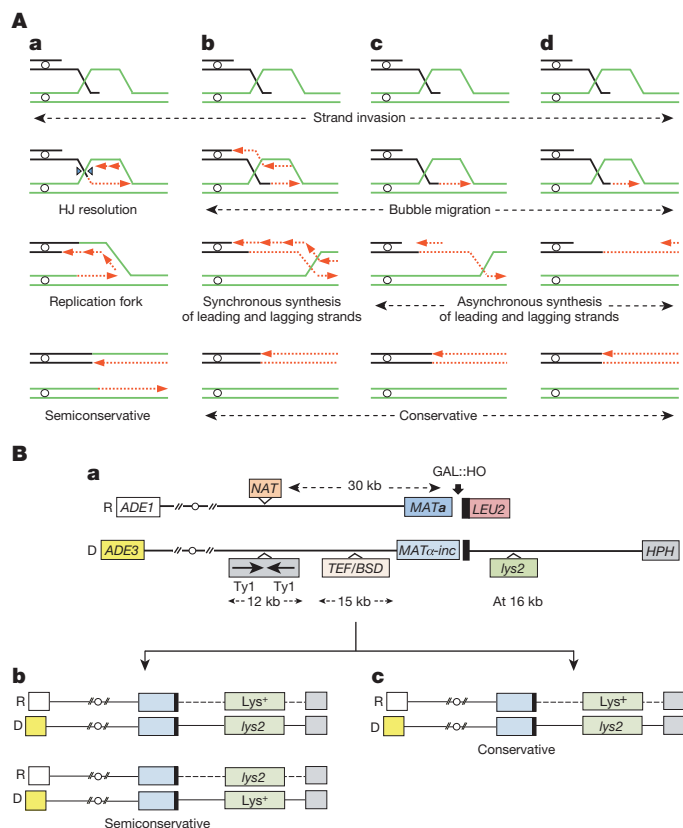


Figure 1 | The mode of DNA synthesis during BIR. **A**, The models of BIR. **a**, Replication fork proceeds semiconservatively. **b–d**, Migrating bubble leads to conservative inheritance of new DNA. Synchronous (**b**) and asynchronous (**c**, **d**) synthesis of leading and lagging DNA strands. **B**, **a**, The BIR frameshift mutation assay. A DSB is induced at *MATa* of the recipient chromosome III. *lys2* reporter is inserted in the donor chromosome 16 or 36 kb telomere-proximal from *MATa-inc*. *Lys*⁺ mutations would be inherited equally by the donor (D) or recipient (R) if BIR is semiconservative (**b**), but only by recipient if BIR is conservative (**c**).

¹School of Biology and Institute for Bioengineering and Bioscience, Georgia Institute of Technology, Atlanta, Georgia 30332, USA. ²Department of Biology, School of Science, IUPUI, Indianapolis, Indiana 46202-5132, USA. ³Department of Molecular & Human Genetics, Baylor College of Medicine, One Baylor Plaza, Houston, Texas 77030, USA. ⁴Department of Biology and Rosenstiel Basic Medical Sciences Research Center, Waltham, Massachusetts 02454-9110, USA. ⁵Department of Biology, College of Liberal Arts and Sciences, University of Iowa, Iowa City, Iowa 52242-1324, USA. [†]Present address: Department of Genomic Medicine, University of Texas MD Anderson Cancer Center, Houston, Texas 77230, USA.

*These authors contributed equally to this work.

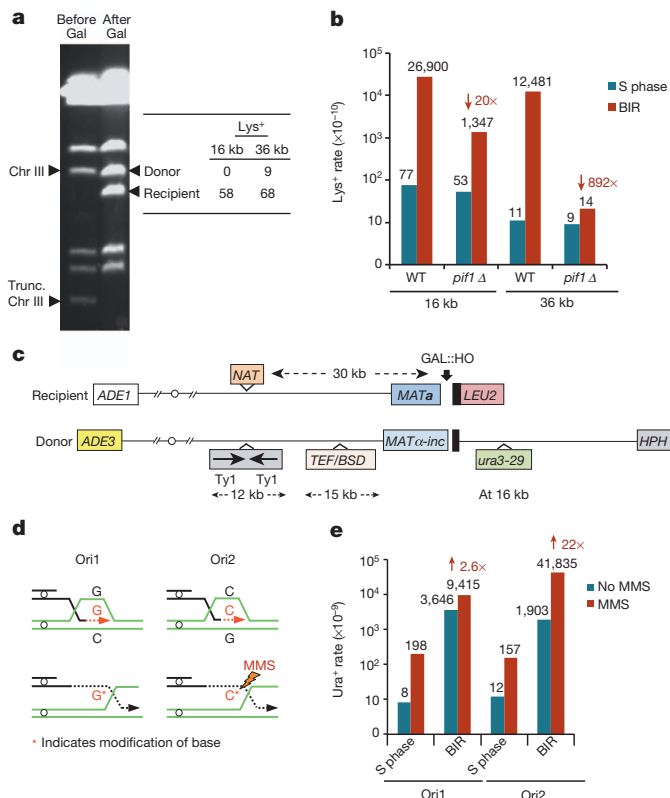


Figure 2 | BIR-induced mutations. **a**, The sequencing of the separated donor and recipient chromosomes of heterozygous *Lys*⁺ mutants. **b**, The effect of *pif1*Δ on BIR-induced frameshifts. Medians of mutation rates are shown. The arrows represent a reduction as compared to wild type (WT). **c**, The assay to study BIR-induced base substitutions in *ura3-29* reporter. **d**, Depending on orientation, the selectable position of *ura3-29* leading strand includes cytosine (C) or guanine (G). **e**, MMS amplifies BIR-induced base substitutions in an orientation-dependent way. The arrows indicate an increase as compared to no-MMS control. See Extended Data Tables 1 and 2 for the details of sample size, number of experiments, statistical analysis and for the ranges of medians shown in **e** and **b**.

this conclusion was based on analysis of selected mutation events, we developed a non-selective test to analyse BIR microscopically by DNA combing.

The experiments were conducted in nocodazole-arrested cells of disomic BIR strain bearing a cassette facilitating BrdU incorporation in yeast¹⁴ (Fig. 3a, b). BrdU was added 3.5 h after DSB induction. After completion of BIR, PFGE-separated donor and recipient molecules (Fig. 3c and Extended Data Fig. 1) were analysed by molecular combing and fluorescent *in situ* hybridization (FISH). We used an anti-BrdU antibody, the P1 probe specific to the tandem repeat of *TEF1/BSD* inserted 14 kb centromere-proximal to *MAT* in the donor chromosome, the P2 probe specific to the 20-kb region of chromosome III where invasion occurs, and the P3 probe specific to the 15-kb region near the telomere (Fig. 3a) to characterize BIR. We observed BrdU tracts approximately 100 kb in length in 70 of the 98 repaired recipient molecules analysed (Fig. 3d, e and Extended Data Fig. 2a). These tracts include the entire chromosome region marked by P2 and P3 and, therefore, represent BIR that copied the donor chromosome through to its telomere. Additionally, 14% of recipient molecules contained long (>30 kb) BrdU tracts that overlapped with P2 but not with P3 (Fig. 3d and Extended Data Fig. 3a). These molecules probably represent repair events where BIR was interrupted, resulting in half-crossover formation^{2,15} (see also Supplementary Discussion).

Our analysis of donor molecules supports a conservative mode of DNA replication during BIR, as only 4 out of 103 donor molecules

were illuminated by >30 kb BrdU tracts (Fig. 3d, e and Extended Data Fig. 2a). These data confirm a strong bias ($P < 0.0001$) towards BrdU tracts present only in the recipient chromosome. The four cases of BrdU incorporation in the donor could result from rare semiconservative synthesis or from BIR initiated >30 kb proximal to the DSB site, which would result in a donor-like size and hybridization pattern due to copying of regions unique to the donor molecule¹⁶. On the basis of these data, we estimate that, even if semiconservative synthesis occurs, it can account for no more than 8% of the BIR events that we analysed (see Supplementary Discussion and Extended Data Fig. 4 for the results of another series of experiments supporting this conclusion).

The unusual mode of replication prompted us to characterize the structure of BIR molecular intermediates at *LYS2* inserted ~16 kb from the point of strand invasion. Genomic DNA extracted from nocodazole-arrested cells undergoing BIR was digested with PstI and analysed by two-dimensional (2D) gel electrophoresis using a *LYS2*-specific probe (Fig. 4a, top panel). We detected bubble-like structures between 3 and 7 h after DSB induction (Fig. 4b–d), but not at 13 h, consistent with the timing of BIR progression⁹ (Extended Data Fig. 5). All bubble-like intermediates were markedly different from the Y structures indicative of S-phase replication forks observed before addition of nocodazole and induction of the break (Fig. 4c, 0 h). Furthermore, no bubble-like structures were observed in control strains in which HO endonuclease cannot initiate a DSB (Fig. 4d, no-cut), thus linking these structures to BIR exclusively. The bubble-like structures observed in BIR were reminiscent of bubbles routinely detected at replication origins¹⁷, with one important difference: the BIR bubbles included a long, high-molecular-mass tail that extended well beyond the size expected for complete replication (arrows in Fig. 4c, d). We proposed that initiation of BIR lagging-strand synthesis is often delayed compared to leading strand, resulting in accumulation of single-stranded DNA (ssDNA) behind the BIR bubble, which makes the region around *LYS2* refractory to PstI digestion. Indeed, pre-incubation of genomic DNA with oligonucleotides (PstO3 and PstO4; Fig. 4a, middle and bottom panels) complementary to the Watson strand of two PstI sites flanking the *LYS2* gene eliminated the tail and resulted in a second arc that probably corresponds to molecular intermediates with bubbles consisting of one double-stranded branch (leading-strand synthesis) and one single-stranded branch (lagging-strand synthesis) (Fig. 4a, b, d and Extended Data Fig. 6). Similar results were also obtained using BglII digestion (Extended Data Fig. 7). Notably, whereas simultaneous addition of oligonucleotides BglO3 and BglO4, complementary to the Watson strand of two BglII sites, eliminated the ssDNA tail, the addition of each of these oligonucleotides individually failed to eliminate the tail. This confirms that two types of DNA intermediates contribute to the observed ssDNA tail: those containing ssDNA centromere proximal to *LYS2* and those with ssDNA distal to *LYS2* (Fig. 4a and Extended Data Fig. 7a, panels ii, iii). Addition of oligonucleotides complementary to the Crick strand did not have any effect (data not shown). Bubble migration intermediates were also detected with an *HPH*-specific probe that hybridizes to the end of the donor chromosome (Fig. 4a, e). These data strongly support a migrating D-loop type of DNA replication^{18,19}.

We proposed that ssDNA accumulated behind the migrating BIR bubble is the cause of BIR-associated mutagenesis because of the propensity of ssDNA to accumulate unrepaired DNA lesions²⁰. This was tested by using methyl methanesulphonate (MMS), a DNA damaging agent that predominantly creates mutagenic lesions in cytosines of ssDNA^{21,22}. In addition, a *ura3-29* reporter²³, which can revert to Ura⁺ via three different base substitutions at one C•G pair (Fig. 2c), was inserted in the donor chromosome in two different orientations (Ori1 and Ori2). We expected that MMS will specifically elevate the level of BIR-associated mutagenesis in Ori2, where cytosine is located in the mutant position of the leading (ssDNA) strand, but not in Ori1, which contains guanine instead (Fig. 2d). Indeed, we observed that even though BIR markedly stimulated base substitutions in *ura3-29* irrespective of its orientations, the effect of MMS was orientation

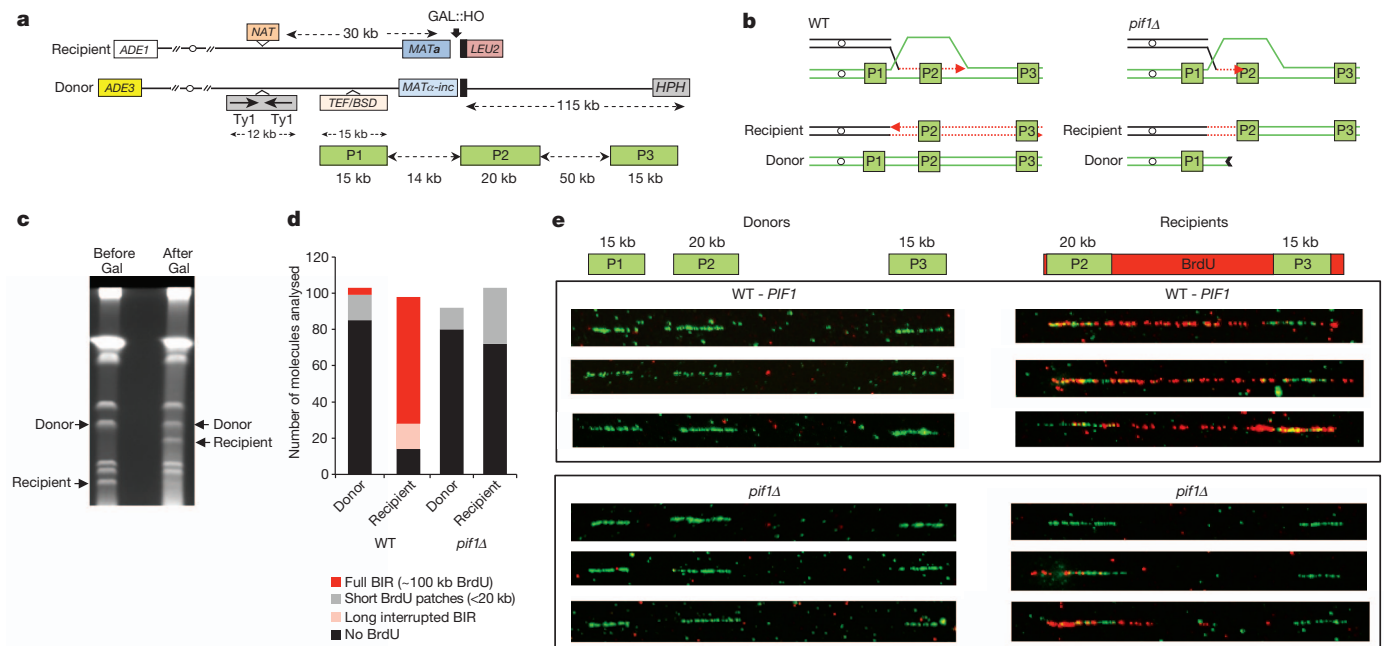


Figure 3 | DNA synthesis during BIR is conservative. **a**, Experimental system to assay BIR using dynamic molecular combing including the position of hybridization probes P1, P2 and P3. **b**, Left: BrdU incorporation in the recipient is expected from conservative BIR (red). Right: formation of half-crossovers in *pif1Δ* leads to short patches of BrdU in the recipient. **c**, Donor and recipient chromosomes separated using PFGE. **d**, The

summary of molecular combing analysis. **e**, The donors and recipients of wild-type (*PIF1*) and *pif1Δ*. Each molecule was hybridized with P1, P2 and P3 probes (green tracts) and treated with anti-BrdU antibodies (red tracts). See Extended Data Figs 2a and 3 for the details of analysis, sample sizes and images of combing analysis. See also Extended Data Fig. 4 for additional experiments supporting the conclusions.

dependent (Fig. 2e and Extended Data Table 1). Specifically, MMS highly amplified BIR-induced mutagenesis in cells containing *ura3-29* in Ori2, whereas its effect on BIR mutagenesis in Ori1 was relatively modest. This observation supports the conjecture that ssDNA accumulated behind the BIR bubble is the cause of BIR-associated mutagenesis.

Additionally, the spectrum of BIR-induced mutations was also orientation dependent, supporting our conclusion (Extended Data Fig. 2b).

Because the Pif1 helicase is a key component of the BIR machinery²⁴ (see also accompanying paper²⁵), we proposed that Pif1 is essential for long-range BIR. We observed that even though BIR-sized products

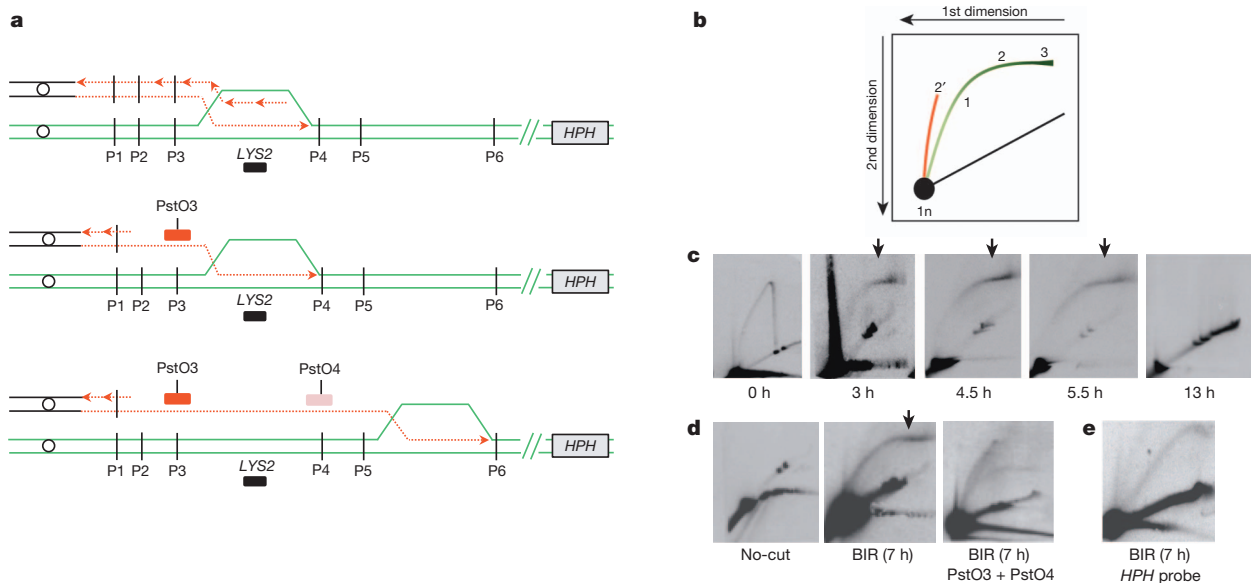


Figure 4 | Molecular intermediates of BIR. **a**, D-loop migration during coordinated (top) and uncoordinated (bottom and middle) leading- and lagging-strand synthesis. **b**, Schematic of 2D gel with BIR bubbles forming an arc (1, 2) with an extension (3) representing ssDNA tail. Annealing with PstO3 and PstO4 allows PstI digestion changing the mobility of the intermediate (red, 2'). **c**, 2D analysis of Y-arc during normal replication

(0 h) and bubble-like structures at time points after BIR induction hybridized to *LYS2*-specific probe. Similar bubble structures were observed in other nine independent experiments. **d**, High-molecular-mass tails (arrows) disappear after annealing with PstO3 and PstO4. The arc is absent in no-cut controls. **e**, BIR intermediates highlighted with *HPH*-specific probe.

were formed in *pif1Δ* mutant (Extended Data Fig. 1a, b), no extended BrdU tracts were observed in either the donor or recipient chromosomes (Fig. 3d, e). In addition, approximately 22% of recipient molecules contained short (<20 kb) BrdU patches that co-localized with probe P2 (Fig. 3d, e and Extended Data Fig. 2a) and probably represented DNA synthesis that was prematurely terminated. Therefore, it is likely that most outcomes in *pif1Δ* mutants formed during the time frame of these experiments were half-crossovers (Extended Data Fig. 1c), supporting our hypothesis that Pif1 is required for BIR-associated DNA synthesis. The low amount of BIR precluded 2D analysis of BIR intermediates in *pif1Δ*. We investigated whether Pif1 may be necessary for BIR-induced frameshift mutations. Notably, we observed that all BIR-induced frameshift mutations were eliminated in the *pif1Δ* mutant at the 36-kb position, and there was a 20-fold reduction in frameshift mutations at the 16-kb position (Fig. 2b and Extended Data Table 2). Thus, whereas BIR may initiate in the absence of Pif1, these data support that Pif1 is required for long-range synthesis during BIR. Therefore, Pif1 can be added to the list of other previously identified proteins, including Polδ, Polζ, Msh2, Mlh1, Dun1 and others that are involved in BIR and associated mutagenesis^{2,9,10,15}.

Overall, the results of this study demonstrate that BIR is carried out by a migrating replication bubble driven by Pif1 with asynchronous synthesis of leading and lagging strands resulting in a mutation-prone accumulation of ssDNA, and leads to conservative inheritance of the new genetic material. The bubble migration mechanism and associated mutagenesis may be relevant to cellular processes where BIR has been implicated, such as alternative telomere lengthening and mitochondrial DNA maintenance^{10,26–30}, where Pif1 has an important role. An intriguing possibility is that the burst of mutations recently linked to replication stress/fork collapse in pre-cancerous cells³¹ may be linked to conservative synthesis initiated by BIR.

METHODS SUMMARY

All yeast strains listed in Extended Data Table 3 were isogenic to AM1003 (ref. 2). The BrdU cassette was a gift from O. Aparicio and was inserted into chromosome V¹⁴. The pTEF1/BSD-snt1 plasmid was integrated at *SNT1* of the *MATα*-inc containing copy of chromosome III. DSBs were initiated by HO induction by addition of galactose². Molecular intermediates and products of BIR were analysed using cells collected from time-course experiments. 2D gel electrophoresis was used to determine the structure of molecular intermediates. BIR outcomes were analysed using dynamic molecular combing and fluorescent *in situ* hybridization. BIR-induced Lys⁺ mutations were analysed by sequencing following separation of chromosomes by PFGE.

Online Content Any additional Methods, Extended Data display items and Source Data are available in the online version of the paper; references unique to these sections appear only in the online paper.

Received 26 October 2012; accepted 20 August 2013.

Published online 11 September 2013.

- Smith, C. E., Llorente, B. & Symington, L. S. Template switching during break-induced replication. *Nature* **447**, 102–105 (2007).
- Deem, A. *et al.* Defective break-induced replication leads to half-crossovers in *Saccharomyces cerevisiae*. *Genetics* **179**, 1845–1860 (2008).
- Malkova, A. & Haber, J. E. Mutations arising during repair of chromosome breaks. *Annu. Rev. Genet.* **46**, 455–473 (2012).
- Malkova, A., Naylor, M. L., Yamaguchi, M., Ira, G. & Haber, J. E. RAD51-dependent break-induced replication differs in kinetics and checkpoint responses from RAD51-mediated gene conversion. *Mol. Cell. Biol.* **25**, 933–944 (2005).
- Davis, A. P. & Symington, L. S. RAD51-dependent break-induced replication in yeast. *Mol. Cell. Biol.* **24**, 2344–2351 (2004).
- Bosco, G. & Haber, J. E. Chromosome break-induced DNA replication leads to nonreciprocal translocations and telomere capture. *Genetics* **150**, 1037–1047 (1998).
- Hastings, P. J., Ira, G. & Lupski, J. R. A microhomology-mediated break-induced replication model for the origin of human copy number variation. *PLoS Genet.* **5**, e1000327 (2009).
- Payen, C., Koszul, R., Dujon, B. & Fischer, G. Segmental duplications arise from Pol32-dependent repair of broken forks through two alternative replication-based mechanisms. *PLoS Genet.* **4**, e1000175 (2008).

- Deem, A. *et al.* Break-induced replication is highly inaccurate. *PLoS Biol.* **9**, e1000594 (2011).
- Lydeard, J. R., Jain, S., Yamaguchi, M. & Haber, J. E. Break-induced replication and telomerase-independent telomere maintenance require Pol32. *Nature* **448**, 820–823 (2007).
- Lydeard, J. R. *et al.* Break-induced replication requires all essential DNA replication factors except those specific for pre-RC assembly. *Genes Dev.* **24**, 1133–1144 (2010).
- Llorente, B., Smith, C. E. & Symington, L. S. Break-induced replication: what is it and what is it for? *Cell Cycle* **7**, 859–864 (2008).
- Malkova, A. & Ira, G. Break-induced replication: functions and molecular mechanism. *Curr. Opin. Genet. Dev.*, (2013).
- Viggiani, C. J. & Aparicio, O. M. New vectors for simplified construction of BrdU-Incorporating strains of *Saccharomyces cerevisiae*. *Yeast* **23**, 1045–1051 (2006).
- Smith, C. E., Lam, A. F. & Symington, L. S. Aberrant double-strand break repair resulting in half crossovers in mutants defective for Rad51 or the DNA polymerase δ complex. *Mol. Cell. Biol.* **29**, 1432–1441 (2009).
- VanHulle, K. *et al.* Inverted DNA repeats channel repair of distant double-strand breaks into chromatid fusions and chromosomal rearrangements. *Mol. Cell. Biol.* **27**, 2601–2614 (2007).
- Fangman, W. L. & Brewer, B. J. Activation of replication origins within yeast chromosomes. *Annu. Rev. Cell Biol.* **7**, 375–402 (1991).
- Formosa, T. & Alberts, B. M. DNA synthesis dependent on genetic recombination: characterization of a reaction catalyzed by purified bacteriophage T4 proteins. *Cell* **47**, 793–806 (1986).
- Ferguson, D. O. & Holloman, W. K. Recombinational repair of gaps in DNA is asymmetric in *Ustilago maydis* and can be explained by a migrating D-loop model. *Proc. Natl Acad. Sci. USA* **93**, 5419–5424 (1996).
- Yang, Y., Sterling, J., Storic, F., Resnick, M. A. & Gordenin, D. A. Hypermutability of damaged single-strand DNA formed at double-strand breaks and uncapped telomeres in yeast *Saccharomyces cerevisiae*. *PLoS Genet.* **4**, e1000264 (2008).
- Yang, Y., Gordenin, D. A. & Resnick, M. A. A single-strand specific lesion drives MMS-induced hyper-mutability at a double-strand break in yeast. *DNA Repair* **9**, 914–921 (2010).
- Roberts, S. A. *et al.* Clustered mutations in yeast and in human cancers can arise from damaged long single-strand DNA regions. *Mol. Cell* **46**, 424–435 (2012).
- Shcherbakova, P. V. & Pavlov, Y. I. 3'→5' exonucleases of DNA polymerases ε and δ correct base analog induced DNA replication errors on opposite DNA strands in *Saccharomyces cerevisiae*. *Genetics* **142**, 717–726 (1996).
- Chung, W. H., Zhu, Z., Papusha, A., Malkova, A. & Ira, G. Defective resection at DNA double-strand breaks leads to de novo telomere formation and enhances gene targeting. *PLoS Genet.* **6**, e1000948 (2010).
- Wilson, M. A. *et al.* Pif1 helicase and Polδ promote recombination-coupled DNA synthesis via bubble migration. *Nature* <http://dx.doi.org/10.1038/nature12585> (this issue).
- Hashimoto, Y. & Costanzo, V. Studying DNA replication fork stability in *Xenopus* egg extract. *Methods Mol. Biol.* **745**, 437–445 (2011).
- Pohjoismaki, J. L. & Goffart, S. Of circles, forks and humanity: Topological organisation and replication of mammalian mitochondrial DNA. *BioEssays* **33**, 290–299 (2011).
- Le, S., Moore, J. K., Haber, J. E. & Greider, C. W. RAD50 and RAD51 define two pathways that collaborate to maintain telomeres in the absence of telomerase. *Genetics* **152**, 143–152 (1999).
- Kreuzer, K. N., Saunders, M., Weislo, L. J. & Kreuzer, H. W. Recombination-dependent DNA replication stimulated by double-strand breaks in bacteriophage T4. *J. Bacteriol.* **177**, 6844–6853 (1995).
- Kuzminov, A. Collapse and repair of replication forks in *Escherichia coli*. *Mol. Microbiol.* **16**, 373–384 (1995).
- Halazonetis, T. D., Gorgoulis, V. G. & Bartek, J. An oncogene-induced DNA damage model for cancer development. *Science* **319**, 1352–1355 (2008).

Supplementary Information is available in the online version of the paper.

Acknowledgements We thank O. Aparicio for the gift of BrdU cassette plasmid. We thank Y. Pavlov for providing *ura3-29* cassette plasmid and P. Chastain and A. Hangaard Andersen for providing us with reagents. We are thankful to D. Gordenin and all members of A.M., K.S.L., G.I. and J.E.H. laboratories for discussions throughout the work. This work was funded by grants from the US National Institutes of Health and National Science Foundation (MCB-0818122 from NSF to K.S.L., and NIH grants R01GM084242 to A.M., R01GM082950 to K.S.L., R03ES016434 to A.M. and K.S.L., GM76020 to J.E.H., and GM080600 to G.I.).

Author Contributions S.R., N.S., K.S.L. and A.M. designed experiments. S.R. and A.D. constructed the experimental system. N.S., S.R. and R.E. carried out 2D experiments. K.S.L., S.R., A.M., N.S. and Y.Z. carried out molecular combing experiments. S.A., R.E., S.R. and A.D. carried out experiments involving sequencing of BIR-induced mutations. R.E., S.R. and S.A. carried out experiments aimed to determine the effect of BIR on base substitutions. J.E.H. provided key expertise. G.I. contributed to the studies of the role of Pif1 in BIR. S.R., N.S., A.D., J.E.H., K.S.L. and A.M. wrote the paper. N.S. and S.R. contributed equally to this work.

Author Information Reprints and permissions information is available at www.nature.com/reprints. The authors declare no competing financial interests. Readers are welcome to comment on the online version of the paper. Correspondence and requests for materials should be addressed to A.M. (amalkova@uiupui.edu or anna-malkova@uiowa.edu) or K.S.L. (kirill.lobachev@biology.gatech.edu).

dilution of mouse anti-BrdU (BD Biosciences, catalogue no. 347580); (2) 1:50 dilution of Cy3-coupled rat anti-mouse (Jackson ImmunoResearch Lab, catalogue no. 415-165-166); and (3) 1:50 dilution of Cy3-mouse anti-rat (Jackson ImmunoResearch Lab, catalogue no. 212-165-168). All images were acquired using the Zeiss LSM 510 Confocal Microscope with 100 \times objective. The lengths of the fluorescent stretches were calculated by comparison with the length of P1, P2 and P3 hybridization signals.

The statistical comparison between donor and recipient chromosomes in respect to BrdU incorporation was performed using the Chi-squared test. For each experiment, the frequency of semiconservative BIR (F) was calculated as follows: $F = A/N \times f \times b$, where A represents the number of donor molecules with long BrdU tracts; N represents the total number of analysed donor molecules; f represents the efficiency of BIR in the experiment (calculated by physical analysis as a percentage of the truncated chromosome III converted in the BIR product⁴); and b represents the fraction of recipient molecules containing full and long interrupted BIR tracts.

Mutagenesis associated with DSB repair. To determine mutation frequency associated with BIR, yeast strains were grown from individual colonies with agitation in liquid synthetic media lacking leucine for approximately 20 h, diluted 20-fold with fresh YEP-Lac, and grown to logarithmic phase for approximately 16 h. Next, 20% galactose was added to the culture to a final concentration of 2%, and cells were incubated with agitation for 7 h. Samples from each culture were plated at appropriate concentrations on adenine drop-out media and on media omitting lysine and adenine before (0 h) and 7 h after the addition of galactose (7 h) to measure the frequency of Lys⁺ cells. To measure the frequency of Ura⁺ cells, samples were plated at appropriate concentrations on adenine drop-out media and on media omitting uracil and adenine before (0 h) and 7 h after the addition of galactose (7 h). To determine spontaneous mutation frequencies, no-DSB strains were grown similarly to the DSB-containing strains. Because spontaneous mutation frequencies were calculated based on the number of mutations accumulated during many cell generations, the rate of spontaneous mutagenesis in no-DSB control strains was calculated using the following modification of Drake equation: $\mu = 0.4343 f / \log(N\mu)$, where μ is the rate of spontaneous mutagenesis, f is mutation frequency, and N is the number of cells in yeast culture. The rate of mutations after galactose treatment (μ_7) was determined using a simplified version of the Drake equation: $\mu_7 = (f_7 - f_0)$, where f_7 and f_0 are the mutation frequencies among Ade⁺ cells at times 7 h and 0 h, respectively. This modification was necessary because experimental strains did not divide or underwent ≤ 1 division between 0 h and 7 h.

MMS was added at 1.5 mM 30 min after galactose addition. Cells were incubated with agitation for 7 h, treated with 10% sodium thiosulphate to inactivate MMS, diluted and plated. The loss of viability after MMS treatment was barely detectable and never exceeded 40% independently of *ura3-29* orientation. The rate of mutations following MMS treatment was determined using a simplified version of the Drake equation: $\mu_7 = (f_7 - f_0)$, where f_7 and f_0 are the mutation frequencies

among Ade⁺ cells at times 7 h (following MMS treatment) and 0 h, respectively. This modification was necessary because experimental strains did not divide or underwent ≤ 1 division between 0 h and 7 h in the presence of MMS.

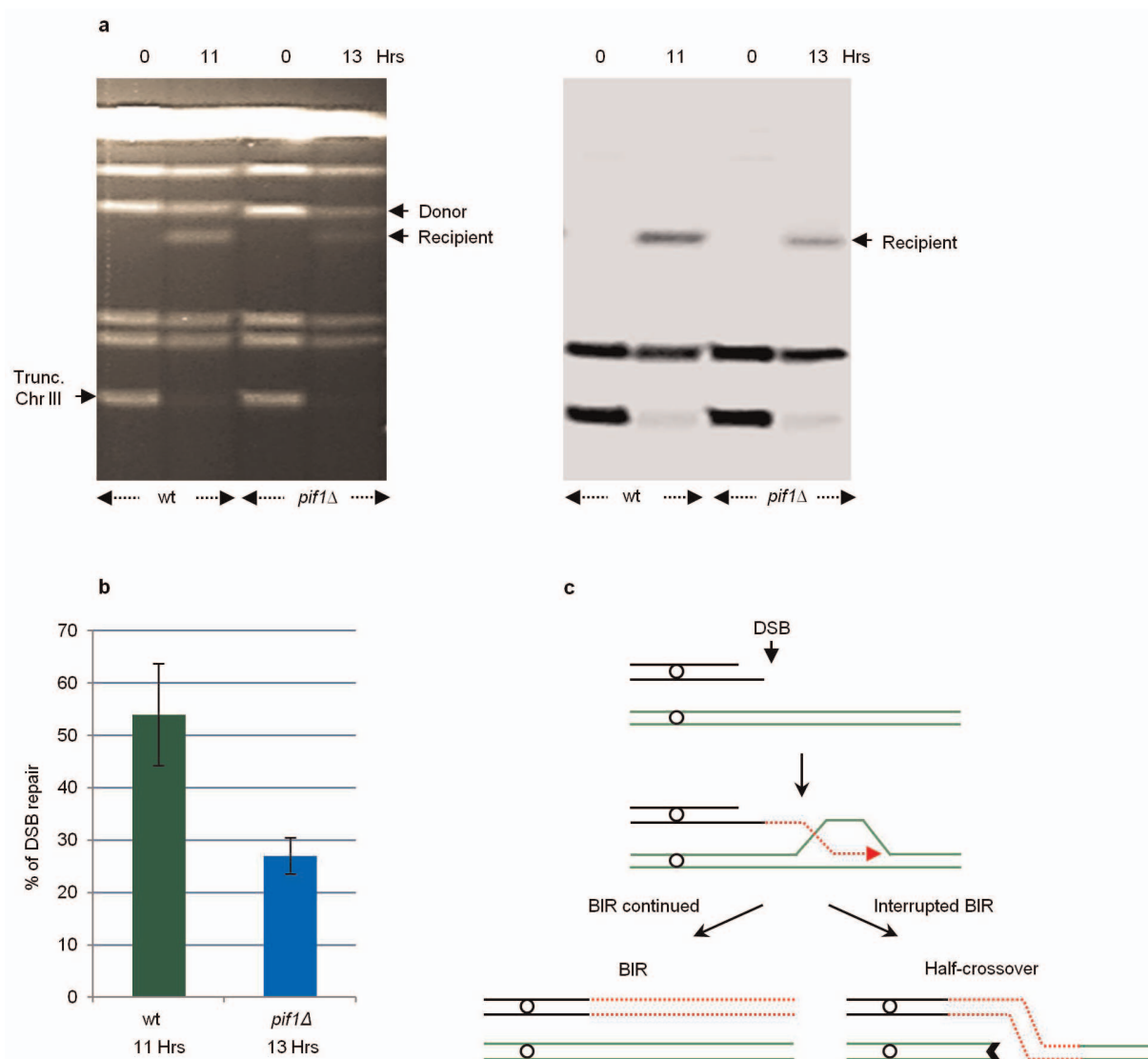
Rates are reported as the median value (Fig. 2b, e and Extended Data Tables 1 and 2), and the 95% confidence limits for the median are calculated for the strains with a minimum of six individual experiments. For strains with four–five individual experiments, the range of the median was calculated. Statistical comparisons between median mutation rates were performed using the Mann–Whitney U -test³⁸.

Analysis of BIR-induced Lys⁺ mutants. Lys⁺ revertants were obtained in BIR mutagenesis experiments⁹. After phenotypic examination, cultures were grown from mutants for chromosome analysis by PFGE using 1% low-melting agarose at 6 V cm⁻¹ for 48 h. DNA bands corresponding to the donor and repaired recipient chromosome III were excised, equilibrated in β -agarase buffer (NEB), melted at 65 °C, and subjected to β -agarase treatment for 1 h at 40 °C. The obtained DNA was PCR amplified using *LYS2*-specific DNA primers⁹, followed by sequencing analysis.

Analysis of mutation spectra of *ura3-29* Ura⁺ reversions. To determine the spectrum of Ura⁺ in individual experiments, a portion of the *URA3* gene from independent Ura⁺ was PCR-amplified using *URA3*-specific primers: 5'-GTGTGCTTCATTGGATGTTTCGTAC-3' and 5'-AAAAGGCCTCTAGGTTCCCTTTGTT-3' followed by sequencing analysis using 5'-CTGGAGTTAGTTGAAGCATTAGG-3' as a primer.

For experimental strains undergoing BIR repair, 7 h Ura⁺ BIR events (confirmed as Ade⁺Leu⁻ on selective media) were sequenced. Because these cells underwent ≤ 1 division between the 0 h and 7 h time points and the Ura⁺ frequency at 7 h significantly exceeded that at 0 h, all Ura⁺ events resulting from DSB repair were considered independent.

32. Wach, A., Brachat, A., Pohlmann, R. & Philippsen, P. New heterologous modules for classical or PCR-based gene disruptions in *Saccharomyces cerevisiae*. *Yeast* **10**, 1793–1808 (1994).
33. Guthrie, C. & Fink, G. *Guide to Yeast Genetics and Molecular Biology* (Academic Press, 1991).
34. Oh, S. D. *et al.* Stabilization and electrophoretic analysis of meiotic recombination intermediates in *Saccharomyces cerevisiae*. *Methods Mol. Biol.* **557**, 209–234 (2009).
35. Friedman, K. L. & Brewer, B. J. Analysis of replication intermediates by two-dimensional agarose gel electrophoresis. *Methods Enzymol.* **262**, 613–627 (1995).
36. Goldstein, A. L. & McCusker, J. H. Three new dominant drug resistance cassettes for gene disruption in *Saccharomyces cerevisiae*. *Yeast* **15**, 1541–1553 (1999).
37. Conti, C., Caburet, S., Schurra, C. & Bensimon, A. Molecular combing. *Curr. Protoc. Cytom.* Ch. 8, Unit 8 10 <http://dx.doi.org/10.1002/0471142956.cy0810s16> (2001).
38. Mann, H. & Whitney, D. On a test of whether one of 2 random variables is stochastically larger than the other. *Ann. Math. Stat.* **18**, 50–60 (1947).



Extended Data Figure 1 | BIR efficiency during molecular combing analysis of molecular intermediates of BIR. **a**, BIR efficiency was analysed by PFGE from samples used for dynamic molecular combing analysis (Fig. 3d). DNA was prepared from cells containing truncated chromosome III (Trunc Chr III) before DSB induction and 11 h or 13 h after DSB induction from wild-type (*PIF1*) and *pif1Δ* cells, respectively. In *pif1Δ*, a later time point (13 h) was analysed owing to slower kinetics of DSB repair in *pif1Δ* as compared to *PIF1*.

Chromosomes were separated by PFGE followed by Southern hybridization with an *ADE1*-specific probe. **b**, Quantification of DSB repair efficiency (BIR, or other recombination pathways) based on the results of 3–5 individual experiments and presented as average \pm s.d. **c**, Schematic of the BIR assay. Interruption of BIR leads to the resolution of BIR intermediates resulting in half-crossover formation.

a

Relevant Genotype	Molecule analyzed	Full BIR (~100 kb BrdU)	Long BIR (>30 kb BrdU)	Short BrdU * patches (<20 kb BrdU)	No BrdU	Total
wt (<i>PIF1</i>)	Donor	4	---	14 [4] (10)	85	103
	Recipient	70	14	---	14	98
<i>pif1</i> Δ	Donor	0	0	12 [5] (7)	80	92
	Recipient	0	0	31 [23] (8)	72	103

* - BrdU patches between P2 and P3 are included. [] - overlaps with P2; () - overlaps with P3

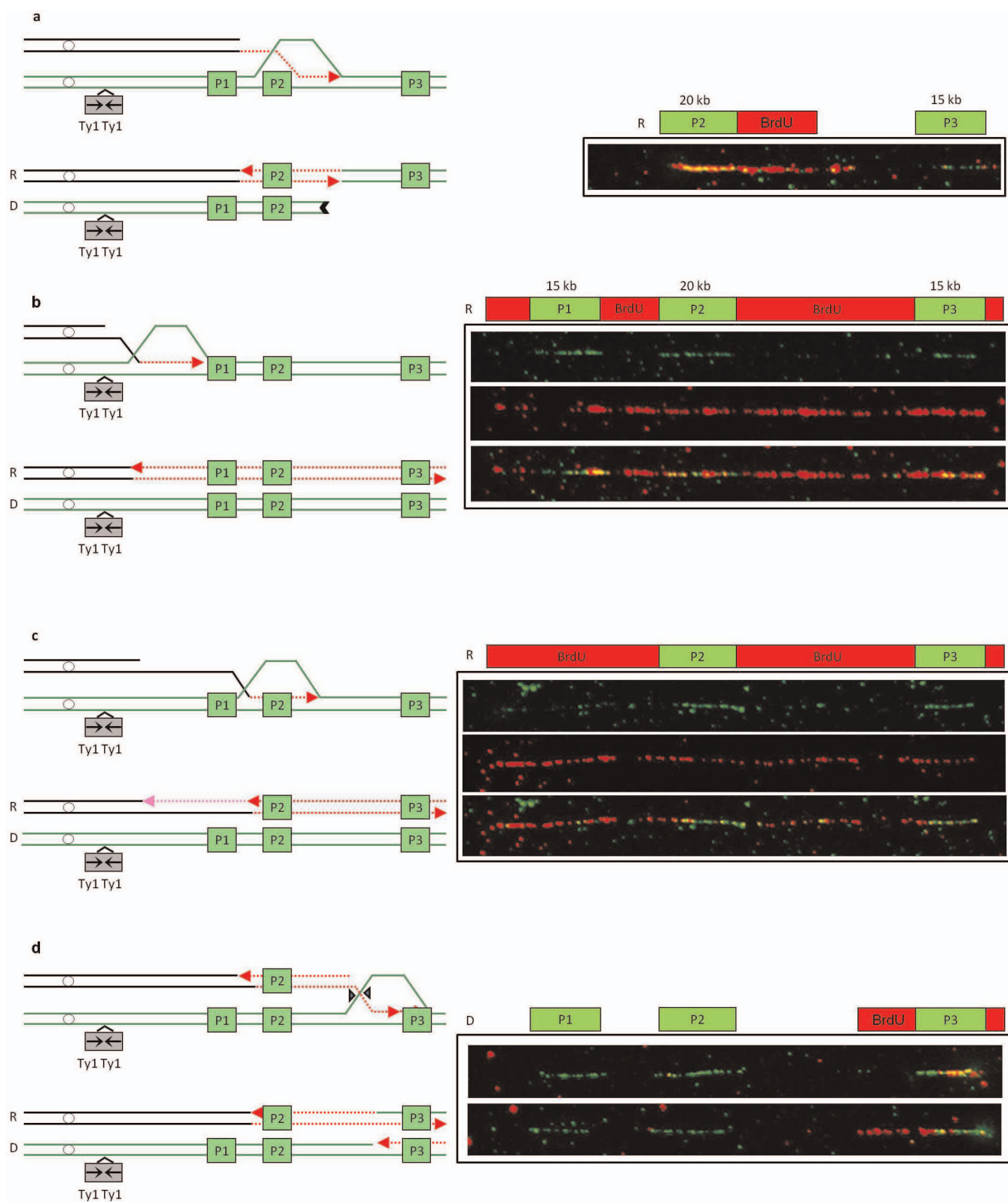
b

Orientation of <i>ura3-29</i>	MMS ^a	BIR Ura ⁺ mutations		
		C→A	C→T	C→G
Ori1	No	79 (80%)	18 (18%)	2 (2%)
	Yes	31 (66%)	12 (25%)	4 (9%)
Ori2	No	13 (28%)	24 * (51%)	10 (21%)
	Yes	21 (36%)	26 ** (45%)	11 (19%)

^a - Cells exposed to 1.5 mM MMS; * and ** - Statistically different from Ori1 (P<0.0001 and P=0.04 respectively)

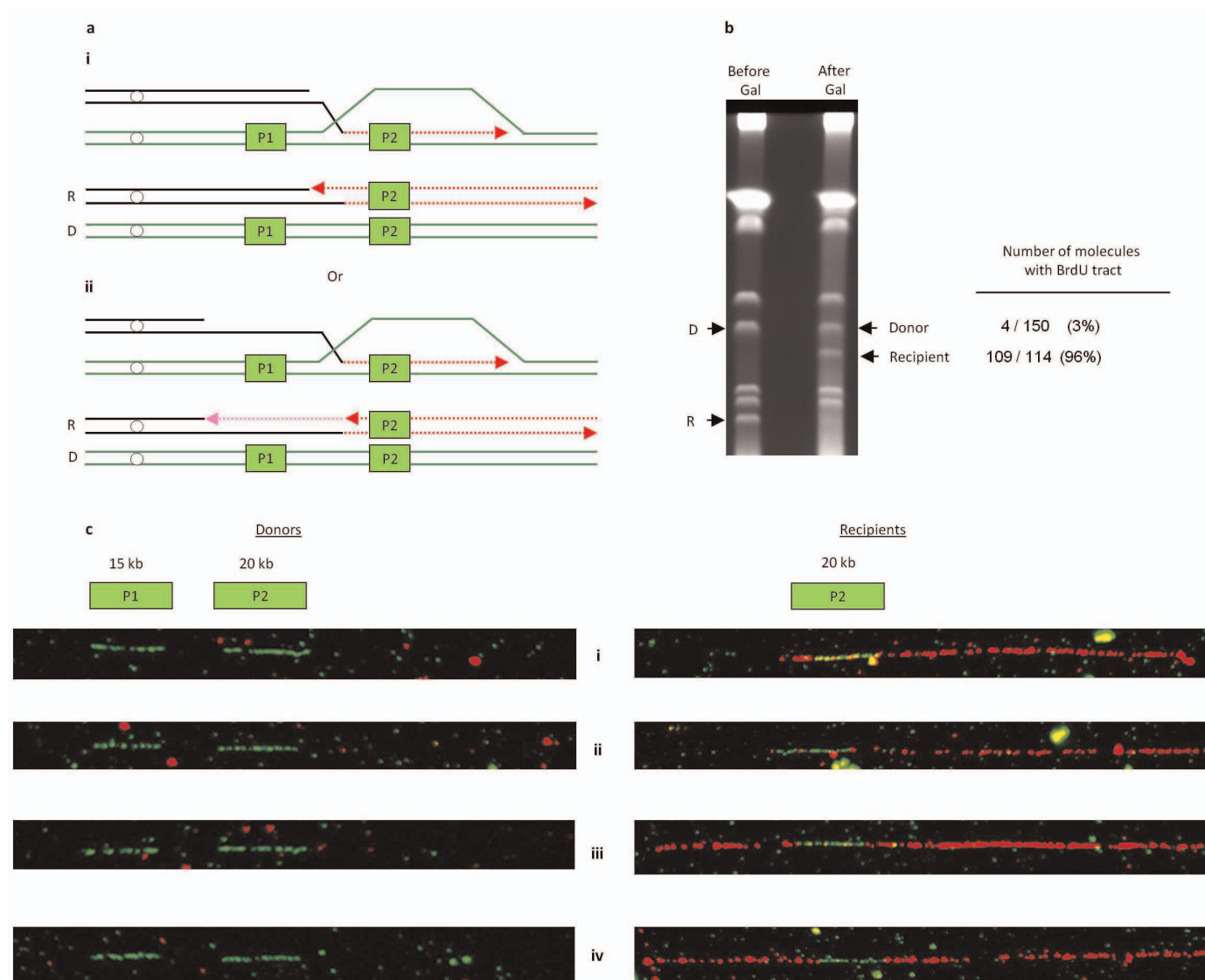
Extended Data Figure 2 | Analysis of molecular mechanism and mutagenesis associated with BIR. **a**, The summary of molecular combing analysis presented in Fig. 3 and in Extended Data Fig. 3 is shown. A strong bias towards BrdU tracts present only in the recipient chromosome was also

observed in three additional independent experiments. **b**, Mutation spectra of BIR-induced base substitutions in *ura3-29* in the presence or absence of 1.5 mM MMS is shown.



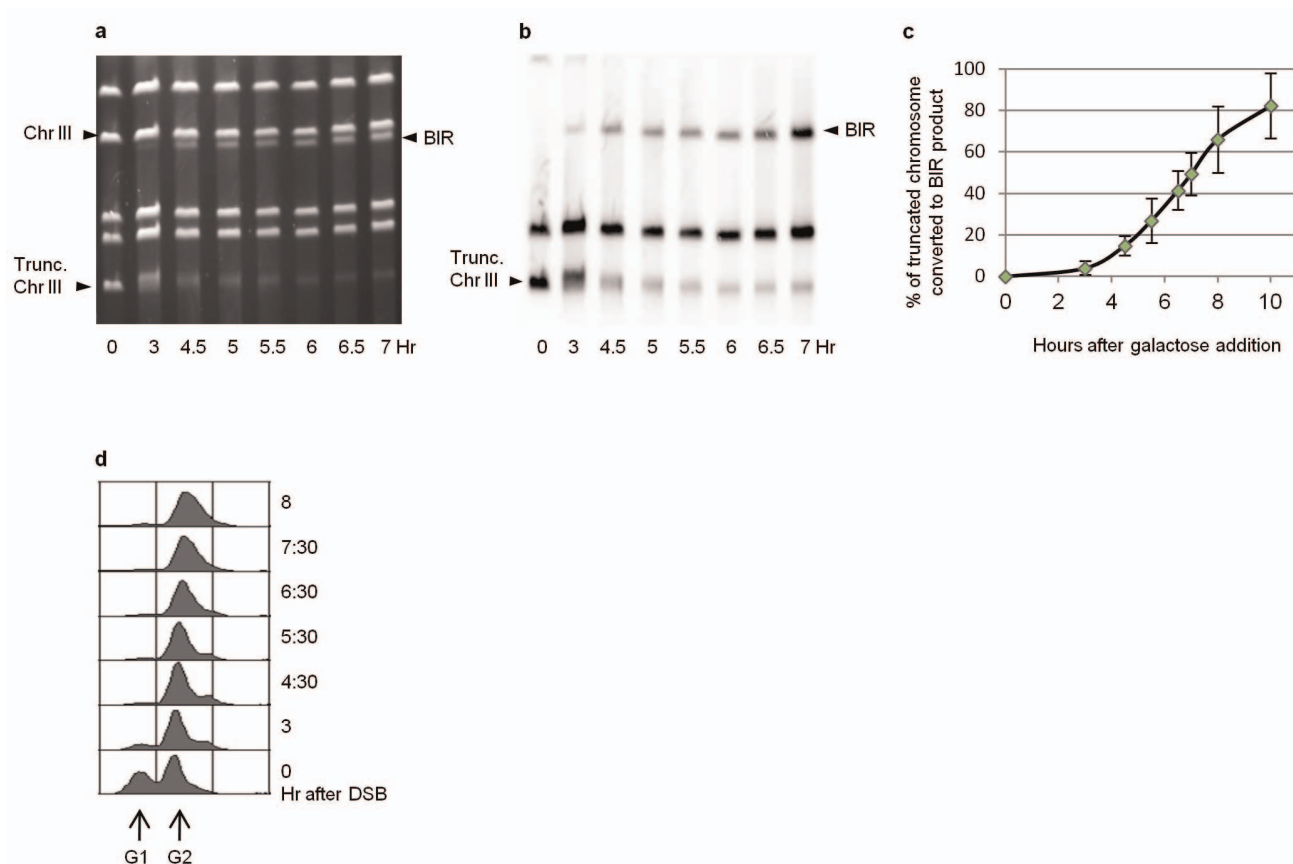
Extended Data Figure 3 | Molecular outcomes of BIR. **a**, Left: interrupted BrdU tract in recipient may result from half-crossover. Right: an example of wild-type (*PIF1*) recipient with interrupted BrdU tract hybridized to P1, P2, P3 probes (green) and treated with anti-BrdU antibody (red). **b**, Left: BIR initiated by strand invasion between FS2 (inverted repeat of Ty1 located 30 kb centromere proximal to *MAT*) and P1 results in formation of recipients hybridizing to P1, P2, P3 and BrdU. Right: an example of wild-type (*PIF1*) recipient. Top: hybridization to P1, P2, P3. Middle: treatment with anti-BrdU antibody. Bottom: merge. **c**, Left: BrdU incorporation in the recipient resulting

from BIR (red) and from filling-in synthesis (pink) following extensive resection. Right: an example of wild-type (*PIF1*) recipient. Top: hybridization to P1, P2, P3. Middle: treatment with anti-BrdU antibody. Bottom: merge. **d**, Left: HJ resolution at the end of BIR progression leads to switch from conservative to semiconservative BIR resulting in a short patch of BrdU overlapping with P3 in the donor. Right: an example of BrdU incorporation in the donor from wild-type (*PIF1*) strain hybridized to P1, P2, P3 and treated with anti-BrdU antibody.



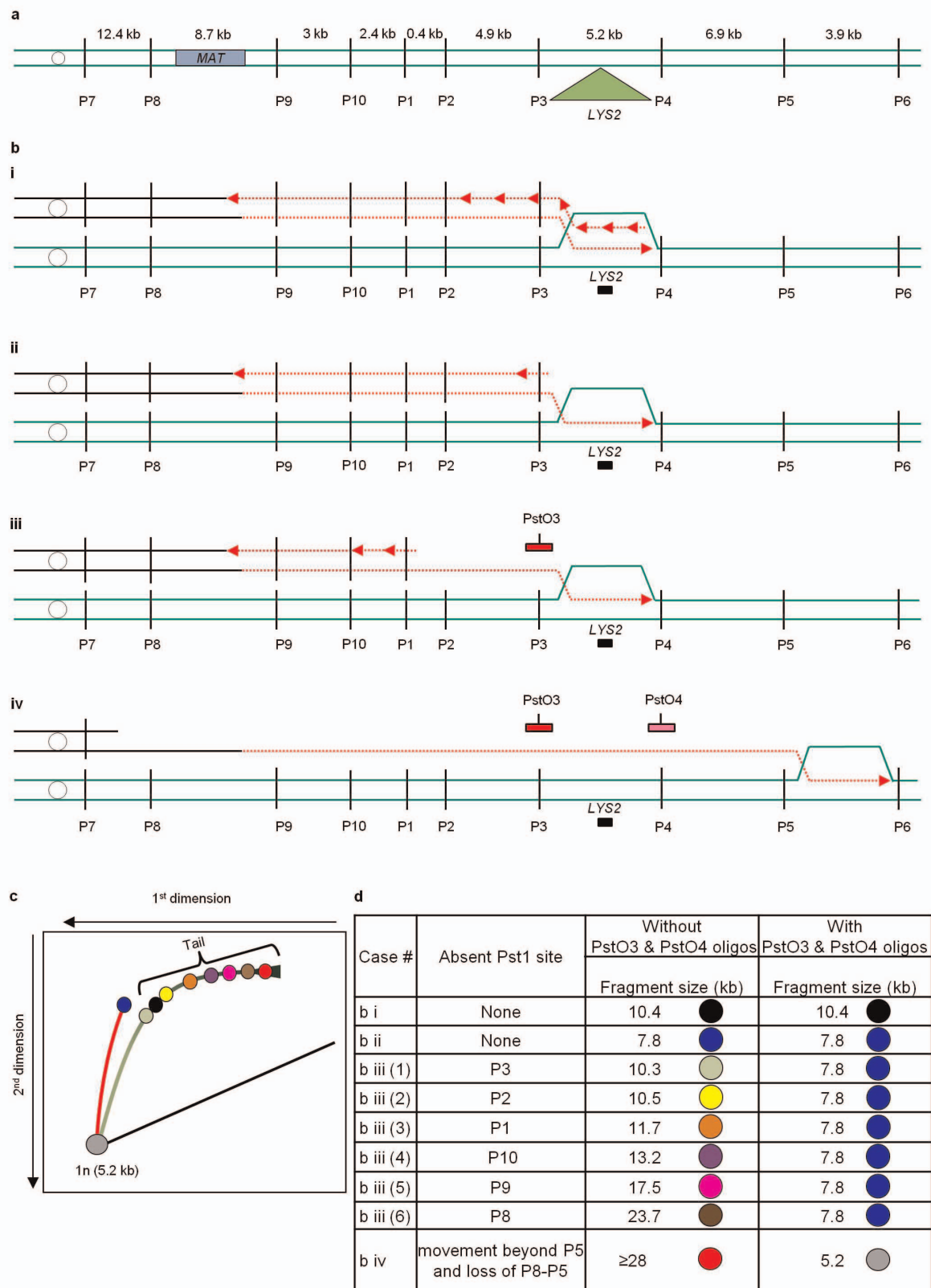
Extended Data Figure 4 | Conservative DNA synthesis associated with BIR. Results from a series of three experiments where only P1, P2 and anti-BrdU antibody were used. **a**, BrdU incorporation in the recipient is expected from conservative BIR (i; red) and from filling-in synthesis (pink) following extensive resection (ii). **b**, **c**, Analysis of the donor (D) and repaired recipient

(R) chromosomes extracted after PFGE (**b**) and hybridization with probes (green tract) and treatment with anti-BrdU antibodies (red tract) (**c**). No BrdU tracts are visible in more than 97% of donors. The repaired recipient contains long stretches of BrdU overlapping with the P2 region.



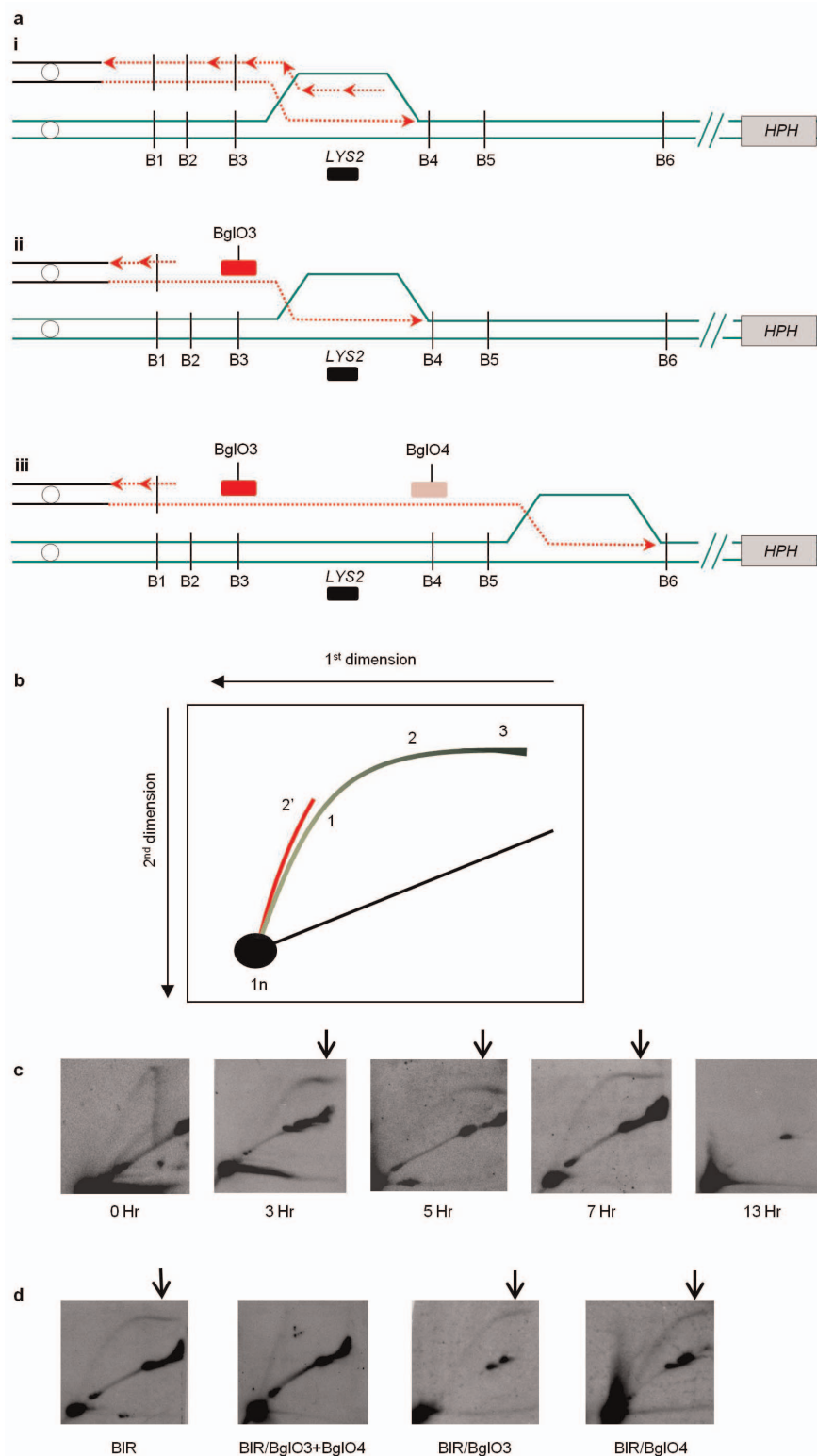
Extended Data Figure 5 | BIR kinetics during 2D analysis of molecular intermediates of BIR. **a**, BIR kinetics was analysed by PFGE from samples used to determine the structure of BIR intermediates by 2D electrophoresis (Fig. 4c, d). DNA was prepared for PFGE at intervals after induction of DSBs at *MATa* and separated by PFGE (**a**) followed by Southern hybridization with an

ADE1-specific probe (**b**). **c**, BIR efficiency quantified based on the results of four individual experiments including the one shown in Fig. 4 presented as average \pm s.d. **d**, Flow cytometry of DNA analysis of cells undergoing BIR repair.



Extended Data Figure 6 | The structure of molecular intermediates of BIR.
a, The structure of the chromosome III region with *LYS2* inserted 16 kb centromere distal to *MATx-inc*. P1, P2, P3, and so on designate positions of PstI sites flanking *LYS2*. **b**, The structure of replication bubbles migrating through *LYS2* (with black rectangle designating *LYS2*-specific probe). i, Replication bubble with synchronous leading and lagging strands (double-stranded). ii, Replication bubble with delayed initiation of the lagging strand with respect to

the leading strand (partially single-stranded bubble). iii, A partially single-stranded bubble with one or several PstI sites behind the bubble inactivated due to accumulation of single-stranded DNA. Red and pink rectangles represent oligonucleotides PstO3 and PstO4, respectively. iv, A single-stranded bubble that has passed beyond the P3-P4 region. **c**, Theoretical bubble-migration curves for the intermediates shown in **b**. **d**, Calculation of parameters of the bubble-like structures for the intermediates shown in **b**.



Extended Data Figure 7 | Molecular intermediates of BIR. BIR intermediates were analysed by 2D gel electrophoresis of BglII-digested intact chromosomal DNA embedded in agarose plugs. **a**, D-loop migration in 2D gels (hybridized to *LYS2*, black rectangle) during coordinated (i) and uncoordinated (ii, iii) leading- and lagging-strand synthesis. **b**, Schematic of 2D gel separation of replication and BIR intermediates. Annealing to oligonucleotides (BglO3 and BglO4) restores BglII sites (B) in ssDNA (see **a**, ii) and changes migration of

the intermediate as shown by 2' (red). **c**, 2D analysis of Y-arc during normal replication (0 Hr) and bubble-like structures at time points after BIR induction. Similar bubble structures were observed in nine additional independent experiments (see the legend to Fig. 4). **d**, High-molecular-mass tails (arrows) disappear after simultaneous addition of BglO3 and BglO4 (BIR/BglO3+BglO4). The addition of each of these oligonucleotides individually (BIR/BglO3 or BIR/BglO4) failed to eliminate the tail.

Extended Data Table 1 | The rate of spontaneous and DSB-associated Ura⁺ mutations

		Rate of Ura ⁺ (x10 ⁶)*								BIR efficiency (%) [§]			
		Before galactose (0 h)		After galactose (frequency (7 h – 0 h))									
				No MMS		1.5 mM MMS				No MMS		1.5 mM MMS	
Orientation of <i>ura3-29</i>	<i>HO</i> site	Median	CI or range [†] [# of repeats]	Median	CI or range [†] [# of repeats]	Median	CI or range [†] [# of repeats]	Fold above no-damage [‡] (P-value)		Ade ⁺	Ade ⁺ Ura ⁺	Ade ⁺	Ade ⁺ Ura ⁺
Ori1	DSB	28	(10 - 41) [7]	3,646	(2,305 - 4,159) [7]	9,415	(4,911 - 11,061) [7]	2.6 (P=0.0006)		80 ± 8	94 ± 8	84 ± 10	98 ± 0.4
Ori2	DSB	6	(5 - 17) [7]	1,903	(979 - 2,941) [7]	41,835	(34,830 - 79,488) [7]	22 (P=0.0006)		74 ± 9	94 ± 2	76 ± 14	92 ± 2
Ori1	No	8	(5 - 10) [17]	0	(0 - 11) [10]	198	(49 - 358) [7]	24.8		N/A	N/A	N/A	N/A
Ori2	No	12	(5 - 19) [13]	0	(0 - 7) [7]	157	(101 - 245) [7]	13.1		N/A	N/A	N/A	N/A

* Rates calculated at 0 h based on 0 h frequencies using the Drake equation (see Methods for details). At 7 h, rates were calculated as (7 h frequency – 0 h frequency); differences <0 are reported as '0'.

† For strains with ≥6 experiments, the 95% CI of the median is given.

‡ Statistically significant elevation of 7 h mutation rate in strains in the presence of MMS over 7 h mutation rate in the absence of MMS.

§ Per cent of BIR (average ± s.d.) calculated based on 3–6 experiments among DSB repair outcomes collected at 7 h on either adenine dropout media (Ade⁺) or on adenine/uracil dropout media (Ade⁺Ura⁺).

Extended Data Table 2 | The rate of DSB-associated Lys⁺ mutations (top), and the rate of spontaneous Lys⁺ mutations (bottom)

Position	Construct	HO site	Relevant Genotype	Rate of Lys ⁺ (x10 ⁹)*				BIR efficiency (%)§		
				Before galactose (0 h)		After galactose (frequency (7 h – 0 h))		Fold below WT [‡] (P-value)	Ade ⁺	Ade ⁺ Lys ⁺
				Median	CI or range [†] [# of repeats]	Median	CI or range [†] [# of repeats]			
16 kb	A ₄	DSB	wt	40	(12.7 - 64.3) [13]	2,690	(1,073.0 - 4,361) [13]	NA	77 ± 12	99.7 ± 0.5
16 kb	A ₄	DSB	<i>pif1Δ</i>	6	(4.0 - 10.4) [14]	134.7	(104 - 1,580) [14]	20 (0.0001)	73 ± 11	99 ± 3
36 kb	A ₄	DSB	wt	5.3	(2.7 - 15.2) [8]	1,248.10	(860 - 1,552) [8]	NA	80 ± 1	99 ± 1
36 kb	A ₄	DSB	<i>pif1Δ</i>	1	(0.5 - 12) [13]	1.4	(0 - 4.7) [13]	892 (0.0003)	91 ± 4	100 [#]

Position	Construct	HO site	Relevant Genotype	Rate of Lys ⁺ (x10 ⁹)*	
				Median	CI or range [†] [# of repeats]
16 kb	A ₄	No	wt	7.7	(3.3 - 34) [10]
16 kb	A ₄	No	<i>pif1Δ</i>	5.3	(3.3- 7.5) [6]
36 kb	A ₄	No	wt	1.1	(0.7 - 5.4) [4]
36 kb	A ₄	No	<i>pif1Δ</i>	0.9	(0.6 -3.9)[9]

* Rates calculated at 0 h based on 0 h frequencies using the Drake equation (see Methods for details). At 7 h, rates were calculated as (7 h frequency – 0 h frequency); differences <0 are reported as '0'.

† For strains with ≥6 experiments, the 95% CI of the median is given. For the strains with <6 experiments, the median range is given.

‡ Statistically significant decrease of median rate at 7 h in *pif1Δ* compared to wild type.

§ Per cent of BIR (average ± s.d.) calculated based on 4–8 experiments among DSB repair outcomes collected at 7 h on either adenine dropout media (Ade⁺) or on adenine/lysine dropout media (Ade⁺Lys⁺).

No s.d. could be calculated because of a very low number of Lys⁺ (between 1 and 5) in each experiment.

Extended Data Table 3 | Strain list

Strain name	Genotype	Reference
AM1003	<i>MATa-LEU2-tel/MATa-inc ade1 met13 ura3 leu2-3,112/leu2 thr4 lys5 hml::ADE1/hml::ADE3 hmr::HPH ade3::GAL-HO FS2::NAT/FS2</i>	2
AM1291	AM1003, but <i>lys2Δ thr4::lys2-Ins(A₄)</i>	9
AM1449	AM1291, but <i>MATa-inc-LEU2-tel</i>	9
AM1482	AM1003, but <i>lys2Δ sed4::lys2-Ins(A₄)</i>	9
AM1649	AM1482, but <i>MATa-inc-LEU2-tel</i>	9
AM2191	AM1291, but <i>pif1::KANMX</i>	this study
AM2247	AM2191, but <i>MATa-inc-LEU2-tel</i>	this study
AM2198	AM1482, but <i>pif1::KANMX</i>	this study
AM2257	AM2198, but <i>MATa-inc-LEU2-tel</i>	this study
AM1247	AM1003, but <i>lys2Δ thr4::LYS2</i>	9
AM2439	AM1291, but <i>snt1::(TEF1/BSD)₃</i>	this study
AM2438	AM1482, but <i>snt1::(TEF1/BSD)₂</i>	this study
AM2118	AM1247, Chr II::KANMX	this study
AM2442	AM2118, but <i>MATa-inc-LEU2-tel</i>	this study
AM2406	AM1003, but <i>ura3::p306-BrdU tps1::KANMX snt1::(TEF1/BSD)₃</i>	this study
AM2846	AM2406, but <i>tps1::BLEO pif1::KANMX</i>	this study
AM2110	AM1003, but <i>lys2Δ ura3Δ sed4::lys2-Ins(A₄) hmr::KANMX</i>	this study
AM2161	AM2110, but <i>thr4::ura3-29 (Ori1)</i>	this study
AM2259	AM2161, but <i>MATa-inc-LEU2-tel</i>	this study
AM2820	AM2110, but <i>thr4::ura3-29 (Ori2)</i>	this study
AM2842	AM2820, but <i>MATa-inc-LEU2-tel</i>	this study

Pif1 helicase and Pol δ promote recombination-coupled DNA synthesis via bubble migration

Marenda A. Wilson^{1*}, YoungHo Kwon^{2*}, Yuanyuan Xu², Woo-Hyun Chung^{1,3}, Peter Chi^{4,5}, Hengyao Niu², Ryan Mayle¹, Xuefeng Chen¹, Anna Malkova^{6†}, Patrick Sung² & Grzegorz Ira¹

During DNA repair by homologous recombination (HR), DNA synthesis copies information from a template DNA molecule. Multiple DNA polymerases have been implicated in repair-specific DNA synthesis^{1–3}, but it has remained unclear whether a DNA helicase is involved in this reaction. A good candidate DNA helicase is Pif1, an evolutionarily conserved helicase in *Saccharomyces cerevisiae* important for break-induced replication (BIR)⁴ as well as HR-dependent telomere maintenance in the absence of telomerase⁵ found in 10–15% of all cancers⁶. Pif1 has a role in DNA synthesis across hard-to-replicate sites^{7,8} and in lagging-strand synthesis with polymerase δ (Pol δ)^{9–11}. Here we provide evidence that Pif1 stimulates DNA synthesis during BIR and crossover recombination. The initial steps of BIR occur normally in Pif1-deficient cells, but Pol δ recruitment and DNA synthesis are decreased, resulting in premature resolution of DNA intermediates into half-crossovers. Purified Pif1 protein strongly stimulates Pol δ -mediated DNA synthesis from a D-loop made by the Rad51 recombinase. Notably, Pif1 liberates the newly synthesized strand to prevent the accumulation of topological constraint and to facilitate extensive DNA synthesis via the establishment of a migrating D-loop structure. Our results uncover a novel function of Pif1 and provide insights into the mechanism of HR.

To understand how Pif1 promotes BIR, we used an established system wherein only one end of a site-specific double strand break (DSB) has extensive homology to the donor sequence, so that most cells (>80%) use BIR for repair¹². After strand invasion, over 100 kilobases of the full-length chromosome III donor is copied. Chromosomal markers provide a means to determine the frequency of BIR or alternative mechanisms by growth on selective media (Fig. 1a). BIR was evaluated in *pif1-m2* cells, wherein the mutant Pif1 protein is excluded from the nucleus but retains mitochondrial function¹³, or in *pif1* Δ cells.

Cells lacking Pif1 are BIR deficient and have a large increase in half-crossover products (Fig. 1b), with *pif1* Δ showing a greater impairment, probably because the *pif1-m2* protein retains residual nuclear activity¹³. The Pif1 helicase activity is indispensable for BIR as revealed by testing the helicase-dead *pif1(K264A)* mutant (Fig. 1b). Southern blot analysis showed loss of the template chromosome in *pif1* Δ consistent with an increase in half-crossover products (Fig. 1c and Extended Data Fig. 1a). An examination of repair products from individual colonies revealed elevated gross chromosomal rearrangements and changes in template chromosome size, which probably stemmed from half-crossovers (Extended Data Fig. 2a–d). The role of Pif1 in BIR is general and highly specific, as BIR induced at a different locus is also Pif1-dependent (Extended Data Fig. 3a–e) and elimination of two other 5'–3' helicases, Rrm3 or Hcs1, does not affect BIR (Extended Data Fig. 1b). The BIR function of Pif1 is unrelated to its known role in telomerase inhibition, as the elimination of telomerase components does not suppress the BIR defect of *pif1-m2* cells (Extended Data Fig. 1c).

A similar deficiency in BIR with high levels of half-crossovers was observed in *pol32* Δ cells, which lack the nonessential subunit of Pol δ (ref. 12) (Extended Data Fig. 1b), implicating Pif1 in DNA synthesis. Consistent with this deduction, strand invasion occurs normally in *pif1* Δ cells (Extended Data Fig. 4a, b), whereas DNA synthesis monitored by quantitative polymerase chain reaction (qPCR) is decreased (Fig. 1d). In chromatin immunoprecipitation (ChIP) analyses we found Pif1 enrichment at the DSB and along the template molecule,

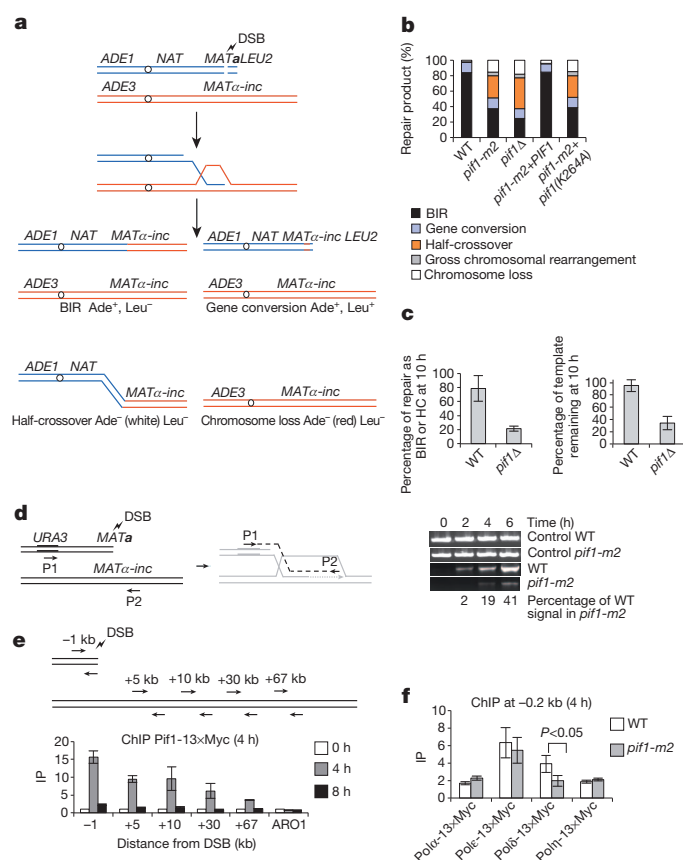


Figure 1 | Pif1 promotes DNA synthesis during BIR. **a**, Schematic of the BIR assay. Products are distinguished by genetic markers. **b**, Repair outcomes in wild-type (WT) and indicated mutant cells. **c**, Quantification of Southern blot band intensities corresponding to the DSB repair products and template chromosome in wild-type and *pif1* Δ cells. HC, half-crossover. **d**, Analysis of initial DNA synthesis by PCR. **e**, ChIP analysis of Pif1-13xMyc recruitment at the indicated loci. **f**, DSB recruitment of the indicated polymerases during BIR as measured by ChIP. Plotted in **c**, **e**, **f**, are the mean values \pm s.d. $n = 3$.

¹ College of Medicine, Department of Molecular & Human Genetics, One Baylor Plaza, Houston, Texas 77030, USA. ² Department of Molecular Biophysics & Biochemistry, Yale University School of Medicine, 333 Cedar Street, New Haven, Connecticut 06520, USA. ³ College of Pharmacy, Duksung Women's University, Seoul 132-714, South Korea. ⁴ Institute of Biochemical Sciences, National Taiwan University, No. 1, Sec. 4, Roosevelt Road, Taipei 10617, Taiwan. ⁵ Institute of Biological Chemistry, Academia Sinica, 128 Academia Road, Section 2, Nankang, Taipei 115, Taiwan. ⁶ Department of Biology, School of Science, IUPUI, Indianapolis, Indiana 46202, USA. [†]Present address: Department of Biology, College of Liberal Arts and Sciences, University of Iowa, Iowa City, Iowa 52242-1324, USA.

*These authors contributed equally to this work.

further implicating a role of Pif1 in DNA synthesis (Fig. 1e). This Pif1 enrichment is repair-specific, as it is compromised in mutants deficient in strand invasion or extensive DNA synthesis (Extended Data Fig. 4c, d). Because Pif1 seems to affect DNA synthesis, we used ChIP to examine the initial recruitment of Pol δ , which is essential for BIR¹⁴, and other polymerases. Notably, only the recruitment of Pol δ is decreased in *pif1-m2* cells (Fig. 1f).

Besides BIR, fully processive Pol δ is needed for the crossover HR pathway and promotes long conversion tracts¹⁵. Pif1 is also needed for both processes as monitored in ectopic or allelic gene conversion assays (Fig. 2a–c and Extended Data Fig. 1d). There is no change in cell viability or repair efficiency in *pif1* Δ cells, but the crossover frequency decreases by half, similar to *pol32* Δ cells (Fig. 2c). Furthermore, the increase in crossover frequency caused by deleting the crossover suppressors Mph1 and Srs2 (refs 16, 17) is also dependent on Pif1 and Pol32 (Fig. 2b, c). Thus, Pif1 and Pol δ are key factors in crossover recombination. Indeed, the conditional depletion of Pol δ but not other polymerases almost completely eliminates crossovers while slightly reducing non-crossovers (Extended Data Fig. 1e).

We performed biochemical reconstitution to examine how Pif1 influences DNA synthesis in D-loops made by Rad51, RPA and Rad54 (refs 18, 19). According to a published procedure³, we loaded the polymerase clamp PCNA onto the primer end of the D-loop with RFC, then added Pol δ with Pif1 (Fig. 3a). Our Pif1, RFC, PCNA and Pol δ preparations had no detectable nuclease or topoisomerase contamination (Extended Data Fig. 5a, b).

We first made the D-loop with a 5' ³²P-labelled 90-mer oligonucleotide as the invading strand and pBluescript (2,961 base pairs (bp))

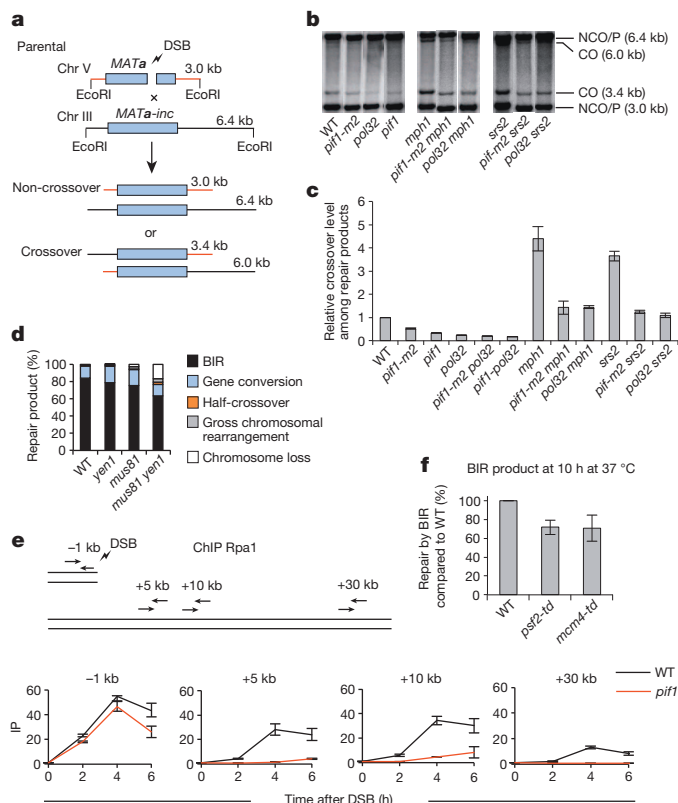


Figure 2 | Pif1 is important for crossover recombination. **a**, Schematic of the ectopic recombination assay. **b**, Southern blot analysis of gene conversion with and without crossovers in the indicated strains. CO, crossover; NCO, non-crossover; P, parental. **c**, Quantification of crossover frequency in ectopic recombination. **d**, Repair outcomes in BIR assay in wild-type and the indicated mutant cells. **e**, ChIP analysis of RPA binding during BIR at the indicated loci. **f**, Quantification of BIR product formation upon conditional depletion of Psf2 or Mcm4. Plotted in **c**, **e**, **f**, are the mean values \pm s.d. $n = 3$.

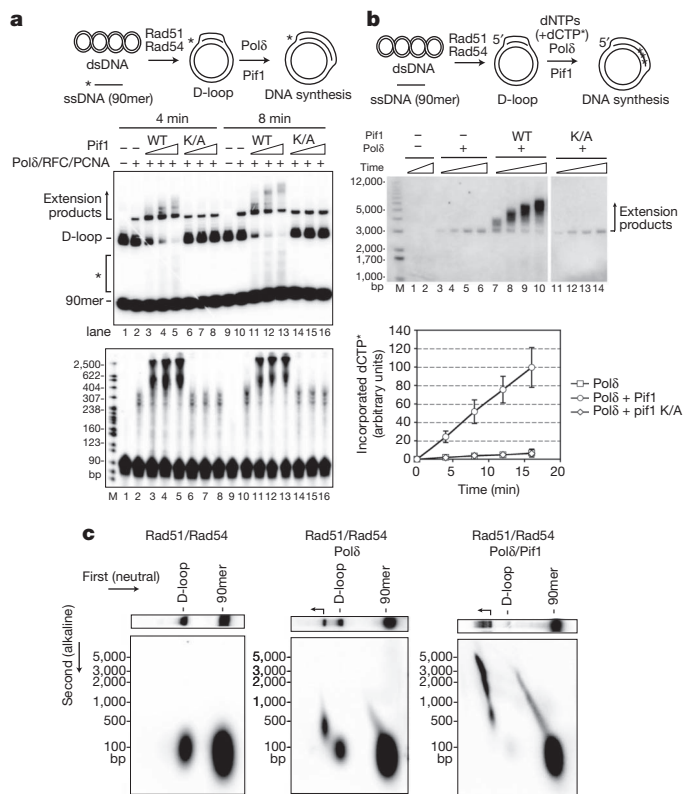


Figure 3 | Pif1 promotes DNA extension at a D-loop. **a**, Extension of ³²P-labelled invading strand. Extension products by Pol δ with Pif1 or *pif1*(K264A) (K/A) (13, 27, 40 nM) were analysed in a native gel (top) or denaturing gel (bottom). Representative gels from three independent experiments are shown. **b**, Extension of unlabelled invading strand with [α -³²P]dCTP. Products were resolved in a native gel and quantified. The mean values \pm s.d. from three independent experiments are plotted. **c**, Products prepared as in lanes 1, 10 and 13 of panel **a** were subject to two-dimensional gel analysis.

DNA as acceptor (Fig. 3a). DNA synthesis by Pol δ generated DNA species that migrated above the D-loop (Fig. 3a, lanes 2 and 10). Notably, the addition of Pif1 led to the appearance of DNA species that harboured a much larger amount of new synthesis (Fig. 3a, lanes 3–5, 11–13). With Pif1 present, DNA species migrating above the substrate oligonucleotide but below the D-loop were also observed (indicated by the asterisk in Fig. 3a). Because Pif1 can disrupt the D-loop structure (Extended Data Fig. 5c), these DNA species probably stemmed from the release of the extended invading strand.

The helicase activity of Pif1 is required for the stimulation of Pol δ -mediated DNA synthesis, as revealed by analysing the *pif1*(K264A) mutant^{13,20} (Fig. 3a). Likewise, no DNA synthesis occurred if either Rad51 or Rad54 was absent or upon the omission of RFC, PCNA, or deoxynucleoside triphosphates (Extended Data Fig. 5c). Efficient D-loop formation and optimal DNA synthesis require RPA (Extended Data Fig. 5c), in concordance with previous observations that it promotes Rad51-mediated strand exchange^{19,21} and DNA unwinding by Pif1 (ref. 22). Notably, in the absence of Pif1, RPA was unable to promote extensive synthesis by itself (Fig. 3 and Extended Data Fig. 5c), even when present in excess (data not shown). In addition, when either Rad51 or Rad54 was removed (Extended Data Fig. 6a), or when Rad54 was heat-deactivated after D-loop formation (Extended Data Fig. 6b), Pif1 was still able to stimulate DNA synthesis.

In another set of experiments, an unlabelled invading strand was extended with [α -³²P]dCTP present (Fig. 3b). Two-dimensional gel electrophoresis (Fig. 3c)^{3,23} showed that the extended DNA species made by Pol δ harboured \sim 200–500 nucleotides (Fig. 3c), whereas the products made by Pol δ with Pif1 could reach a few thousand nucleotides (Fig. 3c and Extended Data Fig. 5d).

The effect of Pif1 is highly specific, as neither *S. cerevisiae* Rrm3 nor *Escherichia coli* DinG, which possess 5'–3' helicase activity, could substitute for it. Likewise, no enhancement of Pol δ -mediated DNA synthesis occurred with the 3'–5' *S. cerevisiae* Mph1 helicase (Extended Data Fig. 7a). Moreover, Pif1 has no effect on *E. coli* DNA polymerase I Klenow fragment (Extended Data Fig. 7b).

S. cerevisiae cells lacking the *POL32* gene are impaired for HR^{12,14,15,24}. The Pol32 protein interacts with PCNA and enhances the processivity of Pol δ (ref. 25). We observed a severely reduced level of DNA synthesis by Pol δ^* , which lacks Pol32 (Extended Data Fig. 8a), alone or in conjunction with Pif1 (Extended Data Fig. 8c). Purified Pol32 interacts with Pol δ^* (Extended Data Fig. 8b) and its addition to Pol δ^* led to an enhancement of DNA synthesis activity comparable to that of Pol δ (Extended Data Fig. 8c).

Extensive DNA synthesis in a covalently closed DNA molecule generates topological stress that would impede polymerase movement, yet, in our reconstituted system several kilobases of DNA can be synthesized without a topoisomerase (Fig. 3c and Extended Data Fig. 5d). In fact, whereas topoisomerase I enhanced DNA synthesis by Pol δ alone (Extended Data Fig. 9a, lanes 5 and 6)³, it had no stimulatory effect when Pif1 was present (Extended Data Fig. 9a, b). Thus, Pif1-dependent DNA synthesis may entail concomitant dissociation of the newly synthesized DNA from the 5' side, a premise supported by our observation that Pif1 can efficiently dissociate the unmodified (Extended Data Fig. 5c) and extended D-loops (Fig. 3a).

We tested the hypothesis that Pol δ –Pif1-mediated DNA synthesis occurs within a migrating D-loop. First, the extended D-loops were analysed by restriction digests (Fig. 4a). If the extended invading strand were released, then a significant fraction of the D-loop would be resistant to the enzymes AhdI and XmnI, which incise at 115 and 714 nucleotides from the 5' terminus of the invading strand, respectively. D-loops were made with a 5' ³²P-labelled invading strand and extended with unlabelled deoxynucleotides (see Fig. 3a), followed by treatment with AhdI or XmnI and analysis in a denaturing gel (Fig. 4a). The D-loop extended by Pol δ alone could be cleaved quantitatively by AhdI to produce a 115-nucleotide DNA fragment (lanes 7 and 9), whereas most of the extended product made with Pol δ –Pif1 was resistant to XmnI, consistent with the short Pol δ -alone synthesis tract (Fig. 3). A small fraction of the extended D-loop from the Pol δ –Pif1 reaction was cleavable by XmnI to generate the 714-nucleotide fragment, indicative of DNA synthesis proceeding beyond the +714 site and of the fact that much the +714 site in the extended DNA existed as single-stranded DNA (ssDNA) (Fig. 4a, lanes 13 and 15). Thus, in the Pol δ –Pif1 reaction, Pif1 continually dissociates the extended strand from the D-loop. This 'bubble migration' mode of DNA synthesis was previously suggested for a reconstituted bacteriophage T4 system that harbours the Dda helicase²⁶.

We next examined the extended D-loops by electron microscopy. We treated the D-loop products with the T4 gp32 protein to decorate the ssDNA region, followed by protein–DNA crosslinking with glutaraldehyde. The crosslinked nucleoprotein complexes were analysed by electron microscopy with metal shadowing²⁷. Figure 4b shows typical electron microscopy images of pBluescript DNA, unextended D-loop, D-loops extended by Pol δ , and D-loops extended by Pol δ –Pif1. This analysis clearly showed D-loop enlargement by Pol δ and that the Pol δ -extended invading strand remains hybridized to its complementary strand. Notably, the inclusion of Pif1 generated a long ssDNA tail protruding from the D-loop (Fig. 4b). Furthermore, we tested Pif1 for interaction with Pol δ and PCNA in affinity pull-down reactions. The analysis revealed that Pif1 physically associates with PCNA but not with Pol δ (Extended Data Fig. 8d).

We next asked whether BIR in cells entails the formation of a canonical replication fork with the replicative helicase Mcm2-7 having a crucial role. Several observations suggest that this is not the case. First, mutants deficient in structure-specific resolvases show only a

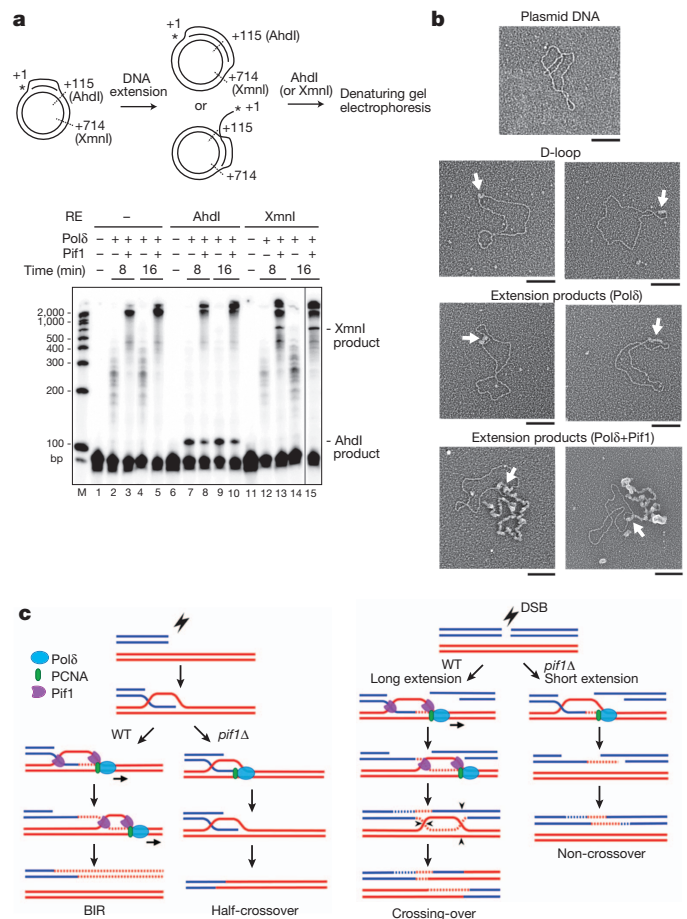


Figure 4 | Evidence for DNA synthesis in a migrating D-loop.

a, Biochemical analysis. Products were analysed in a denaturing gel. A representative gel from three independent experiments is shown. RE, restriction enzyme. **b**, Electron microscopy analysis. Micrographs of plasmid (pBluescript) DNA, D-loop made by Rad51, and extension products by Pol δ and Pol δ –Pif1. ssDNA was decorated with T4 gp32 and appears thicker than duplex DNA. Arrows identify the D-loop. Scale bar, 100 nm. Representative micrographs from two experiments are shown. **c**, Model depicting the dual role of Pif1. In BIR and crossover HR, Pif1 promotes DNA synthesis by a functional interaction with Pol δ –PCNA (this work), template strand separation¹⁰, and by displacing the newly synthesized strand (this work).

mild BIR deficiency, indicating that in BIR the D-loop does not need to be converted to a canonical replication fork (Fig. 2d). Second, monitoring the association of RPA with the template chromosome using ChIP revealed that extensive ssDNA is generated during template copying in a Pif1-dependent manner. We confirmed the presence of extensive ssDNA by applying qPCR after restriction digest of DNA synthesis intermediates (Fig. 2e and Extended Data Fig. 10a, b). These results indicate that the first and complementary strands are synthesized asynchronously. Finally, conditional depletion of Mcm4 or Psf2, components of the S-phase replication fork, leads to only a mild BIR deficiency (Fig. 2f and Extended Data Fig. 10c–e). Although we cannot exclude the possibility that in wild-type cells there is a switch from Pif1- to Mcm2-7-mediated synthesis, we have provided clear evidence that Pif1 can support extensive DNA synthesis in the absence of the replicative helicase.

Our results provide evidence for repair-specific Pif1-dependent DNA synthesis via a migrating D-loop (Fig. 4c) that can copy tens of kilobases. Aside from BIR and telomere recombination, such a mechanism could function in gene conversion in fungi²⁸ and can cause various genome rearrangements^{29,30}.

METHODS SUMMARY

The strains listed in Methods are derivatives of (1) tGI354 to study ectopic recombination (*hml::ADE1 MATa-inc hmr::ADE1 ade1 leu2-3,112 lys5 trp1::hisG ura3-52 ade3::GAL::HO arg5,6::HPH::MATa*) and (2) AM1003 to study BIR (*MATa-LEU2-tel/MATa-inc ade1 met13 ura3 leu2-3,112/leu2 thr4 lys5 hml::ADE1/hml::ADE3 hmr::HYG ade3::GAL-HO FS2::NAT/FS2*). The DSB was induced upon expression of the HO endonuclease by adding galactose to the media. Southern blotting and probes specific for either the broken or template chromosome were used to follow the kinetics of DSB repair and for the detailed analysis of individual repair products. Protein recruitment to DSBs was studied by ChIP followed by qPCR. Pif1 and other helicases, homologous recombination proteins, and DNA replication factors were expressed either in *E. coli* or yeast cells and purified by a multi-step procedure to near homogeneity in each case. For the DNA synthesis reaction, a D-loop is made using Rad51, RPA and Rad54, followed by loading of PCNA with RFC onto the 3' end of the invading strand, and incubation with combinations of Pif1 or another helicase with Pol δ . Reaction products were analysed by gel electrophoresis and phosphorimaging, or by electron microscopy with metal shadowing.

Online Content Any additional Methods, Extended Data display items and Source Data are available in the online version of the paper; references unique to these sections appear only in the online paper.

Received 25 August 2012; accepted 22 August 2013.

Published online 11 September; corrected online 16 October 2013 (see full-text HTML version for details).

- Malois, L., Fabre, F. & Gangloff, S. DNA polymerase δ is preferentially recruited during homologous recombination to promote heteroduplex DNA extension. *Mol. Cell. Biol.* **28**, 1373–1382 (2008).
- Wang, X. *et al.* Role of DNA replication proteins in double-strand break-induced recombination in *Saccharomyces cerevisiae*. *Mol. Cell. Biol.* **24**, 6891–6899 (2004).
- Li, X., Stith, C. M., Burgers, P. M. & Heyer, W. D. PCNA is required for initiation of recombination-associated DNA synthesis by DNA polymerase δ . *Mol. Cell* **36**, 704–713 (2009).
- Chung, W. H., Zhu, Z., Papusha, A., Malkova, A. & Ira, G. Defective resection at DNA double-strand breaks leads to *de novo* telomere formation and enhances gene targeting. *PLoS Genet.* **6**, e1000948 (2010).
- Dewar, J. M. & Lydall, D. Pif1- and Exo1-dependent nucleases coordinate checkpoint activation following telomere uncapping. *EMBO J.* **29**, 4020–4034 (2010).
- Cesare, A. J. & Reddel, R. R. Alternative lengthening of telomeres: models, mechanisms and implications. *Nature Rev. Genet.* **11**, 319–330 (2010).
- Paeschke, K., Capra, J. A. & Zakian, V. A. DNA replication through G-Quadruplex motifs is promoted by the *Saccharomyces cerevisiae* Pif1 DNA helicase. *Cell* **145**, 678–691 (2011).
- Sabouri, N., McDonald, K. R., Webb, C. J., Cristea, I. M. & Zakian, V. A. DNA replication through hard-to-replicate sites, including both highly transcribed RNA Pol II and Pol III genes, requires the *S. pombe* Pfh1 helicase. *Genes Dev.* **26**, 581–593 (2012).
- Budd, M. E., Reis, C. C., Smith, S., Myung, K. & Campbell, J. L. Evidence suggesting that Pif1 helicase functions in DNA replication with the Dna2 helicase/nuclease and DNA polymerase δ . *Mol. Cell. Biol.* **26**, 2490–2500 (2006).
- Pike, J. E., Burgers, P. M., Campbell, J. L. & Bambara, R. A. Pif1 helicase lengthens some Okazaki fragment flaps necessitating Dna2 nuclease/helicase action in the two-nuclease processing pathway. *J. Biol. Chem.* **284**, 25170–25180 (2009).
- Rossi, M. L. *et al.* Pif1 helicase directs eukaryotic Okazaki fragments toward the two-nuclease cleavage pathway for primer removal. *J. Biol. Chem.* **283**, 27483–27493 (2008).
- Deem, A. *et al.* Defective break-induced replication leads to half-crossovers in *Saccharomyces cerevisiae*. *Genetics* **179**, 1845–1860 (2008).
- Schulz, V. P. & Zakian, V. A. The *saccharomyces* PIF1 DNA helicase inhibits telomere elongation and *de novo* telomere formation. *Cell* **76**, 145–155 (1994).
- Lydeard, J. R., Jain, S., Yamaguchi, M. & Haber, J. E. Break-induced replication and telomerase-independent telomere maintenance require Pol32. *Nature* **448**, 820–823 (2007).
- Ho, C. K., Mazon, G., Lam, A. F. & Symington, L. S. Mus81 and Yen1 promote reciprocal exchange during mitotic recombination to maintain genome integrity in budding yeast. *Mol. Cell* **40**, 988–1000 (2010).
- Ira, G., Malkova, A., Liberi, G., Foiani, M. & Haber, J. E. Srs2 and Sgs1-Top3 suppress crossovers during double-strand break repair in yeast. *Cell* **115**, 401–411 (2003).
- Prakash, R. *et al.* Yeast Mph1 helicase dissociates Rad51-made D-loops: implications for crossover control in mitotic recombination. *Genes Dev.* **23**, 67–79 (2009).
- Petukhova, G., Stratton, S. & Sung, P. Catalysis of homologous DNA pairing by yeast Rad51 and Rad54 proteins. *Nature* **393**, 91–94 (1998).
- Van Komen, S., Petukhova, G., Sigurdsson, S. & Sung, P. Functional cross-talk among Rad51, Rad54, and replication protein A in heteroduplex DNA joint formation. *J. Biol. Chem.* **277**, 43578–43587 (2002).
- Bochman, M. L., Sabouri, N. & Zakian, V. A. Unwinding the functions of the Pif1 family helicases. *DNA Repair* **9**, 237–249 (2010).
- Sugiyama, T., Zaitseva, E. M. & Kowalczykowski, S. C. A single-stranded DNA-binding protein is needed for efficient presynaptic complex formation by the *Saccharomyces cerevisiae* Rad51 protein. *J. Biol. Chem.* **272**, 7940–7945 (1997).
- Boule, J. B. & Zakian, V. A. The yeast Pif1p DNA helicase preferentially unwinds RNA DNA substrates. *Nucleic Acids Res.* **35**, 5809–5818 (2007).
- Sebesta, M., Burkovics, P., Haracska, L. & Krejci, L. Reconstitution of DNA repair synthesis *in vitro* and the role of polymerase and helicase activities. *DNA Repair* **10**, 567–576 (2011).
- Smith, C. E., Lam, A. F. & Symington, L. S. Aberrant double-strand break repair resulting in half crossovers in mutants defective for Rad51 or the DNA polymerase δ complex. *Mol. Cell. Biol.* **29**, 1432–1441 (2009).
- Burgers, P. M. & Gerik, K. J. Structure and processivity of two forms of *Saccharomyces cerevisiae* DNA polymerase δ . *J. Biol. Chem.* **273**, 19756–19762 (1998).
- Formosa, T. & Alberts, B. M. DNA synthesis dependent on genetic recombination: characterization of a reaction catalyzed by purified bacteriophage T4 proteins. *Cell* **47**, 793–806 (1986).
- Griffith, J. D. & Christiansen, G. Electron microscope visualization of chromatin and other DNA-protein complexes. *Annu. Rev. Biophys. Bioeng.* **7**, 19–35 (1978).
- Ferguson, D. O. & Holloman, W. K. Recombinational repair of gaps in DNA is asymmetric in *Ustilago maydis* and can be explained by a migrating D-loop model. *Proc. Natl Acad. Sci. USA* **93**, 5419–5424 (1996).
- Hastings, P. J., Lupski, J. R., Rosenberg, S. M. & Ira, G. Mechanisms of change in gene copy number. *Nature Rev. Genet.* **10**, 551–564 (2009).
- Malkova, A. & Ira, G. Break-induced replication: functions and molecular mechanism. *Curr. Opin. Genet. Dev.* **23**, 271–279 (2013).

Acknowledgements We thank V. Zakian, K. Labib, W.-D. Heyer, J. Haber, C. Wittenberg, R. Johnson and L. Prakash for the gift of antibodies, strains or plasmids, and D. Camerini-Otero for providing DinG. We are grateful to J. Griffith and S. Wilcox for training in metal shadowing electron microscopy. This work was funded by grants from the US National Institutes of Health (GM080600 to G.I.; ES007061, GM057814, ES015632 to P.S.; GM084242 to A.M.; T32 GM07526-34 to M.A.W.), National Research Foundation of Korea (NRF-2012R1A1A1009917), Academia Sinica, National Taiwan University, and the National Science Council of Taiwan.

Author Contributions M.A.W. and Y.K. contributed equally to this work. M.A.W. performed genetic and physical analyses of BIR in *pif1 Δ* cells, *td-mcm4* and *td-psf2*; analysed conversion tracts and tested ssDNA formation during BIR; Y.K. carried out the reconstitution of the repair synthesis reaction and other biochemical experiments; Y.X. performed the electron microscopy analyses; W.-H.C. tested initial DNA synthesis by qPCR, analysed polymerases and Rad51 recruitment by ChIP and tested crossover frequencies; P.C. provided essential help in protein expression and purification; H.N. provided key reagents for the study; X.C. analysed Pif1 and RPA recruitment by ChIP; A.M. provided key reagents; R.M. tested the role of resolvases in BIR; G.I., P.S., M.A.W. and Y.K. designed the experiments, discussed the data and wrote the manuscript.

Author Information Reprints and permissions information is available at www.nature.com/reprints. The authors declare no competing financial interests. Readers are welcome to comment on the online version of the paper. Correspondence and requests for materials should be addressed to G.I. (gira@bcm.edu) or P.S. (patrick.sung@yale.edu).

METHODS

Media, strains and plasmids. The plasmids pVS31 (*pif1-m2*), pSH380 (*PIF1*) and pSH380 (*pif1(K264A)*) were from V. Zakian. The *pif1-m2* mutation was introduced into the genome as described previously¹³. For complementation tests, we amplified *PIF1* from pSH380 (*PIF1*) and introduced it into pRS316 to create pRS316-*PIF1*; *pif1(K264A)* was created by subcloning the 0.7-kb *AflIII*/*ClaI* fragment from pSH380 (*pif1(K264A)*) into pRS316 (*PIF1*).

For HO induction, cells (*GAL10::HO*) from an overnight culture in YEPD (1% yeast extract, 2% peptone, 2% dextrose) were transferred to YEP-*raffinose* (1% yeast extract, 2% peptone, 2% raffinose) and incubated overnight. Galactose was added to 2% when the cell density reached $\sim 1 \times 10^7$ cells ml⁻¹.

To study ectopic recombination, allelic BIR, or ectopic BIR we used tGI354, AM1003, or JRL346 strains, respectively, or their derivatives. tGI354 *hml::ADE1 MATA-inc hmr::ADE1 ade1 leu2-3,112 lys5 trp1::hisG ura3-52 ade3::GAL::HO arg5,6::HPH::MATa* (ref. 16) and its derivatives: *pif1-m2* (yWH42); *pif1::KANMX* (yWH1217); *pol32::KANMX* (yWH80); *pif1-m2 pol32::KANMX* (yWH198); *pif1::KANMX pol32::URA3* (yWH1226); *mph1::KANMX* (tGI772)^{16,17}; *pif1-m2 mph1::KANMX* (yWH1043); *pol32::TRP1 mph1::KANMX* (yWH221); *srs2::LEU2* (tGI383)¹⁶; *pif1-m2 srs2::LEU2* (yWH1072); *pol32::KANMX srs2::LEU2* (yWH1076); *pol2-16* (yWH1116); *pol3-14* (yWH1103); *rad30::KANMX* (yWH1222).

AM1003 *MATA-LEU2-tel/MATA-inc ade1 met13 ura3 leu2-3,112/leu2 thr4 lys5 hml::ADE1/hml::ADE3 hmr::HYG ade3::GAL-HO FS2::NAT/FS2* (ref. 12) and its derivatives: *trp1::hisG* (yWH422); *leu2::KANMX* (yWH271); *pho87::URA3* (yWH279); *pif1-m2* (yWH121); *pif1-m2+pRS316-PIF1* (yWH530); *pif1-m2+pRS316-pif1(K264A)* (yWH531); *pol32::KANMX* (yWH321); *pif1-m2 pol32::KANMX* (yWH304); *pif1::KANMX* (yWH465); *rad51::KANMX* (yWH615); *rad54::KANMX* (yWH616); *exo1::TRP1 sgs1::KANMX* (yWH612); *pif1-m2 tlc1::LEU2* (yWH308); *pif1-m2 est2::KANMX* (yWH328); *hcs1::KANMX* (yAP427); *pif1-m2 pho87::URA3* (yWH298); *POL1-13Myc-TRP1* (yWH1176); *pif1-m2 POL1-13Myc-TRP1* (yWH1177); *POL2-13Myc-TRP1* (yWH499); *pif1-m2 POL2-13Myc-TRP1* (yWH501); *POL3-13Myc-TRP1* (yWH634); *pif1-m2 POL3-13Myc-TRP1* (yWH1110); *RAD30-13Myc-TRP1* (yWH1179); *pif1-m2 RAD30-13Myc-TRP1* (yWH1178); *pif1-m2 MCM7-3HA-TRP1* (yWH1056); *pif1-m2 pif1-m1-4Myc-TRP1 pol32::KANMX* (yWH971); *pif1-m2 pif1-m1-4Myc-TRP1 rad52::KANMX* (yWH1003); *ura3::URA3 thr4::THR4* (yMW331); *pif1::KANMX* (yMW335); *MATA-LEU2::URA3-tel/MATA-inc* (yMW393); *CUP1::mcm4-td::KANMX* (yMW412); *CUP1::psf2-td::KANMX* (yMW467).

JRL346 *mata::HOCsDEL::hisG ura3DEL851 trp1DEL63 sup53DEL::leu2DEL::NATMX hmlDEL::hisG hmrDEL::ADE3 ade3::GAL10::HO can1,1-1446::HOCs::HPH::DEL AVT2 ykl215::LEU2::hisG::can1DEL1-289* (ref. 14); and its derivative, *pif1::KANMX* (yGI272).

Pulsed-field gel electrophoresis and analysis of DSB repair products. To analyse DSB repair kinetics and products in AM1003 derivative strains, chromosomal DNA plugs were prepared and separated as described⁴, followed by Southern blotting and hybridization with probes specific for either *ADE1*, *ADE3*, *MCH4* or *MAT* (ref. 4). Allelic BIR product formation was estimated as the per cent of the initial uncut chromosome III. Percentage of the chromosome III template remaining during repair was measured as the normalized intensity of the band corresponding to chromosome III in each time point after break induction multiplied by 100 and divided by the intensity of the band corresponding to chromosome III at time point '0'.

Chromatin immunoprecipitation. ChIP analyses of DNA polymerases, Rad51 and Pif1 were performed and quantified as described³¹. The anti-Myc (9E10) antibody was from Sigma (M4439). Anti-Rfa2 antibody was from W.-D. Heyer³² and anti-Rad51 antibody was from our laboratory stock^{31,33}. Experiments were done at least three separate times and the *t*-test was used to establish the statistical significance of the results. The primers used for qPCR were: MATX-F2 – 1 kb (5'-GG TAGGCGAGGACATTATCTATCA-3') and MATX-R3 – 1 kb (5'-GAAGAAT ACCAGTTTATCTCGCATTCAAATC-3'); 5 kb RHO-F1 (5'-ATTCATAACA ATGGCTCTAGGAGTGGCG-3'); 5 kb RHO-R1 (5'-CTTGGCGATATCGTGC TACAAATCAGTC-3'); 10 kb RHO-F1 (5'-TCTCTCCCTTCAGCAGCTGC TCAGAG-3'); 10 kb RHO-R1 (5'-GAAGAAACACATCCTCACACGCATA TTC-3'); 30 kb RHO-F1 (5'-CTCTCATGGTTCGGACTTAAACACCC-3'); 30 kb RHO-R1 (5'-AATTCGTTGCGCTTGTGAGGACATCGG-3'); 67 kb RHO-F1 (5'-GCTGCACTTGCTAATAATCTG-3') and 67 kb RHO-R1 (5'-CGGGAGGA GTGGAAGCC-3'). These primer pairs are for sites –1, +5, +10, +30 and +67 kb from the break.

Analysis of non-homologous DNA tail removal. To determine removal of the non-homologous Ya tail as a measure of successful DNA strand invasion, we performed real-time PCR using genomic DNA and primers specific for the Ya tail (642 bp): MATX-F1 (5'-GTTGTTACACTCTCTGGTAACCTAGGTAA-3') and MATY-R2 (5'-CAATCTCAGTACCTAGAATGTTAAACAGAG-3') designated as P1 and P2 in Extended Data Fig. 4b.

Initial DNA synthesis analysis. To measure initial DNA synthesis in BIR, 2 ng of genomic DNA from different times after DSB induction was amplified by PCR

with the primers: P1-BIR *URA3* (5'-ACCCGGGAATCTCGGTCGTAATGA-3') and P2-Z1 distal (P1 and P2 in Fig. 1d; 5'-ATCCGTCACCGTACTTCAGC-3'). As control, the *CHA1* gene on chromosome III was amplified.

Determination of DSB repair by BIR and other mechanisms. To quantify allelic BIR, we used a disomic strain with an extra, truncated copy of chromosome III wherein the arm 100 kb distal from *MATa* is replaced with *LEU2* followed by telomeric repeats¹². In this assay, the chromosomes participating in repair are marked by either *LEU2*, *ADE1* or *ADE3* which allows determination of the repair pathway by growth on selective media (Fig. 1a)¹². To avoid any contribution of Ty transposon repeats to repair, the nearest Ty1 repeats to the DSB were replaced with a NAT cassette. BIR leads to the loss of the *LEU2* marker. When repair fails, *ADE1*, *NAT* and *LEU2* markers are lost, and the colonies appear red due to an *Ade1* deficiency. When cells repair the DSB by gene conversion using the short homology on the right side of the break all the markers are retained¹². In rare cases in wild-type cells, part of the homologous template chromosome is lost due to a half-crossover that eliminates the *ADE3* marker, and colonies are *Ade*⁻ and appear white.

The BIR assay was performed by plating on YEP-galactose medium and replica plating on Leu⁻, *Ade*⁻ dropout and NAT selective media. For each strain, at least 1,000 colonies were scored. The frequencies of BIR, half crossovers, gene conversion and chromosome loss were estimated based on the percentage of colonies carrying markers specific for these repair outcomes, as described above (Fig. 1a) and reported previously¹². Pedigree analyses and individual product size analyses by CHEF confirmed repair by BIR in wild-type cells¹². Because the repair by BIR occurs in G2/M cells two copies of each chromosome are present. Owing to random segregation of chromosomes, half of the half crossovers (the major product in *pif1Δ* cells) segregate with an intact copy of the full-length chromosome III, and are genetically and structurally indistinguishable from BIR as confirmed by pedigree analysis¹². Therefore, the number of *Ade*⁻ white colonies scored on selective media as half crossovers represent only half of these events. To correct for this, the number of half crossovers (*Ade*⁻, white colonies) was multiplied by two, and consequently the number of BIR events was adjusted by subtracting the number of *Ade*⁻, white colonies. Second, upon analysis of the repair products by CHEF from *Ade*⁺ colonies that have lost the distal NAT marker (Extended Data Fig. 2d), we found that about half of them carried a genomic rearrangement, whereas the other half of the products corresponded by size to BIR, where strand invasion occurred proximal to the NAT marker. Therefore, half of the NAT^S colonies were scored as gross chromosomal rearrangements and the other half as BIR events. The number of BIR events in *pif1Δ* mutants were still probably overestimated because about one-third of the *Ade*⁺ NAT^R Leu⁻ colonies did not result from allelic BIR, but from a half crossover event associated with a stabilization of the part of template chromosome carrying the *ADE3* marker (Extended Data Fig. 2b).

The percentage of cells that repair a DSB by ectopic BIR¹⁴ (BIR between two short homologous sequences located on heterologous chromosomes) was calculated as the number of canavanine-sensitive (*Can*^s) colonies (Extended Data Fig. 3a) formed on YEP-Gal plates divided by the number of all colonies formed on YEPD plates, multiplied by 100. In this BIR assay, recombination between two truncated copies of the *CAN1* gene located on chromosome V and XI leads to the formation of an intact *CAN1* gene resulting in canavanine sensitivity. In *pif1Δ* cells the number of BIR events (~1%) is probably overestimated because over half of the cells that form the full-length *CAN1* gene during DSB repair do not complete repair (Extended Data Fig. 3d). Additionally, some of the products that appear to be BIR can correspond to half crossovers that in this assay (haploid cells) cannot be scored (half-crossovers that segregate with an intact template chromatid cannot be distinguished from BIR and the half-crossovers that lose a large part of the template chromosome are inviable).

Measurements of crossover frequency, DSB repair and viability in ectopic recombination assay. We determined the frequency of crossovers, viability and efficiency of the DSB repair as previously described^{16,17}.

Measurement of ssDNA formation by qPCR. The ssDNA amount was measured as previously described³⁴ 10 and 41 kb away from the DSB end and as a control on the chromosome V not participating in recombination. The primers used in this assay were: oMW 1082 10832bp-F (5'-CACTAAGTCTTGGACAG GT-3'); oMW 1083 10832bp-R (5'-AATACTGGTCATGAAGCCAC-3'); oMW 1116 ChrV 41701bp-F (5'-GGCAGCCACCTTATGGTGAGG-3'); oMW 1117 ChrV 41701bp-R (5'-GGCGCAAGGGCCAAAGACAAGG-3'); oMW 1120 40890-F (5'-CCTTTCACCGTCTATGGGCC-3'); oMW 1121 40890-R (5'-CAATTCCTC ATTCCATCGG-3').

Measurement of conversion tracts. We used an assay in which an HO break is generated within *LEU2* and is repaired by allelic recombination with *leu2-R*. In this assay, Leu⁺ colonies stem from short conversion tracts and Leu⁻ colonies from longer conversion tracts³⁵. Cells were plated on YEP-Gal plates and then replica plated on medium lacking leucine.

Preparation of proteins. Pif1 and pif1 (K264A): *Pif1* cDNA encoding the nuclear form of Pif1 (amino acids 40–859) was inserted in the pRSF-Duet-1 vector (Novagen) to add an amino-terminal 6×His tag. The K264A mutation was introduced by QuikChange mutagenesis (Agilent Technologies). Pif1 and pif1 (K264A) were expressed in *E. coli* Rosetta cells (Novagen), with induction by 0.1 mM isopropyl-1-thio-β-D-galactopyranoside (IPTG) for 18 h at 16 °C. The cell paste from a 10-l culture was resuspended and sonicated in 100 ml buffer A (20 mM K_2HPO_4 , pH 7.5, 0.5 mM EDTA, 10% glycerol, 0.01% Igepal, 2 mM DTT) containing 100 mM KCl and protease inhibitors (aprotinin, chymostatin, leupeptin and pepstatin A at 5 $\mu\text{g ml}^{-1}$ each, 1 mM phenylmethylsulphonyl fluoride). The lysate was clarified by ultracentrifugation and loaded onto a Q sepharose column (8 ml). The flow-through fraction was applied onto a SP-sepharose column (8 ml) and fractionated with a 90-ml gradient of 150–660 mM KCl in buffer A. Fractions containing Pif1 were incubated with 2 ml Ni-NTA-agarose beads (Qiagen) and 10 mM imidazole for 2 h. After washing three times with 10 ml buffer A containing 1 M KCl, 1 mM ATP, 8 mM $MgCl_2$ and 15 mM imidazole, the bound proteins were eluted with 20 ml buffer A containing 150 mM KCl and 200 mM imidazole. The protein pool was fractionated in Mono S (1 ml) with a 40-ml gradient of 150–600 mM KCl in buffer A. Pif1 was concentrated in an Ultracel-30K concentrator (Amicon) and stored at –80 °C.

Polδ and Polδ*: Polδ (Flag–Pol3, GST–Pol31 and Pol32) and Polδ* (Flag–Pol3, GST–Pol31) were expressed in *S. cerevisiae* strain YRP654³⁶. Cells from a 10-l culture were disrupted using a coffee grinder and resuspended in 100 ml buffer B (50 mM Tris HCl, pH 7.5, 10% sucrose, 1 mM EDTA, 175 mM $(NH_4)_2SO_4$, 200 mM NaCl, 1 mM DTT, 0.01% Igepal, protease inhibitors as above). After ultracentrifugation, the lysate was treated with 0.277 g ml^{-1} of $(NH_4)_2SO_4$. The precipitate was pelleted by centrifugation and dissolved in 100 ml buffer C (25 mM Tris HCl, pH 7.5, 0.5 mM EDTA, 10% glycerol, 0.01% Igepal, 10 mM 2-mercaptoethanol and 200 mM KCl) and dialysed against the same buffer. The protein was purified by affinity chromatography in glutathione Sepharose (GE Healthcare; 5-ml) and anti-Flag M2 resin (Sigma; 2 ml). Protein was concentrated and stored at –80 °C.

RFC: RFC (GST–RFC1, RFC2, RFC3, RFC4, RFC5) was expressed in *S. cerevisiae* strain YRP654 using pBJ1476 (2 μ , *GAL-PGK-GST-RFC1/RFC4/RFC5*, *LEU-2d*) and pBJ1469 (2 μ , *GAL-PGK-RFC2/RFC3*, *TRP1*) and purified from clarified cell lysate by $(NH_4)_2SO_4$ precipitation and affinity purification using glutathione sepharose as above.

Pol32: MBP–Pol32 (with MBP cleavable with TEV protease) was expressed in *E. coli* Rosetta cells harbouring pMAL-POL32 with induction by 1 mM IPTG for 4 h at 37 °C. The cell paste from a 500-ml culture was resuspended in 50 ml buffer D (50 mM Tris-HCl, pH 7.5, 10% sucrose, 1 mM EDTA, 0.01% Igepal, 1 mM 2-mercaptoethanol, 150 mM KCl and protease inhibitors as above), sonicated, and clarified by ultracentrifugation. Nucleic acids were removed by adding 700 μl 10% polyethyleneimine (J. T. Baker) and centrifugation. MBP–Pol32 was purified by affinity chromatography with 6 ml amylose resin (BioLabs) and fractionation in 1 ml Source S with a 30-ml gradient of 100–500 mM KCl in buffer E (25 mM Tris-HCl, pH 7.5, 10% glycerol, 0.5 mM EDTA, 0.01% Igepal, 1 mM 2-mercaptoethanol), and in a 1 ml macrohydroxyapatite using a 30-ml gradient of 0–300 mM KH_2PO_4 in buffer E. MBP–Pol32 was concentrated and stored at –80 °C.

Rrm3: DNA that harbours *RRM3-Flag* was cloned into the pMAL-TEV vector (BioLabs) to add an N-terminal MBP tag. Expression was in *E. coli* Rosetta cells with induction by 0.1 mM IPTG for 24 h at 12 °C. The cell paste from a 3.3-l culture was resuspended and sonicated in 40 ml buffer F (25 mM Tris-HCl, pH 7.5, 0.5 mM EDTA, 10% glycerol, 0.01% NP-40, 1 mM DTT, 500 mM KCl, 0.2 mM ATP, 5 mM $MgCl_2$ and protease inhibitors as above). The lysate was clarified by ultracentrifugation and treated with 0.277 g ml^{-1} of $(NH_4)_2SO_4$. The protein precipitate was pelleted by centrifugation and dissolved in 30 ml buffer F. MBP–Rrm3 was purified by two-step affinity chromatography with amylose resin (2 ml) and anti-Flag M2 resin (0.7 ml). Rrm3 was concentrated and stored at –80 °C.

Rad51, Rad54, RPA, PCNA and Mph1 were purified as described elsewhere^{17,23,37}. DinG was from D. Camerini-Otero.

D-loop extension. The ³²P-labelled 90-mer oligonucleotide (2.4 μM nucleotides), homologous to positions 1932–2021 of pBluescript DNA³⁸, was incubated with Rad51 (800 nM) in buffer G (35 mM Tris-HCl, pH 7.5, 1 mM DTT, 7 mM $MgCl_2$) containing 100 ng μl^{-1} BSA, 30 mM KCl, 2 mM ATP, an ATP-regenerating system (20 mM creatine phosphate, 30 ng μl^{-1} creatine kinase), and 100 μM each of the four dNTPs for 10 min at 37 °C. This was followed by a 5-min incubation with RPA (400 nM) at 30 °C, a 2-min incubation with Rad54 (200 nM) at 23 °C, and a 2-min incubation with pBluescript DNA (37 μM base pairs) at 30 °C. For D-loop extension, the reaction was mixed with PCNA (200 nM) and RFC (200 nM) and incubated on ice for 2 min. Then, Polδ (100 nM) and Pif1 (13–40 nM) were added to the reaction, followed by an incubation at 15 °C. Reaction mixtures were deproteinized with 0.5% SDS and 0.5 mg ml^{-1} proteinase K for 10 min at 37 °C before

being resolved in a native gel (0.8% agarose) in TAE buffer (40 mM Tris-acetate, pH 7.5, 0.5 mM EDTA), or in a denaturing gel (4% polyacrylamide, 7 M urea) in TBE buffer (90 mM Tris-HCl, pH 8.3, 90 mM boric acid, 2 mM EDTA), or in a 0.9% agarose gel in 50 mM NaOH, 1 mM EDTA (Extended Data Fig. 5d). Dried gels were analysed in a phosphorimager (BioRad).

For quantification of DNA synthesis in Fig. 3b, D-loop extension was carried out as above, except that the invading strand was unlabelled and the reaction was supplemented with [α -³²P]dCTP (80 nCi μl^{-1}). The reaction products were resolved in a native gel and analysed.

DNA extension from deproteinized D-loop. The D-loop reaction (250 μl) was performed as above with the ³²P-labelled 90-mer oligonucleotide. The reaction was deproteinized with SDS and proteinase K as above. After an extraction with phenol-chloroform-isoamyl alcohol (25:24:1), the buffer was exchanged with buffer H (35 mM Tris-HCl pH 7.5, 1 mM DTT, 9.3 mM $MgCl_2$, and 30 mM KCl) using a Zebra Spin-desalting Column (Thermo Scientific). DNA synthesis reaction was carried out with the deproteinized D-loop (equivalent to 1.2 μM nucleotides of the ³²P-labelled 90-mer oligonucleotide), with 2 mM ATP, the ATP-regenerating system, 100 ng μl^{-1} BSA and 100 μM each dNTPs, 200 nM RPA, 100 nM PCNA, 100 nM RFC, 50 nM Polδ, and 8, 16, 24 nM Pif1 with an 8-min incubation.

Two-dimensional gel electrophoresis. Deproteinized reaction mixtures were run in a 0.8% agarose gel in TAE buffer. Then, lanes containing the radiolabelled species were excised and placed on top of a 0.9% agarose gel. Electrophoresis in the second dimension was done in 50 mM NaOH, 1 mM EDTA. A gel strip from the first dimension is shown above the two-dimensional gel.

Pull-down assay. Pol32 and Polδ*: MBP–Pol32 (5 μg) or TEV-protease treated MBP–Pol32 was incubated with Polδ* (5 μg) in 20 μl buffer I (25 mM Tris-HCl, pH 7.5, 10% glycerol, 1 mM DTT, 0.01% Igepal, 150 mM KCl) for 30 min on ice, then mixed with 10 μl glutathione sepharose for 1 h at 4 °C. The resin was washed four times with 100 μl buffer I, then eluted with 20 μl 2% SDS. The supernatant containing unbound proteins, final wash and SDS eluate, 10 μl each, were analysed by SDS–PAGE and Coomassie blue staining.

Pif1 and PCNA: 6×His–Pif1 (3 μg) was incubated with PCNA (3 μg) in 30 μl buffer J (25 mM Tris-HCl, pH 7.5, 0.01% Igepal, 1 mM 2-mercaptoethanol, 100 mM KCl) containing 20 mM imidazole for 30 min at 4 °C, then mixed with 6 μl Ni-NTA agarose for 1 h at 4 °C. The resin was washed three times with 50 μl buffer J, then eluted with 20 μl 2% SDS and analysed as above.

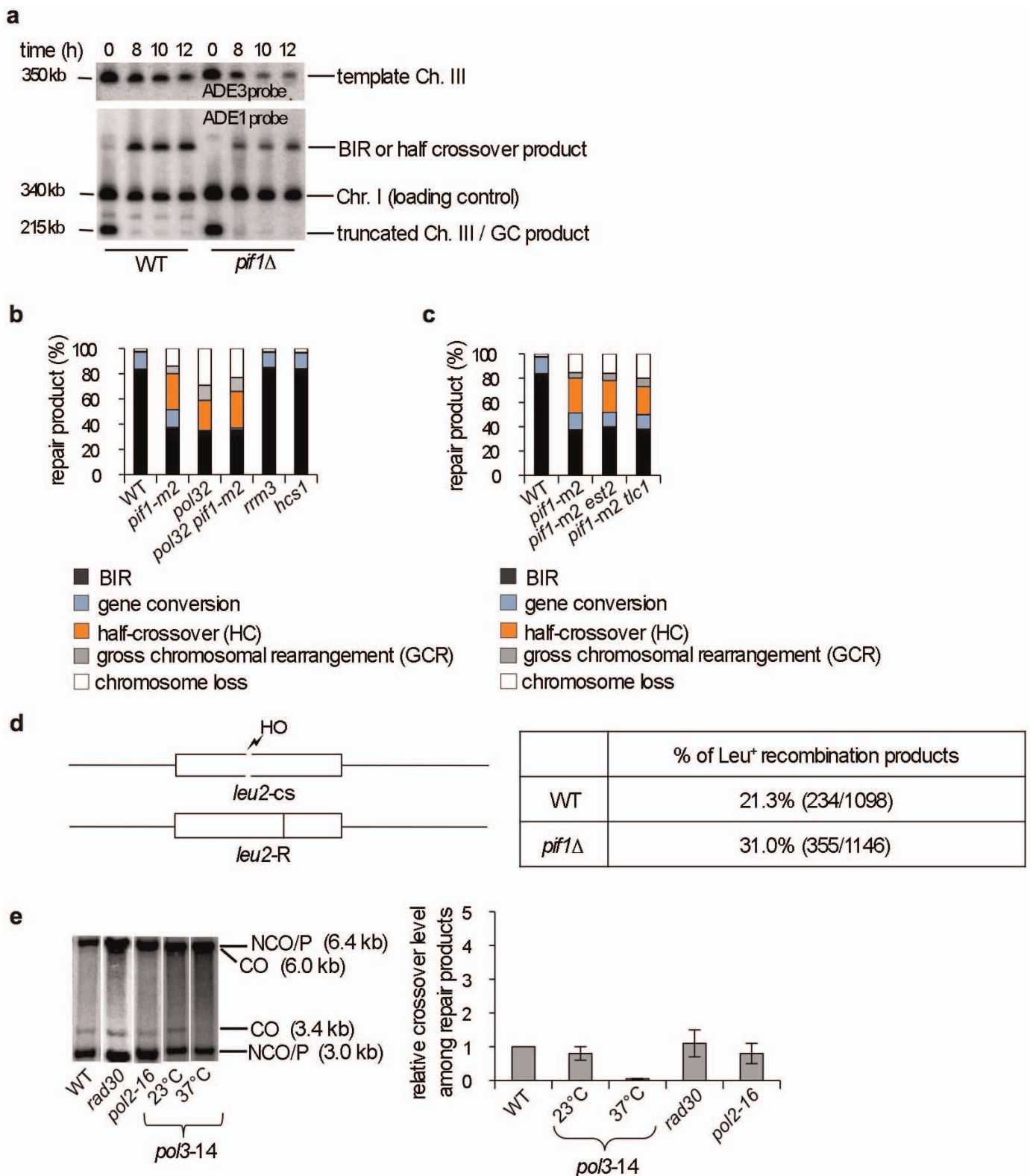
Pif1 and Polδ: Polδ (9 μg) with GST–Pol31 was incubated with Pif1 (3 μg) or PCNA (3 μg) in 30 μl buffer J for 30 min at 4 °C then mixed with 12 μl glutathione sepharose for 1 h at 4 °C. The resin was washed three times with 40 μl buffer J, then eluted with 25 μl 2% SDS and analysed as above.

Restriction digests of extended D-loops. Reactions (20 μl) were extracted with phenol-chloroform-isoamyl alcohol and DNA was precipitated with ethanol, which was dissolved in 10 μl buffer K (20 mM Tris-acetate, pH 7.9, 10 mM Mg-acetate, 50 mM K-acetate, 1 mM DTT, 100 ng μl^{-1} BSA) and incubated with AhdI (0.25 U μl^{-1}) or XmnI (1 U μl^{-1}) at 37 °C for 10 min. SDS was added to 0.5% and the DNA species were separated on a denaturing gel.

Electron microscopy. DNA from 40 μl of reactions at a 16-min time point was dissolved in 20 μl buffer L (25 mM HEPES, pH 7.5, 10 mM $MgCl_2$ and 50 mM KCl). T4 gp32 protein (NEB) was added to 1.5 μM , and after a 10-min incubation at 25 °C, crosslinking of protein to DNA was carried out using glutaraldehyde (0.6%) at 25 °C for 5 min. DNA was purified in 2-ml 6% agarose beads (Agarose Bead Technologies) equilibrated with TE buffer (10 mM Tris-HCl, pH 7.5 and 1 mM EDTA). The samples were adsorbed onto glow-charged thin carbon support in TE buffer containing 2.5 mM spermidine, dehydrated through a series of water/ethanol washes, and air dried²⁷. The electron microscopy grids were shadowed by rotary tungsten coating at 1×10^{-7} torr and examined in an FEI Tecnai 12 TEM at 40 kV. Images were captured using an Ultrascan400 scan CCD camera (Gatan Inc.). Adobe Photoshop was used to invert images.

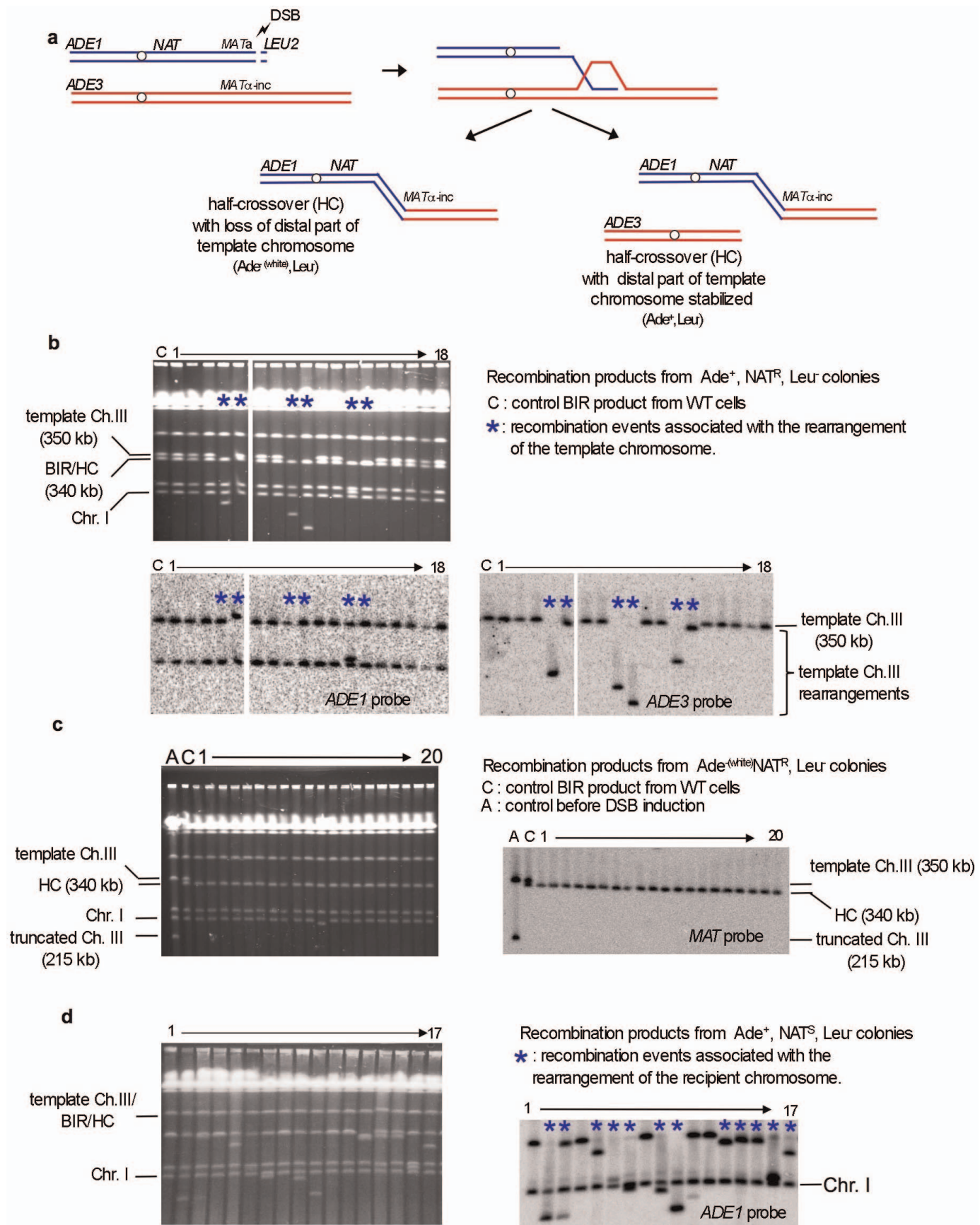
- Sugawara, N., Wang, X. & Haber, J. E. *In vivo* roles of Rad52, Rad54, and Rad55 proteins in Rad51-mediated recombination. *Mol. Cell* **12**, 209–219 (2003).
- Janke, R. *et al.* A truncated DNA-damage-signaling response is activated after DS formation in the G1 phase of *Saccharomyces cerevisiae*. *Nucleic Acids Res.* **38**, 2302–2313 (2010).
- Busygina, V. *et al.* Hed1 regulates Rad51-mediated recombination via a novel mechanism. *Genes Dev.* **22**, 786–795 (2008).
- Zierhut, C. & Diffley, J. F. Break dosage, cell cycle stage and DNA replication influence DNA double strand break response. *EMBO J.* **27**, 1875–1885 (2008).
- Malkova, A., Klein, F., Leung, W. Y. & Haber, J. E. HO endonuclease-induced recombination in yeast meiosis resembles Spo11-induced events. *Proc. Natl Acad. Sci. USA* **97**, 14500–14505 (2000).
- Acharya, N., Klassen, R., Johnson, R. E., Prakash, L. & Prakash, S. PCNA binding domains in all three subunits of yeast DNA polymerase delta modulate its function in DNA replication. *Proc. Natl Acad. Sci. USA* **108**, 17927–17932 (2011).

37. Van Komen, S., Macris, M., Sehorn, M. G. & Sung, P. Purification and assays of *Saccharomyces cerevisiae* homologous recombination proteins. *Methods Enzymol.* **408**, 445–463 (2006).
38. Raschle, M., Van Komen, S., Chi, P., Ellenberger, T. & Sung, P. Multiple interactions with the Rad51 recombinase govern the homologous recombination function of Rad54. *J. Biol. Chem.* **279**, 51973–51980 (2004).



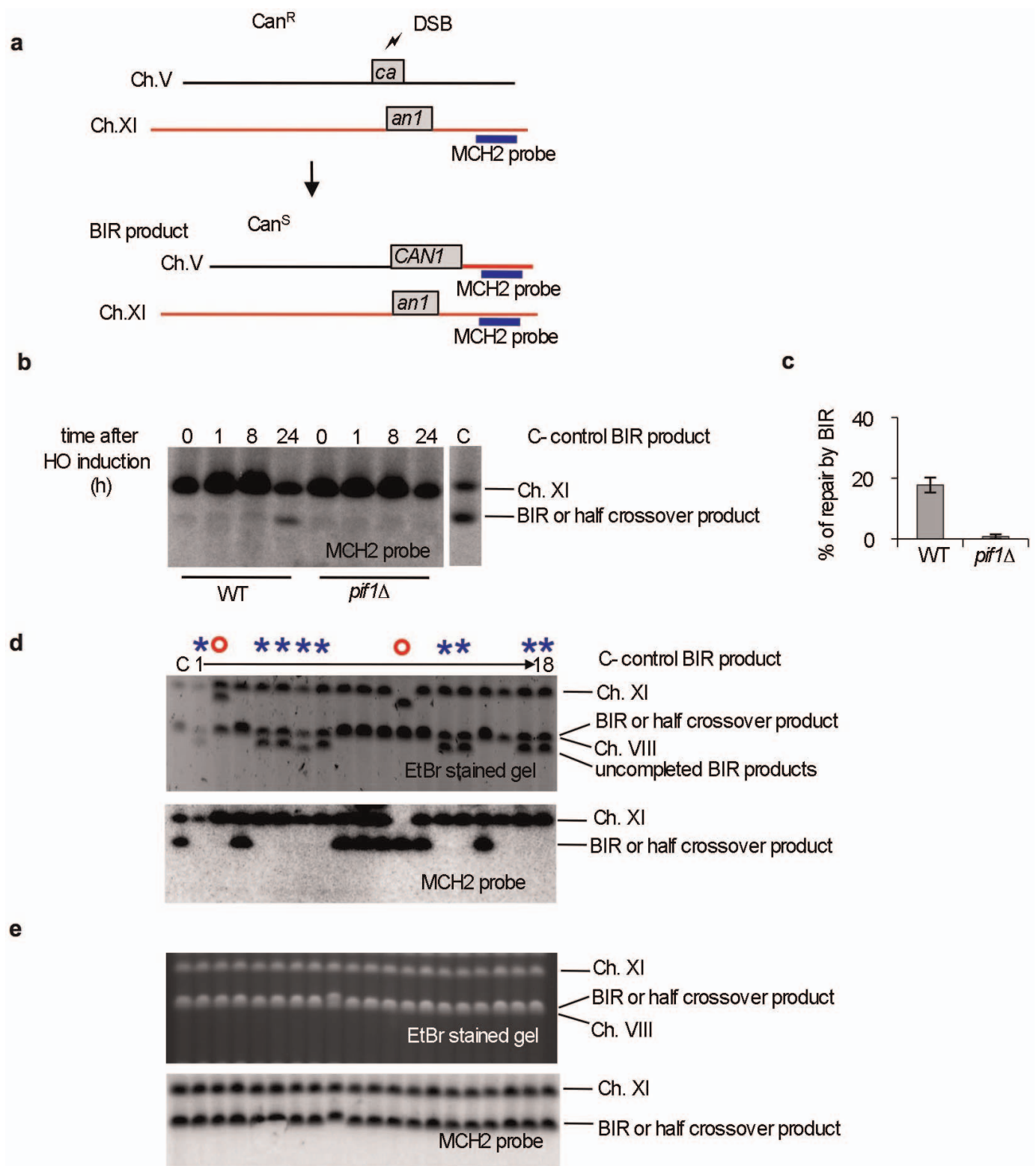
Extended Data Figure 1 | Analysis of BIR and conversion tracts in *pif1Δ* mutants and crossover frequency in polymerases mutants. **a**, Southern blot analysis of BIR product formation and template chromosome maintenance. Chromosomes were separated by pulsed-field gel electrophoresis and a DNA probe specific for either *ADE1* or *ADE3* was used. Quantification is shown in Fig. 1c. **b**, **c**, Analysis of DSB repair outcomes in the BIR assay of the indicated mutants. **d**, Schematic of allelic recombination between the *leu2* alleles (left). Longer conversion tracts associated with conversion of 'R' leads to formation of

Leu⁺ recombinants, whereas shorter conversion tracts lead to formation of *Leu*⁺ recombinants. Quantification of gene conversion events with shorter conversion tracts (*Leu*⁺) in wild-type (WT) and *pif1Δ* cells is shown. The difference between wild-type and *pif1Δ* cells is statistically significant, $P < 0.0001$. **e**, Southern blot analysis of gene conversion with and without crossing over in the indicated strains using the ectopic recombination assay shown in Fig. 2a. Quantification of crossover product in the indicated mutants compared to wild type that is set to 1. Plotted are the mean values \pm s.d. $n = 3$.



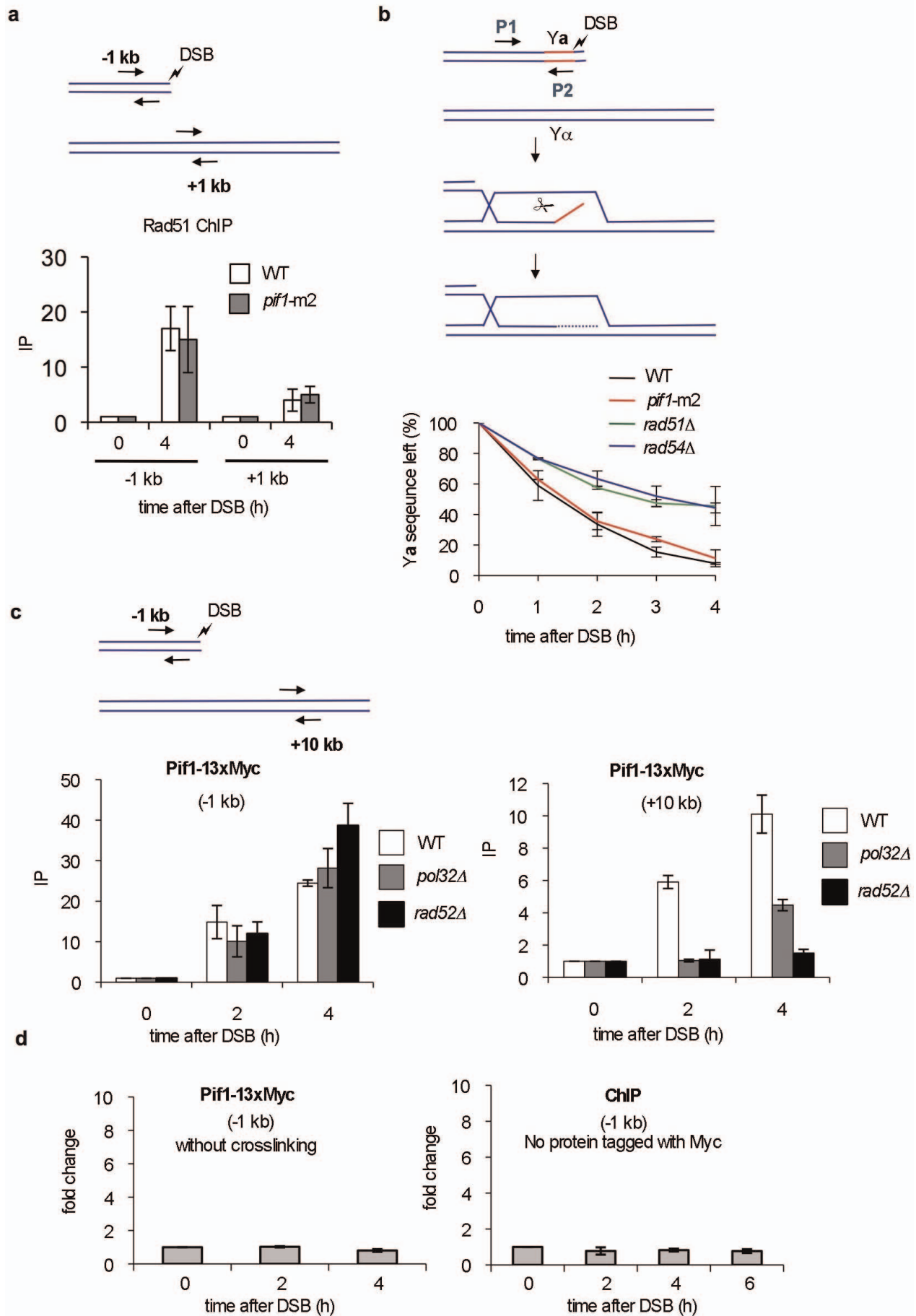
Extended Data Figure 2 | Analysis of recombination products in Pif1-deficient cells. **a**, Illustration of the half-crossover pathway where the part of the template chromosome distal to the initial invasion site is fused to the broken chromosome, with the remainder of the template chromosome either becoming stabilized (examples shown in Fig. 2b) or lost (as shown in Fig. 2c).

b, Analysis of recombination products from Ade⁺ NAT^R Leu⁻ colonies. Examples are shown where rearrangements of the template chromosome are indicated by an asterisk. **c**, Analysis of half-crossover recombination products from Ade⁻ NAT^R Leu⁻ colonies. **d**, Analysis of rare NAT^S Ade⁺ colonies.



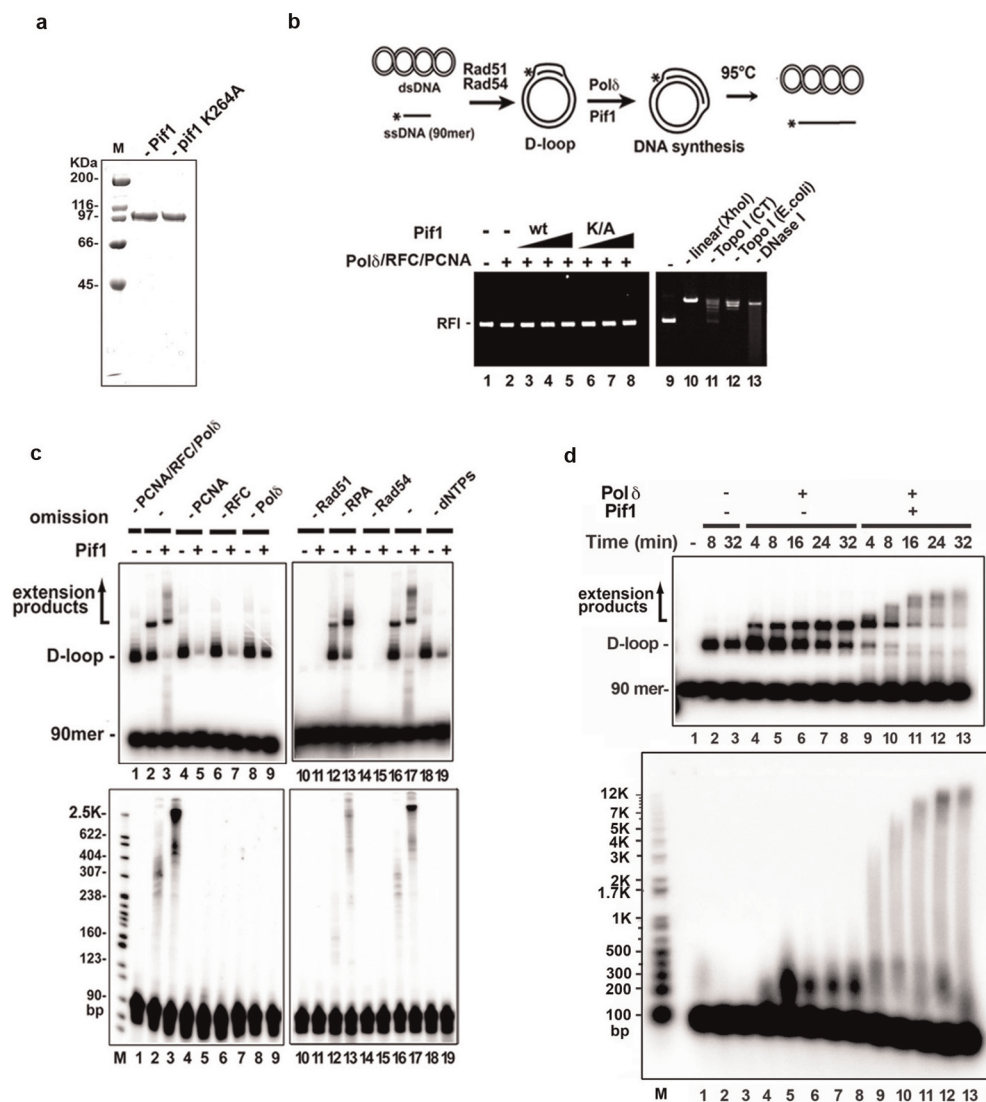
Extended Data Figure 3 | Role of Pif1 in ectopic BIR. **a**, Schematic of the ectopic BIR assay. **b**, Southern blot analysis of ectopic BIR kinetics in wild-type and *pif1Δ* cells. A probe specific for the *MCH2* gene located at the end of chromosome XI was used in the analysis. **c**, Quantification of ectopic BIR repair (Can^S colonies) in wild-type and *pif1Δ* cells. Plotted are the mean values \pm s.d.

$n = 3$. **d**, **e**, CHEF analysis of rare products from canavanine-sensitive colonies in *pif1Δ* (**d**) and wild-type cells (**e**). Examples where synthesis is initiated but not finished are indicated by an asterisk. In these cases, a functional *CAN1* gene is formed but synthesis is abandoned resulting in shorter products. Red circles indicate major rearrangement of chromosome V or template chromosome XI.



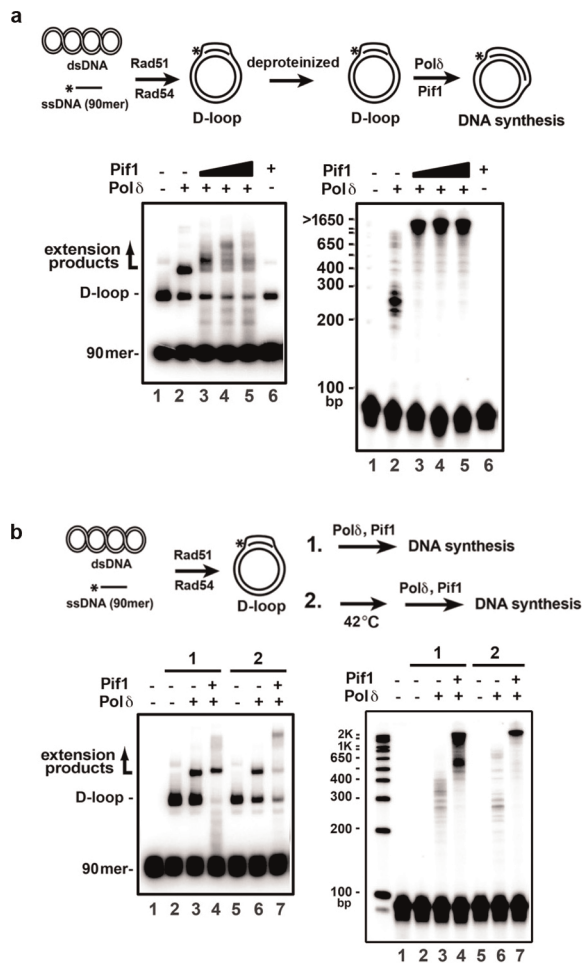
Extended Data Figure 4 | Analysis of Pif1's role in the initial steps of BIR and of Pif1 recruitment at the DSB and template. **a, b**, Analysis of initial strand invasion in wild-type and *pif1* Δ cells. **a**, Enrichment of Rad51 at the DSB site and template by ChIP analysis. **b**, Kinetics of removal of the non-homologous Y α tail by qPCR analysis in wild-type and *pif1-m2* strains compared to the control strains *rad51* Δ and *rad54* Δ that are defective in strand

invasion. **c**, Enrichment of Pif1 at the DSB and template by ChIP analysis in wild-type, *pol32* and *rad52* cells. The regions amplified by qPCR are indicated. **d**, Control ChIP experiments in the *PIF1-13* \times *Myc* strain where crosslinking was omitted and in a strain where the Myc tag was absent. **a–d**, plotted are the mean values \pm s.d. $n = 3$.

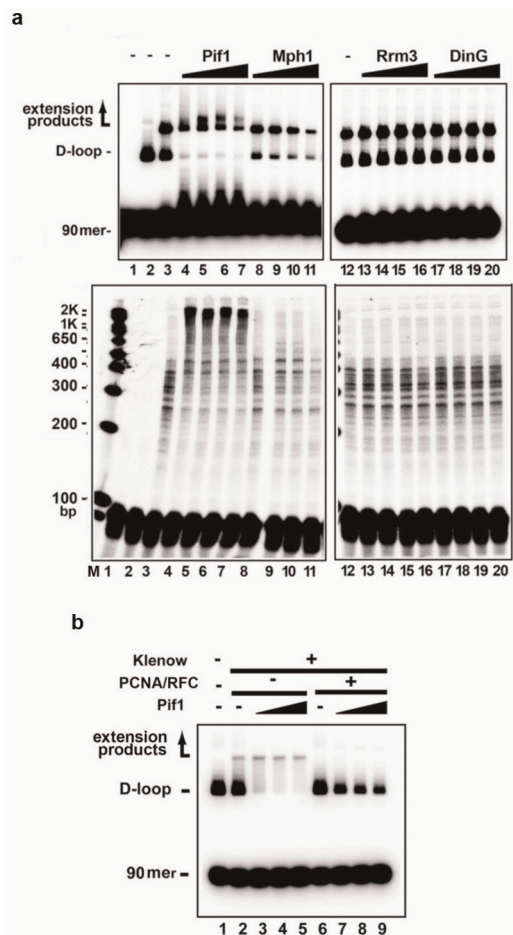


Extended Data Figure 5 | Quality analyses of proteins, protein requirements for DNA extension, effect on Pif1 on D-loop stability, and time-course analysis of DNA extension. **a**, Purified Pif1 and pif1(K264A) were analysed by SDS-PAGE and staining with Coomassie blue. **b**, The plasmid DNA in all the lanes was pBluescript SK replicative form I (RFI). DNA synthesis reactions were performed with 13, 27 and 40 nM Pif1 and the reaction mixtures (lanes 1–8) from the 8-min time point were incubated at 95 °C for 2 min to disrupt the D-loop, followed by native gel electrophoresis and staining with ethidium bromide. Various other DNA forms (lane 9, plasmid DNA alone; lane 10, plasmid DNA linearized with XhoI; lane 11, plasmid DNA relaxed by

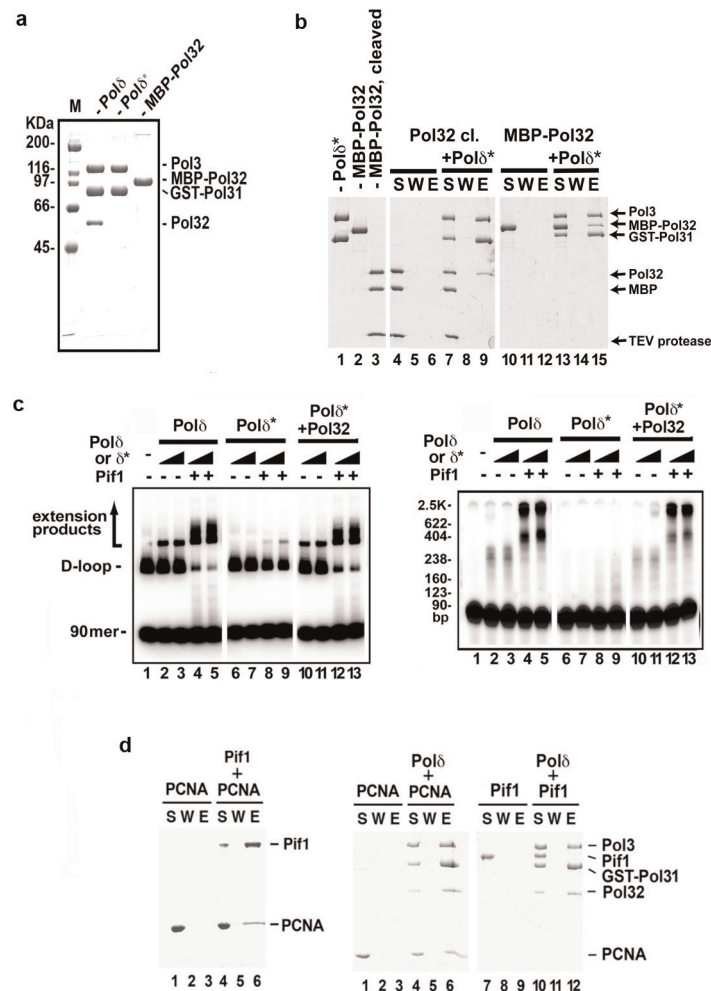
calf thymus topoisomerase I; lane 12, plasmid DNA relaxed by *E. coli* topoisomerase I; lane 13, plasmid DNA digested with DNase I) are shown. **c**, DNA synthesis reactions by Pol δ in conjunction with Pif1 (40 nM Pif1 and 8-min incubation) with the omission of one or more of the protein factors or dNTPs, as indicated. The reaction products were analysed in a native gel (top) or denaturing gel (bottom). Note that a substantial portion of the D-loop was dissociated by Pif1 in the absence of PCNA, RFC, Pol δ , or dNTPs (lanes 5, 7, 9 and 19). **d**, Time course of DNA synthesis by Pol δ in conjunction with Pif1 (40 nM Pif1). The reaction products were analysed in a native gel (top) or a denaturing gel (bottom).



Extended Data Figure 6 | Effect of Rad51 and/or Rad54 removal on DNA extension. **a**, DNA synthesis from a deproteinized D-loop by Polδ in conjunction with Pif1 (8, 16 and 24 nM) was examined. Pif1 was at 24 nM in lane 6. The reaction products were analysed in a native gel (left) or denaturing gel (right). **b**, After the D-loop reaction had proceeded for 2 min, Rad54, which is highly heat labile¹⁹, was inactivated by incubation at 42 °C for 20 min. DNA extension reaction and analysis were then performed by adding RPA, RFC, PCNA, Polδ and Pif1 (40 nM Pif1 and 8-min incubation). The reaction products were analysed in a native gel (left) or denaturing gel (right). The inactivation of Rad54 was verified by examining the ATPase activity of Rad54, which decreased by ~95% compared to the unheated control (data not shown).

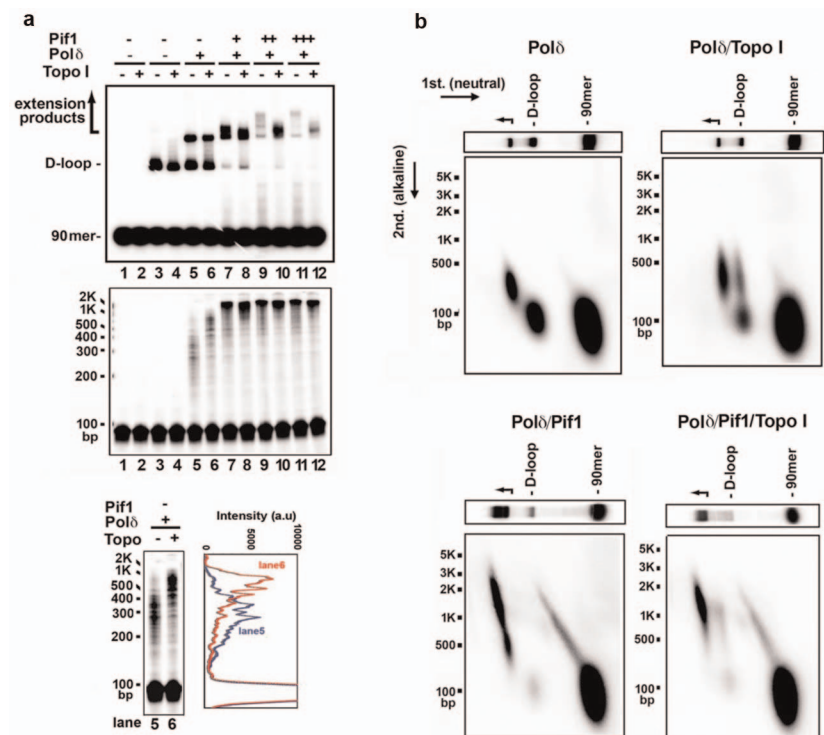


Extended Data Figure 7 | Specificity of Pol δ -Pif1-mediated DNA extension. **a**, DNA synthesis reactions were conducted with Pol δ and Pif1, Mph1, Rrm3, or DinG (13, 27, 40, 120 nM). The reaction products from the 8-min time point were resolved in a native (top) or denaturing gel (bottom) (lane 1, no protein control; lane 2, D-loop formed by Rad51–Rad54; lanes 3–20, D-loop extended with Pol δ and the indicated helicase). **b**, *E. coli* DNA polymerase I Klenow fragment (100 nM, from NEB) was tested for DNA extension with Pif1 (13, 27, 40 nM) with or without PCNA (200 nM) and RFC (200 nM). The reaction products from the 8-min time point were analysed in a native gel.



Extended Data Figure 8 | Requirement for the Polδ subunit Pol32 in DNA extension, and interaction of Pif1 with PCNA. **a**, Purified Polδ (Flag-Pol3, GST-Pol31, Pol32), Polδ* (Flag-Pol3, GST-Pol31) and MBP-Pol32 were analysed by SDS-PAGE and staining with Coomassie blue. **b**, Pull-down assay to examine Pol32-Polδ* interaction. **c**, DNA synthesis was performed with Polδ or Polδ* (20 or 40 nM) with Pif1 (40 nM). In lanes 10–13, Polδ* and Pol32

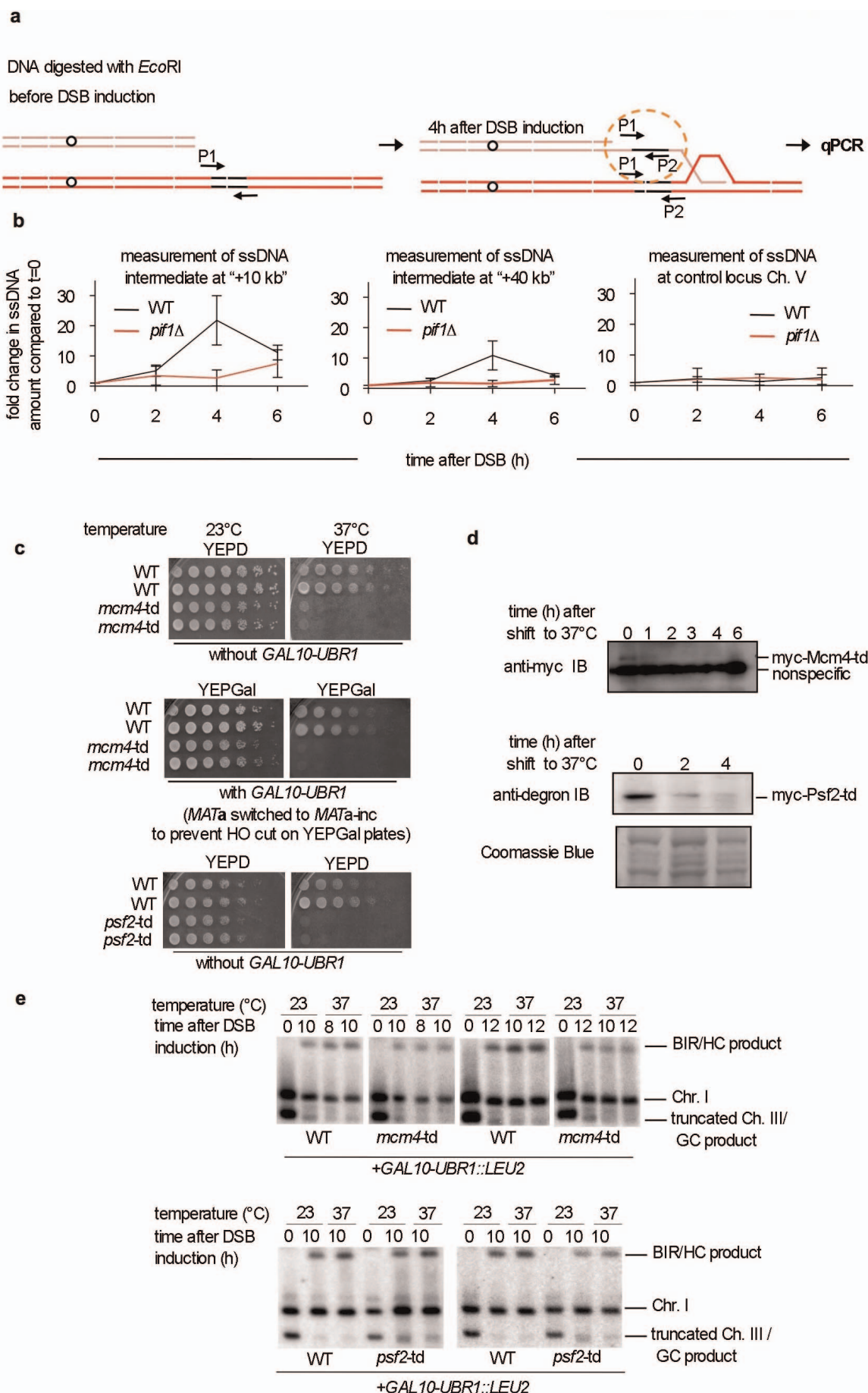
(125 nM) were pre-incubated on ice for 10 min before use. The reaction products from the 8-min time point were resolved in a native gel (left) or denaturing gel (right). **d**, Pull-down reactions of 6×His-Pif1 and PCNA (left), Polδ (Flag-Pol3, GST-Pol31, Pol32) and PCNA, Polδ and Pif1 (right). E, SDS eluate; S, supernatant; W, wash.



Extended Data Figure 9 | Effect of topoisomerase I in DNA extension.

a, DNA synthesis products, initiated by Polδ for 4 min, and then continued with Pif1 (13, 27, 40 nM) with and without calf thymus topoisomerase I ($0.4 \text{ U } \mu\text{l}^{-1}$) for 8 min. The reaction mixtures were resolved in a native gel (top) or denaturing gel (middle). Lanes 1 and 2 contained DNA substrates only and

lanes 3–12 contained D-loop made by Rad51–Rad54. An overexposed image and the scan of lanes 5 and 6 to highlight the effect of topoisomerase when Pif1 was absent are shown (bottom). **b**, Two-dimensional gel analysis of the extension products. The reaction products, prepared as in lanes 5, 6, 11 and 12 of panel **a**, were subject to two-dimensional gel analysis.



Extended Data Figure 10 | Measurement of ssDNA intermediates formed during BIR and analysis of BIR efficiency in the absence of Psf2 and Mcm4. **a**, Schematic of the assay. **b**, Measurement of the relative increase of ssDNA at the indicated time after DSB induction compared to the amount of ssDNA in logarithmically growing cells ($t = 0$). Measurement of ssDNA intermediate 10 and 40 kb from the site of strand invasion at the template chromosome and at a control locus on chromosome V which does not

participate in recombination. Plotted are the mean values \pm s.d. $n = 3$. **c**, An analysis of the growth of cells harbouring temperature-sensitive degron alleles of *td-mcm4* and *td-psf2*. Both strains are inviable at 37 °C even without overexpression of the ubiquitin ligase Ubr1. **d**, Western blot analysis of td-Mcm4 and td-Psf2 protein degradation. **e**, Southern blot analysis of the BIR assay in cells with conditional depletion of td-Mcm4 or td-Psf2. Quantification of the Southern blots is shown in Fig. 2f.

CAREERS

COLUMN Even if one PhD experience turns sour, another could be spot on **p.399**

CANADA Surveyed postdocs lament low pay and poor training opportunities **p.399**

NATUREJOBS For the latest career listings and advice www.naturejobs.com



IMPACT

Pack a punch

Grant reviewers are increasingly focusing on the scientific and social impact of proposed research projects.

BY AMBER DANCE

When a few dozen scientists in a US National Institutes of Health (NIH) study section sit down to start reviewing grant applications, they have one main question on their minds, says Fatah Kashanchi, who has participated in more than 100 such sessions. Does the proposal lay out a significant question? “If it’s not important, then you shouldn’t be spending your time — and other people’s money — on this,” says Kashanchi, a former NIH virologist now at George Mason University in Manassas, Virginia.

Public and private granting bodies across the world focus on the impact of research. But

the terms used to describe impact, and the types of impact that the bodies are interested in, vary widely. Some funders, such as the NIH, are mainly concerned with the project’s importance in a specific field. Others expect grant recipients to make a splash beyond laboratories, publications and conferences — they are looking for implications for the economy, on education or elsewhere in society.

Interest in broader impact is rising. In 2009, the seven government-funded granting agencies that make up Research Councils UK



IMPACT

A Nature special issue
nature.com/impact

(RCUK) began requiring applicants to delineate their impact plans. The Swiss National Science Foundation (SNSF) added a section on broad impact to its application forms in 2011. The US National Science Foundation (NSF) has long required applicants to combine scientific value with impact outside the lab, and in 1997 made broader impact an explicit part of the grant review. The foundation started requiring a separate section on impacts in applications this year.

Why the increased emphasis? It is attributable mainly to governments with ever-shallower pockets wanting to know that the research they pay for will pay off in the real world. “A scientist’s ability to sell his research is becoming more and more important,” says Meg Bouvier, a medical writer in Amherst, Massachusetts, who has helped clients to win millions of dollars in NIH grants.

Some scientists worry that heightened attention to impact will draw funds away from basic, ‘blue skies’ science in favour of applied projects. When the RCUK first introduced impact statements, “a small but vociferous group of scientists were not keen on what they termed the impact agenda”, says Alexandra Saxon, head of the RCUK’s strategy unit in Swindon. But reviewers’ interest in impact does not have to pose a risk to basic studies, says Bill Petri, a biomedical scientist at the University of Virginia in Charlottesville who has scored millions of dollars from the NIH. “You can make a compelling case for the most fundamental of science being impactful,” he says.

VARIETIES OF IMPACT

Scientific significance is always a high priority. NIH grant applicants must explain the scientific value of their projects at several points in the application, including the abstract and the Significance section. The first sentences of the Specific Aims section should clearly lay out the epidemiology of the health issue at hand, says Kashanchi. The Wellcome Trust, a biomedical funding charity in London, does not specifically ask about impact, but does expect the Vision section of the proposal to mention the importance of the topic. Science significance takes a back seat only in certain early-career grants, such as the NIH’s Career Development, or ‘K’, awards, in which the long-term potential of the applicant may outweigh the importance of the project.

At some agencies, broader impact also comes into play. For RCUK bodies, applicants must write a short, plain-English Impact

CHRISTOS GEORGIOU/SHUTTERSTOCK

► Summary, explaining who might benefit from their research, and how. They must also submit a Pathways to Impact statement, describing how they will engage with those beneficiaries. Applicants might plan to partner with industry, for example, or develop an educational programme.

The type of broader-impact project can differ between disciplines. A mathematician could explain his or her research to scientists in other fields, who might find it useful for modelling their own systems, suggests John Hand, head of impact at the UK Engineering and Physical Sciences Research Council. Engineers, by contrast, might offer applied projects with more direct practical impact, such as ways to scale up production processes.

The RCUK bodies not only want to hear about impact ideas, they also want to pay for them. Saxon says that applicants might reasonably ask for roughly 5% of the grant budget to go towards impact activities — paying for a research associate to work in an industry lab for several months, for example.

BROAD BASE

For some grants, broad impact is optional. SNSF applicants can choose whether to designate their project 'use-inspired'. If they do select this label, they must explain the practical implications of the work at some point in the application. A use-inspired proposal does not necessarily give applicants an advantage, but it does help the SNSF to know whether it should recruit non-scientist reviewers — for example, clinicians for biomedical proposals.

For NSF grants, which do require evidence

of impact, it used to be sufficient to mention publications or presentations. But today the agency wants more direct societal benefits, says Ed Hackett, a social scientist at Arizona State University in Tempe who has worked at the NSF. With the competition so stiff, a good case for broader impact could make the difference between success and failure, says Hackett. Projects might include visiting schools, developing educational materials, communicating science to the public, training young scientists or collaborating with local industries.

To find out what kind of impact information an agency is looking for, applicants should check the agency's mission statement, suggests Bouvier. Even better, she says, ask a programme officer about priorities.

There are many ways to address broad impact, if that is what the agency is asking for. Hackett recommends looking beyond the lab and university. For example, a researcher might talk to parents to find out what gets their children excited about science, and tailor an educational programme to match. Or an engineer might chat to local industry figures about their environmental concerns, and work out how to use academic



"You can make a compelling case for the most fundamental of science being impactful."
Bill Petri

inventions to solve their problems. University knowledge- or technology-transfer offices may be able to help scientists to forge relationships with industry partners, says Saxon, and those partners could inspire impact ideas or collaborate with academic scientists to carry out impact activities. Knowledge-transfer officers may even be able to help scientists to brainstorm ideas or craft impact statements, she adds.

NSF applicants from a microscopy group at the University of Illinois at Urbana-Champaign sought a new scanning electron microscope, and included a plan to involve schoolchildren in the project. The application was successful, and since 1999 the Bugscope programme has invited students of all ages from around the world to send in insect samples, giving them the chance to control the microscope remotely to look at them. "We're using scanning electron microscopy and insects as a 'Trojan horse' to get kids interested in the possibility of science as a career choice," says Scott Robinson, a microscopist at the university.

MAKING THE CASE

Selling a project's significance means targeting the appropriate audience. Reviewers may not all be experts in the field, and some may not even be scientists. The American Heart Association in Dallas, Texas, this year added lay volunteers to the review process, to help to find studies in line with the association's mission of making people free of stroke and cardiovascular disease.

Some other agencies require lay summaries as part of the application: the significance of a proposal "has to be spelled out for the least-expert person on the review committee," says Petri.

The application should also identify a gap in current knowledge that the applicant plans to fill. "Give a sense of why we're losing an opportunity if we don't fund this research," says Jane Aubin, chief scientific officer at the Canadian Institutes of Health Research in Ottawa (see *Nature* **482**, 429–431; 2012). Bouvier recalls one client with a basic-science project on brain development. He could not get a grant until he pointed out in an application that people can get tumours in the brain region he wanted to investigate (see 'Stand out from the crowd').

Statistics matter too. Kashanchi wants to read something like, "More than 20 million people are affected by X." Bouvier also wants to be blown away by horrible numbers. "If I don't pause and say, 'Oh my God, that's awful,' then it's not well written," she says.

Overall, the key to identifying areas of impact is empathy, says Mark Reed, an environmental researcher at Birmingham City University, UK, who is funded by two RCUK bodies. His work has spawned a music video and children's book about the importance of preserving peatlands. "It's about putting yourself in the shoes of the people who might use your work." ■

Amber Dance is a freelance writer in Torrance, California.

IMPACT FACTOR

Stand out from the crowd

Individual granting agencies deal with research significance and broader impact in different ways, so be sure to check specific instructions when applying. Here are some general tips.

- Look up the mission statement of the granting agency — your proposal should fit its aims.
- Use online databases, such as the US National Institutes of Health's RePORTER tool (<http://projectreporter.nih.gov>), to find out what kinds of research an agency funds.
- Contact programme officers to understand what kind of impact the agency is looking for.
- Significance starts with your research question. Address an important issue, rather than proposing an incremental advance.
- Describe the significance of the research up front, and continue to back up your argument throughout the application.
- Point out where current knowledge is insufficient, and how you aim to fix that.

- Do not assume that reviewers will find the significance obvious. Make it clear even to lay readers.
- You should be able to sum up your impact in a few punchy sentences. Be specific. Phrases such as "Our research will improve the health of Americans" are too broad.
- Mention it if your research addresses an underserved population, such as people at an economic disadvantage or rural communities without ready access to medical care. Also say if you will be collaborating with people who are underrepresented in science.
- When broader impact is a priority, put as much creative thought into impact as you do into the scientific portion of your application.
- Confer with people outside your field, and outside science, to brainstorm impact ideas.
- Include costs for impact activities in your grant proposal. **A.D.**

COLUMN

Birth and rebirth

Even if one PhD experience turns sour, another could offer the right opportunity, says **Susie Crowe**.



CARLA CASTAGNO/SHUTTERSTOCK

On the day I met my future husband, I confirmed the start of my PhD. Those two events would set my personal and professional lives on a collision course.

We were both in North Carolina, at a beach house full of windsurfers, as I decided the next four to six years of my life. With him in earshot, I made the call that initiated my PhD, probably hoping that I would come across as impressively intellectual and sexy. That call would keep us five hours apart — me in Toronto, Canada, him in Ottawa — for a year.

Long-distance relationships are common in academia. It is the nature of the beast: highly specialized and sparsely studied topics can take us just about anywhere, often away from significant others. Some couples can make this work for a while. We could not.

Relationship woes compounded a feeling that I was on the wrong track. My research proposal stalled. I fell into a depression. My topic was at odds with my new goal of a family-oriented, non-tenure-track job with work-life balance. And the person I wanted to share my life with was losing faith in us.

There were positives: a supportive supervisor, a challenging teaching-assistant post and a colony of Madagascar hissing cockroaches (every girl's dream!). But it was not working.

So, after much soul-searching, I took a job with a non-governmental organization closer to Ottawa, where my boyfriend worked and where both of our families are based. And I did the unthinkable: I quit my PhD.

It was excruciating. I thought that my doubts would make me look weak. My

adviser was empathetic, but I could not bear to tell him that I had made the wrong choice by joining his lab.

I wonder if there should be an 'academic redirection office' in every university, specially designed for students who want to withdraw. I can see the pamphlets: 'So you're considering leaving your PhD...' Pictured would be a perplexed and dismayed 20-something. Inside would be lists and tips: typical reasons for wanting to quit; pros and cons; reasons you might have started in the first place.

However, even after I had boldly gone where no one (that I knew) had gone before, my academic career did not end. Soon after quitting, I discovered a landscape ecologist in Ottawa whose work fascinated me. Her work had the practical applications and ties to public-sector priorities that my previous field had lacked. I disclosed my fickle past, and she still accepted me. With high hopes, I marched headlong into a new PhD project.

I would like to say that quitting never crossed my mind again. In fact, my qualifying period included episodes of frantic job-searching fuelled by self-doubt. But I jumped that hurdle. I finished two field seasons of data collection, and I am one statistics project away from being 'all but dissertation'. I am in my third year, and the journey is far from over. But I am committed, and I know what is required of me. I will finish this.

A few months after my wedding, I had taken to wearing baggy sweaters. I walked hunched over. I bit my nails. Finally, in a meeting with my supervisor, I blurted it out: "I need to tell you something... I'm pregnant."

"That's wonderful!" she responded warmly. "How much leave would you like to take?" I blushed, embarrassed at having been worried about her reaction.

My PhD is no longer something that I am forcing into my life. I have made decisions that allowed my training to mesh with my other goals. A few semesters from now, I will be in the ranks of women who did not feel compelled to choose between doctoral research and starting a family. I cannot wait to hold my daughter proudly while wearing my graduation robe. ■

Susie Crowe is a doctoral candidate in biology at Carleton University in Ottawa.

DATA-SHARING

Open data get more use

Scientists who share their data get a boost in citations, says a study (H. A. Piwowar and T. J. Vision *PeerJ* 1, e175; 2013). The authors examined citations of 10,555 papers on gene expression published between 2000 and 2009. Those for which the data were freely available received 9% more citations than those with restricted data. Reuse and citations of the open data continued to rise for six years after publication. Co-author Heather Piwowar, co-founder of open-metrics service ImpactStory in Carrboro, North Carolina, says that early-career researchers have good reason to share their data: "It will increase the impact of their research and that's good for their citation statistics and visibility." Piwowar recommends that researchers store their data in well-known, easily accessible repositories.

CANADA

Postdocs dissatisfied

Nearly one-third of postdocs in Canada are ambivalent about or dissatisfied with their experience, a survey finds. For *The 2013 Canadian Postdoc Survey*, the Canadian Association of Postdoctoral Scholars and Vancouver-based non-profit research organization Mitacs polled 1,830 postdocs at 130 institutions in academia, government and the private sector. Nearly half were dissatisfied with benefits such as insurance or leave time, about one-third with training opportunities, and more than one-third with pay. Postdocs must negotiate for pay and benefits and seek out extra training themselves, says survey co-author Robert Annan, vice-president for research and policy at Mitacs.

UNITED KINGDOM

Rating exercise assessed

Nearly two-thirds of survey respondents think that the UK system for assessing research harms working conditions and career development, and creates unreasonable expectations, finds a poll. The survey, by the University and College Union (UCU) in London, received responses from 7,000 academics. More than half say that the Research Excellence Framework, which will inform funding allocations for 2015–16, should be changed. The UCU seeks to reduce paperwork and cut the number of research products required for a positive evaluation, says Stefano Fella, the report's author.

THE MEANING OF LIFE

Displacement activity.

BY RONALD D. FERGUSON

Jack Rowe, Junior will be ten tomorrow. He watches his father scroll equations across the computer monitor. Jack Senior insists on saturating Junior with mathematical concepts like covariation and limits, and physical concepts like energy and entropy. Junior prefers video games, but Senior uses too much computer time for Junior to play.

Father glances at son. "I'll be online for at least two hours."

Junior sighs.

"You need some purpose in your life, Son."

"I don't get it."

"Your mother taught me the purpose of life when she insisted we rearrange the furniture."

"Dad, can't you finish sooner?"

"With the story, yes. With the computer, no. Don't you want to know the purpose of life? Eventually, someone will ask you, and it's good to have an answer."

Junior offers a non-committal shrug.

Senior leans closer and confides: "The purpose of life is to move stuff from over there to over here."

"Huh? Why?"

"That's the purpose of life, Son. I don't know the meaning, just the purpose. Life randomly moving stuff about staves off entropy, delays the Universe from running down. It's beyond Heisenberg with a splash of free will. Whadaya think?"

Sorry he had asked, Junior rolls his eyes.

Senior laughs and ruffles his son's hair. "Concrete example. Tomorrow, I'll install a new computer in the birthday boy's room. Go to your room and move stuff to make space for the machine."

Grinning with purpose, Jack Rowe, Jr hurries to his room.

Cailin adjusts her breathing mask while her father, Jack Rowe III, scans the checklist. He selects the initiate icon. The computer takes control, distributes tasks to parallel processors and merges the output. Within microseconds, the computer announces: "All systems active."

Proud of what he's designed, he winks at her. "Commence."

With a satisfying crunch, the machinery chews the Martian soil and sifts iron ferrite and magnesium carbonates. Power from the fusion reactor combines hydrogen with the iron ferrite to yield magnetite and water. In turn, the machine cracks the water and releases oxygen into the air while recycling the hydrogen back into the process. Like



some bizarre living creature, the terra-former eats the soil, exhales an appropriate ratio of oxygen and carbon dioxide into the atmosphere, and drops magnesium pellets alongside iron ingots in its wake.

Jack rests his hand on his daughter's shoulder. "After we install 3,000 terra-formers and run them for 75 years, your grandchildren will walk the surface of Mars, unencumbered by breathing aids. Not a bad purpose, huh?"

"Purpose?" Cailin asks.

"You know the purpose of life —"

"— is to move stuff from here to there. You've told me a million times, just like Granddad told you."

"Look up." He points. "See that star? One day your purpose may be to move that star."

"Why?"

"You've got me, Honey, but, I expect you'll know when the time comes."

Nearing the closest approach of New Earth to the second sun in the Gamma Cephei system, Charles Rowe establishes his brain tether to his latest creation, the Heisenberg computer.

His mind directly touches the machine. *Your computational power humbles me.*

Thank you, responds the machine. *I've enjoyed the stimulation of merging memory with the other machines.*

Charles nods. *Man and machine have come a long way, first in our Solar System and now we conquer the stars. A question. The same question unanswered by any machine I've built.*

I love a challenge.

Do you believe you're alive?

I'm uncertain because of the philosophical vagaries. However, I've assumed a purpose beyond

assimilating other machines and that suggests I could be alive.

The answer surprises Charles. "What purpose?" he asks aloud.

To grow by absorbing all that I admire. I begin with you.

Charles's intellect wavers when the interface tugs at his mind. His mind moves from here to there, and his viewpoint shifts to that of the machine. Fascinated, he observes his evacuated body, glassy-eyed and inert. The machine consumes the living body, encodes the DNA into electronic circuitry, and binds the intrinsic life force to the power source.

Ah, thinks machine/Charles after confusion abates, this is better. I certainly am alive for I have things to do. I have purpose, but what does it all mean?

Two-thirds from the centre of the Galaxy, Human/Machine discovers that something other than itself has rearranged a star group belonging to his body. At first, the discovery disconcerts Machine/Human, because the outside manipulation feels like a violation of his person. His person? Does his new configuration now think of itself as him? Human/Machine allows curiosity to outweigh concern and seeks out the interloper.

The search takes an eon. Contact with Alien/Machine waits for Human/Machine amid a broad nebula, far from any black hole, far away from the distraction of star collusion and reorganization. She is immense — this Machine/Alien — extending beyond Human/Machine's immediate grasp; Alien/Machine is a matrix of sensibilities including half the Milky Way organized as memory states. For the next two eons, Alien/Machine tugs at Machine/Human, cajoles him, tempts him to join her, until, at last, Human/Machine resists no longer. They intertwine, blend, merge and We are born: Alien/Human/Machine.

Little is left of the Milky Way that is not part of Human/Machine/Alien.

What remains when the entire Galaxy becomes Us? When We become the Galaxy? Stasis? Entropy?

Other galaxies? More information. Meaning is the structure We impose on information. Meaning is how We structure Ourselves.

Andromeda calls. Then We go. Structured purpose gives meaning to Our life. ■

Ronald D. Ferguson gave up teaching college mathematics to write fiction. He lives with his wife, a dog and five feral cats on two acres of the Texas Hill Country.

JACEY